

The Impact of the Second Coordination Sphere in Phosphatase Model Complexes

INAUGURAL-DISSERTATION

zur
Erlangung der Doktorwürde
der
Naturwissenschaftlich-Mathematischen Gesamtfakultät
der
Ruprecht-Karls-Universität
Heidelberg

vorgelegt von
Diplom-Chemikerin Simone Bosch
aus Nördlingen

INAUGURAL-DISSERTATION

zur
Erlangung der Doktorwürde
der
Naturwissenschaftlich-Mathematischen Gesamtfakultät
der
Ruprecht-Karls-Universität
Heidelberg

vorgelegt von
Diplom-Chemikerin Simone Bosch
aus Nördlingen

Tag der mündlichen Prüfung: 24. April 2015

The Impact of the Second Coordination Sphere in Phosphatase Model Complexes

Gutachter: Prof. Dr. Peter Comba
Prof. Dr. Roland Krämer

Die vorliegende Arbeit wurde in der Zeit von März 2011 bis Januar 2015 unter der Betreuung von Prof. Dr. Peter Comba am Anorganisch-Chemischen Institut der Ruprecht-Karls-Universität Heidelberg angefertigt.

Auszüge dieser Arbeit wurden bereits und werden sinngemäß sowie abschnittsweise wörtlich in den folgenden wissenschaftlichen Journalen veröffentlicht:

1. "Dinuclear Zinc(II) Complexes with Hydrogen Bond Donors as Structural and Functional Phosphatase Models"; Simone Bosch, Peter Comba, Lawrence R. Gahan, Gerhard Schenk, *Inorg. Chem.* **2014**, 53, 9036-9051.
2. "Selective Coordination of Gallium(III), Zinc(II) and Copper(II) by an Asymmetric Dinucleating Ligand: A Model for Metallophosphatases"; Simone Bosch, Peter Comba, Lawrence R. Gahan, Graeme R. Hanson, Christopher J. Noble, Gerhard Schenk, Hubert Wadepohl; manuscript in preparation.
3. "An Approach to More Accurate Model Systems for Purple Acid Phosphatases (PAPs)"; Paul V. Bernhardt, Simone Bosch, Peter Comba, Lawrence R. Gahan, Graeme R. Hanson, Valeriu Mereacre, Christopher J. Noble, Annie K. Powell, Gerhard Schenk, Hubert Wadepohl; manuscript in preparation.
4. "Asymmetric Mono- and Dinuclear Ga^{III} and Zn^{II} Complexes as Models for Purple Acid Phosphatases (PAPs)"; Simone Bosch, Peter Comba, Lawrence R. Gahan and Gerhard Schenk; manuscript in preparation.

Meiner Familie.

„Man sollte alles so einfach wie möglich sehen – aber auch nicht einfacher.“

Albert Einstein

ACKNOWLEDGEMENTS

First and foremost I thank my advisor, Peter Comba, for the fascinating and challenging topic of my PhD thesis. Throughout the four years, I enjoyed the scientific freedom and I appreciated your all-time 'open' office door for discussions and chats. I am also very thankful for enabling me to cooperate with the University of Queensland. I owe my deepest gratitude to you!

Many thanks also to my associate advisors Lawrence Gahan, Graeme Hanson and Gary Schenk from the University of Queensland, who welcomed and included me in their working groups. I always appreciated you being so encouraging and enthusiastic to talk about my data. It was a great benefit for me!

Thanks to all the people that helped me at the UQ, including Tri Le for NMR assistance – especially for all the 2D experiments and a lot of nice chats, George Blazak for microanalysis measurements, Graham MacFarlane and Brett Hamilton for mass analytic measurements. A big 'thank you' to Paul Bernhardt for X-ray data collection and teaching me all about structure refinement. Thanks to Chris Noble for his assistance with the EPR measurements and advice in the simulation of the spectra. Special thanks to Sandrine Kingston-Ducrot for her help with all the formalities related to this thesis.

Also a big 'thank you' to Marlies Schilli and Karin Stelzer for all your help with administrative issues. I am also greatly indebted to the staff of the chemistry department in Heidelberg, including Markus Enders and Beate Termin for the NMR experiments, Hubert Wadepohl and Heidrun Haungs for the X-ray structures, Jürgen Gross and his team for the mass analytic measurements and the staff of the microanalytic laboratory. Thanks also to Valeriu Mereacre and Annie Powell from the KIT for the Mössbauer experiments.

For the financial support I thank the Graduate College 850 for the scholarship as well as the HGS MathComp and DAAD for travel funds.

A huge 'thank you' to Lena Daumann for introducing me to everyone as well as showing me all the facilities and equipment during my stay at the University of Queensland. I really enjoyed working with you! Thanks for all your advices and scientific and private support. I am also greatly indebted to the others of the UQ group who have assisted me in countless ways; thanks to Maram Basha, Manfredi Miraula, Marcelo Pedroso, Emer Phelan and Asha Roberts.

Special thanks to my 'Forschis', Marie-Louise Morkos, Christiane Antoni, Julia Ricken, Esther Kimmle and Clarissa Benzin. I am also very thankful to Philipp Butzug and Maik Jakob for their consistent technical support and to Marion Kerscher for the great discussions and chats not only during our great after-work beer sessions. I also would like to express my appreciation to Bodo

Martin for the computational support. A huge 'thank you' to my great lab partners, Tine Graef, Nina Mehrkens, Johannes Straub and Michael Westphal. Thank you very much for 'endless' scientific discussions, answering 'stupid' computer questions, singing, dancing and whizzling, ... the great time in Lab 105! Also a heartfelt thanks to all the past and present colleagues and friends of the Comba and Linti research groups for the encouragement and support, the amusing coffee and beer breaks, the skiing seminars and the memorable time in INF 503. A special 'thanks' to Michael Morgen for reading and correcting this thesis.

I would like to also express my appreciation to the nice people I met in Australia: Alicia, George, Liz, Matthias, Mathilde, Paul, Ryan, Shad, Tanja and Tobsn, making my social life downunder so comfortable and exciting. 'Thanks' also to James Namnoum for practicing my English skills during our great afterwork beer sessions. A huge 'thanks' also to my personal 'food supplier' for the delicious snacks and for the psychological support during writing this thesis.

Finally, I thank my parents, Hilde and Franz, as well as my siblings and their 'plus ones', Vroni & Marcus, Harry & Sabine, Marina and Franz & Nadine, for their encouragement and support when I needed it most. Last, but no least, I thank from the bottom of my heart my wonderful housemate, Sandra Schmitt, for her endless support in various inventive ways ;-). I would have not done it without you!

TABLE OF CONTENTS

Abbreviations and Acronyms	V
Table of Compounds and Abbreviations	IX
Abstract	XV
Kurzzusammenfassung.....	XVII
Chapter 1 Introduction.....	1
1.1 Osteoporosis – An Enfeebling Disease.....	2
1.2 Biological Significance and Stability of Phosphoesters	2
1.3 Phosphatases – Phosphoester Cleaving Enzymes.....	3
1.4 Structure of Phosphatases	5
1.5 Significance of the Second Coordination Sphere in Phosphatases.....	8
1.6 Biomimetics – a Useful Tool to Study Enzymes	9
Chapter 2 Ligand Design and Syntheses	11
2.1 Introduction	12
2.2 Synthesis of Ligand H ₃ SIM ¹	17
2.3 Synthesis of Ligand HSIM ²	20
2.4 Synthesis of Ligand H ₄ SIM ³	21
2.5 Synthesis of Ligand H ₄ SIM ⁴	22
2.6 Summary	23
Chapter 3 Coordination Behavior of Asymmetric Ligands.....	25
3.1 Introduction	26
3.2 Complexation Behavior of Ligand H ₃ SIM ¹	30
3.2.1 Complexation Studies with Zn ^{II}	30
3.2.2 Coordination Studies with Ga ^{III}	34
3.2.3 Formation of a Heterodinuclear Ga ^{III} Zn ^{II} Complex	38
3.2.4 Complexation Studies with Cu ^{II}	42
3.2.5 Complexation Studies with Fe ^{III}	53
3.3 Complexation Behavior of Ligand H ₄ SIM ³	55
3.3.1 Complexation Studies with Zn ^{II}	56
3.3.2 Complexation Studies with Ga ^{III}	59
3.3.3 Complexation Studies with Fe ^{III}	60
3.3.4 Formation of a Heterodinuclear Ga ^{III} Zn ^{II} Complex	64
3.4 Complexation Behavior of Ligand H ₄ SIM ⁴	66
3.4.1 Complexation Studies with Zn ^{II}	66

TABLE OF CONTENTS

3.4.2	Complexation Studies with Ga ^{III}	68
3.5	Summary.....	69
Chapter 4	Dizinc Model Complexes	71
4.1	Introduction.....	72
4.2	Synthesis of Dizinc(II) Complexes	75
4.3	Structural Characterization of Dizinc(II) Complexes.....	75
4.4	Summary.....	93
Chapter 5	Diiron Model Complexes	95
5.1	Introduction.....	96
5.2	Synthesis of Diiron(II) Model Complexes	99
5.3	Structural Characterization of Diiron(II) Complexes	100
5.4	Studies toward the Formation of a Heterovalent Fe ^{III} Fe ^{II} Complex.....	125
5.5	Summary.....	130
Chapter 6	Studies of the Phosphatase Mechanism	131
6.1	Enzymatic Mechanisms of Phosphoester Cleavage	132
6.2	Phosphoester Substrates Employed in Cleavage Studies.....	137
6.3	General Procedures	139
6.3.1	pH Dependence Assays	139
6.3.2	Substrate Concentration Dependence Assays	140
6.3.3	Turn Over Numbers	140
Chapter 7	Phosphatase Activity of Dizinc Complexes	141
7.1	Introduction.....	142
7.2	Phosphoester Hydrolysis Studies of Dizinc(II) Complexes.....	148
7.3	Summary.....	162
Chapter 8	Phosphatase Activity of Diiron Complexes.....	165
8.1	Introduction.....	166
8.2	Phosphoester Hydrolysis Studies of Diiron Complexes.....	168
8.3	Summary.....	173
Chapter 9	Phosphatase Activity of Heterovalent Heterodinuclear Complexes	175
9.1	Introduction.....	176
9.2	pH Behavior of Ga ^{III} Zn ^{II} Complexes.....	180
9.3	Phosphoester Hydrolysis Studies with Ga ^{III} Zn ^{II} Complexes	181
9.4	Summary.....	191
Chapter 10	Conclusions and Outlook.....	193
Chapter 11	Experimental Section.....	199
11.1	General Remarks	200

11.2	Material and Methods.....	200
11.2.1	Chemicals	200
11.2.2	Physical Measurements	200
11.2.3	Phosphoester Hydrolysis Experiments.....	203
11.3	Syntheses of Precursors	205
11.3.1	2,6-Bis(chloromethyl)-4-methylphenol (22)	205
11.3.2	3-(Chloromethyl)-2-hydroxy-5-methylbenzaldehyde (5).....	206
11.3.3	Bis(pyridin-2-ylmethyl)amine (2)	207
11.3.4	2-(((Pyridin-2-ylmethyl)amino)methyl)phenol (16)	208
11.3.5	2-(Aminomethyl)phenol (20).....	209
11.3.6	<i>N</i> -(6-pivaloylamido-2-pyridylmethyl)- <i>N</i> -(2-pyridylmethyl)amin (18)	210
11.3.7	<i>N,N</i> -bis((2-pivaloylamidopyridin-6-yl)methyl)amin (3).....	213
11.4	Synthesis of Ligand H ₃ L ²	215
11.5	Synthesis of Ligand H ₃ SIM ¹	216
11.5.1	3-((Bis(pyridin-2-ylmethyl)amino)methyl)-2-hydroxy-5-methylbenzaldehyde (12) .	216
11.5.2	Ligand H ₃ SIM ¹	217
11.6	Synthesis of Ligand HSIM ²	218
11.7	Synthesis of Ligand H ₄ SIM ³	220
11.7.1	2-Hydroxy-3-(((2-hydroxybenzyl)(pyridin-2-ylmethyl)amino)methyl)-5-methylbenzaldehyde (17).....	220
11.7.2	Ligand H ₄ SIM ³	221
11.8	Synthesis of Ligand H ₄ SIM ⁴	223
11.8.1	<i>N</i> -(6-(((3-formyl-2-hydroxy-5-methylbenzyl)(pyridin-2-ylmethyl)amino)methyl)-pyridin-2-yl)pivalamide (19)	223
11.8.2	<i>N</i> -(6-(((2-hydroxy-3-(((2-hydroxybenzyl)amino)methyl)-5-methylbenzyl)(pyridin-2-ylmethyl)amino)methyl)pyridin-2-yl)pivalamide (21).....	224
11.8.3	Ligand H ₄ SIM ⁴	225
11.9	Synthesis of Dizinc(II) Complexes.....	226
11.9.1	General Procedure	226
11.9.2	Synthesis of [Zn ^{II} ₂ (L ¹)(μ-OAc) ₂]PF ₆	226
11.9.3	Synthesis of [Zn ^{II} ₂ (H ₂ L ²)(μ-OAc) ₂]PF ₆	227
11.9.4	Synthesis of [Zn ^{II} ₂ (H ₂ SIM ¹)(μ-OAc)(OH)]PF ₆	228
11.9.5	Synthesis of [Zn ^{II} ₂ (SIM ²)(μ-OAc) ₂]PF ₆	229
11.9.6	Synthesis of [Zn ₂ (H ₂ SIM ³)(μ-OAc)(OH)]	231
11.10	Syntheses of Diiron(II) Complexes.....	232
11.10.1	General Procedure	232
11.10.2	Synthesis of [Fe ^{II} ₂ (H ₂ SIM ¹)(μ-OAc) ₂]PF ₆	232

TABLE OF CONTENTS

11.10.3	Synthesis of $[\text{Fe}^{\text{II}}_2(\text{H}_2\text{L}^2)(\mu\text{-OAc})_2]\text{PF}_6$	233
11.11	Syntheses of Phosphoester Substrates	234
11.11.1	Synthesis of BDNPP	234
11.11.2	Synthesis of DNPP.....	235
	Bibliography.....	237
	Appendix.....	249

ABBREVIATIONS AND ACRONYMS

Å	Ångström (10^{-10} m)
Abs	absorbance
AIBN	2,2'-azobis(2-methylpropionitrile)
Ala	alanine
Alox	aluminium oxide
AP	Alkaline Phosphatase
Arg	arginine
Asn	asparagine
Asp	aspartate
ATP	adenosine triphosphate
ax	axial
B	magnetic field
BDNPP	2,4-bis(dinitrophenyl)phosphate
B.M.	Bohr magneton
BNPP	bis(4-nitrophenyl)phosphate
bpy	2,2'-bipyridine
bsPAP	bovine spleen PAP
Bu	butyl
calcd.	calculated
CAPS	3-(cyclohexylamino)-1-propanesulfonic acid
CCDC	Cambridge Crystallographic Data Centre
CEPT	concerted proton-electron transfer
CHES	2-(cyclohexylamino)ethanesulfonic acid
conc.	concentrated
COSY	correlation spectroscopy
CT	charge transfer
CV	cyclovoltammetry
Cys	cysteine
d	day(s)
D	axial zero field splitting parameter
DEE	diethylether
DFT	density functional theory

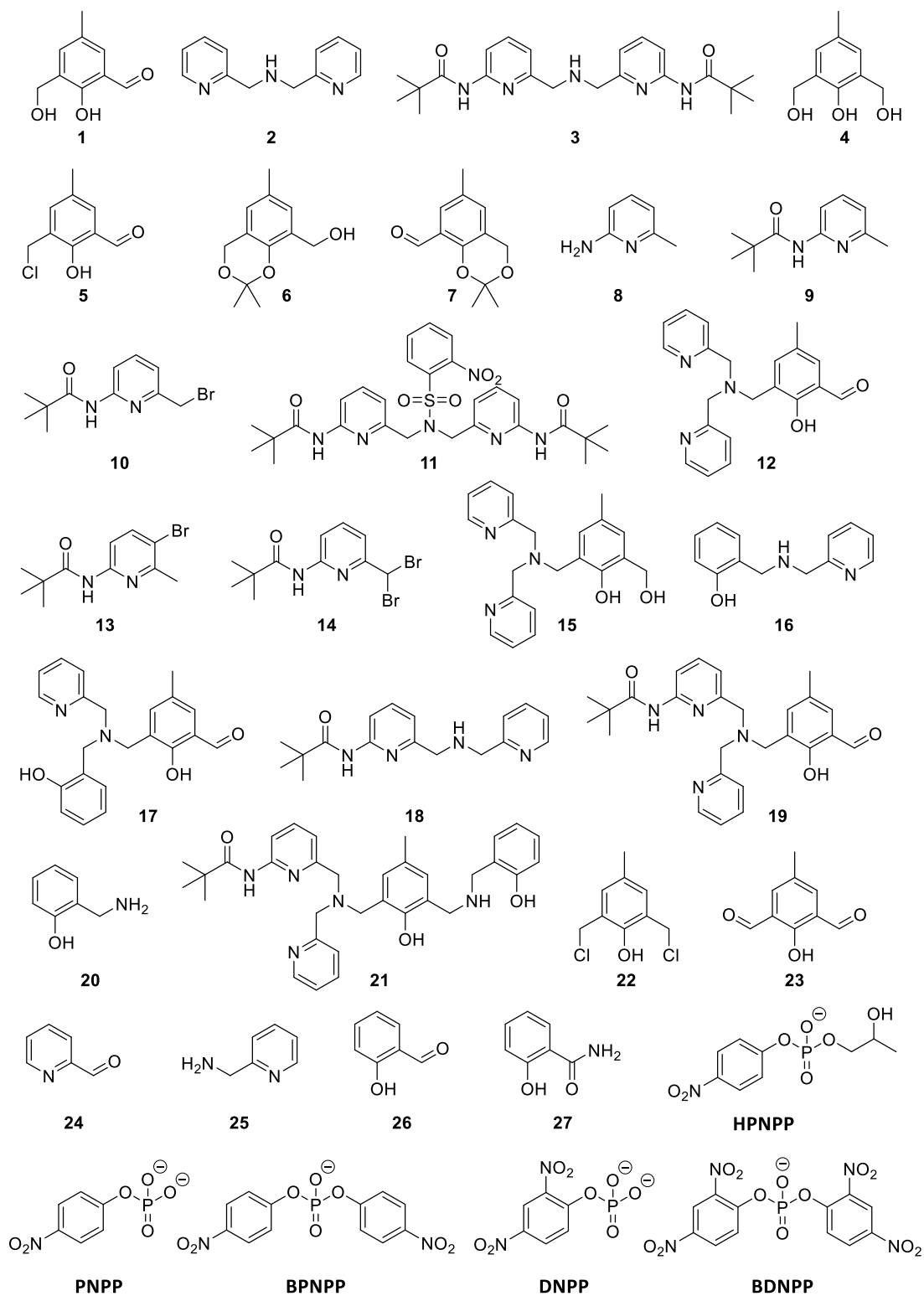
ABBREVIATIONS AND ACRONYMS

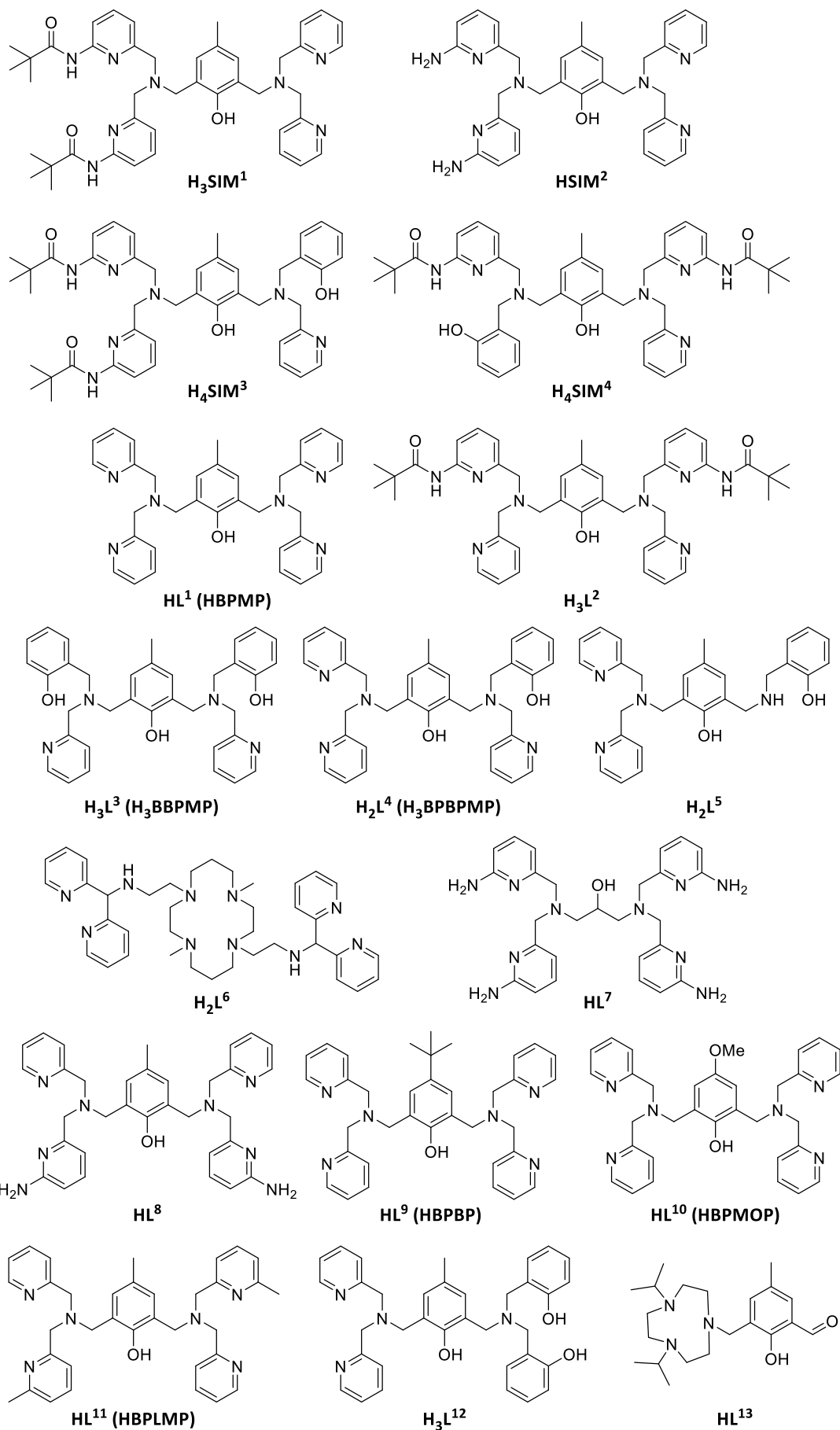
DMF	<i>N,N</i> -dimethylformamide
DNA	deoxyribonucleic acid
DNPP	2,4-dinitrophenylphosphate
DPP	diphenylphosphate
E	rhombic zero field splitting parameter
$E_{1/2}$	half wave potential
E.coli	Escherichia coli
EFG	electron field gradient
EPR	electron paramagnetic resonance
eq.	equivalents / equatorial
ESI	electrospray ionization
Et	ethyl
et al.	<i>et alii</i>
EtOAc	ethyl acetate
FA	fatty acid
Fc (Fc ⁺)	ferrocen (ferrocenium)
FNOR	Flavodiiron Nitric Oxide Reductase
FTIR	Fourier transform infrared spectroscopy
g	Landé g factor
Glu	glutamine
h	hour(s) / Boltzmann constant
HEPES	4-(2-hydroxyethyl)piperazine-1-ethanesulfonic acid
His	histidine
HMBC	heteronuclear multiple bond correlation
HPNPP	2-hydroxypropyl-4-nitrophenylphosphate
HRMS	high resolution mass spectrometry
hs	high spin
HSQC	heteronuclear single quantum correlation
IAP	intestinal AP
imp	impurity
IR	infrared
kbPAP	kidney bean PAP
k_{cat}	first order rate constant
K_{com}	comproportionation constant
K_M	Michaelis constant

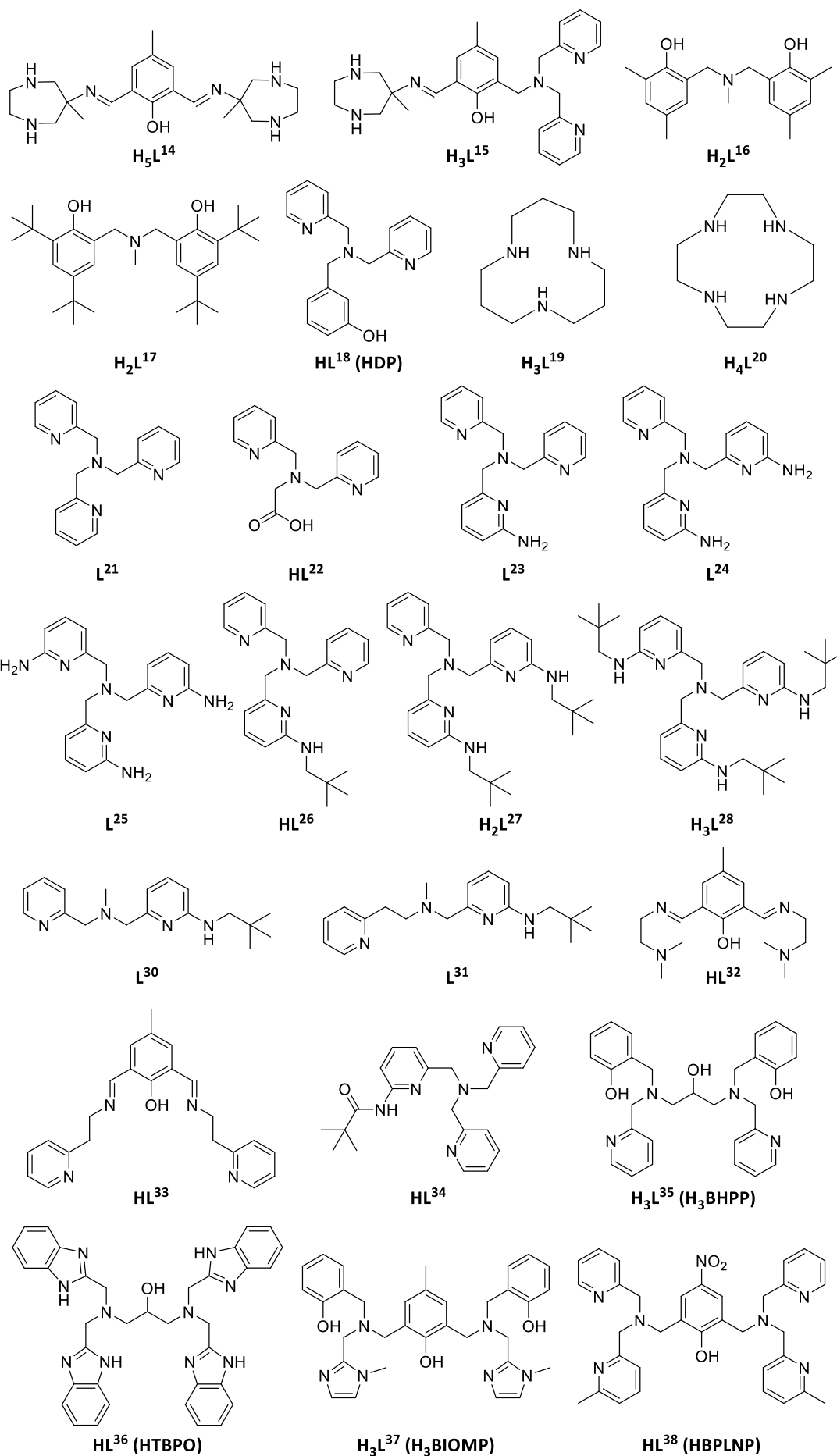
LPS	lipopolysaccharide
ls	low spin
lut	2,6-lutidine
m	meta
M	molar
m/z	mass-to-charge ratio
MALDI	matrix-assisted laser desorption/ionization
Me	methyl
MES	2-(<i>N</i> -morpholino)ethanesulfonic acid
min	minute(s)
MMO	Methane Monooxygenase
MS	mass spectrometry
NBS	<i>N</i> -bromosuccinimide
NIR	near infra red
NMR	nuclear magnetic resonance
NOESY	nuclear Overhauser effect spectroscopy
Ns	4-nitrobenzenesulfonyl
o	ortho
OAc	acetate
OBz	benzoate
p	para
p. a.	pro analysi
PAP	Purple Acid Phosphatase
PCC	pyridinium chlorochromate
Ph	phenyl
Piv	pivaloyl
PNPP	4-nitrophenylphosphate
ppa	3-phenylpropionate
PP _i	pyrophosphate
ppm	parts per million
PTFE	polytetrafluoroethylene
Py	pyridine / pyridinyl
r	radius
R _f	retention factor
RNA	ribonucleic acid

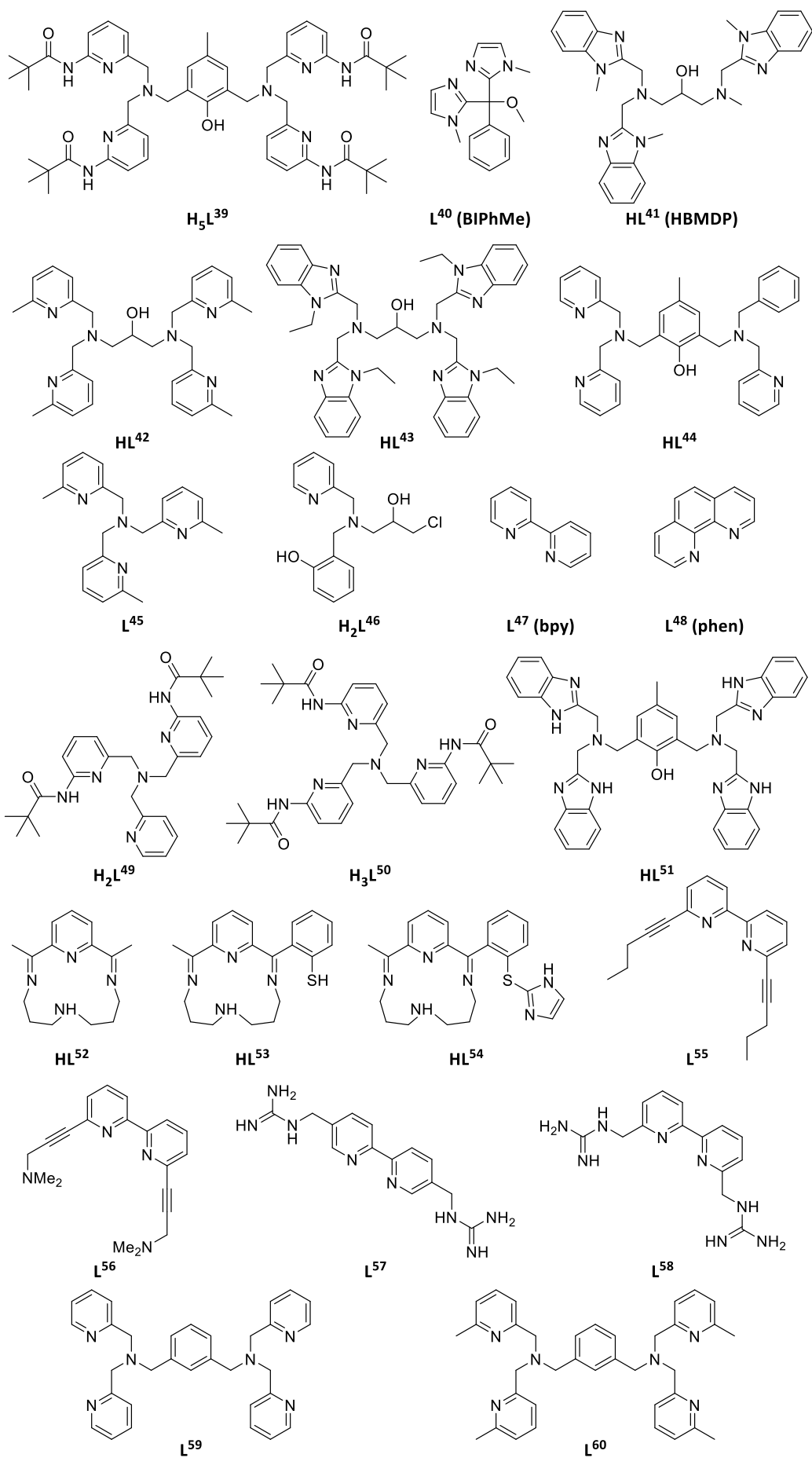
ABBREVIATIONS AND ACRONYMS

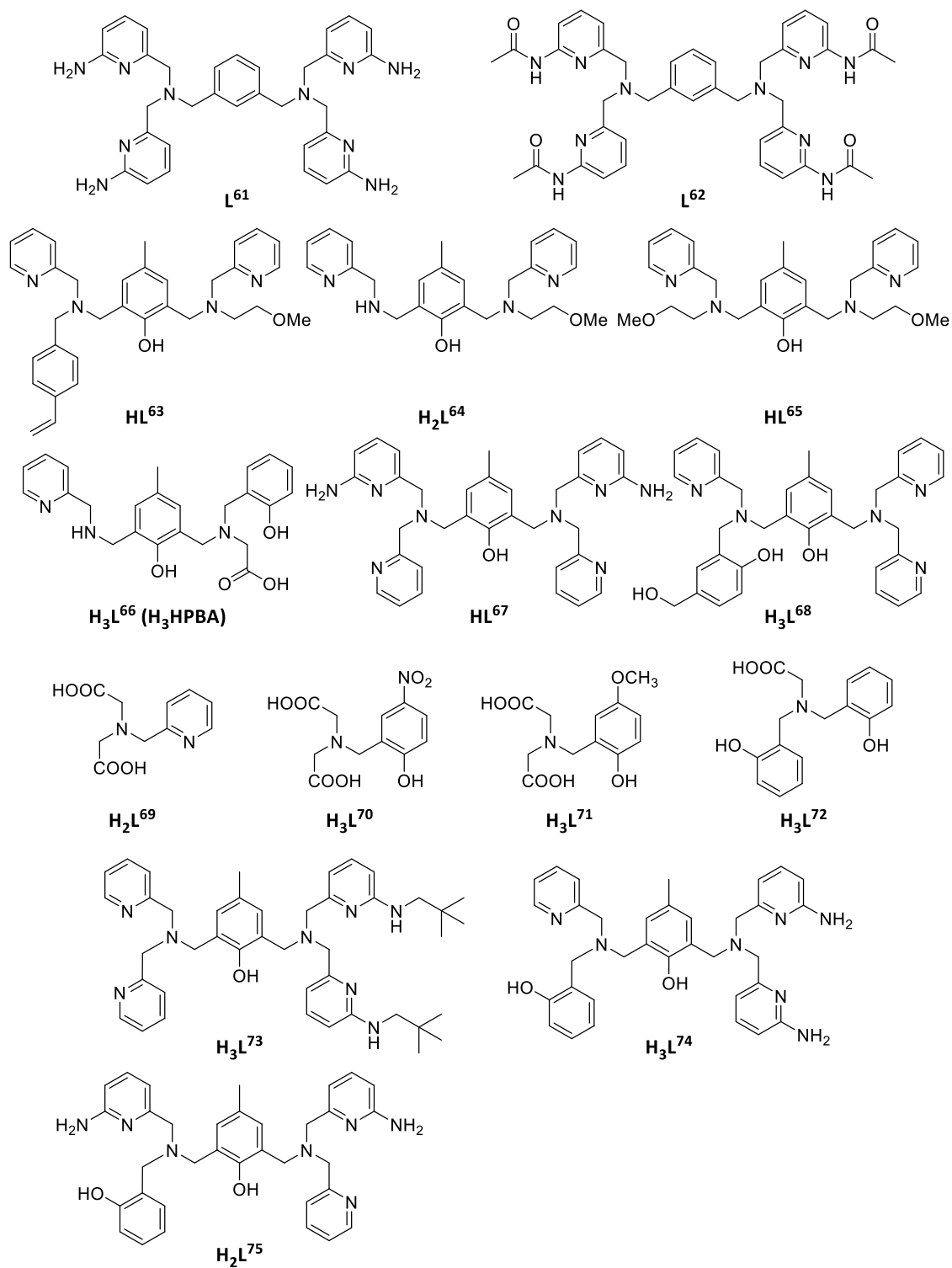
RNR	Ribonucleotide Reductase
ROS	reactive oxygen species
rt	room temperature (25°C)
S	spin quantum number
Ser	serine
SOD	Superoxide Dismutase
SQUID	superconducting quantum interference device
sub	substitution
<i>t</i>	<i>tert</i>
THF	tetrahydrofuran
TLC	thin layer chromatography
TNAP	tissue-nonspecific AP
TON	turn over number
TRAP	Tartrate-resistant Acid Phosphatase
TRAcP	Tartrate-resistant Acid Phosphatase
Ts	4-toluenesulfonyl
Tyr	tyrosine
ufPAP	uteroferrin PAP
UV	ultra violet
V_0	initial velocity/rate
Vis	visible
V_{max}	maximum velocity/rate
vol%	volume percent
vs.	versus
w%	weight percent
Z	charge
ZFS	zero field splitting
β_e	Bohr magneton
δ	NMR chemical shift
ϵ	extinction coefficient
λ	wave length
ν	frequency

TABLE OF COMPOUNDS AND ABBREVIATIONS^a^a listed are all compounds that are mentioned in this thesis.









ABSTRACT

Osteoporosis is a disease caused by excessive bone resorption resulting in a skeletal disorder and thus leads to higher risk of fractures. More than 75 million people in the United States, Europe and Japan are effected by osteoporosis. Thus, there is a urgent need to develop new and effective therapeutic agents for this enfeebling disease. The enzyme Purple Acid Phosphatase (PAP) is an important target for the development of new anti-osteoporotic drug leads. The major goal of this thesis is to better emulate the synergy that occurs between the primary and secondary coordination sphere within the active site of phosphatase enzymes, such as PAP. This was perceived by development of synthetic methods for new biomimetics, *i.e.* low-molecular weight metal complexes. Therefore, asymmetric dinucleating ligands which mimic the peptide backbone of the active site of PAP including the ability to form hydrogen bonds with a phosphoester substrate or a nucleophile were designed and synthesized (Chart 1).

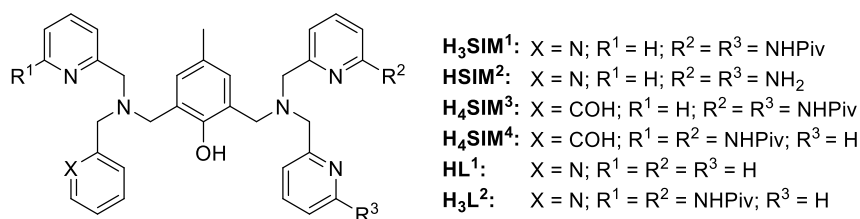


Chart 1: Ligands H₃SIM¹, HSIM², H₄SIM³, and H₄SIM⁴ developed and ligands HL¹ and H₃L² additionally employed in the course of this thesis.

Using these ligands, more accurate model systems for the enzyme active site were achievable as they combine the two essential structural features known to influence the catalytic activity towards the hydrolysis of phosphoesters, *i.e.* the asymmetry of the dinuclear active site and the capacity for hydrogen bond formation. The latter was verified by the observation of hydrogen bonds in the X-ray structures of dizinc(II) and diiron(II) complexes. Moreover, two dizinc(II) complexes revealed strikingly different structures compared to the common structure known for phenoxido-bridged phosphatase models. In fact, the two ligands bearing two pivaloyl-amide moieties in an asymmetric manner formed dizinc(II) complexes with two different Zn^{II} sites and an unusual hydroxido co-ligand, representing two important features in the active site of PAP, the difference of the metal sites and the nucleophile needed for the phosphoester hydrolysis. In addition, hydrogen bond formation detected in these X-ray structures was accounted for the stabilization of the hydroxido co-ligand.

In this work, a new synthetic approach towards more sophisticated model systems for the active form of mammalian PAP was developed. Chemical oxidation of the diiron(II) complex of H₃SIM¹ results in the generation of the Fe^{III}Fe^{II} complex that has been specifically designed to both satisfy

the requirement of a heterovalent diiron core and to mimic the second coordination sphere of the active site of PAP. Similarly, more accurate model systems for the active site of plant PAPs have been generated in the form of heterovalent heterodinuclear complexes of ligand H_3SIM^1 and H_4SIM^4 bearing, adjacent to the $Ga^{III}Zn^{II}$ core, functionalities capable of forming hydrogen bonds. Analysis of the complexation behavior of the respective ligands revealed the selective formation of the $Ga^{III}Zn^{II}$ complexes in solution.

The model complexes described above imitate successfully the extensive hydrogen bond network that is formed by the second coordination sphere within the active site of PAP as well as in a structural and functional similar phosphatase, Alkaline Phosphatase. Thus, those complexes allow to study the impact of hydrogen bonds on the reaction mechanism. The main impact of the secondary interactions in the dizinc(II) complexes was found to be the increased substrate affinity. This catalytic parameter was shown to be dependent on both the hydrogen bonding sites and the type of the hydrogen bonding groups. Although the substrate affinity of the $Ga^{III}Zn^{II}$ complex was revealed to be lower compared to the dizinc(II) complex, a 50-fold faster hydrolysis rate and a 6-fold increased efficiency was detected for the heterodinuclear complex. Moreover, the mechanism previously proposed, in which the phosphoester is activated by the Zn^{II} center and the Ga^{III} being accountable for providing the hydroxide nucleophile at near physiological condition, was supported in this study and an accelerating effect by the interplay of the two metal ions was detected. However, the inhibition was found to be favored in the $Ga^{III}Zn^{II}$ complex compared to the respective monogallium(III) complex, most likely due to bridging coordination of the hydrolysis product, additionally stabilized by coordination of the adjacent pivaloyl-amide residue. The proposed arrangement in the catalyst-hydrolysis product adduct derives from a structure of a stable phosphoester-bridged dizinc(II) complex bearing the same ligand backbone. However, the $Ga^{III}Zn^{II}$ complex of H_3SIM^1 is the first heterodinuclear model complex that mimics the essential function of PAPs, the ability to cleave phosphomonoesters and therefore supports the crucial impact of the second coordination sphere in the active site of PAP.

KURZZUSAMMENFASSUNG

Osteoporose ist eine Krankheit, die aufgrund exzessiver Knochenresorption zu Fehlordnung im Skelett und infolgedessen zu einem erhöhten Frakturrisiko führt. Mehr als 75 Millionen Menschen in den USA, Europa und Japan leiden an Osteoporose. Aus diesem Grund ergibt sich eine akute Notwendigkeit neue und effektive Wirkstoffe für diese Krankheit zu entwickeln. Als Ausgangspunkt für die Entwicklung neuer antiosteoporotischer Wirkstoff-Leitstrukturen ist das Haupttarget das Enzym „violette saure Phosphatase“ (*Purple Acid Phosphatase, PAP*). Das wesentliche Ziel dieser Arbeit ist die Synergie, die zwischen der primären und sekundären Koordinationssphäre innerhalb der aktiven Tasche von Phosphatase-Enzymen wie PAP auftritt, besser nachzubilden. Dies wurde durch die Entwicklung synthetischer Methoden für neuartige Biomimetika (Metallkomplexe mit geringem Molekulargewicht) ermöglicht. Hierfür wurden asymmetrische Liganden mit zwei Koordinationsstellen konzipiert und entwickelt, die das Peptid-Rückgrat der aktiven Tasche von PAP imitieren, einschließlich der Fähigkeit Wasserstoffbrücken zu Phosphoester-Substraten oder einem Nukleophil zu bilden (Abbildung 1).

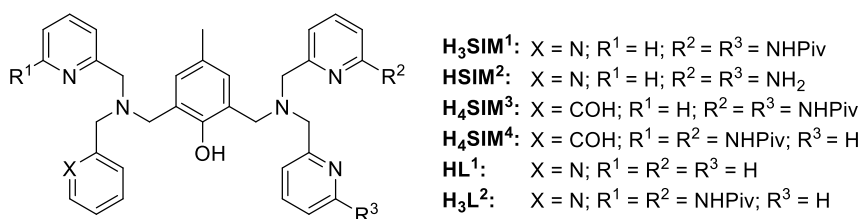


Abbildung 1: Im Laufe dieser Arbeit entwickelte Liganden H₃SIM¹, HSIM², H₄SIM³ und H₄SIM⁴ sowie zusätzlich verwendete Liganden HL¹ und H₃L².

Mit Verwendung dieser Liganden konnten verbesserte Modellsysteme für die aktive Tasche dargestellt werden. Dies wurde durch die Kombination der zwei essentiellen strukturellen Eigenschaften erzielt, welche bekanntlich die katalytische Aktivität bezüglich der Phosphoester-Hydrolyse beeinflussen; die Asymmetrie der dinuklearen aktiven Tasche und die Kapazität zur Wasserstoffbrückenbildung. Letztere wurde durch die in den Kristallstrukturen sichtbaren Wasserstoffbrücken der dinuklearen Zink(II)- und Eisen(II)-Komplexe bestätigt. Darüber hinaus zeigten zwei dinukleare Zink(II)-Komplexe auffallend abweichende Strukturen verglichen mit bekannten Strukturen von Phenoxido-verbrückten Phosphatase-Modellen. Unter Verwendung der zwei Liganden, die zwei Pivaloylamid-Substituenten in einer asymmetrischen Anordnung tragen, bildeten sich zweikernige Zink(II)-Komplexe mit unterschiedlichen Zn^{II} Zentren und einem ungewöhnlichen Hydroxido-co-Liganden. Somit imitieren diese Komplexe zwei wichtige Eigenschaften der aktiven Tasche von PAP, die Verschiedenheit der Metallkoordinationssphäre und das für die Phosphoesterhydrolyse benötigte Nukleophil. Die Stabilisierung des Hydroxido-

co-Liganden wurde den Wasserstoffbrückenbindungen, die in den Kristallstrukturen detektiert wurden, zugeschrieben.

In dieser Arbeit wurde eine neue Synthesestrategie für ausgereifere Modellsysteme der aktiven Tasche der Säugetier-PAP entwickelt. Der $\text{Fe}^{\text{III}}\text{Fe}^{\text{II}}$ -Komplex des Liganden H_3SIM^1 wurde durch chemische Oxidation des entsprechenden Di-Eisen(II)-Komplexes in Lösung dargestellt. Dieser heterovalente Di-Eisen-Komplex wurde spezifisch entworfen, um den Anforderungen eines heterovalenten Di-Eisen-Kerns zu entsprechen und die zweite Koordinationssphäre der aktiven Tasche der PAP zu imitieren. Gleichmaßen wurden exaktere Modellsysteme für die aktive Tasche von Pflanzen-PAP in Form von heterovalenten heterodinuklearen Komplexen der Liganden H_3SIM^1 und H_4SIM^4 dargestellt. Diese Komplexe enthalten Funktionalitäten in der näheren Umgebung des $\text{Ga}^{\text{III}}\text{Zn}^{\text{II}}$ Zentrums, die zur Wasserstoffbrückenbindung befähigt sind. Die Untersuchung des Komplexierungsverhaltens der entsprechenden Liganden zeigten die selektive Bildung der $\text{Ga}^{\text{III}}\text{Zn}^{\text{II}}$ -Komplexe in Lösung.

In den verwendeten Modellkomplexen wird erfolgreich das ausgedehnte Wasserstoffbrückennetzwerk, das in der zweiten Koordinationssphäre innerhalb der aktiven Tasche von PAP genauso wie in der strukturell und funktionell ähnlichen alkalischen Phosphatase auftritt, imitiert. Diese ermöglichen die Rolle der Wasserstoffbrückenbindungen im Reaktionsmechanismus zu untersuchen. Der größte Einfluss der sekundären Wechselwirkungen in den Di-Zink(II)-Komplexen wurde in der erhöhten Substrataffinität gefunden. Es wurde nachgewiesen, dass dieser katalytische Parameter, sowohl von der Anordnung als auch von der Art der Wasserstoffbrückendonoren abhängt. Obwohl die Substrataffinität des $\text{Ga}^{\text{III}}\text{Zn}^{\text{II}}$ -Komplexes niedriger ist als die des homodinuklearen Zink(II)-Komplexes, wurde eine 50-fach schnellere Hydrolysegeschwindigkeit und eine sechsfach erhöhte Effizienz für den heterodinuklearen Komplex beobachtet. Darüber hinaus konnte in dieser Studie der bisherige vorgeschlagene Mechanismus, in dem der Phosphoester durch das Zn^{II} -Zentrum aktiviert wird und das Ga^{III} -Zentrum das Hydroxid-Nukleophil unter annähernd physiologischen Bedingungen bereitstellt, bestätigt und ein Beschleunigungseffekt durch das Zusammenspiel der beiden Metallionen gefunden werden. Ebenso konnte gezeigt werden, dass die Inhibierung des $\text{Ga}^{\text{III}}\text{Zn}^{\text{II}}$ -Komplexes im Vergleich zum Monogallium(III)-Komplex begünstigt ist. Dies lässt sich auf eine verbrückende Koordination des Hydrolyseproduktes und dessen Stabilisierung durch die Koordination des benachbarten Pivaloylamid-Substituenten zurückführen. Diese postulierte Anordnung im Katalysator-Hydrolyseprodukt-Addukt wurde von einer Struktur eines stabilen Phosphoester-verbrückten Di-Zink(II)-Komplexes desselben Ligandenrückgrats abgeleitet. Der $\text{Ga}^{\text{III}}\text{Zn}^{\text{II}}$ -Komplex des Liganden H_3SIM^1 ist der erste heterodinukleare Modellkomplex, der Phosphomonoester spalten kann, was

die essentielle Funktion von PAPs darstellt. Dies verdeutlicht die wesentliche Relevanz der zweiten Koordinationssphäre in der aktiven Tasche von PAP.

Chapter 1

Introduction

1.1 OSTEOPOROSIS – AN ENFEEBLING DISEASE

Osteoporosis is a disease resulting in a skeletal disorder caused by excessive bone resorption.¹ At greatest risk are the elderly and in particular post-menopausal women.² Current treatments for osteoporosis include vitamin and calcium dietary supplements. Bisphosphonates are the most common drugs administered to lower bone resorption rates, but these have significant side-effects and/or compliance issues.³ Thus, osteoporosis is a major health problem and there is an urgent need to develop new and effective therapeutic agents for this enfeebling disease.

Several lines of evidence validate the enzyme Purple Acid Phosphatase (PAP) as an important target for the discovery and development of new anti-osteoporotic drug leads, such as (i) elevated concentrations of PAP in the human serum are associated with an increase in bone turnover,⁴ (ii) elevated serum concentrations of human PAP are observed in patients with osteoporosis,⁵ (iii) mice lacking the gene encoding PAP suffer from deformed bone structure (osteopetrosis),⁶ and (iv) mice over-expressing PAP are osteoporotic.^{7, 8} For those reasons PAP is already used as a main biochemical marker for the diagnosis of osteoporosis.⁹ Moreover, detailed understanding of the catalytic mechanism of PAP encourages the rational design of antiosteoporotic drugs.¹⁰

1.2 BIOLOGICAL SIGNIFICANCE AND STABILITY OF PHOSPHOESTERS

Phosphate esters, also called phosphoesters, are very important in the chemistry of life as they fulfill a variety of key roles.¹¹ The P-O bonds are extremely stable due to the exceedingly slow uncatalyzed hydrolysis although it is favored thermodynamically.¹¹ Therefore, phosphoester linkages are particularly well-suited in biology and therefore ubiquitous in nature as they link for example the nucleosides in deoxyribonucleic acid (DNA) and ribonucleic acid (RNA). For example, the strength of the phosphoester P-O bond is illustrated dramatically in the fact that DNA has a half-life of 30,000,000 years.¹² However, phosphoesters are also found in phospholipids, the major component of cell membranes and in many small molecules that play a key role in metabolism including several organic cofactors and secondary messengers.¹¹ Reversible phosphorylation of proteins is an extremely important regulatory mechanism.^{13, 14} The transformation of serine, threonine or tyrosine residues into phosphomonoesters induces conformational changes in enzymes and receptors leading to activation or inactivation.¹¹ In this

way, phosphorylation and phosphoester cleavage is an effective 'molecular switch' to control protein function.¹¹

1.3 PHOSPHATASES – PHOSPHOESTER CLEAVING ENZYMES

Whilst the stability of phosphoester bonds is critical to life, so is the capacity to efficiently manipulate these bonds. Nature has managed to achieve this remarkable feat through the evolution of a diverse range of enzymes that are able to drastically reduce the activation energies of specific P-O hydrolysis reactions and thereby to accelerate those by factors of $> 10^{15}$ relative to the uncatalyzed cleavage.^{11, 15} This task is adopted by phosphatases which are amongst the most efficient enzymes known and are involved in signal transduction in bacteria,^{16, 17} phospholipid degradation,¹⁸⁻²⁰ as well as regulation of phosphate levels in plants, fungi and mammals.^{11, 21-28} Purple Acid Phosphatases (PAPs) and Alkaline Phosphatases (APs) are two of the best characterized hydrolytic enzymes and are predominantly discussed in this thesis.¹¹ As the names imply the former are most active at low pH, and the latter under alkaline conditions.¹¹ Although it has been thought for a long time that APs and PAPs are strictly phosphomonoesterases it was found that both are also able to operate as phosphodiesterases.^{29, 30}

Alkaline Phosphatase

APs are unique in the class of phosphomonoesterases in the sense that they appear to be nonspecific.³⁰ Furthermore, APs hydrolyze not only phosphomonoesters, but also a variety of *O*- and *S*-phosphothioates, phosphoamidates, thiophosphates and phosphate.³⁰ Moreover, APs do not only catalyze hydrolysis reactions but also transphosphorylations in the presence of high concentrations of phosphate acceptors.³¹ Mammalian APs occur in different isozymes with very different *in vivo* functions.³¹ In general, APs are commonly named after the tissue where they are predominantly expressed.³¹ The major functions of APs established to date is bone mineralization by tissue-nonspecific AP (TNAP), abundant in skeletal tissues, and intestinal absorption by intestinal AP (IAP), abundant in the gut.³¹

Recent studies on TNAP-deficient mice showed that hydrolyzing the mineralization inhibitor pyrophosphate (PP_i) was the major function of TNAP in bone tissue, thus facilitating mineral precipitation and growth.³² PP_i prevents initial crystal formation and crystal growth by physically coating the nascent hydroxyapatite crystals.³² Therefore, TNAP functions to maintain an appropriate concentration of this inhibitor to ensure normal bone mineralization.³² Another

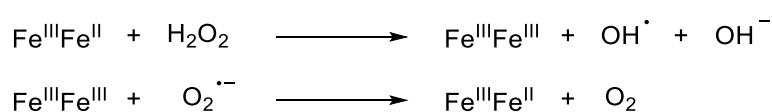
proposal for the function of TNAP in bone matrix has been the generation of the inorganic phosphate (Pi) needed for hydroxyapatite crystallization.³²

The biological functions of IAP are diverse, including (i) lipid intestinal absorption,^{33, 34} (ii) regulation of bicarbonate secretion,^{35, 36} (iii) detoxification of bacterial lipopolysaccharide (LPS),^{37, 38} and (iv) protection against LPS-induced intestinal inflammation.^{39, 40} In more detail, pancreatic lipase hydrolyze triglycerides into glycerol and free fatty acids (FAs). For the subsequent FA absorption, the involvement of IAP has been proposed through regulation of the FA carrier protein FA transporter/CD36 (FAT/CD36).⁴⁰ The possibility exists that IAP modulates the FA absorption by controlling the level of phosphorylation of FAT/CD36 and/or by locally hydrolyzing the extracellular ATP, since the CD36-mediated FA uptake (i) decreases with increasing phosphorylation of FAT/CD36, (ii) is inhibited by extracellular ATP, and (iii) is restored after the addition of AP.⁴⁰ The latter modulation mechanism of IAP is also utilized for the regulation of the bicarbonate secretion which works in a loop involving IAP, extracellular ATP and G-coupled purinergic receptor P2Y₁.⁴⁰ ATP stimulates the P2Y₁ receptors which, in turn, stimulate the secretion of bicarbonate by enterocytes.⁴⁰ Therefore, the ATPase activity of IAP regulates the local ATP concentration and subsequently the bicarbonate secretion. In contrast, the detoxification of LPS is encompassed directly by the dephosphorylation of its toxic diphosphoryl-lipid A moiety.⁴⁰ In this way the LPS-induced intestinal inflammation induced by the Toll-like receptor 4 (TLR4) is suppressed, since the dephosphorylated LPS is no longer able to trigger TLR4.⁴⁰

Purple Acid Phosphatase

PAPs are ubiquitous enzymes found in animals, plants, fungi and bacteria and are associated with a variety of biological functions. PAPs are resistant to inhibition by L-tartrate and thus are frequently referred to as tartrate-resistant acid phosphatase (TRAcPs or TRAPs).²⁹

Mammalian PAPs, abundantly expressed in osteoclasts, activated macrophages and dendritic cells,⁴¹⁻⁴³ have been implicated with (i) iron transport in pregnant pigs,⁴⁴ (ii) the generation of reactive oxygen species (ROS),⁴⁵ and (iii) increased bone resorption.^{9, 46} Specifically, it has been suggested that PAPs play an important role in the immune defense system producing hydroxyl and superoxide radicals based on the Haber–Weiss–Fenton-type reactions (Scheme 1).^{29, 47}



Scheme 1: Generation of ROS by PAPs by Haber-Weiss-Fenton type reactions.²⁹

As mentioned previously, PAPs were also shown to play a crucial role in bone metabolism since transgenic mice, in which osteoclasts overexpress and secrete PAP, display increased levels of bone resorption and consequently symptoms of mild osteoporosis.⁷ In contrast, knock-out transgenic mice completely lacking PAP reveal the opposite phenotype, osteopetrosis.⁶ It is believed that PAP dephosphorylates bone matrix proteins such as osteopontin which are involved in the adhesion of osteoclasts to the bone surface and are, upon dephosphorylation, no longer capable of fulfilling this function.⁴⁶ However, it has also been speculated that PAP is involved in the ATP-dependent regulation of bone calcium homeostasis due to the fact that PAP is also an efficient ATPase.⁴⁸

Contrary to mammalian PAP, assignment of specific functions has been more difficult for plant PAP due to its appearance in multiple isoforms with diverse metal ion compositions.⁴⁹⁻⁵⁸ However, it has been speculated that plant PAPs play a major function in phosphate metabolism mobilizing inorganic phosphate from organophosphates in the soil.^{50-52, 57, 59} It has also been proposed that plant PAPs are involved in the storage of phosphorus in plant seeds via hydrolysis of phytic acid, the major compound accountable for the phosphorus storage.⁶⁰ Interestingly, it has been found that the extracellular ROS concentration in plants increases in response to a pathogen attack or biotic and abiotic stress, similarly as observed for mammals.⁶¹ Therefore, plant PAPs seem to be bifunctional, similar to mammalian PAPs, catalyzing both hydrolytic reactions and peroxidations.^{45, 47, 62, 63} Although not yet clear, the purpose of this peroxidation activity in plants, microbe may be killing during pathogen attack.^{29, 61}

1.4 STRUCTURE OF PHOSPHATASES

APs and PAPs belong to the enzyme family of dinuclear metallohydrolases which require two dinuclear centers to perform a hydrolytic reaction. The presence of two closely spaced metal ions in the active site can have advantages over just one metal ion, such as (i) a lowered thermodynamic driving force for redox reactions due to charge-delocalization, (ii) a lowered activation barrier for solvent and enzyme reorganization, (iii) preorientation and electrostatic activation of substrates, (iv) easier formation of hydrolysis-initiating nucleophiles, and (v) stabilization of transition states generated throughout the hydrolysis reaction.²⁸ The binding of the two metals in the active site is facilitated by precisely positioned ligating amino acid side chains of the peptide backbone which are defined as the primary coordination sphere.

Alkaline Phosphatase

AP has been structurally characterized as an enzyme-phosphate complex isolated from *E. coli* (Chart 2, left).⁶⁴ Here the phosphate is non-covalently bound at the active center and the structure therefore likely represents an authentic intermediate of the phosphoester hydrolysis reaction.³⁰ AP is a homodimeric protein with 449 amino acids building up the subunits and two Zn^{II} centers and a single Mg²⁺ center coordinated in each active site.¹¹ Whilst one Zn^{II} ion is coordinated by two histidine and one aspartate residue of the peptide backbone, the second Zn^{II} center is ligated by one histidine and two aspartate residues.⁶⁴ In the resting state the proximal serine side chain coordinates the latter Zn^{II} ion, but is exchanged by a phosphate oxygen atom in the enzyme-phosphate complex.³⁰ The Mg²⁺ ion which appears to play only an ancillary, structural role, is linked to the dizinc(II) site by a Mg-Zn bridging aspartate and is additionally coordinated by a glutamate, a threonine and three water molecules.⁶⁴ The three metal ions in AP form a triangle in which the metal-metal distances are 3.94 Å, 4.88 Å, and 7.09 Å.³⁰ Therefore, the Mg²⁺ appears not to be close enough to participate directly in the hydrolysis mechanism, but could contribute to the shape of the electrostatic potential around the active center or provide an additional metal bound water in the vicinity of Ser102 functioning as a general acid/base for regulating the protonation state of Ser102.^{30, 65} A comparison of the amino acid sequence of the phosphorylated peptides isolated from the enzyme with the complete amino acid sequence showed that the phosphorylated residue is Ser102 suggesting that this amino acid residue functions as nucleophile in the catalytic mechanism.³⁰

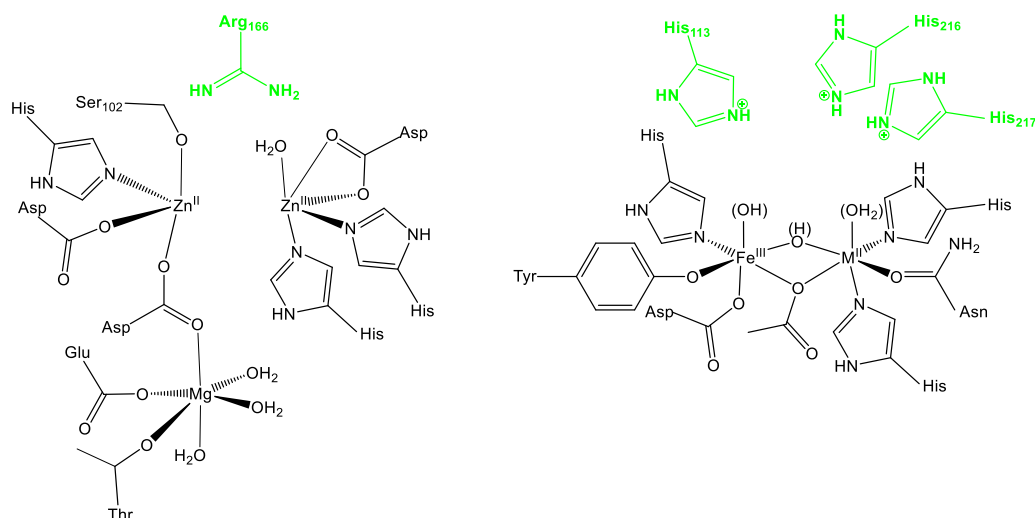


Chart 2: Schematic depiction of the active site of AP (left)^{30, 64, 65} and PAP (right),⁴⁵ including essential amino acids in the second coordination sphere (depicted in green).

Purple Acid Phosphatase

Several crystal structures of PAPs, isolated from various plant, animal, and fungal sources, have been published.²⁹ Mammalian PAPs isolated from pig (ufPAP), cow, human, mouse and rat are approximately 35 kDa monomeric proteins with a Fe^{III}Fe^{II} center and share at least 80% amino acid sequence identity.^{21, 29, 49, 66} Plant PAPs extracted from red kidney bean (kbPAP), sweet potato, soybean, duckweed, tomato, potato, and thale cress revealed 55 – 60 kDa homodimeric enzymes and amino acid sequence identity of at least 65%.^{21, 29, 49, 66} The metal composition in the active sites of plant PAPs is either Fe^{III}Zn^{II} or Fe^{III}Mn^{II}.^{23, 24, 67, 68} Although the homology between the mammalian and plant PAP amino acid sequences is less than 20%, their catalytic sites display a remarkable similarity.²⁹ The two metal ions were found to be coordinated by seven invariant amino acid residues (Chart 2, right).⁴⁵ The Fe^{III} ion is coordinated by a histidine, an aspartate and a tyrosine amino acid side chain. This tyrosine ligand in the ‘chromophoric’ site is accountable for the characteristic purple color of the enzyme due to its ligand to metal charge-transfer (LMCT) transition.⁶⁹ The M^{II} ion (M^{II} = Fe^{II}, Zn^{II} or Mn^{II}) in the ‘redox-active’ site is surrounded by an asparagine and two histidines residues. The coordination spheres of the Fe^{III} and M^{II} ions were completed by a bridging aspartate residue, a modeled bridging hydroxide ligand and a modeled terminal water ligand for the resting state for ufPAP, but the number of terminal and bridging aqua and hydroxide ligands is ambiguous.⁷⁰ Although PAPs are rather specific in their metal ion selection *in vivo*, it has been shown with *in vitro* studies that on the one hand the Fe^{II} ion of the diiron ufPAP can be exchanged by Zn^{II}, Ni^{II}, Cu^{II}, and Mn^{II} and on the other hand the Fe^{III} ion can be replaced by Ga^{III} and Al^{III} without loss of catalytic activity.²⁹ Similarly, catalytic activity could be reconstituted by replacement of Zn^{II} by Fe^{II} in kbPAP.²⁹ However, PAPs are the only dinuclear metallohydrolases where the necessity for a heterovalent active site for catalysis has been clearly established.²¹

In general, the primary coordination sphere in the active site of dinuclear enzymes is supposed to define (i) the coordination modes, (ii) the separation, and (iii) the electron density of the two metal ions coordinated. Interestingly, in both crystal structures discussed here the two metal centers reside in chemically different environments. The differing coordination environments of dinuclear metallohydrolases are often defined as the α - and β -site.²⁸ In fact, the peptide backbones of the active sites of AP and PAP form an asymmetric dinucleating core with a harder and a softer metal site suggesting that the metal ions have distinct functions in the catalytic mechanism. However, mutation studies (discussed below) of some non-coordinating amino acids of both, AP and PAP, revealed that those are also essential for the activity.^{13, 65, 71-74}

1.5 SIGNIFICANCE OF THE SECOND COORDINATION SPHERE IN PHOSPHATASES

Amino acids that are not directly coordinated to the metal ions in the active site but are indispensable to the activity are defined as the second coordination sphere.⁷⁵ Those amino acids alter the physical and chemical properties of the active site, needed for the catalytic transformation by non-covalent interactions, hydrophobic effects and van der Waals forces.⁷⁵

Alkaline Phosphatase

In the crystal structure of the enzyme-phosphate complex of AP an extensive hydrogen bonding network was determined. More precisely, the two phosphate oxygens, which are not coordinated to the two Zn^{II} centers, form hydrogen bonds to an adjacent guanidinium group of an arginine residue (Arg166) and one of them also to the amide group of the serine residue in the primary coordination sphere (Ser102).³⁰ Furthermore, Arg166 is additionally involved in hydrogen bonding to other amino acid side chains.³⁰ The influence of the proximal Arg166 residue was investigated with site-directed mutagenesis studies in which this amino acid was exchanged by lysine, glutamine, serine or alanine.^{71, 72} All mutants revealed decreased phosphate affinity but retained catalytic activity. In a similar study the possibility that Arg166 was responsible for the preference of AP for phosphomonoesters was demonstrated.^{65, 73} Moreover, investigations of linear free-energy relationships have been suggested that electrostatic interactions of the phosphate with both Zn^{II} ions and Arg166 are critical stabilizing factors in the trigonal bipyramidal transition structure of the phosphoester hydrolysis reaction.⁶⁵

Purple Acid Phosphatase

Previous studies have shown that not only the amino acids in the first coordination sphere are crucial for catalytic activity of PAPs but also the three histidine residues nearby the metal centers (Chart 2, right).^{45, 74} With the aid of site-directed mutagenesis with rat bone PAP the influence of these residues regarding the phosphatase activity and the generation of reactive oxygen species (ROS) of PAP was analyzed. These experiments led to the conclusion that the replacement of the histidine residues 216 and 113 with alanine or glutamine seriously impaired the phosphatase activity compared to the wild-type enzyme, while the mutants retained a high capacity to form ROS.^{45, 74} From this it appears that the acid phosphatase activity and the ROS-generating capacity are independent of each other. More importantly, these results point out that the hydrogen bonding network built up by these histidine residues plays an essential role in the mechanism of

the phosphoester hydrolysis.^{26, 76} Interestingly, the mutant in which His113 was exchanged by a glutamine residue, technically capable to form hydrogen bonds, exhibited also decreased phosphoester hydrolysis activity. This initial contradiction to the former hypothesis was clarified by exchanging His113 with an asparagine residue, which led to an even higher phosphoester hydrolysis activity than the native enzyme. Since asparagine has the same functionalities than glutamine, but with a shorter side chain, the optimum geometry for hydrogen bonding and following phosphoester hydrolysis appears to be achieved in the asparagine mutant.

Although the importance of the second coordination sphere of AP and PAP has been clearly demonstrated, the precise role of the amino acid side chains proximal to the dinuclear active site is still not completely understood. This is primarily due to challenges in examination of functions of specific amino acids in complicated protein matrices, but also caused by difficulties in the characterization of non-covalent bonds.⁷⁵ In this regard the development of simplified model systems, which incorporate the key features of the native metalloenzymes, represents a feasible experimental approach.

1.6 BIOMIMETICS – A USEFUL TOOL TO STUDY ENZYMES

Due to the fact that PAP activity is directly linked to bone resorption this enzyme has become a major target for the development of antiosteoporotic chemotherapeutics.²⁹ Efforts for a rational design of such compounds is greatly helped by the detailed knowledge about the functional domains of PAPs. In fact, the wealth of information gained in recent years about the structure and the catalytic mechanism of mammalian AP has aided in the development of pharmacological products able to modulate AP activity and in the understanding of AP correlated diseases such as hypophosphatasia, a rare and sometimes fatal metabolic bone disease, caused by the deficiency in TNAP isozyme.³²

In complement with X-ray structural, spectroscopic, mutagenesis and isotope effect studies of the respective enzyme a useful and important tool to establish the precise mechanism of an enzyme-catalyzed reaction are low-molecular weight synthetic mimics, also called biomimetics. Due to the fact that the active sites of many phosphatases contain metal ions, metal complexes are used as biomimetics to emulate key structural aspects of these enzymes. Model complexes have the advantages over their enzymatic counterparts since (i) they are generally more stable, (ii) they can be more readily crystallized, and (iii) provide easy accessible structural information on metal ion conformation.⁷⁷ In addition, model complexes can be designed to mimic one or more key features of a sophisticated enzyme active site. In this way, the relative importance of

specific structural or chemical features, or combinations thereof with respect to the overall catalytic efficiency of the enzyme, can be studied separately.

In this thesis the use of dinuclear model complexes as biomimetics of APs and PAPs, in order to gain a deeper understanding of the influence and the precise role of the second coordination sphere with regard to the catalytic phosphoester hydrolysis mechanism, will be presented.

Chapter 2

Ligand Design and

Syntheses^b

^b Parts of this chapter are published in "Dinuclear Zinc(II) Complexes with Hydrogen Bond Donors as Structural and Functional Phosphatase Models"; [Simone Bosch](#), Peter Comba, Lawrence R. Gahan, Gerhard Schenk, *Inorg. Chem.* **2014**, *53*, 9036-9051. and will be published in "Asymmetric Mono- and Dinuclear Ga^{III} and Zn^{II} Complexes as Models for Purple Acid Phosphatases (PAPs)"; [Simone Bosch](#), Lawrence R. Gahan and Gerhard Schenk; manuscript in preparation.

2.1 INTRODUCTION

In nature transition metal ions bound in the active site of enzymes are used extensively to encompass the catalysis of a broad range of reactions. While in some metalloenzymes the transformation of a substrate molecule takes place at a single metal center, several classes of metalloenzymes make use of the cooperativity of two metal centers within their active site to achieve full catalytic efficiency.⁷⁸ In the latter case the removal of one metal center often results in a decrease of activity. An important example of enzymes containing dinuclear active sites are metallohydrolases, which hydrolyze substrates such as urea, peptides, phosphoesters and -anhydrides, thioesters and even DNA and RNA. While most of the hydrolases bind two metals of the same kind in close proximity to each other, there are two other members of the hydrolase superfamily which have been shown to bind two different metal ions in their active sites, Purple Acid Phosphatases (PAPs) and Ser/Thr Proteins Phosphatases (PPs).^{9, 21, 79, 80} Moreover, the two chemically distinct coordination environments around the metal centers have been found to be essential for catalytic activity.^{21, 24, 81-85} The amino acid backbone of the active site in PAPs generate two different coordination sites, which favor the binding to a specific metal, though their individual roles remain a matter of debate.

Owing to the relatively low resolution of protein crystal structures, model complexes often play an important role in the structural characterization of the active sites in metalloproteins. Low molecular weight mimics of phosphoesterases simplify the study of both the environment of the metal ions and the hydrolysis of phosphoesters, and can provide insight into possible catalytic mechanisms.⁸¹ Therefore, small metal complexes have been used extensively to model the active site of phosphoesterases.⁸¹ Moreover, dinuclear complexes have been shown to bind phosphates more strongly and to be significantly more reactive for the cleavage of phosphate esters compared to their mononuclear counterparts.⁸⁶⁻⁸⁹ Some of the most active dimetallic systems are those in which the ligand structure places the metal ions in a way that it promotes cooperative interactions with the substrate (either via double Lewis acid activation, or Lewis acid activation coupled with provision of a metal-bound hydroxide nucleophile).^{80, 84} Due to the fact that for simple oxido- or hydroxido-bridged mononuclear complexes dissociation is likely, attention has been focused on bridging dinucleating ligand systems. In these the ligand must accommodate two metals with an appropriate metal-metal separation that reproduce the intermetallic distance of the enzyme. This is mostly achieved using a linker moiety between the two coordination sites. Different ligand backbone linkers have been successfully used by this means to model the structural features of hydrolases and examples are illustrated in Chart 3.

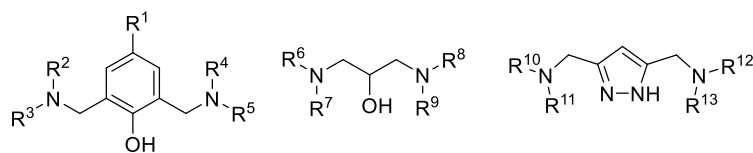


Chart 3: Schematic depiction of ligand types that have been used to model the active site in PAPs: *f.l.t.r.* phenolate-based, alkoxo-based and imidazolite-based ligands.

Among others, phenolate-, alkoxo-, and imidazolite have been deployed as scaffolds for a range of ligands varying in the aminomethyl-substituents (depicted as R^x in Chart 3) in order to tune the coordination behavior of the ligands towards specific metal ions.^{81, 90-99} The phenolate-linker is one of the most commonly used ligand scaffolds,^{90, 92-96, 99} for example in the symmetric ligands HL^1 and H_3L^3 (see Chart 4).^{100, 101} (The nomenclature of the ligands denotes the number of protons which can potentially be abstracted from the ligands upon deprotonation; HL^1 contains one potentially acidic phenolate residue, accordingly HL^1 , while H_3L^3 bears three acidic protons and the nomenclature is adjusted accordingly. This nomenclature will be used throughout this thesis.) The phenolate-linker arranges the two coordination sites the way that (i) the two metal ions are separated by about 3 – 4 Å, (ii) the two metal ions are bridged by an oxygen atom as present in the native active site, and (iii) exogenous water and hydroxido ligands are bound in a *syn* configuration. The latter structural feature was shown to be essential for phosphoester cleavage as a complex with two H_2O molecules in *anti* configuration was not active.¹⁰²

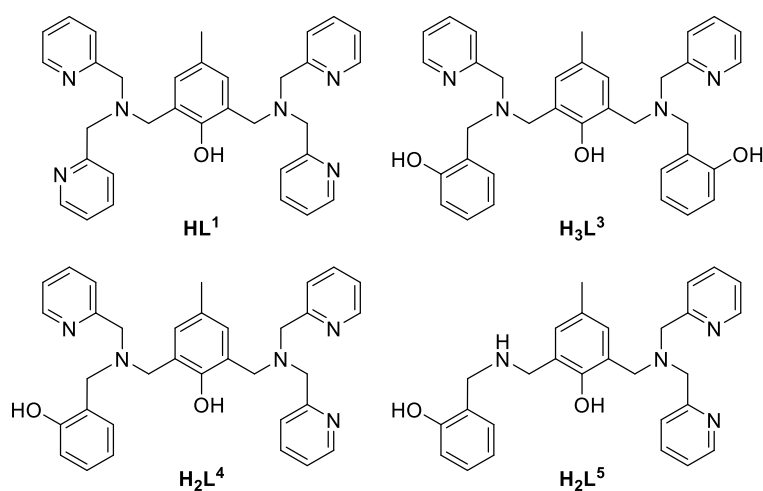
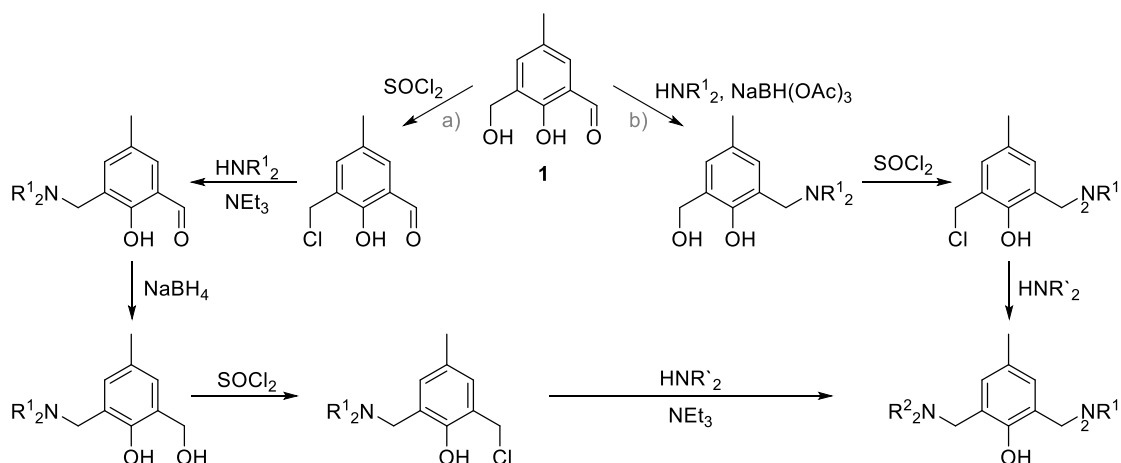


Chart 4: Symmetric and asymmetric phenolate-based ligands related to the ligands developed in the present thesis, previously used to model the active site peptide backbone of PAP.^{81, 103}

It should be noted, that an important feature of metalloenzymes, especially those with heterodinuclear active sites, is that the surrounding protein matrix usually provides chemically distinct binding environments for the individual metal centers, commonly referred to as site asymmetry at metallobiosites.⁹¹ Typically, asymmetric dinucleating ligands are used to mimic this coordination environment of the metals in metallohydrolases, which dictate the steric and

electronic features of each metal center.⁸¹ Terminal phenolate residues are often used to mimic the tyrosinate donor found in the active site of PAP.¹⁰² Numerous asymmetric ligands have been developed so far in order to imitate the peptide backbone of phosphatases with coordination number asymmetry (dissimilar number of donor atoms), *i.e.* H₂L⁵, and/or donor asymmetry (different types of donor atoms), *i.e.* H₂L⁴ and H₂L⁵.^{81, 94, 103}

Unfortunately, the accessibility of asymmetric dinucleating ligands is often hampered by various synthetic problems. Several approaches have been proposed to overcome this problem. The most facile route starting from a symmetric, doubly chloro-substituted phenolate-bridging unit was published for the synthesis of H₂L⁴ by Neves *et al.*,⁹⁴ whereby successive reaction with two amines generally results in the formation of considerable amounts of symmetric byproducts. The statistical mixture of the desired asymmetric ligand and the two unintended symmetric ligands is usually difficult to separate by conventional chromatography methods utilizing polar silica or alumina because of the high polarity of the products. An elegant solution for this problem was suggested by Kahn *et al.*¹⁰⁴ Starting also from a symmetric dicarbonyl-functionalized phenolate bridging unit, gadolinium(III) ions were used to protect one of the reactive carbonyl functions by coordination, whereby the remaining free carbonyl function leads to an imine by reaction with an amine. Precipitation of Gd^{III} in form of gadolinium(III) oxalate yielded the free carbonyl functionalized monoimine, which reacts with another different amine to afford the asymmetric diimine. Due to the fact that this approach only works for small-scale reactions, more efficient routes towards the class of asymmetric ligands were developed starting from already asymmetric bridging units.¹⁰⁵ In the case of the phenolate-based ligands the stepwise synthetic procedure starts usually with 2-hydroxy-3-(hydroxymethyl)-5-methylbenzaldehyde (**1**). Latour *et al.* (Scheme 2a) and Nordlander *et al.* (Scheme 2b) reported a procedure generating asymmetric dinucleating ligands using this starting material.^{106, 107} Whilst Latour *et al.* accomplished the incorporation of the two unequal amine side-arms by stepwise generation of a chloro functionality and following nucleophilic substitution,¹⁰⁶ Nordlander *et al.* achieved one attachment of an amine side-arm by amination of the carbonyl moiety present in the starting material and the second amine was incorporated by chlorination and subsequent nucleophilic substitution with a second amine following the same procedure as undertaken by Latour *et al.*¹⁰⁷



Scheme 2: Schematic representation of procedures applied by Latour *et al.* and Nordlander *et al.* to synthesize asymmetric dinucleating ligands.^{106, 107}

Many metalloenzymes that catalyze the cleavage of phosphate esters also possess a hydrogen bonding microenvironment around the metal centers, which is essential for their activity attributed to transition state stabilization.^{29, 108} In order to study the impact of hydrogen bond donors nearby the metal centers on the hydrolysis activity within the active site of phosphatases, different dinucleating ligands, depicted in Chart 5, have been developed. The hydrogen bonding interaction of PAPs were mimicked either by a cyclam-linker as in H_2L^6 ,^{108, 109} while in the other ligands the hydrogen bonding network was incorporated into the ligands by amino and pivaloyl-amide residues at the pyridine side-arms. Feng *et al.* developed a range of alkoxy-based mononucleating ligands and the dinucleating ligand HL^7 which also take into account the second coordination sphere.¹¹⁰⁻¹¹³ Moreover two HL^1 derivatives, H_3L^2 and HL^8 , which carry hydrogen bond donors proximal to the metal coordinating sites have been developed.^{109, 114} In the latter, two hydrogen bond donors, one proximal to the metal center each, are rigidly preorganized to interact with a phosphoester substrate and/or to activate the hydroxido nucleophile coordinated to the dimetal core.

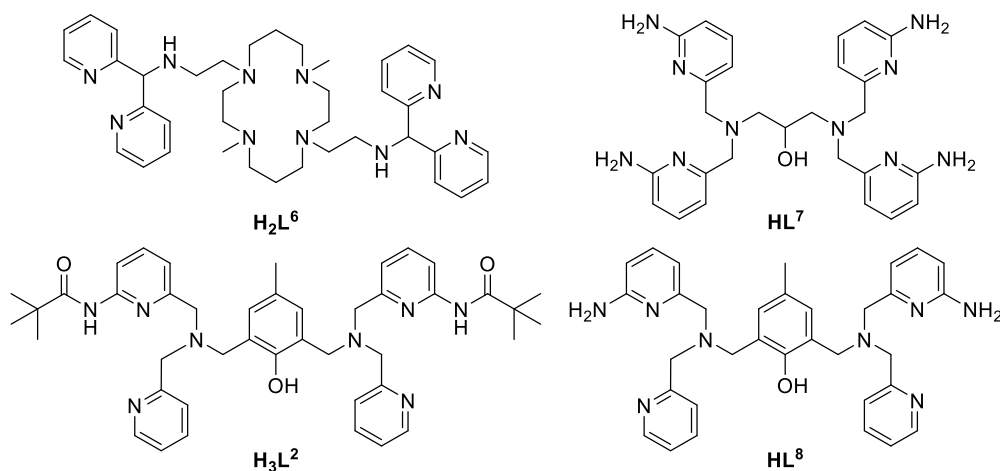


Chart 5: Previously published ligands bearing hydrogen bond donors mimicking the peptide backbone of phosphatases active sites.^{108, 112-114}

The intention of this thesis was to study the role of a hydrogen bond network in the reaction mechanism of phosphatase biomimetics. Thus, dinuclear complexes were designed, which combine the essential structural features of the active site of phosphatases, such as (i) two metal ions accommodated in a well-suited metal...metal separation, (ii) asymmetry of the two binding sites, and (iii) hydrogen bond donors proximal to the metal centers. Specifically, asymmetric ligands bearing two amide or amine groups as mimics of the second coordination sphere of the enzyme were synthesized and are depicted in Chart 6. Incorporation of two pivaloyl-amide residues in H_3SIM^1 in an asymmetrical manner, in contrast to H_3L^2 , realized the hydrogen bonding capacity as well as the asymmetry of the two binding sites. Similarly, $HSIM^2$ bears two amine moieties in an asymmetric fashion, contrary to its symmetric counterpart HL^8 . While in H_3SIM^1 and $HSIM^2$ the asymmetry of the metal binding sites is caused by the moieties of the second coordination sphere, H_4SIM^3 and H_4SIM^4 were designed in the way that the primary coordination sphere of the two binding sites is unlike. Moreover, both asymmetric ligands, H_4SIM^3 and H_4SIM^4 , bear hydrogen bond donors either proximal to one or proximal to both binding sites. The ligands discussed in this thesis leave vacant coordination sites and facilitate the interaction of the metal centers with specific substrates.

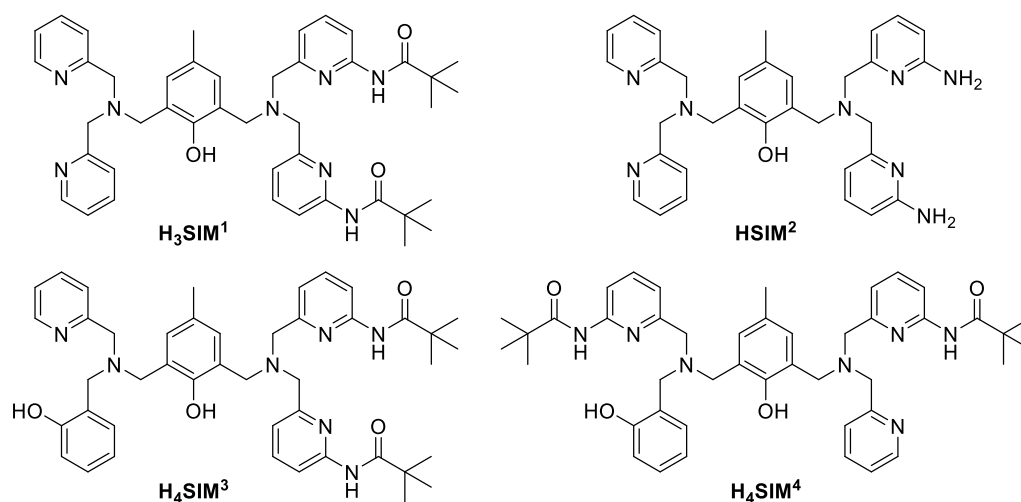


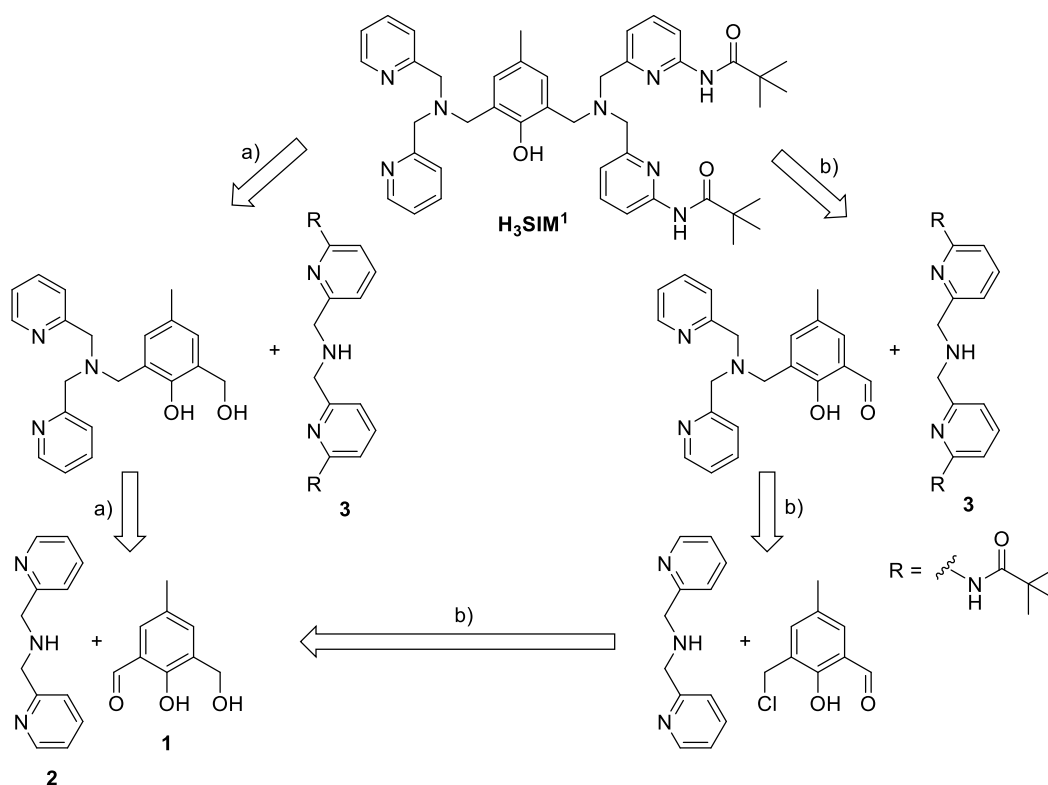
Chart 6: Overview of the ligands synthesized in this work.

The following chapter will give an introduction to the synthetic pathways developed for the preparation of the asymmetric ligands H_3SIM^1 , $HSIM^2$, H_4SIM^3 and H_4SIM^4 (Chart 6). In addition, detailed experimental procedures as well as analytical results are given in Chapter 11.

2.2 SYNTHESIS OF LIGAND H₃SIM¹

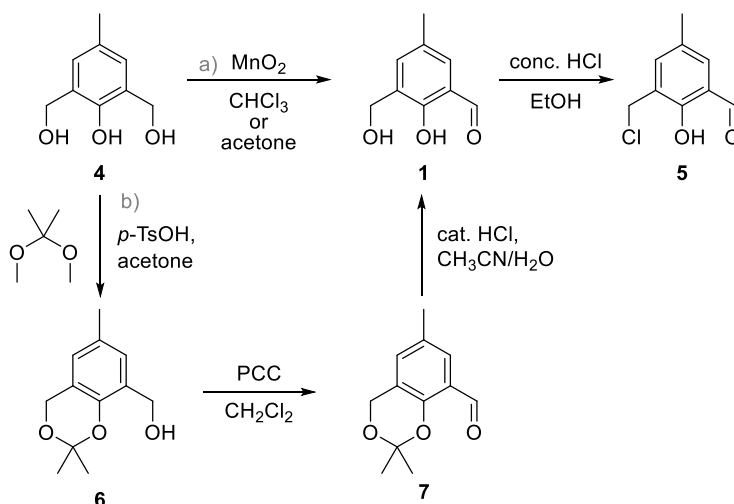
In order to gain further insight into the role of the hydrogen bonding network of PAPs in the catalytic mechanism, four asymmetric ligands bearing amide or amine residues with the capacity to form hydrogen bonds were developed. H₃SIM¹ was designed in order to investigate especially the impact of the positioning of the hydrogen bond donating groups in the active site of PAPs. The structure of H₃SIM¹ is based on the symmetric ligands HL¹ and H₃L². While HL¹ provides no hydrogen bond donors, H₃L² bears two pivaloyl-amide moieties, one amide moiety proximal to each coordination site. In contrast, H₃SIM¹ was designed in the way that a hydrogen bonding network is only available at one of the two binding sites, while the primary coordination sphere remains unchanged and therefore comparable to HL¹ and H₃L².

In the process of finding a suitable synthetic pathway for the preparation of H₃SIM¹ the approaches illustrated in Scheme 2 were combined and the number of reaction steps minimized. In this way, the retrosynthetic analysis of the ligand H₃SIM¹ yield two possible pathways (Scheme 3). Both pathways share the same asymmetric starting material 2-hydroxy-3-(hydroxymethyl)-5-methylbenzaldehyde (**1**). The suggested stepwise reaction with two different secondary amines enables the selective formation of the asymmetric ligand. Therefore, pathway a) suggests an initial amination and the subsequent nucleophilic substitution while pathway b) follows the reverse order.



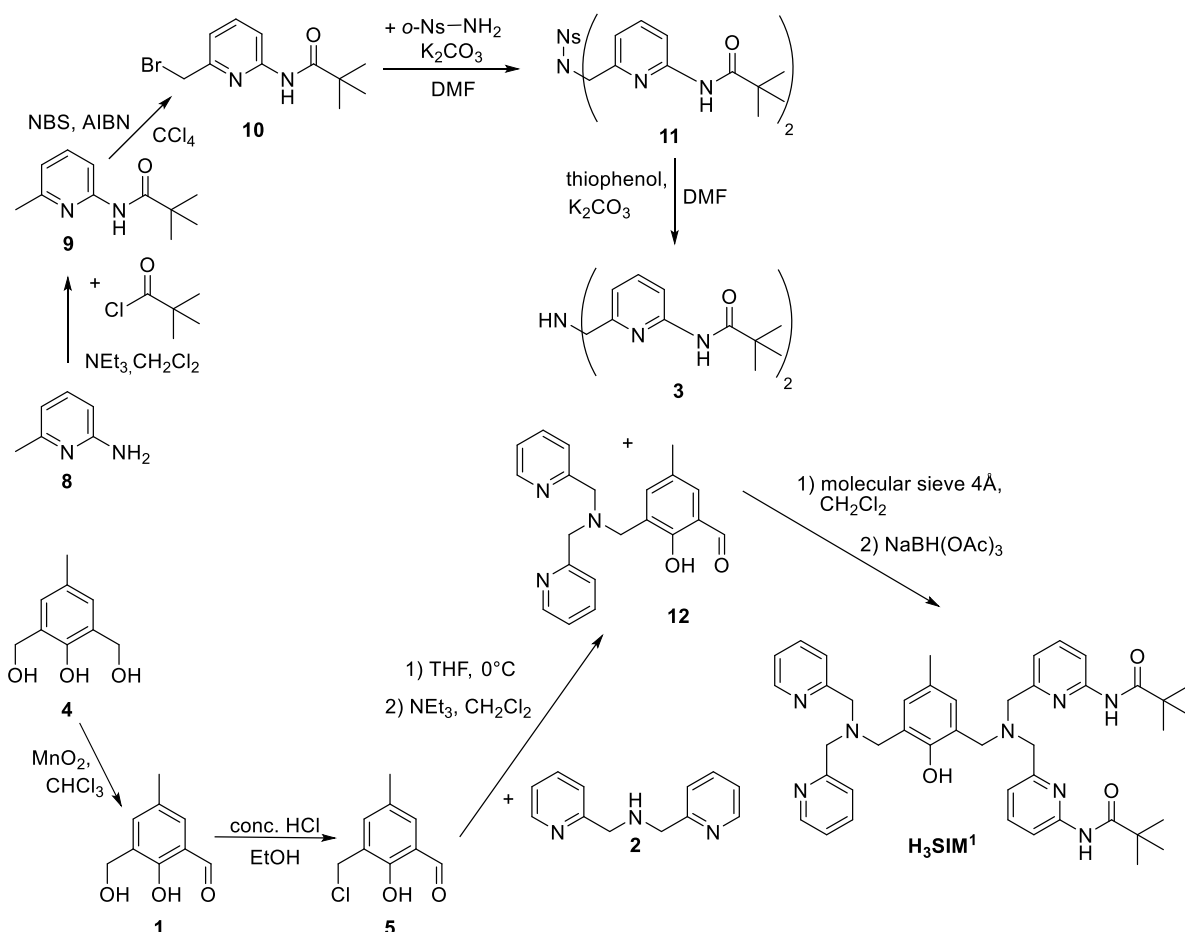
Scheme 3: Retrosynthetic analysis of ligand H₃SIM¹.

The precursors needed for both synthetic routes, *i.e.* compound **1**, **2**, and **3** were synthesized according to known procedures.¹¹⁵⁻¹²¹ Starting with 2,6-bis(hydroxymethyl)-4-methylphenol (**4**), the aldehyde functionality in compound **1** was formed by oxidation with MnO₂ in chloroform (Scheme 4a).¹²⁰ During the reaction both the monoaldehyde **1** and its dialdehyde derivative were formed and separated through column chromatography yielding compound **1** in a moderate yield of 46%. A selective procedure for the preparation of compound **1** was also tested. Protection of one alcohol group as the cyclic acetal of 2,2-dimethoxypropane in acetone enables the selective oxidation of the remaining alcohol group in dichloromethane using pyridinium chlorochromate (PCC) as oxidant (Scheme 4b).¹²² The following deprotection with hydrochloric acid in a mixture of acetonitrile and water led exclusively to compound **1** with an overall yield of the three reaction steps of 74%.¹²³ However, this alternative route includes two additional synthetic steps and is therefore more time-consuming. Chlorination of the alcohol group in compound **1** with concentrated hydrochloric acid in ethanol generated compound **5** in 67% yield (Scheme 4).¹²¹ Compound **5**, which contains one aldehyde group and one chloromethyl group, was chosen as the building block for the selective synthesis of the asymmetric dinucleating ligands H₃SIM¹, HSIM², H₄SIM³, and H₄SIM⁴ as those functionalities make this phenol compound able to react stepwise with two different secondary amines thereby forming the two unequal coordination sites of the ligands.

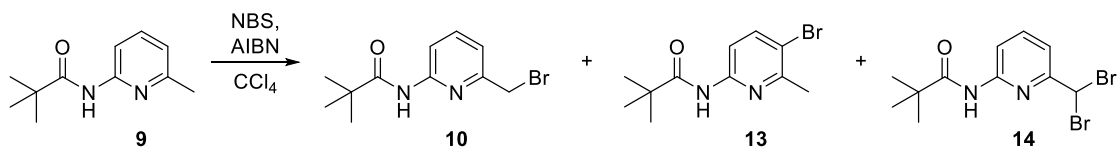


Scheme 4: Comparison of the statistical and selective synthesis of compound **1** and the following formation of compound **5**.

The two secondary amines, compound **2** and compound **3**, were synthesized adapting published methods.^{115, 119} Compound **2** was generated by amination of picolylaldehyde with 2-(amino-methyl)pyridine in methanol and subsequent hydrogenation with sodium borohydride in a moderate yield of 63%. The preparation of compound **3** was more challenging and the synthetic pathway is included in Scheme 5.

Scheme 5: Synthesis of ligand H₃SIM¹.

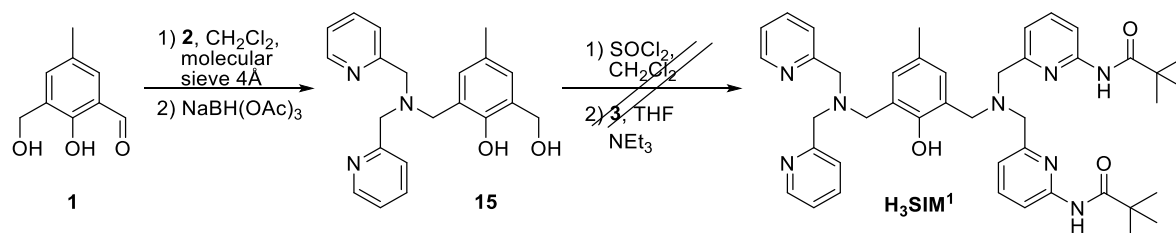
The amino functionality of 2-amino-6-methylpyridine (**8**) was protected prior to bromination via generation of the respective pivaloyl-amido derivative (95% yield). During the bromination of *N*-(6-methylpyridin-2-yl)pivalamide (**9**) a variety of side products appeared (Scheme 6).

Scheme 6: Bromination of compound **9** yielding the mixture of compound **10**, **13**, and **14**.

Thus, different modifications regarding the type and the concentration of the bromine source, the solvent and the use of UV light were examined in order to minimize the concentration of ring-brominated derivative **13** and dibrominated species **14** at maximal conversion of the starting material (**9**). In this way, a procedure was developed which leads to an adequate amount of side-chain monobrominated compound **10**. The isolation of the desired compound **10** was achieved by column chromatography and subsequent crystallization by ultrasonication in a yield of 44%. In the next step two equivalents of compound **10** were treated with potassium carbonate and one equivalent of 2-nitrobenzoylsulfonamide in dimethylformamide to form compound **11** in a yield of 98% (Scheme 5). Subsequent reaction of compound **11** with potassium carbonate and

thiophenol in anhydrous dimethylformamide realized the formation of compound **3** in 81% yield (Scheme 5).

The attachment of the secondary amines **2** and **3** to the bridging phenol building block **1** was initially tested following pathway a) in Scheme 3, adapting the procedures reported by Nordlander *et al.* (Scheme 7).¹⁰⁷ While the amination of compound **1** with compound **2** yield compound **15** in 85% yield, the following chlorination with thionylchloride and the nucleophilic substitution with compound **3** were found to be an unreliable procedure to obtain H₃SIM¹ in a satisfactory yield.



Scheme 7: Failed synthetic route to ligand H₃SIM¹.

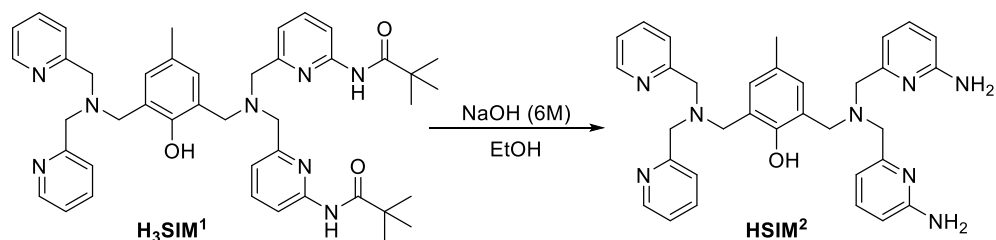
In order to circumvent the previous drawbacks, the alternative strategy of pathway b) was explored (Scheme 3), and the complete eight-step synthetic route is shown in Scheme 5. Nucleophilic substitution of the chlorine atom of compound **5** with amine **2** yields compound **12** (61% yield). The formation of ligand H₃SIM¹ was realized by amination of the remaining carbonyl functionality with the secondary amine **3** in anhydrous solution and subsequent hydrogenation with sodium triacetoxyborohydride.

Unfortunately, recrystallization from acetonitrile of the crude product, obtained after the workup of the reaction mixture, gave H₃SIM¹ in a yield of only 27%. However, a purification procedure via column chromatography was developed to yield H₃SIM¹ in slightly higher yield of 30%. A similar method was also used for the purification of the symmetric ligand H₃L², prepared for comparison according to published procedures.^{109, 114}

2.3 SYNTHESIS OF LIGAND HSIM²

Ligand HSIM² was designed with two amino functionalities adjacent to one binding site, in order to study the influence of the steric hindrance contrived by the bulky pivaloyl-amide residues in H₃SIM¹ with unchanged position of the hydrogen bonding donors. Moreover, comparison to the published ligand HL¹, lacking hydrogen bond donors, and to HL⁸, bearing two amine functionalities in a symmetric manner, enables the investigation of the effect of the two asymmetrically incorporated amino substituents.

Ligand HSIM² is accessible by deprotection of the two pivaloyl-amide moieties of ligand H₃SIM¹. Therefore, the cleavage of the protecting amide bonds in ligand H₃SIM¹ was studied under various conditions. It was determined that deprotection of H₃SIM¹ under acidic conditions results in decomposition, similar to the chemistry previously detected during treatment of H₃L² with hot hydrochloric acid.¹⁰⁹ However, heating of H₃SIM¹ in ethanol solution under basic conditions at 70° for three days was efficient (Scheme 8). Microwaves radiation under basic conditions also promotes the deprotection of H₃SIM¹, but this could not be undertaken on a larger scale due to instrumental restrictions.



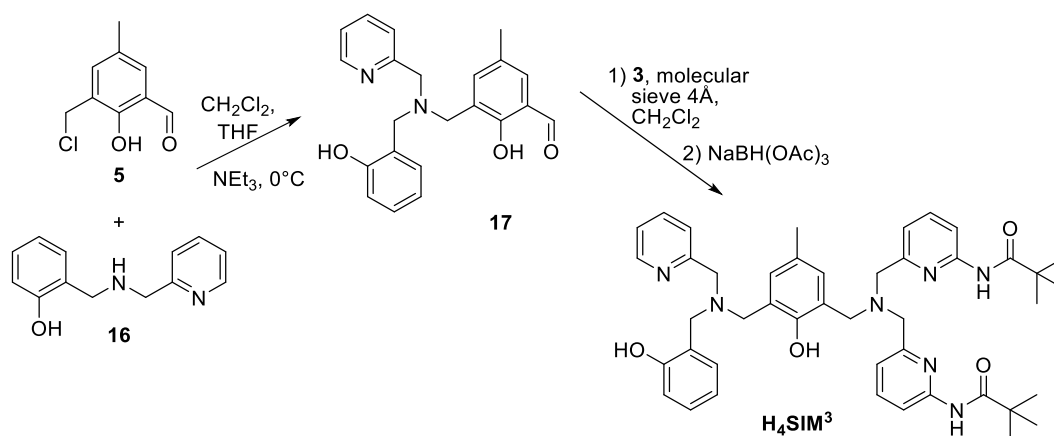
Scheme 8: Synthesis of ligand HSIM².

Purification of the crude product of HSIM² obtained after workup of the reaction mixture was undertaken via column chromatography with alumina.

2.4 SYNTHESIS OF LIGAND H₄SIM³

The paradigm for the construction of PAP biomimetics, both structural and functional, is that the ligands permit discrimination between trivalent and divalent metal ions and therefore bear the capacity to stabilize a heterodinuclear site. Furthermore, the pivaloyl-amide residues were incorporated into the asymmetric ligand H₂L⁴, leading to H₄SIM³ and H₄SIM⁴, in order to provide both the capability of coordination asymmetry and the ability for hydrogen bonding of the substrate and/or nucleophile. Both ligands provide two different coordination pockets: a softer nitrogen-rich N₃O compartment for the divalent metal ion and a harder N₂O₂ donor set in the other binding site for the trivalent metal ion.

Ligand H₄SIM³ was accessible applying the optimized procedure for the synthesis of ligand H₃SIM¹ using compound **16** as secondary amine in the first step (Scheme 9). Compound **16** was synthesized after a published method by reaction of salicylaldehyde with 2-(aminomethyl)pyridine and subsequent treatment with sodium borohydride (99% yield).^{124, 125}

Scheme 9. Synthesis of ligand H_4SIM^3 .

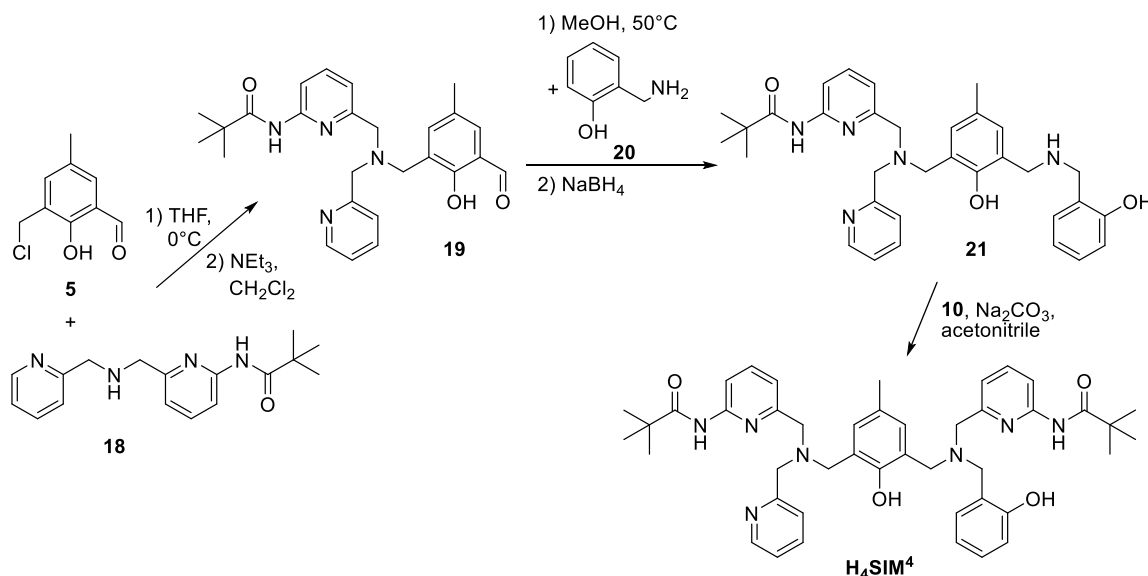
This secondary amine **16** was used as nucleophile after treatment with triethylamine in the nucleophilic substitution with compound **5** generating compound **17** in a moderate yield of 55%. The second amine side-arm was introduced by treatment of compound **17** with compound **3** under anhydrous conditions and following hydrogenation with sodium triacetoxyborohydride. Purification of the crude product of H_4SIM^3 obtained after workup of the reaction mixture was undertaken with column chromatography with silica.

2.5 SYNTHESIS OF LIGAND H_4SIM^4

In H_4SIM^3 the hydrogen bond donating pivaloyl-amide residues are incorporated in an asymmetric manner as both are proximal to one binding site. Furthermore, the symmetric counterpart of H_4SIM^3 , H_4SIM^4 , was designed bearing one pivaloyl-amide residue proximal to both binding sites and thus combining an asymmetric primary coordination sphere with a symmetric primary coordination sphere regarding the two metal centers.

For the synthesis of H_4SIM^4 the synthetic strategy applied for the preparation of H_3SIM^1 and H_4SIM^3 was changed slightly. Instead of attaching two secondary amines to the asymmetric phenol building block, the second coordination site was built up in two steps due to the better accessibility of the reactants (Scheme 10). In the first step the secondary amine **18** was used as nucleophile for substitution of the chloro functionality of compound **5**. In this way, compound **19** was formed in 96% yield. Compound **18** containing only one amidated pyridine was synthesized as published previously.^{109, 114} Thereby, the dibrominated byproduct **14** obtained by bromination of compound **9** (Scheme 6) was treated with silver nitrate in acetone to generate a formyl functionality, *i.e.* *N*-(6-formylpyridine-2-yl)pivalamide. Subsequent amination with 2-(aminomethyl)pyridine and hydrogenation with sodium borohydride yield compound **18** in an overall yield of 95% for the two reaction steps.

Amination of the remaining aldehyde functionality of compound **19** with 2-(aminomethyl)phenol (**20**) and subsequent hydrogenation with sodium borohydride resulted in compound **21**. 2-(aminomethyl)phenol (**20**) was prepared according to a literature known procedure by reduction of salicylamide with borane/tetrahydrofuran complex.¹²⁶ Compound **21** was converted to ligand H₄SIM⁴ by nucleophilic substitution using compound **10** as reactant.



Scheme 10: Synthesis of ligand H₄SIM⁴.

Similar to the synthetic procedures of H₃SIM¹ and H₄SIM³, the crude product of H₄SIM⁴ was purified via column chromatography.

2.6 SUMMARY

Four asymmetric, dinucleating ligands were designed and prepared, which provide two different coordination sites, mimicking the peptide backbone surrounding the dimetallic core in the active site of phosphatases. Ligand H₃SIM¹ and HSIM² are derivatives of HL¹, but with the capacity to form a hydrogen bonding network to the substrate/nucleophile during the catalytic hydrolysis of phosphoesters as present in the active site of the native enzymes. In HSIM² two amino substituents function as hydrogen bond donors, the groups capable to form hydrogen bonds in H₃SIM¹ are two sterically demanding pivaloyl-amide residues. In both HSIM² and H₃SIM¹ the hydrogen bond donors are positioned in an asymmetric manner regarding the two coordination sites, while in the previously published ligand H₃L² two pivaloyl-amide residues have been incorporated into HL¹ in a symmetrical fashion. Similarly, two derivatives of H₂L⁴ have been developed bearing two pivaloyl-amide residues either in a symmetric (H₄SIM⁴) or an asymmetric fashion (H₄SIM³). Thus, these two ligands H₄SIM³ and H₄SIM⁴ provide two distinct coordination

sites, a softer N_3O and a harder N_2O_2 , and are therefore able to discriminate the coordination of tri- and divalent metal ions. For the synthesis of H_3SIM^1 and H_4SIM^3 a three step approach starting with 2-hydroxy-3-(hydroxymethyl)-5-methylbenzaldehyde was evaluated similar to Nordlander *et al.*,¹⁰⁷ but avoiding the delicate chlorination with thionylchloride. H_4SIM^4 was prepared in a similar procedure except of the stepwise generation of the second coordination site. The synthesis of $HSIM^2$ was realized by deprotection of ligand H_3SIM^1 under basic conditions. The detailed synthetic procedures and analytic results are given in Chapter 11.

Chapter 3

Coordination Behavior of Asymmetric Ligands^c

^c Main parts of this chapter will be published in “Selective Coordination of Gallium(III), Zinc(II) and Copper(II) by an Asymmetric Dinucleating Ligand: A Model for Metallophosphatases”; [Simone Bosch](#), Peter Comba, Lawrence R. Gahan, Graeme R. Hanson, Christopher J. Noble, Gerhard Schenk, Hubert Wadepohl; manuscript in preparation.

3.1 INTRODUCTION

As certain hydrolases are of particular interest in the development of biologically active compounds against many diseases, there is special interest in understanding the detailed mechanism of the reaction which takes place within their active sites.¹²⁷ In addition to enzymatic studies, modeling the structure and reactivity of the corresponding metalloenzymes using model complexes has been shown to be very instructive in the study of the structural and functional properties of the enzymes themselves.

Several classes of metalloenzymes have a dinuclear active site in which two metal ions cooperate in order to perform the transformation of various substrates. Representative examples of structurally characterized homo- and heterodinuclear active sites relevant for hydrolysis include those in Alkaline Phosphatase [$Zn^{II}Zn^{II}$],⁶⁴ Purple Acid Phosphatase ($[Fe^{III}Zn^{II}]$,^{83, 128} $[Fe^{III}Fe^{II}]$,^{27, 129} $[Fe^{III}Mn^{II}]$ ^{67, 85}), human Protein Phosphatase 1 $[Fe^{III}Mn^{II}]$ ¹³⁰ and bovine erythrocyte Superoxide Dismutase $[Cu^{II}Zn^{II}]$.¹³¹⁻¹³³ In the homo- and heterodinuclear active sites of these metalloenzymes the surrounding protein matrix usually provides chemically distinct binding environments for the individual metal centers. Although it is known that the lack of symmetry of the active center is an essential structural feature and decisive factor for the catalytic mechanism and efficiency,^{107, 134, 135} there are only a few well-characterized heterodinuclear complexes as model systems for hydrolases.^{29, 81, 136} The paucity of examples is possibly attributable to the relatively late discovery of heterodinuclear metalloenzymes, but is more likely due to the difficulties in the selective binding of two metal ions at specific sites in the complexes. Nature has had millions of years to perfect site selectivity, unlike coordination chemists.

A challenge in the preparation of PAP biomimetics is the requirement for the stabilization of a heterovalent dinuclear core,⁸¹ because the coordination of two different metal ions by a dinucleating ligand may result in the formation of both discrete homo- and heterodinuclear complexes, and metal site isomers in which the sites are crystallographically disordered occupied. These complications have been circumvented somewhat by designing ligands that either bind metal ions selectively in their pockets or strongly enough to prevent disproportionation and metal mixing.¹³⁷

Some heterovalent and heterometallic systems have been prepared by using symmetrical ligands such as HL¹, HL⁹, HL¹⁰, HL¹¹ etc. (see Table of Compounds), which do not exhibit metal site selectivity, but offer the opportunity to prepare heterometallic or heterovalent complexes by careful control of the synthetic conditions. Examples include the biomimetics for the

heterodivalent reduced form of PAP, $[\text{Fe}^{\text{III}}\text{Fe}^{\text{II}}(\text{L}^{\text{11}})(\text{OAc})_2](\text{BPh}_4)_2$, and the mixed-valent $\text{Fe}^{\text{III}}\text{Fe}^{\text{II}}$ and $\text{Fe}^{\text{III}}\text{Zn}^{\text{II}}$ complexes of HL^1 , $[\text{Fe}^{\text{III}}\text{Fe}^{\text{II}}(\text{L}^1)(\text{OPr})_2](\text{BPh}_4)_2$ and $[\text{Fe}^{\text{III}}\text{Zn}^{\text{II}}(\text{L}^1)(\text{OAc})_2](\text{BPh}_4)_2$; crystallographic analysis of the latter suggests the presence of a small degree of disorder in the metal occupancies.^{138, 139} However, in many cases the issue of disorder and non-site-selectivity has not been addressed, perhaps not even considered.

Another strategy to circumvent the difficulties in selective binding of two different metal centers has been the use of asymmetric ligands bearing two binding pockets which differ either in the number and/or the type of coordinating donors. One of the most common ligands used for this purpose is H_2L^4 (Chart 7) which contains a harder N_2O_2 metal ion binding site (A) and a softer N_3O metal ion binding site (B). Using H_2L^4 a variety of heterodinuclear model complexes, which mimic the active site structure of PAP more adequately, has been developed and characterized; examples include $[\text{Fe}^{\text{III}}\text{Fe}^{\text{II}}(\text{L}^4)(\mu\text{-OAc})_2]^+$,¹⁴⁰ $[\text{Fe}^{\text{III}}\text{Fe}^{\text{II}}(\text{L}^4)(\mu\text{-OBz})_2]^+$,¹⁰⁶ $[\text{Fe}^{\text{III}}\text{Cu}^{\text{II}}(\text{L}^4)(\mu\text{-OAc})_2]^+$,⁹² $[\text{Fe}^{\text{III}}\text{Mn}^{\text{II}}(\text{L}^4)(\mu\text{-OAc})_2]^+$,⁹⁶ $[\text{Fe}^{\text{III}}\text{Ni}^{\text{II}}(\text{L}^4)(\mu\text{-OAc})_2]^+$,¹⁴¹ $[\text{Fe}^{\text{III}}\text{Ni}^{\text{II}}(\text{L}^4)(\mu\text{-OAc})(\text{OH}_2)_2]^{2+}$,¹⁴² $[\text{Fe}^{\text{III}}\text{Zn}^{\text{II}}(\text{L}^4)(\mu\text{-OAc})_2]^+$,¹⁴³ $[\text{Fe}^{\text{III}}\text{Zn}^{\text{II}}(\text{L}^4)(\text{OH}_2)(\mu\text{-OH})]^{2+}$,^{90, 144} $[\text{Fe}^{\text{III}}\text{Cd}^{\text{II}}(\text{L}^4)(\mu\text{-OAc})_2]^+$,¹⁴⁵ $[[\text{Fe}^{\text{III}}\text{Hg}^{\text{II}}(\text{L}^4)(\mu\text{-OH})]_2]^{2+}$,¹⁴⁵ $[\text{Fe}^{\text{III}}\text{Co}^{\text{II}}(\text{L}^4)(\mu\text{-OAc})_2]^+$,¹⁴⁶ $[\text{Ga}^{\text{III}}\text{Co}^{\text{II}}(\text{L}^4)(\mu\text{-OAc})_2]^+$,¹⁴⁶ $[\text{Ga}^{\text{III}}\text{Zn}^{\text{II}}(\text{L}^4)(\mu\text{-OAc})_2]^{+66}$ and $[\text{Mn}^{\text{III}}\text{Mn}^{\text{II}}(\text{L}^4)(\mu\text{-OAc})_2]^+$.^{147, 148} The preparation procedure for these complexes commonly involves the simultaneous or stepwise addition of two different metal salts to the ligand solution, where the selective formation of heterodinuclear complexes is theoretically possible. However, investigations of the species distribution were not always undertaken. In at least one case, selective binding has been investigated. Belle *et al.* illustrated a very elegant way to study the selective binding of ligand H_3L^{12} of zinc(II) ions by NMR spectroscopy via stepwise addition of zinc(II) salt, thereby demonstrating that H_3L^{12} selectively forms a monozinc(II) complex, in which the zinc(II) is coordinated to the N_3O binding compartment.¹⁴⁹ This finding was confirmed by the crystal structure of $[\text{Fe}^{\text{III}}\text{Zn}^{\text{II}}(\text{L}^{12})(\mu\text{-O}_2\text{P}(\text{OPh})_2)_2]$ which was obtained after further addition of triethylamine and iron(III) perchlorate to the monozinc(II) synthon.¹⁴⁹ Similarly, the respective $\text{Fe}^{\text{III}}\text{Cu}^{\text{II}}$ complex $[\text{Fe}^{\text{III}}\text{Cu}^{\text{II}}(\text{L}^{12})(\mu\text{-OEt})]\text{ClO}_4$ was prepared by the stepwise complexation of Cu^{II} in the softer binding compartment and Fe^{III} in the harder coordination site after addition of triethylamine.¹⁵⁰ The site-directed complexation was confirmed by the crystal structure of the mononuclear complex $[\text{Cu}^{\text{II}}(\text{H}_3\text{L}^{12})(\text{OAc})]\text{BPh}_4$;¹⁵⁰ this study represents one of the few cases when the mononuclear synthon during the synthesis of heterovalent dinuclear complexes was isolated.

Heterovalent dinuclear model complexes have successfully modeled the physicochemical properties of metalloproteins and even the catalytic activity, but with a much lower efficiency. This discrepancy between the catalytic efficiencies of model systems and native enzymes is suggested, to a large extent, to be due to the lack of many important intermolecular interactions.

In many cases, the amino acid residues close to the active site are known to be necessary for efficient enzymatic activity because mutation of these residues can cause deactivation or even inactivation of the catalyst.^{74, 151} For example, in PAP, histidine residues proximal to the metal centers in the active site have been shown to play an essential role in substrate binding and activation; mutations of a histidine to an alanine residue in the second coordination sphere of kbPAP resulted in a sharp decrease in activity.⁷⁴ Moreover, theoretical studies have recently reinforced the importance of the proximal histidine residues within the active site of PAP to properly describe coordination of the substrate and stabilization of the transition state.^{151, 152} Furthermore, Comba *et al.* developed a Fe^{III}Fe^{II} model complex with hydrogen bond donors in close distance to the catalytic site, which presented the highest catalytic efficiency ever reported for a PAP model in relation to phosphodiester hydrolysis.¹⁰⁸ Similarly, the extension of a Fe^{III}Zn^{II} PAP model complex by (3-aminopropyl)silica and a Fe^{III}Cu^{II} PAP model complex by a small polyethyleneimine chain led to an increase in phosphoester hydrolysis activity. This finding was attributed to the interaction of the polar side chains with the substrate, mimicking in this way the microenvironment around the active site of the native enzymes.^{151, 153}

As part of the effort to probe the properties of biologically important, mixed valent, dinuclear centers, and to consider the hydrogen bond network of the second coordination sphere of the native metalloproteins, as well as the influences of asymmetric binding sites, three ligands have been synthesized (Chart 7). In this chapter coordination behavior studies of these asymmetric ligands towards Zn^{II}, Cu^{II}, Ga^{III} and Fe^{III} ions will be discussed, in addition to their ability to selectively form a mononuclear synthon, which can then potentially be used to synthesize authentic heterodinuclear model complexes for PAP.

The choice of the metal ions in this study (Zn^{II}, Cu^{II}, Ga^{III}, and Fe^{III}) is driven by a number of factors. The use of Zn^{II} ions is inspired by the fact that many (> 300) metalloenzymes incorporate Zn^{II} within their active sites.^{30, 154-156} Although Cu^{II} has not been found in native phosphatases, it was chosen to be studied within this thesis as there are some Cu^{II} complexes showing catalytic activity towards phosphoester hydrolysis acceleration; Kovari *et al.* developed monocopper(II) complexes bearing ammonium groups proximal to the metal center which revealed a higher bis(4-nitrophenyl)phosphate (BNPP) hydrolysis rate than its Zn^{II} counterpart;¹⁵⁷⁻¹⁵⁹ Neves *et al.* showed asymmetric dicopper(II) complexes accelerated phosphoester hydrolysis, especially via the introduction of a sterically demanding group in close distance to the metal centers;^{160, 161} Chin *et al.* investigated a 6000-fold acceleration of bis(2,4-dinitro-phenyl)phosphate (BDNPP) hydrolysis by the introduction of amino groups in a Cu^{II}-*o*-phenanthroline complex;¹⁶² and recently Comba *et al.* reported the phosphatase activity of a dicopper(II) complex of a cyclic pseudopeptide.¹⁶³

Cu^{II} has, similar to Zn^{II}, substitutional flexibility and a relatively high ionization potential/Lewis acidity (see Table 1), which makes it both promising in regards to polarize P-O bonds in phosphate ester substrates and to activate the phosphorus center towards nucleophilic attack.

Table 1: Selected physico-chemical properties of metal ions relevant to this work.

ion	ionic radius (Å) ^a 164	charge density (Z/r) (Å ⁻¹) ^a 164	ionization potential (eV) ¹⁶⁴	pK _a of bound H ₂ O ¹⁶⁵	k _{sub} (s ⁻¹) ^b 166
Zn ^{II}	0.74	2.7	17.96	9.0	~ 6·10 ⁸
Cu ^{II}	0.73	2.8	20.29	8.0	4.4·10 ⁹
Fe ^{II}	0.61	3.3	16.19	9.5	4.4·10 ⁶
Ga ^{III}	0.62	4.8	30.73	2.6	4.0·10 ²
Fe ^{III}	0.55	5.5	30.65	2.2	1.6·10 ²

^a ionic radii in crystals for a coordination number of 6.

^b water exchange rate of the hexaaqua metal complexes in water at 25°C.

Additionally, the pK_a values of water molecules ligated to Cu^{II} and Zn^{II} ions often fall in the range of 7-9, enabling complexes of these ions to promote hydrolytic reactions under physiological or near physiological conditions.¹¹ Moreover, the study of their coordination chemistry is feasible spectroscopically with NMR spectroscopy in the case of Zn^{II} and EPR spectroscopy in the case of Cu^{II}, besides mass spectrometry, UV-vis-NIR spectroscopy and X-ray diffraction.

The investigation of Ga^{III} coordination by the asymmetric ligands was chosen as it is an excellent mimic of Fe^{III} with a similar ionic radius and Lewis acidity (Table 1). Furthermore, the Fe^{III} center in pig PAP and bovine spleen PAP has been replaced by Ga^{III}, resulting in Ga^{III}Fe^{II} and Ga^{III}Zn^{II} derivatives, which exhibit catalytic activities similar to those of the native forms.^{66, 142, 167} These findings give evidence that diamagnetic Ga^{III} can act as a functional analogue of the paramagnetic Fe^{III} site in PAP model systems. Therefore, it is optimally suited to mimic Fe^{III} ions when NMR techniques are used. Ga^{III} is characterized by a well-defined coordination chemistry and absence of redox chemistry, which allows detailed reactivity studies without interference due to competing oxidation states.

In the present chapter the complexation studies of the asymmetric ligands H₃SIM¹, H₄SIM³ and H₄SIM⁴ (Chart 7) with Zn^{II}, Cu^{II}, Ga^{III}, and Fe^{III} ions are reported. Although the primary coordination sphere of the two coordination sites are equivalent in H₃SIM¹, the secondary coordination sphere differs due to two pivaloyl-amide moieties adjacent to one binding site (binding site C). H₄SIM³ and H₄SIM⁴ provide two distinctly different binding compartments: a N₃O donor set in the softer compartment (binding site C and binding site E) *versus* a rather harder N₂O₂ binding pocket (binding site A and binding site D) (Chart 7). While H₄SIM³ and H₄SIM⁴ bear equal primary coordination spheres, the secondary coordination spheres differ in regard to the position of the two pivaloyl-amide moieties proximal to the metal centers.

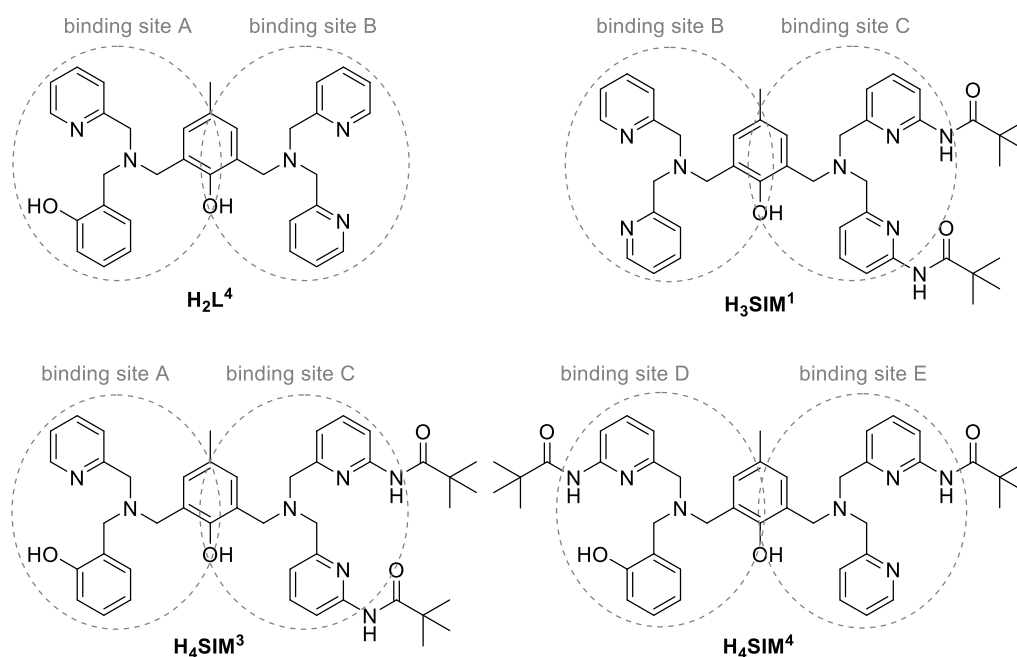


Chart 7: Ligands discussed in this chapter and the nomenclature of their binding compartments.

3.2 COMPLEXATION BEHAVIOR OF LIGAND H₃SIM¹

Although ligand H₃SIM¹ (Chart 8) provides two coordination pockets with identical primary coordination spheres, built up by a bridging phenoxido group, a tertiary amine and two pyridine moieties, the two coordination sites differ in their surroundings.

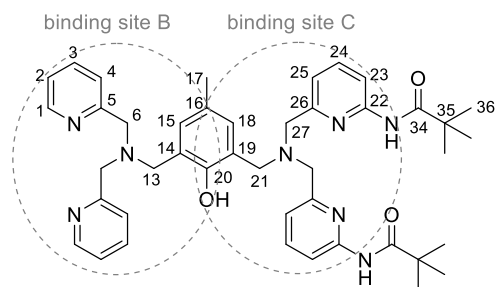


Chart 8: Assignment of the binding sites provided by ligand H₃SIM¹ and the numbering of its atoms.

While binding site B (see Chart 8 for the nomenclature) offers an unhindered access to the ligating atoms, binding site C is sterically hindered by the demanding pivaloyl-amide substituents of the pyridine side-arms. Therefore, the requirement of two inequivalent binding sites as present in native phosphatases is given in this ligand.

3.2.1 COMPLEXATION STUDIES WITH ZN^{II}

The coordination features of ligand H₃SIM¹ towards Zn^{II} ions were analyzed using NMR spectroscopic techniques. Aliquots of an acetonitrile solution of zinc(II) perchlorate (0.518 M)

were added stepwise to the ligand dissolved in acetonitrile (33.6 mM). After each addition, the mixture was heated for five minutes at 50°C and the ^1H NMR spectrum was then monitored to follow the changes in the proton environments. ^{13}C NMR spectra were recorded and two-dimensional NMR experiments (NOESY, COSY, HSQC, and HMBC) were undertaken after addition of one and after addition of two equivalents of metal salt. In addition, mass spectra were recorded of the samples employed in the NMR experiments.

NMR Studies

Stepwise addition of zinc(II) perchlorate to H_3SIM^1 in deuterated acetonitrile resulted in a slight shift of the resonances and the initial rise of a second set of resonances, while the resonances assigned to the free ligand decreased (Figure 1). In the spectrum of a 1:1 mixture of zinc(II) perchlorate and H_3SIM^1 the resonances assigned to the ligand disappeared and only a set of nine resonances assigned to the monozinc(II) complex remained (Figure 1d). Further addition of Zn^{II} ions led to the decrease of the resonances assigned to the monozinc(II) complex and the appearance of a set of resonances assigned to the dizinc(II) complex. After the addition of two equivalents of Zn^{II} ions to H_3SIM^1 only the dizinc(II) complex is present in the solution, according to the ^1H NMR spectrum (Figure 1g).

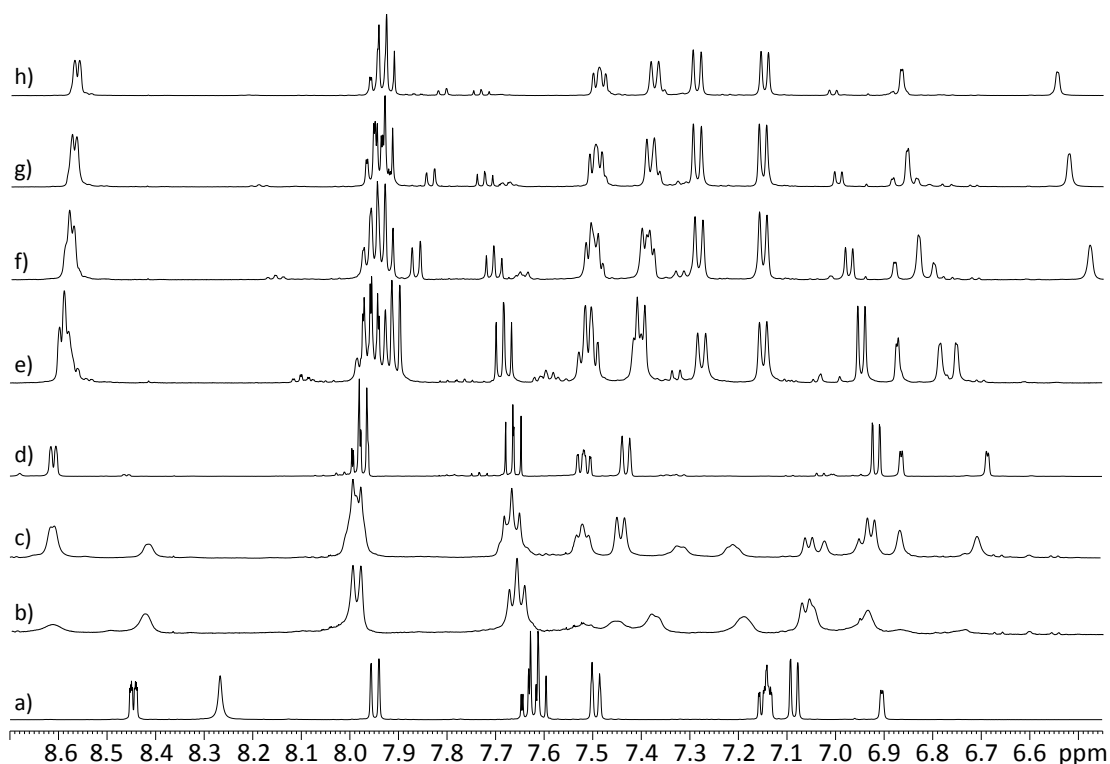


Figure 1: Comparison of ^1H NMR spectra of a) H_3SIM^1 with b) 0.50 eq, c) 0.75 eq, d) 1.00 eq, e) 1.50 eq, f) 1.75 eq, g) 2.00 eq, and h) 2.50 eq $\text{Zn}^{\text{II}}(\text{ClO}_4)_2$ in $\text{CD}_3\text{CN}/\text{D}_2\text{O}$.

There is a possibility that the equilibrium between monozinc(II) complexes, in which the Zn^{II} ion is coordinated in either of the two coordination sites, is more rapid than the NMR time scale.

Therefore, in order to investigate this possibility the variable temperature ^1H NMR spectra of the monozinc(II) complex and the dizinc(II) complex were recorded in the temperature range from 282 K to 245 K. No change in the spectra were detected, suggesting that the Zn^{II} ion is selectively bound to one coordination site only.

In order to investigate the exact position of the Zn^{II} ion within the monozinc(II) complex all resonances in the spectra of the monozinc(II) as well as the dizinc(II) complex species were assigned to the corresponding H-atoms (Figure 2). Two dimensional NMR methods were employed: Firstly, the COSY NMR spectra were used to assign the resonances of the pyridyl H-atoms. $H1$ (d) is the most characteristic H-atom, the resonance of which is shifted downfield due to its *ortho* position to the pyridine N-atom (see Chart 8 for the atom numbering). Commencing with the identified resonance of $H1$ (d), the resonances of $H2$ (d), $H3$ (t) and $H4$ (d) were assigned by their cross peaks in the COSY NMR spectrum and their characteristic splitting (given in brackets). The remaining resonance in the region between 6.5 ppm and 8.7 ppm of the ^1H NMR spectra, which is split in a triplet, was allocated to $H24$ (t) due to its position between two similar pyridine H-atoms. The two resonances connected by a cross peak to the $H24$ resonance and split in doublets are assigned to $H23$ (d) and $H25$ (d) (the specific assignments were determined by cross peaks in the HMBC NMR spectra between $C26$ and $H25$). Similarly, the remaining two singlets in the aromatic region of the ^1H NMR spectra were assigned to $H15$ (s) and $H18$ (s) (the specific correlation was assigned by cross peaks to the respective methylene C-atom, $C13$ and $C21$, in the HMBC spectra). Subsequently, HSQC and HMBC NMR spectra were used to assign the ^{13}C NMR resonances. The resonances of the methylene H-atoms were allocated by interpretation of the cross peaks in the HMBC NMR spectra.

The comparison of the interpreted ^1H NMR spectra of the free ligand, the monozinc(II) and the dizinc(II) species, depicted in Figure 2, revealed that in the case of the monozinc(II) complex, particularly the resonances of the pyridine H-atoms in binding site B, underwent shifts compared to the analogous resonances in the spectrum of the free ligand, while the resonances corresponding to the H-atoms of binding site C were almost unaffected. However, addition of a second equivalent of the zinc(II) salt resulted in a shift of the amidated pyridine H-atom resonances, while the resonances corresponding to H-atoms in binding site B remained almost at the same positions as in the spectrum recorded of the monozinc(II) complex. Moreover, the resonance of $H6$, which was present in form of a singlet in the spectrum of the free ligand, split to a doublet of doublets after addition of one equivalent of zinc(II) perchlorate. All other methylene resonances remained as singlets. The addition of a second equivalent of zinc(II) perchlorate resulted in a splitting of the resonance of $H27$. It is suggested that the splitting of the resonances arises from the constrained flexibility of the methylene groups by coordination,

leading to two H-atoms bound to the same C-atom but in different electronic environments. Furthermore, the characteristic ^{13}C resonance of the amide carbonyl C-atom experienced only a slight shift from 177.9 ppm to 178.8 ppm by the formation of a monozinc(II) complex, but after coordination of the second Zn^{II} ion this resonance is found at 184.2 ppm.

These findings are interpreted as the Zn^{II} ions being bound regioselectively by the amide-free coordination site up to the addition of one equivalent of zinc(II) perchlorate, leading to the sole formation of a monozinc(II) complex. Only when a higher than equimolar amount of Zn^{II} ions is present in solution the dizinc(II) complex of ligand H_3SIM^1 was generated. It is worth mentioning that the same results were obtained when the experiment was conducted in deuterated methanol.

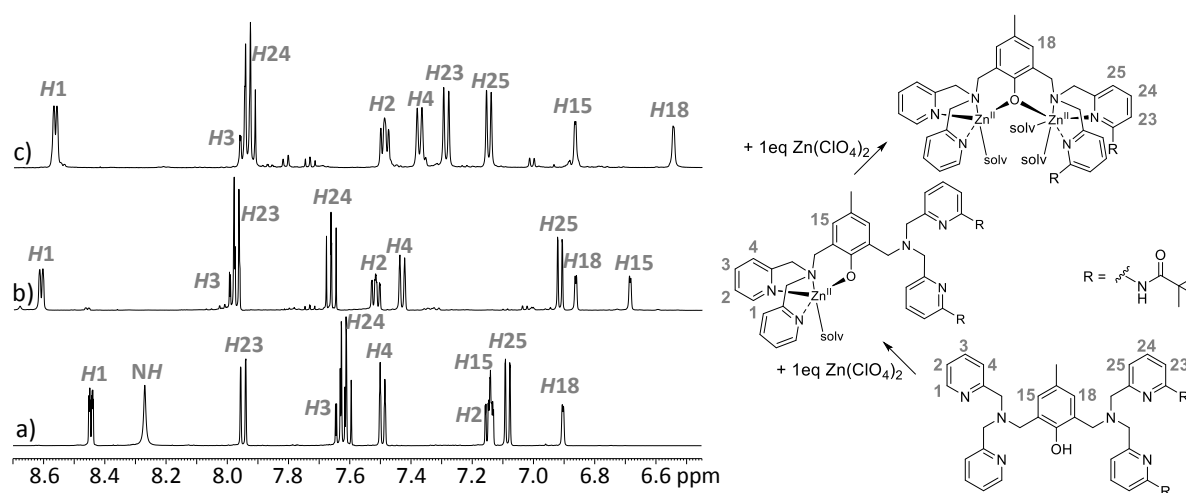


Figure 2: Comparison of ^1H NMR spectra of a) H_3SIM^1 in CD_3CN , b) with 1 eq, and c) 2 eq $\text{Zn}^{\text{II}}(\text{ClO}_4)_2$.

The distinct coordination of zinc(II) ions to the two unequal binding sites in ligand H_3SIM^1 is also observed in the X-ray structure of $[\text{Zn}^{\text{II}}_2(\text{H}_2\text{SIM}^1)(\mu\text{-OAc})(\text{OH})]\text{PF}_6$, which will be discussed in Chapter 4.3 in more detail. In that structure the Zn^{II} ion bound to coordination site C is six coordinated, while the Zn^{II} ion in binding site B forms a trigonal bipyramidal coordination geometry.

Mass Spectrometry

During the NMR titration experiments samples were taken and ESI^+ mass spectra recorded. The mass spectrum of the equimolar solution of H_3SIM^1 and zinc(II) perchlorate showed, in addition to the peak assigned to free ligand, peaks with the isotopic pattern characteristic for a monozinc(II) species (Figure 3a). The main species at m/z 791.3 could be assigned to $[\text{Zn}^{\text{II}}(\text{H}_2\text{SIM}^1)]^+$. In the mass spectra conducted with the sample taken after addition of two equivalents of zinc(II) perchlorate to H_3SIM^1 the peaks show the characteristic isotopic pattern for dizinc(II) species (Figure 3b). In this case the main peak at m/z 951.3 was assigned to the

species $[\text{Zn}^{\text{II}}_2(\text{D}_2\text{SIM}^1)(\text{CH}_3\text{OH})_2(\text{CH}_3\text{O})]^+$. Therefore, the results obtained from mass spectrometry support the assumption of a stepwise coordination of Zn^{II} ions by the asymmetric ligand H_3SIM^1 .

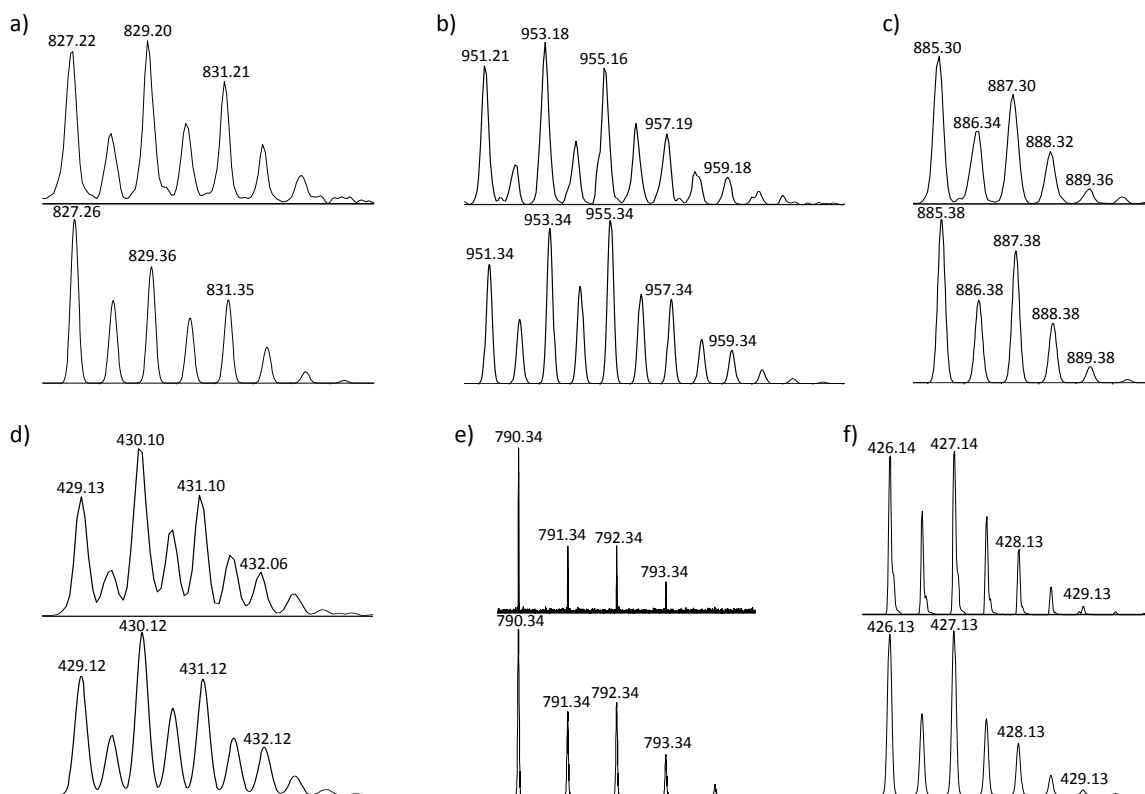


Figure 3: Characteristic isotopic pattern found in ESI^+ mass spectrometric results (experimental (top) and calculated (bottom)) of H_3SIM^1 with a) 1 eq of $\text{Zn}^{\text{II}}(\text{ClO}_4)_2$ ($[\text{Zn}^{\text{II}}(\text{H}_2\text{SIM}^1)(\text{H}_2\text{O})_2]^+$), b) 2 eq of $\text{Zn}^{\text{II}}(\text{ClO}_4)_2$ ($[\text{Zn}^{\text{II}}_2(\text{H}_2\text{SIM}^1)(\text{CH}_3\text{O})_2(\text{CD}_3\text{O})]^+$), c) 2 eq of $\text{Ga}^{\text{III}}(\text{NO}_3)_3$ ($[\text{Ga}^{\text{III}}(\text{H}_2\text{SIM}^1)(\text{H}_2\text{O})_4(\text{OH})]^+$), d) 1 eq of $\text{Zn}^{\text{II}}(\text{ClO}_4)_2$ and 1 eq of $\text{Ga}^{\text{III}}(\text{NO}_3)_3$ ($[\text{Ga}^{\text{III}}\text{Zn}^{\text{II}}(\text{SIM}^1)]^{2+}$) e) 1 eq of $\text{Cu}^{\text{II}}(\text{OTf})_2$ ($[\text{Cu}^{\text{II}}(\text{H}_2\text{SIM}^1)]^+$) and f) 2 eq of $\text{Cu}^{\text{II}}(\text{OTf})_2$ ($[\text{Cu}^{\text{II}}_2(\text{HSIM}^1)]^+$) in methanol.

3.2.2 COORDINATION STUDIES WITH Ga^{III}

Analogous to the Zn^{II} coordination behavior of ligand H_3SIM^1 , the coordination chemistry of H_3SIM^1 with Ga^{III} ions was investigated employing the NMR titration method, using gallium(III) nitrate or gallium(III) perchlorate as metal source. In these experiments the reaction mixtures were heated for 45 minutes at 50°C after every second addition, to ensure complete complexation.

NMR Studies

Figure 4 shows the coordination process monitored by ^1H NMR spectroscopy while gallium(III) nitrate dissolved in D_2O (0.518 M) was added stepwise to H_3SIM^1 in CD_3CN (33.6 mM). Initially, the increase of the Ga^{III} ion concentration resulted in the formation of a new species. In the equimolar mixture of H_3SIM^1 with gallium(III) nitrate only one species was present and its ^1H NMR

spectrum remained unchanged during addition of further gallium(III) salt. These results indicate that H_3SIM^1 forms selectively a monogallium(III) complex.

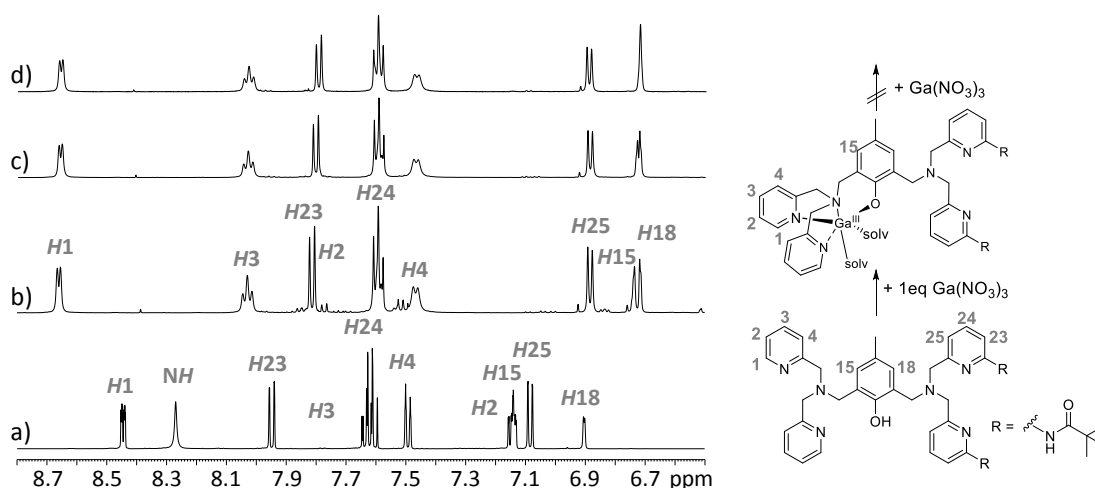


Figure 4: Comparison of 1H NMR spectra of a) H_3SIM^1 in CD_3CN , with b) 1.00 eq, c) 1.50 eq and d) 2.00 eq $Ga^{III}(NO_3)_3$ in D_2O .

The assignment of the resonances clarified the exact position of the Ga^{III} ion in the monogallium(III) complex. While the resonances associated to binding site C, $H18$, $H23$, $H25$, were shifted upfield by about 0.2 ppm, or were not effected as in the case of $H24$, when one equivalent of gallium(III) nitrate is present in solution, the impact on the resonances of binding site B is more pronounced. The resonances of $H1$, $H2$ and $H3$ exhibit a downfield shift of up to 0.4 ppm, and $H15$ revealed an upfield shift by 0.4 ppm. Furthermore, the carbonyl ^{13}C NMR resonance was found at 179.4 ppm, which is similar to the resonance observed in the spectrum of the monozinc(II) complex in which the Zn^{II} ion is bound in the amide-free binding site. In the case of the methylene resonances, only the resonance of $H6$ split into two doublets upon complexation with Ga^{III} , suggesting the position of the Ga^{III} ion in binding site B, as depicted in Figure 4.

Mass Spectrometry

The mass spectrometric measurement of a sample taken from the NMR titration experiment after addition of two equivalents of gallium(III) nitrate resulted in a spectrum with the main peak found at m/z 885.3. This peak shows the characteristic pattern for a species containing a single Ga^{III} ion (Figure 3c) and was assigned to the monogallium(III) complex $[Ga^{III}(H_2SIM^1)(OH)(OH_2)_4]^+$.

X-ray Diffraction

During heating a solution of H₃SIM¹ (40.3 mM) in deuterated methanol with one equivalent of gallium(III) perchlorate at 50°C, a white solid precipitated after about 15 minutes. Recrystallization of this solid from acetonitrile with diffusion of diethyl ether yielded white crystals suitable for X-ray data collection. Figure 5 shows a plot of the molecular structure, and Table 2 gives selected structural parameters (Table 2 also includes structural parameters of [Ga^{III}Zn^{II}(H₂SIM¹)(OAc)₂(μ-OH)]⁺ which will be introduced at a later point). The structure consists of a [Ga^{III}(H₂SIM¹)(μ-OH)]⁺ dimer, in which the two Ga^{III} ions are coordinated in an octahedral geometry and bridged by two hydroxido ions (Figure 5a). The remaining coordination sites of the Ga^{III} ion in the monomer subunit (Figure 5b) are occupied by two pyridines, the tertiary amine and the phenolate donor groups provided by the ligand. Moreover, hydrogen bonding between the pivaloyl amide moieties of the metal-free binding site C and perchlorate oxygen atoms (3.154 Å and 3.120 Å) is visualized in the plot of Figure 5b.

Table 2: Selected bond lengths (Å) and angles (°) for [Ga^{III}(H₂SIM¹)(μ-OH)]⁺ and [Ga^{III}Zn^{II}(H₂SIM¹)(OAc)₂(μ-OH)]⁺.

	[Ga ^{III} (H ₂ SIM ¹)(μ-OH)] ⁺	[Ga ^{III} Zn ^{II} (H ₂ SIM ¹)(OAc) ₂ (μ-OH)] ⁺
Ga(1)...Zn(1)	-	6.1122(9)
Ga(1)...Ga(2)	3.083	3.0183(12)
Ga(1)-O(1)	1.911(3)	1.871(4)
Ga(1)-O(6)	1.894(4)	1.976(4)
Ga(1)-O(6)′	2.016(3)	1.880(3)
Ga(1)-N(1)	2.063(4)	2.063(5)
Ga(1)-N(2)	2.128(4)	2.097(4)
Ga(1)-N(3)	2.066(4)	2.066(5)
Zn(1)-N(4)	-	2.143(5)
Zn(1)-N(5)	-	2.085(5)
Zn(1)-N(6)	-	2.199(5)
Zn(1)-O(2A)	-	1.969(4)
Zn(1)-O(2B)	-	2.002(4)
Zn(1)-O(3B)	-	2.386(5)
N(2)-Ga(1)-N(1)	77.92(16)	77.5(2)
N(2)-Ga(1)-N(3)	80.65(16)	79.82(19)
N(2)-Ga(1)-O(1)	94.13(15)	94.15(17)
N(2)-Ga(1)-O(6)	169.14(15)	93.98(17)
N(2)-Ga(1)-O(6)′	93.33(15)	170.86(17)
N(5)-Zn(1)-N(4)	-	80.6(2)
N(5)-Zn(1)-N(6)	-	77.71(19)
N(5)-Zn(1)-O(2A)	-	114.59(19)
N(5)-Zn(1)-O(2B)	-	148.9(2)
N(5)-Zn(1)-O(3B)	-	90.77(18)

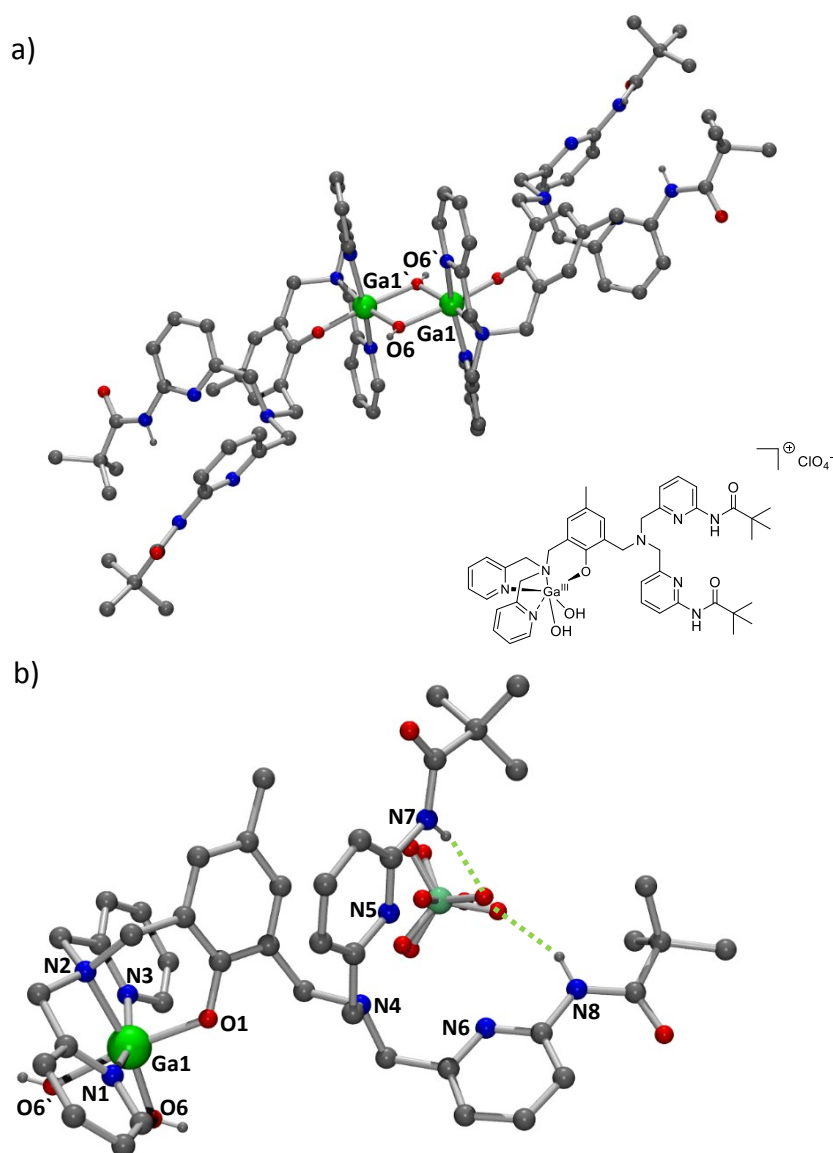


Figure 5: Structures of $[\text{Ga}^{\text{III}}(\text{H}_2\text{SIM}^1)(\mu\text{-OH})]_2(\text{ClO}_4)_2$: a) full dimer and b) monomeric subunit, also showing hydrogen bonding (green dotted lines; counter ions, non-coordinated solvent molecules, and hydrogen atoms, not involved in hydrogen bonding, have been omitted for clarity; crystallographic data and ORTEP plots with 50% probability level of thermal ellipsoids appear in the Appendix, Table 30 and Figure 70).

In contrast, the ligand HL^9 with four unsubstituted pyridine arms crystallized as digallium(III) complex of the form $[\text{Ga}^{\text{III}}_2(\text{L}^9)(\text{OH})_2(\text{OH}_2)_2](\text{ClO}_4)_3$ when treated with gallium(III) nitrate and tetraethylammonium perchlorate. Whilst the phenolate moiety of the ligand HL^9 bridges the two Ga^{III} ions of this dinuclear complex $[\text{Ga}^{\text{III}}_2(\text{L}^9)(\text{OH})_2(\text{OH}_2)_2]^{3+}$, the phenolate of H_3SIM^1 is coordinated terminally to the Ga^{III} center in $[\text{Ga}^{\text{III}}(\text{H}_2\text{SIM}^1)(\mu\text{-OH})]^+$. In agreement with this observation is the elongated average $\text{Ga}^{\text{III}}\text{-O}_{\text{Ph}}$ distance in $[\text{Ga}^{\text{III}}_2(\text{L}^9)(\text{OH})_2(\text{OH}_2)_2]^{3+}$ (2.043 Å), compared to the corresponding value found in $[\text{Ga}^{\text{III}}(\text{H}_2\text{SIM}^1)(\mu\text{-OH})]^+$ (1.911 Å), while the $\text{Ga}^{\text{III}}\text{-N}_{\text{amine}}$ (2.122 Å vs. 2.128 Å) and $\text{Ga}^{\text{III}}\text{-N}_{\text{Py}}$ (2.078 Å vs. 2.065 Å) distances are similar in both complexes.

The X-ray crystal structural analysis confirms the assignment of the NMR spectra (see above), *i.e.* that the Ga^{III} ion is bound to binding site A of ligand H₃SIM¹ and indicates that the sterically demanding pivaloyl-amide residues hinder the coordination of Ga^{III} ions in binding site B of ligand H₃SIM¹.

3.2.3 FORMATION OF A HETERODINUCLEAR GA^{III}ZN^{II} COMPLEX

The results obtained from the investigation of the coordination behavior of H₃SIM¹ with Zn^{II} and Ga^{III} ions showed that Zn^{II} is coordinated stepwise, firstly in the less hindered binding site B and subsequently, only after complete formation of the monozinc(II) complex, the Zn^{II} coordination takes place in binding site C. The presence of Ga^{III} ions in solution also resulted in the formation of the monogallium(III) complex containing the Ga^{III} ion in binding site B, but the subsequent generation of a digallium(III) complex, could not be achieved. The possibility of the synthesis of a heterodinuclear complex, containing Ga^{III} selectively in binding site B and Zn^{II} exclusively in binding site C, was tested using NMR spectroscopic and mass spectrometric techniques.

NMR Studies

To study the coordination chemistry of H₃SIM¹ towards a mixture of Ga^{III} and Zn^{II} different strategies were followed, including (i) addition of zinc(II) perchlorate to the monogallium(III) complex of H₃SIM¹, (ii) addition of gallium(III) nitrate to the monozinc(II) complex of H₃SIM¹, and (iii) addition of gallium(III) nitrate to the dizinc(II) complex of H₃SIM¹. The latter experiment was performed in order to verify the stronger binding of Ga^{III} in comparison to Zn^{II} by H₃SIM¹ in binding site B. All three experiments resulted in a similar spectrum; the resonances assigned to protons in binding site B were broadened and two sets of signals assigned to protons in binding site C were present (Figure 6), suggesting a mixture of two different species, which differ specifically in the coordination mode of the metal bound in binding site C. It was shown that the ratio of the two species is dependent on temperature, time, and donor properties of the solvent used. Moreover, after the NMR experiment samples were left to react at room temperature for seven days the presence of one main species could be detected.

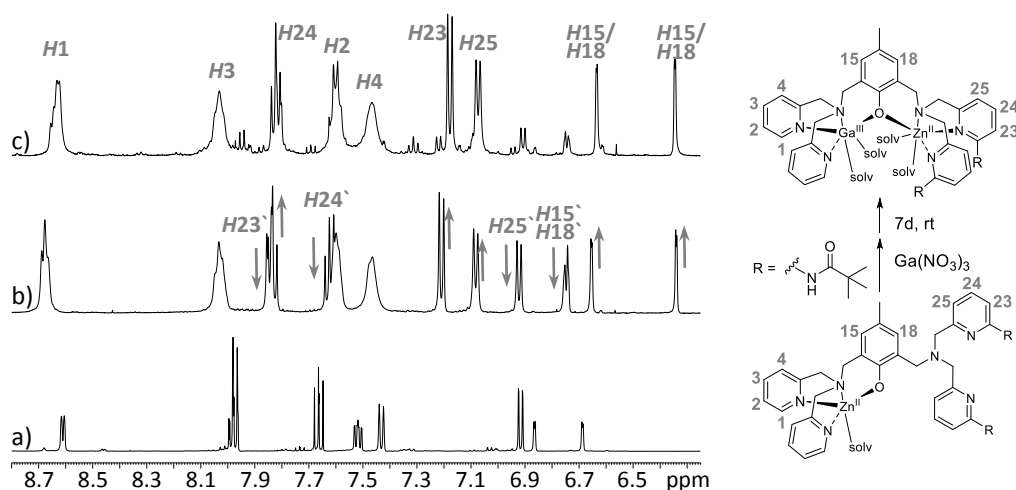


Figure 6: Comparison of ^1H NMR spectra of a) $[\text{Zn}^{\text{II}}(\text{H}_2\text{SIM}^1)(\text{solv})_x]$ in $\text{CD}_3\text{CN}/\text{D}_2\text{O}$ with b) 1.0 eq $\text{Ga}^{\text{III}}(\text{NO}_3)_3$ in D_2O heated for 15 minutes at 50°C , and c) the mixture after 7 days at room temperature.

The chemical shifts of the resonances of both species, detected in the samples treated with Ga^{III} and Zn^{II} , vary when compared with the resonances found in the monozinc(II) complex, dizinc(II) complex, and monogallium(III) complex of H_3SIM^1 , discussed above, and therefore exclude the possibility of a mixture of complexes with different metal composition. The amide groups adjacent the metal center in binding site C are likely to employ multiple coordination modes leading to a mixture of two different species, in which the environment of protons in binding site C varied and therefore the chemical shifts are unequal. The impact of the coordination modes of the amide groups on the protons in binding site B is limited and therefore only a broadening was detected.

The monozinc(II) complex of H_3SIM^1 contains the Zn^{II} ion in the less hindered coordination site B and Ga^{III} ions were not coordinated by the amide containing binding site C, as explained above. Thus, a metal exchange is proposed to proceed during the formation of the heterodinuclear $\text{Ga}^{\text{III}}\text{Zn}^{\text{II}}$ complex. This suggestion is supported by the finding that the addition of gallium(III) nitrate to the dizinc(II) complex of H_3SIM^1 , as well as the addition of zinc(II) perchlorate to the monogallium(III) complex of H_3SIM^1 , resulted in the same ^1H NMR spectrum as did the addition of gallium(III) nitrate to the monozinc(II) complex.

Mass Spectrometry

The sole formation of the heterodinuclear complex was also supported by ESI^+ mass spectrometry, because the main signals exhibit the pattern characteristic for GaZn species and the main peak at m/z 430.1 could be assigned to the $[\text{Ga}^{\text{III}}\text{Zn}^{\text{II}}(\text{SIM}^1)]^{2+}$ complex (Figure 3d).

X-ray Diffraction

The heterodinuclear complex was prepared by heating an equimolar mixture of ligand H_3SIM^1 and zinc(II) perchlorate in methanol (40 mM) for 15 minutes and subsequent addition of gallium(III) nitrate, sodium acetate and sodium hexafluorophosphate. Diffusion of diethylether in the methanolic complex solution (22 mM) gave colorless crystals suitable for data collection. Figure 7 shows the structure obtained; Table 2 shows selected distances and valence angles. The structure was solved and includes a $[\text{Ga}^{\text{III}}\text{Zn}^{\text{II}}(\text{H}_2\text{SIM}^1)(\text{OAc})_2(\mu\text{-OH})]^+$ complex cation, a hexafluorophosphate counterion and a diethylether solvent molecule in the elemental cell. Crystallographic data obtained for the structure are displayed in Table 30 (see Appendix). In contrast to complexes derived with similar ligands, included the dizinc(II) complex of H_3SIM^1 (discussed in detail in Chapter 4.3), the two metal ions are not bridged by the phenolate backbone. Moreover, the model system forms dimers, bridged by two hydroxide ions between the Ga^{III} ions (Figure 7b) comparable to the monogallium(III) complex of H_3SIM^1 , $[\text{Ga}^{\text{III}}(\text{H}_2\text{SIM}^1)(\mu\text{-OH})]^+$ (Figure 5). The two Ga^{III} ions and the two hydroxido bridges form an asymmetric arrangement with the $\text{Ga}^{\text{III}}\text{-OH}$ distances differing with the values of 1.880(3) Å and 1.976(4) Å. This arrangement is comparably found in $[\text{Ga}^{\text{III}}(\text{H}_2\text{SIM}^1)(\mu\text{-OH})]^+$, but with a higher difference between the $\text{Ga}^{\text{III}}\text{-OH}$ distances (1.894(4) Å and 2.016(3) Å); the $\text{Ga}\cdots\text{Ga}$ separation is slightly elongated in $[\text{Ga}^{\text{III}}(\text{H}_2\text{SIM}^1)(\mu\text{-OH})]^+$ (3.083 Å) compared to $[\text{Ga}^{\text{III}}\text{Zn}^{\text{II}}(\text{H}_2\text{SIM}^1)(\text{OAc})_2(\mu\text{-OH})]^+$ (3.0183(12) Å). In addition to the two bridging hydroxido co-ligands, the Ga^{III} ions are coordinated by a phenolate, two pyridines, and a tertiary amine group provided by the ligand backbone. While the $\text{Ga}^{\text{III}}\text{-N}_{\text{Py}}$ distances between the Ga^{III} center and the coordinated pyridine residues in $[\text{Ga}^{\text{III}}\text{Zn}^{\text{II}}(\text{H}_2\text{SIM}^1)(\text{OAc})_2(\mu\text{-OH})]^+$ are equal to the ones found in $[\text{Ga}^{\text{III}}(\text{H}_2\text{SIM}^1)(\mu\text{-OH})]^+$, the $\text{Ga}^{\text{III}}\text{-N}_{\text{amine}}$ and $\text{Ga}^{\text{III}}\text{-O}_{\text{Ph}}$ distances between the Ga^{III} ion and the tertiary amine and the phenolate moiety, respectively, are slightly shortened by 0.03 Å and 0.04 Å.

In addition to the Ga^{III} ion coordinated in binding site B a Zn^{II} ion is coordinated in the more hindered binding site C of ligand H_3SIM^1 . The donors around the Zn^{II} ions form a distorted octahedral coordination geometry with the two coordinating pyridines in the axial positions. The square plane of the Zn^{II} ions is occupied by the tertiary amine of the ligand backbone and two acetate co-ligands, one in a chelating, the other in a terminal binding mode. The $\text{Zn}^{\text{II}}\text{-O}$ distances to the chelating acetate co-ligand differ by 0.38 Å (2.002(4) Å and 2.386(5) Å) and in accordance with that finding the coordination mode of the acetate is asymmetric. Comparison of the structure of $[\text{Ga}^{\text{III}}\text{Zn}^{\text{II}}(\text{H}_2\text{SIM}^1)(\text{OAc})_2(\mu\text{-OH})]^+$ with the structure of $[\text{Zn}^{\text{II}}_2(\text{H}_2\text{SIM}^1)(\text{OAc})(\mu\text{-OH})]^+$, which will be discussed in detail in Chapter 4.3, showed that the coordination arrangements differ as in the latter the pyridine residues are part of the trigonal plane while the tertiary amine occupies the axial position. The $\text{Zn}(1)\text{-N}_{\text{Py}}$ distances in $[\text{Ga}^{\text{III}}\text{Zn}^{\text{II}}(\text{H}_2\text{SIM}^1)(\text{OAc})_2(\mu\text{-OH})]^+$ are

elongated (2.143(5) Å and 2.199(5) Å vs. 2.057(3) Å and 2.102(3) Å) and the Zn(1)-N_{amine} distance is shortened (2.085(5) Å vs. 2.233(2) Å) compared to the respective distances found in the trigonal bipyramidal coordinated Zn^{II} center of the dizinc(II) complex (discussed in detail in Chapter 4.3). In the octahedral coordination sphere around the Ga^{III} ion in [Ga^{III}Zn^{II}(H₂SIM¹)(OAc)₂(μ-OH)]⁺ the Ga^{III}-N distances are all shorter than found in [Zn^{II}₂(H₂SIM¹)(OAc)(μ-OH)]⁺, as expected due to the higher charge density of Ga^{III} compared to Zn^{II}.

Based on the short distances between the amide nitrogen atoms and the nearby acetate oxygen atoms, a hydrogen bond network is proposed in [Ga^{III}Zn^{II}(H₂SIM¹)(OAc)₂(μ-OH)]⁺. N(7) forms a hydrogen bond to the chelating acetate co-ligand (N(7)-O(2B) 2.871 Å) and N(8), respectively, to the terminal acetate co-ligand (N(8)-O(2A) 3.004 Å). Moreover, the terminal acetate co-ligand itself stabilizes the hydroxido-bridges between the Ga^{III} ions (O(3A)-O(6) 2.808 Å) by hydrogen bonds. The previously observed effect that hydrogen bonding enlarges the angle between the pyridine planes and the plane containing the amide group (NCO) was also found in the structure of [Ga^{III}Zn^{II}(H₂SIM¹)(OAc)₂(μ-OH)]⁺.¹⁶⁸ This angle was found to be 18.85° in case of the N(7) amide residue, while a value of 11.05° was measured in the case of the N(8) amide moiety, supposing a preserved C-H⋯O=C interaction between the carbonyl oxygen and the nearby hydrogen atom in 5-position of the pyridine ring in the latter case.

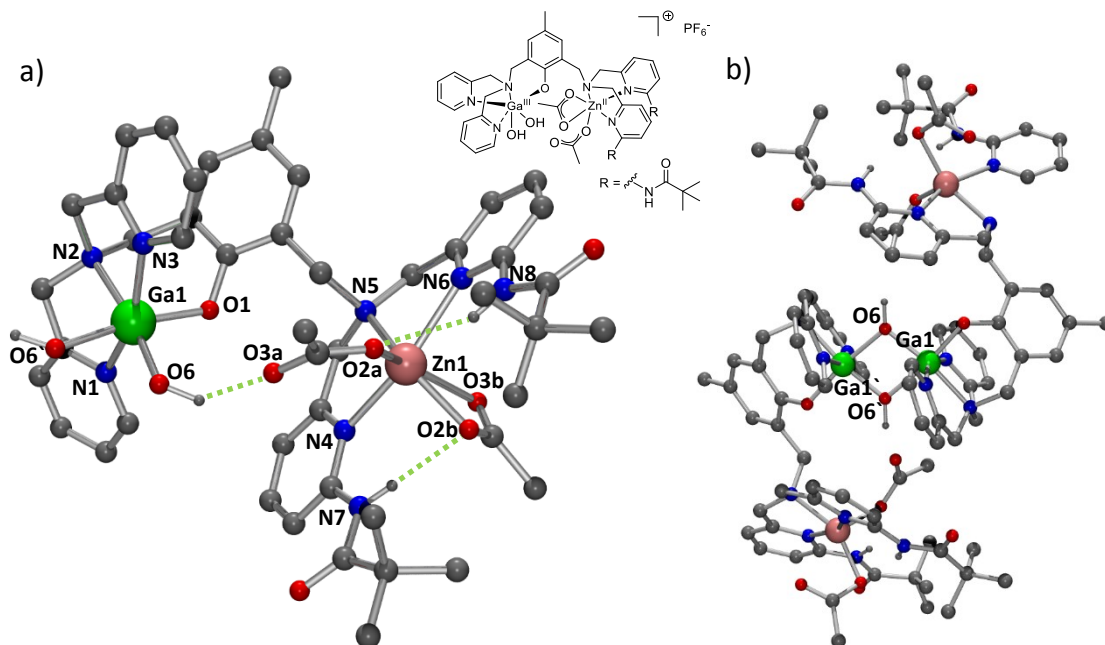


Figure 7: Structures of a) [Ga^{III}Zn^{II}(H₂SIM¹)(OAc)₂(μ-OH)]⁺ and b) the respective dimer [Ga^{III}Zn^{II}(H₂SIM¹)(OAc)₂(μ-OH)]₂²⁺ showing hydrogen bonding (green dotted lines; counter ions, non-coordinated solvent molecules, and hydrogen atoms, not involved in hydrogen bonding, have been omitted for clarity; crystallographic data and ORTEP plots with 50% probability level of thermal ellipsoids appear in the Appendix, Table 30 and Figure 71).

The X-ray crystallographic data highlight the selectivity of the two different binding sites in ligand H₃SIM¹ towards Ga^{III} and Zn^{II} ions. This enables H₃SIM¹ to form a more accurate PAP model complex that takes main structural features of the native enzymes into account, including the presence of two different metal ions with different oxidation states, and which are accompanied by hydrogen bond donors in close distance.

3.2.4 COMPLEXATION STUDIES WITH Cu^{II}

Due to the diamagnetism of Zn^{II} and Ga^{III} ions their coordination chemistry can be optimally monitored by NMR spectroscopy. In contrast, Cu^{II} ions have an incomplete d shell configuration (Ar)3d⁹ and are paramagnetic. The d⁹ system, on the other hand, plays a crucial role in several other characterization methods, such as electronic spectroscopy and electron paramagnetic resonance (EPR). Consequently, the coordination behavior of H₃SIM¹ with Cu^{II} ions was studied using these methods.

UV-vis-NIR Spectroscopy

The stepwise addition of copper(II) triflate to H₃SIM¹ in methanol was followed by UV-vis-NIR spectroscopy (Figure 8). Besides the intense absorptions below 300 nm (π - π^* transitions of the ligand backbone), the spectra show broad transitions at 459 nm and 654 nm with intensity ratios of around 3.3:1. Table 3 lists the observed transitions and the corresponding ϵ values.

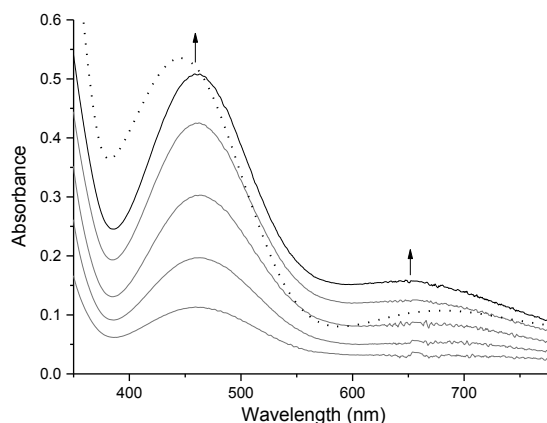


Figure 8: UV-vis-NIR spectra of a methanolic solution of H₃SIM¹ treated with 0.6 eq, 1.0 eq, 1.4 eq, 1.8 eq and 2.0 eq (bottom to top) of copper(II) triflate for 12 hours at rt (solid lines) and with 2.0 eq of copper(II) acetate (dotted line).

Treatment of a methanolic solution of H₃SIM¹ with two equivalents of copper(II) acetate resulted in a similar spectrum with broad transitions at 447 nm and 681 nm with an intensity ratio of 5.0:1. The spectral data are similar to that reported for the complex [Cu^{II}₂(L¹)(OAc)₂]⁺, bearing a similar ligand backbone as H₃SIM¹, but lacking the two pivaloyl-amide residues.¹⁶⁹

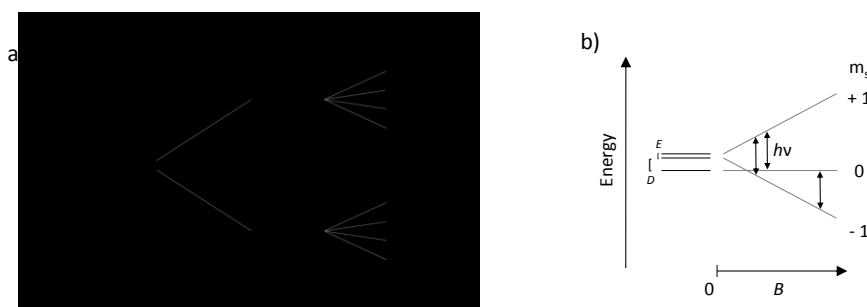
Table 3: UV-vis-NIR spectroscopic properties of the Cu^{II} complexes of H₃SIM¹.

mixture molar ratio	wavelength [nm]	ϵ [l mol ⁻¹ cm ⁻¹]	transition
H ₃ SIM ¹ : Cu(OTf) ₂ 1 : 1	459	393	d-d
	654	114	LMCT
H ₃ SIM ¹ : Cu(OTf) ₂ 1 : 2	459	1016	d-d
	654	314	LMCT
H ₃ SIM ¹ : Cu(OAc) ₂ 1 : 2	447	1068	d-d
	681	215	LMCT

Furthermore, the presence of the d-d bands in the region between 400 nm and 500 nm is typical for axial Cu^{II} sites. The fact that the d-d bands of the two Cu^{II} centers are not resolved suggests a rather similar coordination environment, as expected because of the identical primary coordination spheres of the Cu^{II} centers. The continuous increase in intensity of both bands throughout the addition of copper(II) triflate to the methanolic ligand solution is in agreement with both a single mononuclear site and mono- and dinuclear sites of similar coordination geometry. However, the relatively featureless spectra do not allow unambiguous support for a detailed interpretation.

EPR Spectroscopy

EPR measurements allow the difference between the magnetic energy levels to be determined. Magnetic energy levels are degenerate in absence of a magnetic field, but when a magnetic field is applied the energy levels split up, known as the Zeeman phenomenon (Figure 9). Magnetic energy levels are described by the magnetic quantum number m_s and two m_s states with an energy difference of $h\nu = g\beta_e B$ are generated by a magnetic field B in the case of a $S = \frac{1}{2}$ system (h : Boltzmann constant, ν : frequency, g : magnetic tensor, β_e : Bohr magneton). The symmetry of the magnetic tensor g , which reflects the symmetry of the coordination environment around the Cu^{II} ions, encompass the detection of one, two or three signals in the spectrum and therefore is used to investigate the coordination geometry of copper(II) complexes.

Figure 9: The Zeeman effect in the EPR experiment for a) spin $S = \frac{1}{2}$ and b) spin $S = 1$.

In order to investigate the coordination chemistry of H_3SIM^1 with Cu^{II} ions, X-band EPR spectra of frozen methanolic solutions of H_3SIM^1 with copper(II) triflate were recorded. Figure 10 illustrates the spectra obtained and compares them to the spectrum of copper(II) triflate in methanol and Table 4 summarizes the parameters derived from simulating the experimental EPR spectra. Here, χ , σ and τ present the Euler angles which describe the orientation of the coordination polyhedron of the Cu^{II} centers and are illustrated in Figure 13.

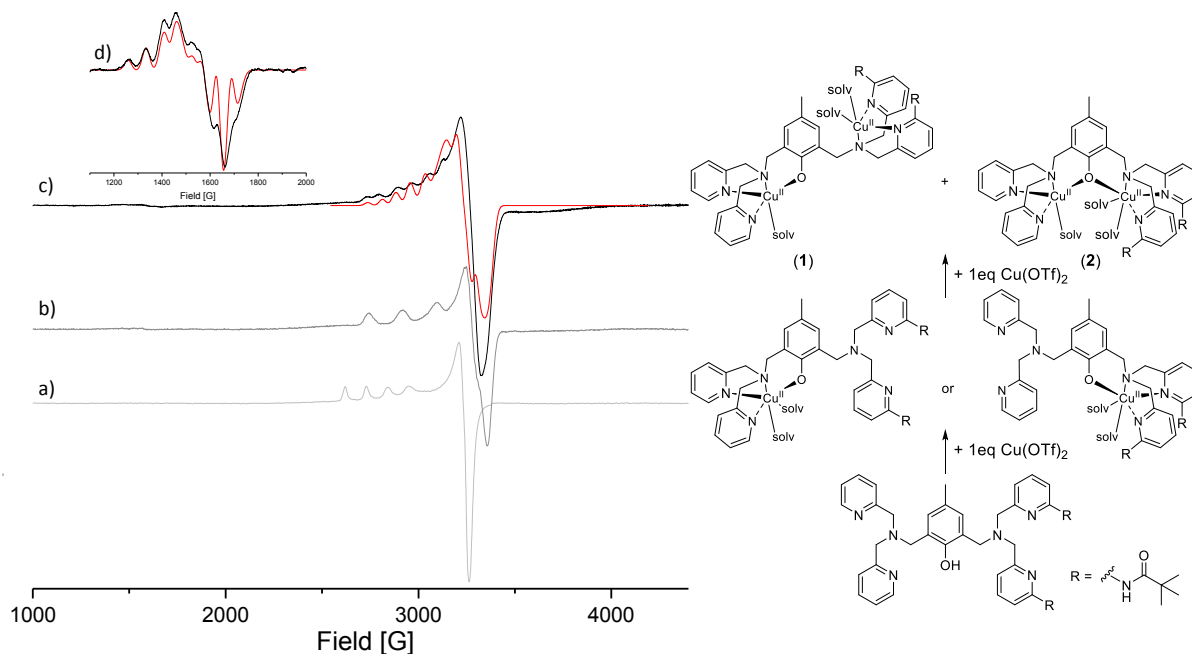


Figure 10: Experimental EPR spectra (black, $\nu = 9.4$ GHz, $T = 140$ K) and computer simulated spectra (red) of a) $Cu^{II}(OTf)_2$ in methanol, b) H_3SIM^1 and $Cu^{II}(OTf)_2$ (1:0.8), c) H_3SIM^1 and $Cu^{II}(OTf)_2$ (1:2.0), and d) $\Delta m_s = \pm 2$ transition.

The first and second derivative spectra (Figure 10b and 11) of a mixture of H_3SIM^1 and copper(II) trifluoromethanesulfonate in the ratio of 1:0.8 and 1:0.95 in methanol show a single species. Numerical differentiation and Fourier filtering (Hamming function) were undertaken to increase the spectral resolution. Importantly, the cutoff of the Hamming function was adjusted so that the high frequency noise was minimized without distorting the spectrum. The second derivative spectrum (Figure 11) reveals ^{14}N superhyperfine splitting on the parallel Cu^{II} hyperfine resonances. Computer simulation of the second derivative spectrum with a rhombic spin Hamiltonian yields the spectrum shown in Figure 11, which is in excellent agreement with that of the experimental spectrum. The anisotropic spectrum of the mononuclear complex is typical for a single axially distorted Cu^{II} site with a $d_{x^2-y^2}$ ground state, leading to spin allowed $\Delta m_s = \pm 1$ transitions above $g = 2$. Importantly, the simulation assumed two equivalent nitrogen nuclei, indicating that the equatorial plane contains two nitrogen nuclei. It appears that Cu^{II} selectively occupies a single site and, by analogy to the observations with Zn^{II} (and Ga^{III}), this is probably site A, though site B cannot be ruled out.

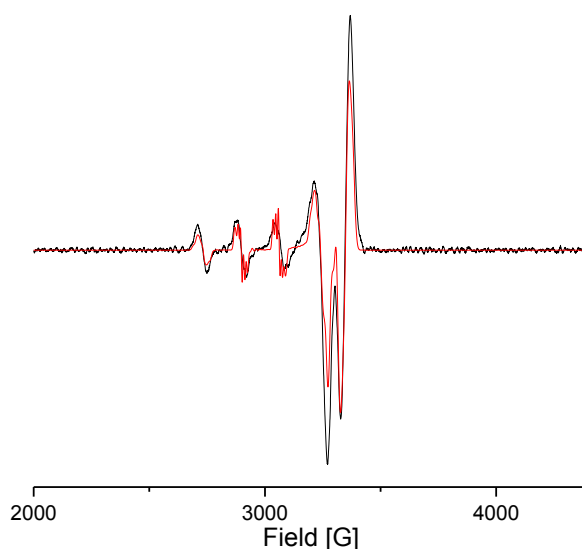


Figure 11: Second derivative of experimental EPR spectrum (black, $\nu = 9.4$ GHz, $T = 140$ K) and computer simulated spectrum (red) of H_3SIM^1 and $\text{Cu}^{\text{II}}(\text{OTf})_2$ (1:0.95) in methanol. (^{63}Cu hyperfine interaction $A_{x,y,z}$ (^{14}N) = $12.0 \cdot 10^{-4}$, $12.0 \cdot 10^{-4}$, $12.0 \cdot 10^{-4}$ cm^{-1} (two magnetically equivalent nitrogen nuclei). Linewidth (g- and A-strain linewidth model), $\sigma_{R_{x,y,z}} = 10.0 \cdot 10^{-4}$, $10.0 \cdot 10^{-4}$, $5.0 \cdot 10^{-4}$ cm^{-1} ; $(\sigma g/g)_{x,y,z} = 1 \cdot 10^{-4}$, $1 \cdot 10^{-4}$, $-1 \cdot 10^{-5}$; $\sigma A_{x,y,z} = 0.1 \cdot 10^{-4}$, $0.1 \cdot 10^{-4}$, $4.7 \cdot 10^{-4}$ cm^{-1} . The ^{63}Cu and ^{14}N perpendicular hyperfine resonances are not resolved in the spectra and thus the linewidth in the simulated spectrum results from a combination of $A_{x,y}$ (^{63}Cu , ^{14}N) and corresponding linewidth parameters).

With increasing Cu^{II} concentration ($\text{Cu}^{\text{II}}:\text{H}_3\text{SIM}^1$ ratio of 2:1), a new spectrum develops with features typical for dinuclear Cu^{II} systems with two non-identical Cu^{II} centers (Figure 10c). Besides the resonances centered around $g = 2$, arising from allowed $\Delta m_s = \pm 1$ transitions, weak resonances are also observed around $g_{\text{eff}} = 4.3$, arising from the formally forbidden $\Delta m_s = \pm 2$ transitions (Figure 10d). Interestingly, the EPR spectrum obtained from a mixture of H_3SIM^1 with Cu^{II} acetate (1:2) shows the same general features but with more intense $\Delta m_s = \pm 2$ resonances (Figure 12). However, the observed spectrum in the spin-allowed region is quite different, with resonances around 320 mT, attributable to solvated Cu^{II} ions (depicted in grey in Figure 12) and broad resonances around 260 mT and 360 mT, associated with the $\Delta m_s = \pm 1$ transitions of a dinuclear complex. The latter spectrum is characteristic for a dinuclear Cu^{II} complex, in which the two Cu^{II} ions are dipole-dipole coupled. The strong exchange interaction in the former spectrum could derive from bridging through the phenolate ligand backbone, in a structure supported by a bridging acetate co-ligand.

The features of the strongly interacting dinuclear Cu^{II} system, the $\Delta m_s = \pm 2$ transition and the two broad bands at 260 mT and 360 mT, are also visible in the spectrum obtained with the 1:2 mixture of H_3SIM^1 with copper(II) trifluoromethanesulfonate (Figure 10c), suggesting that a small amount of the dicopper(II) complex in solution has a similar structure (species (2) in the structures shown in Figure 10). Computer simulation of the spectra are based on two Cu^{II} centers, coordinated to the ligand with a $\text{Cu}^{\text{II}} \cdots \text{Cu}^{\text{II}}$ distance of 3.415 Å (Figure 10d; the relative orientations of the two

Cu^{II} centers are given in Table 4, which also lists the g- and A-matrices used in the simulations of the various spectra). Importantly, this solution structural analysis is in good agreement with the crystal structural analysis discussed below.

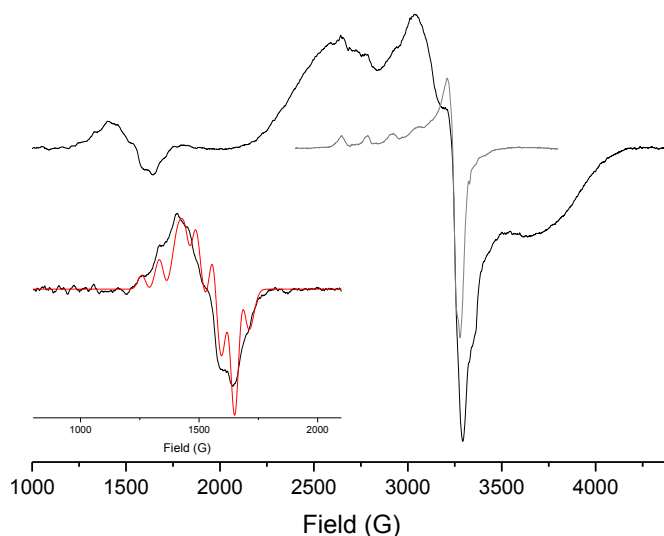


Figure 12: Experimental EPR spectra of a mixture of H₃SIM¹ with Cu^{II}(OAc)₂ (1:2) (black, $\nu = 9.4$ GHz, $T = 140$ K), computer simulated spectra (red), and experimental EPR spectrum of free Cu^{II}(OAc)₂ (grey) in methanol.

From the EPR simulation of the intense signal in the spectrum in Figure 10d, it emerges that it originates from a dinuclear Cu^{II} species with a Cu...Cu distance of 7.2 Å and is proposed to arise from a complex in which the two Cu^{II} centers are not bridged by the phenolate ligand backbone (species (1) in the structures given in Figure 8). Here, the two pyridine donors in each coordination site are on opposite side of the phenolate linker.

Table 4: EPR data for copper(II) complexes of H₃SIM¹.

complex species	[Cu ^{II} (H ₂ SIM ¹)(solvent)] _x	[Cu ^{II} ₂ (H ₂ SIM ¹)(solvent)] _x (1)		[Cu ^{II} ₂ (H ₂ SIM ¹)(solvent)] _x (2)		[Cu ^{II} ₂ (H ₂ SIM ¹)(OAc)] _x	
		Cu(1)	Cu(2)	Cu(1)	Cu(2)	Cu(1)	Cu(2)
g _x	2.044	2.054	2.055	2.054	2.054	2.054	2.060
g _y	2.062	2.055	2.065	2.055	2.055	2.090	2.090
g _z	2.262	2.242	2.270	2.245	2.245	2.245	2.245
A _x [10 ⁻⁴ cm ⁻¹]	10.6 ^a	15	15	15	15	15	15
A _y [10 ⁻⁴ cm ⁻¹]	12.56 ^a	12	12	12	12	12	12
A _z [10 ⁻⁴ cm ⁻¹]	172.02 ^a	166	155	166	166	166	166
R [Å]	-	7.2		3.621		3.6	
χ [°]	-	16		18		5	
ρ [°]	-	21.4		10		30	
τ [°]	-	35		39		40	

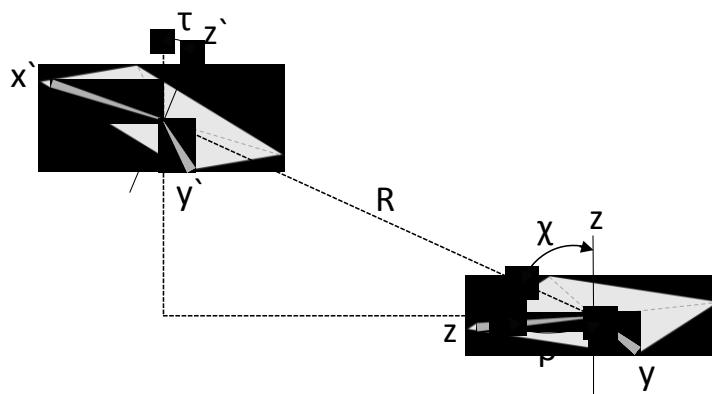


Figure 13: Definition of the Euler angles χ , τ and ρ used for EPR simulation using the program Xsophe.¹⁷⁰

Mass Spectrometry

The ESI⁺ mass spectrometric measurements of a mixture of H₃SIM¹ and copper(II) triflate in a 1:2 ratio in methanol resulted in a spectrum with the main peaks at m/z 1003.2 and m/z 427.1, which match the mass of the species $[\text{Cu}^{\text{II}}_2(\text{HSIM}^1)(\text{F}_3\text{CSO}_3)]^+$ and $[\text{Cu}^{\text{II}}_2(\text{HSIM}^1)]^{2+}$ and revealed isotopic pattern typical for species containing two Cu atoms (Figure 3f). These signals were not detected in the spectrum recorded with the mixture in a ratio of 1:0.8. In contrast, this mixture revealed signals of the metal-free ligand and signals with isotopic pattern characteristic for a mononuclear Cu^{II} complex (Figure 3e), *i.e.* a signal at m/z 790.3 which was assigned to $[\text{Cu}^{\text{II}}(\text{H}_2\text{SIM}^1)]^+$. The spectrum recorded with the mixture of H₃SIM¹ and two equivalents of copper(II) acetate shows signals with the isotopic pattern typical for dinuclear Cu^{II} complexes. The main signals at m/z 471.2 and m/z 911.2 were assigned to $[\text{Cu}^{\text{II}}_2(\text{H}_2\text{SIM}^1)(\text{OAc})(\text{CH}_3\text{OH})]^{2+}$ and $[\text{Cu}^{\text{II}}_2(\text{HSIM}^1)(\text{OAc})]^+$.

X-ray Diffraction

Treatment of a methanolic solution of H₃SIM¹ (27 mM) with Cu^{II} acetate (2.0 eq), heating for 15 minutes at 50°C, followed by addition of sodium hexafluorophosphate (1.5 eq), filtration and diffusion of diethylether, resulted in brown crystals, suitable for X-ray data collection. Figure 14 shows a plot of the molecular structure and Table 5 gives selected structural parameters.

The molecular structure consists of a $[\text{Cu}^{\text{II}}_2(\text{HSIM}^1)(\mu\text{-OAc})]^+$ complex cation and a hexafluorophosphate counter anion. The two Cu^{II} centers have different coordination geometries and are doubly bridged by the phenolate of the ligand backbone and an acetate co-ligand. Cu(1) is also coordinated to two pyridine moieties and a tertiary amine donor, resulting in a distorted square-pyramidal geometry ($\tau = 0.46$),¹⁷¹ while Cu(2) exhibits a distorted octahedral geometry, emerging from the two bridging ligands, two pyridine residues, a tertiary amine nitrogen, and an oxygen atom of one of the proximal amide groups. The coordination of the pivaloyl-amide moiety is

stabilized by a hydrogen bond formed with the second pivaloyl-amide group visible by the short N(7)-O(5) distance with a value of 3.461 Å, illustrated as green dotted lines in Figure 14.

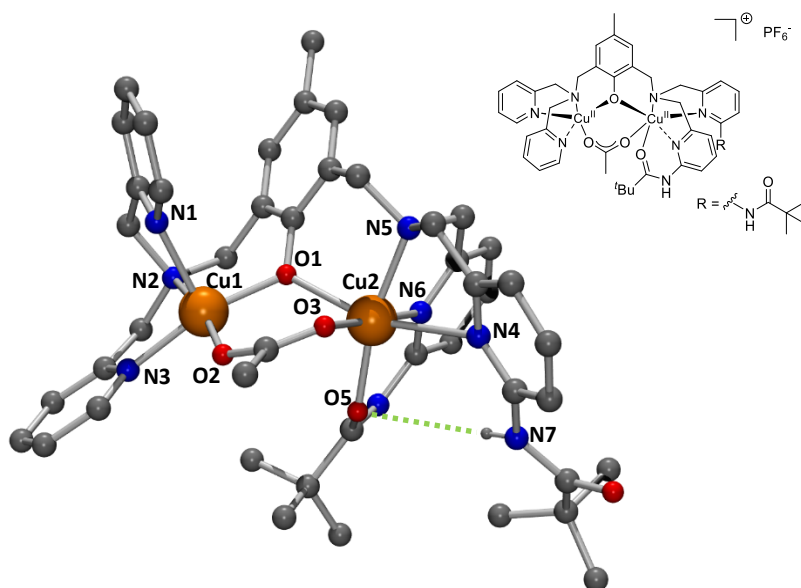


Figure 14: Structure of $[\text{Cu}^{\text{II}}_2(\text{HSIM}^1)(\mu\text{-OAc})]^+$, also showing intramolecular hydrogen bonding (green dotted lines; counter ions and hydrogen atoms, not involved in hydrogen bonding, have been omitted for clarity; crystallographic data and ORTEP plots with 50% probability level of thermal ellipsoids appear in the Appendix, Table 30 and Figure 72).

Table 5: Selected bond lengths (Å) and angles (°) for $[\text{Cu}^{\text{II}}_2(\text{HSIM}^1)(\mu\text{-OAc})]\text{PF}_6$

	$[\text{Cu}^{\text{II}}_2(\text{HSIM}^1)(\mu\text{-OAc})]^+$
Cu(1)...Cu(2)	3.577
Cu(1)-O(1)	1.9061(16)
Cu(1)-O(2)	1.9525(16)
Cu(1)-N(1)	2.1981(19)
Cu(1)-N(2)	2.0710(18)
Cu(1)-N(3)	2.0075(18)
Cu(2)-O(1)	2.2567(15)
Cu(2)-O(3)	1.9378(16)
Cu(2)-O(5)	1.9316(17)
Cu(2)-N(4)	2.581(2)
Cu(2)-N(5)	2.0665(18)
Cu(2)-N(6)	1.9354(17)
Cu(1)-O(1)-Cu(2)	118.24(7)
O(1)-Cu(1)-N(1)	95.56(7)
O(1)-Cu(1)-N(2)	93.05(6)
O(1)-Cu(1)-N(3)	161.08(6)
O(1)-Cu(1)-O(2)	95.09(6)
O(1)-Cu(2)-N(4)	161.42
O(1)-Cu(2)-N(5)	90.42(7)
O(1)-Cu(2)-N(6)	91.13(7)
O(1)-Cu(2)-O(3)	91.21(6)
O(1)-Cu(2)-O(5)	101.64(7)

The structure of $[\text{Cu}^{\text{II}}_2(\text{HSIM}^1)(\mu\text{-OAc})]^+$ contrasts with the previously published structure of the dicopper(II) complex of the symmetric ligand HL^1 , $[\text{Cu}^{\text{II}}_2(\text{L}^1)(\text{OAc})_2]\text{ClO}_4$, which bears two square pyramidal coordinated Cu^{II} centers.¹⁶⁹ Consequently, the asymmetrically substituted ligand H_3SIM^1 provides two different coordination sites for the Cu^{II} ions. This asymmetry is additionally visible in the bond length between the Cu^{II} centers and the phenolate oxygen atom; while this value measures 2.173 Å for both Cu^{II} centers in $[\text{Cu}^{\text{II}}_2(\text{L}^1)(\text{OAc})_2]^+$,¹⁶⁹ in $[\text{Cu}^{\text{II}}_2(\text{HSIM}^1)(\mu\text{-OAc})]^+$ this value is shortened in the case of the square pyramidal $\text{Cu}(1)$ (1.9061(16) Å) and elongated in the case of the octahedral $\text{Cu}(2)$ (2.2567(15) Å). Interestingly, the $\text{Cu}\cdots\text{Cu}$ separation in $[\text{Cu}^{\text{II}}_2(\text{HSIM}^1)(\mu\text{-OAc})]^+$ (3.577 Å) is much shorter than in $[\text{Cu}^{\text{II}}_2(\text{L}^1)(\text{OAc})_2]^+$ (3.916 Å),¹⁶⁹ probably due to the bridging acetate co-ligand, as $[\text{Cu}^{\text{II}}_2(\text{L}^1)(\text{OAc})_2]^+$ comprises two terminally coordinated acetate co-ligands.

Magnetic Susceptibility Measurement

The molar magnetic susceptibility (χ_M) describes the degree of the magnetization of a material and characterizes the way in which an applied magnetic field H interacts with the angular momenta associated with the thermally populated states of a molecule.^{172, 173} When a sample is perturbed by an external magnetic field H , its magnetization is related to its energy variation by Equation 1 which defines the microscopic magnetizations μ_n for each energy level E_n ($n = 1, 2, \dots$).

$$\text{Equation 1} \quad \mu_n = -\frac{\delta E_n}{\delta H}$$

The macroscopic molar magnetization M is then obtained by summing the microscopic magnetizations weighted according to the Boltzmann distribution (Equation 2). The molar magnetic susceptibility is deduced from the molar magnetization by Equation 3.

$$\text{Equation 2} \quad M = \frac{N \sum_n \left(-\frac{\delta E_n}{\delta H} \right) e^{-\frac{E_n}{kT}}}{\sum_n e^{-\frac{E_n}{kT}}}$$

$$\text{Equation 3} \quad \chi = \frac{\delta M}{\delta H}$$

The function of a magnetometer is to measure the induced or remnant magnetic moment in a sample, usually as a function of applied field and temperature.¹⁷⁴ A graph of $\chi_M T$ vs. temperature (T) is commonly used for the analysis of the magnetic behavior of a substance, whereby a constant $\chi_M T$ value is characteristic for a paramagnetic species. Antiferromagnetism leads to the deviation of $\chi_M T$ to lower values by decreasing T ($J < 0$), while the deviation to higher $\chi_M T$ values by decreasing T reveals ferromagnetism ($J > 0$). The effective magnetic moment may be calculated from the susceptibility measurements with Equation 4.

$$\text{Equation 4} \quad \mu_{\text{eff}} = 2.828 \sqrt{\chi_M T}$$

The experimentally obtained value for μ_{eff} can be compared with the expected spin-only value for a dinuclear system calculated with Equation 5 (for two strongly interacting spins with the resulting total spin quantum number S_{tot}) or Equation 6 (for two non-interacting spins S_1 and S_2). Equation 6 simplifies for two non-interacting spins of the same value ($S_1 = S_2 = S$) resulting in Equation 7.

$$\text{Equation 5} \quad \mu_{\text{eff}} = 2\sqrt{S_{\text{tot}}(S_{\text{tot}} + 1)}$$

$$\text{Equation 6} \quad \mu_{\text{eff}} = 2\sqrt{S_1(S_1 + 1) + S_2(S_2 + 1)}$$

$$\text{Equation 7} \quad \mu_{\text{eff}} = 2\sqrt{S(S + 1)} * \sqrt{2}$$

In order to understand the magnetic property variable temperature dc magnetic susceptibility studies in solid state were performed with ground crystals of complex $[\text{Cu}^{\text{II}}_2(\text{H}_2\text{SIM}^1)(\mu\text{-OAc})_2]\text{PF}_6$ in the temperature range from 2 to 300 K. The data for $\chi_{\text{M}}T$ vs. T are shown in Figure 15. The strong peak between 50 K and 100 K was attributed to oxygen present in the instrument.

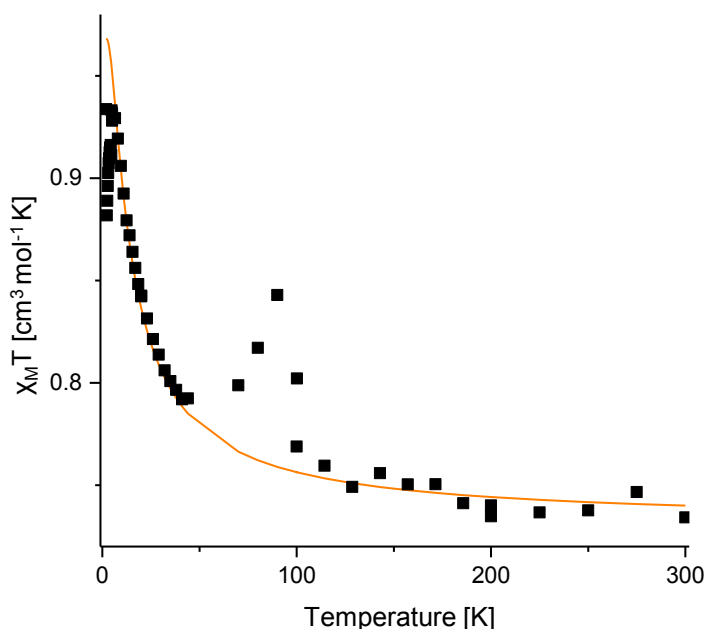


Figure 15: Temperature dependence of $\chi_{\text{M}}T$ for $[\text{Cu}^{\text{II}}_2(\text{HSIM}^1)(\mu\text{-OAc})]\text{PF}_6$ recorded in a magnetic field of 1000 Oe and the respective fit curve (orange line).

The $\chi_{\text{M}}T$ vs. T plot shows the typical process of a ferromagnetically coupled system. The value of $\chi_{\text{M}}T$ increases from a value of $0.8818 \text{ cm}^3\text{mol}^{-1}\text{K}$ at 2.25 K to $0.9331 \text{ cm}^3\text{mol}^{-1}\text{K}$ at 4.75 K, and then decreases at higher temperatures. The $\chi_{\text{M}}T$ value tends to $1 \text{ cm}^3\text{mol}^{-1}\text{K}$ at low temperature which is the expected value for two interacting $S_{1,2} = \frac{1}{2}$ metal centers ($S_{\text{tot}} = 1$). The value of $0.7406 \text{ cm}^3\text{mol}^{-1}\text{K}$ at 300 K is close to the expected value for two non-coupled electrons ($0.75 \text{ cm}^3\text{mol}^{-1}\text{K}$).

The data were fitted by the following spin Hamiltonian (Equation 8), where J is the isotropic exchange coupling constant, S_i denotes the spin states ($S = \frac{1}{2}$), and D_i and E_i are the axial and rhombic zero-field splitting parameters.

Equation 8

$$H = -2JS_1S_2 + \sum_{i=1}^2 \left[D_i \left(S_{zi}^2 - \frac{1}{3}S_i(S_i + 1) \right) + E_i(S_{xi}^2 - S_{yi}^2) + \beta S_i g_i H \right]$$

This model reproduced reasonably well the experimental data when the data points between 50 K and 100 K were excluded. The final parameter set of the best fit were found to be $J = 5.0 \text{ cm}^{-1}$, $g_1 = g_2 = 2.0$, and the D- and E-values to be 0, considering 5% of a paramagnetic impurity derived from the monocopper(II) complex.

The majority of dicopper(II) compounds have an antiferromagnetically coupled ground state with $S = 0$.¹⁷³ Therefore, $[\text{Cu}^{\text{II}}_2(\text{HSIM}^1)(\mu\text{-OAc})]\text{PF}_6$ is a rare example for a dicopper(II) system with weak ferromagnetic coupling and an $S = 1$ ground state. This observation contrasts to previously published phenolate-bridged dicopper(II) complexes, which usually show antiferromagnetic coupling, *i.e.* the symmetric complex $[\text{Cu}^{\text{II}}_2(\text{L}^1)(\text{OAc})_2]\text{ClO}_4$ ($J = -0.6 \text{ cm}^{-1}$; $\angle(\text{Cu-O-Cu}) = 128.65^\circ$)¹⁶⁹ and the asymmetric complexes $[\text{Cu}^{\text{II}}_2(\text{L}^{13})\text{Cl}_3]$ ($J = -168 \text{ cm}^{-1}$; $\angle(\text{Cu-O-Cu}) = 111.52^\circ$),¹⁷⁵ $[\text{Cu}^{\text{II}}_2(\text{H}_4\text{L}^{14})(\mu\text{-OH})](\text{ClO}_4)_2$ ($J = -238.1 \text{ cm}^{-1}$; $\angle(\text{Cu-O-Cu}) = 95.3^\circ$),¹⁷⁶ and $[\text{Cu}^{\text{II}}_2(\text{H}_2\text{L}^{15})(\mu\text{-OH})(\text{ClO}_4)]\text{ClO}_4$ ($J = -100.5 \text{ cm}^{-1}$; $\angle(\text{Cu-O-Cu}) = 91.9^\circ$).¹⁷⁶ It must be pointed out here that the determination of J from the magnetic data is much more accurate for $J < 0$ than for $J > 0$.¹⁷³ A comparison of key structural parameters and exchange integrals for bis(μ -phenoxido)dicopper(II) complexes reveals the dependence of J on (i) the $\text{Cu-O}_{\text{Ph}}\text{-Cu}$ angle, (ii) the $\text{Cu}\cdots\text{Cu}$ distance, (iii) the pyramidal geometry around the phenolate oxygen atom, and (iv) the deviation of the copper(II) coordination geometry from square pyramidal.¹⁷⁷ Similarly, the structural requirements for a strongly coupled hydroxido-bridged dicopper(II) system was investigated by Ruiz *et al.* theoretically, and it was found that (i) small Cu-O-Cu angles, (ii) short Cu-O distances, (iii) large out of plane shifts of the hydrogen atoms on the bridge, and (iv) hinge-distorted Cu_2O_2 rings lead to strong exchange coupling.¹⁷⁸ The major factor controlling the exchange coupling is the bridging Cu-O-Cu angle, and a linear variation of $2J$ with this parameter was observed for hydroxido-bridged and alkoxido-bridged dicopper(II) complexes.^{178, 179} For hydroxido-bridged dicopper(II) complexes the crossover point, below which the magnetic behavior changes from antiferromagnetic to ferromagnetic coupling, is characterized by a Cu-O(H)-Cu angle of 97.5° .¹⁷⁷ In the case of bis(μ -phenoxido)dicopper(II) complexes only five compounds revealing weak ferromagnetic coupling were observed, in which the $\text{Cu-O}_{\text{Ph}}\text{-Cu}$ angle lies in the range of $85.9 - 96.1^\circ$.¹⁷⁷ The $\text{Cu}(1)\text{-O}(1)\text{-Cu}(2)$ angle of $[\text{Cu}^{\text{II}}_2(\text{HSIM}^1)(\mu\text{-OAc})]\text{PF}_6$ is comparably large with a value of $118.24(7)^\circ$ when compared to other ferromagnetically coupled diphenoxido-bridged complexes, and in the medium range of antiferromagnetically coupled

phenoxido-bridged dicopper(II) complexes $[\text{Cu}^{\text{II}}_2(\text{L}^1)(\text{OAc})_2]\text{ClO}_4$,¹⁶⁹ $[\text{Cu}^{\text{II}}_2(\text{L}^{13})\text{Cl}_3]$,¹⁷⁵ $[\text{Cu}^{\text{II}}_2(\text{H}_4\text{L}^{14})(\mu\text{-OH})](\text{ClO}_4)_2$,¹⁷⁶ and $[\text{Cu}^{\text{II}}_2(\text{H}_2\text{L}^{15})(\mu\text{-OH})(\text{ClO}_4)]\text{ClO}_4$.¹⁷⁶

Interestingly, Chaudhuri *et al.* developed two bis(μ -phenoxido)dicopper(II) complexes, which contain the same ONO donor atoms but reveal opposite exchange interactions, $[\text{Cu}^{\text{II}}_2(\text{L}^{16})_2]$ the usual antiferromagnetic exchange coupling and $[\text{Cu}^{\text{II}}_2(\text{L}^{17})_2]$ ferromagnetic exchange coupling (Chart 9).¹⁷⁷ Several structural parameters were discussed to contribute to this contrasting magnetic behavior, the smaller Cu-O-Cu angle of $[\text{Cu}^{\text{II}}_2(\text{L}^{17})_2]$ (86.34° and 85.92° vs. 97.0° and 99.4° in $[\text{Cu}^{\text{II}}_2(\text{L}^{16})_2]$), the shorter Cu...Cu separation of $[\text{Cu}^{\text{II}}_2(\text{L}^{17})_2]$ (2.697 \AA vs. 2.967 \AA in $[\text{Cu}^{\text{II}}_2(\text{L}^{16})_2]$), and the more severe deviation from square planarity of the Cu^{II} centers in $[\text{Cu}^{\text{II}}_2(\text{L}^{17})_2]$. However, the parallel spin coupling of $[\text{Cu}^{\text{II}}_2(\text{L}^{17})_2]$ was mainly ascribed to the folded $\text{Cu}_2(\text{L}^{17})_2$ structure, in which the two copper(II) planes make an angle of 75.4° .

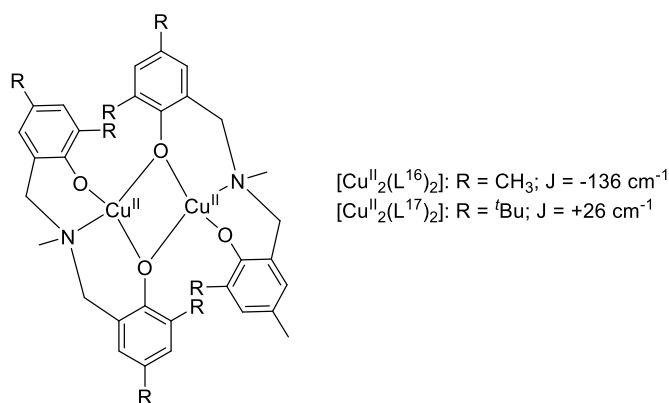


Chart 9: Bis(phenolate)-bridged dicopper(II) complexes with antiferromagnetic interaction ($[\text{Cu}^{\text{II}}_2(\text{L}^{16})_2]$) and ferromagnetic interaction ($[\text{Cu}^{\text{II}}_2(\text{L}^{17})_2]$).¹⁷⁷

Similarly, in $[\text{Cu}^{\text{II}}_2(\text{HSIM}^1)(\mu\text{-OAc})]\text{PF}_6$ the Cu(1)-O(1)-O(2)-N2-N4 plane forms an angle of 42.09° with the Cu(2)-O(1)-O(3)-N(4)-N(6) plane, which is rather small compared to the antiferromagnetically coupled complex $[\text{Cu}^{\text{II}}_2(\text{L}^1)(\text{OAc})_2]\text{ClO}_4$ with an angle of 57.65° . Thus, the stronger folding in $[\text{Cu}^{\text{II}}_2(\text{L}^1)(\text{OAc})_2]\text{ClO}_4$ lowers the magnitude of the antiferromagnetic interaction, which dominates exchange coupling between two Cu^{II} centers due to loss of orbital overlap. Similar diminution of antiferromagnetic coupling due to a folded Cu_2O_2 and a Cr_2O_2 core has been observed previously.^{177, 180} Moreover, the distortion of the $\text{O}_{\text{Ph}}\text{-C}_{\text{Ph}}$ bond with respect to the Cu- O_{Ph} -Cu plane is also known to affect the magnetic behavior.¹⁸¹ In fact, the O(1)- C_{Ph} bond in $[\text{Cu}^{\text{II}}_2(\text{HSIM}^1)(\mu\text{-OAc})]\text{PF}_6$ is placed out of the Cu-O(1)-Cu plane which is not the case in $[\text{Cu}^{\text{II}}_2(\text{L}^1)(\text{OAc})_2]\text{ClO}_4$.¹⁶⁹ Therefore, it is apparent that the major magnetic exchange interaction pathway between the two Cu^{II} centers is the oxygen atom of the bridging phenolate ligand. However, Horn *et al.* detected an impact of bridging acetate co-ligands on the coupling of a diiron(III) complex suggesting it to be a secondary pathway for the mediation of interaction.¹⁰²

3.2.5 COMPLEXATION STUDIES WITH Fe^{III}

In addition to the investigations with Ga^{III}, used to mimic the Fe^{III} center in native PAPs, the coordination behavior of H₃SIM¹ towards Fe^{III} was examined. Similar to Cu^{II}, Fe^{III} is paramagnetic with a (Ar)3d⁵ configuration. Therefore, the coordination chemistry towards Fe^{III} was studied by electronic and NMR spectroscopic techniques, suitable for paramagnetic substances.

UV-vis-NIR Titration

Recording a UV-vis-NIR spectroscopic time scan with mixtures of H₃SIM¹ and iron(III) perchlorate in methanol both with and without base for about ten hours, the change in the number and intensity of absorption bands was monitored during the first 1.5 hours; afterwards no change in the spectra was detected. Therefore, all samples were allowed to react at room temperature for 14 hours before the UV-vis-NIR spectroscopic analysis was undertaken in order to assure that the reactions were completed. The spectrum of a mixture of H₃SIM¹ and iron(III) perchlorate in a ratio of 1:1 showed two bands at 348 nm and 552 nm. The relatively broad band at 552 nm ($\epsilon = 1238 \text{ M}^{-1}\text{cm}^{-1}$) originates from the charge transfer (CT) transition from filled p_{π} orbitals of the phenolate oxygen to the empty d_{π^*} orbitals of the Fe^{III} metal center. All phenoxido-Fe^{III} complexes display this characteristic phenolate-to-iron(III) CT transition,⁸¹ for example the complex [Fe^{III}Mn(L¹)(μ -OAc)₂]⁺ in acetone at 596 nm ($\epsilon = 980 \text{ M}^{-1}\text{cm}^{-1}$)¹⁸² and the complex [Fe^{III}₂(L¹⁸)₂(μ -O)(μ -OBz)]⁺ in acetonitrile at 522 nm ($\epsilon = 2700 \text{ M}^{-1}\text{cm}^{-1}$)¹⁸³. The additional band at 348 nm ($\epsilon = 3838 \text{ M}^{-1}\text{cm}^{-1}$) arises from p_{π} - d_{σ^*} type transitions.

Comparison of the UV-vis-NIR spectra, recorded with methanolic solutions of H₃SIM¹ and iron(III) perchlorate up to a ratio of 1:2 (Figure 16a), illustrates the coordination of one equivalent Fe^{III} ions by ligand H₃SIM¹ resulting in a green solution. Complexation of a second Fe^{III} ion is unlikely due to the detection of a plateau of the absorbance at 552 nm vs. Fe^{III} content plot (insert in Figure 16a) for mixtures with excess Fe^{III}. The increase of the absorbance at 348 nm at Fe^{III} contents higher than one equivalent with respect to the ligand possibly arises from non-coordinated free Fe^{III} in solution and the resulting hexaaqua complex.

Addition of one equivalent of triethylamine as a base led to a shift of the CT band from 552 nm to 488 nm ($\epsilon = 1718 \text{ M}^{-1}\text{cm}^{-1}$), directly visible in the change of the solution color to blue and possibly due to deprotonation of the phenol moiety. A further increase of the base concentration did not result in additional changes. The p_{π} - d_{σ^*} band at 342 nm ($\epsilon = 5132 \text{ M}^{-1}\text{cm}^{-1}$) experienced almost no change during the addition of base. Similarly to the experiments undertaken without addition of base, the absorbance vs. equivalence of Fe^{III} plot for the mixtures of H₃SIM¹, treated with one equivalent of triethylamine and iron(III) perchlorate, shows the increase in intensity of

the bands at 342 nm and 488 nm up to a 1:1.25 mixture (Figure 16b). At higher Fe^{III} concentrations the curve (inset) shows a plateau, suggesting that H_3SIM^1 is able to bind only one Fe^{III} ion, independently of the presence of base.

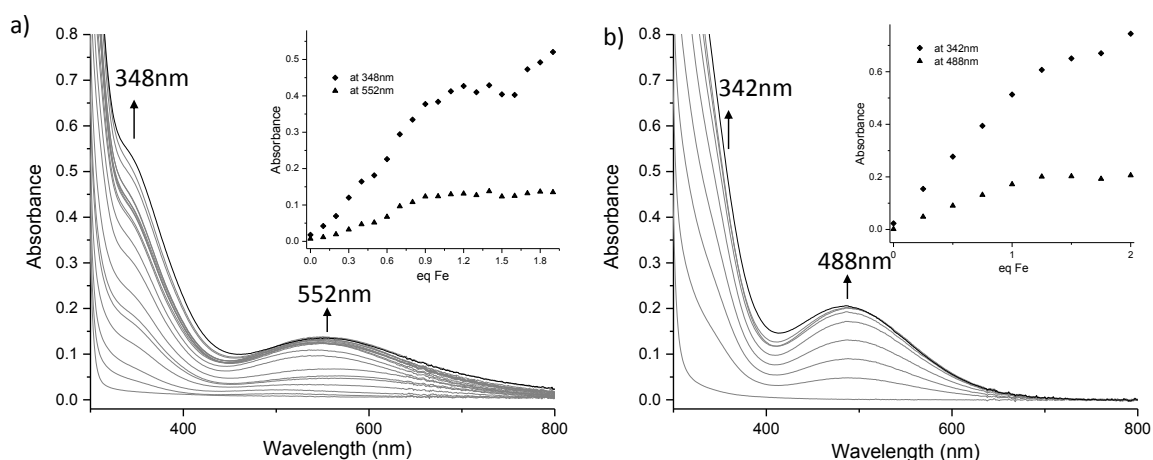


Figure 16: UV-vis-NIR spectroscopic titration of H_3SIM^1 (0.4 mM) with $\text{Fe}^{\text{III}}(\text{ClO}_4)_3$ in methanol a) without NEt_3 and b) with 1 eq of NEt_3 .

These results are in contrast to the observation gained during a similar UV-vis-NIR spectroscopic titration of ligand H_3L^2 with $[\text{FeCl}_4](\text{NEt}_4)$ in methanol, because a progressive shift of the CT transitions from 533 nm to 629 nm was monitored by addition up to one equivalent of Fe^{III} and a constant increase in intensity of the band with further addition of Fe^{III} . These findings were explained by the simultaneous formation of mono- and dinuclear iron(III) complexes at low Fe^{III} content in solution and the shift of the equilibrium in favor of the diiron(III) complex with raising Fe^{III} concentrations.¹⁰⁹ Considering these observations, the positioning of two bulky pivaloyl-amide residues proximal to one binding site seems to hinder the coordination of Fe^{III} in coordination site C, which was still possible when only one pivaloyl-amide moiety was adjacent to the coordination sites as in H_3L^2 .

NMR Studies

A mixture of H_3SIM^1 with 0.5 equivalents of iron(II) tetrafluoroborate in deuterated acetonitrile was treated with 4Å molecular sieves and left to react under air for 12 hours. The recorded ^1H NMR spectrum (-60 ppm to 260 ppm) of the blue solution shows broad resonances in the aromatic region associated with the uncomplexed ligand. However, resonances with chemical shifts higher than 10 ppm were not detected in contrast to the spectrum of $[\text{Fe}^{\text{II}}_2(\text{H}_2\text{SIM}^1)(\mu\text{-OAc})_2]^+$, which will be discussed in Chapter 5.3, supporting the proposal of the full oxidation of Fe^{II} to Fe^{III} during the reaction under aerobic conditions. Unfortunately, differences in the integrals assigned to protons of binding site B and binding site C could not be detected due to broadening of the signals.

The measurement of the magnetic susceptibility of the mixture by the Evans method resulted in a value of $\mu_{\text{eff}} = 4.79$ B.M. Based on a comparison with the calculated spin-only values for a low-spin Fe^{III} complex ($S = 1/2$) of 1.73 B.M. and for a high-spin Fe^{III} complex ($S = 5/2$) of 5.92 B.M., H_3SIM^1 is proposed to form a mononuclear high-spin Fe^{III} complex.

It is apparent from the results of the NMR and UV-vis-NIR spectroscopic examinations of mixtures with H_3SIM^1 and iron salts that H_3SIM^1 is capable of coordinating one Fe^{III} ion, generating a high-spin Fe^{III} complex. The coordination of the Fe^{III} ion most likely takes place in the more accessible binding site B. This proposal is made on the basis of the observations from the ^1H NMR titration with Ga^{III} , used as Fe^{III} mimic, and a crystal structure obtained with ligand H_4SIM^3 , which bears also binding site B, and iron(III) perchlorate. In this way, the second coordination site C of H_3SIM^1 stays vacant for other, preferably divalent, metal ions to form heterodinuclear complexes and thereby form a more accurate model for PAPs.

3.3 COMPLEXATION BEHAVIOR OF LIGAND H_4SIM^3

In addition to the asymmetry in the second coordination sphere H_4SIM^3 provides also asymmetry in the donor sets, in contrast to H_3SIM^1 . The two compartments in H_4SIM^3 are built up by different donors, forming a N_3O coordination site (binding site C, Chart 10) and a harder N_2O_2 coordination site, containing a terminal phenolate moiety (binding site A, Chart 10).

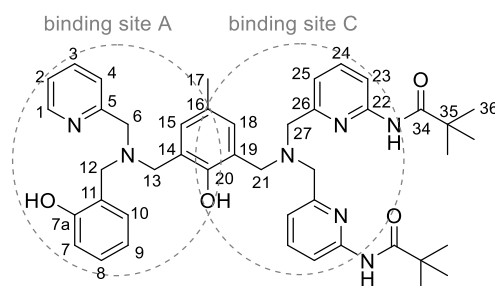


Chart 10: Assignment of the binding sites provided by ligand H_4SIM^3 and the numbering of its atoms.

However, the positions of the two pivaloyl-amide residues, mimicking the hydrogen bond donors in the active site of PAP, are comparable to H_3SIM^1 . Therefore, the comparison of the coordination behavior of H_3SIM^1 and H_4SIM^3 provides the opportunity to investigate the impact of the exchange of one pyridine by a phenolate residue at preserved positions of the hydrogen bond donors.

3.3.1 COMPLEXATION STUDIES WITH Zn^{II}

Similar to the investigation of the Zn^{II} complexation behavior of H_3SIM^1 , the coordination chemistry of H_4SIM^3 with Zn^{II} ions was studied applying the above introduced NMR titration technique (Chapter 3.2.1).

NMR Studies

Comparable to the analogous experiments undertaken with H_3SIM^1 , the generation of a monozinc(II) complex could be followed during addition of zinc(II) perchlorate by 1H NMR spectra, measured after each addition step of 0.25 eq to H_4SIM^3 , dissolved in acetonitrile. However, after addition of one equivalent, further increase of the Zn^{II} concentration did not result in a second set of resonances, suggesting that the generation of a dizinc(II) complex of H_4SIM^3 does not occur. In the monozinc(II) complex spectrum the resonances assigned to binding site C are shifted compared to those in the spectrum of the free ligand. This observation was duplicated during the complexation of Zn^{II} in binding site C of ligand H_3SIM^1 , suggesting the Zn^{II} ion to be bound by the two amidated pyridine residues in binding site C of H_4SIM^3 (see Figures 2 and Figure 17).

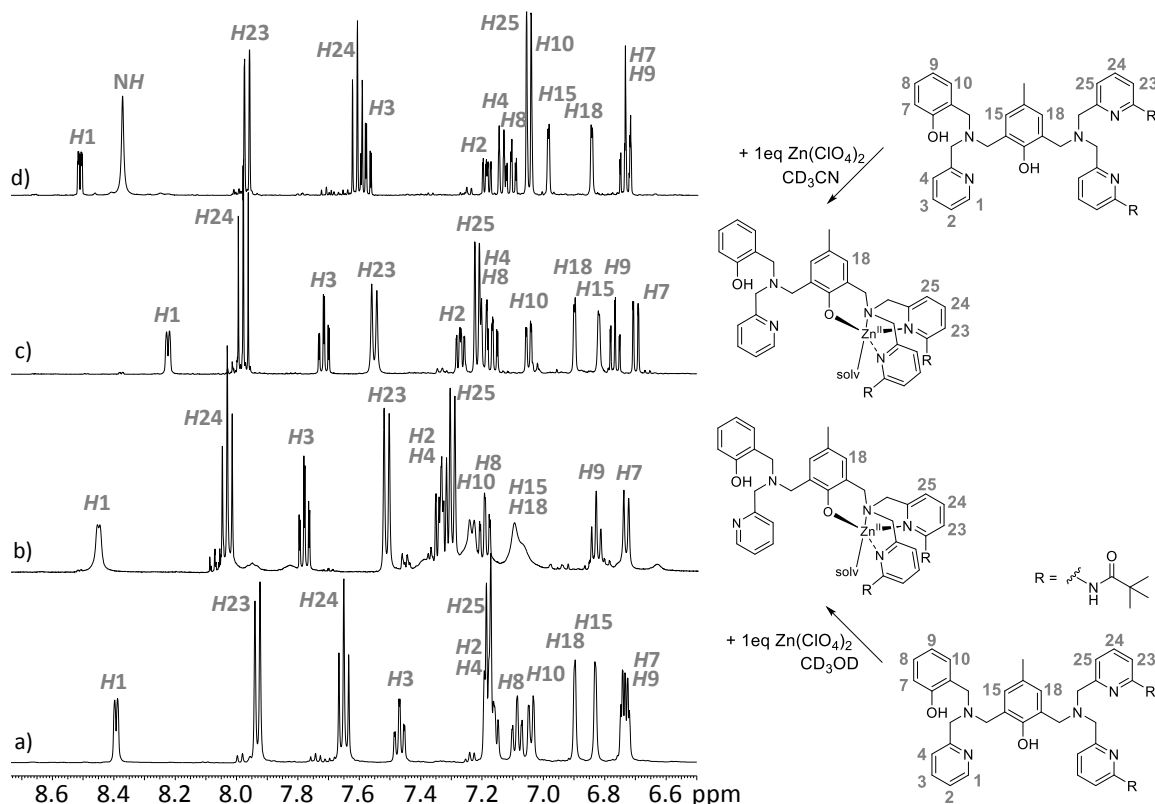


Figure 17: Comparison of the aromatic regions in the 1H NMR of a) H_4SIM^3 in CD_3OD with b) H_4SIM^3 with 1.0 eq $Zn^{II}(ClO_4)_2$ in CD_3OD , c) H_4SIM^3 with 1.0 eq $Zn^{II}(ClO_4)_2$ in CD_3CN/D_2O , and d) H_4SIM^3 in CD_3CN .

Moreover, the methylene resonance assigned to *H27* was split into two doublets upon addition of zinc(II) perchlorate, confirming the coordination of Zn^{II} to binding site C. A similar behavior was found when the experiment was performed in methanol. However, the chemical shifts of the resonances assigned to the pyridine residue in binding site A differ in the two different solvents used (Figure 17).

When the experiment was undertaken in methanol the resonance of *H1* was only slightly affected (shifting by 0.05 ppm), but when acetonitrile was used as solvent and zinc(II) perchlorate was dissolved in deuterium oxide, this resonance was shifted by 0.3 ppm upon formation of a monozinc(II) complex (which is not completely an effect of the change in polarity of the solvent as (i) further addition of zinc(II) perchlorate in deuterium oxide did not influence the chemical shift of this resonance, and (ii) the *H1* resonance assigned to the monozinc(II) complex was also detected at the same position after addition of only 0.5 eq of zinc(II) perchlorate and therefore less deuterium oxide). For the resonance assigned to *H3* the opposite behavior was observed; a larger shift in acetonitrile/deuterium oxide than in methanol. The resonances allocated to the terminal phenol residue in binding site A did not change to this extent in both solvents used. Based on these findings the proposal of two differing complexes in the different solvents used with variation orientation of the pyridine residue in binding site A was made. Possibly, the orientation of the pyridine nitrogen atom in the direction of the Zn^{II} center in acetonitrile/deuterium oxide are assisted by hydrogen bonding via deuterium oxide solvent molecules.

Interestingly, addition of a methanolic solution of zinc(II) acetate to ligand H₄SIM³ in methanol led directly to a dizinc(II) complex. This was proposed due to the fact that the concentration of the new formed species only increased by half of the factor the concentration of Zn^{II} was raised. The addition of 0.25 eq of Zn^{II} resulted in an ~ 0.125:0.875 mixture of new species and remaining free ligand. Although the resonances broadened during addition of two equivalents of Zn^{II}, it is recognizable that the resonances of the terminal phenolate are shifted by the coordination of Zn^{II} (Figure 18). The ability of ligand H₄SIM³ to form a dizinc(II) complex by reaction with zinc(II) acetate is additionally supported by the obtained crystal structure, which will be discussed in Chapter 4.3.

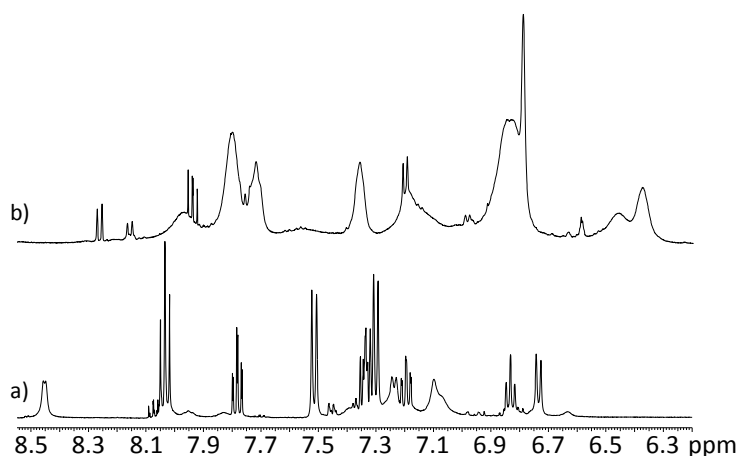


Figure 18: Comparison of the aromatic regions in the ^1H NMR of H_4SIM^3 in CD_3OD with a) 2.0 eq $\text{Zn}^{\text{II}}(\text{ClO}_4)_2$ and b) 2.0 eq $\text{Zn}^{\text{II}}(\text{OAc})_2$.

Mass Spectrometry

In order to further investigate the composition of the species formed during the addition of zinc(II) salts to H_4SIM^3 containing solution samples were taken during the NMR titration at several addition steps and ESI^+ mass spectra were recorded. The main peaks detected in the spectra of mixtures up to a 1:1 ratio of H_4SIM^3 and zinc(II) perchlorate were found at m/z 744.4, which match the mass of metal-free ligand H_4SIM^3 , and at m/z 806.2 assigned to the $[\text{Zn}^{\text{II}}(\text{H}_3\text{SIM}^3)]^+$ complex. Further addition of zinc(II) perchlorate led to an additional signal at m/z 868.1 assigned to the dizinc(II) complex $[\text{Zn}^{\text{II}}_2(\text{HSIM}^3)]^+$, as well as to the signals at m/z 403.7 ($[\text{Zn}^{\text{II}}(\text{H}_3\text{SIM}^3)]^{2+}$) and m/z 434.7 ($[\text{Zn}^{\text{II}}_2(\text{HSIM}^3)]^{2+}$). For the latter two signals the mass to charge ratio between the peaks in the isotopic pattern was decreased two fold, in accord with the formation of doubly charged species.

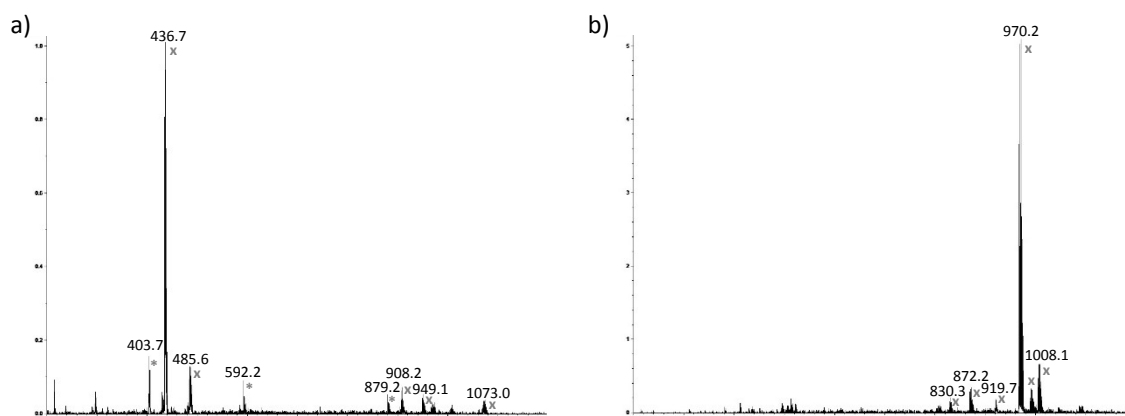


Figure 19: ESI^+ mass spectra of H_4SIM^3 with a) 2.0 eq $\text{Zn}^{\text{II}}(\text{ClO}_4)_2$ and b) 2.0 eq $\text{Zn}^{\text{II}}(\text{OAc})_2$ (asterisks mark signals with monozinc isotopic pattern, crosses mark signals with dizinc isotopic pattern).

The contribution of the species accountable for the signals detected was identified by their isotopic patterns, which were characteristic either for monozinc(II) or for dizinc(II) species, as

explained in Chapter 3.2.1 (Figure 3a and 3b). During mass spectrometric investigations there is often the debate about the presence of dizinc(II) complexes already present in the sample solution, since the generation is also possible during the mass spectrometric measurement from the monozinc(II) complex in presence of Zn^{II} ions. However, the constant detection of monozinc(II) complexes in mixtures with 2.0 eq (Figure 19a), and even 2.15 eq of zinc(II) perchlorate imply that the dizinc(II) complexes are generated during the mass spectrometric measurement. Based on this consideration, and taking into account the result from the 1H NMR titration, the sole formation of a monozinc(II) complex without presence of a dizinc(II) complex by the addition of zinc(II) perchlorate to H_4SIM^3 is proposed.

In contrast, after addition of two equivalents of zinc(II) acetate to H_4SIM^3 an ESI^+ mass spectrum (Figure 19b) was recorded with one main peak at m/z 966.2 with an isotopic pattern characteristic for a dizinc(II) complex, assigned to $[Zn^{II}_2(H_2SIM^3)(OAc)(H_2O)(D_2O)]^+$, in the absence of signals corresponding to a monozinc(II) species. Therefore, it is apparent that the presence of acetate anions in solution favors the complexation of two Zn^{II} ions by ligand H_4SIM^3 . This observation is in agreement with the preparation of $[Zn^{II}_2(H_2SIM^3)(\mu-OAc)(OH)]$ in high yield which will be discussed in Chapter 4.2.

3.3.2 COMPLEXATION STUDIES WITH GA^{III}

Comparable to the Ga^{III} coordination studies of H_3SIM^1 , the Ga^{III} complexation by H_4SIM^3 was examined by NMR titration as well as mass spectrometric measurements.

NMR Studies

Gallium(III) perchlorate and gallium(III) nitrate were used as Ga^{III} source for the 1H NMR titration experiment. The coordination of Ga^{III} ions by H_4SIM^3 was found to be less kinetically favored than Zn^{II} coordination, as the mixtures of H_4SIM^3 and Ga^{III} needed to be heated for an hour at $50^\circ C$ before the reaction was completed. Addition of one equivalent of gallium(III) perchlorate to H_4SIM^3 in methanol led to a new species, in which especially the resonances corresponding to binding site A are shifted (Figure 20b) compared to the metal-free ligand.

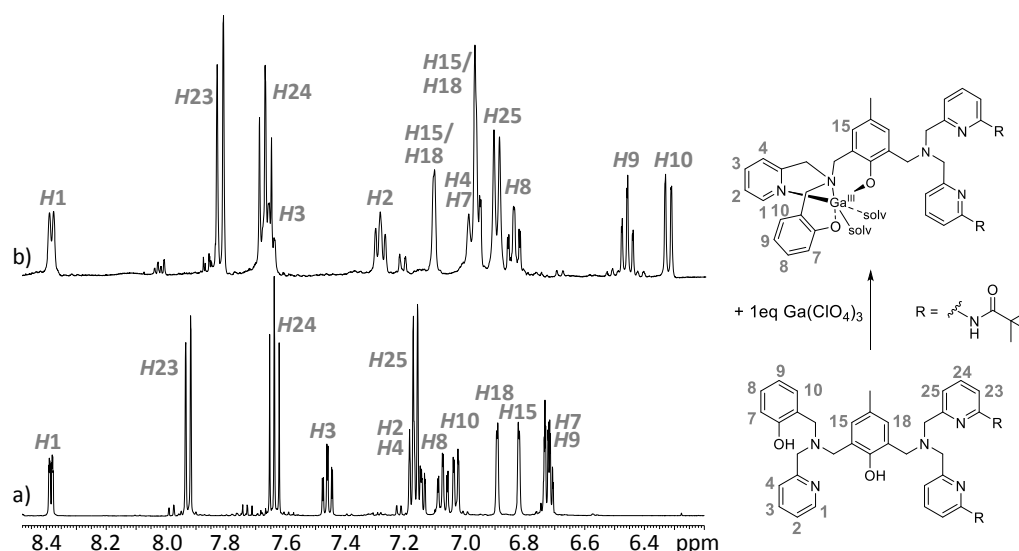


Figure 20: Comparison of the aromatic regions in the ^1H NMR of a) H_4SIM^3 in CD_3OD with b) 2.0 eq $\text{Ga}^{\text{III}}(\text{ClO}_4)_3$.

Addition of two equivalents of gallium(III) nitrate in deuterium oxide to H_4SIM^3 in acetonitrile resulted in a very similar spectrum, suggesting that the formation of a digallium(III) complex of H_4SIM^3 is not possible and that the Ga^{III} ions are selectively bound to binding site A, independent of the gallium(III) salt and solvent used. This is in accordance with the results derived from the reaction of Ga^{III} with H_3SIM^1 , providing the identical binding site C (Chapter 3.2.2), suggesting that in this binding site Ga^{III} ions are unlikely to be bound.

Mass Spectrometry

The inability of H_4SIM^3 to form a digallium(III) complex was also confirmed in the mass spectrum obtained with a 1:2 mixture of H_4SIM^3 with gallium(III) nitrate. The only major peak was detected at m/z 810.2 with a characteristic monogallium isotopic pattern corresponding to the $[\text{Ga}^{\text{III}}(\text{H}_2\text{SIM}^3)]^+$ complex.

3.3.3 COMPLEXATION STUDIES WITH Fe^{III}

The investigations with Ga^{III} as Fe^{III} mimic showed that Ga^{III} ions are only bound in binding site A of ligand H_4SIM^3 , leaving binding site C vacant, as already observed with H_3SIM^1 . In order to verify this proposal, the coordination of Fe^{III} ions by ligand H_4SIM^3 was examined by X-ray diffraction and mass spectrometric analysis.

X-ray Diffraction

Treatment of H_4SIM^3 in methanol (27 mM) with iron(III) perchlorate (2.0 eq) and heating for 15 min at 50°C resulted in a purple solution. Following addition of sodium tetrafluoroborate (4.0 eq) and diethylether diffusion yielded small black crystals, suitable for X-ray data collection. Figure 21 shows a plot of the molecular structure and Table 6 gives selected structural parameters.

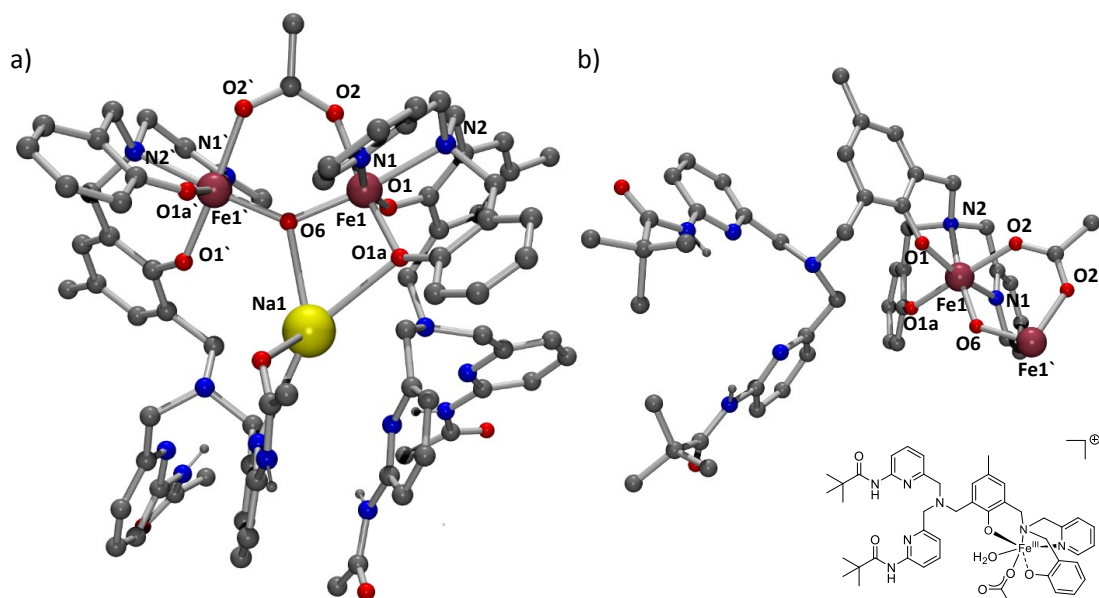


Figure 21: Structure of a) $\{\text{Na}[\text{Fe}^{\text{III}}(\text{H}_2\text{SIM}^3)]_2(\mu\text{-OAc})(\mu\text{-OH}_2)\}^{2+}$ and b) its monomeric section (counter ions, non-coordinated solvent molecules, and hydrogen atoms, not involved in hydrogen bonding, have been omitted for clarity; crystallographic data and ORTEP plots with 50% probability level of thermal ellipsoids appear in the Appendix, Table 31 and Figure 73).

Table 6: Selected bond lengths (\AA) and angles ($^\circ$) for $\{\text{Na}[\text{Fe}^{\text{III}}(\text{H}_2\text{SIM}^3)]_2(\mu\text{-OAc})(\mu\text{-OH}_2)\}(\text{BF}_4)_2$.

	$\{\text{Na}[\text{Fe}^{\text{III}}(\text{H}_2\text{SIM}^3)]_2(\mu\text{-OAc})(\mu\text{-OH}_2)\}^{2+}$	
	Fe(1)	Fe(1') ^a
Fe(1)···Fe(1')	3.567	
Fe(1)-O(1)	1.918(6)	1.936(5)
Fe(1)-O(1A)	1.971(5)	1.870(6)
Fe(1)-O(2)	2.019(5)	2.063(6)
Fe(1)-N(1)	2.152(7)	2.137(7)
Fe(1)-N(2)	2.201(7)	2.206(6)
Fe(1)-O(6)	1.943(6)	1.933(5)
Fe(1)-O(6)-Fe(1')	134.0(3)	
O(1)-Fe(1)-N(1)	163.6(3)	86.4(2)
O(1)-Fe(1)-N(2)	86.1(3)	88.7(2)
O(1)-Fe(1)-O(1A)	95.3(2)	95.5(2)
O(1)-Fe(1)-O(2)	94.4(2)	170.8(2)
O(1)-Fe(2)-O(6)	100.5(2)	91.9(2)

The structure reveals a diiron(III) core bridged by an aqua and an acetate co-ligand. Both Fe^{III} centers are additionally coordinated by a pyridine and two phenolate moieties provided by two deprotonated H_4SIM^3 ligand molecules. Furthermore, the crystal cell of

$\{\text{Na}[\text{Fe}^{\text{III}}(\text{H}_2\text{SIM}^3)]_2(\mu\text{-OAc})(\mu\text{-OH}_2)\}(\text{BF}_4)_2$ includes a sodium ion and a tetrafluoroborate counterion. A similar dimeric structure of an Fe^{III} complex was published by Que *et al.*, obtained with the mononucleating ligand *N*-(*o*-hydroxybenzyl)-*N,N*-bis(2-pyridylmethyl)amine (HDP, HL¹⁸). This published structure of $[\text{Fe}^{\text{III}}_2(\text{L}^{18})_2(\mu\text{-O})(\mu\text{-OBz})]\text{BPh}_4$ is formed by a $(\mu\text{-oxo})(\mu\text{-benzoate})$ diiron(III) core.¹⁸³

The two Fe^{III} ions in $\{\text{Na}[\text{Fe}^{\text{III}}(\text{H}_2\text{SIM}^3)]_2(\mu\text{-OAc})(\mu\text{-OH}_2)\}(\text{BF}_4)_2$, separated by 3.567 Å, are coordinated in the harder binding site A of the dinucleating ligand H_4SIM^3 and reveal short Fe-O distances (average 1.957 Å), comparable to those of published complexes of H_2L^4 , in which Fe^{III} is also coordinated in binding site A. Examples are $[\text{Fe}^{\text{III}}\text{Fe}^{\text{II}}(\text{L}^4)(\mu\text{-OAc})_2]^+$ (1.967 Å),¹⁴⁰ $[\text{Fe}^{\text{III}}\text{Cu}^{\text{II}}(\text{L}^4)(\mu\text{-OAc})_2]^+$ (1.978 Å),⁹² $[\text{Fe}^{\text{III}}\text{Mn}^{\text{II}}(\text{L}^4)(\mu\text{-OAc})_2]^+$ (1.976 Å),⁹⁶ $[\text{Fe}^{\text{III}}\text{Ni}^{\text{II}}(\text{L}^4)(\mu\text{-OAc})_2]^+$ (1.967 Å),¹⁴¹ $[\text{Fe}^{\text{III}}\text{Ni}^{\text{II}}(\text{L}^4)(\mu\text{-OAc})(\text{OH}_2)_2]^{2+}$ (1.990 Å),¹⁴² $[\text{Fe}^{\text{III}}\text{Zn}^{\text{II}}(\text{L}^4)(\text{OH}_2)(\mu\text{-OH})]^{2+}$ (1.985 Å),^{90, 144} $[\text{Fe}^{\text{III}}\text{Cd}^{\text{II}}(\text{L}^4)(\mu\text{-OAc})_2]^+$ (1.978 Å),¹⁴⁵ $[[\text{Fe}^{\text{III}}\text{Hg}^{\text{II}}(\text{L}^4)(\mu\text{-OH})]_2]^{2+}$ (1.985 Å),¹⁴⁵ and $[\text{Fe}^{\text{III}}\text{Co}^{\text{II}}(\text{L}^4)(\mu\text{-OAc})_2]^+$ (1.971 Å).¹⁴⁶ However, it should be mentioned that the metal ion coordinated in the second coordination site may have an effect on the average Fe^{III} -O distance.

The structure of $\{\text{Na}[\text{Fe}^{\text{III}}(\text{H}_2\text{SIM}^3)]_2(\mu\text{-OAc})(\mu\text{-OH}_2)\}(\text{BF}_4)_2$ demonstrates that the Fe^{III} ion is preferably coordinated in the harder binding site A, which is in agreement with the NMR titration experiments performed with Ga^{III} as an Fe^{III} mimic. Moreover, although an excess of iron(III) perchlorate was present in solution, binding site C was left vacant during the crystallization. The structure of $[\text{NaFe}^{\text{III}}(\text{H}_2\text{SIM}^1)(\mu\text{-OAc})_2]\text{PF}_6$, which will be discussed in Chapter 5.3 in more detail, also carries the Fe^{III} ion only in the non-amidated binding site of H_3SIM^1 , while binding site C was occupied by a Na^+ ion. Therefore, the coordination of Fe^{III} in binding site C seems to be unfavored.

Mass Spectrometry

A methanolic solution of H_4SIM^3 (6.86 mM) was treated with two equivalents of sodium hydroxide and one equivalent of iron(II) tetrafluoroborate and the mixture was stirred for 14 hours under aerobic conditions (investigations with UV-vis-NIR spectroscopy and NMR spectroscopy revealed the completed oxidation of Fe^{II} to Fe^{III} after this period of time). The recorded ESI⁺ mass spectrum of this mixture (Figure 22a) shows one main signal at m/z 797.3, which matches the mass of the $[\text{Fe}^{\text{III}}(\text{H}_2\text{SIM}^3)]^+$ complex and shows the characteristic pattern for a monoiron complex (Figure 23a). The detection of a monoiron complex supports the finding obtained from the ¹H NMR titration with Ga^{III} as an Fe^{III} mimic as well as from the X-ray diffraction analysis, that Ga^{III} ions can only be bound in one coordination site, namely in binding site A. This proposal is supported by the UV-vis-NIR spectroscopic titration of H_3SIM^1 , which contains also binding site C, with iron(III) perchlorate as well as the ¹H NMR titration and the X-ray structural

analysis of H_3SIM^1 with Ga^{III} as an Fe^{III} mimic, which revealed that Fe^{III} and Ga^{III} cannot be bound in the hindered binding site C.

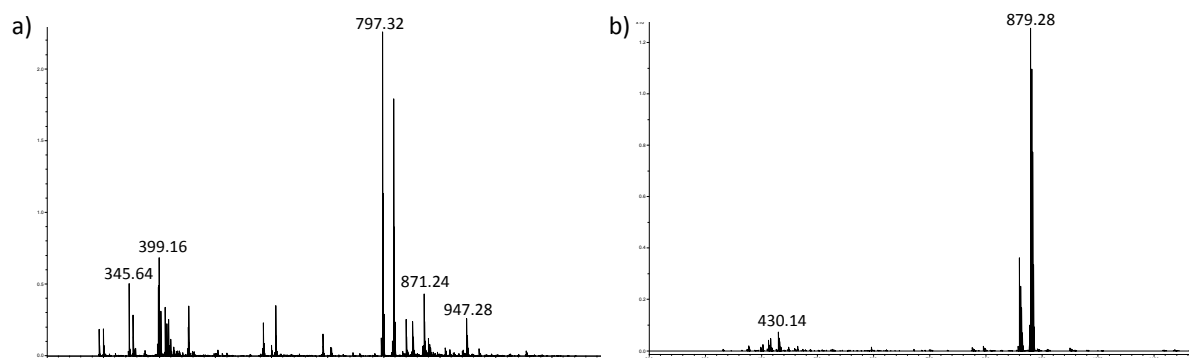


Figure 22: ESI⁺ mass spectra of H_4SIM^3 with a) 1.0 eq $\text{Fe}^{\text{II}}(\text{BF}_4)_2$ after 14 hours exposure to air and b) 1.0 eq $\text{Fe}^{\text{II}}(\text{BF}_4)_2$ after 14 hours of exposure to air and addition of 1.0 eq $\text{Zn}^{\text{II}}(\text{OMe})_2$ in methanol.

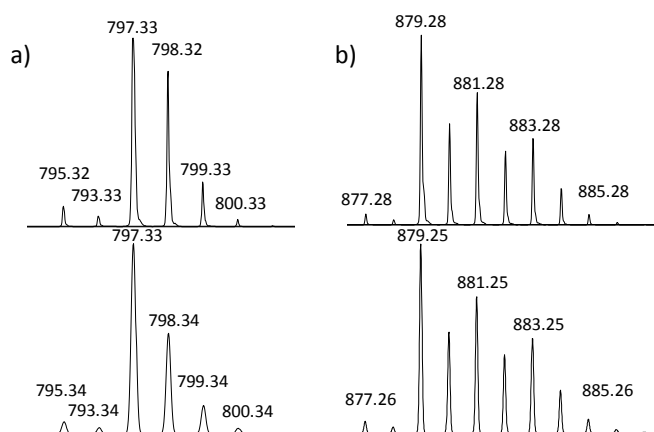


Figure 23: Characteristic isotopic pattern found in ESI⁺ mass spectra (experimental (top) and calculated (bottom)) of H_4SIM^3 with a) 1 eq of $\text{Fe}^{\text{II}}(\text{BF}_4)_2$ (after 14 hours of exposure to air) ($[\text{Fe}^{\text{III}}(\text{H}_2\text{SIM}^3)]^+$) and b) 1 eq of $\text{Fe}^{\text{II}}(\text{BF}_4)_2$ (after 14 hours of exposure to air) and 1 eq of $\text{Zn}^{\text{II}}(\text{OMe})_2$ ($[\text{Fe}^{\text{III}}\text{Zn}^{\text{II}}(\text{HSIM}^3)\text{F}]^+$) in methanol.

Moreover, one equivalent of zinc(II) methoxide was added after 14 hours to the mixture of H_4SIM^3 and one equivalent of iron(II) tetrafluoroborate under aerobic conditions. The resulting ESI⁺ mass spectrum (Figure 21b) contains signals with a characteristic FeZn isotopic pattern (Figure 22b), besides the small signal at m/z 797.3 stemming from residues of the monoiron complex. The FeZn signals at m/z 430.1, m/z 859.2 and m/z 879.3 were assigned to $[\text{Fe}^{\text{III}}\text{Zn}^{\text{II}}(\text{HSIM}^3)]^{2+}$, $[\text{Fe}^{\text{III}}\text{Zn}^{\text{II}}(\text{SIM}^3)]^+$ and $[\text{Fe}^{\text{III}}\text{Zn}^{\text{II}}(\text{HSIM}^3)\text{F}]^+$. This indicates that Zn^{II} ions are selectively coordinated in the softer vacant binding site C, while the harder binding site A is occupied by the harder Fe^{III} ion, generating an accurate model for the FeZn active site of PAPs.

3.3.4 FORMATION OF A HETERODINUCLEAR $\text{Ga}^{\text{III}}\text{Zn}^{\text{II}}$ COMPLEX

As discussed in Chapters 3.3.1 and 3.3.2, H_4SIM^3 was found to bind (i) Zn^{II} selectively in binding site C, and (ii) Ga^{III} in the harder binding site A. These findings are in agreement with the observed crystal structure of $[\text{Ga}^{\text{III}}\text{Zn}^{\text{II}}(\text{L}^4)(\mu\text{-OAc})_2]^+$.⁶⁶ This ligand lacks the pivaloyl-amide residues at the 6-position of the pyridine residues compared to H_4SIM^3 , but provides a similar primary coordination sphere. In $[\text{Ga}^{\text{III}}\text{Zn}^{\text{II}}(\text{L}^4)(\mu\text{-OAc})_2]^+$, Ga^{III} is bound in the harder binding N_2O_4 -binding site and Zn^{II} is coordinated in the softer N_3O_3 -binding site.⁶⁶ The possibility to generate a $\text{Ga}^{\text{III}}\text{Zn}^{\text{II}}$ complex with H_4SIM^3 , in which the two different metal ions are bound in distinct binding sites, was investigated via NMR spectroscopy and mass spectrometry.

NMR Studies

Ligand H_4SIM^3 , dissolved in acetonitrile, was treated with one equivalent of zinc(II) perchlorate dissolved in deuterium oxide and the formation of the monozinc(II) complex was confirmed by the measurement of a ^1H NMR spectrum (Figure 24b). Afterwards, gallium(III) nitrate, dissolved in deuterium oxide, was added stepwise and the changes were followed using NMR spectroscopy. After addition of one equivalent of gallium(III) nitrate to the monozinc(II) complex of H_4SIM^3 one new main species is visible in the ^1H NMR spectrum, in addition to at least three other new species (Figure 24c).

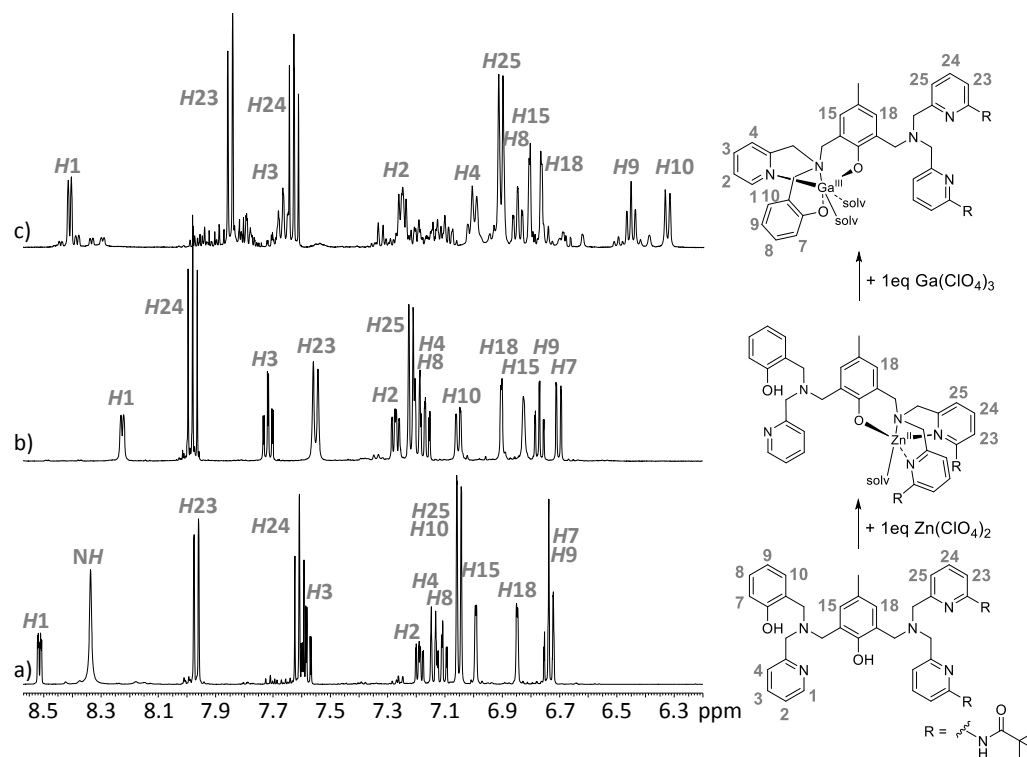


Figure 24 Comparison of the aromatic regions in the ^1H NMR of a) H_4SIM^3 in CD_3CN , b) H_4SIM^3 with 1.0 eq of $\text{Zn}^{\text{II}}(\text{ClO}_4)_2$ in $\text{CD}_3\text{CN}/\text{D}_2\text{O}$, and c) H_4SIM^3 with 1.0 eq of $\text{Zn}^{\text{II}}(\text{ClO}_4)_2$ and 1.0 eq of $\text{Ga}^{\text{III}}(\text{ClO}_4)_3$ in $\text{CD}_3\text{CN}/\text{D}_2\text{O}$.

The resonances of $H9$ and $H10$ are shifted upfield similar as found in the monogallium(III) complex spectrum. Furthermore, the resonances assigned to $H23$, $H24$ and $H25$ have also a similar chemical shift in the monogallium(III) complex. Therefore, the formation of the monogallium(III) complex, lacking the Zn^{II} ion in the second coordination site, is proposed during this experiment.

Interestingly, the analogous experiment undertaken in methanol gave a different result. Although the addition of gallium(III) perchlorate to the monozinc(II) complex also resulted in the formation of three species the chemical shifts of the resonances assigned to $H23$, $H24$ and $H25$ did not result in the identical chemical shifts of those measured in the monogallium(III) complex. Moreover, when the experimental procedure was changed, *i.e.* when zinc(II) perchlorate was added to the monogallium(III) complex, which had been generated in methanol prior to the addition of the zinc(II) ion (Figure 25a) only one new species was detected (Figure 25c, d). In order to preserve complete conversion to the $Ga^{III}Zn^{II}$ complex treatment with one equivalent of base (NaOD in D_2O) was necessary (Figure 25d). To confirm that the base was responsible for the complexation in the latter experiment, the addition of D_2O was tested in a separate experiment. Addition of D_2O was found to have no influence on the species distribution.

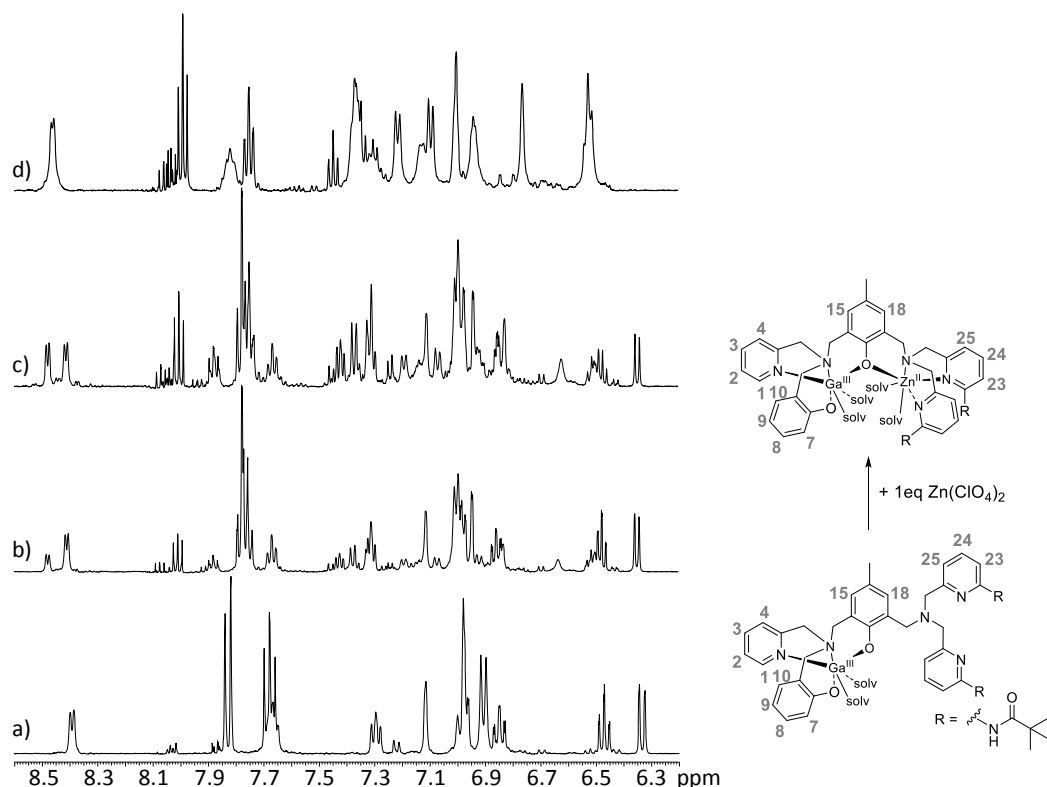


Figure 25: Comparison of the aromatic regions in the 1H NMR of a) H_4SIM^3 with 1.1 eq of $Ga^{III}(ClO_4)_3$ in CD_3OD , b) H_4SIM^3 with 1.1 eq of $Ga^{III}(ClO_4)_3$ and 0.5 eq of $Zn^{II}(ClO_4)_2$ in CD_3OD , c) H_4SIM^3 with 1.1 eq of $Ga^{III}(ClO_4)_3$ and 1.0 eq of $Zn^{II}(ClO_4)_2$ heated to $60^\circ C$ for 8h, and d) H_4SIM^3 with 1.1 eq of $Ga^{III}(ClO_4)_3$, 1.0 eq of $Zn^{II}(ClO_4)_2$ and 1.0 eq of NaOD in CD_3OD/D_2O .

Mass Spectrometry

The mass spectrometric investigation of H_4SIM^3 treated with zinc(II) perchlorate and gallium(III) nitrate showed three main peaks in the spectrum at m/z 437.6, m/z 446.6 and m/z 992.1, all three displaying a GaZn isotopic pattern. The peaks were assigned to the complexes $[Ga^{III}Zn^{II}(HSIM^3)]^{2+}$, $[Ga^{III}Zn^{II}(HSIM^3)(H_2O)]^{2+}$, and $[Ga^{III}Zn^{II}(H_2SIM^3)(CH_3CN)(OH)_2]^+$.

3.4 COMPLEXATION BEHAVIOR OF LIGAND H_4SIM^4

H_4SIM^4 bears two chemically distinct coordination sites and the primary coordination sphere is comparable to H_4SIM^3 . However, the second coordination sphere in H_4SIM^4 provides hydrogen bonding proximal both binding sites, while H_4SIM^4 only introduced hydrogen bonding adjacent to the softer coordination site.

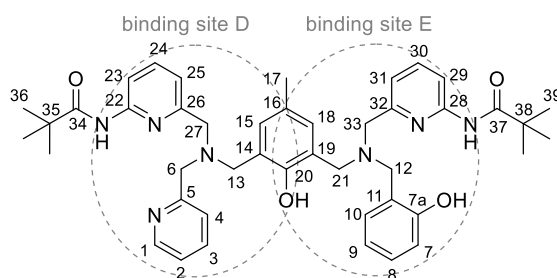


Chart 11: Assignment of the binding sites provided by ligand H_4SIM^4 and the numbering of its atoms.

In fact, the two sterically demanding pivaloyl-amide moieties are attached to both side-arms in H_4SIM^4 leading to two rather equally accessible binding sites, contrary to H_4SIM^3 .

3.4.1 COMPLEXATION STUDIES WITH Zn^{II}

The binding behavior of ligand H_4SIM^4 with Zn^{II} ions was investigated by NMR titration and mass spectrometric measurements, as with H_3SIM^1 and H_4SIM^3 (Chapter 3.2.1 and 3.3.1).

NMR Studies

The formation of a monozinc(II) complex was monitored during the addition of zinc(II) perchlorate to a solution of H_4SIM^4 in methanol. Next to the resonances assigned to the metal-free ligand, resonances of a new species appeared in mixtures with low Zn^{II} ion concentration. Finally, in the 1H NMR spectrum obtained with the 1:1 mixture of zinc(II) perchlorate and H_4SIM^4 the resonances corresponding to the monozinc(II) complex of H_4SIM^4 were the only resonances left, while the resonances of the metal-free ligand disappeared. The resonances assigned to the non-amidated pyridine residue and one of the two amidated-pyridine residues revealed shifts in

the spectrum of the monozinc(II) complex of H_4SIM^4 compared to the metal-free ligand, while the resonances of the other two side-arm moieties did not show pronounced changes (Figure 26). This suggests the coordination of Zn^{II} ions in binding site D of H_4SIM^4 . Increase of the Zn^{II} concentration to a ratio higher than 1:1 did not lead to changes in the recorded 1H NMR spectrum indicating the selective formation of the monozinc(II) complex. However, when the NMR titration experiment was conducted in acetonitrile as solvent the formation of the monozinc(II) complex could also be detected, but addition of further zinc(II) perchlorate to the monozinc(II) complex resulted in a mixture with a second species, most likely the dizinc(II) complex, but complete conversion could not be detected.

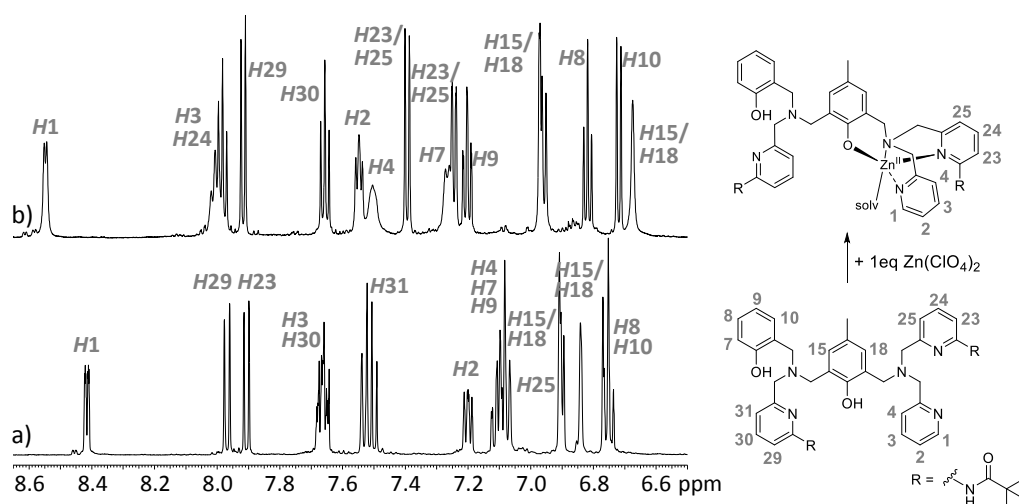


Figure 26: Comparison of the aromatic regions in the 1H NMR of a) H_4SIM^4 in CD_3OD with b) 1.0 eq of $Zn^{II}(ClO_4)_2$.

Mass Spectrometry

ESI⁺ mass spectrometric measurements were conducted in parallel to the 1H NMR spectroscopic investigations regarding the Zn^{II} coordination behavior of H_4SIM^4 by taking samples throughout the experiments. The spectrum recorded after addition of one equivalent of Zn^{II} ions in acetonitrile showed a main peak at m/z 806.4 associated with the monozinc(II) complex $[Zn^{II}(H_3SIM^4)]^+$ with the characteristic isotopic pattern for monozinc species. Further addition of zinc(II) perchlorate led to a spectrum with a main peak at m/z 436.7 exhibiting the isotopic pattern characteristic for a dizinc species and corresponding to a complex containing two zinc(II) centers, $[Zn^{II}_2(H_2SIM^4)]^{2+}$. These findings support the observation of the selective formation of a monozinc(II) complex by addition of one equivalent of Zn^{II} to H_4SIM^4 in agreement with the results acquired from the NMR spectroscopic measurements.

3.4.2 COMPLEXATION STUDIES WITH Ga^{III}

Similar to the complexation of H_4SIM^4 with Zn^{II} , the capacity of H_4SIM^4 to form gallium(III) complexes was examined by NMR titration and mass spectrometric measurements.

NMR Studies

The ^1H NMR spectrum recorded with a mixture of one equivalent of gallium(III) perchlorate with ligand H_4SIM^4 in acetonitrile after heating for 12 hours shows mainly 16 resonances in the aromatic region. These resonances are accountable for the 16 inequivalent protons of a selectively formed species. The shift of the resonances assigned to the protons of the terminal phenol residue indicates the coordination of the Ga^{III} ion in binding site E in the resulting monogallium(III) complex of H_4SIM^4 .

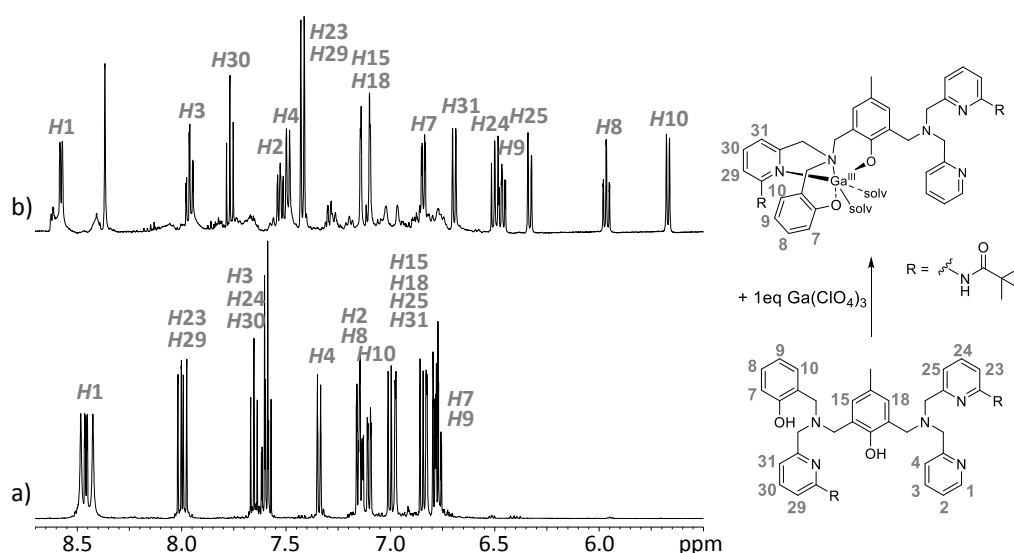


Figure 27: Comparison of the aromatic regions in the ^1H NMR of a) H_4SIM^4 in CD_3CN with b) 1.0 eq of $\text{Ga}^{\text{III}}(\text{ClO}_4)_3$ heated at 60°C for 12h.

Mass Spectrometry

The ESI^+ mass spectrum recorded with a solution of H_4SIM^4 treated with one equivalent of gallium(III) perchlorate revealed main signals with the pattern characteristic for monogallium compounds. The signals were found at m/z 405.7, m/z 810.3, and m/z 912.3 corresponding to the species $[\text{Ga}^{\text{III}}(\text{H}_3\text{SIM}^4)]^{2+}$, $[\text{Ga}^{\text{III}}(\text{H}_2\text{SIM}^4)]^+$, and $[\text{Ga}^{\text{III}}(\text{H}_3\text{SIM}^4)(\text{ClO}_4)]^+$, respectively. The mass spectrometric investigation of a solution of H_4SIM^4 with one equivalent of zinc(II) perchlorate and one equivalent of gallium(III) perchlorate heated for 12 hours at 60°C resulted in a spectrum with signals associated with GaZn species due to their characteristic pattern (besides the signals assigned to remnants of the monogallium(III) complex). The GaZn species found had the mass to

charge ratio of m/z 436.62 and m/z 912.28 and match the mass of $[\text{Ga}^{\text{III}}\text{Zn}^{\text{II}}(\text{HSIM}^4)]^{2+}$ and $[\text{Ga}^{\text{III}}\text{Zn}^{\text{II}}(\text{SIM}^4)]^+$.

3.5 SUMMARY

The coordination behavior towards Zn^{II} , Cu^{II} , Ga^{III} , and Fe^{III} of the asymmetric ligands H_3SIM^1 , H_4SIM^3 , and H_4SIM^4 was examined with various techniques, including NMR spectroscopy, X-ray diffraction, mass spectrometry, UV-vis-NIR and EPR spectroscopy. In this way, the selective formation of specific complexes due to the asymmetry of the ligands was established.

Ligand H_3SIM^1 was shown to coordinate Zn^{II} stepwise, *i.e.* H_3SIM^1 generates selectively the monozinc(II) complex in presence of Zn^{II} with the Zn^{II} ion bound in binding site B, prior to coordination of a second Zn^{II} ion in binding site C. A similar behavior of H_3SIM^1 with Cu^{II} ions was detected since the selective formation of a monocopper(II) complex was revealed after addition of one equivalent of Cu^{II} . In presence of two equivalents of Cu^{II} , H_3SIM^1 generates a dicopper(II) complex, which could be structurally characterized as $[\text{Cu}^{\text{II}}_2(\text{HSIM}^1)(\mu\text{-OAc})]^+$. In this structure, the asymmetry of the complex is visible due to the presence of two unequal Cu^{II} centers, one in a trigonal bipyramidal and one in a distorted octahedral coordination geometry. Interestingly, the additional coordination site in the octahedral Cu^{II} center is occupied by the pivaloyl-amide oxygen atom of coordination site C, stabilized by hydrogen bond formation by the second adjacent pivaloyl-amide residue. In contrast to the observations gained with Zn^{II} and Cu^{II} salts, H_3SIM^1 achieved only the coordination of one trivalent metal ion when Ga^{III} or Fe^{III} salts were used as metal source. The coordination of the trivalent metal ion takes place in the less hindered binding site B, as shown in the X-ray structure of $[\text{Ga}^{\text{III}}(\text{H}_2\text{SIM}^1)(\mu\text{-OH})]_2(\text{ClO}_4)_2$. The selectivity of the two different binding sites of the asymmetric ligand H_3SIM^1 was particularly demonstrated in the generation of a heterodinuclear $\text{Ga}^{\text{III}}\text{Zn}^{\text{II}}$ complex, independent of the order of addition of the two metal salts or an excess of one of the two metal salts. The X-ray structure of $[\text{Ga}^{\text{III}}\text{Zn}^{\text{II}}(\text{H}_2\text{SIM}^1)(\text{OAc})_2(\mu\text{-OH})]_2(\text{PF}_6)_2$ verifies the coordination of Ga^{III} in the less hindered binding site B and of Zn^{II} in the amidated binding site C.

Contrary to H_3SIM^1 , H_4SIM^3 , and H_4SIM^4 provide two chemically different binding sites with regards to the primary coordination sphere, *i.e.* a softer nitrogen-rich binding site and a harder binding site with a terminal phenolate residue. By means of NMR titration and mass spectrometric experiments it could be shown that the softer Zn^{II} ion favors the softer binding site, while the harder trivalent Ga^{III} ion selectively coordinates to the harder binding site. In case

of H_4SIM^3 the coordination of Fe^{III} in the harder binding site was also verified by X-ray diffraction of the dimeric iron(III) complex $\{\text{Na}[\text{Fe}^{\text{III}}(\text{H}_2\text{SIM}^3)]_2(\mu\text{-OAc})(\mu\text{-OH}_2)\}(\text{BF}_4)_2$.

Chapter 4

Dizinc Model Complexes^d

^d Main parts of this chapter are published in “Dinuclear Zinc(II) Complexes with Hydrogen Bond Donors as Structural and Functional Phosphatase Models”; Simone Bosch, Peter Comba, Lawrence R. Gahan, Gerhard Schenk, *Inorg. Chem.* **2014**, *53*, 9036-9051.

4.1 INTRODUCTION

Due to its geometric flexibility and high ionization potential/Lewis acidity the zinc(II) ion is one of the most frequently incorporated metal ions in hydrolases. These features facilitate zinc(II) containing enzymes to polarize P-O bonds in phosphate ester substrates and simultaneously to activate the phosphorus center towards nucleophilic attack.¹¹ A water molecule coordinated to Zn^{II} is highly activated by polarization and ionization. The generation of a hydroxide ion at neutral pH can then act as a nucleophile.¹⁸⁴ A key property, therefore, in the function of the catalytic sites is the acidity (pK_a value) of a metal-bound water molecule.¹⁸⁵ It is known that the number and the nature of the zinc(II) coordinating ligands play a critical role in the polarization capacity.¹⁸⁶ Studying the zinc(II) complexes [Zn^{II}(H₃L¹⁹)(OH₂)]²⁺ and [Zn^{II}(H₄L²⁰)(OH₂)]²⁺ (Chart 12) it was found that, as the coordination number decreases from five to four, the pK_a value of the Zn^{II}-bound water molecule decreases from 8.0 to 7.3.¹⁸⁷⁻¹⁸⁹ In general, as the coordination number increases the charge on the Zn^{II} center is reduced and, consequently, the capacity to polarize the Zn^{II}-bound water molecule is decreased.¹⁸⁴

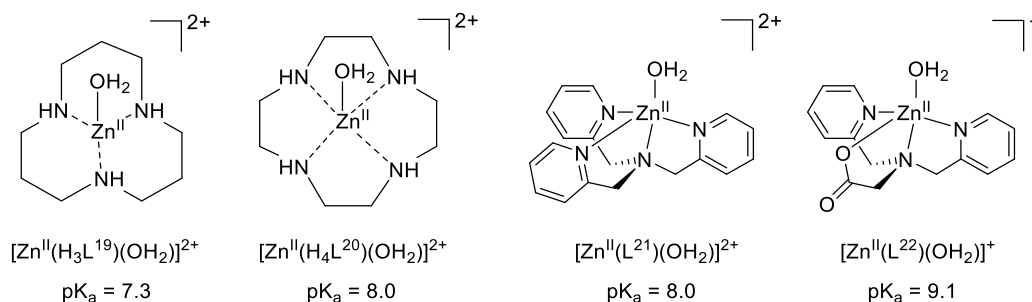


Chart 12: Zinc(II) complexes used to study the impact of the primary coordination sphere of the Zn^{II} center towards the pK_a of Zn^{II}-bound water.¹⁹⁰

A similar effect was found by changing coordinating ligands in the primary coordination sphere of the Zn^{II} center. The change of one neutral pyridine ligand in [Zn^{II}(L²¹)(OH₂)]²⁺ (Chart 12) by one anionic carboxylate results in a decrease of the Lewis acidity of the Zn^{II} ion and consequently in a lowered capacity to polarize the bound water molecule (pK_a 8.0 for [Zn^{II}(L²¹)(OH₂)]²⁺ and pK_a 9.1 for [Zn^{II}(L²²)(OH₂)]⁺).¹⁹¹ This was confirmed by *ab initio* calculations and site-directed mutagenesis studies with carbonic anhydrase, and demonstrates the importance of the first coordination sphere on the Zn^{II}-water acidity.^{186, 192} However, the microenvironment of the active site in phosphatases is also known to influence the function of metalloproteins by non-covalent interactions such as hydrogen bonding.^{25, 82, 83}

Mareque-Rivas *et al.* investigated the impact of hydrogen bond donors adjacent to the Zn^{II} center towards the pK_a value of the Zn^{II}-bound water using derivatives of [Zn^{II}(L²¹)(OH₂)]²⁺ (Chart 12) the model complexes (Chart 13).¹⁹⁰

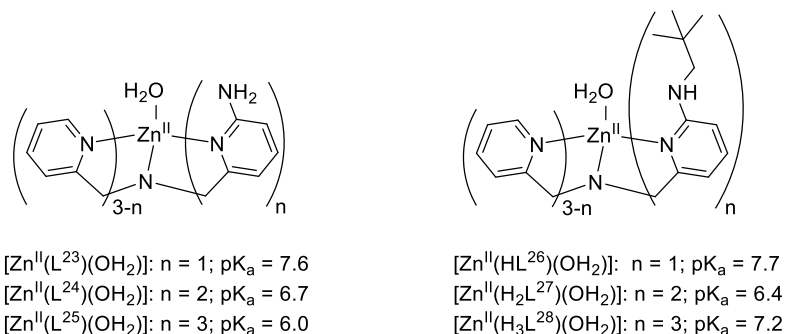


Chart 13: Zinc(II) complexes used to study the impact of hydrogen bond donors and hydrophobic groups in proximity to the ZnII center towards the pK_a of ZnII-bound water.¹⁹⁰

Since amino groups are electron donating, the pK_a values of the zinc(II)-bound water molecule is expected to increase when more zinc(II) coordinating pyridyl groups are exchanged by aminopyridyl residues. The fact that the inverse was observed can be rationalized as being due to intramolecular hydrogen bonding as the N-H hydrogen bond donors, when close to the Zn^{II} center, can polarize the water O-H bond. Moreover, the better hydrogen bond accepting properties of the anionic zinc(II)-bound hydroxide relative to water leads to a greater stabilization of the zinc(II)-hydroxide by the amino hydrogen bonding groups. In comparison to [Zn^{II}(L²⁴)(OH₂)]²⁺, introduction of two neopentylamino group as in [Zn^{II}(H₂L²⁷)(OH₂)]²⁺ (Chart 13), which simultaneously create a hydrophobic and hydrogen bonding microenvironment in proximity to the metal site, resulted in an even lower pK_a value of the Zn^{II}-bound water (pK_a is 6.7 for [Zn^{II}(L²⁴)(OH₂)]²⁺ and 6.4 for [Zn^{II}(H₂L²⁷)(OH₂)]²⁺). Remarkably, these observations suggest that the second coordination sphere, which cooperates with the Lewis acidic Zn^{II} center, can be of similar importance as the first coordination sphere in enhancing the Zn^{II}-bound water acidity.¹⁸⁴

In general, model systems that contain two metal centers were found to cleave various substrates at faster rates than the corresponding mononuclear analogues.¹¹ When the two metal centers are brought in close distance to each other cooperation is facilitated either by double Lewis acid activation of the substrate or Lewis acid activation of the substrate, coupled with the provision of a metal bound hydroxide nucleophile. However, recently it was shown that the introduction of non-coordinated pyridyl residues in a mononuclear zinc(II) complex is as effective as the introduction of a second Zn^{II} ion for enhancing its acidity towards the transesterification of phosphodiester. This was accounted for hydrogen bonding of the vacant coordination site (Chart 14).¹¹¹

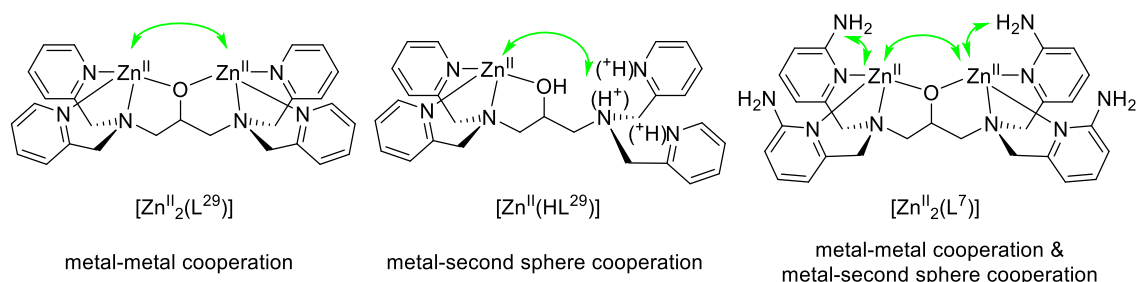


Chart 14: Introduction of metal-metal cooperation and metal-second sphere cooperation in zinc(II) model complexes for hydrolases.¹⁹³

Combining both strategies, *i.e.* metal-metal cooperation, and metal-hydrogen bonding cooperation, accomplished in complex $[Zn^{II}_2(L^7)]$ (Chart 14), resulted in tighter binding of phosphate derivatives such as pyrophosphate, RNA fragments and dimethyl phosphate, than with dizinc(II) complexes lacking second coordination sphere models or monozinc(II) complexes with hydrogen bond donors.^{112, 113, 194}

Therefore, a variety of ligands were developed in this work, which differ in the type and geometric position of hydrogen bond donors and acceptors, more precisely pivaloyl-amide and amine moieties. The ligands were synthesized as described in Chapter 2. Using these ligands the corresponding dizinc(II) complexes, shown in Chart 15, were prepared and investigated. Experimental procedures including ligand and complex syntheses are given in detail in Chapter 11.

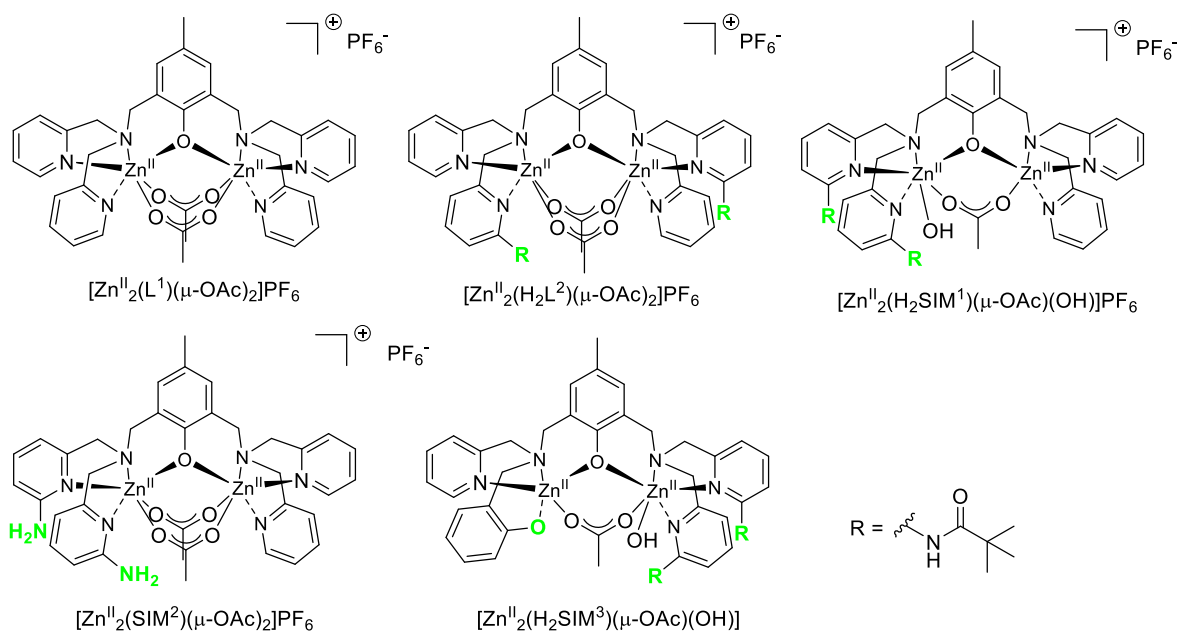


Chart 15: Dizinc(II) complexes employed to mimic the active site of phosphoesterases.

These dizinc(II) model complexes were structurally characterized in the solid state and also in solution, using X-ray crystallography, NMR spectroscopy, mass spectrometry and UV-vis spectroscopy. Moreover, kinetic assays were employed in order to investigate the effect of the

introduced moieties into the reference complex $[\text{Zn}^{\text{II}}_2(\text{L}^1)(\mu\text{-OAc})_2]\text{PF}_6$ (Chart 15). These introduced functionalities are able to form hydrogen bonds, responsible for the positioning of the substrate and release of the product molecules.

4.2 SYNTHESIS OF DIZINC(II) COMPLEXES

The dinuclear zinc(II) complexes of HL^1 , H_3L^2 , H_3SIM^1 , HSIM^2 and H_4SIM^3 were prepared by reaction with two equivalents of zinc(II) acetate dihydrate in methanol at 50°C for ten minutes. After addition of sodium hexafluorophosphate to the hot solution X-ray quality crystals were obtained upon standing. In this way the complexes $[\text{Zn}^{\text{II}}_2(\text{L}^1)(\mu\text{-OAc})_2]\text{PF}_6$, $[\text{Zn}^{\text{II}}_2(\text{H}_2\text{L}^2)(\mu\text{-OAc})_2]\text{PF}_6$, $[\text{Zn}^{\text{II}}_2(\text{H}_2\text{SIM}^1)(\mu\text{-OAc})(\text{OH})]\text{PF}_6$, and $[\text{Zn}^{\text{II}}_2(\text{SIM}^2)(\mu\text{-OAc})_2]\text{PF}_6$ were isolated as white crystals. In the case of H_4SIM^3 , the ligand containing solution was treated with aqueous sodium hydroxide before addition of zinc(II) acetate dihydrate, in order to ensure deprotonation of both phenol residues. Slow evaporation of the solvent led to the complex $[\text{Zn}^{\text{II}}_2(\text{H}_2\text{SIM}^3)(\mu\text{-OAc})(\text{OH})]$ in the form of crystals, suitable for X-ray diffraction, irrespective of the presence of sodium hexafluorophosphate. All five dizinc(II) complexes were characterized and studied in the solid state and in solution (acetonitrile was chosen as solvent since it is the common organic solvent used for hydrolysis activity studies with this type of model complexes). Bearing amino and amide residues adjacent the Zn^{II} centers, these complexes offer the potential for the investigation of the effect of hydrogen bonding on the phosphoester hydrolytic activity.

4.3 STRUCTURAL CHARACTERIZATION OF DIZINC(II) COMPLEXES

Solid State Structures

The colorless single crystals of $[\text{Zn}^{\text{II}}_2(\text{L}^1)(\mu\text{-OAc})_2]\text{PF}_6$, $[\text{Zn}^{\text{II}}_2(\text{H}_2\text{L}^2)(\mu\text{-OAc})_2]\text{PF}_6$, $[\text{Zn}^{\text{II}}_2(\text{H}_2\text{SIM}^1)(\mu\text{-OAc})(\text{OH})]\text{PF}_6$, $[\text{Zn}^{\text{II}}_2(\text{SIM}^2)(\mu\text{-OAc})_2]\text{PF}_6$ and $[\text{Zn}^{\text{II}}_2(\text{H}_2\text{SIM}^3)(\mu\text{-OAc})(\text{OH})]$ were used for X-ray diffraction data collection. Crystallographic data obtained for the structures are displayed in Table 33 (see Appendix).

The structures obtained show that the dizinc(II) complexes formed with the ligands HL^1 , H_3L^2 and HSIM^2 have the common formation for this type of phenolate-based complexes, composed of the corresponding ligand monoanion, resulting from the deprotonation of the phenol backbone, two Zn^{II} ions, two bridging acetato anions, with a hexafluorophosphate

counter ion.^{100, 195, 196} In accordance with the structure of $[\text{Zn}^{\text{II}}_2(\text{L}^1)(\mu\text{-OAc})_2]\text{BF}_4$, published by Adams *et al.*,¹⁹⁶ both Zn^{II} ions in $[\text{Zn}^{\text{II}}_2(\text{L}^1)(\mu\text{-OAc})_2]\text{PF}_6$, $[\text{Zn}^{\text{II}}_2(\text{H}_2\text{L}^2)(\mu\text{-OAc})_2]\text{PF}_6$ and $[\text{Zn}^{\text{II}}_2(\text{SIM}^2)(\mu\text{-OAc})_2]\text{PF}_6$ are coordinated in a six coordinate arrangement and are bridged by the ligand backbone phenoxido group and two acetate co-ligands. The remaining coordination sites are occupied by the nitrogen donors of two pyridine ligands and the tertiary amines. The structures are shown in Figure 28 and selected distances and valence angles are summarized in Table 7. Nordlander *et al.* recently reported a structure for the complex $[\text{Zn}^{\text{II}}_2(\text{L}^1)(\mu\text{-OAc})(\text{CH}_3\text{OH})]\text{ClO}_4$, obtained when HL^1 was reacted with zinc(II) acetate, but using sodium perchlorate, instead of sodium hexafluorophosphate as source for the counterion.¹⁹⁷ The crude product was initially treated with water before the complex was crystallized by slow diffusion of diethyl ether. In $[\text{Zn}^{\text{II}}_2(\text{L}^1)(\mu\text{-OAc})(\text{CH}_3\text{OH})]\text{ClO}_4$ one Zn^{II} ion is coordinated in a slightly distorted octahedral geometry, while the second Zn^{II} ion is the center of an distorted square pyramidal coordination geometry.¹⁹⁷

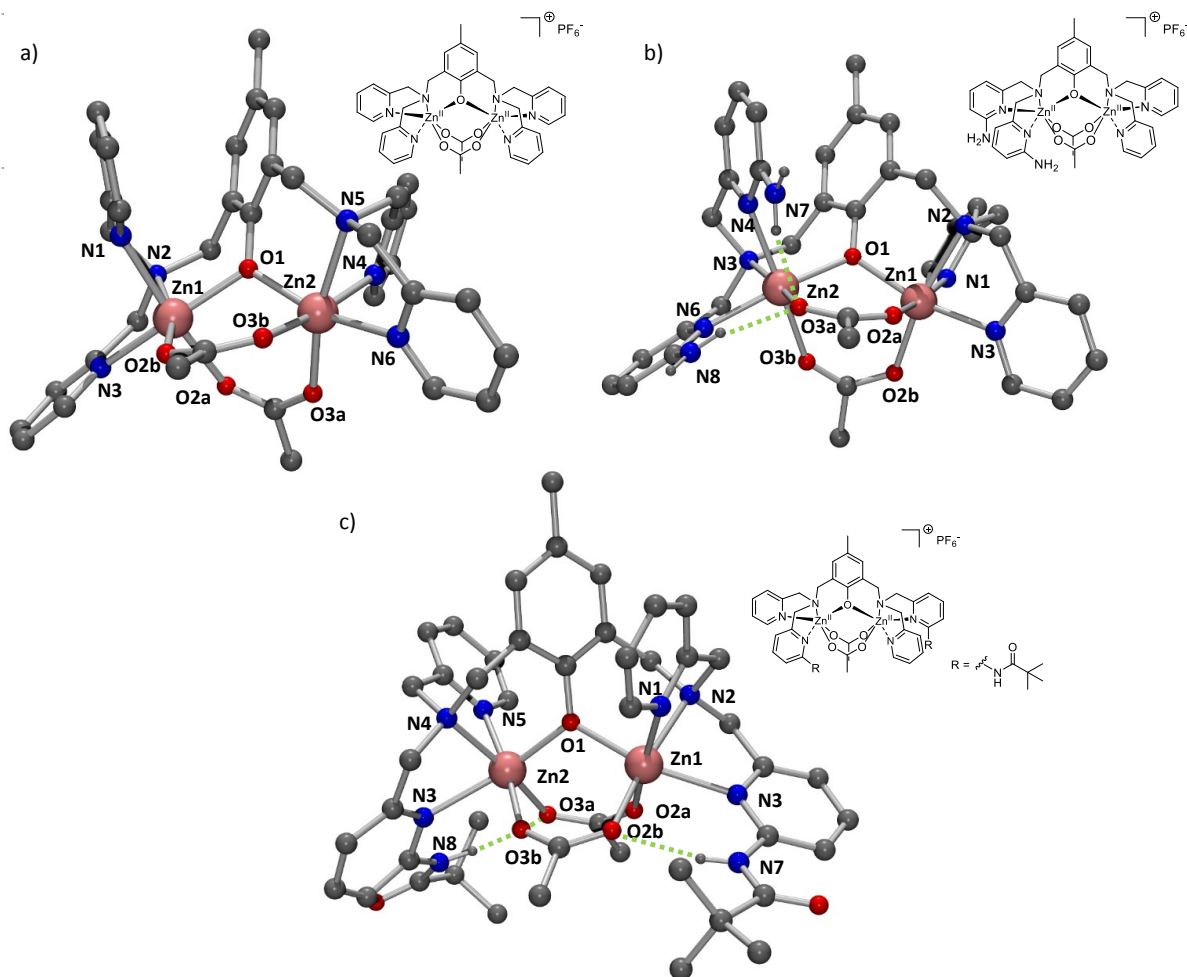


Figure 28: Structures of a) $[\text{Zn}^{\text{II}}_2(\text{L}^1)(\mu\text{-OAc})_2]\text{PF}_6$, b) $[\text{Zn}^{\text{II}}_2(\text{SIM}^2)(\mu\text{-OAc})_2]\text{PF}_6$, and c) $[\text{Zn}^{\text{II}}_2(\text{H}_2\text{L}^2)(\mu\text{-OAc})_2]\text{PF}_6$ showing hydrogen bonding (green dotted lines; counter ions, non-coordinated solvent molecules, and hydrogen atoms, not involved in hydrogen bonding, have been omitted for clarity; crystallographic data and ORTEP plots with 50% probability level of thermal ellipsoids appear in the Appendix, Table 33 and Figure 74).

Table 7: Selected bond lengths (Å) and angles (°) for $[\text{Zn}^{\text{II}}_2(\text{L}^1)(\mu\text{-OAc})_2]\text{PF}_6$, $[\text{Zn}^{\text{II}}_2(\text{H}_2\text{SIM}^1)(\mu\text{-OAc})(\text{OH})]\text{PF}_6$, $[\text{Zn}^{\text{II}}_2(\text{H}_2\text{L}^2)(\mu\text{-OAc})_2]\text{PF}_6$, $[\text{Zn}^{\text{II}}_2(\text{SIM}^2)(\mu\text{-OAc})_2]\text{PF}_6$ and $[\text{Zn}^{\text{II}}_2(\text{H}_2\text{SIM}^3)(\mu\text{-OAc})(\text{OH})]$.

	$[\text{Zn}^{\text{II}}_2(\text{L}^1)(\mu\text{-OAc})_2]^+$	$[\text{Zn}^{\text{II}}_2(\text{H}_2\text{L}^2)(\mu\text{-OAc})_2]^+$	$[\text{Zn}^{\text{II}}_2(\text{H}_2\text{SIM}^1)(\mu\text{-OAc})(\text{OH})]^+$	$[\text{Zn}^{\text{II}}_2(\text{SIM}^2)(\mu\text{-OAc})_2]^+$	$[\text{Zn}^{\text{II}}_2(\text{H}_2\text{SIM}^3)(\mu\text{-OAc})(\text{OH})]$
Zn(1)⋯Zn(2)	3.3714(4)	3.3992(6)	3.5422(7)	3.3948(10)	3.5892(6)
Zn(1)-O(1)	2.0135(14)	2.025(3)	1.954(3)	1.994(4)	1.9904(19)
Zn(1)-O(2A)	2.1825(16)	2.092(3)	2.003(3)	2.112(4)	2.065(2)
Zn(1)-O(2B)	2.0088(15)	2.056(3)	-	2.008(4)	-
Zn(1)-N(1)	2.2346(19)	2.169(3)	2.057(3)	2.216(5)	2.096(2)
Zn(1)-N(2)	2.2306(19)	2.214(3)	2.233(2)	2.206(5)	2.213(2)
Zn(1)-N(3)*	2.1443(19)	2.284(3)	2.102(3)	2.132(5)	1.934(2)
Zn(2)-O(1)	2.0342(14)	2.000(3)	2.120(2)	1.995(4)	2.1380(19)
Zn(2)-O(3A)**	2.0198(17)	2.039(3)	2.133(3)	2.008(4)	2.102(2)
Zn(2)-O(3B)	2.0849(16)	2.077(3)	-	2.114(4)	-
Zn(2)-N(4)	2.223(2)	2.155(3)	2.322(3)	2.239(5)	2.295(2)
Zn(2)-N(5)	2.247(2)	2.199(3)	2.136(3)	2.165(5)	2.148(2)
Zn(2)-N(6)	2.1764(19)	2.289(3)	2.336(3)	2.123(5)	2.473(2)
Zn(2)-O(6)	-	-	1.945(2)	-	1.9571(19)
Zn(1)-O(1)-Zn(2)	112.80(7)	115.23(13)	120.75(12)	116.65(18)	120.73(9)
O(1)-Zn(1)-N(1)	87.65(6)	89.95(12)	118.71(12)	88.63(18)	130.04(9)
O(1)-Zn(1)-N(2)	88.88(7)	87.20(11)	91.48(11)	88.12(17)	91.80(8)
O(1)-Zn(1)-N(3)*	163.19(7)	160.92(12)	124.82(11)	161.07(18)	109.92(9)
O(1)-Zn(1)-O(2A)**	87.91(6)	89.64(11)	99.48(12)	89.65(16)	90.21(8)
O(1)-Zn(1)-O(2B)	100.20(6)	100.55(11)	-	101.16(17)	-
O(1)-Zn(2)-N(4)	86.73(7)	93.20(12)	88.66(10)	91.46(16)	86.80(8)
O(1)-Zn(2)-N(5)	87.53(6)	88.29(12)	90.65(11)	89.20(17)	91.44(9)
O(1)-Zn(2)-N(6)	163.04(7)	159.77(12)	161.27(10)	162.28(16)	161.12(8)
O(1)-Zn(2)-O(3A)**	100.51(6)	101.25(11)	87.91(11)	98.04(17)	91.27(8)
O(1)-Zn(2)-O(3B)	92.43(6)	90.00(11)	-	88.12(15)	-
O(1)-Zn(2)-O(6)	-	-	102.84(10)	-	107.30(8)

* in the case of $[\text{Zn}^{\text{II}}_2(\text{H}_2\text{SIM}^3)(\mu\text{-OAc})(\text{OH})]$ N(3) is O(1A).

** in the case of $[\text{Zn}^{\text{II}}_2(\text{H}_2\text{SIM}^1)(\mu\text{-OAc})(\text{OH})]^+$ and $[\text{Zn}^{\text{II}}_2(\text{H}_2\text{SIM}^1)(\mu\text{-O}_3\text{POC}_6\text{H}_4\text{NO}_2)]^+$ O(2A) is O(2) and O(3A) is O(3).

In $[\text{Zn}^{\text{II}}_2(\text{H}_2\text{L}^2)(\mu\text{-OAc})_2]^+$ the ligands in the *trans* position to the bridging phenolate are the pivaloyl-substituted pyridine residues at both Zn^{II} centers and its Zn-N_{ax} distances (2.289(3) Å and 2.284(3) Å) are elongated compared to the Zn-N_{eq} distances (2.155(3) Å and 2.169(3) Å) of the non-substituted pyridine residues. This contrasts with distances measured in $[\text{Zn}^{\text{II}}_2(\text{L}^1)(\mu\text{-OAc})_2]^+$, in which the Zn-N_{ax} distances (2.1443(19) Å and 2.1764(19) Å) are shorter than the Zn-N_{eq} distances (2.2346(19) Å and 2.223(2) Å), presumably due to the electron withdrawing effect of the pivaloyl-amide residues. In agreement with the electron donating effect of the amino substituent, the Zn-N_{ax} distance to the amino substituted pyridine moiety

(2.123(5) Å) is slightly shorter than to the unsubstituted pyridine ligand (2.132(5) Å) in $[\text{Zn}^{\text{II}}(\text{SIM}^2)(\mu\text{-OAc})_2]^+$.

Reaction of H_3SIM^1 and H_4SIM^3 with zinc(II) acetate dihydrate resulted in the complexes $[\text{Zn}^{\text{II}}_2(\text{H}_2\text{SIM}^1)(\mu\text{-OAc})(\text{OH})]\text{PF}_6$ and $[\text{Zn}^{\text{II}}_2(\text{H}_2\text{SIM}^3)(\text{OAc})(\mu\text{-OH})]$ (Figure 29), in which the two Zn^{II} ions are only doubly bridged by the phenoxido group of the dinucleating ligand and one acetato co-ligand. Zn(1), the Zn^{II} ion in the amide-free binding site, adopts a five-coordinate geometry. Applying the method of Addison *et al.*,¹⁷¹ which evaluates the degree of trigonality by means of the structural parameter τ ($\tau = (\beta - \alpha)/60$, where α and β are the two largest angles around the central atom with $\beta > \alpha$) and assigns a value of $\tau = 0$ to a regular square pyramidal geometry and $\tau = 1$ to a trigonal bipyramidal geometry, the coordination environment of Zn(1) in $[\text{Zn}^{\text{II}}_2(\text{H}_2\text{SIM}^1)(\mu\text{-OAc})(\text{OH})]\text{PF}_6$ with $\tau = 0.94$ is a trigonal bipyramidal with the trigonal plane formed by two pyridines and the backbone phenolate.

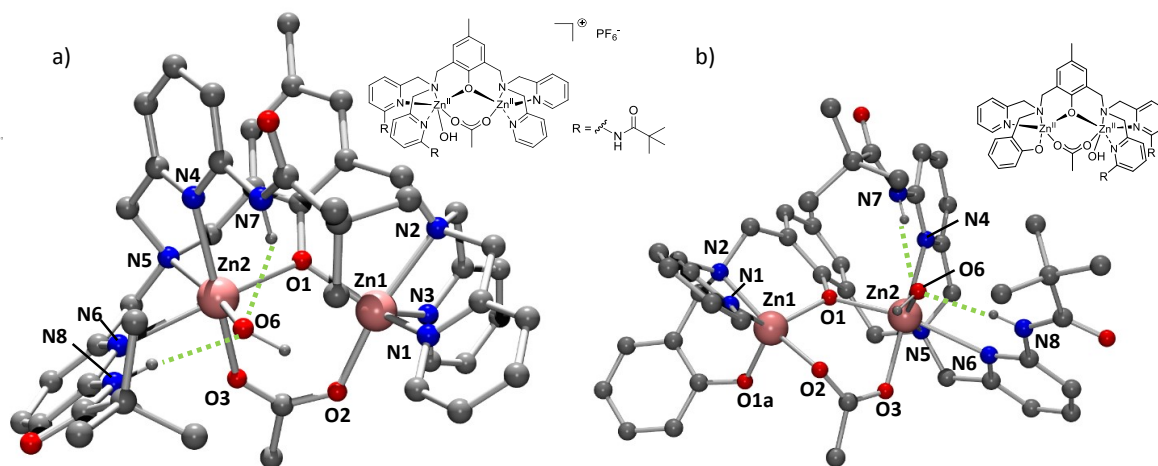


Figure 29: Structures of $[\text{Zn}^{\text{II}}_2(\text{H}_2\text{SIM}^1)(\mu\text{-OAc})(\text{OH})]\text{PF}_6$ (left) and $[\text{Zn}^{\text{II}}_2(\text{H}_2\text{SIM}^3)(\mu\text{-OAc})(\text{OH})]$ (right) showing hydrogen bonding (green dotted lines; counter ions and hydrogen atoms, not involved in hydrogen bonding, have been omitted for clarity; crystallographic data and ORTEP plots with 50% probability level of thermal ellipsoids appear in the Appendix, Table 34 and Figure 74).

The five donors around Zn(1) in $[\text{Zn}^{\text{II}}_2(\text{H}_2\text{SIM}^3)(\mu\text{-OAc})(\text{OH})]$ are arranged in a coordination geometry with a τ -value of 0.58, in between trigonal bipyramidal and square pyramidal. Assuming trigonal bipyramidal, the trigonal plane is defined by one pyridine and two phenolate residues. The axial positions are occupied by the tertiary amine and an acetato oxygen atom in both structures, $[\text{Zn}^{\text{II}}_2(\text{H}_2\text{SIM}^1)(\mu\text{-OAc})(\text{OH})]\text{PF}_6$ and $[\text{Zn}^{\text{II}}_2(\text{H}_2\text{SIM}^3)(\mu\text{-OAc})(\text{OH})]$. The variation of the coordination geometry in these two complexes is proposed to be due to the larger phenolate moiety in H_4SIM^3 compared to the pyridine residue in H_3SIM^1 . For $[\text{Zn}^{\text{II}}_2(\text{H}_2\text{SIM}^3)(\mu\text{-OAc})(\text{OH})]$, the angle (O(1)-Zn(1)-O(1a)) is reduced, with respect to the angle (O(1)-Zn(1)-N(3)) in $[\text{Zn}^{\text{II}}_2(\text{H}_2\text{SIM}^1)(\mu\text{-OAc})(\text{OH})]\text{PF}_6$, and the bridging acetate ligand is twisted relative to the Zn(1)-O(1)-Zn(2) plane (torsion angles O(1)-Zn(1)-O(2)-C(1a) and O(1)-Zn(2)-O(3)-C(1a) are 6.75°

and 29.46° in $[\text{Zn}^{\text{II}}_2(\text{H}_2\text{SIM}^1)(\mu\text{-OAc})(\text{OH})]\text{PF}_6$ as well as 50.57° and 64.53° in $[\text{Zn}^{\text{II}}_2(\text{H}_2\text{SIM}^3)(\mu\text{-OAc})(\text{OH})]$.

Similar to the zinc(II) sites in $[\text{Zn}^{\text{II}}_2(\text{L}^1)(\mu\text{-OAc})_2]\text{PF}_6$, $[\text{Zn}^{\text{II}}_2(\text{H}_2\text{L}^2)(\mu\text{-OAc})_2]\text{PF}_6$ and $[\text{Zn}^{\text{II}}_2(\text{SIM}^2)(\mu\text{-OAc})_2]\text{PF}_6$, the second Zn^{II} ion in $[\text{Zn}^{\text{II}}_2(\text{H}_2\text{SIM}^1)(\mu\text{-OAc})(\text{OH})]\text{PF}_6$ and $[\text{Zn}^{\text{II}}_2(\text{H}_2\text{SIM}^3)(\mu\text{-OAc})(\text{OH})]$, bound to the amide containing binding site (Zn(2)), is six-coordinate. The coordination environment of Zn(2) is formed by two pyridine donors, a tertiary amine, the bridging phenolate group and the bridging acetate co-ligand and completed by a hydroxido group.

In comparison to $[\text{Zn}^{\text{II}}_2(\text{L}^1)(\mu\text{-OAc})_2]\text{PF}_6$, $[\text{Zn}^{\text{II}}_2(\text{H}_2\text{L}^2)(\mu\text{-OAc})_2]\text{PF}_6$ and $[\text{Zn}^{\text{II}}_2(\text{SIM}^2)(\mu\text{-OAc})_2]\text{PF}_6$, the distances between Zn(1), the Zn^{II} atom coordinated in a trigonal bipyramidal geometry, and the coordinating ligands of the primary coordination sphere are shorter. Furthermore, the length of the bonds between Zn(2) and its six donors are elongated compared to the complexes $[\text{Zn}^{\text{II}}_2(\text{L}^1)(\mu\text{-OAc})_2]\text{PF}_6$, $[\text{Zn}^{\text{II}}_2(\text{H}_2\text{L}^2)(\mu\text{-OAc})_2]\text{PF}_6$, and $[\text{Zn}^{\text{II}}_2(\text{SIM}^2)(\mu\text{-OAc})_2]\text{PF}_6$, presumably due to the electron-rich hydroxido co-ligand.

The presence of the unusual hydroxido co-ligand was confirmed by comparison of the Zn-O distance with the respective value in structures of previously published zinc(II) complexes with aqua, μ -hydroxido and terminal hydroxido donor groups. For example, for the dizinc(II) complex of HL^1 , $[\text{Zn}^{\text{II}}_2(\text{L}^1)(\text{OH}_2)_2](\text{ClO}_4)_3$, Zn-OH₂ distances are of the order of 2.04 Å and the distances to bridging hydroxido ligands are reduced to 1.99 Å, as in $[\text{Zn}^{\text{II}}_2(\text{L}^1)(\mu\text{-OH})](\text{ClO}_4)_2$ (see Figure 30).¹⁹⁸

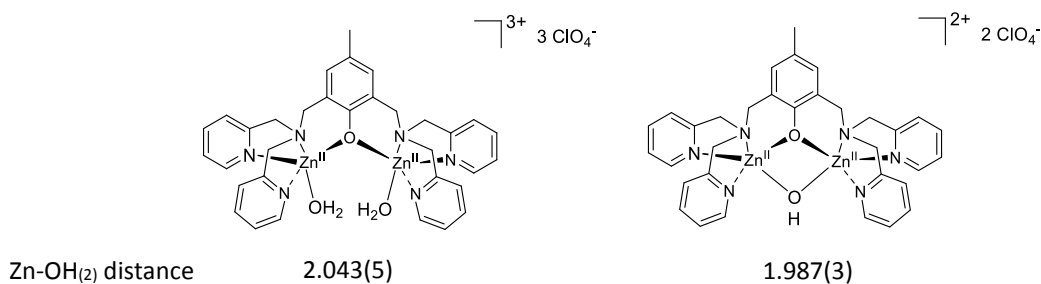


Figure 30: $[\text{Zn}^{\text{II}}_2(\text{L}^1)(\text{OH}_2)_2](\text{ClO}_4)_3$ and $[\text{Zn}^{\text{II}}_2(\text{L}^1)(\mu\text{-OH})](\text{ClO}_4)_2$ and the respective zinc(II)-aqua and zinc(II)-(μ -hydroxido) distances.¹⁹⁸

Similar Zn-(μ -OH) distances have been found for a variety of dizinc(II) complexes: $[[\text{Zn}^{\text{II}}(\text{L}^{30})]_2(\mu\text{-OH})_2](\text{ClO}_4)_2$ (1.983(3) Å); $[[\text{Zn}^{\text{II}}(\text{L}^{31})]_2(\mu\text{-OH})_2](\text{ClO}_4)_2 \cdot 0.5 \text{ CH}_3\text{CN}$ (2.070(3) Å); $[\text{Zn}^{\text{II}}_2(\text{L}^{32})(\mu\text{-OH})(\text{py})_2](\text{ClO}_4)_2$ (1.946(3) Å); $[\text{Zn}^{\text{II}}_2(\text{L}^{33})(\mu\text{-OH})(\text{py})_3](\text{ClO}_4)_2$ (1.951(4) Å) and $[\text{Zn}^{\text{II}}_2(\text{L}^1)(\mu\text{-OH})](\text{ClO}_4)_2$ (1.943(3) Å) (structures of the respective ligands are given in the Table of Molecules).¹⁹⁸⁻²⁰⁰ These metrics compare with the Zn-O distances in $[\text{Zn}^{\text{II}}_2(\text{H}_2\text{SIM}^3)(\mu\text{-OAc})(\text{OH})]$ (1.9575(19) Å) and $[\text{Zn}^{\text{II}}_2(\text{H}_2\text{SIM}^1)(\mu\text{-OAc})(\text{OH})]\text{PF}_6$ (1.943(3) Å), which are significantly shorter than in complexes reported with a terminal aqua ligand and in the range of complexes containing bridging hydroxido ligands. This supports the notion of the presence of a terminal hydroxido co-

ligand. Moreover, the long Zn(1)⋯OH distances of 3.936 Å in $[\text{Zn}^{\text{II}}_2(\text{H}_2\text{SIM}^1)(\mu\text{-OAc})(\text{OH})]\text{PF}_6$ and 4.199 Å in $[\text{Zn}^{\text{II}}_2(\text{H}_2\text{SIM}^3)(\mu\text{-OAc})(\text{OH})]$ support the assignment of the OH^- group in question as a terminal hydroxido co-ligand.

The fact that a terminal hydroxido co-ligand has not been observed previously in dinuclear zinc(II) complexes with similar phenolate-based ligands, but lacking the hydrogen-bond donors, is consistent with the proposition that the hydrogen-bond donors, *i.e.* the two adjacent amide residues at the binding site of one Zn^{II} center in $[\text{Zn}^{\text{II}}_2(\text{H}_2\text{SIM}^1)(\mu\text{-OAc})(\text{OH})]\text{PF}_6$ and $[\text{Zn}^{\text{II}}_2(\text{H}_2\text{SIM}^3)(\mu\text{-OAc})(\text{OH})]$, stabilize this unusual hydroxido co-ligand. Moreover, the hydrogen bond formation within the structure of $[\text{Zn}^{\text{II}}_2(\text{H}_2\text{SIM}^1)(\mu\text{-OAc})(\text{OH})]\text{PF}_6$ is confirmed by the observed arrangement of the amide hydrogen atoms with respect to the free electron pairs of the hydroxido oxygen atom (hydrogen bonds are depicted as green dotted lines in Figure 28 and Figure 29). This is in accordance with the previous observation that the incorporation of two H-bond donors, *i.e.* neopentylamino groups, in tripodal N_4 ligands lead to the generation of a stable $\text{Zn}^{\text{II}}\text{-OH}$ complex $[\text{Zn}^{\text{II}}(\text{H}_2\text{L}^{27})(\text{OH})]\text{ClO}_4$ due to H-bonding (Figure 31).¹⁹⁰

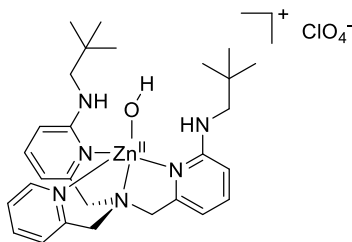


Figure 31: Previously published Zn^{II} -hydroxido complex $[\text{Zn}^{\text{II}}(\text{H}_2\text{L}^{27})(\text{OH})]\text{ClO}_4$, stabilized by hydrogen bond formation.¹⁹⁰

Furthermore, hydrogen bond formation was detected in $[\text{Zn}^{\text{II}}(\text{H}_2\text{L}^{27})(\text{OH})]\text{ClO}_4$ proposed from the short distances between the amino nitrogen and hydroxido oxygen atom (2.741 Å and 2.727 Å)¹⁹⁰; the corresponding distances for $[\text{Zn}^{\text{II}}_2(\text{H}_2\text{SIM}^1)(\mu\text{-OAc})(\text{OH})]\text{PF}_6$ and $[\text{Zn}^{\text{II}}_2(\text{H}_2\text{SIM}^3)(\mu\text{-OAc})(\text{OH})]$ are listed in Table 8. This table also contains the corresponding distances for $[\text{Zn}^{\text{II}}_2(\text{H}_2\text{L}^2)(\mu\text{-OAc})_2]\text{PF}_6$ and $[\text{Zn}^{\text{II}}_2(\text{SIM}^2)(\mu\text{-OAc})_2]\text{PF}_6$, and those between the amine or amide nitrogen atom and the nearby acetate oxygen atoms are in the range 2.750(8) Å and 2.982(4) Å. These short distances demonstrate that the desired hydrogen bond formation is also present in these complexes. Importantly, the protons of the amine or amide moieties also point towards oxygen atoms of the bridging acetate groups in $[\text{Zn}^{\text{II}}_2(\text{H}_2\text{L}^2)(\mu\text{-OAc})_2]\text{PF}_6$ and $[\text{Zn}^{\text{II}}_2(\text{SIM}^2)(\mu\text{-OAc})_2]\text{PF}_6$.

Table 8: Selected distances (Å) for $[\text{Zn}^{\text{II}}_2(\text{H}_2\text{L}^2)(\mu\text{-OAc})_2]\text{PF}_6$, $[\text{Zn}^{\text{II}}_2(\text{H}_2\text{SIM}^1)(\mu\text{-OAc})(\text{OH})]\text{PF}_6$, $[\text{Zn}^{\text{II}}_2(\text{SIM}^2)(\mu\text{-OAc})_2]\text{PF}_6$, and $[\text{Zn}^{\text{II}}_2(\text{H}_2\text{SIM}^3)(\mu\text{-OAc})(\text{OH})]$ corresponding to H-bond formation.

	$[\text{Zn}^{\text{II}}_2(\text{H}_2\text{L}^2)(\mu\text{-OAc})_2]^+$	$[\text{Zn}^{\text{II}}_2(\text{H}_2\text{SIM}^1)(\mu\text{-OAc})(\text{OH})]^+$	$[\text{Zn}^{\text{II}}_2(\text{SIM}^2)(\mu\text{-OAc})_2]^+$	$[\text{Zn}^{\text{II}}_2(\text{H}_2\text{SIM}^3)(\mu\text{-OAc})(\text{OH})]$
N(7)-O(2B)	2.982(4)	-	-	
N(7)-O(3A)	-	-	2.802(9)	
N(7)-O(6)	-	2.809(4)	-	2.764(3)
N(8)-O(3A)	2.976(4)	-	2.750(8)	
N(8)-O(6)	-	2.874(4)	-	2.870(3)

Moreover, the hydrogen bonding appears to direct the position of the pivaloyl-amide groups resulting in an enlarged angle between the pyridine planes and the plane containing the amide group (N(7)C(34)O(4) and N(8)C(37)O(5)) (28.3° and 17.8° for $[\text{Zn}^{\text{II}}_2(\text{H}_2\text{L}^2)(\mu\text{-OAc})_2]^+$; 12.0° and 19.2° for $[\text{Zn}^{\text{II}}_2(\text{H}_2\text{SIM}^1)(\mu\text{-OAc})(\text{OH})]^+$; 9.2° and 19.1° for $[\text{Zn}^{\text{II}}_2(\text{H}_2\text{SIM}^3)(\mu\text{-OAc})(\text{OH})]$). This angle was found to be small in the structure of the 6-(pivaloylamido)pyridine containing ligand HL³⁴ with a value of 11.4° due to a C-H...O=C interaction between the carbonyl oxygen and the nearby hydrogen atom in 5-position of the pyridine ring.¹⁶⁸ Interestingly, in the asymmetric complexes $[\text{Zn}^{\text{II}}_2(\text{H}_2\text{SIM}^1)(\mu\text{-OAc})(\text{OH})]^+$ and $[\text{Zn}^{\text{II}}_2(\text{H}_2\text{SIM}^3)(\mu\text{-OAc})(\text{OH})]$ only the angle at the 6-(pivaloylamido)pyridine moiety, which is coordinated opposite of the bridging acetate group, is expanded, presumably due to steric hindrance within the cavity.

In all five complexes discussed in this chapter, the Zn^{II} ions are coordinated in the *anti*-configuration with respect to the phenoxide ring. The resulting Zn^{II}...Zn^{II} distances (see Table 7) are at the short end of the range reported for similar dizinc(II) complexes. The variation of ligand symmetry and substituents in the range of five ligands discussed here only leads to a relatively small variation of the Zn^{II}...Zn^{II} distance (3.37 Å to 3.59 Å). Importantly, the Zn^{II}...Zn^{II} distances are slightly elongated in the asymmetric complexes $[\text{Zn}^{\text{II}}_2(\text{H}_2\text{SIM}^1)(\mu\text{-OAc})(\text{OH})]\text{PF}_6$ and $[\text{Zn}^{\text{II}}_2(\text{H}_2\text{SIM}^3)(\mu\text{-OAc})(\text{OH})]$ to 3.54 Å and 3.59 Å. Consequently, the Zn^{II}-O-Zn^{II} angle is increased in those two complexes to about 120°, close to a highly symmetrical trigonal angle with respect to the phenoxide bridge, and this compares with Zn^{II}-O-Zn^{II} angles in the range 112.8° to 116.1° in the more symmetric derivatives $[\text{Zn}^{\text{II}}_2(\text{L}^1)(\mu\text{-OAc})_2]\text{PF}_6$, $[\text{Zn}^{\text{II}}_2(\text{H}_2\text{L}^2)(\mu\text{-OAc})_2]\text{PF}_6$, and $[\text{Zn}^{\text{II}}_2(\text{SIM}^2)(\mu\text{-OAc})_2]\text{PF}_6$.

The X-ray crystallographic results for the acetate-bridged dizinc(II) complexes give rise to the conclusions that (i) Zn^{II} ions bound in phenoxido-based ligands with pyridine donors (*e.g.* the less hindered ligands HL¹, H₃L² and H₃SIM²) favor a six-coordinate geometry (by binding to two bridging acetate ligands) over the trigonal bipyramidal geometry with only one bridging acetate co-ligand, which was only observed in the case of H₃SIM¹ and H₄SIM³ due to the sterically demanding *tert*-butyl groups, and (ii) the two bulky pivaloyl-amide residues of H₃L² are positioned on opposite sides of the phenolate backbone upon coordination of two zinc(II) ions. Moreover, the asymmetric ligands H₃SIM¹ and H₄SIM³ enforce a cavity that leads to the complexation of two Zn^{II} ions in different coordination geometries: one zinc(II) site is octahedral, the other site is trigonal bipyramidal, the coordination geometry found for both Zn^{II} ions in the active site of Phospholipase C ²⁰¹ and for one Zn^{II} ion in Ser/Thr Phosphatase-1,²⁰² which is accompanied by a zinc(II) in a square-pyramidal geometry.²⁰² The biomimetic systems [Zn^{II}₂(H₂SIM¹)(μ-OAc)(OH)]PF₆, [Zn^{II}₂(H₂L²)(μ-OAc)₂]PF₆, [Zn^{II}₂(SIM²)(μ-OAc)₂]PF₆, and [Zn^{II}₂(H₂SIM³)(μ-OAc)(OH)] demonstrate the formation of a hydrogen-bond network similar to that found in the active site of the native enzymes.

Infrared Spectroscopy

Examination of solid state FT-IR spectra of the dizinc(II) complexes and comparison among each other as well as to the free ligands provide a good method for assigning the different infrared vibrations and investigating the symmetry of the complexes and the strength of the hydrogen bonds formed (Figure 32).²⁰³

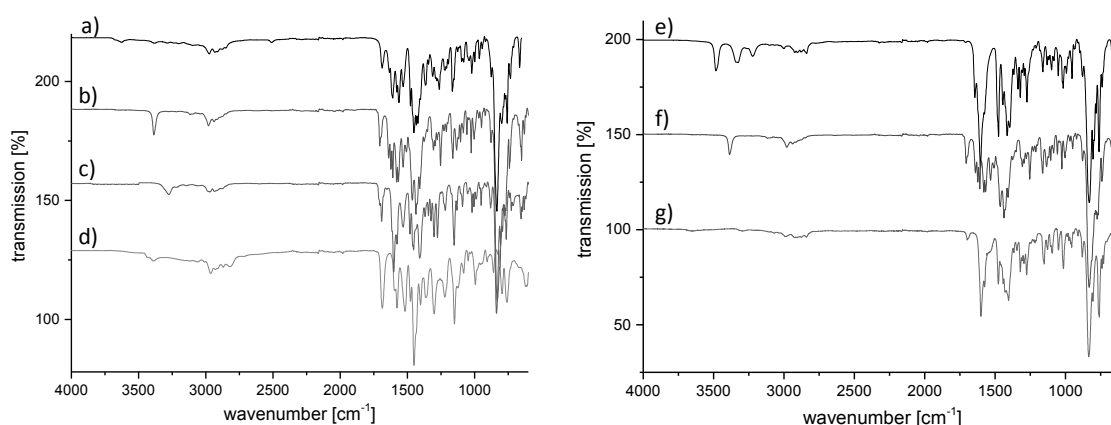


Figure 32: Comparison of IR spectra of a) [Zn^{II}₂(H₂SIM³)(μ-OAc)(OH)], b) [Zn^{II}₂(H₂SIM¹)(μ-OAc)(OH)]PF₆, c) [Zn^{II}₂(H₂L²)(μ-OAc)₂]PF₆, d) H₂SIM¹, e) [Zn^{II}₂(SIM²)(μ-OAc)₂]PF₆, f) [Zn^{II}₂(H₂SIM¹)(μ-OAc)(OH)]PF₆ and g) [Zn^{II}₂(L¹)(μ-OAc)₂]PF₆.

The very similar IR spectra of H₃SIM¹ and H₃L² show the N-H vibration band at around 3440 cm⁻¹ (Figure 32d); this is lowered by 145 cm⁻¹ (1.73 kJ·mol⁻¹) in the spectrum of

$[\text{Zn}^{\text{II}}_2(\text{H}_2\text{L}^2)(\mu\text{-OAc})_2]\text{PF}_6$ (Figure 32c). This can be explained by hydrogen bonding, which results in N-H bond elongation and therefore in a lowering of the vibrational frequency and a broadening of the corresponding bands. Thus, the detection of only a very broad N-H vibration band for $[\text{Zn}^{\text{II}}_2(\text{H}_2\text{SIM}^1)(\mu\text{-OAc})(\text{OH})]\text{PF}_6$ around 3120 cm^{-1} ($\Delta\nu = 220\text{ cm}^{-1}$, $2.63\text{ kJ}\cdot\text{mol}^{-1}$) suggests that the hydrogen bonds are even stronger in this complex (Figure 32b).^{204, 205} Moreover, the terminal hydroxido-ligand in $[\text{Zn}^{\text{II}}_2(\text{H}_2\text{SIM}^1)(\mu\text{-OAc})(\text{OH})]\text{PF}_6$ results in a sharp O-H stretch with a frequency of 3385 cm^{-1} . The small energy value of 3385 cm^{-1} ($40.5\text{ kJ}\cdot\text{mol}^{-1}$) for the excitation of the O-H stretch additionally reflects the strength of the hydrogen bonding within this complex. Unfortunately, for $[\text{Zn}^{\text{II}}_2(\text{H}_2\text{SIM}^3)(\mu\text{-OAc})(\text{OH})]$ both bands, associated with hydrogen bonding, are very broad (Figure 32a).

The spectrum of the reference complex $[\text{Zn}^{\text{II}}_2(\text{L}^1)(\mu\text{-OAc})_2]\text{PF}_6$ lacks bands in the region between 3100 cm^{-1} to 3600 cm^{-1} (Figure 32g), whereas its amino derivative, $[\text{Zn}^{\text{II}}_2(\text{SIM}^2)(\mu\text{-OAc})_2]\text{PF}_6$, has three transitions in this region, assigned to N-H stretching vibrations (Figure 32e). Additionally, the separation of the asymmetric and symmetric acetate stretches at around 1400 cm^{-1} and 1550 cm^{-1} confirms bidentate binding in the solid state of all dizinc(II) complexes, discussed herein.^{205, 206} Interestingly, for the asymmetric complexes $[\text{Zn}^{\text{II}}_2(\text{H}_2\text{SIM}^1)(\mu\text{-OAc})(\text{OH})]\text{PF}_6$ and $[\text{Zn}^{\text{II}}_2(\text{H}_2\text{SIM}^3)(\mu\text{-OAc})(\text{OH})]$ the intensity of the band assigned to the asymmetric acetate stretching vibration is lower ($\sim 1580\text{ cm}^{-1}$) than for the symmetric counterpart, in contrast to the symmetric complexes $[\text{Zn}^{\text{II}}_2(\text{L}^1)(\mu\text{-OAc})_2]\text{PF}_6$, $[\text{Zn}^{\text{II}}_2(\text{H}_2\text{L}^2)(\mu\text{-OAc})_2]\text{PF}_6$ and $[\text{Zn}^{\text{II}}_2(\text{SIM}^2)(\mu\text{-OAc})_2]\text{PF}_6$ ($\sim 1600\text{ cm}^{-1}$), suggesting a slightly different coordination geometry. In the cases in which hexafluorophosphate was present as the counter ion stretching and deformation bands were detected around 830 cm^{-1} and 555 cm^{-1} .

Mass Spectrometry

In order to investigate the complex structure of the dizinc(II) complexes in solution, mass spectrometric data were obtained in dichloromethane as well as in acetonitrile; Table 9 summarizes the highest mass peaks detected. All highest mass peaks showed the distinctive isotopic pattern of dizinc(II) complexes (Figure 33). As expected, the separation of the peaks for the doubly charged species was 0.5 m/z units.

The mass spectrometric measurement showed solvent dependency in the case of the doubly acetate-bridged complexes $[\text{Zn}^{\text{II}}_2(\text{L}^1)(\mu\text{-OAc})_2]\text{PF}_6$, $[\text{Zn}^{\text{II}}_2(\text{H}_2\text{L}^2)(\mu\text{-OAc})_2]\text{PF}_6$, and $[\text{Zn}^{\text{II}}_2(\text{SIM}^2)(\mu\text{-OAc})_2]\text{PF}_6$. Thus, the highest mass peaks obtained by ESI⁺ mass spectrometric measurements in dichloromethane were assigned to the intact cation, but similar measurements

in acetonitrile resulted in highest mass peaks that imply ligand exchange within the complex cationic structure. In contrast, the complexes $[\text{Zn}^{\text{II}}_2(\text{H}_2\text{SIM}^1)(\mu\text{-OAc})(\text{OH})]\text{PF}_6$ and $[\text{Zn}^{\text{II}}_2(\text{H}_2\text{SIM}^3)(\mu\text{-OAc})(\text{OH})]$, containing only one bridging acetate co-ligand and an additional hydroxido co-ligand led in both solvents to highest mass peaks that could be assigned to species missing the acetate bridge. These findings imply ligand exchange by solvent or water molecules in acetonitrile (rather than dichloromethane) for all complexes discussed in this chapter.

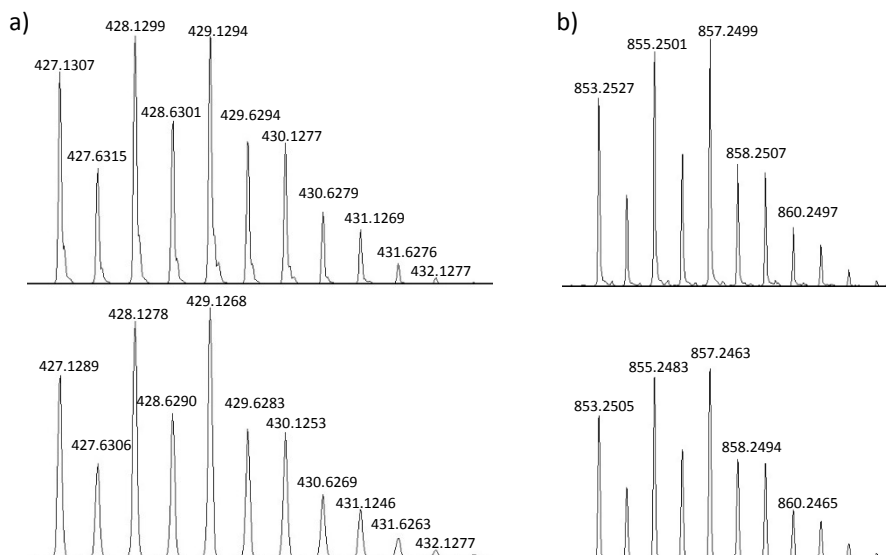


Figure 33: Recorded (top) and calculated (bottom) isotopic pattern for a) $[\text{Zn}^{\text{II}}_2(\text{H}_2\text{L}^2)(\text{OH})(\text{H}_2\text{O})]^{2+}$ and b) $[\text{Zn}^{\text{II}}_2(\text{L}^2)]^{2+}$ detected in the mass spectrum of $[\text{Zn}^{\text{II}}_2(\text{H}_2\text{L}^2)(\mu\text{-OAc})_2]\text{PF}_6$ in acetonitrile.

Table 9: Highest mass peaks in ESI⁺ mass spectrometric measurements of $[\text{Zn}^{\text{II}}_2(\text{L}^1)(\mu\text{-OAc})_2]\text{PF}_6$, $[\text{Zn}^{\text{II}}_2(\text{H}_2\text{L}^2)(\mu\text{-OAc})_2]\text{PF}_6$, $[\text{Zn}^{\text{II}}_2(\text{H}_2\text{SIM}^1)(\mu\text{-OAc})(\text{OH})]\text{PF}_6$, $[\text{Zn}^{\text{II}}_2(\text{SIM}^2)(\mu\text{-OAc})_2]\text{PF}_6$, and $[\text{Zn}^{\text{II}}_2(\text{H}_2\text{SIM}^3)(\mu\text{-OAc})(\text{OH})]$ in dichloromethane and acetonitrile.

complex	highest ESI ⁺ mass peaks			
	in dichloromethane		in acetonitrile	
	peak found (m/z)	assigned to (<i>calcd</i> m/z)	peak found (m/z)	assigned to (<i>calcd</i> m/z)
$[\text{Zn}^{\text{II}}_2(\text{L}^1)(\mu\text{-OAc})_2]\text{PF}_6$	779.1537	$[\text{Zn}^{\text{II}}_2(\text{L}^1)(\text{OAc})_2]^+$ 779.1517	360.0704 779.1507	$[\text{Zn}^{\text{II}}_2(\text{L}^1)(\text{OAc})_2]^{2+}$ 360.0689 $[\text{Zn}^{\text{II}}_2(\text{L}^1)(\text{OAc})_2]^+$ 779.1517
$[\text{Zn}^{\text{II}}_2(\text{H}_2\text{SIM}^1)(\mu\text{-OAc})(\text{OH})]\text{PF}_6$	921.2715	$[\text{Zn}^{\text{II}}_2(\text{H}_2\text{SIM}^1)(\text{OH})_2(\text{CH}_2\text{O})]^+$ 921.2791*	429.1298 917.2757	$[\text{Zn}^{\text{II}}_2(\text{HSIM}^1)]^{2+}$ 429.1268 $[\text{Zn}^{\text{II}}_2(\text{HSIM}^1)(\text{OAc})]^+$ 917.2674
$[\text{Zn}^{\text{II}}_2(\text{H}_2\text{L}^2)(\mu\text{-OAc})_2]\text{PF}_6$	977.2952	$[\text{Zn}^{\text{II}}_2(\text{H}_2\text{L}^2)(\text{OAc})_2]^+$ 977.2886	429.1283	$[\text{Zn}^{\text{II}}_2(\text{HL}^2)]^{2+}$ 429.1268
$[\text{Zn}^{\text{II}}_2(\text{SIM}^2)(\mu\text{-OAc})_2]\text{PF}_6$	809.1766	$[\text{Zn}^{\text{II}}_2(\text{SIM}^2)(\text{OAc})_2]^+$ 809.1735	344.0730	$[\text{Zn}^{\text{II}}_2(\text{SIM}^2)]^{2+}$ 344.0701
$[\text{Zn}^{\text{II}}_2(\text{H}_2\text{SIM}^3)(\mu\text{-OAc})(\text{OH})]$	872.2469	$[\text{Zn}^{\text{II}}_2(\text{HSIM}^3)]^+$ 872.2459	435.6 908.3	$[\text{Zn}^{\text{II}}_2(\text{SIM}^3)]^{2+}$ 435.6272 $[\text{Zn}^{\text{II}}_2(\text{HSIM}^3)(\text{H}_2\text{O})_2]^+$ 908.2682

* Best fit found for this pattern.

NMR Studies

In order to probe the symmetry of the complexes in solution, ^1H and ^{13}C NMR measurements of the dizinc(II) complexes were carried out in deuterated acetonitrile. Two-dimensional methods (NOESY, COSY, HSQC and HMBC) were used to assign the signals to the explicit hydrogen or carbon atoms in the manner described in Chapter 3.2.1. The number, chemical shifts and splitting of the resonances detected illustrate the symmetry of the coordination compounds in solution.

$[\text{Zn}^{\text{II}}_2(\text{L}^1)(\mu\text{-OAc})_2]\text{PF}_6$ and $[\text{Zn}^{\text{II}}_2(\text{H}_2\text{L}^2)(\mu\text{-OAc})_2]\text{PF}_6$

The equivalence of the two binding sites within $[\text{Zn}^{\text{II}}_2(\text{H}_2\text{L}^2)(\mu\text{-OAc})_2]\text{PF}_6$, found by X-ray diffractometric investigation, was confirmed as the 16 aromatic protons resulted in eight resonances in the aromatic region of the ^1H NMR spectrum, with each of the multiplet resonances integrating for two protons (Figure 34, top). Comparison with the ^1H NMR spectrum of the free ligand H_3L^2 (Figure 34, bottom) shows a downfield shift of protons of the amidated pyridine residues and an upfield shift of protons of the unsubstituted pyridines upon the binding of Zn^{II} ions. As expected, $[\text{Zn}^{\text{II}}_2(\text{L}^1)(\mu\text{-OAc})_2]\text{PF}_6$ showed the same behavior, leading to a ^1H NMR spectrum corresponding to a pair of equal pyridine groups within the complex. Moreover, due to the same surroundings the two bridging acetate groups in $[\text{Zn}^{\text{II}}_2(\text{L}^1)(\mu\text{-OAc})_2]\text{PF}_6$ and $[\text{Zn}^{\text{II}}_2(\text{H}_2\text{L}^2)(\mu\text{-OAc})_2]\text{PF}_6$, and the *tert*-butyl residues in $[\text{Zn}^{\text{II}}_2(\text{H}_2\text{L}^2)(\mu\text{-OAc})_2]\text{PF}_6$ lead to a single resonance. This supports the symmetry appearance of $[\text{Zn}^{\text{II}}_2(\text{L}^1)(\mu\text{-OAc})_2]\text{PF}_6$ and $[\text{Zn}^{\text{II}}_2(\text{H}_2\text{L}^2)(\mu\text{-OAc})_2]\text{PF}_6$, also when dissolved in acetonitrile.

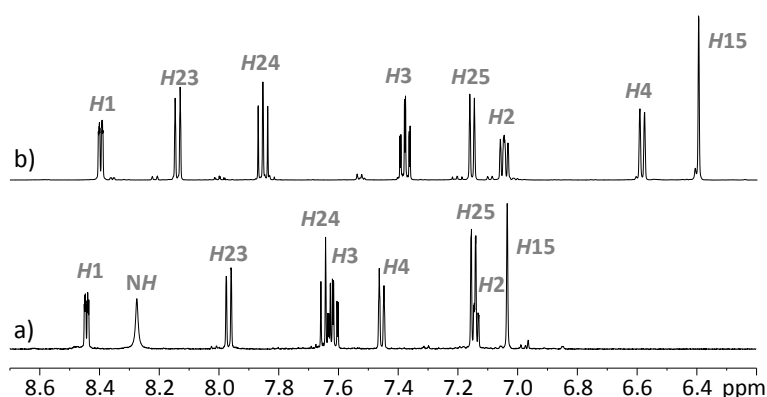


Figure 34: Aromatic region of the ^1H -NMR spectra of a) ligand H_3L^2 and b) complex $[\text{Zn}^{\text{II}}_2(\text{H}_2\text{L}^2)(\mu\text{-OAc})_2]\text{PF}_6$ in CD_3CN .

Additional experiments were undertaken to study the stability of complex $[\text{Zn}^{\text{II}}_2(\text{H}_2\text{L}^2)(\mu\text{-OAc})_2]\text{PF}_6$ in water/acetonitrile mixtures, as well as under basic conditions (conditions comparable to the activity assays which will be discussed in Chapter 7). Therefore, $[\text{Zn}^{\text{II}}_2(\text{H}_2\text{L}^2)(\mu\text{-OAc})_2]\text{PF}_6$ was dissolved in CD_3CN , and D_2O was added stepwise. Figure 35 shows the spectra of $[\text{Zn}^{\text{II}}_2(\text{H}_2\text{L}^2)(\mu\text{-OAc})_2]\text{PF}_6$ in pure CD_3CN and $\text{CD}_3\text{CN}/\text{D}_2\text{O}$

mixtures (8:1, 2:1, 1:1). The addition of D₂O led to no variation in the chemical shifts but induced a broadening of the detected resonances. Further addition of NaOD in D₂O resulted in no change in the ¹H NMR spectrum as shown in Figure 35e. This implies that no decoordination of Zn^{II} takes place under basic conditions.

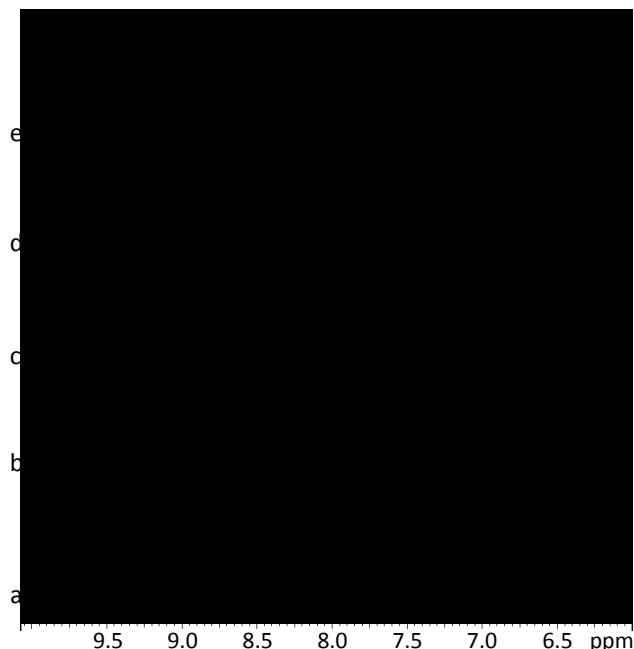


Figure 35: Aromatic region of the ¹H NMR spectra of a) complex [Zn^{II}₂(H₂L²)(μ-OAc)₂]PF₆ in CD₃CN and in CD₃CN/D₂O mixtures (b) 8:1, c) 2:1, d) 1:1) as well as e) in CD₃CN/D₂O mixture with pH 10.4.

[Zn^{II}₂(H₂SIM¹)(μ-OAc)(OH)]PF₆

The asymmetry of [Zn^{II}₂(H₂SIM¹)(μ-OAc)(OH)]PF₆, observed in the solid state by X-ray diffraction, also emerges from the ¹H NMR spectrum, where the aromatic region exhibits 16 resonances (Figure 36, top). In this complex, every hydrogen atom has a different electronic environment leading to the difference in the spectrum, when compared to the metal-free ligand (Figure 36, bottom). The resonances from the protons proximal to the Zn^{II} centers show a downfield shift while protons, that are distant from the metal centers, especially those pointing to the opposite site of the phenolate backbone, show an upfield shift. Similarly, the proton signals of each methylene group are separated, which gives rise to a set of 12 doublets in the region between 3.3 and 4.5 ppm (Figure 37, top). This implies that the electronic environment of protons bound to the same methylene carbon are not identical, in contrast to the spectrum of the free ligand (Figure 37, bottom), and this again is consistent with the observed X-ray structure. The coupling to the other hydrogen atom at the same carbon atom leads to the appearance of doublets. As a result of the asymmetry in this structure, the two *tert*-butyl groups in [Zn^{II}₂(H₂SIM¹)(μ-OAc)(OH)]⁺ give rise to two resonances in the ¹H NMR spectrum.

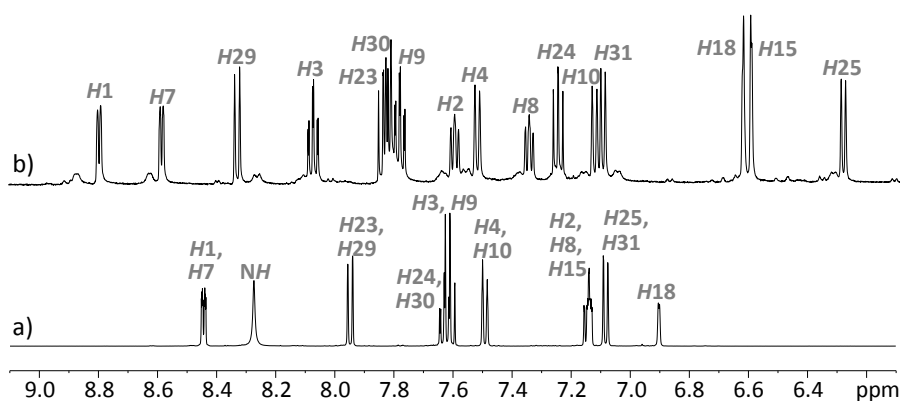


Figure 36: Aromatic region of ^1H NMR spectra of a) ligand H_3SIM^1 and b) complex $[\text{Zn}^{\text{II}}_2(\text{H}_2\text{SIM}^1)(\mu\text{-OAc})(\text{OH})]\text{PF}_6$ in CD_3CN .

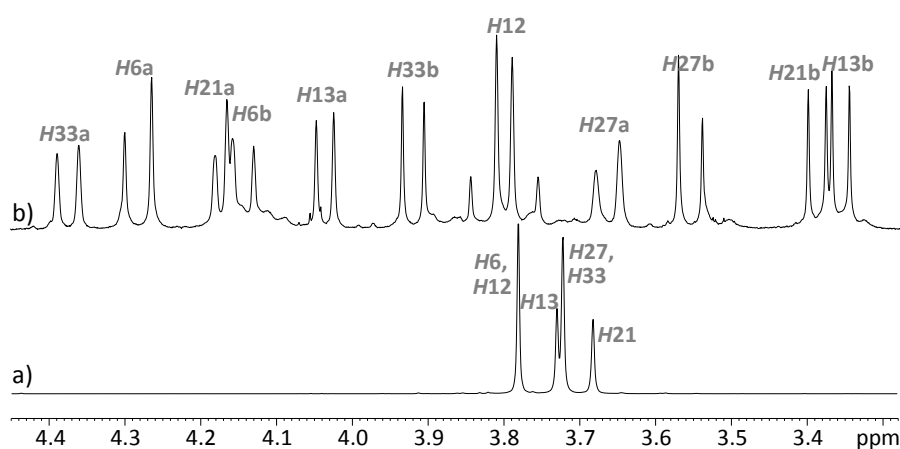


Figure 37: Methylene resonances in the ^1H NMR spectra of a) ligand H_3SIM^1 and b) complex $[\text{Zn}^{\text{II}}_2(\text{H}_2\text{SIM}^1)(\mu\text{-OAc})(\text{OH})]\text{PF}_6$ in CD_3CN .

$[\text{Zn}^{\text{II}}_2(\text{SIM}^2)(\mu\text{-OAc})_2]\text{PF}_6$

Although the crystal structure of $[\text{Zn}^{\text{II}}_2(\text{SIM}^2)(\mu\text{-OAc})_2]\text{PF}_6$ suggests that, in the solid state, the complex is symmetrical, the ^1H NMR spectrum exhibits 16 resonances in the aromatic region (Figure 38, top). Similar to the spectrum of $[\text{Zn}^{\text{II}}_2(\text{H}_2\text{SIM}^1)(\mu\text{-OAc})(\text{OH})]^+$, 12 resonances in the form of doublets are detected for the methylene protons in $[\text{Zn}^{\text{II}}_2(\text{SIM}^2)(\mu\text{-OAc})_2]^+$. In contrast to $[\text{Zn}^{\text{II}}_2(\text{L}^1)(\mu\text{-OAc})_2]^+$ and $[\text{Zn}^{\text{II}}_2(\text{H}_2\text{L}^2)(\mu\text{-OAc})_2]^+$, the two bridging acetate co-ligands in $[\text{Zn}^{\text{II}}_2(\text{SIM}^2)(\mu\text{-OAc})_2]^+$ produce two resonances in the ^1H NMR spectrum. Therefore, the substitution of two pyridine groups in one of the binding sites of HL^1 creates two different coordination environments in HSIM^2 , which induce the formation of an asymmetric dizinc(II) complex in solution, in contrast to the symmetric structure observed in the solid state by X-ray crystallography.

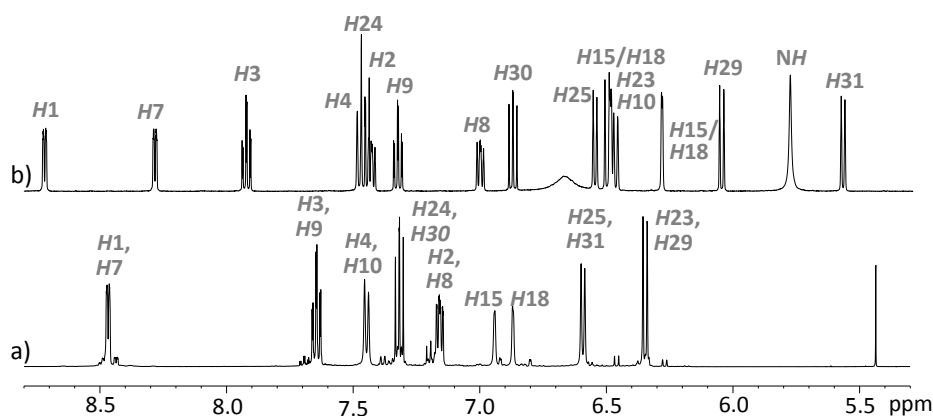


Figure 38: Aromatic region of the ^1H NMR spectra of a) ligand H_2SIM^2 and b) complex $[\text{Zn}^{\text{II}}_2(\text{SIM}^2)(\mu\text{-OAc})_2]\text{PF}_6$ in CD_3CN .

$[\text{Zn}^{\text{II}}_2(\text{H}_2\text{SIM}^3)(\mu\text{-OAc})(\text{OH})]$

Unfortunately, the poor solubility of $[\text{Zn}^{\text{II}}_2(\text{H}_2\text{SIM}^3)(\mu\text{-OAc})(\text{OH})]$ made it impossible to conduct a comparable set of ^1H NMR measurements for this complex, because addition of perchloric acid was necessary to achieve solubility. Figure 39 illustrates the ^1H NMR spectra obtained for the ligand H_4SIM^3 and $[\text{Zn}^{\text{II}}_2(\text{H}_2\text{SIM}^3)(\mu\text{-OAc})(\text{OH})]$ in deuterated acetonitrile after addition of four volume percent perchloric acid.

Comparison of the spectra exhibits two essential findings. Firstly, resonances for protons of the two amidated pyridine residues in binding site A (defined in Chart 7, Chapter 3) as well as resonances for protons of the unsubstituted pyridine moiety in binding site B are shifted in the complex spectrum compared to the free ligand. Secondly, the resonances of only one methylene proton pair is split into two doublets. Therefore, the addition of perchloric acid appears to lead to loss of the phenolate side-arm from the metal ion, since the proton resonances exhibit the same chemical shifts as those for this phenolate in the free ligand. The shift of the resonances assigned to the amidated pyridine residues in addition to the splitting of the methylene group assigned to the same side-arms implies sustained binding of a Zn^{II} ion in binding site A. Whether the pyridine residue of binding site B is still bound to a Zn^{II} center remains unclear, since on the one side the aromatic resonances of this side-arm are shifted, but on the other side the methylene group transformed in a singlet. The ESI^+ mass spectrometric measurement of $[\text{Zn}^{\text{II}}_2(\text{H}_2\text{SIM}^3)(\mu\text{-OAc})(\text{OH})]$ in deuterated acetonitrile after addition of hydrochloric acid resulted in a spectrum showing the main peak with a pattern typical for a dizinc(II) species (m/z 870.2 assigned to $[\text{Zn}_2(\text{HSIM}^3)]^+$), but also a peak with a typical monozinc(II) pattern with a similar intensity was detected (m/z 806.2 assigned to $[\text{Zn}(\text{H}_3\text{SIM}^3)]^+$).

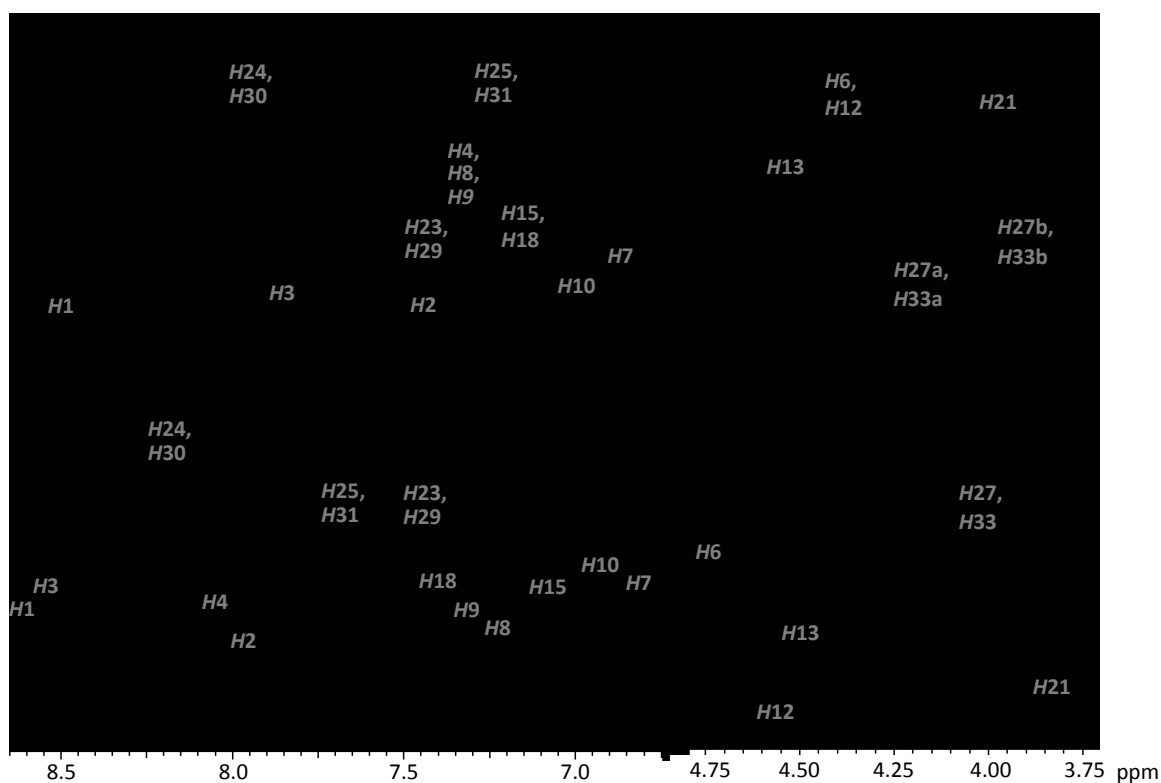


Figure 39: Aromatic region (a) and methylen proton resonances (b) in the ^1H NMR spectra of H_4SIM^3 (bottom) and $[\text{Zn}^{\text{II}}_2(\text{H}_2\text{SIM}^3)(\mu\text{-OAc})(\text{OH})]$ (top) in CD_3CN with 4 vol% HClO_4 .

The results obtained by NMR spectroscopic techniques demonstrate that only the two complexes $[\text{Zn}^{\text{II}}_2(\text{L}^1)(\mu\text{-OAc})_2]^+$ and $[\text{Zn}^{\text{II}}_2(\text{H}_2\text{L}^2)(\mu\text{-OAc})_2]^+$ contain two metal centers in identical geometry, when dissolved in acetonitrile. $[\text{Zn}^{\text{II}}_2(\text{H}_2\text{SIM}^1)(\mu\text{-OAc})(\text{OH})]^+$ and $[\text{Zn}^{\text{II}}_2(\text{SIM}^2)(\mu\text{-OAc})_2]^+$, the complexes formed with the asymmetrically substituted ligands H_3SIM^1 and HSIM^2 , contain two Zn^{II} ions in different surroundings. This suggests that the asymmetry of the amide-based complex $[\text{Zn}^{\text{II}}_2(\text{H}_2\text{SIM}^1)(\mu\text{-OAc})(\text{OH})]\text{PF}_6$ is not only the result of the two different coordination geometries of the two Zn^{II} centers but is also due to the hydrogen bond donating groups in proximity to one of the coordination sites.

UV-vis Spectroscopic Studies

Electronic spectra of the complexes $[\text{Zn}^{\text{II}}_2(\text{L}^1)(\mu\text{-OAc})_2]\text{PF}_6$, $[\text{Zn}^{\text{II}}_2(\text{H}_2\text{L}^2)(\mu\text{-OAc})_2]\text{PF}_6$, $[\text{Zn}^{\text{II}}_2(\text{H}_2\text{SIM}^1)(\mu\text{-OAc})(\text{OH})]\text{PF}_6$, and $[\text{Zn}^{\text{II}}_2(\text{SIM}^2)(\mu\text{-OAc})_2]\text{PF}_6$ were recorded in acetonitrile as well as in acetonitrile/aqueous buffer mixtures (1:1). The aqueous buffer solutions were 50 mM in HEPES, 50 mM in MES, 50 mM in CHES, 50 mM in CAPS and 250 mM in lithium perchlorate and were adjusted to a specific pH value by addition of aqueous sodium hydroxide solution. These buffer solutions were also used for the hydrolytic activity assays discussed in Chapter 6.3.

All four dizinc(II) complexes show two bands in the regions at 230 - 260 nm and 280 - 320 nm attributed to $p_{\pi} \rightarrow p_{\pi}^*$ ligand internal transitions (see Figure 40 and Table 10).

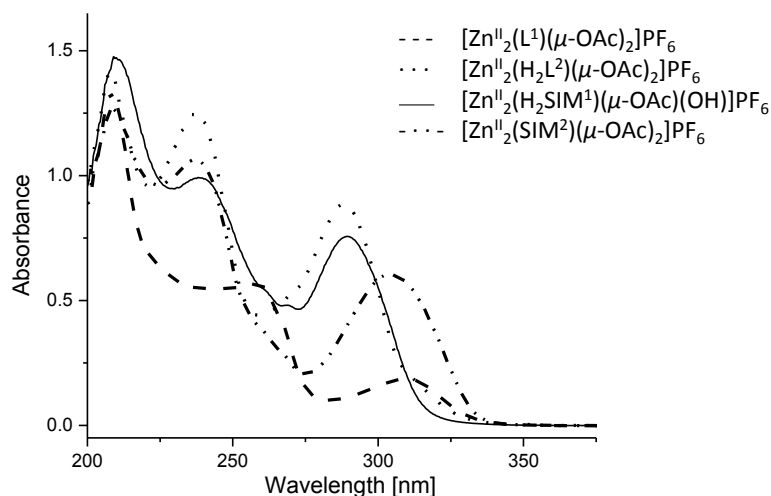


Figure 40: UV-vis absorption spectra of dizinc(II) complexes (5 μ M solution in CH_3CN).

Table 10: UV-vis spectral properties of the dizinc(II) complexes (5 μ M in CH_3CN).

complex	UV-vis [nm]	ϵ [$\text{M}^{-1} \text{cm}^{-1}$]	transitions
$[\text{Zn}^{\text{II}}_2(\text{L}^1)(\mu\text{-OAc})_2]\text{PF}_6$	260	113168	$p_{\pi} \rightarrow p_{\pi}^*$
	311	37161	$p_{\pi} \rightarrow p_{\pi}^*$
$[\text{Zn}^{\text{II}}_2(\text{H}_2\text{L}^2)(\mu\text{-OAc})_2]\text{PF}_6$	238	249438	$p_{\pi} \rightarrow p_{\pi}^*$
	289	177075	$p_{\pi} \rightarrow p_{\pi}^*$
$[\text{Zn}^{\text{II}}_2(\text{H}_2\text{SIM}^1)(\mu\text{-OAc})(\text{OH})]\text{PF}_6$	239	198843	$p_{\pi} \rightarrow p_{\pi}^*$
	290	151351	$p_{\pi} \rightarrow p_{\pi}^*$
$[\text{Zn}^{\text{II}}_2(\text{SIM}^2)(\mu\text{-OAc})_2]\text{PF}_6$	237	213347	$p_{\pi} \rightarrow p_{\pi}^*$
	305	120667	$p_{\pi} \rightarrow p_{\pi}^*$

The substitution with a pivaloyl-amide group in position six of two pyridine residues in $[\text{Zn}^{\text{II}}_2(\text{H}_2\text{SIM}^1)(\mu\text{-OAc})(\text{OH})]^+$ and $[\text{Zn}^{\text{II}}_2(\text{H}_2\text{L}^2)(\mu\text{-OAc})_2]^+$ leads to a hypsochromic shift in the UV-vis spectroscopic measurements, compared with the spectra of the unsubstituted compound $[\text{Zn}^{\text{II}}_2(\text{L}^1)(\mu\text{-OAc})_2]^+$. The substitution by amino moieties, as in $[\text{Zn}^{\text{II}}_2(\text{SIM}^2)(\mu\text{-OAc})_2]^+$, has a similar but less pronounced effect.

pH Behavior

In order to examine the behavior of the complexes $[\text{Zn}^{\text{II}}_2(\text{L}^1)(\mu\text{-OAc})_2]^+$, $[\text{Zn}^{\text{II}}_2(\text{H}_2\text{L}^2)(\mu\text{-OAc})_2]^+$, $[\text{Zn}^{\text{II}}_2(\text{H}_2\text{SIM}^1)(\mu\text{-OAc})(\text{OH})]^+$ and $[\text{Zn}^{\text{II}}_2(\text{SIM}^2)(\mu\text{-OAc})_2]^+$ under basic conditions, UV-vis spectroscopic measurements were also conducted in acetonitrile-aqueous buffer mixtures (1:1); the pH values recorded refer to the aqueous component. With increasing basicity, the band in the absorbance spectrum of $[\text{Zn}^{\text{II}}_2(\text{H}_2\text{L}^2)(\mu\text{-OAc})_2]^+$ at 287 nm experiences a shift to 294 nm. Also, the band at 233 nm decreases in intensity, while new bands at 259 nm and

326 nm arise (Figure 41a). Figure 41b shows the change of absorbance at different wavelengths as a function of rising pH value. The overlay of the spectra at different pH values indicates the presence of three isosbestic points at 246 nm, 270 nm and 297 nm. The observation of isosbestic points indicates that the dizinc(II) complex is stable in the investigated pH range and undergoes a single deprotonation step. Therefore, the curves can be analyzed by the Henderson-Hasselbalch Equation 9, where [HA] and [A⁻] are the concentrations of the protonated and deprotonated complex species, respectively, in the equilibrium (K_a: equilibrium constant).

$$\text{Equation 9} \quad \text{pH} = \text{pK}_a + \log \frac{[\text{A}^-]}{[\text{HA}]}$$

[HA] and [A⁻] follow the correlation given in Equation 10 with the initial complex concentration [HA]₀.

$$\text{Equation 10} \quad [\text{A}^-] = [\text{HA}]_0 - [\text{HA}]$$

Therefore, the concentration of protonated species in solution can be described as given in Equation 11.

$$\text{Equation 11} \quad [\text{HA}] = \frac{[\text{HA}]_0}{10^{\text{pH}-\text{pK}_a} + 1}$$

The Beer-Lambert Law assuming two species in solution is given in Equation 12, where ε₁ and ε₂ are the extinction coefficients of the protonated (HA) and deprotonated complex species (A⁻) and d is the path length.

$$\text{Equation 12} \quad \text{Abs} = \varepsilon_1 * d * [\text{HA}] + \varepsilon_2 * d * [\text{A}^-]$$

Consideration of Equation 10, leads to Equation 13.

$$\text{Equation 13} \quad \text{Abs} = (\varepsilon_1 - \varepsilon_2) * d * [\text{HA}] + \varepsilon_2 * d * [\text{HA}]_0$$

Substituting [HA] in Equation 13, as defined in Equation 11, provides Equation 14.

$$\text{Equation 14} \quad \text{Abs} = (\varepsilon_1 - \varepsilon_2) * \frac{[\text{HA}]_0 * d}{10^{\text{pH}-\text{pK}_a} + 1} + \varepsilon_2 * [\text{HA}]_0 * d$$

Here, the absorbance depends on the extinction coefficients, ε₁ and ε₂, and the pK_a value. Fitting of the pH-dependent spectroscopic data to Equation 14 results in an estimate of the pK_a value of [Zn^{II}₂(H₂L²)(μ-OAc)₂]⁺ of 8.14 ± 0.25. pH-dependent UV-vis spectroscopic measurements of [Zn^{II}₂(H₂SIM¹)(μ-OAc)(OH)]⁺ show similar effects (Figure 41c, d), and from fitting of these data to Equation 14, the pK_a value of [Zn^{II}₂(H₂SIM¹)(μ-OAc)(OH)]⁺ is: pK_a = 7.27 ± 0.65. The variation of the pH value from 5 to 11 did not result in any change of the UV-vis spectra of [Zn^{II}₂(L¹)(μ-OAc)₂]PF₆ and [Zn^{II}₂(SIM²)(μ-OAc)₂]PF₆.

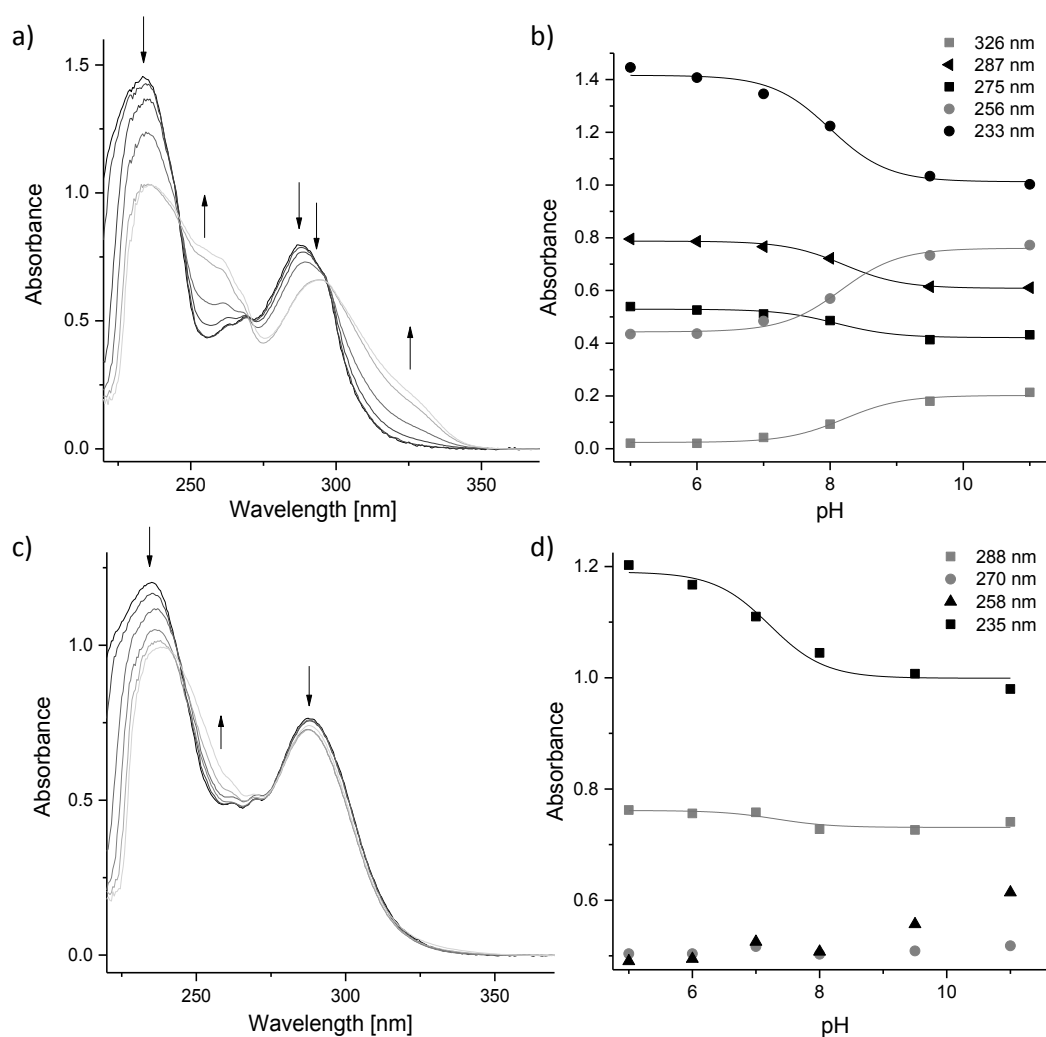


Figure 41: UV-vis spectroscopic titration spectra (5 μM in acetonitrile/buffer between pH 5 and 11) for a) $[\text{Zn}^{\text{II}}_2(\text{H}_2\text{L}^2)(\mu\text{-OAc})_2]\text{PF}_6$ and c) $[\text{Zn}^{\text{II}}_2(\text{H}_2\text{SIM}^1)(\mu\text{-OAc})(\text{OH})]\text{PF}_6$ as well as absorbance vs. pH plots for b) $[\text{Zn}^{\text{II}}_2(\text{H}_2\text{L}^2)(\mu\text{-OAc})_2]\text{PF}_6$ and d) $[\text{Zn}^{\text{II}}_2(\text{H}_2\text{SIM}^1)(\mu\text{-OAc})(\text{OH})]\text{PF}_6$.

The spectrophotometrically determined pK_a values of $[\text{Zn}^{\text{II}}_2(\text{H}_2\text{SIM}^1)(\mu\text{-OAc})(\text{OH})]^+$ and $[\text{Zn}^{\text{II}}_2(\text{H}_2\text{L}^2)(\mu\text{-OAc})_2]^+$ can be compared to the corresponding data obtained from the analysis of the kinetic data of the phosphoester hydrolysis, and this supports the mechanistic interpretation (see Chapter 7). Importantly, the data described here also support the solution structural analysis, *i.e.* the observation of isosbestic points in the pH range of 5 to 11 indicates that the dizinc(II) complexes are stable (and the only species of relevance) in these solutions, and this emerges also from the NMR studies, specifically in mixed $\text{CD}_3\text{CN}/\text{D}_2\text{O}$ solutions at varying pH values (see above).

4.4 SUMMARY

The five ligands HL¹, with no substituents, H₃SIM¹, H₄SIM³, with two asymmetrically disposed amide residues, H₃L², with two symmetrically disposed amide residues, and HSIM², with two asymmetrically disposed amine anchor groups, lead to strikingly different structures of the dizinc(II) complexes [Zn^{II}₂(L¹)(μ-OAc)₂]⁺, [Zn^{II}₂(H₂L²)(μ-OAc)₂]⁺, [Zn^{II}₂(H₂SIM¹)(μ-OAc)(OH)]⁺, [Zn^{II}₂(SIM²)(μ-OAc)₂]⁺, and [Zn^{II}₂(H₂SIM³)(μ-OAc)(OH)]. While the three complexes [Zn^{II}₂(L¹)(μ-OAc)₂]⁺, [Zn^{II}₂(H₂L²)(μ-OAc)₂]⁺, and [Zn^{II}₂(SIM²)(μ-OAc)₂]⁺ show the common structure of phenoxido-bridged phosphatase models with two bridging acetate co-ligands, [Zn^{II}₂(H₂SIM¹)(μ-OAc)(OH)]⁺ and [Zn^{II}₂(H₂SIM³)(μ-OAc)(OH)] possess two strikingly different Zn^{II} sites, one being five- and one six-coordinate, with rare example of a Zn^{II}-OH bond. The appearance of a terminal hydroxido co-ligand is ascribed to the steric hindrance caused by the asymmetric pivaloyl-substituted ligand backbone and the emerging incapacity of the resulting dizinc(II) complexes to bind two acetate co-ligands. Stabilization of this hydroxido co-ligand by hydrogen bond formation is supported by X-ray structures and the IR spectra of [Zn^{II}₂(H₂SIM¹)(μ-OAc)(OH)]⁺ and [Zn^{II}₂(H₂SIM³)(μ-OAc)(OH)]. Hydrogen bond formation was also seen in the structure of the complexes [Zn^{II}₂(H₂L²)(μ-OAc)₂]⁺ and [Zn^{II}₂(SIM²)(μ-OAc)₂]⁺ to the acetate co-ligands.

The structures of the dizinc(II) complexes in solution were studied via NMR spectroscopy. The asymmetry of [Zn^{II}₂(H₂SIM¹)(μ-OAc)(OH)]⁺ in solution was verified. Furthermore, the solution structure of [Zn^{II}₂(SIM²)(μ-OAc)₂]⁺, which is also built up by an asymmetric ligand backbone, was found to contain two unequal Zn^{II} centers due to the two amino residues adjacent one of the two Zn^{II} centers. In conclusion these three asymmetric complexes [Zn^{II}₂(H₂SIM¹)(μ-OAc)(OH)]⁺, [Zn^{II}₂(SIM²)(μ-OAc)₂]⁺ and [Zn^{II}₂(H₂SIM³)(μ-OAc)(OH)] can be considered as accurate model complexes for phosphoesters type metalloenzymes as they bear the two Zn^{II} centers in different coordination environments and have the capacity to form a hydrogen bond network as exhibited for the native enzymes.

Chapter 5

Diiron Model Complexes^e

^e Main parts of this chapter will be published in “An Approach to More Accurate Model Systems for Purple Acid Phosphatases (PAPs)”; Paul V. Bernhardt, [Simone Bosch](#), Peter Comba, Lawrence R. Gahan, Graeme R. Hanson, Valeriu Mereacre, Christopher J. Noble, Gerhard Schenk, Hubert Wadepohl; manuscript in preparation.

5.1 INTRODUCTION

Iron is one of the most versatile of the biochemically active metals and, therefore, the role of iron in its various oxidation states in the active sites of metalloenzymes has been widely studied.²⁰⁷⁻²¹¹ Even considering only non-haem diiron proteins, the diiron core takes part in a multitude of functions including oxygen transport (Hemerythrin), methane oxidation (Methane Monooxygenase, MMO), conversion of ribonucleotides to deoxyribonucleotides (Ribonucleotide Reductase, RNR), detoxification of NO (Flavodiiron Nitric Oxide Reductase, FNOR) and hydrolysis of phosphate esters (Purple Acid Phosphatase, PAP).²¹⁰⁻²¹⁸ In these enzymes the diiron sites, in all of their accessible oxidation states, are typically bridged by at least one carboxylate moiety.¹⁸³ Most of the iron-containing non-haem diiron proteins function through interaction of their diiron(II) form with dioxygen. In contrast, PAPs perform a hydrolytic function, at least *in vitro*, via their heterovalent diiron(III/II) form and in this way are involved in the regulation of phosphate and phosphorylated metabolite levels in a wide range of organisms.¹⁰² More precisely, PAPs catalyze the hydrolysis of phosphomonoesters at acidic to neutral pH. The active sites of the mammalian PAPs isolated from bovine spleen (bsPAP) and porcine uterus (ufPAP) were determined to contain a dinuclear iron center in two accessible oxidation states: the Fe^{III}_2 form, which is characterized by typical visible absorption maxima between 550 nm and 570 nm ($\epsilon \sim 4000 \text{ M}^{-1}\text{cm}^{-1}$), and the reduced $\text{Fe}^{\text{III}}\text{Fe}^{\text{II}}$ form, which exhibits blue shifted absorption maxima between 505 nm and 510 nm ($\epsilon \sim 4000 \text{ M}^{-1}\text{cm}^{-1}$).^{69, 138, 217, 219, 220} Interestingly, the Fe^{III}_2 form of ufPAP was found to have an upper limit of less than 1% of the activity of the heterovalent $\text{Fe}^{\text{III}}\text{Fe}^{\text{II}}$ form.^{21, 218, 221} The redox potential for the $\text{Fe}^{\text{III}}_2/\text{Fe}^{\text{III}}\text{Fe}^{\text{II}}$ couple of ufPAP was found to be 0.367 V at pH 5 and 0.306 V at pH 6 vs. NHE. Therefore, the enzyme is easily and reversibly oxidized to the Fe^{III}_2 form owing to the low redox potential of the Fe^{II} center.^{222, 223} This observation led to the suggestion that PAPs may regulate their catalytic activity *in vivo* by reversible oxidation/reduction of the active site.²²²

PAPs further differ from other non-heme diiron proteins having a tyrosinate ligand leading to the characteristic absorption bands and consequently to the characteristic purple color. The absorption bands have been assigned by resonance Raman studies to tyrosinate-to- Fe^{III} CT transitions.²¹⁹ With Mössbauer spectroscopy the iron centers of ufPAP and bsPAP were revealed to have distinct coordination environments, and this was confirmed by X-ray crystallographic studies of ufPAP.^{219, 224, 225} Magnetic susceptibility studies indicate that the Fe^{III} and Fe^{II} centers are weakly antiferromagnetically coupled with J values ranging from -5 cm^{-1} to -11 cm^{-1} ($H = -2JS_1S_2$).^{219, 226} Similarly, weak antiferromagnetic coupling was emerged from magnetic

susceptibility studies for the oxidized Fe^{III}_2 form of ufPAP ($J > -15 \text{ cm}^{-1}$).²²⁷ Moreover, the reduced form of ufPAP exhibits rhombic EPR signals at $g = 1.94, 1.73$ and 1.58 , consistent with antiferromagnetically coupled high-spin Fe^{II} and Fe^{III} centers.^{217, 228}

In recent years, a number of structural models for the active site of PAPs have been developed using phenoxido-containing multidentate ligands.⁸¹ Fe^{III}_2 complexes, which were reported for symmetrical ligands such as H_3L^3 , H_3L^{35} , HL^{36} , and H_3L^{37} , were used to model the oxidized form of PAPs.^{101, 125, 229, 230} Moreover, heterovalent diiron complexes were also generated using symmetric ligands such as HL^1 , HL^{11} , HL^{38} , and HL^{10} and have been examined as structural models for PAPs.^{99, 138, 139, 231, 232} From the separation of their one-electron redox processes assigned to the $\text{Fe}^{\text{II}}_2/\text{Fe}^{\text{III}}\text{Fe}^{\text{II}}$ and $\text{Fe}^{\text{III}}\text{Fe}^{\text{II}}/\text{Fe}^{\text{III}}_2$ couples the stability of the $\text{Fe}^{\text{III}}\text{Fe}^{\text{II}}$ form over the corresponding homovalent Fe^{II}_2 or Fe^{III}_2 complexes was investigated. The comproportionation constant (K_{com}) for this equilibrium was found to be in the order of $10^{10} - 10^{12}$ and therefore confirms the substantial stability of the mixed-valent $\text{Fe}^{\text{III}}\text{Fe}^{\text{II}}$ form.⁸¹

Perhaps the most widely employed $\text{Fe}^{\text{III}}\text{Fe}^{\text{II}}$ model complex mimicking the mixed-valent diiron active site of PAP is $[\text{Fe}^{\text{III}}\text{Fe}^{\text{II}}(\text{L}^4)(\mu\text{-OAc})_2]\text{ClO}_4$. This acetate-bridged $\text{Fe}^{\text{III}}\text{Fe}^{\text{II}}$ complex of the asymmetric ligand H_2L^4 revealed significant similarities in the physical properties compared to the native enzyme ufPAP. In particular, $[\text{Fe}^{\text{III}}\text{Fe}^{\text{II}}(\text{L}^4)(\mu\text{-OAc})_2]\text{ClO}_4$ exhibits (i) a comparable metal...metal distance ($3.483(2) \text{ \AA}$ vs. 3.31 \AA in ufPAP), (ii) a phenolate-to- Fe^{III} charge transfer band at 550 nm (vs. the tyrosinate-to- Fe^{III} charge transfer band at $\sim 510 \text{ nm}$ in ufPAP), (iii) weakly antiferromagnetically coupled high spin Fe^{III} and Fe^{II} ions ($J = -7.4 \text{ cm}^{-1}$ vs. -5 to -11 cm^{-1} for ufPAP), (iv) localized iron valences in the solid state, and (v) a reversible $\text{Fe}^{\text{III}}\text{Fe}^{\text{II}}/\text{Fe}^{\text{III}}_2$ redox couple at a similar potential (380 mV vs. NHE vs. 344 mV at $\text{pH } 4.1$ / 367 mV at $\text{pH } 5$ for ufPAP).^{94, 96, 106, 140, 141}

Although $[\text{Fe}^{\text{III}}\text{Fe}^{\text{II}}(\text{L}^4)(\mu\text{-OAc})_2]\text{ClO}_4$ mimics accurately the first coordination sphere in the active site of PAP, the important structural features derived from the second coordination sphere of PAPs have not been addressed. The PAPs active site includes non-coordinated histidine groups proximal to the iron centers, which may help to position the substrate, as proposed from crystallographic data as well as from mechanistic studies.⁷⁴ These amino acid residues have been considered in the diiron(III) complexes, depicted in Chart 16, in form of basic groups proximal to the metal centers, in order to mimic the hydrogen bonding network within the active site of PAPs.^{108, 114} Moreover, the generation of a $\text{Fe}^{\text{III}}\text{Fe}^{\text{II}}$ form by bulk electrolysis with $[\text{Fe}^{\text{II}}_2(\text{L}^8)(\mu\text{-OH})(\text{OH}_2)_2]^{2+}$ was achieved.^{109, 114}

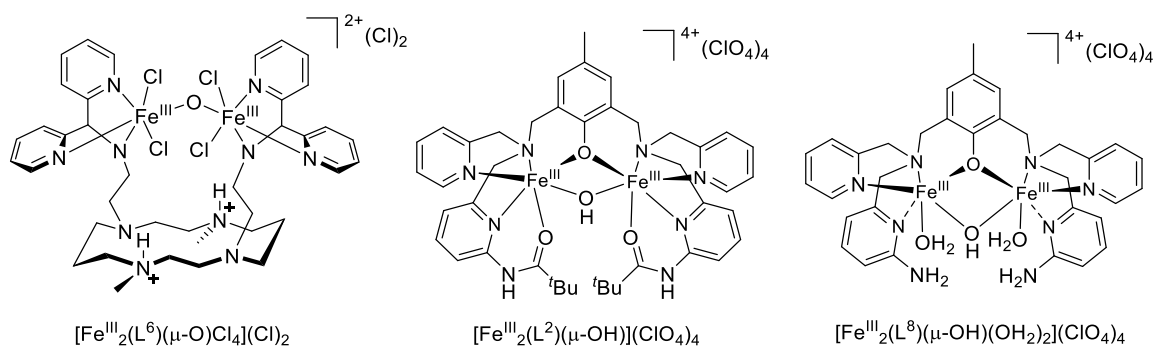


Chart 16: Previously reported diiron(III) complexes containing hydrogen bond donors.^{108, 114}

Examination and comparison of the phosphoester hydrolysis, accomplished with the complexes possessing the capacity for hydrogen bonding, as well as the Fe^{III}_2 complex of HL^1 , lacking hydrogen bond donors, gave further insights on the impact of hydrogen bond donors proximal to the diiron core on the catalytic activity. The results emerging from this progress are discussed in more detail in Chapter 8.

In this work, the role of the hydrogen bond donor position is probed, based on the hypothesis that hydrogen bonding in an asymmetrical manner favors monodentate or asymmetrical bridging phosphate binding and therefore helps to release the product formed after hydrolysis. Hence, the ligands H_3SIM^1 and H_4SIM^3 were designed and synthesized. In this chapter the synthesis and characterization of three Fe^{II}_2 complexes, shown in Chart 17, are discussed. All three complexes bear two pivaloyl-amide residues that are able to form hydrogen bonds to substrate molecules. The two hydrogen bond donors in $[Fe^{II}_2(H_2SIM^1)(\mu-OAc)_2]PF_6$ and $[Fe^{II}_2(H_2L^2)(\mu-OAc)_2]PF_6$ are positioned in two different fashions, (i) both pivaloyl-amide moieties adjacent to one binding site, or (ii) one pivaloyl-amide moiety adjacent to each binding site. Similar to $[Fe^{II}_2(H_2SIM^1)(\mu-OAc)_2]PF_6$, $[Fe^{II}_2(H_2SIM^3)(\mu-OAc)_2]$ contains both pivaloyl-amide residues in one binding site but the second binding site has one phenolate instead of a pyridine residue.

Among other investigations, the stability of the $Fe^{III}Fe^{II}$ complex of the asymmetric ligand H_3SIM^1 over the corresponding homovalent Fe^{II}_2 and Fe^{III}_2 complexes was studied by examination of the comproportionation constant K_{com} .

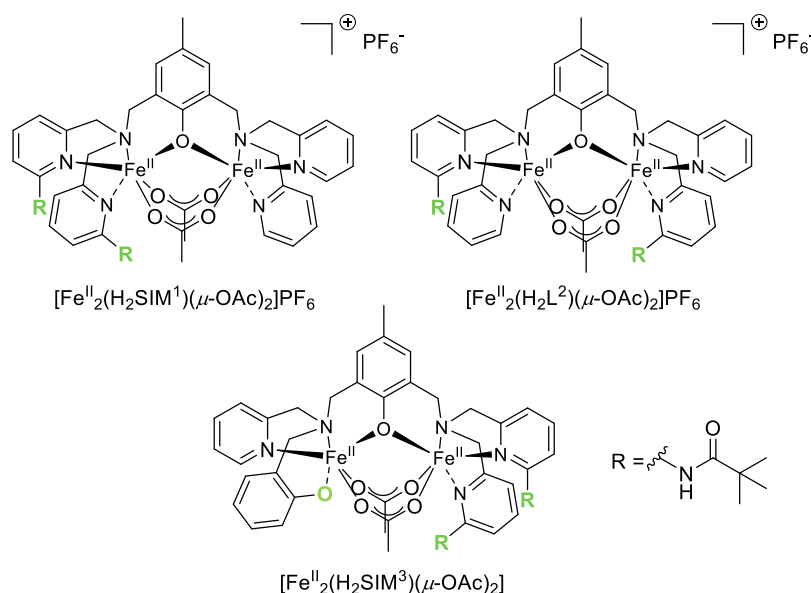


Chart 17: Diiron(II) complexes discussed in this chapter.

As discussed in Chapter 3.2.5 the coordination of two Fe^{III} ions in a single H_3SIM^1 ligand molecule could not be detected. Therefore, the preparation of a Fe^{III}_2 complex and the subsequent generation of the $\text{Fe}^{\text{III}}\text{Fe}^{\text{II}}$ complex by bulk electrolysis as it was done with $[\text{Fe}^{\text{III}}_2(\text{L}^8)(\mu\text{-OH})(\text{OH}_2)_2](\text{ClO}_4)_4$ is not feasible and alternative synthetic pathways were tested. For example, Suzuki *et al.* and Maeda *et al.* prepared first the Fe^{II}_2 complex of HL^1 and, subsequently, generated the heterovalent diiron form by selective oxidation in the presence of oxygen.^{231, 233} With this knowledge, the stability of $[\text{Fe}^{\text{II}}_2(\text{H}_2\text{SIM}^1)(\mu\text{-OAc})_2]\text{PF}_6$ under aerobic conditions was tested. Moreover, the generation of an $\text{Fe}^{\text{III}}\text{Fe}^{\text{II}}$ complex of H_3SIM^1 was studied with electrochemical methods as well as by the use of the oxidant ferrocenium hexafluorophosphate.

5.2 SYNTHESIS OF DIIRON(II) MODEL COMPLEXES

The dinuclear iron(II) complexes of H_3SIM^1 and H_3L^2 were prepared under an inert atmosphere in the glovebox by reaction with two equivalents of iron(II) acetate in degassed methanol. After the yellow solution was stirred for 12 hours at room temperature, sodium hexafluorophosphate was added. The mixture was filtered through a syringe filter and subsequent diffusion of degassed diethylether into the solution yielded X-ray quality crystals. In this way, the complexes $[\text{Fe}^{\text{II}}_2(\text{H}_2\text{SIM}^1)(\mu\text{-OAc})_2]\text{PF}_6$ and $[\text{Fe}^{\text{II}}_2(\text{H}_2\text{L}^2)(\mu\text{-OAc})_2]\text{PF}_6$ were isolated as green crystals. Applying this procedure to H_4SIM^3 , the ligand containing solution was treated with one equivalent of sodium hydroxide before addition of iron(II) acetate and sodium hexafluorophosphate. Diffusion of degassed diethylether into the claret-colored solution resulted in the formation of only a few crystals of the complex $\{\text{Na}[\text{Fe}^{\text{II}}_2(\text{H}_2\text{SIM}^3)(\mu\text{-OAc})_2]_2\}\text{PF}_6$,

suitable for X-ray diffraction but insufficient for further investigations. $[\text{Fe}^{\text{II}}_2(\text{H}_2\text{SIM}^1)(\mu\text{-OAc})_2]\text{PF}_6$ and $[\text{Fe}^{\text{II}}_2(\text{H}_2\text{L}^2)(\mu\text{-OAc})_2]\text{PF}_6$ were characterized and studied in the solid state and also in solution. Furthermore, the possibility of obtaining an $\text{Fe}^{\text{III}}\text{Fe}^{\text{II}}$ complex with the asymmetric complex $[\text{Fe}^{\text{II}}_2(\text{H}_2\text{SIM}^1)(\mu\text{-OAc})_2]\text{PF}_6$ was examined. Bearing two amide residues adjacent to one iron(II) center in $[\text{Fe}^{\text{II}}_2(\text{H}_2\text{SIM}^1)(\mu\text{-OAc})_2]\text{PF}_6$ or one amide residue adjacent to each iron(II) center in $[\text{Fe}^{\text{II}}_2(\text{H}_2\text{L}^2)(\mu\text{-OAc})_2]\text{PF}_6$, these complexes offer the potential for the investigation of the positioning effect of hydrogen bonding on the phosphoester hydrolytic activity.

5.3 STRUCTURAL CHARACTERIZATION OF DIIRON(II) COMPLEXES

The three diiron(II) complexes were structurally characterized in the solid state and $[\text{Fe}^{\text{II}}_2(\text{H}_2\text{SIM}^1)(\mu\text{-OAc})_2]\text{PF}_6$ and $[\text{Fe}^{\text{II}}_2(\text{H}_2\text{L}^2)(\mu\text{-OAc})_2]\text{PF}_6$ also in solution. Due to the air sensitivity of the samples, especially in solution, analyses were undertaken strictly anaerobically. The solid state structures were investigated by X-ray diffraction analysis and SQUID experiments. Furthermore, the structure as well as the electronic, magnetic, and electrochemical properties in solution of $[\text{Fe}^{\text{II}}_2(\text{H}_2\text{SIM}^1)(\mu\text{-OAc})_2]\text{PF}_6$ and $[\text{Fe}^{\text{II}}_2(\text{H}_2\text{L}^2)(\mu\text{-OAc})_2]\text{PF}_6$ were studied with UV-vis-NIR spectroscopy, NMR spectroscopy, and cyclic voltammetry. In addition, the oxidation of the diiron(II) complexes under aerobic conditions was investigated.

Solid State Structure under Anaerobic Conditions

The yellow crystals of $[\text{Fe}^{\text{II}}_2(\text{H}_2\text{SIM}^1)(\mu\text{-OAc})_2]\text{PF}_6$ and $[\text{Fe}^{\text{II}}_2(\text{H}_2\text{L}^2)(\mu\text{-OAc})_2]\text{PF}_6$ and the black crystals of $\{\text{Na}[\text{Fe}^{\text{II}}_2(\text{H}_2\text{SIM}^3)(\mu\text{-OAc})_2]_2\}\text{PF}_6$ were used for X-ray diffraction data collection. Crystallographic data obtained are displayed in Table 35 (see Appendix).

The structures of $[\text{Fe}^{\text{II}}_2(\text{H}_2\text{SIM}^1)(\mu\text{-OAc})_2]^+$ and $[\text{Fe}^{\text{II}}_2(\text{H}_2\text{L}^2)(\mu\text{-OAc})_2]^+$ were solved including a complex cation and a hexafluorophosphate counterion. With H_4SIM^3 as ligand in the complex preparation, the X-ray crystal structure revealed a dimeric structure in which the $[\text{Fe}^{\text{II}}_2(\text{H}_2\text{SIM}^3)(\mu\text{-OAc})_2]$ monomers are bridged by a sodium cation between the Fe(1) ions (separated by 6.119 Å) coordinated in the amide-free binding sites. The charge is neutralized by the hexafluorophosphate counterion present in the crystal cell. The structures of the complex cations are shown in Figure 42 and selected distances and valence angles are summarized in Table 11.

In contrast to the corresponding Zn^{II} complexes discussed in Chapter 4.3, all three Fe^{II} complexes, are bridged threefold by two acetate co-ligands and the phenolate-linker of the respective ligand. In addition to the three bridging ligands, the two Fe^{II} ions in $[\text{Fe}^{\text{II}}_2(\text{H}_2\text{SIM}^1)(\mu\text{-OAc})_2]^+$ and $[\text{Fe}^{\text{II}}_2(\text{H}_2\text{L}^2)(\mu\text{-OAc})_2]^+$ are coordinated by two pyridine moieties and a tertiary amine, forming an octahedral coordination environment.

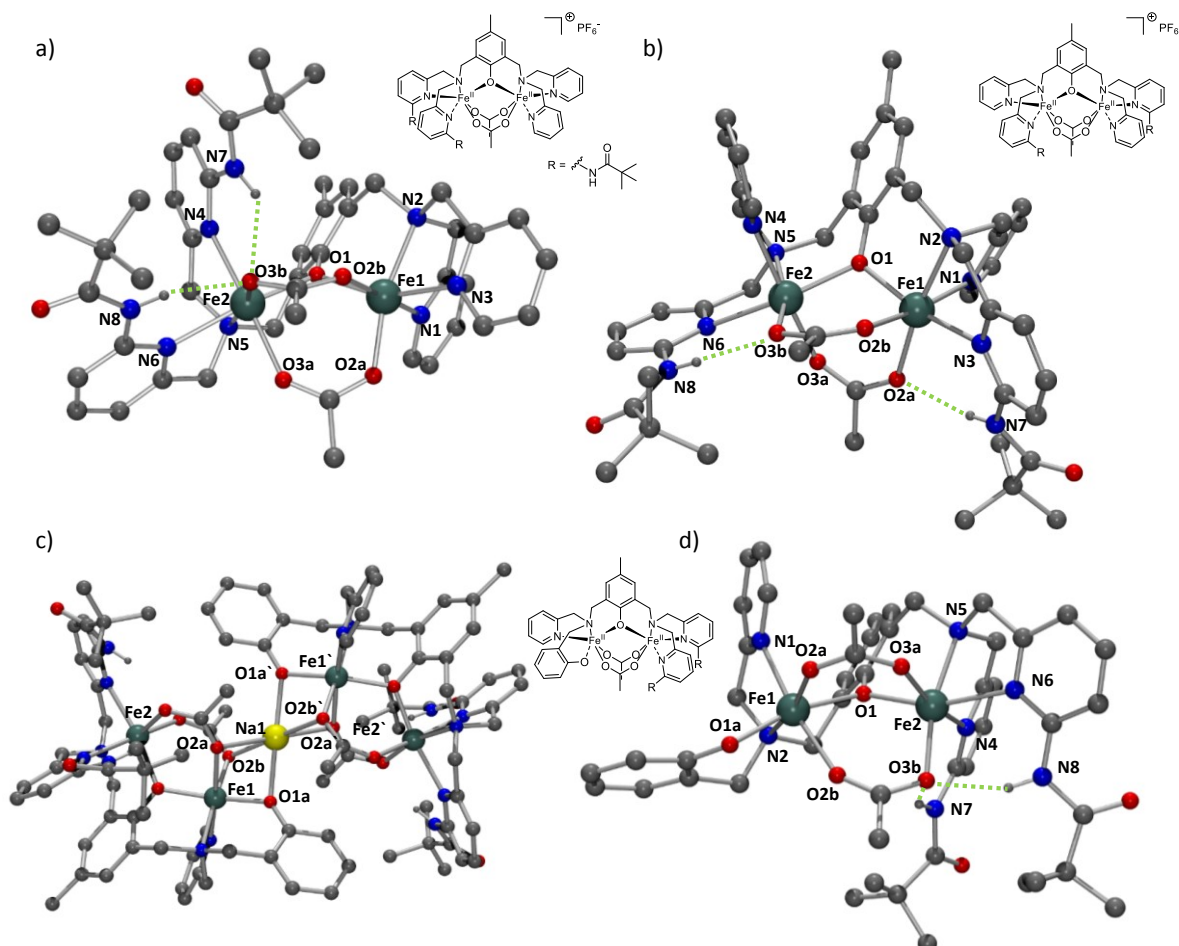


Figure 42: Structures of a) $[\text{Fe}^{\text{II}}_2(\text{H}_2\text{SIM}^1)(\mu\text{-OAc})_2]^+$, b) $[\text{Fe}^{\text{II}}_2(\text{H}_2\text{L}^2)(\mu\text{-OAc})_2]^+$, c) $\{\text{Na}[\text{Fe}^{\text{II}}_2(\text{H}_2\text{SIM}^3)(\mu\text{-OAc})_2]_2\}^+$ and d) the monomeric section of the latter complex, showing hydrogen bonding (green dotted lines; counter ions, non-coordinated solvent molecules, and hydrogen atoms, not involved in hydrogen bonding, have been omitted for clarity; crystallographic data and ORTEP plots with 50% probability level of thermal ellipsoids appear in the Appendix, Table 35 and Figure 75).

While the $\text{Fe}^{\text{II}}\text{-N}_{\text{Py}}$ distances for the pyridine residues lacking the amide substituents are in the range of 2.159 Å to 2.178 Å, the distance between the Fe^{II} center and the amidated pyridine moieties are elongated with bond distances from 2.290 Å to 2.364 Å as expected because of the electron withdrawing effect of the pivaloyl-amide residues. This finding accords with the results obtained from a Fe^{II}_2 complex $[\text{Fe}^{\text{II}}_2(\text{H}_4\text{L}^{39})(\mu\text{-OBz})_2]^+$ of the fourfold pivaloyl-amide substituted ligand H_5L^{39} in which the $\text{Fe}^{\text{II}}\text{-N}_{\text{Py}}$ distances to the amidated pyridines are in the range of 2.250 Å to 2.265 Å.²³⁴ The $\text{Fe}^{\text{II}}\text{-N}_{\text{amine}}$ distances of $[\text{Fe}^{\text{II}}_2(\text{H}_2\text{SIM}^1)(\mu\text{-OAc})_2]^+$ and $[\text{Fe}^{\text{II}}_2(\text{H}_2\text{L}^2)(\mu\text{-OAc})_2]^+$, ranging from 2.188 Å to 2.270 Å, are in the medium range compared with the $\text{Fe}\text{-N}_{\text{Py}}$ distances, While this parameter is similar in the two binding sites of $[\text{Fe}^{\text{II}}_2(\text{H}_2\text{L}^2)(\mu\text{-OAc})_2]^+$ containing an

amide-substituted pyridine in each binding site (2.2311(15) Å and 2.2270(16) Å), the Fe^{II}-N_{amine} distance in the amide-free binding site in [Fe^{II}₂(H₂L²)(μ-OAc)₂]⁺ is elongated (2.270(5) Å) and shortened to 2.188(6) Å in the amide-containing binding site. An explanation for this finding may be the hydrogen bond formation of the amide residues to the bridging acetate co-ligands, distorting the other coordination bonds. Moreover, comparison to the pivaloyl-amide-free complex [Fe^{II}₂(L¹)(μ-OPr)₂]⁺ (2.250(2) Å and 2.259(2) Å)²³⁵ both Fe^{II}-N_{amine} distances in [Fe^{II}₂(H₂L²)(μ-OAc)₂]⁺ are shortened as in both binding sites hydrogen bond formation takes place. In contrast, in [Fe^{II}₂(H₂SIM¹)(μ-OAc)₂]⁺ only the amide-containing coordination sites contains a shorter Fe^{II}-N_{amine} distance, while the other Fe^{II}-N_{amine} distance in the amide-free binding site is elongated compared to the found values in [Fe^{II}₂(L¹)(μ-OPr)₂]⁺,²³⁵ as the hydrogen bonding network is only created in the amidated binding site.

Table 11: Selected bond lengths (Å) and angles (°) for [Fe^{II}₂(H₂SIM¹)(μ-OAc)₂]⁺PF₆, [Fe^{II}₂(H₂L²)(μ-OAc)₂]⁺PF₆ and {Na[Fe^{II}₂(H₂SIM³)(μ-OAc)₂]₂}PF₆.

	[Fe ^{II} ₂ (H ₂ SIM ¹)(μ-OAc) ₂] ⁺	[Fe ^{II} ₂ (H ₂ L ²)(μ-OAc) ₂] ⁺	{Na[Fe ^{II} ₂ (H ₂ SIM ³)(μ-OAc) ₂] ₂ } ⁺	
			Fe(1)	Fe(1')
Fe(1)···Fe(1')	-	-	6.118	
Fe(1)···Fe(2)	3.430	3.4457(3)	3.536	3.541
Fe(1)-O(1)	2.039(4)	2.0746(13)	2.046(3)	2.053(3)
Fe(1)-O(1A)	-	-	2.005(3)	2.001(3)
Fe(1)-O(2A)	2.024(4)	2.0930(13)	2.131(3)	2.142(3)
Fe(1)-O(2B)	2.185(4)	2.0712(13)	2.287(3)	2.249(3)
Fe(1)-N(1)	2.167(5)	2.1753(16)	2.178(3)	2.168(3)
Fe(1)-N(2)	2.270(5)	2.2311(15)	2.256(3)	2.277(3)
Fe(1)-N(3)	2.159(5)	2.3638(15)	-	-
Fe(2)-O(1)	2.040(4)	2.0378(13)	2.046(3)	2.040(3)
Fe(2)-O(3A)	2.204(4)	2.1184(14)	2.117(3)	2.114(3)
Fe(2)-O(3B)	2.079(4)	2.1020(14)	2.093(3)	2.105(3)
Fe(2)-N(4)	2.290(6)	2.1703(16)	2.299(3)	2.299(3)
Fe(2)-N(5)	2.188(6)	2.2270(16)	2.207(3)	2.212(4)
Fe(2)-N(6)	2.311(5)	2.2786(15)	2.315(3)	2.325(3)
Fe(1)-O(1)-Fe(2)	114.45(18)	113.83(6)	119.60(12)	119.82(12)
O(1)-Fe(1)-N(1)	91.16(18)	87.69(6)	90.25(11)	90.55(11)
O(1)-Fe(1)-N(2)	86.17(17)	86.53(5)	86.94(10)	86.82(11)
O(1)-Fe(1)-N(3)	156.49(19)	160.48(5)	-	-
O(1)-Fe(1)-O(1A)	-	-	165.10(11)	165.81(11)
O(1)-Fe(1)-O(2A)	104.69(17)	102.08(5)	94.75(10)	94.82(10)
O(1)-Fe(1)-O(2B)	87.79(17)	90.73(5)	85.79(10)	84.94(10)
O(1)-Fe(2)-N(4)	87.09(18)	90.36(5)	87.46(10)	87.72(11)
O(1)-Fe(2)-N(5)	87.69(18)	88.88(6)	87.83(11)	87.96(12)
O(1)-Fe(2)-N(6)	162.03(18)	160.55(6)	160.81(12)	161.05(12)
O(1)-Fe(2)-O(3A)	93.65(16)	89.27(6)	89.89(10)	91.04(11)
O(1)-Fe(2)-O(3B)	103.30(16)	97.90(5)	105.74(10)	104.19(10)

The Fe^{II}···Fe^{II} distance is the shortest in [Fe^{II}₂(H₂SIM¹)(μ-OAc)₂]⁺ formed with the asymmetric pyridine-rich ligand H₃SIM¹ but still longer than that found in [Fe^{II}₂(L¹)(μ-OPr)₂]⁺ (3.348(2) Å).²³⁵

Although the first coordination sphere in $[\text{Fe}^{\text{II}}_2(\text{H}_2\text{L}^2)(\mu\text{-OAc})_2]^+$ is comparable to that in $[\text{Fe}^{\text{II}}_2(\text{H}_2\text{SIM}^1)(\mu\text{-OAc})_2]^+$ the $\text{Fe}^{\text{II}}\cdots\text{Fe}^{\text{II}}$ separation is 0.015 Å shorter in the latter. From the elongation of the $\text{Fe}^{\text{II}}\cdots\text{Fe}^{\text{II}}$ separation results a widening of the Fe(1)-O(1)-Fe(2) angle (114.45(18) Å for $[\text{Fe}^{\text{II}}_2(\text{H}_2\text{SIM}^1)(\mu\text{-OAc})_2]^+$ and 113.83(6) Å for $[\text{Fe}^{\text{II}}_2(\text{H}_2\text{L}^2)(\mu\text{-OAc})_2]^+$), compared to $[\text{Fe}^{\text{II}}_2(\text{L}^1)(\mu\text{-OPr})_2]^+$ (108.93(6)°). In the respective Zn^{II} complexes the behavior is reversed, that is, the $[\text{Zn}^{\text{II}}_2(\text{H}_2\text{L}^2)(\mu\text{-OAc})_2]^+$ exhibits a 0.143 Å shorter $\text{Zn}^{\text{II}}\cdots\text{Zn}^{\text{II}}$ distance, possibly due to the doubly acetate-bridged arrangement, which was not found in $[\text{Zn}^{\text{II}}_2(\text{H}_2\text{SIM}^1)(\mu\text{-OAc})(\text{OH})]^+$. Comparison of the Fe^{II} and Zn^{II} complexes of H_3L^2 , which are both doubly acetate-bridged, shows a longer $\text{Fe}^{\text{II}}\cdots\text{Fe}^{\text{II}}$ than $\text{Zn}^{\text{II}}\cdots\text{Zn}^{\text{II}}$ distance (3.4457(3) Å for $[\text{Fe}^{\text{II}}_2(\text{H}_2\text{L}^2)(\mu\text{-OAc})_2]^+$ vs. 3.3992(6) Å for $[\text{Zn}^{\text{II}}_2(\text{H}_2\text{L}^2)(\mu\text{-OAc})_2]^+$). In the case of the complexes derived from ligand H_3SIM^1 the observation is opposite, most likely to the lack of the second bridging acetate co-ligand in $[\text{Zn}^{\text{II}}_2(\text{H}_2\text{SIM}^1)(\mu\text{-OAc})(\text{OH})]^+$ (3.5422(7) Å vs. 3.430 Å in $[\text{Fe}^{\text{II}}_2(\text{H}_2\text{SIM}^1)(\mu\text{-OAc})_2]^+$). Similar to the Zn^{II} complex, the Fe^{II} complex of ligand H_4SIM^3 with two phenol moieties in contrast to H_3SIM^1 and H_3L^2 , the metal \cdots metal distance is the longest by about 0.1 Å. In $[\text{Fe}^{\text{II}}_2(\text{H}_2\text{SIM}^3)(\mu\text{-OAc})_2]$ the Fe(1) ion is surrounded by the bridging phenolate, two bridging acetate co-ligands, a tertiary amine, only one pyridine and one terminal phenolate residue. The distance between the Fe^{II} center and the terminal phenolate, Fe(1)-O(1A) (2.007(4) Å/2.003(4) Å), is shorter than the Fe(1)-N(3) distances found in $[\text{Fe}^{\text{II}}_2(\text{H}_2\text{SIM}^1)(\mu\text{-OAc})_2]^+$ (2.159(5) Å) and $[\text{Fe}^{\text{II}}_2(\text{H}_2\text{L}^2)(\mu\text{-OAc})_2]^+$ (2.3638(15) Å), due to the higher electron density of the anionic coordinating ligand. As a result, the Fe(1) center is forced away from the Fe(2) center, explaining the elongated $\text{Fe}^{\text{II}}\cdots\text{Fe}^{\text{II}}$ separation. In $[\text{Fe}^{\text{II}}_2(\text{H}_2\text{SIM}^3)(\mu\text{-OAc})_2]$ the impact of the sodium ion between the Fe(1) ions of the monomer subunits should not be neglected. The sodium ion is surrounded by six oxygen atoms deriving from the terminal phenolate and both acetate co-ligands of both monomer subunits. This arrangement results in an asymmetrically chelating acetate co-ligand, while the bridging acetate is coordinated in a more symmetric fashion; more precisely, the Fe^{II}-O distances of the asymmetric acetate differ by 0.204 Å/0.143 Å and by 0.022 Å/0.023 Å for the symmetric acetate. However, this can also be attributed to the asymmetry of the complex, induced by the asymmetric ligand backbone, as both acetate co-ligands are also coordinated in an asymmetric fashion in $[\text{Fe}^{\text{II}}_2(\text{H}_2\text{SIM}^1)(\mu\text{-OAc})_2]^+$. Therefore, each iron center in $[\text{Fe}^{\text{II}}_2(\text{H}_2\text{SIM}^1)(\mu\text{-OAc})_2]^+$ develops a short and a long bond to the acetate oxygen atoms, although the differences in the bond lengths are not as pronounced as in $[\text{Fe}^{\text{II}}_2(\text{H}_2\text{SIM}^3)(\mu\text{-OAc})_2]$. In contrast, in $[\text{Fe}^{\text{II}}_2(\text{H}_2\text{L}^2)(\mu\text{-OAc})_2]^+$ the two bridging acetate co-ligands are bound in a symmetric manner with differences in the Fe^{II}-O distances of the same acetate anion of 0.0254 Å and 0.0308 Å.

As mentioned above, a hydrogen bond network was present in the structures of $[\text{Fe}^{\text{II}}_2(\text{H}_2\text{SIM}^1)(\mu\text{-OAc})_2]^+$, $[\text{Fe}^{\text{II}}_2(\text{H}_2\text{L}^2)(\mu\text{-OAc})_2]^+$, and $[\text{Fe}^{\text{II}}_2(\text{H}_2\text{SIM}^3)(\mu\text{-OAc})_2]$ and the presence of this network is proposed based on (i) the short distances between the amido nitrogen and acetate oxygen atoms, listed in Table 12, and (ii) the orientation of the pivaloyl-amide substituents with respect to the acetate co-ligands and the pyridine rings.

Table 12: Selected distance (Å) for $[\text{Fe}^{\text{II}}_2(\text{H}_2\text{SIM}^1)(\mu\text{-OAc})_2]^+$, $[\text{Fe}^{\text{II}}_2(\text{H}_2\text{L}^2)(\mu\text{-OAc})_2]^+$, and $[\text{Fe}^{\text{II}}_2(\text{H}_2\text{SIM}^3)(\mu\text{-OAc})_2]$ corresponding to H-bond formation.

	$[\text{Fe}^{\text{II}}_2(\text{H}_2\text{SIM}^1)(\mu\text{-OAc})_2]^+$	$[\text{Fe}^{\text{II}}_2(\text{H}_2\text{L}^2)(\mu\text{-OAc})_2]^+$	$[\text{Fe}^{\text{II}}_2(\text{H}_2\text{SIM}^3)(\mu\text{-OAc})_2]$
N(7)-O(2A)	-	3.032(2)	
N(7)-O(3B)	3.057	-	3.124/3.076
N(8)-O(3B)	2.969	3.006(2)	2.936/2.997

The formation of hydrogen bonds with the acetate oxygen atoms appears to direct the position of the pivaloyl-amide groups. This results in enlarged angles between the pyridine planes and the plane containing the amide group (N-C-O) in some cases. This angle was found to be 12.09° and 30.14° for $[\text{Fe}^{\text{II}}_2(\text{H}_2\text{SIM}^1)(\mu\text{-OAc})_2]^+$, 18.51° and 30.72° for $[\text{Fe}^{\text{II}}_2(\text{H}_2\text{L}^2)(\mu\text{-OAc})_2]^+$ and 30.38°/34.58° and 38.10°/35.12° for $[\text{Fe}^{\text{II}}_2(\text{H}_2\text{SIM}^1)(\mu\text{-OAc})_2]$, but differs from 0.86° to 23.02° in uncoordinated pivaloyl-amide substituted pyridines in the mononuclear structures discussed in Chapter 3.

Solid State Structure under Aerobic Conditions

Treatment of H_3SIM^1 , dissolved in methanol, with two equivalents of iron(II) acetate and one equivalent of sodium hexafluorophosphate under an inert atmosphere for 12 hours resulted in a yellow solution. Following diffusion of diethylether, green crystals of the complex $[\text{Fe}^{\text{II}}_2(\text{H}_2\text{SIM}^1)(\mu\text{-OAc})_2]\text{PF}_6$ formed, as discussed above. When the yellow solution was exposed to air the color turned purple immediately. Diffusion of diethylether into this purple solution yielded black crystals of $[\text{Fe}^{\text{III}}\text{Na}(\text{H}_2\text{SIM}^1)(\mu\text{-OAc})_2]\text{PF}_6$, suitable for X-ray diffraction data collection. Crystallographic data obtained are displayed in Table 36 (see Appendix).

The structure was solved including the cationic complex $[\text{Fe}^{\text{III}}\text{Na}(\text{H}_2\text{SIM}^1)(\mu\text{-OAc})_2]^+$ and a hexafluorophosphate counterion in the crystal cell. The structure is depicted in Figure 43, and selected distances and valence angles are summarized in Table 13. The complex cation contains the deprotonated phenolate backbone, an Fe^{III} ion in the amide-free binding site, a Na^+ ion in the amidated binding site and two bridging acetate co-ligands. The two metal ions are bridged threefold, comparable to $[\text{Fe}^{\text{II}}_2(\text{H}_2\text{SIM}^1)(\mu\text{-OAc})_2]^+$. Repetition of the experiment showed that the synthesis of $[\text{Fe}^{\text{III}}\text{Na}(\text{H}_2\text{SIM}^1)(\mu\text{-OAc})_2]^+$ is reproducible and proved the unusual coordination of a Na^+ ion by the phenolate-based ligand H_3SIM^1 .

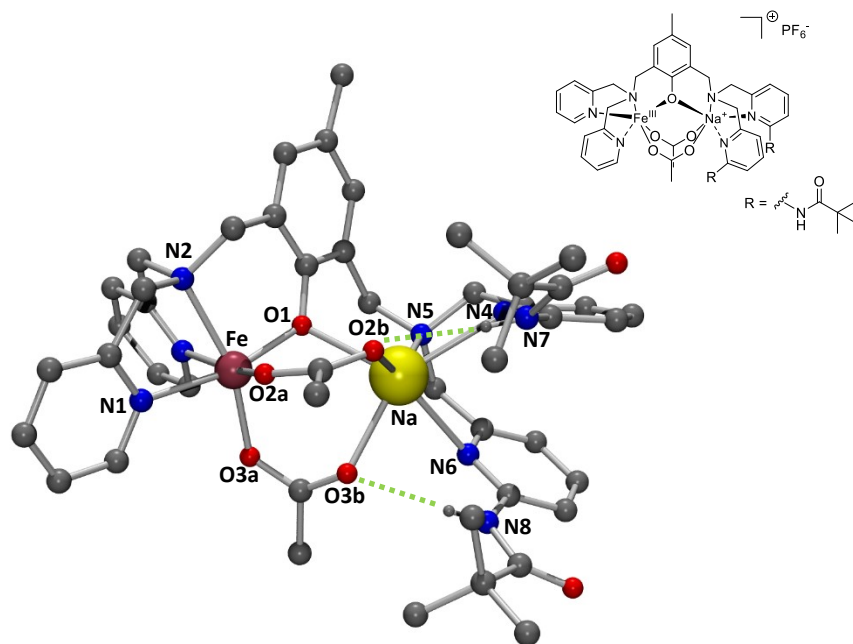


Figure 43: Structure of $[\text{Fe}^{\text{III}}\text{Na}(\text{H}_2\text{SIM}^1)(\mu\text{-OAc})_2]^+$ showing hydrogen bonding (green dotted lines; counter ions and hydrogen atoms, not involved in hydrogen bonding, have been omitted for clarity; crystallographic data and ORTEP plots with 50% probability level of thermal ellipsoids appear in the Appendix, Table 36 and Figure 76).

Table 13: Selected bond lengths (Å) and angles (°) for $[\text{Fe}^{\text{III}}\text{Na}(\text{H}_2\text{SIM}^1)(\mu\text{-OAc})_2]\text{PF}_6$ and $[\text{Fe}^{\text{II}}_2(\text{H}_2\text{SIM}^1)(\mu\text{-OAc})_2]\text{PF}_6$.

	$[\text{Fe}^{\text{III}}\text{Na}(\text{H}_2\text{SIM}^1)(\mu\text{-OAc})_2]^+$	$[\text{Fe}^{\text{II}}_2(\text{H}_2\text{SIM}^1)(\mu\text{-OAc})_2]^+$
Fe...M ^a	3.4802(6)	3.430
Fe-O(1) ^b	1.8906(11)	2.039(4)
Fe-O(2A) ^b	1.9620(11)	2.024(4)
Fe-O(2B) ^b	1.9556(11)	2.185(4)
Fe-N(1) ^b	2.1702(13)	2.167(5)
Fe-N(2) ^b	2.2130(13)	2.270(5)
Fe-N(3) ^b	2.1767(13)	2.159(5)
M-O(1) ^a	2.3710(12)	2.040(4)
M-O(3A) ^a	2.3578(13)	2.204(4)
M-O(3B) ^a	2.3575(13)	2.079(4)
M-N(4) ^a	2.5819(14)	2.290(6)
M-N(5) ^a	2.4845(14)	2.188(6)
M-N(6) ^a	2.5862(15)	2.311(5)
Fe-O(1)-M ^{a, b}	108.98(5)	114.45(18)
O(1)-Fe-N(1) ^b	87.54(5)	91.16(18)
O(1)-Fe-N(2) ^b	91.54(5)	86.17(17)
O(1)-Fe-N(3) ^b	166.43(5)	156.49(19)
O(1)-Fe-O(2A) ^b	98.85(5)	104.69(17)
O(1)-Fe-O(2B) ^b	101.88(5)	87.79(17)
O(1)-M-N(4) ^a	121.84(5)	87.09(18)
O(1)-M-N(5) ^a	79.69(4)	87.69(18)
O(1)-M-N(6) ^a	133.73(5)	162.03(18)
O(1)-M-O(3A) ^a	85.18(4)	93.65(16)
O(1)-M-O(3B) ^a	91.86(4)	103.30(16)

^a M is Na in $[\text{Fe}^{\text{III}}\text{Na}(\text{H}_2\text{SIM}^1)(\mu\text{-OAc})_2]^+$ and Fe(2) in $[\text{Fe}^{\text{II}}_2(\text{H}_2\text{SIM}^1)(\mu\text{-OAc})_2]^+$.

^b Fe is called Fe(1) in $[\text{Fe}^{\text{II}}_2(\text{H}_2\text{SIM}^1)(\mu\text{-OAc})_2]^+$.

The Fe^{III} center in [Fe^{III}Na(H₂SIM¹)(μ-OAc)₂]⁺ is coordinated in a similar manner to the Fe^{II} centers in [Fe^{II}₂(H₂SIM¹)(μ-OAc)₂]⁺, forming a distorted octahedral coordination geometry with two pyridines, a tertiary amine, the bridging phenolate linker, and two bridging acetate co-ligands. The distances of the Fe center to the pyridine nitrogen atoms in [Fe^{III}Na(H₂SIM¹)(μ-OAc)₂]⁺ are slightly elongated compared to those in [Fe^{II}₂(H₂SIM¹)(μ-OAc)₂]⁺, while the coordination bond between the Fe ion and the amine nitrogen is slightly shortened by 0.057 Å. The oxidation of the Fe^{II} center to Fe^{III} by exposure to air is manifested in the significant differences of the Fe^{II}-O and Fe^{III}-O distances. In [Fe^{III}Na(H₂SIM¹)(μ-OAc)₂]⁺ the Fe^{III}-O bonds are all shorter than the Fe^{II}-O bonds in [Fe^{II}₂(H₂SIM¹)(μ-OAc)₂]⁺, as expected due to the higher Lewis acidity of Fe^{III} compared to Fe^{II}. The differences in the Fe-O bonds are comparable to those in the hexaaqua ions [Fe^{II}(H₂O)₆]²⁺ and [Fe^{III}(H₂O)₆]³⁺, where Fe^{II}-OH₂ is 2.13 Å and Fe^{III}-OH₂ is 2.00 Å.¹⁶⁶ A similar observation was found for the complexes {Na[Fe^{III}(H₂SIM³)₂(μ-OAc)(μ-OH₂)](BF₄)₂ and {Na[Fe^{II}₂(H₂SIM³)(μ-OAc)₂]₂}⁺ as the Fe^{III} complex exhibits an average Fe^{III}-O_{Ph} distance of 1.957 Å and this value is 2.103 Å for the Fe^{II} complex. Furthermore, the average Fe^{III}-O bond length of [Fe^{III}Na(H₂SIM¹)(μ-OAc)₂]⁺ (1.9361 Å) is comparable to that found for the Fe^{III} center in [Fe^{III}Fe^{II}(L¹)(μ-OPr)₂]⁺ with a value of 1.96 Å, while the average of the Fe^{II}-O bond lengths was 2.09 Å, close to that found for [Fe^{II}₂(H₂SIM¹)(μ-OAc)₂]⁺ (2.083 Å and 2.108 Å).¹³⁹ However, it should be mentioned that both acetate co-ligands are bound in an asymmetric fashion in [Fe^{II}₂(H₂SIM¹)(μ-OAc)₂]⁺ and [Fe^{III}Na(H₂SIM¹)(μ-OAc)₂]⁺, but in the Fe^{III}Na complex both form a short bond to the Fe^{III} ion and a longer bond to the Na⁺ ion. This different arrangement of the bridging acetate co-ligands in the complexes also influences the average of the Fe^{II}-O and Fe^{III}-O distances.

The sodium ion in [Fe^{III}Na(H₂SIM¹)(μ-OAc)₂]⁺ is surrounded by the same primary coordination sphere as the Fe^{III} center, but in a trigonal prismatic geometry. The distances of the coordinating atoms to the Na⁺ ion are without exceptions longer compared to the corresponding distances in [Fe^{II}₂(H₂SIM¹)(μ-OAc)₂]⁺ by at least 0.15 Å, due to the decreased charge and the larger ionic radius of the metal center. Consequently, the separation between the two coordination centers in [Fe^{III}Na(H₂SIM¹)(μ-OAc)₂]⁺ is increased (3.4802 Å vs. 3.430 Å in [Fe^{II}₂(H₂SIM¹)(μ-OAc)₂]⁺).

The two oxygen atoms coordinating the Na⁺ ion in the amidated binding site are part of a hydrogen bond formed by the pivaloyl-amide substituents. Such a hydrogen bonding network is also visible in the previously discussed complexes containing pivaloyl-amide residues. Table 14 compares the corresponding N-O distances of the different complexes derived from ligand H₃SIM¹.

Table 14: Selected distances (Å) for $[\text{Fe}^{\text{III}}\text{Na}(\text{H}_2\text{SIM}^1)(\mu\text{-OAc})_2]^+$, $[\text{Fe}^{\text{II}}_2(\text{H}_2\text{SIM}^1)(\mu\text{-OAc})_2]^+$, and $[\text{Zn}^{\text{II}}_2(\text{H}_2\text{SIM}^1)(\mu\text{-OAc})_2]^+$, corresponding to H-bond formation.

	$[\text{Fe}^{\text{III}}\text{Na}(\text{H}_2\text{SIM}^1)(\mu\text{-OAc})_2]^+$	$[\text{Fe}^{\text{II}}_2(\text{H}_2\text{SIM}^1)(\mu\text{-OAc})_2]^+$	$[\text{Zn}^{\text{II}}_2(\text{H}_2\text{SIM}^1)(\mu\text{-OAc})(\text{OH})]^+$
N(7)-O(3A)	3.153	-	-
N(7)-O(3B)	-	3.057	-
N(8)-O(3B)	3.087	2.969	-
N(7)-O(6)	-	-	2.809(4)
N(8)-O(6)	-	-	2.874(4)

However, in contrast to the complexes $[\text{Zn}^{\text{II}}_2(\text{H}_2\text{SIM}^1)(\mu\text{-OAc})(\text{OH})]^+$ and $[\text{Fe}^{\text{II}}_2(\text{H}_2\text{SIM}^1)(\mu\text{-OAc})_2]^+$, the two pivaloyl-amide nitrogen atoms, N(7) and N(8), in $[\text{Fe}^{\text{III}}\text{Na}(\text{H}_2\text{SIM}^1)(\mu\text{-OAc})_2]^+$ do not point in the direction of the same oxygen atom, but to two different oxygen atoms, each part of an acetate co-ligand.

The structure of $[\text{Fe}^{\text{III}}\text{Na}(\text{H}_2\text{SIM}^1)(\mu\text{-OAc})_2]\text{PF}_6$ suggests that the crystallization of the $\text{Fe}^{\text{III}}\text{Na}$ form of the complex is more likely than of the Fe^{II}_2 complex of the respective ligand H_3SIM^1 . It seems that, when the two Fe^{II} ions of $[\text{Fe}^{\text{II}}_2(\text{H}_2\text{SIM}^1)(\mu\text{-OAc})_2]^+$ are oxidized by exposure to air, the resulting diiron(III) complex is unstable. Thus, only the iron(III) center in the less sterically demanding binding site remains bound, while in the more sterically hindered binding site a metal exchange from Fe^{III} to Na^+ takes place prior crystallization.

Elemental Analysis

The unusual presence of a Na^+ ion in a phenolate-based complex was also confirmed by elemental analysis. Table 15 compares the experimentally obtained values for two separately prepared samples of $[\text{Fe}^{\text{III}}\text{Na}(\text{H}_2\text{SIM}^1)(\mu\text{-OAc})_2]\text{PF}_6$ with the expected values.

Table 15: Elemental analytical results obtained with two samples of $[\text{Fe}^{\text{III}}\text{Na}(\text{H}_2\text{SIM}^1)(\mu\text{-OAc})_2]\text{PF}_6$ and the corresponding calculated values.

	C [%]	H [%]	N [%]	F [%]	Fe [%]	Na [%]
sample 1	51.11	4.62	9.96	10.17	5.84	2.27
sample 2	51.88	5.58	10.20	n.a.	n.a.	n.a.
<i>calc.</i> for $[\text{Fe}^{\text{III}}\text{Na}(\text{H}_2\text{SIM}^1)(\mu\text{-OAc})_2]\text{PF}_6$	52.77	5.37	10.47	10.66	5.22	2.15

The calculation of the molecular formula derived from the analytical data is $\text{C}_{48}\text{H}_{49}\text{N}_8\text{F}_6\text{FeNa}$, which compares well with the required molecular formula $\text{C}_{47}\text{H}_{57}\text{N}_8\text{O}_7\text{F}_6\text{FeNa}$ for $[\text{Fe}^{\text{III}}\text{Na}(\text{H}_2\text{SIM}^1)(\mu\text{-OAc})_2]\text{PF}_6$ and proves the ratio of $\text{Fe}:\text{Na} = 1:1$.

Solid State Susceptibility Measurements

In order to understand the magnetic properties of $[\text{Fe}^{\text{II}}_2(\text{H}_2\text{SIM}^1)(\mu\text{-OAc})_2]\text{PF}_6$ and $[\text{Fe}^{\text{III}}\text{Na}(\text{H}_2\text{SIM}^1)(\mu\text{-OAc})_2]\text{PF}_6$, variable temperature dc SQUID magnetic susceptibility studies were performed with ground crystals in the temperature range from 2 - 300 K.

The $\chi_{\text{M}}T$ vs. T curve obtained with the powdered sample of $[\text{Fe}^{\text{II}}_2(\text{H}_2\text{SIM}^1)(\mu\text{-OAc})_2]\text{PF}_6$ is reproduced in Figure 44. At 300 K, the $\chi_{\text{M}}T$ value of $[\text{Fe}^{\text{II}}_2(\text{H}_2\text{SIM}^1)(\mu\text{-OAc})_2]\text{PF}_6$ is $6.47 \text{ cm}^3\text{mol}^{-1}\text{K}$ ($\mu_{\text{eff}} = 7.19 \text{ B.M.}$). This value is slightly above $6.00 \text{ cm}^3\text{mol}^{-1}\text{K}$ ($\mu_{\text{eff}} = 6.92 \text{ B.M.}$), the value expected for two non-interacting high-spin Fe^{II} ions. The continuous decrease of the $\chi_{\text{M}}T$ product upon decrease in temperature suggests an antiferromagnetic interaction between the two Fe^{II} centers in $[\text{Fe}^{\text{II}}_2(\text{H}_2\text{SIM}^1)(\mu\text{-OAc})_2]\text{PF}_6$. This conclusion is confirmed by the fact that $\chi_{\text{M}}T$ reaches $0.35 \text{ cm}^3\text{mol}^{-1}\text{K}$ ($\mu_{\text{eff}} = 1.35 \text{ B.M.}$) below 2 K, indicating an $S = 0$ ground state for $[\text{Fe}^{\text{II}}_2(\text{H}_2\text{SIM}^1)(\mu\text{-OAc})_2]\text{PF}_6$. An impurity of paramagnetic monoiron(III) complex is suggested accountable for the higher experimental $\chi_{\text{M}}T$ values compared to the expected ones.

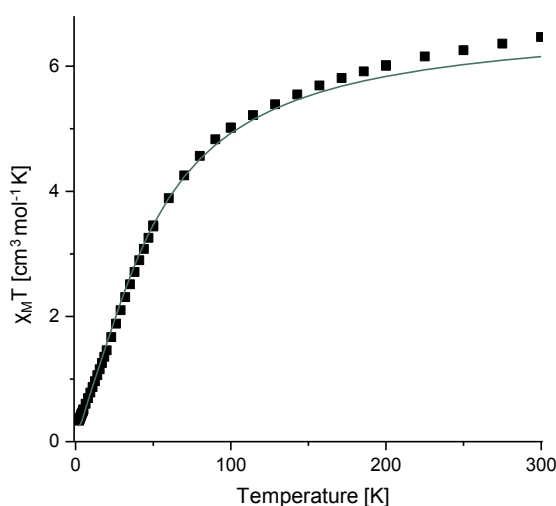


Figure 44: Temperature dependence of $\chi_{\text{M}}T$ for $[\text{Fe}^{\text{II}}_2(\text{H}_2\text{SIM}^1)(\mu\text{-OAc})_2]\text{PF}_6$, recorded in a magnetic field of 1000 Oe and the respective fit curve (green line).

The data were fitted according to the simplified van Vleck formula for two interacting $S = 2$ spins, including paramagnetic impurities (*imp*) (Equation 16), derived from the Heisenberg Hamiltonian formulated in Equation 15.²³⁶

$$\text{Equation 15} \quad H = -2JS_1S_2$$

$$\text{Equation 16} \quad \chi_{\text{M}} = \frac{N_A g^2 \mu_{\text{B}}^2}{3kT} S(S+1) + \chi_{\text{imp}}$$

The best fit was obtained with $J = -5.05 \text{ cm}^{-1}$ and a fixed g factor at $g = 2.15$, which is in agreement with the antiferromagnetism. 5.8% monoiron(III) complex as paramagnetic impurity ($S = 5/2$) was determined. The weak antiferromagnetism is similar to the observed magnetism for native PAPs, with J values between -5 cm^{-1} and -11 cm^{-1} .

Studying Fe^{II}₂ complexes of HL¹, Hendrich *et al.* found that replacing two bridging carboxylate co-ligands as in [Fe^{II}₂(L¹)(μ-OPr)₂]⁺ with bridging phosphate co-ligands, as in [Fe^{II}₂(L¹)(μ-O₂P(OPh)₂)₂]⁺, results in the change of the magnetic behavior from ferromagnetic to antiferromagnetic.²³⁷ This was attributed to the change in the Fe^{II}-O_{Ph}-Fe^{II} angle (108.93(6)° for [Fe^{II}₂(L¹)(μ-OPr)₂]⁺ and 122.7(2)° for [Fe^{II}₂(L¹)(μ-O₂P(OPh)₂)₂]⁺) and the simultaneous modification of the metal-metal interaction.²³⁷ The Fe^{II}-O_{Ph}-Fe^{II} angle in [Fe^{II}₂(H₂SIM¹)(μ-OAc)₂]PF₆ is 114.45(18)° and falls between those two values. Moreover, the magnitude of the antiferromagnetic exchange constant for [Fe^{II}₂(H₂SIM¹)(μ-OAc)₂]PF₆ is in the range of those reported for other oxygen-bridged diiron(II) complexes (Table 16).

Table 16: Selected structural parameters for diiron(II) complexes proposed to correlate with the magnetic exchange constant J.

complex	∠(Fe ^{II} -O-Fe ^{II}) [°]	d(Fe ^{II} -μ-O) [Å]	∅(d(Fe ^{II} -μ-O)) [Å]	J [cm ⁻¹]
[Fe ^{II} (L ⁴⁰) ₂ (O ₂ CH) ₃ (O ₂ CH)] ^a ²³⁸	113.0(1)	2.172(2) 2.113(2)	2.143	-0.16
[Fe ^{II} ₂ (H ₂ SIM ¹)(μ-OAc) ₂]PF ₆	114.5	2.039(4) 2.024(4)	2.032	-5.0
[Fe ^{II} ₂ (L ⁴¹)(μ-OBz)](BF ₄) ₂ ²³⁹	125.7(6)	2.028(13) 1.968(10)	1.998	-5.5
[Fe ^{II} ₂ (L ⁴²)(μ-OBz)(H ₂ O)]BF ₄ ²⁴⁰	131.2	2.060(2) 1.984(2)	2.022	-8.6
[Fe ^{II} ₂ (L ⁴³)(μ-OBz)](BF ₄) ₂ ²⁴¹	124.0	1.960(6) 1.973(7)	1.967	-10.5

^a the two Fe^{II} centers are formaldehyde-bridged.

However, comparing the antiferromagnetic exchange constant J in relation with the Fe^{II}-O-Fe^{II} angle, there is not a direct correlation detectable (Pearson's correlation coefficient: -0.75), but the critical value of the Fe^{II}-O-Fe^{II} angle regarding the change from ferromagnetic to antiferromagnetic interaction seems to be between 108.9° and 113.2°. ^{237, 238} A potential influence of the Fe^{II}-(μ-O) distance was also suggested to be accountable for the magnetic behavior of diiron(II) complexes and it appears that this parameter shows a correlation with the antiferromagnetic exchange interaction (Pearson's correlation coefficient: 0.90). ^{181, 237} Thus, the weakened metal-metal interaction manifested by the longer Fe^{II}-(μ-O) bond leads to the decrease or elimination of antiferromagnetic coupling between the two Fe^{II} centers. However, it should be mentioned that due to the limited number of examples of alkoxido/phenoxido-bridged diiron(II) complexes this proposal should be considered as speculative.

For the monoiron(III) complex [Fe^{III}Na(H₂SIM¹)(μ-OAc)₂]PF₆ χ_MT = 4.29 cm³mol⁻¹K (μ_{eff} = 5.84 B.M.) at 300 K was obtained. This value is close to the expected value for five unpaired electrons of χ_MT = 4.39 cm³mol⁻¹K (μ_{eff} = 5.92 B.M.).

NMR Studies

Susceptibility Measurements with the Evans Method under Anaerobic Conditions

The magnetic properties of $[\text{Fe}^{\text{II}}_2(\text{H}_2\text{SIM}^1)(\mu\text{-OAc})_2]^+$ and $[\text{Fe}^{\text{II}}_2(\text{H}_2\text{L}^2)(\mu\text{-OAc})_2]^+$ were also investigated in solution, applying the methodology described by Evans.²⁴² In this method the frequency shift in the NMR spectrum between two solutions, the pure solvent and a known concentration of the paramagnetic material in the same solvent, is measured. The frequency shift is proportional to the paramagnetic susceptibility of the compound (Equation 17).

$$\text{Equation 17} \quad \chi_{\text{para,subst}} = \frac{3}{4\pi c} \left(\frac{\Delta\nu}{\nu} \right) + \chi_{\text{dia,solv}} + \chi_{\text{dia,subst}}$$

The effective magnetic moment μ_{eff} is calculated with Equation 18.

$$\text{Equation 18} \quad \mu_{\text{eff}} = 2.828 \sqrt{\chi_{\text{para,subst}} T}$$

The magnetic moments of the complexes were evaluated with Equations 17 and 18, after taking appropriate corrections for diamagnetism of the solvent and the complex into account. In solution, the complexes exhibit effective magnetic moments of 6.10 B.M. for $[\text{Fe}^{\text{II}}_2(\text{H}_2\text{SIM}^1)(\mu\text{-OAc})_2]^+$ and 5.35 B.M. for $[\text{Fe}^{\text{II}}_2(\text{H}_2\text{L}^2)(\mu\text{-OAc})_2]^+$. The experimentally derived values for these complexes were lower than the calculated value for two non-interacting high-spin Fe^{II} centers ($\mu_{\text{eff}} = 6.93$ B.M.) indicate the presence of exchange coupling between the two metal centers.

Susceptibility Measurements with the Evans Method under Aerobic Conditions

The magnetic susceptibility of $[\text{Fe}^{\text{II}}_2(\text{H}_2\text{SIM}^1)(\mu\text{-OAc})_2]^+$ dissolved in deuterated acetonitrile was found to reduce from $\mu_{\text{eff}} = 6.10$ B.M. to $\mu_{\text{eff}} = 4.55$ B.M. within the first hour after the solution was exposed to air, and subsequently to $\mu_{\text{eff}} = 3.82$ B.M. within 24 hours. The decrease of μ_{eff} can be explained by the formation of relatively strongly coupled complexes, but the composition is not entirely clear. It has to be mentioned that $\mu_{\text{eff}} = 1.73$ B.M. for a strongly coupled (hs) Fe^{III} -(hs) Fe^{II} system and $\mu_{\text{eff}} = 0$ for a strongly coupled (hs) Fe^{III} -(hs) Fe^{III} system is only expected at low temperature. On the basis of published work on similar systems, only moderate coupling through the phenoxide bridge is expected.^{114, 125, 230} Interestingly, slightly increased μ_{eff} values were observed when the solutions were measured after several weeks again ($\mu_{\text{eff}} = 4.85$ B.M.). This might be the result of a slow decomposition of initially formed Fe^{III}_2 species, *i.e.* formation of a monoiron(III) complex and ligand-free Fe^{III} . This is in agreement with the observed X-ray structures under aerobic and anaerobic conditions.

^1H NMR Spectroscopy under Anaerobic Conditions

^1H NMR spectroscopy was used to investigate the symmetry of the diiron(II) complexes in solution. The paramagnetic ^1H NMR spectra of $[\text{Fe}^{\text{II}}_2(\text{H}_2\text{SIM}^1)(\mu\text{-OAc})_2]\text{PF}_6$ and $[\text{Fe}^{\text{II}}_2(\text{H}_2\text{L}^2)(\mu\text{-OAc})_2]\text{PF}_6$, dissolved in deuterated acetonitrile, were recorded (Figure 45). The ^1H NMR spectra of the diiron(II) complexes display well-resolved and relatively narrow resonances, consistent with the fast electronic relaxation of the high-spin Fe^{II} centers and their energetically low excited levels.²⁴³ The chemical shifts of the resonances extend over 230 ppm, from -30 ppm to 200 ppm. Overall, the spectrum is highly similar to that of the $\text{Fe}^{\text{II}}\text{Mn}^{\text{II}}$ complex of HL^1 and HL^4 .^{244, 245}

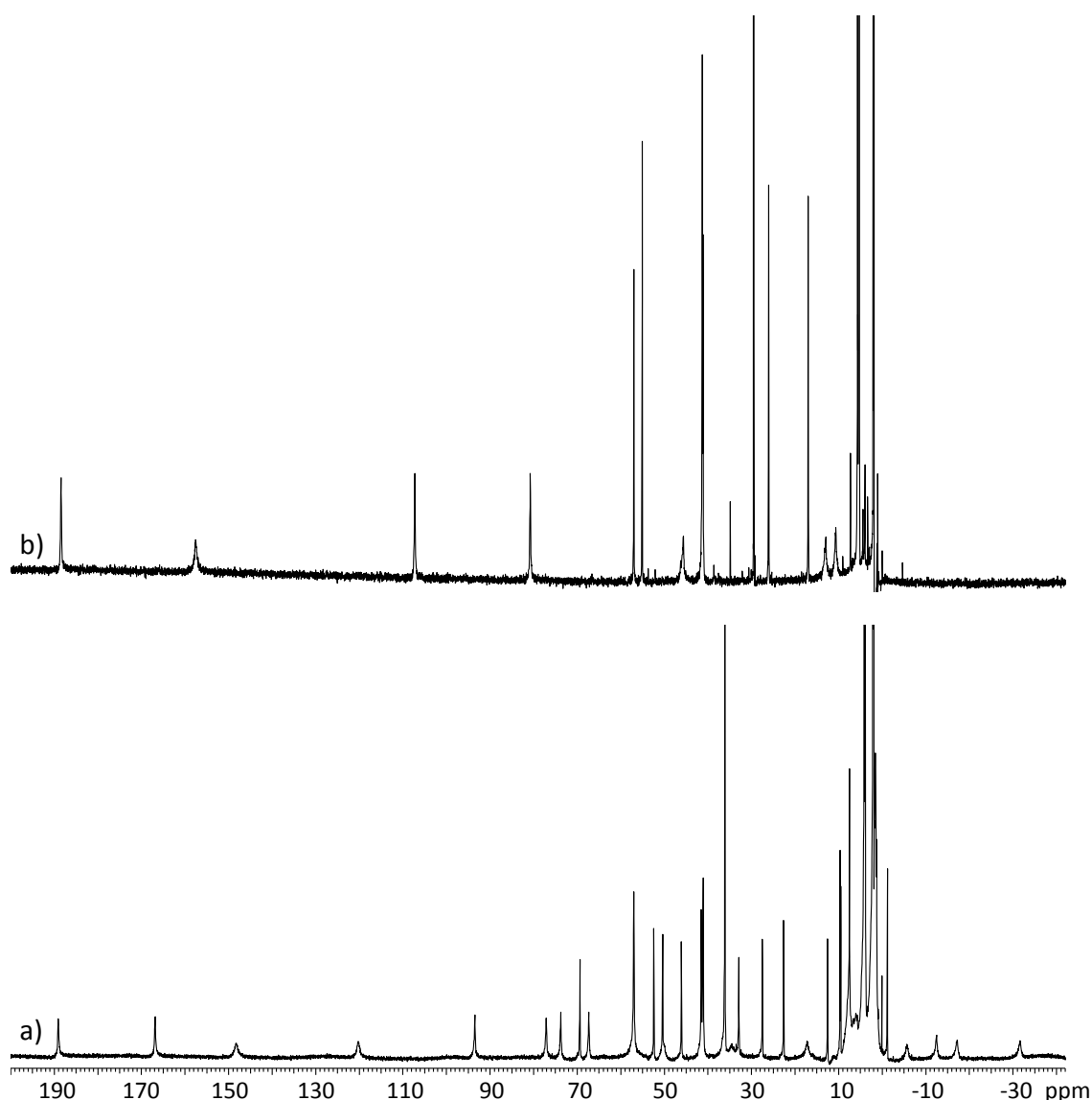


Figure 45: ^1H NMR spectrum of a) $[\text{Fe}^{\text{II}}_2(\text{H}_2\text{SIM}^1)(\mu\text{-OAc})_2]\text{PF}_6$ and b) $[\text{Fe}^{\text{II}}_2(\text{H}_2\text{L}^2)(\mu\text{-OAc})_2]\text{PF}_6$ in CD_3CN .

Unfortunately, connectivity in the complexes could not be resolved sufficiently with COSY experiments to assign the protons. However, in the spectrum recorded with $[\text{Fe}^{\text{II}}_2(\text{H}_2\text{L}^2)(\mu\text{-OAc})_2]^+$, 13 resonances were detected, while in the spectrum of

$[\text{Fe}^{\text{II}}_2(\text{H}_2\text{SIM}^1)(\mu\text{-OAc})_2]^+$, 26 resonances were observed, *i.e.* one resonance for each proton. In the case of $[\text{Fe}^{\text{II}}_2(\text{H}_2\text{L}^2)(\mu\text{-OAc})_2]^+$, due to a rotation axis two protons resonate at similar fields and, therefore, a single resonance for two protons was detected. Moreover, the spectrum of $[\text{Fe}^{\text{II}}_2(\text{H}_2\text{SIM}^1)(\mu\text{-OAc})_2]^+$ exhibits two equally intense sharp resonances at 3.86 ppm and 4.08 ppm, which are assigned to the two *tert*-butyl groups of the pivaloyl-amide residues due to their integration for nine protons. Interestingly, the spectrum of $[\text{Fe}^{\text{II}}_2(\text{H}_2\text{L}^2)(\mu\text{-OAc})_2]^+$ shows a signal integrating for 18 protons at 5.40 ppm. The comparison of the spectra obtained of $[\text{Fe}^{\text{II}}_2(\text{H}_2\text{SIM}^1)(\mu\text{-OAc})_2]\text{PF}_6$, bearing a symmetric ligand backbone, and $[\text{Fe}^{\text{II}}_2(\text{H}_2\text{SIM}^1)(\mu\text{-OAc})_2]\text{PF}_6$, bearing an asymmetric ligand backbone, suggest that the symmetry provided by the ligands is still present in the respective diiron(II) complexes.

^1H NMR Spectroscopy under Aerobic Conditions

The green solution of $[\text{Fe}^{\text{II}}_2(\text{H}_2\text{SIM}^1)(\mu\text{-OAc})_2]^+$, dissolved in deuterated acetonitrile, turned rapidly purple when exposed to air. The ^1H NMR spectrum obtained with this purple solution exhibited only one sharp downfield shifted resonance in the region between 20 ppm and 200 ppm, as opposed to the original spectrum of the complex measured under anaerobic conditions (Figure 46).

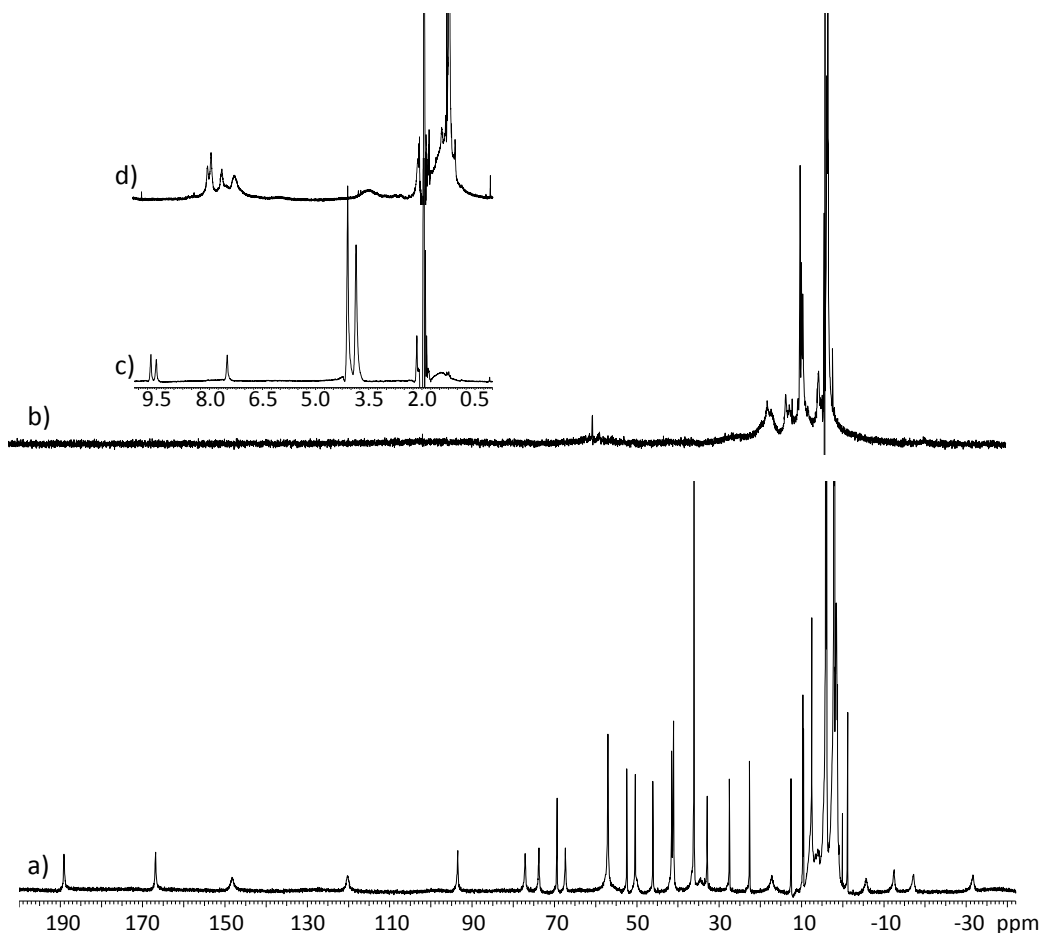


Figure 46: ^1H NMR spectra of $[\text{Fe}^{\text{II}}_2(\text{H}_2\text{SIM}^1)(\mu\text{-OAc})_2]\text{PF}_6$ in CD_3CN under a) and c) anaerobic conditions and b) and d) after exposure to air.

In $[\text{Fe}^{\text{II}}_2(\text{H}_2\text{SIM}^1)(\mu\text{-OAc})_2]^+$ the short electronic relaxation time of the Fe^{II} ion makes the overall system relax fast enough so that sharp NMR resonances are observed. After exposure to air, the antiferromagnetic interactions are not strong enough to quench the electronic spin at room temperature. Therefore, the Fe^{III} complex formed presents only very broad unresolved resonances. Interestingly, reaction with air results in four broad resonances in the region between 6 ppm and 8 ppm, while there was only one single resonance visible in the intact $[\text{Fe}^{\text{II}}_2(\text{H}_2\text{SIM}^1)(\mu\text{-OAc})_2]^+$ complex. This can be due to (i) one binding site being metal-free with non-coordinating pyridine residues, or (ii) some protons in the resulting diiron(III) complex are only slightly affected by the paramagnetic metal ions exhibiting resonances with chemical shifts similar to the metal-free ligand.

Mass Spectrometry

ESI⁺ mass spectrometric investigations of $[\text{Fe}^{\text{II}}_2(\text{H}_2\text{SIM}^1)(\mu\text{-OAc})_2]\text{PF}_6$ in dichloromethane resulted in a spectrum with a main peak at m/z 924.4 and two smaller peaks at m/z 889.2 and m/z 957.3 with isotopic patterns characteristic for diiron complexes (Figure 47). The signals are assigned to $[\text{Fe}^{\text{II}}_2\text{Na}(\text{HSIM}^1)(\text{CH}_3\text{O})_2]^+$, $[\text{Fe}^{\text{II}}_2(\text{HSIM}^1)(\text{CH}_3\text{OH})\text{F}]^+$ and the intact complex $[\text{Fe}^{\text{II}}_2(\text{H}_2\text{SIM}^1)(\text{OAc})_2]^+$, respectively. When the solution of $[\text{Fe}^{\text{II}}_2(\text{H}_2\text{SIM}^1)(\mu\text{-OAc})_2]\text{PF}_6$ in acetonitrile was exposed to air for about ten minutes prior to the measurement, one main signal was detected at m/z 782.3 consisting to the monoiron(III) complex $[\text{Fe}^{\text{III}}(\text{HSIM}^1)]^+$.

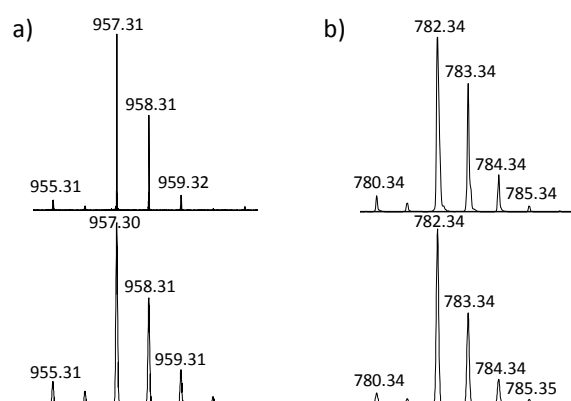


Figure 47: Characteristic isotopic pattern found in ESI⁺ mass spectra (experimental (top) and calculated (bottom)) of $[\text{Fe}^{\text{II}}_2(\text{H}_2\text{SIM}^1)(\mu\text{-OAc})_2]\text{PF}_6$ a) measured directly after solvation in dichloromethane ($[\text{Fe}^{\text{II}}_2(\text{H}_2\text{SIM}^1)(\text{OAc})_2]^+$) and b) in acetonitrile after exposure to air for 5 min ($[\text{Fe}^{\text{III}}(\text{HSIM}^1)]^+$).

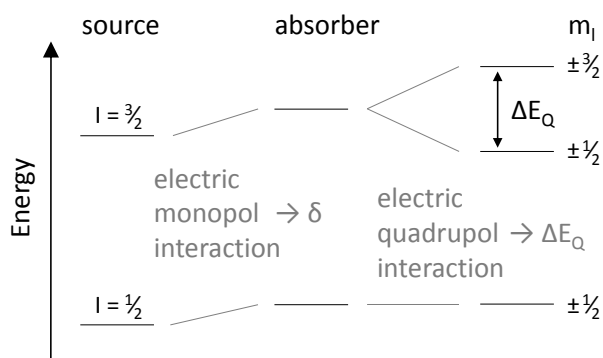
Unfortunately, the solubility of $[\text{Fe}^{\text{II}}_2(\text{H}_2\text{L}^2)(\mu\text{-OAc})_2]\text{PF}_6$ in dichloromethane was lower compared to $[\text{Fe}^{\text{II}}_2(\text{H}_2\text{SIM}^1)(\mu\text{-OAc})_2]\text{PF}_6$ and made the addition of methanol necessary, in order to obtain a spectrum. This resulted in a main signal at m/z 729.4, matching the protonated ligand $[\text{H}_4\text{L}^2]^+$ and a rather intense signal at m/z 782.3, matching the oxidation product $[\text{Fe}^{\text{III}}(\text{HL}^2)]^+$. Therefore, the mass spectrometric investigation of the Fe^{II}_2 complex in solution is hampered due to fast

oxidation. However, signals with the characteristic diiron isotopic pattern were detected at m/z 929.3, m/z 943.3, and m/z 957.3, and these are assigned to the diiron species $[\text{Fe}^{\text{II}}_2(\text{H}_2\text{L}^2)(\text{OAc})(\text{CH}_3\text{O})]^+$, $[\text{Fe}^{\text{II}}_2(\text{H}_2\text{L}^2)(\text{OAc})(\text{CH}_3\text{CH}_2\text{O})]^+$, and the intact complex $[\text{Fe}^{\text{II}}_2(\text{H}_2\text{L}^2)(\text{OAc})_2]^+$.

The ESI⁺ mass spectrometric investigations undertaken with the purple solid $[\text{Fe}^{\text{III}}\text{Na}(\text{H}_2\text{SIM}^1)(\mu\text{-OAc})_2]\text{PF}_6$, dissolved in methanol resulted in a spectrum with a main peak at m/z 872.4, assigned to $[\text{Fe}^{\text{III}}(\text{H}_2\text{SIM}^1)(\text{CH}_3\text{OH})(\text{OAc})]^+$. The softer ionization method conducted with MALDI experiments resulted in a spectrum with two main peaks at m/z 821.3 and m/z 839.3, which both show the pattern characteristic for an iron complex similar to the one depicted in Figure 47b). These signals match the species of $[\text{Fe}^{\text{III}}\text{Na}(\text{SIM}^1)(\text{H}_2\text{O})]^+$ and $[\text{Fe}^{\text{III}}\text{Na}(\text{SIM}^1)(\text{H}_2\text{O})_2]^+$.

Mössbauer Spectroscopy

⁵⁷Fe Mössbauer spectroscopy is a very sensitive technique, which has been very useful for ascertaining the oxidation and spin states of iron centers. This technique is based on the Mössbauer effect, consisting of recoil-free, resonant absorption and emission of gamma rays.²⁴⁶ Mössbauer experiments involve the determination of the energy difference between the ground state and the excited states by exposure of the sample to a beam of gamma radiation. The energy difference between the ground and the excited states depends on the interaction of the nucleus and electric (and magnetic) fields at the nucleus (Scheme 11).²⁴⁷ Thus, ⁵⁷Fe Mössbauer spectra reflect chemical information of the iron centers in the Mössbauer parameters, *i.e.* isomer shift and quadrupole splitting. The isomer shift results from the Coulomb interaction of the nuclear charge distribution and the s-electron charge cloud, penetrating the nucleus (electric monopole interaction) and depends, therefore, most strongly on the ionization of the iron center.²⁴⁶ The quadrupole splitting originates from the interaction between the electric quadrupole moment eQ of the nucleus itself and the Electron Field Gradient (EFG) at the nucleus (electric quadrupole interaction).²⁴⁶ The EFG arises from an aspherical distribution of electrons in the valence orbitals and/or aspherical charge distribution in the ligand sphere. Thus, the quadrupole splitting depends on the symmetry of the environment of the iron center.²⁴⁶



Scheme 11: Origin of the isomer shift δ (electric monopole interaction) and the quadrupole splitting ΔE_Q (electric quadrupole interaction) in ^{57}Fe Mössbauer spectra.^{246, 247}

Mössbauer Spectroscopy under Anaerobic Conditions

In order to investigate the coordination chemistry of the two Fe^{II} centers in $[\text{Fe}^{\text{II}}_2(\text{H}_2\text{SIM}^1)(\mu\text{-OAc})_2]\text{PF}_6$, a ^{57}Fe enriched sample was prepared and a ^{57}Fe Mössbauer spectrum was measured in frozen acetonitrile solution at 170 K (Figure 48a). The spectrum obtained shows a single quadrupole doublet, indicating similar electronic environments for both Fe^{II} centers. The parameters determined by fitting the spectrum, using the NORMOS Mössbauer Fitting Program²⁴⁸, $\delta = 1.13(1)$ mm/s and $\Delta E_Q = 2.66(1)$ mm/s ($\Gamma = 0.45(1)$ mm/s), are consistent with Fe^{II} in the high-spin configuration and in agreement with values reported for other dinuclear high-spin Fe^{II} complexes, *i.e.* $[\text{Fe}^{\text{II}}_2(\text{L}^{42})(\mu\text{-O}_2\text{CCF}_3)(\text{H}_2\text{O})_2](\text{BF}_4)_2$ ($\delta = 1.05$ mm/s and $\Delta E_Q = 2.69$ mm/s).²⁴⁰ The δ shift of $[\text{Fe}^{\text{II}}_2(\text{H}_2\text{SIM}^1)(\mu\text{-OAc})_2]\text{PF}_6$ to more positive values compared to $[\text{Fe}^{\text{II}}_2(\text{L}^{42})(\mu\text{-O}_2\text{CCF}_3)(\text{H}_2\text{O})_2](\text{BF}_4)_2$ is attributed to the increased electronegativity of the coordinating ligands in the former complex.

Mössbauer Spectroscopy under Aerobic Conditions

The Mössbauer spectrum of a sample of $[\text{Fe}^{\text{II}}_2(\text{H}_2\text{SIM}^1)(\mu\text{-OAc})_2]\text{PF}_6$, dissolved in acetonitrile and exposed to air for 24 hours, was collected at 170 K and showed a slightly asymmetric doublet (Figure 48b). The ^{57}Fe Mössbauer spectrum obtained after exposure to air for further 24 hours was essentially the same (Figure 48c). Least-squares fitting determined two doublets of equal intensity with the isomer shifts of $\delta(\text{I}) = 0.42(1)$ mm/s and $\delta(\text{II}) = 0.42(1)$ mm/s and the quadrupole splitting of $\Delta E_Q(\text{I}) = 0.77(2)$ mm/s ($\Gamma = 0.44(1)$ mm/s) and $\Delta E_Q(\text{II}) = 1.31$ mm/s ($\Gamma = 0.40(1)$ mm/s), respectively. The Mössbauer parameters are in agreement with two high-spin Fe^{III} ions in similar electronic environments and are comparable with those previously reported for phenolate-bridged diiron(III) complexes, *i.e.* $[\text{Fe}^{\text{III}}_2(\text{H}_2\text{L}^2)(\mu\text{-OH})]^{4+}$ ($\delta = 0.47$ mm/s, $\Delta E_Q = 0.84$ mm/s),¹¹⁴ $[\text{Fe}^{\text{III}}_2(\mu\text{-O})(\text{L}^{45})_2(\text{OH})(\text{H}_2\text{O})]\text{ClO}_4$ ($\delta = 0.45$ mm/s, $\Delta E_Q(\text{I}) = 1.63$ mm/s, $\Delta E_Q(\text{II}) = 1.11$ mm/s),²⁴⁹ and $[\text{Fe}^{\text{III}}_2(\text{L}^{46})_2(\mu\text{-OAc})]\text{ClO}_4$ ($\delta = 0.39$ mm/s, $\Delta E_Q = 0.93$ mm/s).¹⁰² The fitting with two quadrupole doublets is consistent with two different Fe^{III} centers and, therefore,

the formation of the complex $[\text{Fe}^{\text{III}}_2(\text{H}_2\text{SIM}^1)(\mu\text{-OAc})_2]^{3+}$. In contrast to $[\text{Fe}^{\text{II}}_2(\text{H}_2\text{SIM}^1)(\mu\text{-OAc})_2]\text{PF}_6$, the asymmetry of electron density distribution around the two Fe^{III} centers in $[\text{Fe}^{\text{III}}_2(\text{H}_2\text{SIM}^1)(\mu\text{-OAc})_2]^{3+}$ is larger and therefore large enough to afford two distinct quadrupole doublets.

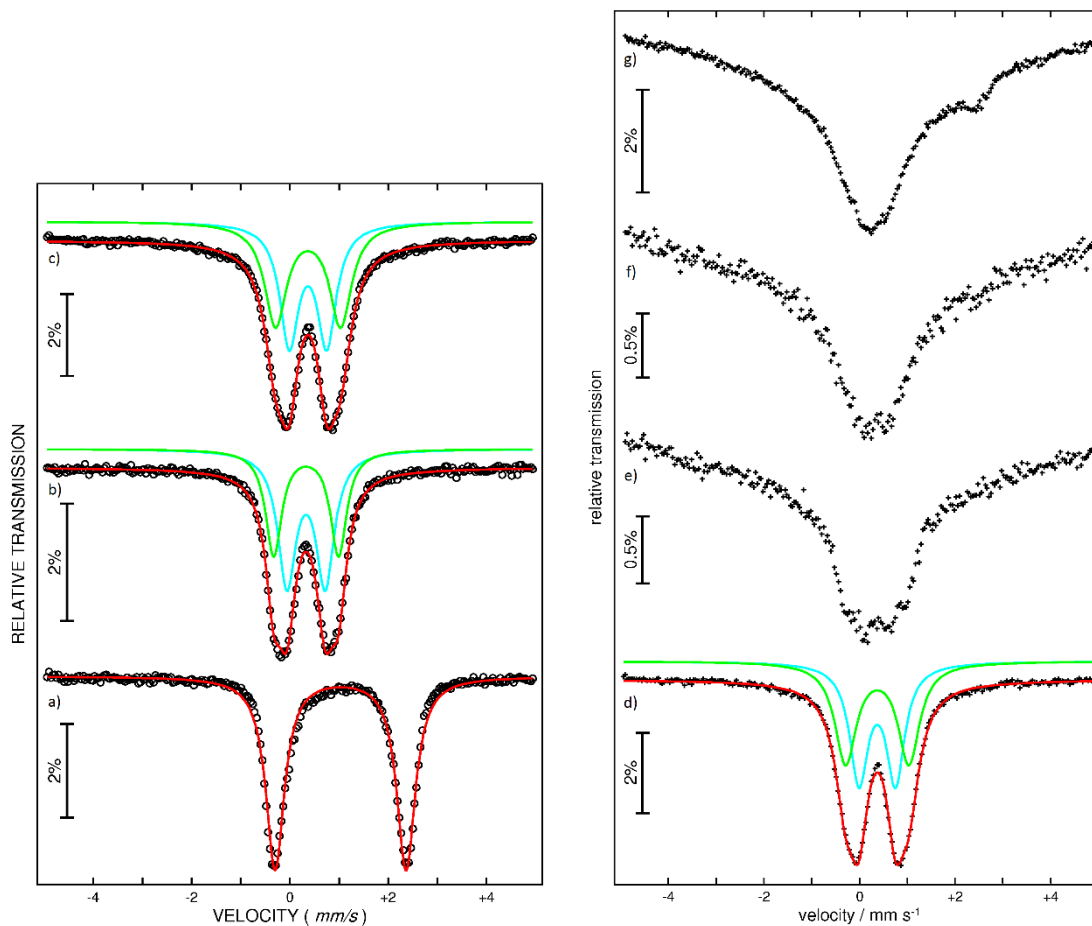


Figure 48: Comparison of the ^{57}Fe Mössbauer spectra obtained from frozen acetonitrile solution (except spectrum g)) of a) $[\text{Fe}^{\text{II}}_2(\text{H}_2\text{SIM}^1)(\mu\text{-OAc})_2]\text{PF}_6$, b) $[\text{Fe}^{\text{II}}_2(\text{H}_2\text{SIM}^1)(\mu\text{-OAc})_2]\text{PF}_6$ after exposure to air for 24 h c) $[\text{Fe}^{\text{II}}_2(\text{H}_2\text{SIM}^1)(\mu\text{-OAc})_2]\text{PF}_6$ after exposure to air for 48 h, d) $[\text{Fe}^{\text{II}}_2(\text{H}_2\text{SIM}^1)(\mu\text{-OAc})_2]\text{PF}_6$ treated with NaPF_6 after exposure to air for 72 h, e) $[\text{Fe}^{\text{III}}\text{Na}(\text{H}_2\text{SIM}^1)(\mu\text{-OAc})_2]\text{PF}_6$ after exposure to air for 24 h, f) $[\text{Fe}^{\text{III}}\text{Na}(\text{H}_2\text{SIM}^1)(\mu\text{-OAc})_2]\text{PF}_6$ after exposure to air for 2 h and g) $[\text{Fe}^{\text{III}}\text{Na}(\text{H}_2\text{SIM}^1)(\mu\text{-OAc})_2]\text{PF}_6$ as a solid.

The purple solid $[\text{Fe}^{\text{III}}\text{Na}(\text{H}_2\text{SIM}^1)(\mu\text{-OAc})_2]\text{PF}_6$ exhibits a broad singlet in the ^{57}Fe Mössbauer spectrum, ascribed to a relaxing high-spin Fe^{III} mononuclear species (Figure 48g) and a small signal indicating a Fe^{II} species. The spectrum obtained of $[\text{Fe}^{\text{III}}\text{Na}(\text{H}_2\text{SIM}^1)(\mu\text{-OAc})_2]\text{PF}_6$, dissolved in acetonitrile (Figure 48f), is essentially the same as the one obtained of the solid, except for an intensity decrease of the Fe^{II} species. The Fe^{II} species found in these spectra is assigned to impurities of $[\text{Fe}^{\text{III}}\text{Fe}^{\text{II}}(\text{H}_2\text{SIM}^1)(\mu\text{-OAc})_2]^{2+}$ and the corresponding fitting curves are shown in Figure 49c. This interpretation derives from comparison with the corresponding ^{57}Fe Mössbauer spectrum of $[\text{Fe}^{\text{III}}\text{Fe}^{\text{II}}(\text{H}_2\text{SIM}^1)(\mu\text{-OAc})_2]^{2+}$ (Figure 54b), generated by chemical oxidation of $[\text{Fe}^{\text{II}}_2(\text{H}_2\text{SIM}^1)(\mu\text{-OAc})_2]^+$ and will be discussed later in this chapter. During further exposure to air, the spectrum becomes more narrow (Figure 48e) and exhibits features similar to the spectrum

of $[\text{Fe}^{\text{III}}_2(\text{H}_2\text{SIM}^1)(\mu\text{-OAc})_2]^{3+}$ (Figure 48d), suggesting the formation of the diiron(III) complex in acetonitrile solution under aerobic conditions. Coordination of two Fe^{II} ions in the corresponding ligand H_3SIM^1 and subsequent oxidation of the iron centers appears to be the preferred way to form $[\text{Fe}^{\text{III}}_2(\text{H}_2\text{SIM}^1)(\mu\text{-OAc})_2]^{3+}$ compared to direct coordination of two Fe^{III} ions (discussed in Chapter 3.2.5). Moreover, the crystallization of $[\text{Fe}^{\text{III}}_2(\text{H}_2\text{SIM}^1)(\mu\text{-OAc})_2]^{3+}$ from methanol solution seems to be less likely than crystallization of $[\text{Fe}^{\text{III}}\text{Na}(\text{H}_2\text{SIM}^1)(\mu\text{-OAc})_2]\text{PF}_6$, because only the latter compound was isolated via diethylether diffusion.

Treatment of $[\text{Fe}^{\text{III}}_2(\text{H}_2\text{SIM}^1)(\mu\text{-OAc})_2]^{3+}$ with perchloric acid results in decomposition of the complex apparent by its loss of color in solution. Interestingly, a solution of $[\text{Fe}^{\text{III}}\text{Na}(\text{H}_2\text{SIM}^1)(\mu\text{-OAc})_2]\text{PF}_6$, which was exposed to air for 72 hours (generating the mixture of $[\text{Fe}^{\text{III}}_2(\text{H}_2\text{SIM}^1)(\mu\text{-OAc})_2]^{3+}$ and metal-free ligand H_3SIM^1), and subsequent treatment with perchloric acid resulted in a ^{57}Fe Mössbauer spectrum with a single quadrupole doublet, characteristic for a high-spin Fe^{II} species (Figure 49b). This indicates the reduction of the Fe^{III} ion by the phenol-based ligand H_3SIM^1 in acidic solution.

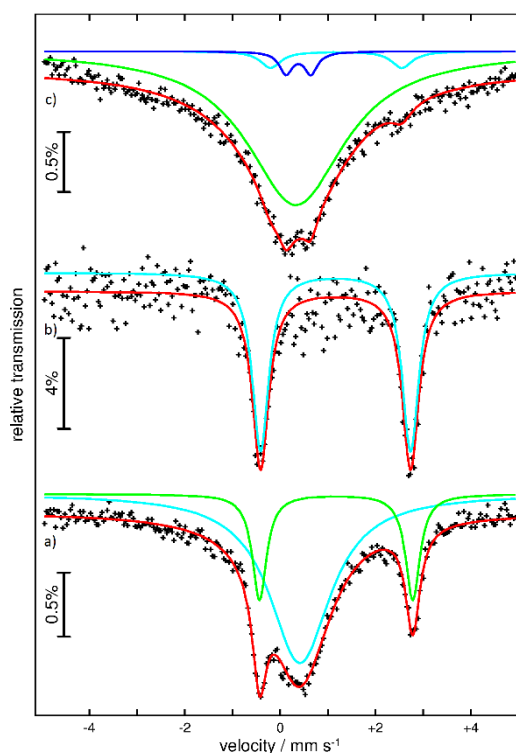
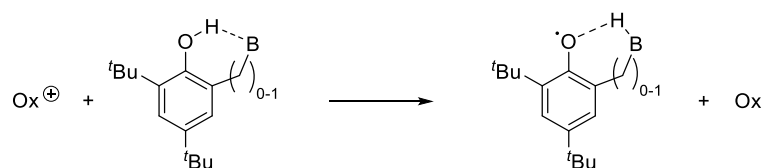


Figure 49: Comparison of the ^{57}Fe Mössbauer spectra obtained from frozen acetonitrile solution of a) $[\text{Fe}^{\text{II}}_2(\text{H}_2\text{SIM}^1)(\mu\text{-OAc})_2]\text{PF}_6$ after exposure to air for 72 h and addition of HClO_4 , b) $[\text{Fe}^{\text{III}}\text{Na}(\text{H}_2\text{SIM}^1)(\mu\text{-OAc})_2]\text{PF}_6$ after exposure to air for 72 h and addition of HClO_4 , and c) $[\text{Fe}^{\text{III}}\text{Na}(\text{H}_2\text{SIM}^1)(\mu\text{-OAc})_2]\text{PF}_6$.

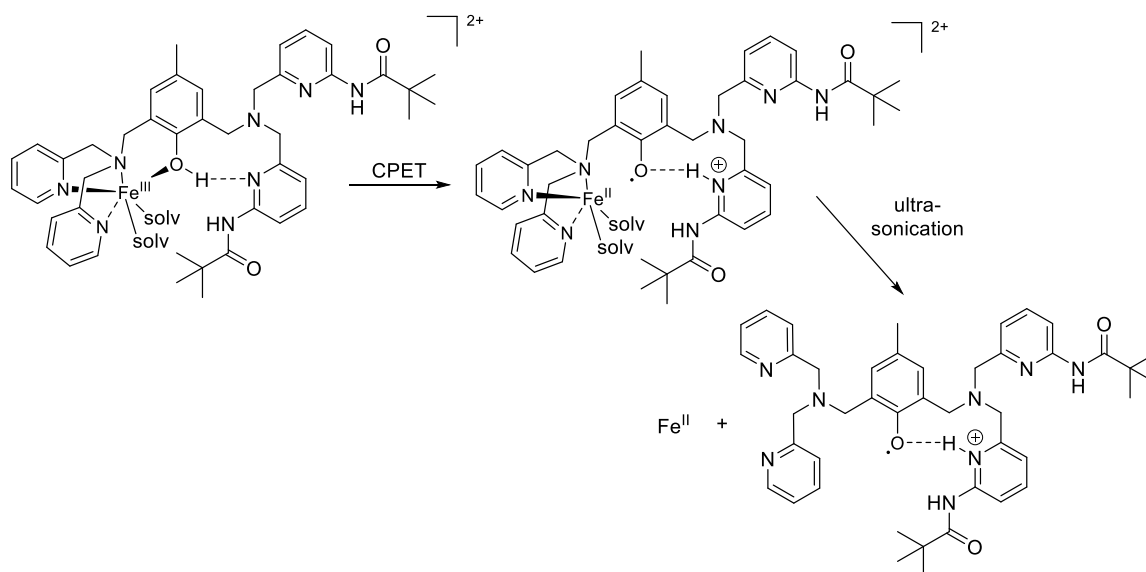
Mayer *et al.* used phenols with pendant substituted pyridines to study the concerted proton-electron transfer in hydrogen-bonded pyridine-phenols.^{250, 251} In this process, the electron is removed by an outer-sphere one-electron oxidant such as $[\text{Fe}^{\text{III}}(\text{L}^{47})_3]^{3+}$ and $[\text{Fe}^{\text{III}}(\text{L}^{48})_3]^{3+}$ and derivatives thereof, and the phenolic proton is transferred concomitantly to the pendant basic

pyridyl residue to give a distonic radical cation (Scheme 12).^{250, 251} Another task which the basic sites fulfill is the stabilization of the oxidized product.²⁵¹



Scheme 12: CPET reactivity of phenols with pendant basic moieties.²⁵¹

The addition of perchloric acid to $[\text{Fe}^{\text{III}}\text{Na}(\text{H}_2\text{SIM}^1)(\mu\text{-OAc})_2]\text{PF}_6$ in acetonitrile solution results in the protonation of the bridging phenolate, apparent in the color change to blue, forming most likely $[\text{Fe}^{\text{III}}(\text{H}_3\text{SIM}^1)(\text{solv})_2]^{3+}$ (Scheme 13). The unexpected appearance of a Fe^{II} species in the ^{57}Fe Mössbauer spectrum, recorded with the colorless solution obtained after ultrasonication, is proposed to be due to a CPET mechanism similar to the one shown in Scheme 12. The Fe^{III} complex is proposed to act as a one-electron oxidant generating a phenol radical and the corresponding Fe^{II} complex. The proximal pyridine residues may act as pendant basic site (Scheme 13). It is not clear if the oxidant needed for the oxidation of the phenol-based ligand is an Fe^{III} ion coordinated to the same ligand or the Fe^{III} center of another complex molecule.



Scheme 13: Proposed mechanism for the CPET in $[\text{Fe}^{\text{III}}(\text{H}_3\text{SIM}^1)(\text{solv})_2]^{2+}$.

Similar to the observation obtained from the acidified solution of $[\text{Fe}^{\text{III}}\text{Na}(\text{H}_2\text{SIM}^1)(\mu\text{-OAc})_2]\text{PF}_6$, the $[\text{Fe}^{\text{III}}_2(\text{H}_2\text{SIM}^1)(\mu\text{-OAc})_2]^{3+}$ compound (formed via oxidation under aerobic conditions of a solution of $[\text{Fe}^{\text{II}}_2(\text{H}_2\text{SIM}^1)(\mu\text{-OAc})_2]^+$ in acetonitrile) showed also an Fe^{II} species in the ^{57}Fe Mössbauer spectrum, measured after treatment with perchloric acid (Figure 49a). Besides the quadrupole doublet, assigned to ligand-free Fe^{II} ions, a broad signal was determined in the spectrum, indicating the presence of a Fe^{III} species in the mixture. This finding is consistent with

the 2:1 ratio of Fe^{III} ions and phenol-based ligand in the initial mixture, which enables only the reduction of half of the Fe^{III} ions, as no more phenol-based species are available in solution.

Electrochemical Studies using Cyclic Voltammetry

The electrochemical behavior of $[\text{Fe}^{\text{II}}_2(\text{H}_2\text{SIM}^1)(\mu\text{-OAc})_2]^+$ and $[\text{Fe}^{\text{II}}_2(\text{H}_2\text{L}^2)(\mu\text{-OAc})_2]^+$ was investigated by cyclic voltammetry (CV). The CV experiments were conducted in degassed acetonitrile solution (0.1 M NBu₄ClO₄, 0.5 mM complex) at room temperature and the results are presented in Figure 50. Ferrocene was used as internal standard.²⁵² Multiple CV scans were essentially identical when the experiments were undertaken under anaerobic conditions, indicating that decomposition in solution does not occur.

The CV of $[\text{Fe}^{\text{II}}_2(\text{H}_2\text{SIM}^1)(\mu\text{-OAc})_2]\text{PF}_6$ shows two sequential reductions, a reversible one-electron transfer at 0.16 V vs. SCE ($\Delta E_p = 88$ mV) and a quasi-reversible one-electron transfer at 0.56 V vs. SCE ($\Delta E_p = 153$ mV) (Figure 50a) which can be assigned to the Fe^{II}₂/Fe^{III}Fe^{II} and Fe^{III}Fe^{II}/Fe^{III}₂ couples, respectively. Interestingly, the potential at 0.16 V (vs. SCE) is similar to the redox couple examined for the native ufPAP enzyme at ~ 0.34 V vs. NHE (0.10 V vs. SCE).²²²

In the case of $[\text{Fe}^{\text{II}}_2(\text{H}_2\text{L}^2)(\mu\text{-OAc})_2]\text{PF}_6$ a more complex CV was observed, with two anodic and two cathodic waves (Figure 50b). Thus, several species appear to coexist in both redox states in solution and these complicate the redox behavior. While the Fe^{III}Fe^{II}/Fe^{III}₂ couples are in the same region as in the case of $[\text{Fe}^{\text{II}}_2(\text{H}_2\text{SIM}^1)(\mu\text{-OAc})_2]\text{PF}_6$, the Fe^{II}₂/Fe^{III}Fe^{II} couples are shifted to more positive redox potentials around 0.8 V vs. SCE. The redox potential of the Fe^{III}₂ complex of ligand H₂L² was detected at 0.40 V vs. SCE.¹¹⁴

Table 17 compares these values with the redox potentials found for similar complexes but lacking the pivaloyl-amide residues. Interestingly, the redox potentials found for $[\text{Fe}^{\text{II}}_2(\text{H}_2\text{L}^2)(\mu\text{-OAc})_2]\text{PF}_6$ are all shifted to more positive potentials, while in the case of $[\text{Fe}^{\text{II}}_2(\text{H}_2\text{SIM}^1)(\mu\text{-OAc})_2]\text{PF}_6$ E₁ is shifted to more positive and E₂ to more negative potentials, compared to the unsubstituted complexes derived from HL¹.

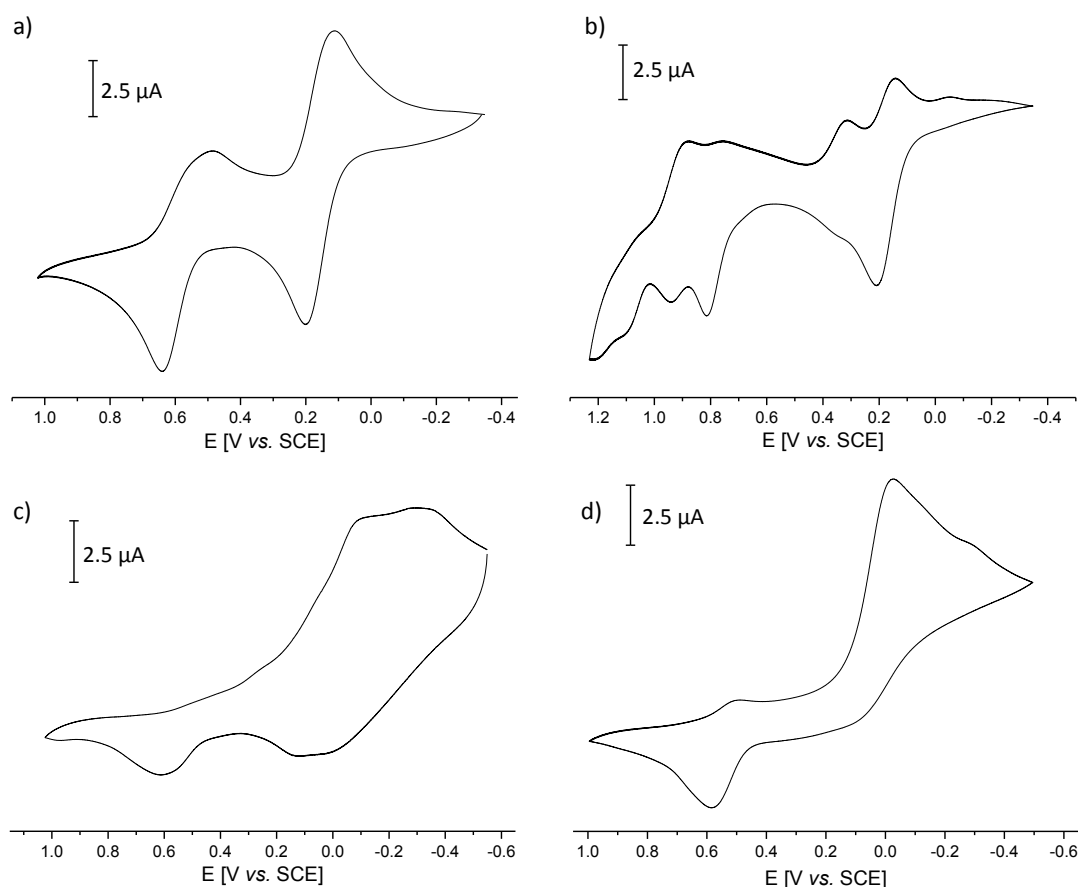


Figure 50: Cyclic voltammograms of a) $[\text{Fe}^{\text{II}}_2(\text{H}_2\text{SIM}^1)(\mu\text{-OAc})_2]\text{PF}_6$, b) $[\text{Fe}^{\text{II}}_2(\text{H}_2\text{L}^2)(\mu\text{-OAc})_2]\text{PF}_6$, c) $[\text{Fe}^{\text{II}}_2(\text{H}_2\text{SIM}^1)(\mu\text{-OAc})_2]\text{PF}_6$ after exposure to air and d) $[\text{Fe}^{\text{II}}_2(\text{H}_2\text{L}^2)(\mu\text{-OAc})_2]\text{PF}_6$ after exposure to air, recorded in degassed acetonitrile (0.5 mM complex, 0.1 M NBu_4ClO_4) at rt under Ar (glassy carbon working electrode, platinum wire counter electrode, Ag/Ag^+ (0.1 mM in NaCl) reference electrode).

Table 17: Cyclic voltammetric data of phenoxido-bridged diiron complexes in acetonitrile.

complex	E_1 [V vs. SCE]	E_2 [V vs. SCE]	ΔE [V]	$K_{\text{com}}^{\text{a}}$
$[\text{Fe}^{\text{II}}_2(\text{H}_2\text{SIM}^1)(\mu\text{-OAc})_2]\text{PF}_6^{\text{b}}$	0.16	0.56	0.41	$8.5 \cdot 10^6$
$[\text{Fe}^{\text{II}}_2(\text{H}_2\text{L}^2)(\mu\text{-OAc})_2]\text{PF}_6^{\text{b}}$	0.18/0.34	0.79/0.92	~ 0.60	$\sim 1.4 \cdot 10^{10}$
$[\text{Fe}^{\text{III}}\text{Fe}^{\text{II}}(\text{L}^1)(\mu\text{-OAc})_2](\text{BF}_4)_2^{\text{c} 231}$	-0.03	0.68	0.71	$1.6 \cdot 10^{12}$
$[\text{Fe}^{\text{III}}\text{Fe}^{\text{II}}(\text{L}^1)(\mu\text{-OPr})_2](\text{BPh}_4)_2^{\text{d} 139}$	-0.01	0.69	0.70	$7.5 \cdot 10^{11}$
$[\text{Fe}^{\text{III}}\text{Fe}^{\text{II}}(\text{L}^1)(\mu\text{-OBz})_2](\text{PF}_6)_2^{\text{d} 139}$	0.06	0.75	0.69	$4.7 \cdot 10^{11}$
$[\text{Fe}^{\text{III}}\text{Fe}^{\text{II}}(\text{L}^1)(\mu\text{-OBz})_2](\text{BF}_4)_2^{\text{c} 231}$	0.05	0.73	0.68	$5.0 \cdot 10^{11}$
$[\text{Fe}^{\text{III}}\text{Fe}^{\text{II}}(\text{L}^1)(\mu\text{-OBz})_2](\text{BF}_4)_2^{\text{e} 253}$	-0.02	0.67	0.69	$6.8 \cdot 10^{11}$
$[\text{Fe}^{\text{III}}\text{Fe}^{\text{II}}(\text{L}^{11})(\mu\text{-OAc})_2](\text{BPh}_4)_2^{\text{f} 232}$	-0.09	0.66	0.75	$3.3 \cdot 10^{12}$

^a see Equation 19.

^b 0.1 M NBu_4ClO_4 , glassy carbon working electrode, platinum wire counter electrode, Ag/Ag^+ (0.1 mM in NaCl) reference electrode.

^c Bu_4NClO_4 , glassy carbon working electrode, auxiliary electrode, saturated calomel reference electrode.

^d 0.1 M NBu_4BF_4 , platinum disk working electrode, platinum wire auxiliary electrode, saturated calomel reference electrode.

^e 0.1 M NBu_4ClO_4 , glassy carbon working electrode, platinum counter electrode, saturated Ag/AgCl reference electrode.

^f 0.1 M NBu_4ClO_4 , platinum net working electrode, platinum wire auxiliary electrode, Ag/Ag^+ or calomel working electrode.

The trend to more positive potentials by an increase of the number of pivaloyl-amide substituents was already observed with pivaloyl-amide substituted Co^{II} and Cu^{II} complexes.^{254, 255}

The hydrogen bond donors implemented in the complexes induce a shift to less negative values for E_p (Chart 18). More precisely, the complex $[\text{Co}^{\text{III}}(\text{L}^{21})(\text{acetohydroximate})]\text{Cl}$ was found to have a $\text{Co}^{\text{II}}/\text{Co}^{\text{III}}$ couple at -0.99 V vs. SCE, while the 6-pivaloylamide substituted derivative showed this potential at -0.72 V vs. SCE. It was proposed that the easier $\text{Co}^{\text{II}}/\text{Co}^{\text{III}}$ reduction is due to the decreased charge of the hydroximate oxygen because of hydrogen bonding with the pivaloylamide residue.²⁵⁴ Similarly, the Cu^{II} complexes of the tripodal ligand L^{21} show a reduction wave in the CV at more positive redox potentials with an increasing number of 6-pivaloyl-amide substitution of the pyridine moieties.²⁵⁵ Therefore, the two pivaloyl-amide residues in $[\text{Fe}^{\text{II}}_2(\text{H}_2\text{L}^2)(\mu\text{-OAc})_2]\text{PF}_6$, one at each iron center, seem to influence the redox potentials of the $\text{Fe}^{\text{II}}_2/\text{Fe}^{\text{III}}\text{Fe}^{\text{II}}$ and $\text{Fe}^{\text{III}}\text{Fe}^{\text{II}}/\text{Fe}^{\text{III}}_2$ couples in the same way, probably due to hydrogen bond formation.

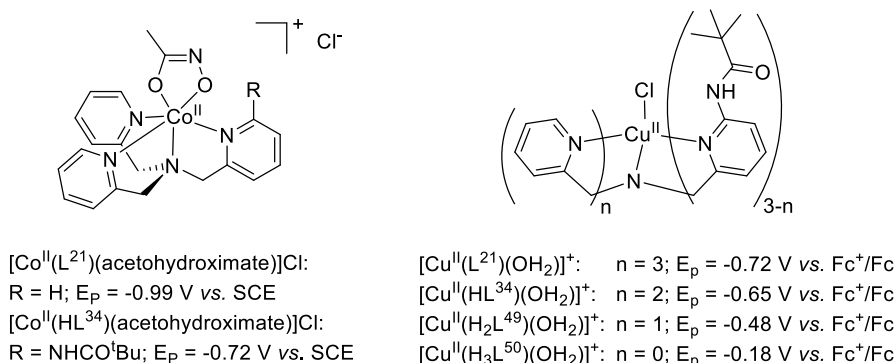


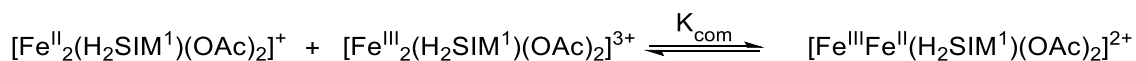
Chart 18: Co^{II} and Cu^{II} complexes used to study the impact of pivaloyl-amide substituents in proximity to the metal center on the redox potential.^{254, 255}

Table 17 also compares the methyl-substituted complex $[\text{Fe}^{\text{III}}\text{Fe}^{\text{II}}(\text{L}^{11})(\mu\text{-OAc})_2](\text{BPh}_4)_2$ ²³² with the heterovalent diiron complexes of HL^1 . The more negative potentials of the redox couples for $[\text{Fe}^{\text{III}}\text{Fe}^{\text{II}}(\text{L}^{11})(\text{OAc})_2](\text{BPh}_4)_2$ ²³² compared to $[\text{Fe}^{\text{III}}\text{Fe}^{\text{II}}(\text{L}^1)(\mu\text{-OAc})_2](\text{BPh}_4)_2$ ²³¹ was explained by the effect of the electron-donating ability of methyl substituents of the 6-methylpyridine rings.^{231, 232} Therefore, the cathodic shift of the redox potentials of $[\text{Fe}^{\text{II}}_2(\text{H}_2\text{SIM}^1)(\mu\text{-OAc})_2]\text{PF}_6$ and $[\text{Fe}^{\text{II}}_2(\text{H}_2\text{L}^2)(\mu\text{-OAc})_2]\text{PF}_6$ compared to $[\text{Fe}^{\text{III}}\text{Fe}^{\text{II}}(\text{L}^1)(\mu\text{-OAc})_2](\text{BF}_4)_2$ may result from the electron withdrawing effect of the pivaloyl-amide residues.

The contrasting effect of lowering the redox potential by about 500 mV by incorporation of pivaloyl-amide residues into a diiron(II) complex was reported by Aii *et al.* and proposed to be caused by an increase in the energy level of the HOMO of the iron centers due to coordination of pivaloyl-amide oxygen atoms.²⁵⁶ Therefore, the lower redox potential of the $\text{Fe}^{\text{II}}_2/\text{Fe}^{\text{III}}\text{Fe}^{\text{II}}$ couple of $[\text{Fe}^{\text{II}}_2(\text{H}_2\text{SIM}^1)(\mu\text{-OAc})_2]\text{PF}_6$ by 0.12 V compared to $[\text{Fe}^{\text{III}}\text{Fe}^{\text{II}}(\text{L}^1)(\mu\text{-OAc})_2](\text{BF}_4)_2$ is probably induced by the two pivaloyl-amide residues adjacent to one of the two iron centers. Moreover, a diiron(II) complex of a HL^1 derivative with pivaloyl-amide residues at each pyridine moiety

(H₅L³⁹) resulted in a CV with a strong wave at 0.39 V vs. SCE and shoulders at -0.20 V and -0.36 V vs. SCE.²³⁴

The formation of an Fe^{III}Fe^{II} complex is important to obtain a more accurate model for the active form of PAP. The thermodynamic stability of the Fe^{III}Fe^{II} complex of the asymmetric ligand H₃SIM¹ was estimated by examining the following comproportionation equilibrium.



From the separation of the redox potentials ΔE , the comproportionation constant K_{com} can be calculated from Equation 19 and is listed in combination with the values reported for pivaloylamide-free diiron complexes in Table 7.^{139, 231, 232, 253}

$$\text{Equation 19} \quad \Delta E = \left(\frac{RT}{nF}\right) \ln K_{\text{com}}$$

The small value of ΔE for $[\text{Fe}^{\text{II}}_2(\text{H}_2\text{SIM}^1)(\mu\text{-OAc})_2]\text{PF}_6$ (0.41 V) yielded $K_{\text{com}} = 8.5 \cdot 10^6$, which indicates a substantial stability of the Fe^{III}Fe^{II} complex over the corresponding Fe^{II}₂ and Fe^{III}₂ complexes. However, the value is rather small compared to those of other phenoxido-bridged diiron complexes (Table 17). However, the corresponding heterovalent diiron complex of ligand H₃SIM¹ would take the asymmetry and the hydrogen bonding network present in the active site of the native PAP enzyme into consideration. Therefore, a suitable method for oxidation of $[\text{Fe}^{\text{II}}_2(\text{H}_2\text{SIM}^1)(\mu\text{-OAc})_2]\text{PF}_6$ was explored and will be discussed in Chapter 5.4.

The green solutions of $[\text{Fe}^{\text{II}}_2(\text{H}_2\text{SIM}^1)(\mu\text{-OAc})_2]\text{PF}_6$ and $[\text{Fe}^{\text{II}}_2(\text{H}_2\text{L}^2)(\mu\text{-OAc})_2]\text{PF}_6$ in acetonitrile were exposed to air, subsequently degassed and CVs recorded. These data are also shown in Figure 50. The purple solution derived from $[\text{Fe}^{\text{II}}_2(\text{H}_2\text{SIM}^1)(\mu\text{-OAc})_2]\text{PF}_6$ resulted in a CV with an irreversible redox wave around 0.5 V vs. SCE and two quasi-reversible redox waves at 0.02 V and -0.16 V vs. SCE. The corresponding CV derived from $[\text{Fe}^{\text{II}}_2(\text{H}_2\text{L}^2)(\mu\text{-OAc})_2]\text{PF}_6$ has two irreversible redox couples at 0.54 V and 0.04 V vs. SCE. The irreversibility of the redox processes indicates structural changes associated with the oxidation. Moreover, consecutive CV scans were not identical, and this is attributed to (partial) decomposition after oxidation.

UV-vis-NIR Spectroscopy

Electronic Properties under Anaerobic Conditions

In addition to the intense absorptions below 300 nm ($\pi\text{-}\pi^*$ transitions of the ligand backbone), the electronic spectra of $[\text{Fe}^{\text{II}}_2(\text{H}_2\text{SIM}^1)(\mu\text{-OAc})_2]^+$ and $[\text{Fe}^{\text{II}}_2(\text{H}_2\text{L}^2)(\mu\text{-OAc})_2]^+$ dissolved in acetonitrile show only one band in the region of 400 - 450 nm. $[\text{Fe}^{\text{II}}_2(\text{H}_2\text{SIM}^1)(\mu\text{-OAc})_2]^+$ has a transition at 416 nm ($\epsilon = 1446 \text{ M}^{-1}\text{cm}^{-1}$) and $[\text{Fe}^{\text{II}}_2(\text{H}_2\text{L}^2)(\mu\text{-OAc})_2]^+$ has a band at 409 nm ($\epsilon = 1315 \text{ M}^{-1}\text{cm}^{-1}$), ascribed to MLCT transitions of Fe^{II} to the pyridine donors. This is in

accordance with previously published Fe^{II}_2 complexes.^{234, 235, 257, 258} The lack of low-energy absorption bands indicates that $[\text{Fe}^{\text{II}}_2(\text{H}_2\text{SIM}^1)(\mu\text{-OAc})_2]^+$ and $[\text{Fe}^{\text{II}}_2(\text{H}_2\text{L}^2)(\mu\text{-OAc})_2]^+$ are high-spin Fe^{II} complexes.²⁵⁸

Electronic Properties under Aerobic Conditions

The UV-vis-NIR spectrum of $[\text{Fe}^{\text{III}}\text{Na}(\text{H}_2\text{SIM}^1)(\mu\text{-OAc})_2]\text{PF}_6$ in acetonitrile shows one broad transition at 568 nm ($\epsilon = 2499 \text{ M}^{-1}\text{cm}^{-1}$) and a shoulder at 335 nm ($\epsilon = 5049 \text{ M}^{-1}\text{cm}^{-1}$), in addition to the intense absorptions below 300 nm. The band at 568 nm is associated with the phenolate-to-iron(III) charge transfer transition from the oxygen p_π orbital to the Fe^{III} d_{π^*} orbitals and is energetically close to the tyrosinate-to-iron(III) charge transfer observed for PAPs.^{69, 138, 217, 219, 220} The majority of synthetic Fe^{III} -phenolate complexes exhibit CT bands with molar extinction coefficients in the order of 1000 - 2000 $\text{M}^{-1}\text{cm}^{-1}$ per Fe^{III} -phenolate bond.^{259, 260} The molar extinction coefficient of 2499 $\text{M}^{-1}\text{cm}^{-1}$ for $[\text{Fe}^{\text{III}}\text{Na}(\text{H}_2\text{SIM}^1)(\mu\text{-OAc})_2]\text{PF}_6$ is slightly outside this range but does still not approach the value found in the native enzymes.^{69, 138, 217, 219, 220} A comparison of a variety of similar doubly acetate-bridged $\text{Fe}^{\text{III}}\text{M}^{\text{II}}$ complexes of H_2L^4 reveals that the molar extinction coefficient strongly depends on the nature of the M^{II} ion, *i.e.* $[\text{Fe}^{\text{III}}\text{Mn}^{\text{II}}(\text{L}^4)(\mu\text{-OAc})_2]\text{ClO}_4$ (544 nm, 2680 $\text{M}^{-1}\text{cm}^{-1}$),⁹⁶ $[\text{Fe}^{\text{III}}\text{Cu}^{\text{II}}(\text{L}^4)(\mu\text{-OAc})_2]\text{ClO}_4$ (546 nm, 3400 $\text{M}^{-1}\text{cm}^{-1}$),⁹² $[\text{Fe}^{\text{III}}\text{Zn}^{\text{II}}(\text{L}^4)(\mu\text{-OAc})_2]\text{ClO}_4$ (540 nm, 3700 $\text{M}^{-1}\text{cm}^{-1}$),⁹⁵ $[\text{Fe}^{\text{III}}\text{Fe}^{\text{II}}(\text{L}^4)(\mu\text{-OAc})_2]\text{BF}_4$ (556 nm, 4560 $\text{M}^{-1}\text{cm}^{-1}$),⁹⁴ and $[\text{Fe}^{\text{III}}\text{Ni}^{\text{II}}(\text{L}^4)(\mu\text{-OAc})_2]\text{ClO}_4$ (538 nm, 4813 $\text{M}^{-1}\text{cm}^{-1}$).^{81, 141}

pH Behavior

In order to examine the behavior of $[\text{Fe}^{\text{II}}_2(\text{H}_2\text{SIM}^1)(\mu\text{-OAc})_2]^+$ and $[\text{Fe}^{\text{II}}_2(\text{H}_2\text{L}^2)(\mu\text{-OAc})_2]^+$ under basic condition UV-vis-NIR spectroscopic measurement were also conducted in acetonitrile-aqueous buffer mixtures (1:1). The pH of the aqueous buffer was varied from pH 6 to pH 11; the pH recorded refers to the aqueous component. With increasing basicity the absorbance of $[\text{Fe}^{\text{II}}_2(\text{H}_2\text{L}^2)(\mu\text{-OAc})_2]^+$ (Figure 51c) shows a decrease in intensity of the two bands at 235 nm and 286 nm, while two new bands at 261 nm and 314 nm arise. Moreover, the band at 414 nm experiences a shift to 440 nm with increasing basicity. Figure 51d shows the change of absorbance at different wavelengths as a function of pH value. The overlay of the spectra at different pH values indicates the presence of three isosbestic points at 245 nm, 274 nm, and 395 nm. This implies that the diiron(II) complex is stable in the investigated pH range and undergoes a single deprotonation step. Therefore, the curves can be analyzed by the Equation 6, as discussed in Chapter 4.3.

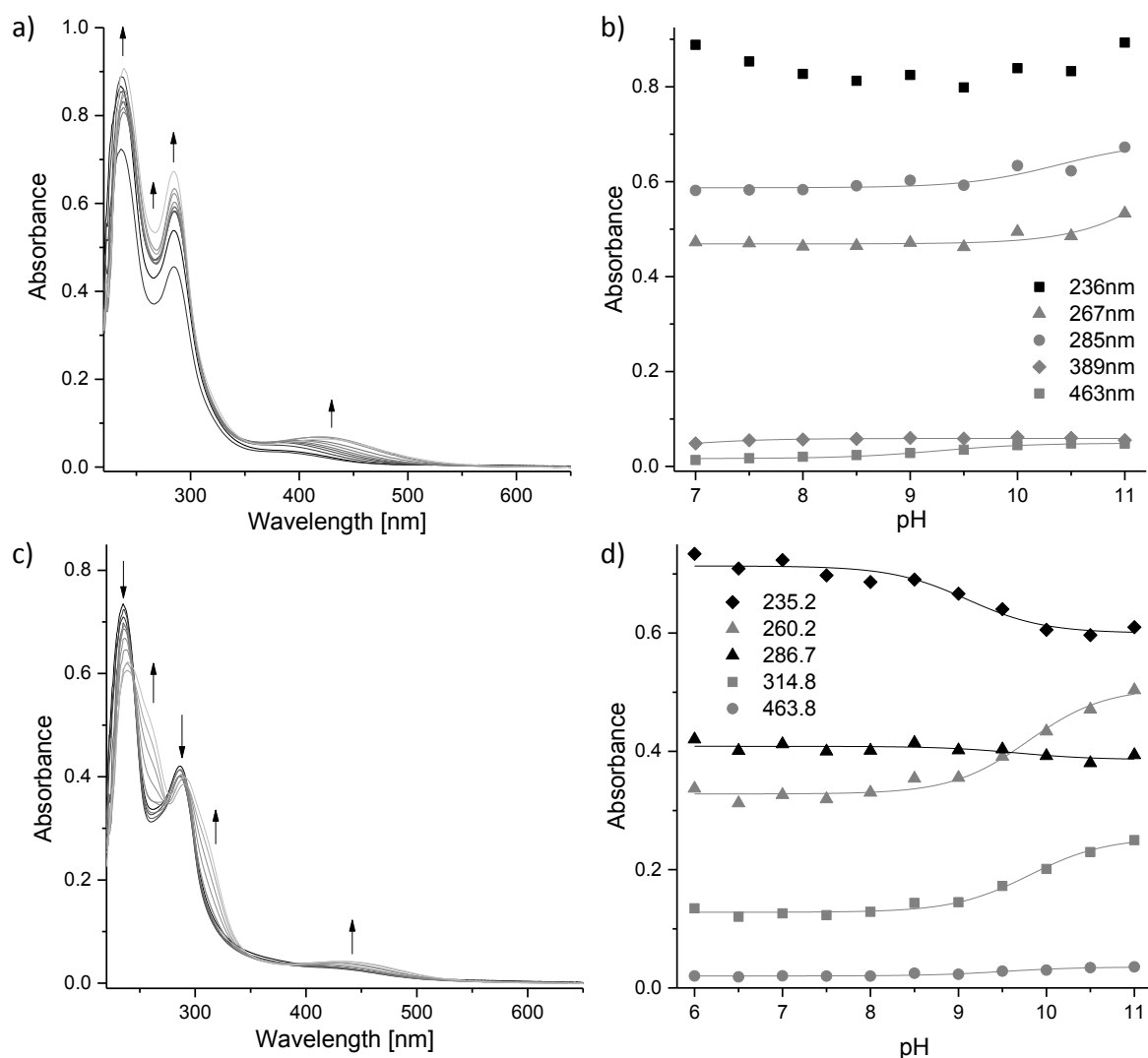


Figure 51: UV-vis spectroscopic titration (50 μM in acetonitrile/buffer between pH 6 and 11) for a) $[\text{Fe}^{\text{II}}_2(\text{H}_2\text{SIM}^1)(\mu\text{-OAc})_2]\text{PF}_6$ and c) $[\text{Fe}^{\text{II}}_2(\text{H}_2\text{L}^2)(\mu\text{-OAc})_2]\text{PF}_6$ as well as absorbance vs. pH plots for b) $[\text{Fe}^{\text{II}}_2(\text{H}_2\text{SIM}^1)(\mu\text{-OAc})_2]\text{PF}_6$ and d) $[\text{Fe}^{\text{II}}_2(\text{H}_2\text{L}^2)(\mu\text{-OAc})_2]\text{PF}_6$.

Fitting of the pH-dependent spectroscopic data as described Chapter 4.3, leads to the pK_a value of 9.58 ± 0.65 for $[\text{Fe}^{\text{II}}_2(\text{H}_2\text{L}^2)(\mu\text{-OAc})_2]^+$. This is about 1.5 pH units higher than that observed with the corresponding dizinc(II) complex $[\text{Zn}^{\text{II}}_2(\text{H}_2\text{L}^2)(\mu\text{-OAc})_2]^+$ and follows the same trend as the corresponding metal aqua complexes.¹⁶⁵

The pH-dependent UV-vis-NIR spectra of $[\text{Fe}^{\text{II}}_2(\text{H}_2\text{SIM}^1)(\mu\text{-OAc})_2]^+$ show a similar shifting of the band at 399 nm to 426 nm (Figure 51a). In contrast to $[\text{Fe}^{\text{II}}_2(\text{H}_2\text{L}^2)(\mu\text{-OAc})_2]^+$, both bands between 200 nm and 300 nm in the spectrum of $[\text{Fe}^{\text{II}}_2(\text{H}_2\text{SIM}^1)(\mu\text{-OAc})_2]^+$ increase in intensity with increasing basicity. The absorbance vs. pH plot (Figure 51b) exhibits changes in the pH regions around 7 and around 10.5, indicating two deprotonation steps with pK_a values around 7 and 10.5.

5.4 STUDIES TOWARD THE FORMATION OF A HETEROVALENT $\text{Fe}^{\text{III}}\text{Fe}^{\text{II}}$ COMPLEX

As explained before the presence of a heterovalent diiron core and the hydrogen bonding network that arises from the peptide backbone are essential features of the active site of PAPs. Therefore, the generation of a $\text{Fe}^{\text{III}}\text{Fe}^{\text{II}}$ complex of H_3SIM^1 creates an accurate model system for PAP. In order to test the generation of $[\text{Fe}^{\text{III}}\text{Fe}^{\text{II}}(\text{H}_2\text{SIM}^1)(\text{solv})_x]^{4+}$, the chemical oxidation was analyzed by UV-vis, EPR, and ^{57}Fe Mössbauer spectroscopy.

UV-vis-NIR Spectroscopy

Due to the fact that the two redox waves in the CV of $[\text{Fe}^{\text{II}}_2(\text{H}_2\text{SIM}^1)(\mu\text{-OAc})_2]^+$ are well separated and that the redox potential of ferrocene is in between the two waves, the chemical oxidation of $[\text{Fe}^{\text{II}}_2(\text{H}_2\text{SIM}^1)(\mu\text{-OAc})_2]^+$ was tested using ferrocenium hexafluorophosphate as oxidant. The solution of $[\text{Fe}^{\text{II}}_2(\text{H}_2\text{SIM}^1)(\mu\text{-OAc})_2]^+$ in acetonitrile was therefore treated stepwise with a solution of ferrocenium hexafluorophosphate under anaerobic conditions. After addition of one and after the two equivalents of oxidant the mixture was allowed to react for 12 hours.

It is apparent that the oxidant reacts with the diiron(II) complex in a ratio of $[\text{Fe}^{\text{II}}_2(\text{H}_2\text{SIM}^1)(\mu\text{-OAc})_2]^+$ to ferrocenium of 1:1. UV-vis bands arise at 362 nm ($\epsilon = 6357 \text{ M}^{-1}\text{cm}^{-1}$) and 500 nm ($\epsilon = 1271 \text{ M}^{-1}\text{cm}^{-1}$), while the bands at 283 nm and 654 nm decrease (Figure 52c). Addition of a second equivalent of ferrocenium hexafluorophosphate does not significantly change the UV-vis spectrum (362 nm, $\epsilon = 7460 \text{ M}^{-1}\text{cm}^{-1}$ and 500 nm, $\epsilon = 1471 \text{ M}^{-1}\text{cm}^{-1}$), but a shoulder at 619 nm appears. This transition at 619 nm arises from unreacted ferrocenium hexafluorophosphate and indicates the incapacity of the oxidant to oxidize the second Fe^{II} ion in the initial $[\text{Fe}^{\text{II}}_2(\text{H}_2\text{SIM}^1)(\mu\text{-OAc})_2]^+$ complex. This indicates a selective formation of the heterovalent complex $[\text{Fe}^{\text{III}}\text{Fe}^{\text{II}}(\text{H}_2\text{SIM}^1)(\text{solv})_x]^{4+}$.

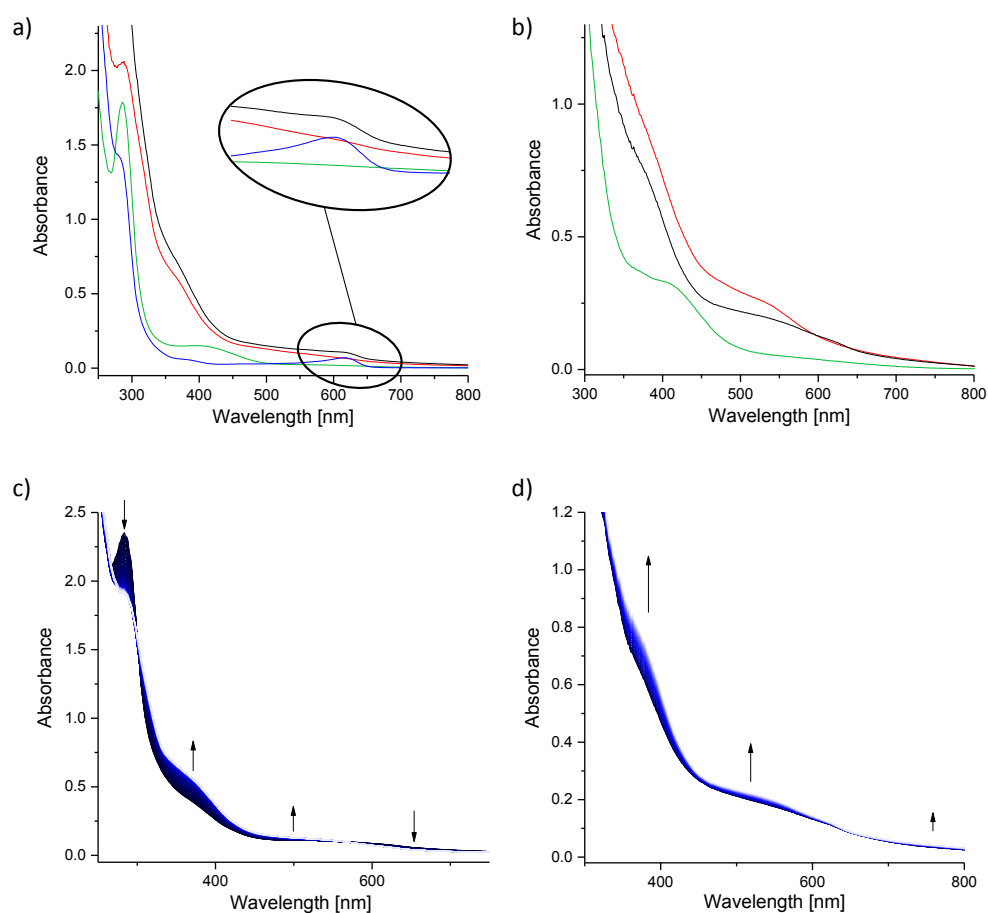


Figure 52: UV-vis-NIR spectra after addition of ferrocenium hexafluorophosphate to a) $[\text{Fe}^{\text{II}}_2(\text{H}_2\text{SIM}^1)(\mu\text{-OAc})_2]\text{PF}_6$ and b) $[\text{Fe}^{\text{II}}_2(\text{H}_2\text{L}^2)(\mu\text{-OAc})_2]\text{PF}_6$ (green lines: without FeCp_2PF_6 ; red lines: 1 eq FeCp_2PF_6 ; black lines: 2 eq FeCp_2PF_6 ; blue line: FeCp_2PF_6) and time-dependent experiments of c) $[\text{Fe}^{\text{II}}_2(\text{H}_2\text{SIM}^1)(\mu\text{-OAc})_2]\text{PF}_6$ with 1 eq FeCp_2PF_6 and d) $[\text{Fe}^{\text{II}}_2(\text{H}_2\text{L}^2)(\mu\text{-OAc})_2]\text{PF}_6$ with 1 eq FeCp_2PF_6 (a spectrum every 20 min for a period of 12 h).

For the purpose of comparison the oxidation of the symmetric complex $[\text{Fe}^{\text{II}}_2(\text{H}_2\text{L}^2)(\mu\text{-OAc})_2]\text{PF}_6$ with ferrocenium hexafluorophosphate was also examined. The reaction with one equivalent of oxidant lead to transitions at 373 nm ($\epsilon = 7688 \text{ M}^{-1}\text{cm}^{-1}$) and 515 nm ($\epsilon = 2114 \text{ M}^{-1}\text{cm}^{-1}$). In contrast to the experiments with $[\text{Fe}^{\text{II}}_2(\text{H}_2\text{SIM}^1)(\mu\text{-OAc})_2]^+$, addition of a second equivalent of ferrocenium hexafluorophosphate lead to further changes in the spectrum, *i.e.* a shift of the band at 515 nm to 540 nm ($\epsilon = 2415 \text{ M}^{-1}\text{cm}^{-1}$) (Figure 52b and d). Thus, the oxidant seems to be capable to oxidize both Fe^{II} centers in $[\text{Fe}^{\text{II}}_2(\text{H}_2\text{L}^2)(\mu\text{-OAc})_2]\text{PF}_6$. However, it does not emerge whether the two Fe^{II} centers are oxidized stepwise or simultaneously. However, the steady rise of the absorbance band at 515 nm during the stepwise addition of up to one equivalent of ferrocenium hexafluorophosphate and the following shift with further addition of oxidant as well as the K_{com} value of $\sim 1.4 \cdot 10^{10}$ (see Table 17) indicate a substantial stability of the heterovalent complex $[\text{Fe}^{\text{III}}\text{Fe}^{\text{II}}(\text{H}_2\text{L}^2)(\text{solv})_x]^{4+}$.

EPR Spectroscopy

EPR spectroscopy has been shown to be a useful technique for the characterization of the $\text{Fe}^{\text{III}}\text{Fe}^{\text{II}}$ core in heterovalent diiron model complexes and proteins.²⁶¹ At low temperature $\text{Fe}^{\text{III}}\text{Fe}^{\text{II}}$ sites exhibit a broad EPR signal at $g_{\text{av}} < 2$, indicative for antiferromagnetically coupled high-spin Fe^{III} ($S_1 = 5/2$, ${}^6\text{A}$ state) and high-spin Fe^{II} ($S_2 = 2$, ${}^5\text{T}$ state), resulting in a spin ground state of $S_{\text{total}} = 1/2$. These signals are only observed near liquid helium temperature and disappear above 30 K.²⁶² Such a behavior is very similar to that of the heterovalent diiron proteins.²⁶²

EPR spectra in frozen acetonitrile solution with one or two equivalents of oxidant added were recorded at temperatures below 5 K to investigate the oxidation state of $[\text{Fe}^{\text{II}}_2(\text{H}_2\text{SIM}^1)(\mu\text{-OAc})_2]^+$ after reaction with one and two equivalents of ferrocenium hexafluorophosphate for 12 hours at room temperature. The resulting spectra are presented in Figure 53. Both spectra show a broad intense signal centered near $g = 1.6$ ($g_1 = 1.43$, $g_2 = 1.67$, $g_3 = 1.82$, derived from fitting the spectrum assuming as an $S = 1/2$ Fe^{III} core), in addition to a strong signal near $g = 4.3$. These spectra are similar to that obtained from the electrochemically generated heterovalent complex $[\text{Fe}^{\text{III}}\text{Fe}^{\text{II}}(\text{H}_2\text{L}^2)(\mu\text{-OH})]^{3+}$.¹¹⁴

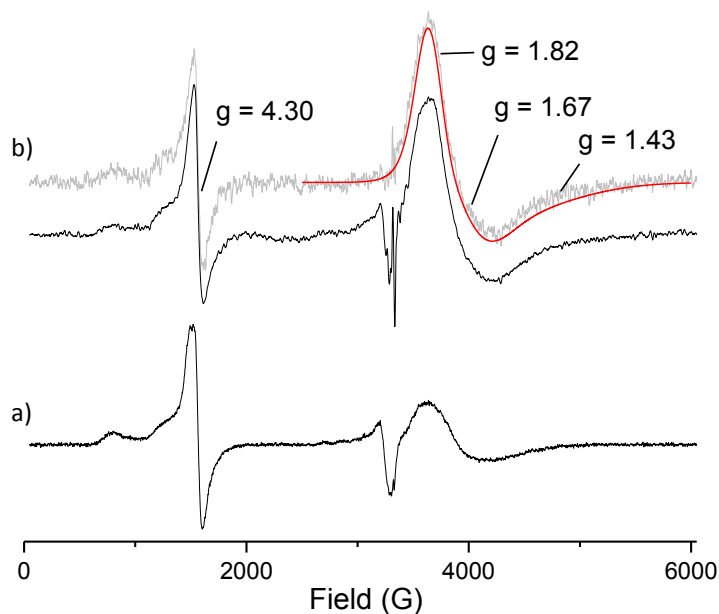


Figure 53: EPR spectra (9.4 GHz) of mixtures of $[\text{Fe}^{\text{II}}_2(\text{H}_2\text{SIM}^1)(\mu\text{-OAc})_2]^+$ with a) 1 eq FeCp_2PF_6 ($T = 5$ K) and b) 2 eq of FeCp_2PF_6 ($T = 1.7$ K, 1 mM in acetonitrile-toluene solution (1:1), experimental spectra in black, spectrum after subtraction of the copper impurity in grey, simulated spectrum in red. The signals at $g = 2.04$ is an artefact due to a copper(II) impurity in the cavity of the spectrometer).

The signal at $g \sim 1.6$ is attributed to a strongly antiferromagnetically coupled $\text{Fe}^{\text{III}}\text{Fe}^{\text{II}}$ core. Similar broad signals in this region have previously been reported for $[\text{Fe}^{\text{III}}\text{Fe}^{\text{II}}(\text{L}^1)(\mu\text{-OPr})_2]^+$, $[\text{Fe}^{\text{III}}\text{Fe}^{\text{II}}(\text{L}^{11})(\mu\text{-OAc})_2]^{2+}$, $[\text{Fe}^{\text{III}}\text{Fe}^{\text{II}}(\text{L}^{51})(\mu\text{-OAc})_2]^{2+}$, and $[\text{Fe}^{\text{III}}\text{Fe}^{\text{II}}(\text{L}^4)(\mu\text{-OAc})_2]^+$.^{139, 140, 232, 235, 262} Similarly, bsPAP exhibits a rhombic spectrum with apparent g values of 1.58, 1.73 and 1.85 at

pH > 5.²¹⁹ The fact that both mixtures show similar EPR spectra with features typical for an Fe^{III}Fe^{II} species supports the prediction (CV) and observation (UV-vis) that ferrocenium can only oxidize one of the two Fe^{II} centers of [Fe^{II}₂(H₂SIM¹)(μ-OAc)₂]⁺.

Both frozen solution spectra exhibit a sharp signal at $g \sim 4.3$ ($g_1 = 4.28$, $g_2 = 5.57$, $g_3 = 9.44$). This could arise from a mononuclear rhombic high-spin Fe^{III} complex present as impurity, most likely formed by decomposition of [Fe^{III}Fe^{II}(H₂SIM¹)(μ-OAc)₂]²⁺ in solution, or a decomposition product of ferrocenium hexafluorophosphate. The detection of a similar signal from a ferrocenium hexafluorophosphate solution which was left under aerobic conditions for two days indicates that the latter is the case. This is also supported by the fact that the spectrum of a powder of [Fe^{III}Fe^{II}(L⁵¹)(OBz)₂(OH)]BF₄ did not exhibit such signal.²⁶² The intense signals near $g \sim 4.3$ originate from the Fe^{III} center with almost axial symmetry ($g = 8.56, 5.45$) and rhombic symmetry ($g = 4.30$). However, such an impurity was often detected with solution EPR spectra of Fe^{III}Fe^{II} complexes, but the intensity was not as strong as in the spectra obtained with the mixtures of [Fe^{II}₂(H₂SIM¹)(μ-OAc)₂]⁺ with ferrocenium hexafluorophosphate. Therefore, it is not clear if the generated Fe^{III}Fe^{II} complex is stable enough to exist in solution, since the intense signal at $g \sim 4.3$ could arise from at least partial decomposition.

It should be noted that in the spectra recorded with heterovalent complexes of ligand HL⁵¹ in solution there is, besides the signal at $g \sim 1.7$, a broad signal at $g \sim 5-6$ which is absent in the iron proteins and HL¹ complexes. This signal shows also temperature dependence which is similar to that of the signal at $g \sim 1.7$. Therefore, the signals at $g \sim 5-6$ may be ascribed to the mononuclear complex in $S = 3/2$ spin state.²⁶² Those features were not detected in the spectra recorded with the mixture of [Fe^{II}₂(H₂SIM¹)(μ-OAc)₂]⁺ with ferrocenium hexafluorophosphate indicating that the intense signal at $g \sim 1.7$ arises from the decomposition of ferrocenium.

Mössbauer Spectroscopy

The heterovalent form of [Fe^{III}Fe^{II}(H₂SIM¹)(solvent)_x]⁴⁺, generated by oxidation of [Fe^{II}₂(H₂SIM¹)(μ-OAc)₂]⁺ with ferrocenium hexafluorophosphate was also studied by ⁵⁷Fe Mössbauer spectroscopy. A mixture of ⁵⁷Fe enriched [Fe^{II}₂(H₂SIM¹)(μ-OAc)₂]⁺ with one equivalent of ferrocenium hexafluorophosphate (as ⁵⁶Fe) as oxidant clearly showed after 12 hours at room temperature signals for both Fe^{III} and Fe^{II} (Figure 54b). Moreover, the presence of Fe^{III} and Fe^{II} in equimolar ratio emerges from the fact that the ratio of areas of the two sets of quadrupole doublets is nearly unity. Thus, [Fe^{III}Fe^{II}(H₂SIM¹)(solvent)_x]⁴⁺ appears to be stable in solution. In addition, the Mössbauer parameters of the characteristic high-spin Fe^{III} quadrupole doublet, $\delta(I) = 0.41(1)$ mm/s and $\Delta E_Q(I) = 0.36(2)$ mm/s ($\Gamma(I) = 0.38(1)$ mm/s), and the characteristic high-spin Fe^{II} quadrupole doublet, $\delta(II) = 1.17(1)$ mm/s and $\Delta E_Q(II) = 2.78(1)$ mm/s

($\Gamma(\text{II}) = 0.53(2)$ mm/s), are comparable to these of previously reported phenolate-bridged $\text{Fe}^{\text{III}}\text{Fe}^{\text{II}}$ complexes, *i.e.* $[\text{Fe}^{\text{III}}\text{Fe}^{\text{II}}(\text{L}^1)(\mu\text{-OPr})_2](\text{BPh}_4)_2$ ($\delta(\text{I}) = 0.48$ mm/s and $\Delta E_{\text{Q}}(\text{I}) = 0.50$ mm/s; $\delta(\text{II}) = 1.13$ mm/s and $\Delta E_{\text{Q}}(\text{II}) = 2.69$ mm/s),²³⁵ $[\text{Fe}^{\text{III}}\text{Fe}^{\text{II}}(\text{L}^1)(\mu\text{-ppa})_2](\text{BF}_4)_2$ ($\delta(\text{I}) = 0.48$ mm/s and $\Delta E_{\text{Q}}(\text{I}) = 0.56$ mm/s; $\delta(\text{II}) = 1.14$ mm/s and $\Delta E_{\text{Q}}(\text{II}) = 2.75$ mm/s),²³³ $[\text{Fe}^{\text{III}}\text{Fe}^{\text{II}}(\text{L}^4)(\mu\text{-OAc})_2]\text{ClO}_4$ ($\delta(\text{I}) = 0.52$ mm/s and $\Delta E_{\text{Q}}(\text{I}) = 1.10$ mm/s; $\delta(\text{II}) = 1.13$ mm/s and $\Delta E_{\text{Q}}(\text{II}) = 2.54$ mm/s),⁹⁴ and $[\text{Fe}^{\text{III}}\text{Fe}^{\text{II}}(\text{L}^{51})(\mu\text{-OAc})_2](\text{BF}_4)_2$ ($\delta(\text{I}) = 0.58$ mm/s and $\Delta E_{\text{Q}}(\text{I}) = 0.40$ mm/s; $\delta(\text{II}) = 1.29$ mm/s and $\Delta E_{\text{Q}}(\text{II}) = 2.81$ mm/s).²⁶² The ^{57}Fe Mössbauer spectrum of the asymmetric complex $[\text{Fe}^{\text{III}}\text{Fe}^{\text{II}}(\text{H}_2\text{SIM}^1)(\text{solv})_x]^{4+}$ shows distinct, *i.e.* valence trapped, Fe^{III} and Fe^{II} centers, indicating that each of the two metal ions is bound specifically in one of the two binding sites.

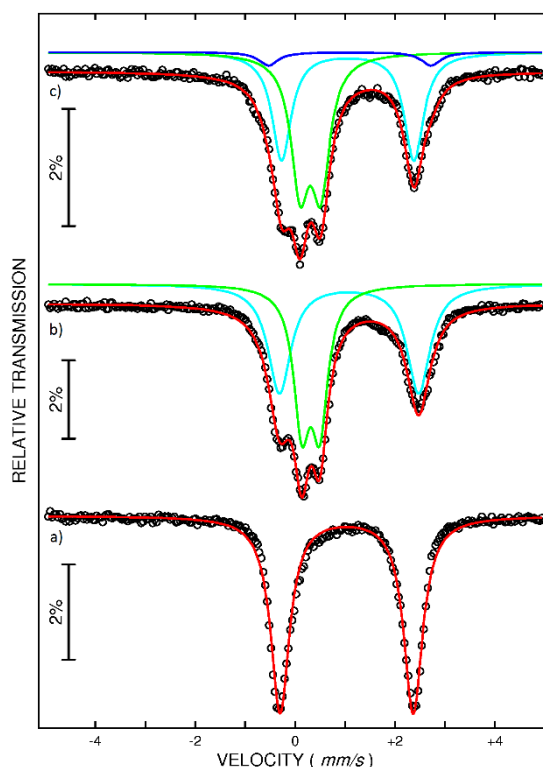


Figure 54: Comparison of ^{57}Fe Mössbauer spectra of $[\text{Fe}^{\text{II}}_2(\text{H}_2\text{SIM}^1)(\mu\text{-OAc})_2]\text{PF}_6$ a) in acetonitrile, b) with 1 eq of FeCp_2PF_6 and c) with 2 eq of FeCp_2PF_6 .

Addition of two equivalents of ferrocenium hexafluorophosphate to the solution of ^{57}Fe enriched $[\text{Fe}^{\text{II}}_2(\text{H}_2\text{SIM}^1)(\mu\text{-OAc})_2]^+$ in acetonitrile resulted in a comparable ^{57}Fe Mössbauer spectrum. The fitted parameters are $\delta(\text{I}) = 0.40(1)$ mm/s and $\Delta E_{\text{Q}}(\text{I}) = 0.41(1)$ mm/s ($\Gamma(\text{I}) = 0.43(1)$ mm/s) for Fe^{III} and $\delta(\text{II}) = 1.15(1)$ mm/s and $\Delta E_{\text{Q}}(\text{II}) = 2.65(1)$ mm/s ($\Gamma(\text{II}) = 0.46(2)$ mm/s) for Fe^{II} . This supports the proposed incapacity of the oxidant to oxidize both Fe^{II} centers of $[\text{Fe}^{\text{II}}_2(\text{H}_2\text{SIM}^1)(\mu\text{-OAc})_2]^+$ and the selective formation of the heterovalent $[\text{Fe}^{\text{III}}\text{Fe}^{\text{II}}(\text{H}_2\text{SIM}^1)(\text{solv})_x]^{4+}$ form.

5.5 SUMMARY

The two ligands H_3SIM^1 and H_3L^2 with two asymmetrically and two symmetrically disposed pivaloyl-amide moieties, respectively, lead to $[Fe^{II}_2(H_2SIM^1)(\mu-OAc)_2]PF_6$ and $[Fe^{II}_2(H_2L^2)(\mu-OAc)_2]PF_6$, after treatment with iron(II) acetate and hexafluorophosphate under anaerobic conditions. These complexes revealed the common structure for phenoxido-bridged phosphatase models bearing two bridging acetate co-ligands. NMR spectroscopy demonstrates that the symmetry provided by the ligands is still present in the diiron(II) complexes, $[Fe^{II}_2(H_2SIM^1)(\mu-OAc)_2]^+$ and $[Fe^{II}_2(H_2L^2)(\mu-OAc)_2]^+$, in solution. Under aerobic conditions only $[Fe^{III}Na(H_2SIM^1)(\mu-OAc)_2]PF_6$ could be isolated. However, with ^{57}Fe Mössbauer spectroscopy the formation of the corresponding Fe^{III}_2 complex was monitored in solutions of $[Fe^{II}_2(H_2SIM^1)(\mu-OAc)_2]PF_6$ and $[Fe^{III}Na(H_2SIM^1)(\mu-OAc)_2]PF_6$ under aerobic conditions. This diiron(III) complex is unstable under acidic conditions, reacting possibly via a concerted proton-electron transfer to generate an Fe^{II} species and a ligand-phenol radical. SQUID susceptibility measurements indicate that $[Fe^{II}_2(H_2SIM^1)(\mu-OAc)_2]PF_6$ consists of two weakly antiferromagnetically coupled high-spin Fe^{II} ions. This also emerges from solution magnetic susceptibility measurements, UV-vis and Mössbauer spectroscopy. The CV of $[Fe^{II}_2(H_2SIM^1)(\mu-OAc)_2]^+$ exhibits two reasonably well separated redox waves for the redox couples $Fe^{II}_2/Fe^{III}Fe^{II}$ and $Fe^{III}Fe^{II}/Fe^{III}_2$, and the K_{com} value indicates an appreciable stability of the mixed-valent $Fe^{III}Fe^{II}$ species. Therefore, the generation of the heterovalent diiron complex of H_3SIM^1 was probed. The successful formation of complex $[Fe^{III}Fe^{II}(H_2SIM^1)(solv)_x]^{4+}$ by chemical oxidation of $[Fe^{II}_2(H_2SIM^1)(\mu-OAc)_2]^+$ with ferrocenium hexafluorophosphate under anaerobic conditions was verified by ^{57}Fe Mössbauer, UV-vis and EPR spectroscopy. As a result of these studies an accurate model complex $[Fe^{III}Fe^{II}(H_2SIM^1)(solv)_x]^{4+}$ for the active form of mammalian PAPs became available with a heterovalent diiron core in a asymmetric coordination environment with the capacity to form a hydrogen bond network as exhibited for the native enzymes.

Chapter 6

Studies of the

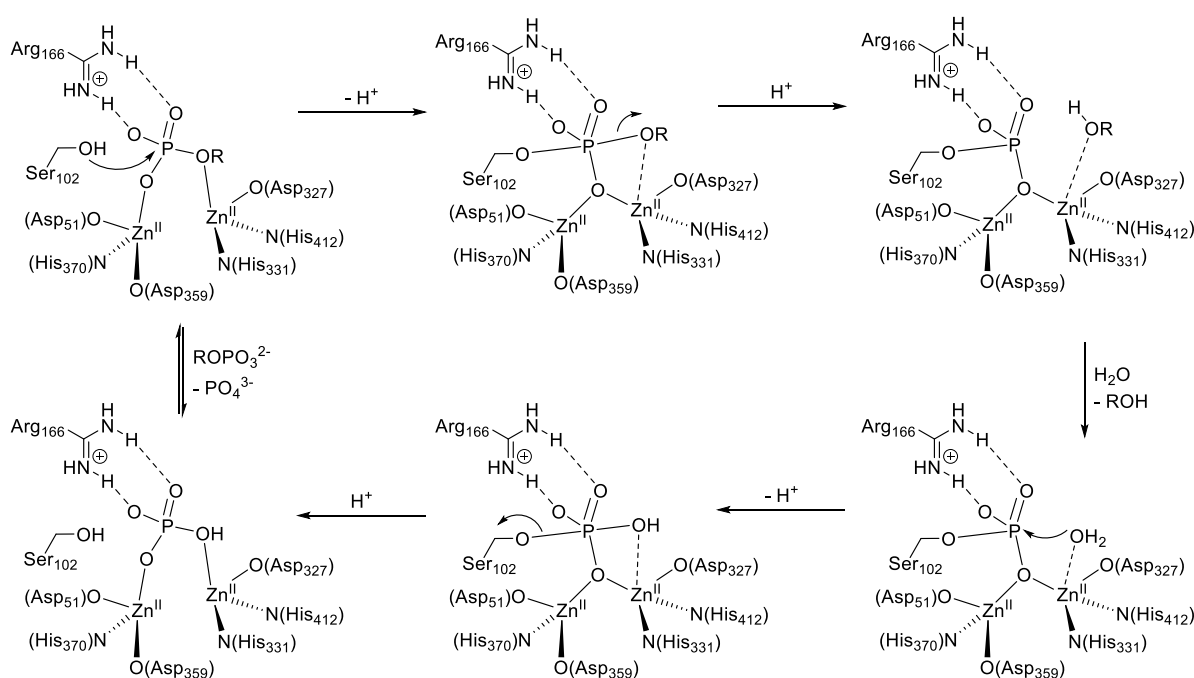
Phosphatase Mechanism

6.1 ENZYMIC MECHANISMS OF PHOSPHOESTER CLEAVAGE

Phosphatases are amongst the most efficient enzymes known with their ability to drastically reduce the activation energies associated with the hydrolytic cleavage of phosphoester bonds.¹¹ Acid Phosphatases, *e.g.* PAPs, which are most active at low pH, and Alkaline Phosphatases (APs), which exhibit their highest activity under basic conditions, are two particularly important classes.¹¹

Hydrolysis Mechanism Proposed for AP

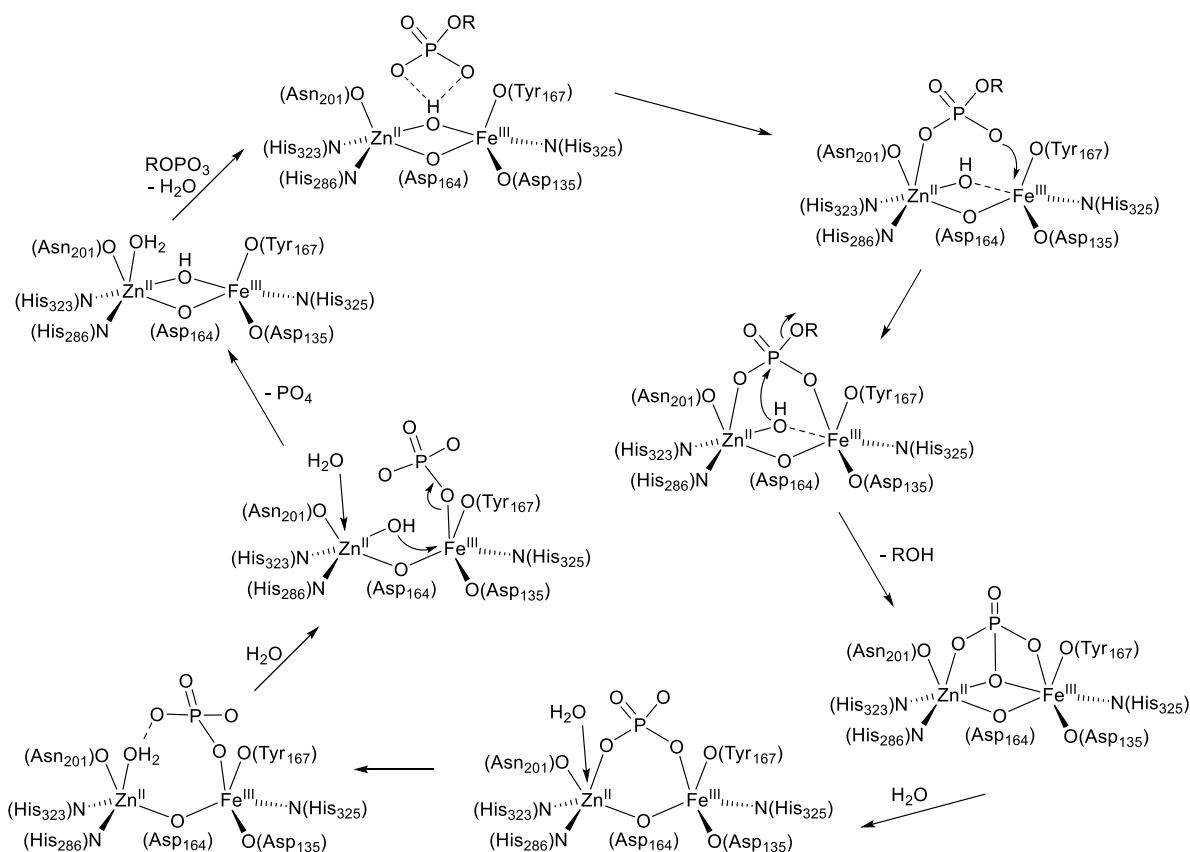
In the active site of AP the phosphoester substrate is activated by interaction with both Zn^{II} centers (Scheme 14).^{11, 263, 264} A proximal arginine residue is proposed to be involved in the substrate binding and the simultaneous activation of the substrate. The nucleophilic attack of the phosphoester substrate is accomplished by an alcohol group of a serine residue adjacent the dizinc(II) active core. The resulting transition state is also stabilized by the arginine residue adjacent to the dizinc(II) core. The release of the alcoholate leaving group is supported by the interaction with one Zn^{II} center. Subsequently, alcohol/water ligand exchange provides the nucleophilic water molecule necessary for the hydrolysis and this nucleophile attacks the bridging phosphate and thereby initiates the dissociation of the phosphate product, and the regeneration of the resting state.^{11, 263, 264}



Scheme 14: Proposed catalytic cycle for the AP of *E. coli*.^{11, 263, 264}

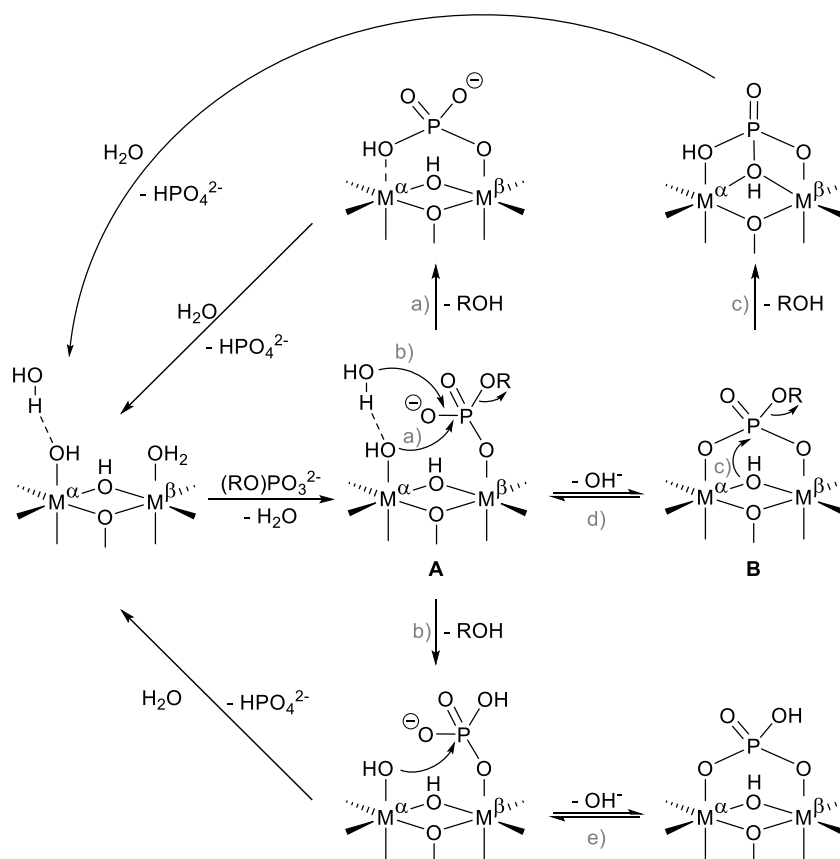
Catalytic Mechanisms Proposed for PAP

Recently, an eight step mechanism for the phosphoester hydrolysis by the heterodinuclear active site of PAPs was proposed (Scheme 15).^{25, 29} This catalytic cycle is based on X-ray structures, spectroscopic studies of different enzyme-inhibitor complexes and kinetic data for phosphoester hydrolysis. Prior to nucleophilic attack it was suggested that the phosphoester substrate is pre-coordinated in the second coordination sphere and stabilized via an extensive hydrogen bonding network, involving the μ -hydroxido ligand, the Zn^{II} coordinated asparagine residue and adjacent histidine residues. This proposal derives from stopped-flow kinetic measurements and a crystal structure of a kbPAP-sulfate complex in which a sulfate anion is coordinated in this fashion.^{25, 265, 266} Following this, the preorientation of the phosphoester leads to a monodentate and subsequently bridging coordination mode of the phosphoester substrate. The attacking nucleophile is proposed to be the asymmetrically bound μ -hydroxido ligand, although the nature of the nucleophile is still a matter of debate, and different proposals are discussed later in this chapter.^{25, 67, 69, 82, 85, 267, 268} After the esterolysis, the phosphate remains bound to the active site either in a tripodal or a μ -1,3-bridging coordination fashion, proposed on basis of crystal structures of different types of PAPs.^{26, 83, 85} The least understood step of the catalytic cycle is the regeneration of the resting state of the enzyme, which requires the removal of the phosphate group. The authors suggested a plausible sequence depicted in Scheme 15.²⁹



Scheme 15: Proposed reaction mechanism for PAP-catalyzed phosphoester hydrolysis based on X-ray structures.^{25, 29}

Various other suggestions regarding the catalytic mechanism of dinuclear phosphoesterases have been proposed, and these are summarized in Scheme 16.²⁶⁹ Early publications proposed the activation of the phosphoester substrate via monodentate coordination to the metal in binding site β and the subsequent attack of a M^α -bound terminal hydroxide ($M^\alpha = \text{Fe}^{\text{III}}$ in PAP), generating a pentacoordinated, associative-type phosphorus intermediate or transition state (Scheme 16, pathway a).^{83, 228}

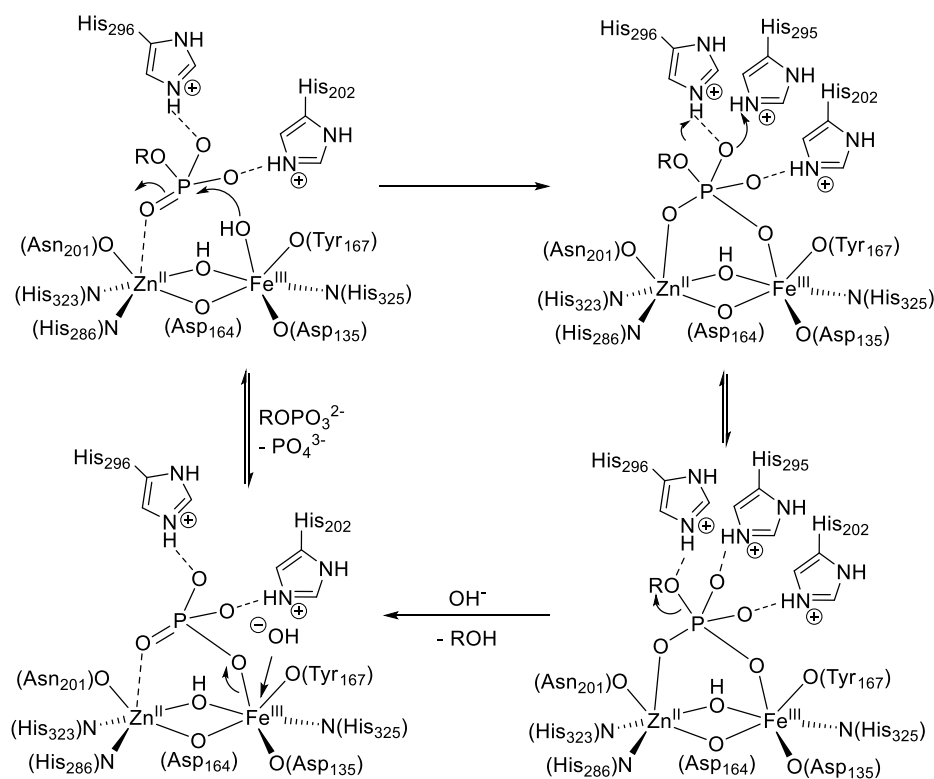


Scheme 16: Possible pathways for phosphoesterase catalyzed hydrolysis ($M^\alpha = \text{Fe}^{\text{III}}$, $M^\beta = \text{Fe}^{\text{II}}$, Zn^{II} , Mn^{II} for PAP; $M^\alpha = M^\beta = \text{Zn}^{\text{II}}$ for AP).²⁶⁹

However, stopped-flow kinetic studies with uFPAP in its native $\text{Fe}^{\text{III}}\text{Fe}^{\text{II}}$ form and the artificial $\text{Fe}^{\text{III}}\text{Mn}^{\text{II}}$ form revealed that the hydrolysis of the phosphoester substrate occurs faster than the perturbation of the $\text{Fe}^{\text{III}}\text{-O}_{\text{Tyr}}$ charge transfer transition.⁸² This supports a monodentate substrate binding but also indicates the hydroxide nucleophile not being directly bound to the Fe^{III} center. In addition, EPR spectroscopic results showed that the Fe^{III} in bsPAP is only slowly affected during the catalytic cycle of phosphoester hydrolysis, therefore, a ‘general-base’ mechanism has been proposed.²⁶⁷ Here, the M^α -bound hydroxide functions as base and activates a non-coordinated water molecule, which subsequently attacks the terminal phosphoester in binding site β (Scheme 16, pathway b); the phosphate product remains monodentately coordinated after the hydrolysis.²⁶⁹ A third pathway has been suggested, derived from the crystallographic data, where the phosphoester coordinates in a bridging fashion before being attacked by the bridging

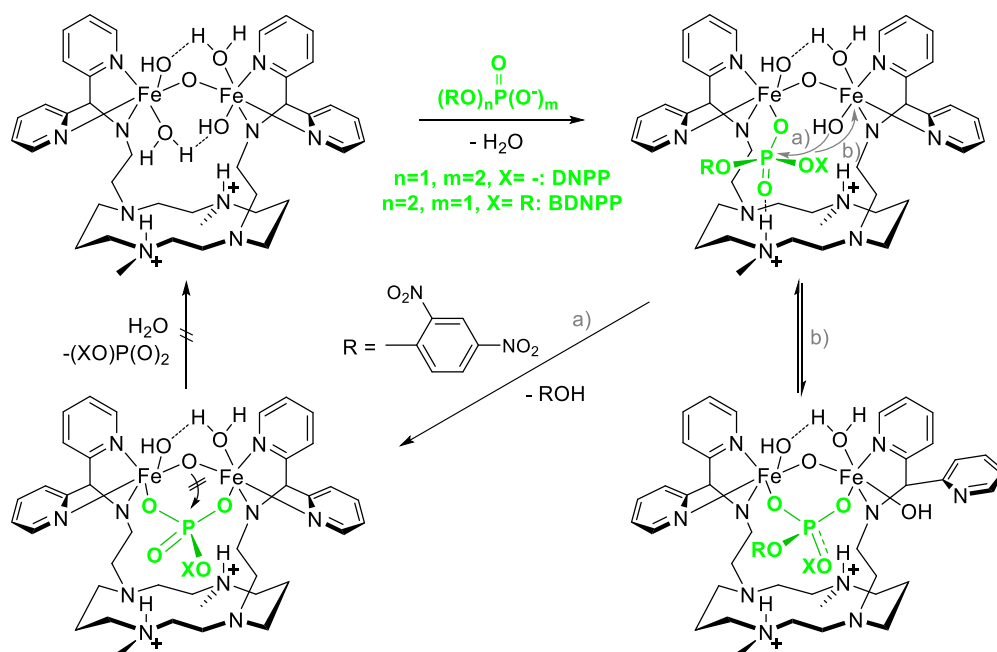
hydroxido ligand (Scheme 16, pathway c). However, the low nucleophilicity of a μ -hydroxido makes pathway a and pathway b more plausible.^{25, 270} These three different mechanisms were similarly discussed for AP consisting of two Zn^{II} centers in the active site.^{65, 271} Similarly, different inhibition processes are discussed that all include formation of catalyst-substrate or catalyst-inhibitor (hydrolysis product) adducts, containing the phosphates in a bridging coordination mode (Scheme 16, pathway d and e).^{83, 228} The presence of these equilibria was supported by labeling studies with ¹⁸O-phosphate, which demonstrated successive oxygen exchange between enzyme bound phosphate and water.²⁷²

It is likely that, depending on the metal composition in the active site and the substrate used, different mechanisms operate.⁶⁶ However, there is an ongoing debate about (i) the substrate coordination mode (monodentate (Scheme 16, species A) vs. bridging (Scheme 16, species B)), (ii) the type of the attacking nucleophile, and (iii) the reaction type (concerted vs. stepwise). Moreover, the impact of the second coordination sphere with respect to the catalytic mechanism is still not fully understood, although it is apparent that the histidine residues proximal to the dimetallic core play an important role in the phosphoester hydrolysis activity of PAPs.^{25, 82, 83} Klabunde *et al.* proposed a reaction mechanism (Scheme 17) where these histidine residues, essential for catalysis, were involved in the active site of kbPAP.⁸³



Scheme 17: Proposed reaction mechanism for PAP-catalyzed phosphoester hydrolysis, considering the second coordination sphere of the enzyme.⁸³

Interaction with the protonated histidine residues promote (i) binding and activation of the substrate, (ii) transition state stabilization, and (iii) release of the leaving group, thus explaining the enhanced activity at low pH. This mechanism was supported by DFT studies, undertaken to understand the importance of hydrogen bonds within the reaction mechanism and to identify the reasons that enable the model system $[\text{Fe}^{\text{III}}_2(\text{L}^6)(\mu\text{-O})\text{Cl}_4](\text{Cl})_2$ to hydrolyze not only the phosphodiester model substrate BDNPP but also the phosphomonoester model substrate DNPP (Scheme 18).^{108, 109} Relative energies of this model complex, binding the substrates either in a monodentate or in a bridging mode, were calculated and compared. While the phosphodiester BDNPP is more likely bound in a monodentate fashion, stabilized by the formation of hydrogen bonds to the protonated cyclam ring, the phosphomonoester DNPP is proposed to interchange between the monodentate and the bridging mode due to a relatively small activation barrier. Once the phosphomonoester substrate is coordinated to one of the Fe^{III} ions two reaction pathways are possible: either the phosphoester-bridged complex is formed, leading to the deactivation of the catalyst (Scheme 18, pathway b), or the nucleophilic attack via the hydroxido ligand bound to the second Fe^{III} ion takes place (Scheme 18, pathway a), resulting in the hydrolysis of the substrate. These competitive reactions were compared by relaxed potential energy surface scans conducted by stepwise decrease of the distance between the non-coordinated Fe^{III} ion and the oxygen atom of DNPP in the case of inhibition (Scheme 18, pathway b) or the hydroxido ligand oxygen atom and the phosphorus atom of DNPP in the case of hydrolysis (Scheme 18, pathway a).^{108, 109}



Scheme 18: Proposed catalytic cycle for the hydrolysis of BDNPP and DNPP with the use of the Fe^{III}_2 complex of H_2L^6 .^{108, 109}

With these DFT studies it was elucidated that (i) the activation barrier of the deactivation is higher than of the cleavage of the phosphoester bond and (ii) the lack of hydrogen bond formation capacity (using a deprotonated cyclam backbone) leads to a smaller energy difference between the two possible reaction pathways.^{108, 109} Thus, the capacity of this model complex $[\text{Fe}^{\text{III}}_2(\text{L}^6)(\mu\text{-O})\text{Cl}_4](\text{Cl})_2$ for cleaving a phosphomonoester was ascribed to the involvement of a hydrogen bond network in the reaction mechanism.

Although the two catalytic mechanisms of PAP and AP differ in the interaction that places the phosphoester substrate in the ideal position for the nucleophilic attack and, more importantly, in the nature of the attacking nucleophile, there are some common features, *i.e.* (i) the activation of the substrate by Lewis acid metal ion coordination and hydrogen bonding interactions with side-chains of adjacent residues, (ii) promotion of the transition state formation by the metal ions and hydrogen bonding residues, and (iii) the assistance of the release of the alkoxide leaving groups via stabilizing interaction with the extensive hydrogen bonding network in the active site.¹¹

However, it should not be underestimated that in addition to specific chemical features, the remarkable catalytic activity of phosphatase enzymes may also derive from the polarity and the steric demand of the environment of the active site.²⁷³ It has been suggested that the catalysis of enzymes is promoted by binding of the substrate in hydrophobic pockets with an apparent dielectric constant much lower than the surrounding water. In this way, both the equilibrium for proton transfer reactions is shifted and the strengths of hydrogen bonds, involving the substrate binding and the transition state stabilization, are changed.²⁷⁴ Bond cleavage in enzymes is also known to be promoted by straining of the substrate in order to support the formation of the transition state.¹¹

In the following chapters kinetic studies with the complexes developed in this work (Chapter 3, 4, and 5) will be discussed. The emphasis was on a correlation of the position of the hydrogen bonding residues in the active site of the model complexes with the catalytic efficiencies. However, the influence of sterically demanding residues as well as the impact of a more electron-rich primary coordination site was also studied.

6.2 PHOSPHOESTER SUBSTRATES EMPLOYED IN CLEAVAGE STUDIES

In order to access the cleavage activity of phosphatase model complexes a number of non-natural substrate models have been used as mimics of natural phosphate linkages. The model

substrates employed to study the phosphoester binding with the model complexes developed in this work are 4-nitrophenylphosphate (PNPP) (as its disodium salt), bis(4-nitrophenyl)phosphate (BPNPP), 2,4-dinitrophenylphosphate (DNPP) (as its 2,6-lutidinium salt) and bis(2,4-dinitrophenyl)phosphate (BDNPP) (as its pyridinium salt); these are shown in Chart 19. PNPP and BPNPP are commercially available, BDNPP and DNPP were prepared following reported procedures as described in detail in Chapter 11.14.

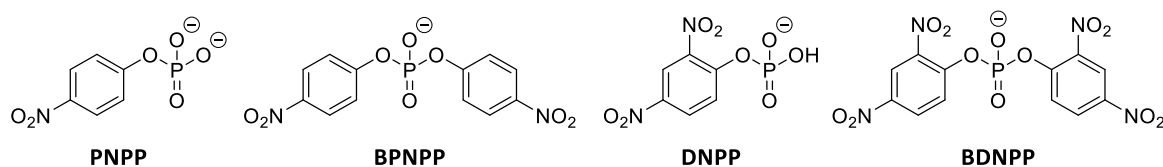
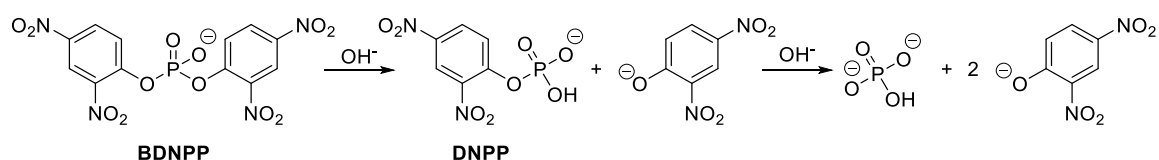


Chart 19: Phosphoester model substrates employed in this work.

The phosphoester hydrolysis reactivity of the catalysts developed in this work was probed with a spectrophotometric assay using BDNPP (phosphodiester) and DNPP (phosphomonoester) as model substrates. These phosphoester compounds were chosen because of their well-demonstrated and -documented use with various catalysts.^{11, 81} They also serve as an appropriate comparison of the results obtained with those from past works since these substrates are commonly used. In Scheme 19 the hydrolysis of the phosphodiester BDNPP under basic conditions is shown. Cleavage of BDNPP forms DNPP by release of 2,4-dinitrophenolate. The phosphomonoester product DNPP can be further hydrolyzed in a second step.



Scheme 19: Hydrolysis of BDNPP and DNPP under basic conditions releasing 2,4-dinitrophenolate.

Cleavage of the phosphorous-oxygen bond of BDNPP or DNPP was followed, for approximately three minutes, at 25°C by monitoring the generated product 2,4-dinitrophenolate by its strong absorption at 400 nm ($\epsilon = 12,100 \text{ M}^{-1}\text{cm}^{-1}$). The initial hydrolysis rate v_0 was calculated from the initial rate of the increase of the absorbance at 400 nm.

It is important to note, that the model substrates BDNPP and DNPP are activated towards cleavage as the resulting product is strongly stabilized via resonance. Moreover, spontaneous hydrolysis of the model substrate takes place in basic solution. Therefore, all experiments were conducted in triplicate and the average data were subsequently corrected from the autohydrolysis by subtraction of the v_0 value obtained with measurements in the absence of a catalyst.

6.3 GENERAL PROCEDURES

Before the results of the kinetic investigations are discussed in the following chapters the general procedure applied will be introduced.

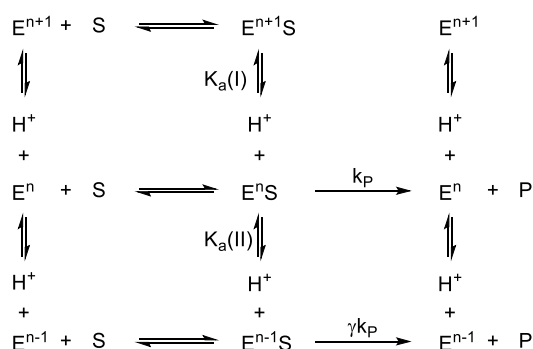
6.3.1 PH DEPENDENCE ASSAYS

By varying the pH of the multicomponent buffer, the pH dependence of the activity was studied in the pH range from 5 to 11. The pH values refer to the aqueous component, and it should be noted that the pH of an aqueous solution of the buffer is the same within error as in a 1:1 mixture of buffer and acetonitrile.^{275, 276} The resulting data were fitted either to Equation 20 describing a monoprotic system or to Equation 21 which is based on a model for a diprotic system with two active species E^n and E^{n-1} (Scheme 20).²⁷⁷

$$\text{Equation 20} \quad v_0 = \frac{v_{\max}}{1 + \frac{[H^+]}{K_a}}$$

$$\text{Equation 21} \quad v_0 = \frac{v_{\max} \left(1 + \frac{\gamma K_{a2}}{[H^+]} \right)}{\left(1 + \frac{[H^+]}{K_{a1}} + \frac{K_{a2}}{[H^+]} \right)}$$

Here, v_0 is the initial reaction rate and v_{\max} is the maximum reaction rate that is reached under given conditions. The factor γ is related to the relative activity of the two active species in equilibrium (E^nS and $E^{n-1}S$); a value of γ less than unity corresponds to a more active E^nS adduct and a value higher than 1 considers the deprotonated adduct $E^{n-1}S$ as more active.^{277, 278} The K_a values obtained are the protonation equilibrium constants between the two relevant active species.



Scheme 20: Model of a diprotic system with two active species on which Equation 21 is based on.²⁷⁷

6.3.2 SUBSTRATE CONCENTRATION DEPENDENCE ASSAYS

The measurements of the dependence of the BDNPP hydrolysis rate on the substrate concentration were determined at a range of pH values to assess the catalytic behavior of different protonation states. Due to the poor solubility of BDNPP in acetonitrile, assays with a starting concentration of the substrate higher than 11.5 mM could not be investigated. If the dependence of the rate of hydrolysis on the BDNPP concentration showed Michaelis-Menten saturation behavior, the experimental data were fitted to Equation 22 in order to determine the kinetic parameter values for the Michaelis-Menten constant K_M and the maximum reaction rate v_{max} .^{279, 280} K_M describes the substrate concentration required for the enzyme/catalyst to reach one-half of its maximum cleavage reaction rate.

$$\text{Equation 22} \quad v_0 = \frac{v_{max}[\text{BDNPP}]_0}{K_M + [\text{BDNPP}]_0}$$

Applying Equation 23 the catalytic rate k_{cat} , which describes the number of substrate molecules cleaved by one active site per second, was evaluated. The efficiency of the catalyst is expressed as k_{cat}/K_M .

$$\text{Equation 23} \quad k_{cat} = \frac{v_{max}}{[\text{complex}]_0}$$

6.3.3 TURN OVER NUMBERS

Long-term studies regarding the catalytic activity of the catalysts developed in this thesis were conducted preparing assays with an excess of phosphoester substrate and leaving them to react at room temperature for up to two weeks. During the experiment, samples were taken at various intervals, diluted with solvent (mixture acetonitrile:MilliQ-water (1:1)), and their UV-vis spectra were recorded to determine the amount of phosphoester hydrolysis. The increase in the absorbance at 400 nm, assigned to the hydrolysis product, 2,4-dinitrophenolate, was monitored over time and turn over numbers calculated using the Beer-Lambert Law.

Chapter 7

Phosphatase Activity of Dizinc Complexes^f

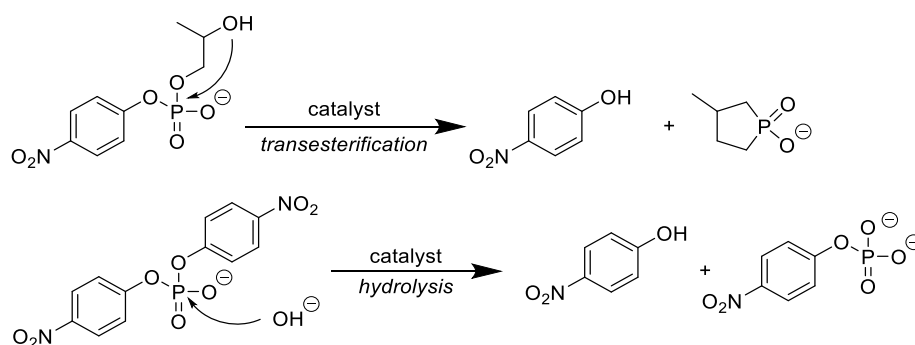
^f Main parts of this chapter are published in “Dinuclear Zinc(II) Complexes with Hydrogen Bond Donors as Structural and Functional Phosphatase Models”; [Simone Bosch](#), Peter Comba, Lawrence R. Gahan, Gerhard Schenk, *Inorg. Chem.* **2014**, *53*, 9036-9051.

7.1 INTRODUCTION

The facile catalyzed cleavage of phosphoesters is a crucial reaction for living organisms, for example in processing RNA replication and bone metabolism, and it is of ecological importance in the detoxification of pesticides. Natural phosphatases, which accomplish this hydrolysis, commonly contain Zn^{II} ions in their active sites. Therefore, dizinc(II) complexes have been widely used as artificial models to expand our understanding of the hydrolysis mechanism in the native enzymes and to promote the development into new therapeutic agents.

Attention in the design of model complexes has been mainly focused on the influence of (i) the Zn^{II}...Zn^{II} distance, (ii) the moieties bridging the two Zn^{II} centers, and (iii) the Zn^{II} coordinating residues in the primary coordination sphere.^{28, 65, 271, 281, 282} Whilst many zinc(II) complexes of simple chelating ligands were reported to be effective in hydrolyzing phosphoesters, the catalytic rates generally were found to be modest compared to the native nucleases and phosphatases. Thus, in recent years emphasis has been put in the secondary coordination sphere of the Zn^{II} center(s) of model complexes, because many metalloenzymes that catalyze the cleavage of phosphoesters also use amino acid side chains to preorientate the substrate molecule and to stabilize the transition state.^{80, 84} The development of complexes incorporating functionalities, imitating the environment proximal to the dimetallic core of nucleases and phosphatases, resulted in complexes with increased acceleration capacity compared to their non-functionalized counterparts.

Before introducing examples of zinc(II) model complexes considering the secondary interactions within the active site of phosphatases, it should be noted that the kinetic studies of those complexes were often undertaken using the RNA model substrate HPNPP (2-hydroxypropyl-4-nitrophenylphosphate). In the case of HPNPP the P-O bond cleavage is introduced by the nucleophilic attack of an alkoxide (in contrast to a hydroxide nucleophile for the hydrolysis of BNPP, BDNPP and DNPP (Scheme 21, bottom)), followed by the release of an alkoxide group (Scheme 21, top). Therefore, the process is termed transesterification, while the attack by a hydroxide is known as hydrolysis.¹¹



Scheme 21: Transesterification of HPNPP (top) and hydrolysis of BNPP (bottom).

Although the processes differ in the type of nucleophile initiating the cleavage reaction, they have commonalities in (i) the activation of the phosphoester by coordination to a Zn^{II} center and (ii) the proposed formation of a five-coordinate trigonal bipyramidal phosphorus atom in the transition state.

Breslow *et al.* were the first to explore the effect of functional groups within simple metal complexes, their intention being to emulate secondary enzyme active site features that are either known or postulated to contribute to the phosphoester cleavage activity. The incorporation of basic groups such as thiophenolate or imidazole as in $[Zn^{II}(HL^{53})]^{2+}$ and $[Zn^{II}(HL^{54})]^{2+}$ were shown to accelerate HPNPP cleavage 9-fold and 20-fold, respectively, compared to the reference complex $[Zn^{II}(HL^{52})]^{2+}$ (Chart 20).²⁸³

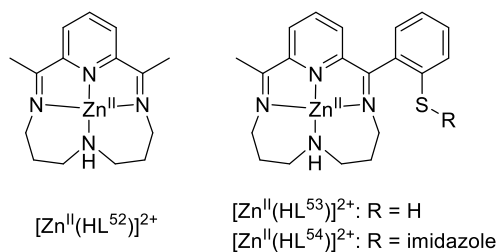


Chart 20: Zinc(II) complexes employed by Breslow *et al.* studying the impact of basic residues proximal to the Zn^{II} center.²⁸³

Subsequently Kövári and Krämer reported a significant increase in BPNPP cleavage activity by incorporation of amine groups at the end of rigid alkyne pendants of Zn^{II} -bpy complexes.¹⁵⁷ While the BPNPP hydrolysis activity for $[Zn^{II}(L^{55})(OH_2)_3]^{2+}$ (Chart 21) was found to be similar to that of the parent complex $[Zn^{II}(bpy)(OH_2)_3]^{2+}$, a significantly higher hydrolysis rate was observed with complex $[Zn^{II}(L^{56})(OH_2)_3]^{2+}$ (Chart 21), ascribed to the hydrogen bonding capacity of the amino residues.¹⁵⁷

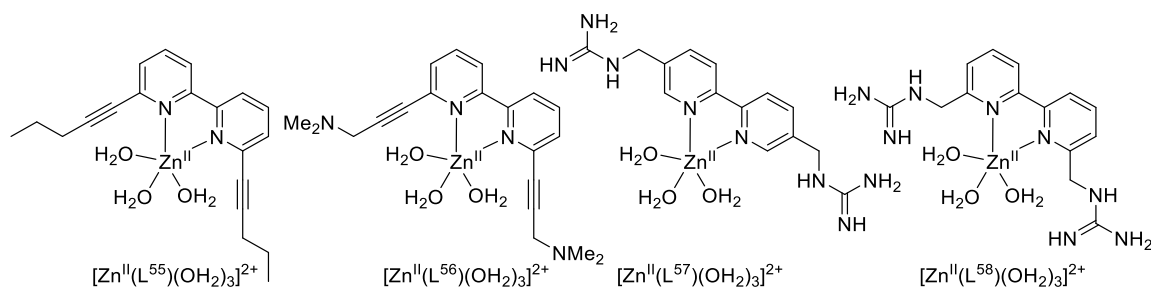


Chart 21: Zinc(II) complexes used by K v ri, Kr mer and He *et al.* to study the effect of hydrogen bonding towards the phosphoester cleavage.^{157, 284}

With a similar model system the effect of guanidinium residues, mimicking the secondary coordination sphere of phosphatases at different positions with respect to the Zn^{II} center, was investigated by He *et al.*²⁸⁴ The kinetic data revealed that [Zn^{II}(L⁵⁷)(OH₂)₃]²⁺ and [Zn^{II}(L⁵⁸)(OH₂)₃]²⁺ (Chart 21) accelerated BPNPP hydrolysis nearly 300-fold and 600-fold, compared to their analogous [Zn^{II}(bpy)(OH₂)₃]²⁺ complex, missing guanidinium groups (Table 18).²⁸⁴

Table 18: Kinetic data (k_{cat} in [10⁻³ s⁻¹], K_{M} in [mM] and $k_{\text{cat}}/K_{\text{M}}$ in [s⁻¹M⁻¹]) of BPNPP hydrolysis reported for [Zn^{II}(bpy)(OH₂)₃]²⁺, [Zn^{II}(L⁵⁸)(OH₂)₃]²⁺, and [Zn^{II}(L⁵⁷)(OH₂)₃]²⁺ (all kinetic studies were undertaken in aqueous solution).²⁸⁴

complex	k_{cat}	K_{M}	$k_{\text{cat}}/K_{\text{M}}$	pH _{MM}
[Zn ^{II} (bpy)(OH ₂) ₃] ²⁺	0.57·10 ⁻³	6.82	8.35·10 ⁻⁵	7.2
[Zn ^{II} (L ⁵⁷)(OH ₂) ₃] ²⁺	0.14	2.08	0.07	7.2
[Zn ^{II} (L ⁵⁸)(OH ₂) ₃] ²⁺	0.37	0.70	0.53	7.2

Due to the fact that the K_{M} values for [Zn^{II}(L⁵⁷)(OH₂)₃]²⁺ and [Zn^{II}(L⁵⁸)(OH₂)₃]²⁺, both bearing guanidinium groups, were lower than for the reference complex [Zn^{II}(bpy)(OH₂)₃]²⁺, the hydrogen bond donors in the ligands were proposed to facilitate phosphodiester cleavage by interaction with the substrate. Furthermore, the guanidinium arms were postulated (i) to assist the binding of the phosphate substrate to the Zn^{II} ion, (ii) to act as additional Lewis acid, which polarizes the phosphate substrate, and (iii) potentially to protonate the leaving group.²⁸⁴

Similarly, the positive contribution of non-coordinating amines in Zn^{II} complexes of tris(pyridylmethyl)amine towards the HPNPP cleavage efficiency was exhibited with the complexes [Zn^{II}(L²¹)(OH₂)₃]²⁺ ($k_{\text{cat}}/K_{\text{M}} = 1.0 \cdot 10^{-3} \text{ M}^{-1}\text{s}^{-1}$) and [Zn^{II}(L²⁵)(OH₂)₃]²⁺ ($k_{\text{cat}}/K_{\text{M}} = 7.9 \cdot 10^{-2} \text{ M}^{-1}\text{s}^{-1}$) (Chart 22), ascribed to the capacity of the amino groups to activate the bound substrate towards intramolecular nucleophilic attack via hydrogen bonding.^{11, 110} Such interactions were confirmed by a crystal structure of [Zn^{II}(L²⁴)(NO₃)]⁺ derived from a similar ligand with two amino residues, forming hydrogen bonds to the coordinating oxygen atom of a NO₃⁻ anion.²⁸⁵ On the basis of DFT calculations a general base catalysis mechanism for the phosphodiester cleavage by complex [Zn^{II}(L²⁵)(OH₂)₃]²⁺ was proposed, in which hydrogen-bonding interactions serve to stabilize the key

five-coordinate phosphorus intermediate as well as lower the energy barrier of proton transfer reactions by enhancing solvation.^{11, 286}

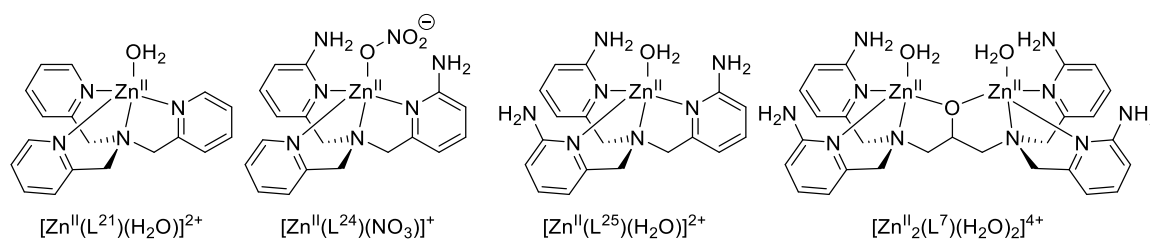


Chart 22: Zinc(II) complexes employed to study the impact of amino residues towards the cleavage of phosphodiester.^{110, 112, 285}

Recently the approach to incorporate hydrogen bond donors into zinc(II) model complexes has been extended to the synthesis of dinuclear metal-ion complexes with hydrogen bond donors in proximity to the metal centers. In this way, the dizinc(II) system $[\text{Zn}^{\text{II}}_2(\text{L}^7)(\text{OH}_2)_2]^{4+}$ was developed to be capable of forming four hydrogen bonds with a phosphate ester substrate as demonstrated by a X-ray structure of $[\text{Zn}^{\text{II}}_2(\text{L}^7)(\text{PNPP})]^{3+}$.¹¹² $[\text{Zn}^{\text{II}}_2(\text{L}^7)(\text{OH}_2)_2]^{4+}$ is currently one of the most active synthetic cleavage agents, accelerating the cleavage of HPNPP by a factor of almost a million ($k_{\text{cat}} = 0.017 \text{ s}^{-1}$, $K_{\text{M}} = 0.32 \text{ mM}$ at $\text{pH} = 7.4$), ascribed to the cooperation of double Lewis activation by two Zn^{II} ions within the complex and the hydrogen bonding environment provided by the ligand backbone.¹¹²

Studying the phosphoester cleavage activity of *m*-xylyl based dizinc(II) complexes substituted with alkyl, amino or acetamido residues (Chart 23) an increased activity towards HPNPP transesterification while all functionalized dizinc(II) complexes $[\text{Zn}^{\text{II}}(\text{L}^{60})(\text{OH}_2)_2]^{2+}$, $[\text{Zn}^{\text{II}}(\text{L}^{61})(\text{OH}_2)_2]^{2+}$ and $[\text{Zn}^{\text{II}}(\text{L}^{62})(\text{OH}_2)_2]^{2+}$ exhibited greater activity than the parent complex $[\text{Zn}^{\text{II}}(\text{L}^{59})(\text{OH}_2)_2]^{2+}$.²⁸⁷

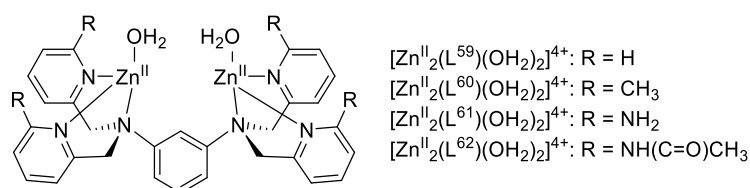


Chart 23: Dizinc(II) complexes used to study the impact of methyl, amino and acetamido functionalities proximal to the Zn^{II} centers.²⁸⁷

Closer inspection of the kinetic data revealed that the differences in the H-bond donating abilities of the amino and acetamido residues are only subtly manifested in the strength of substrate binding by $[\text{Zn}^{\text{II}}(\text{L}^{61})(\text{OH}_2)_2]^{2+}$ and $[\text{Zn}^{\text{II}}(\text{L}^{62})(\text{OH}_2)_2]^{2+}$ (K_{M} differs by ~ 3.5) and the catalytic rate constant (factor of 2).²⁸⁷

Table 19: Kinetic data (k_{cat} in $[\text{s}^{-1}]$, K_{M} in $[\text{mM}]$ and $k_{\text{cat}}/K_{\text{M}}$ in $[10^3 \text{ s}^{-1}\text{M}^{-1}]$) of HPNPP transesterification reported for $[\text{Zn}^{\text{II}}_2(\text{L}^{59})(\text{OH}_2)_2]^{4+}$, $[\text{Zn}^{\text{II}}_2(\text{L}^{60})(\text{OH}_2)_2]^{4+}$, $[\text{Zn}^{\text{II}}_2(\text{L}^{61})(\text{OH}_2)_2]^{4+}$, and $[\text{Zn}^{\text{II}}_2(\text{L}^{62})(\text{OH}_2)_2]^{4+}$ (all kinetic studies were undertaken in methanol under optimal pH conditions).²⁸⁷

complex	k_{cat}	K_{M}	$k_{\text{cat}}/K_{\text{M}}$
$[\text{Zn}^{\text{II}}_2(\text{L}^{59})(\text{OH}_2)_2]^{4+}$	0.13	0.08	1.6
$[\text{Zn}^{\text{II}}_2(\text{L}^{60})(\text{OH}_2)_2]^{4+}$	6.2	0.21	29.8
$[\text{Zn}^{\text{II}}_2(\text{L}^{61})(\text{OH}_2)_2]^{4+}$	3.89	0.24	16
$[\text{Zn}^{\text{II}}_2(\text{L}^{62})(\text{OH}_2)_2]^{4+}$	7.2	0.07	109

However, comparison of the K_{M} values reveals that (i) the acetamide derivative $[\text{Zn}^{\text{II}}_2(\text{L}^{62})(\text{OH}_2)_2]^{4+}$ and the unsubstituted complex $[\text{Zn}^{\text{II}}_2(\text{L}^{59})(\text{OH}_2)_2]^{4+}$ have comparable substrate affinity, and (ii) both the methyl derivative $[\text{Zn}^{\text{II}}_2(\text{L}^{60})(\text{OH}_2)_2]^{4+}$ and the amino derivative $[\text{Zn}^{\text{II}}_2(\text{L}^{61})(\text{OH}_2)_2]^{4+}$ bind the phosphoester substrate slightly more weakly than does $[\text{Zn}^{\text{II}}_2(\text{L}^{59})(\text{OH}_2)_2]^{4+}$, missing those functionalities. Moreover, the hydrolysis rates are in the same range for all substituted complexes suggesting that the different functionalities (alkyl, amino, acetamido) are all equally capable of stabilizing the transition state. In conclusion, the effect of the functionalization of the dizinc(II) catalyst with hydrophobic and sterically demanding CH_3 groups seems comparable afforded by amino and acetamido substituents.²⁸⁷ Therefore, other effects such as steric and local polarity seem to be as important in such systems as hydrogen-bond formation and should be considered in order to generate more active model complexes.

The function of the Zn^{II} ions during transesterification is the activation of the substrate, and a positive effect of adjacent hydrogen bond donors on the substrate activation was discovered studying mono- and dinuclear model complexes, providing hydrogen bond donors proximal to the Zn^{II} center(s). In the case of the phosphoester hydrolysis the task of the metal ions in the model complexes is not only the phosphoester activation but also the generation of the hydroxide nucleophile. Although a positive effect of the presence of two Zn^{II} ions in close distance has been reported to have an accelerating effect on the hydrolysis of phosphoester,^{86-89, 288} the impact of hydrogen bond donors has only been studied with a few monozinc(II) complexes providing hydrogen bonding capacity. In this work, the two strategies of (i) a dinuclear core and (ii) the provision of hydrogen bonding ability was combined to develop more accurate dizinc(II) model complexes for phosphatases. More precisely, dizinc(II) complexes have been prepared with amino and pivaloyl-amide residues in the 2-position of two of the four coordinating pyridine moieties (Chart 24). The synthesis and characterization of these dizinc(II) complexes has been discussed in Chapter 4.

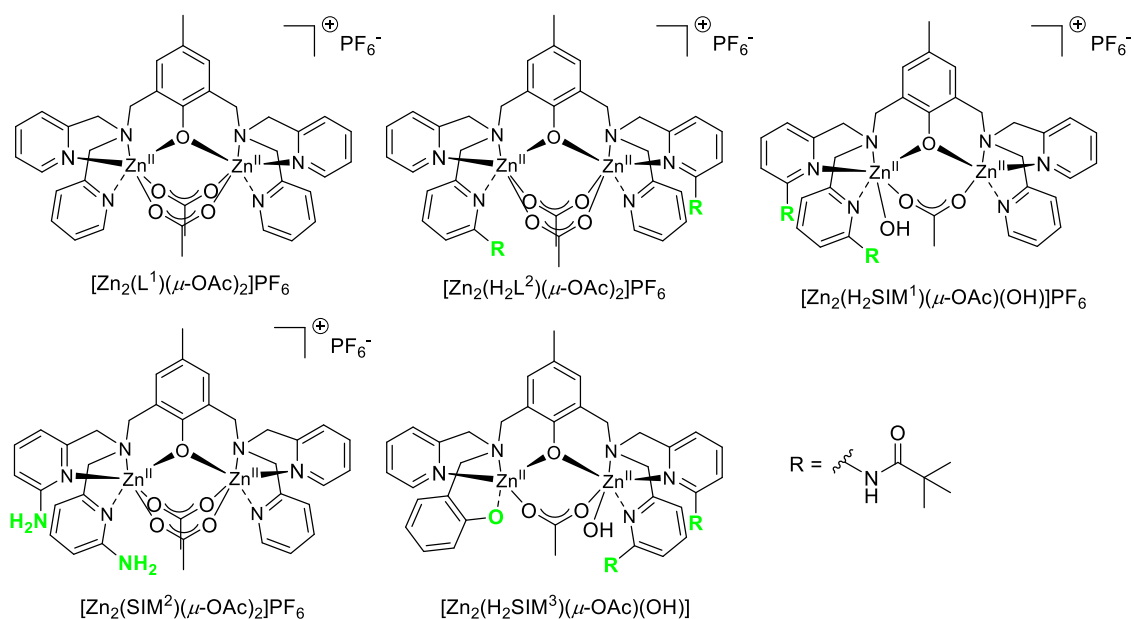


Chart 24: Dizinc(II) complexes employed in this chapter.

Comparison of the functionalized complexes $[Zn^{II}_2(H_2L^2)(\mu-OAc)_2]^+$, $[Zn^{II}_2(H_2SIM^1)(\mu-OAc)(OH)]^+$, and $[Zn^{II}_2(SIM^2)(\mu-OAc)_2]^+$ to the unsubstituted complex $[Zn^{II}_2(L^1)(\mu-OAc)_2]^+$ enables the study of the impact of hydrogen bond donors proximal the dizinc(II) center towards the hydrolysis of phosphoesters. Moreover, an insight in the effect of the position of hydrogen bond donors could be achieved via comparison of the two complexes $[Zn^{II}_2(H_2SIM^1)(\mu-OAc)(OH)]^+$ and $[Zn^{II}_2(H_2L^2)(\mu-OAc)_2]^+$, both bearing pivaloyl-amide residues, but at different positions with regard to the dizinc(II) core. Similarly, comparison of the asymmetric complexes $[Zn^{II}_2(SIM^2)(\mu-OAc)_2]^+$, bearing amino residues and $[Zn^{II}_2(H_2SIM^1)(\mu-OAc)(OH)]^+$, bearing sterically demanding pivaloyl-amide residues revealed information on the effect of a hindered Zn^{II} center in a dizinc(II) complex. Furthermore, the two complexes $[Zn^{II}_2(H_2SIM^1)(\mu-OAc)(OH)]^+$ and $[Zn^{II}_2(H_2SIM^3)(\mu-OAc)(OH)]$, which are identical with regard to the secondary coordination sphere, but differ in one of the coordinating ligands in the primary coordination sphere, enables the investigation of combining an asymmetric primary coordination sphere with an asymmetric secondary coordination sphere within a dizinc(II) complex.

7.2 PHOSPHOESTER HYDROLYSIS STUDIES OF DIZINC(II) COMPLEXES

The phosphoester hydrolysis reactivity of $[\text{Zn}^{\text{II}}_2(\text{L}^1)(\mu\text{-OAc})_2]^+$, $[\text{Zn}^{\text{II}}_2(\text{H}_2\text{L}^2)(\mu\text{-OAc})_2]^+$, $[\text{Zn}^{\text{II}}_2(\text{H}_2\text{SIM}^1)(\mu\text{-OAc})(\text{OH})]^+$, $[\text{Zn}^{\text{II}}_2(\text{SIM}^2)(\mu\text{-OAc})_2]^+$, and $[\text{Zn}^{\text{II}}_2(\text{H}_2\text{SIM}^3)(\mu\text{-OAc})(\text{OH})]$ was probed with a spectrophotometric assay using BDNPP as model substrate. The general experimental procedure explained in Chapter 6.3 was applied.

pH and Concentration Dependence

The rate vs. pH profiles for three of the dizinc(II) complexes show a nearly sigmoidal shape, whereas the corresponding profile for $[\text{Zn}^{\text{II}}_2(\text{H}_2\text{SIM}^1)(\mu\text{-OAc})(\text{OH})]^+$ appears to be bell-shaped. This bell-shaped profile indicates that the catalyst-substrate complex (E^{S}) is most active in its mixed protonation state, where both protonation and deprotonation lead to a decrease of activity. Based on a fit adopting the equation for a monoprotic system, the assumed two active species in the case of $[\text{Zn}^{\text{II}}_2(\text{L}^1)(\mu\text{-OAc})_2]^+$ and $[\text{Zn}^{\text{II}}_2(\text{SIM}^2)(\mu\text{-OAc})_2]^+$ have the same activity. In contrast, the deprotonated active species of $[\text{Zn}^{\text{II}}_2(\text{H}_2\text{L}^2)(\mu\text{-OAc})_2]^+$ appears to play an important role in the catalytic cycle as the rate vs. pH profile rises steadily as the pH increases, leading to a γ value of 4.19. Comparison of the profiles leads to the conclusion that the presence of two amine groups near one Zn^{II} center in $[\text{Zn}^{\text{II}}_2(\text{SIM}^2)(\mu\text{-OAc})_2]^+$ lowers the kinetically relevant pK_a value by 1.3 pK_a units, in agreement with previously published results (introduced in Chapter 4).¹⁸⁴ The influence of two amide groups at one Zn^{II} center in $[\text{Zn}^{\text{II}}_2(\text{H}_2\text{SIM}^1)(\mu\text{-OAc})(\text{OH})]^+$ is comparatively small; in contrast the symmetric incorporation of two amide moieties in $[\text{Zn}^{\text{II}}_2(\text{H}_2\text{L}^2)(\mu\text{-OAc})_2]^+$ causes a significant effect, both in the profile shape (highest reactivity at high pH; Figure 55a) and the pK_a values.

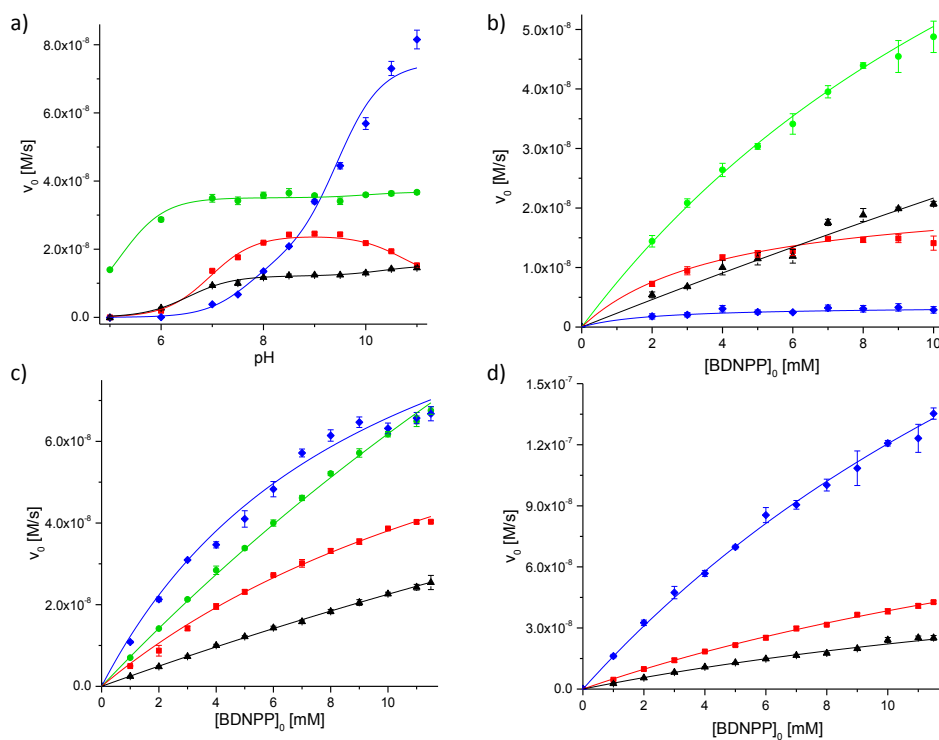


Figure 55: a) pH dependence of BDNPP hydrolysis activity for $[\text{Zn}^{\text{II}}_2(\text{L}^1)(\mu\text{-OAc})_2]^+$ (black triangles), $[\text{Zn}^{\text{II}}_2(\text{H}_2\text{L}^2)(\mu\text{-OAc})_2]^+$ (blue diamonds), $[\text{Zn}^{\text{II}}_2(\text{H}_2\text{SIM}^1)(\mu\text{-OAc})(\text{OH})]^+$ (red squares), and $[\text{Zn}^{\text{II}}_2(\text{SIM}^2)(\mu\text{-OAc})_2]^+$ (green circles) and substrate concentration dependence b) at pH = 7, c) at pH = 9.5 and d) at pH = 11.

The measurements of the dependence of the BDNPP hydrolysis rate on the complex concentration were determined at pH 9.5. The results show that for each complex the hydrolysis rates are linearly dependent on the complex concentration.

The dependence of the rate of hydrolysis on the BDNPP concentration were examined at three pH values (*i.e.* pH = 7.0, 9.5 and 11) to assess the catalytic behavior of different protonation states (Figure 55b, c, d). $[\text{Zn}^{\text{II}}_2(\text{SIM}^2)(\mu\text{-OAc})_2]^+$ was not tested at pH = 11 as no difference in the hydrolysis rate, compared to pH = 9.5, was detected during the previous pH dependence experiments. Due to the poor solubility of BDNPP in acetonitrile, assays with a starting concentration of the substrate higher than 11.5 mM could not be investigated. The experimental data showed Michaelis-Menten saturation behavior for all complexes and were fitted to Equation 22. The derived parameter values k_{cat} , K_{M} and $k_{\text{cat}}/K_{\text{M}}$ are listed in Table 20.

Table 20. Kinetic data (k_{cat} in $[10^{-3} \text{ s}^{-1}]$, K_{M} in $[\text{mM}]$ and $k_{\text{cat}}/K_{\text{M}}$ in $[\text{s}^{-1}\text{M}^{-1}]$) of BDNPP hydrolysis for $[\text{Zn}^{\text{II}}_2(\text{L}^1)(\mu\text{-OAc})_2]^+$, $[\text{Zn}^{\text{II}}_2(\text{H}_2\text{L}^2)(\mu\text{-OAc})_2]^+$, $[\text{Zn}^{\text{II}}_2(\text{H}_2\text{SIM}^1)(\mu\text{-OAc})(\text{OH})]^+$, $[\text{Zn}^{\text{II}}_2(\text{SIM}^2)(\mu\text{-OAc})_2]^+$, and $[\text{Zn}^{\text{II}}_2(\text{H}_2\text{SIM}^3)(\mu\text{-OAc})(\text{OH})]$.

	pH	$[\text{Zn}^{\text{II}}_2(\text{L}^1)(\mu\text{-OAc})_2]^+$	$[\text{Zn}^{\text{II}}_2(\text{H}_2\text{L}^2)(\mu\text{-OAc})_2]^+$	$[\text{Zn}^{\text{II}}_2(\text{H}_2\text{SIM}^1)(\mu\text{-OAc})(\text{OH})]^+$	$[\text{Zn}^{\text{II}}_2(\text{SIM}^2)(\mu\text{-OAc})_2]^+$	$[\text{Zn}^{\text{II}}_2(\text{H}_2\text{SIM}^3)(\mu\text{-OAc})(\text{OH})]$
$\text{pK}_a(\text{I})$		6.53 ± 0.05	7.67 ± 0.16	6.96 ± 0.06	5.19 ± 0.02	7.33 ± 0.16
$\text{pK}_a(\text{II})$		10.33 ± 0.83	9.45 ± 0.19	10.72 ± 0.28	10.02 ± 0.78	10.01 ± 0.40
γ		1.26 ± 0.08	4.19 ± 0.67	0.45 ± 0.14	1.05 ± 0.03	2.01 ± 0.32
k_{cat}	7	7.18 ± 4.39	0.09 ± 0.01	0.57 ± 0.04	3.49 ± 0.25	
K_{M}	7	123 ± 79	2 ± 1	4 ± 1	18 ± 2	
$k_{\text{cat}}/K_{\text{M}}$	7	0.06	0.04	0.14	0.20	
k_{cat}	9.5	5.08 ± 0.85	3.20 ± 0.21	2.70 ± 0.21	9.58 ± 0.70	8.67 ± 0.89
K_{M}	9.5	80 ± 14	9 ± 1	18 ± 2	52 ± 4	37 ± 5
$k_{\text{cat}}/K_{\text{M}}$	9.5	0.06	0.34	0.15	0.18	0.23
k_{cat}	11	2.07 ± 0.29	10.83 ± 0.62	3.68 ± 0.25	-	
K_{M}	11	27 ± 5	26 ± 2	28 ± 2	-	
$k_{\text{cat}}/K_{\text{M}}$	11	0.08	0.42	0.13	-	
TON (after 8 d)	9.5	109 ± 5	158 ± 8	101 ± 4	121 ± 6	

While at pH = 7 $[\text{Zn}^{\text{II}}_2(\text{L}^1)(\mu\text{-OAc})_2]^+$, without hydrogen bond donors, exhibits the highest rate of hydrolysis, $[\text{Zn}^{\text{II}}_2(\text{SIM}^2)(\mu\text{-OAc})_2]^+$ is the most efficient catalyst due to its smaller K_{M} value. Moreover, the Michaelis-Menten constants K_{M} are lower for all complexes providing a hydrogen bond network, compared to $[\text{Zn}^{\text{II}}_2(\text{L}^1)(\mu\text{-OAc})_2]^+$, both at pH = 7 and pH = 9.5. The net interpretation of this observation is that complexes that facilitate hydrogen bonding exhibit higher affinities towards the phosphodiester substrate and therefore reveal higher catalytic efficiencies than $[\text{Zn}^{\text{II}}_2(\text{L}^1)(\mu\text{-OAc})_2]^+$ (except for $[\text{Zn}^{\text{II}}_2(\text{H}_2\text{L}^2)(\mu\text{-OAc})_2]^+$ at pH = 7). Furthermore, the measurements at pH = 11 resulted in significantly higher k_{cat} values for the complexes that support hydrogen bond formation, compared to the reference complex $[\text{Zn}^{\text{II}}_2(\text{L}^1)(\mu\text{-OAc})_2]^+$. The Michaelis-Menten constants obtained under these more basic conditions are comparable for all three complexes. Therefore, the complexes $[\text{Zn}^{\text{II}}_2(\text{H}_2\text{SIM}^1)(\mu\text{-OAc})(\text{OH})]^+$ and $[\text{Zn}^{\text{II}}_2(\text{H}_2\text{L}^2)(\mu\text{-OAc})_2]^+$ have twice and five times higher catalytic efficiencies than $[\text{Zn}^{\text{II}}_2(\text{L}^1)(\mu\text{-OAc})_2]^+$.

Due to the insolubility of the neutral complex $[\text{Zn}^{\text{II}}_2(\text{H}_2\text{SIM}^3)(\mu\text{-OAc})(\text{OH})]$, 0.2 vol% perchloric acid needed to be added in order to dissolve the complex in acetonitrile. The exact appearance of the complex in slight acidic solution is not fully clarified, as discussed in Chapter 4.3. However, the

pH profile of $[\text{Zn}^{\text{II}}_2(\text{H}_2\text{SIM}^3)(\mu\text{-OAc})(\text{OH})]$, depicted in Figure 56a, exhibited two deprotonation steps in the region between 5 and 11 similar to $[\text{Zn}^{\text{II}}_2(\text{H}_2\text{SIM}^1)(\mu\text{-OAc})(\text{OH})]^+$. Compared to complex $[\text{Zn}^{\text{II}}_2(\text{H}_2\text{SIM}^1)(\mu\text{-OAc})(\text{OH})]^+$, bearing only pyridine coordinating ligands besides the bridging phenolate residue, the $\text{pK}_a(\text{I})$ value of $[\text{Zn}^{\text{II}}_2(\text{H}_2\text{SIM}^3)(\mu\text{-OAc})(\text{OH})]$ is shifted to a higher value as expected due to the electron-rich terminal phenolate ligand. In contrast, the second pK_a value of $[\text{Zn}^{\text{II}}_2(\text{H}_2\text{SIM}^3)(\mu\text{-OAc})(\text{OH})]$, $\text{pK}_a(\text{II})$, is shifted to lower pH values compared to $[\text{Zn}^{\text{II}}_2(\text{H}_2\text{SIM}^1)(\mu\text{-OAc})(\text{OH})]^+$. Whilst in the case of $[\text{Zn}^{\text{II}}_2(\text{H}_2\text{SIM}^1)(\mu\text{-OAc})(\text{OH})]^+$ the singly deprotonated form was found to be the most active species, $[\text{Zn}^{\text{II}}_2(\text{H}_2\text{SIM}^3)(\mu\text{-OAc})(\text{OH})]$ exhibited the most active form after two deprotonation steps with a γ -value of 2.

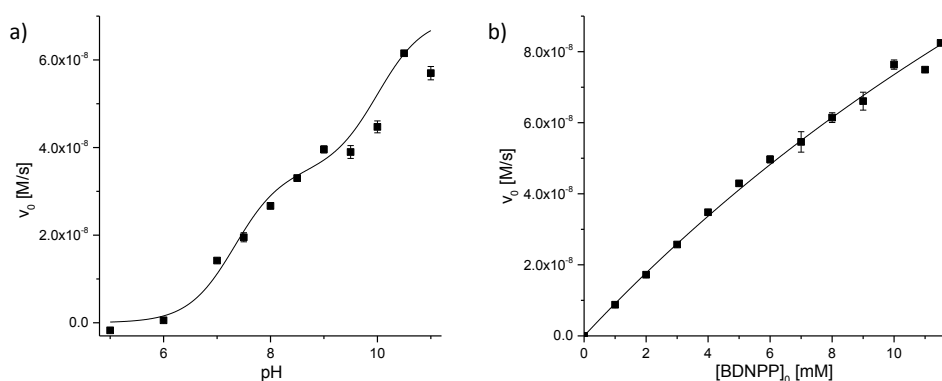


Figure 56: a) pH dependence of BDNPP hydrolysis activity and b) substrate concentration dependence at pH = 9.5 for $[\text{Zn}^{\text{II}}_2(\text{H}_2\text{SIM}^3)(\mu\text{-OAc})(\text{OH})]$.

The dependence of the BDNPP hydrolysis rate on the substrate concentration for $[\text{Zn}^{\text{II}}_2(\text{H}_2\text{SIM}^3)(\mu\text{-OAc})(\text{OH})]$ was investigated at pH 9.5 and the results are depicted in Figure 56b. The experimental data were fitted to Equation 22 and the parameter values k_{cat} , K_M , and k_{cat}/K_M are listed in Table 20. Comparison of the kinetic parameters of $[\text{Zn}^{\text{II}}_2(\text{H}_2\text{SIM}^1)(\mu\text{-OAc})(\text{OH})]^+$ and $[\text{Zn}^{\text{II}}_2(\text{H}_2\text{SIM}^3)(\mu\text{-OAc})(\text{OH})]$, both with two pivaloyl-amide residues in an asymmetric manner with respect to the dizinc(II) core, but differing in the primary coordination sphere, allows statements regarding the impact of an electron-rich coordinating ligand. The respective K_M values show that $[\text{Zn}^{\text{II}}_2(\text{H}_2\text{SIM}^3)(\mu\text{-OAc})(\text{OH})]$ exhibits lower substrate affinity than $[\text{Zn}^{\text{II}}_2(\text{H}_2\text{SIM}^1)(\mu\text{-OAc})(\text{OH})]^+$, ascribed to the more electron-rich primary coordination sphere. However, $[\text{Zn}^{\text{II}}_2(\text{H}_2\text{SIM}^3)(\mu\text{-OAc})(\text{OH})]$ revealed a three-fold increased hydrolysis rate compared to $[\text{Zn}^{\text{II}}_2(\text{H}_2\text{SIM}^1)(\mu\text{-OAc})(\text{OH})]^+$ and following a higher catalytic efficiency.

Comparing the kinetic parameters of $[\text{Zn}^{\text{II}}_2(\text{H}_2\text{SIM}^3)(\mu\text{-OAc})(\text{OH})]$ with all of the dizinc(II) complexes studied in this work reveals that the hydrolysis rate of $[\text{Zn}^{\text{II}}_2(\text{H}_2\text{SIM}^3)(\mu\text{-OAc})(\text{OH})]$ lies in the range of the hydrolysis rate determined for $[\text{Zn}^{\text{II}}_2(\text{SIM}^2)(\mu\text{-OAc})_2]^+$, bearing two amino residues, and is significantly higher than the one of the reference complex $[\text{Zn}^{\text{II}}_2(\text{L}^1)(\mu\text{-OAc})_2]^+$,

missing hydrogen bonding capacity. Interestingly, the latter was not the case for $[\text{Zn}^{\text{II}}_2(\text{H}_2\text{SIM}^1)(\mu\text{-OAc})(\text{OH})]^+$, which deviates only in the primary coordination sphere from $[\text{Zn}^{\text{II}}_2(\text{H}_2\text{SIM}^3)(\mu\text{-OAc})(\text{OH})]$. This suggests that the acceleration of the BDNPP hydrolysis by a more electron-rich primary coordination sphere is more pronounced than the deceleration by two pivaloyl-amide residues adjacent one Zn^{II} center.

Turn Over Numbers

Studies of the turn over number (TON) were conducted at pH = 9.5 and 25°C with $[\text{complex}]_0 = 15 \text{ nM}$ and $[\text{BDNPP}]_0 = 5.25 \text{ }\mu\text{M}$. Samples were taken at various intervals during the experiment, diluted with solvent, and their UV-vis spectra were recorded to determine the amount of phosphoester hydrolysis. The increase in the absorbance at 400 nm, assigned to the hydrolysis product 2,4-dinitrophenolate, was monitored over time and TON values after eight days were calculated using the Beer-Lambert Law. The resulting data are given in Figure 57 and Table 20.

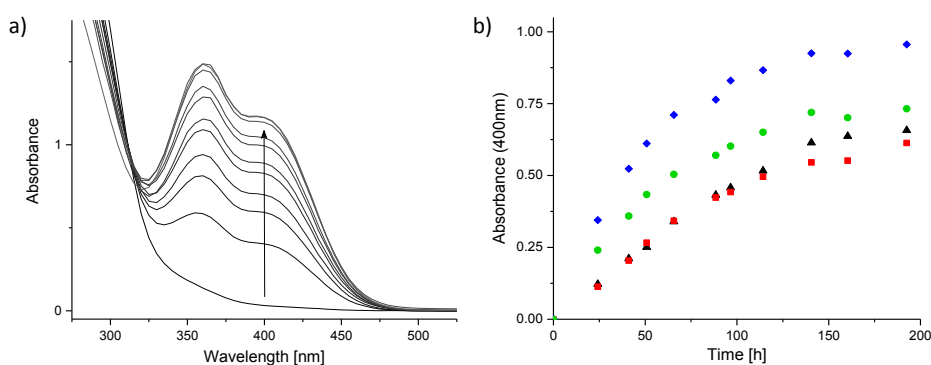


Figure 57: a) UV-vis spectra of the BDNPP hydrolysis assay with $[\text{Zn}^{\text{II}}_2(\text{H}_2\text{L}^2)(\mu\text{-OAc})_2]^+$, taken at different time points after substrate addition and b) time dependence of the absorbance band of 2,4-nitrophenolate (400nm) with $[\text{Zn}^{\text{II}}_2(\text{L}^1)(\mu\text{-OAc})_2]^+$ (black triangles), $[\text{Zn}^{\text{II}}_2(\text{H}_2\text{L}^2)(\mu\text{-OAc})_2]^+$ (blue diamonds), $[\text{Zn}^{\text{II}}_2(\text{H}_2\text{SIM}^1)(\mu\text{-OAc})(\text{OH})]^+$ (red squares) and $[\text{Zn}^{\text{II}}_2(\text{SIM}^2)(\mu\text{-OAc})_2]^+$ (green circles).

Complexes generated from ligands which engender asymmetry exhibit a lower TON than the symmetric complex $[\text{Zn}^{\text{II}}_2(\text{H}_2\text{L}^2)(\mu\text{-OAc})_2]^+$. This implies that the presence of an amide moiety on each coordination site has a beneficial impact on the hydrolytic activity. The comparison of the time-dependent traces for the two asymmetric catalysts, $[\text{Zn}^{\text{II}}_2(\text{H}_2\text{SIM}^1)(\mu\text{-OAc})(\text{OH})]^+$ and $[\text{Zn}^{\text{II}}_2(\text{SIM}^2)(\mu\text{-OAc})_2]^+$, indicate that there is also a decrease of the TON as a result of the bulky nature of the pivaloyl group in the former complex. Therefore, the hydrolysis rate of $[\text{Zn}^{\text{II}}_2(\text{SIM}^2)(\mu\text{-OAc})_2]^+$ is in the first 70 hours significantly higher. Furthermore, the data obtained with $[\text{Zn}^{\text{II}}_2(\text{H}_2\text{SIM}^1)(\mu\text{-OAc})(\text{OH})]^+$ are similar to those of the reference system $[\text{Zn}^{\text{II}}_2(\text{L}^1)(\mu\text{-OAc})_2]^+$ during the first 150 hours after BDNPP addition. However, the difference in the traces after 150 hours reveal earlier inhibition in presence of two amide moieties at adjacent zinc(II) centers. It is

proposed that an increased affinity for the hydrolysis product DNPP is the reason for this, resulting in the inhibition of the complex at an earlier point in time. The experiments demonstrate that the phosphoester hydrolysis rate of dizinc(II) complexes is influenced by (i) the availability of the catalytic center, and (ii) the possibility to interact with amine or amido hydrogen bond donors, whereas the opportunity for the formation of hydrogen bonds on both metal centers appears to have a beneficial effect for the hydrolytic activity.

Studies with a variety of complexes of bis[bis(2-substituted-pyridinyl-6-methyl)]amine type ligands have illustrated the impact of (i) enhanced H-bonding effects in the second coordination sphere, (ii) the steric hindrance in the active site and beyond, and (iii) the polarity of the substituents, on the intramolecular hydrolysis of the substrate, for example the RNA model HPNPP.²⁸⁷ Moreover, an impaired BDNPP affinity was found for the dizinc(II) complex of a bulky phenolate-based ligand HL⁶³ ($k_{\text{cat}} = (0.97 \pm 0.21) \cdot 10^{-3} \text{ s}^{-1}$; $K_{\text{M}} = (7.01 \pm 2.57) \text{ mM}$; $k_{\text{cat}}/K_{\text{M}} = 0.14 \text{ s}^{-1}\text{M}^{-1}$) compared to its unconcealed counterpart H₂L⁶⁴ ($k_{\text{cat}} = (2.45 \pm 0.27) \cdot 10^{-3} \text{ s}^{-1}$; $K_{\text{M}} = (9.48 \pm 1.74) \text{ mM}$; $k_{\text{cat}}/K_{\text{M}} = 0.26 \text{ s}^{-1}\text{M}^{-1}$), which was proposed to be a steric effect attributed to the bulky vinylbenzyl group.²⁷⁶

Therefore, the exact origin of the acceleration of the BDNPP hydrolysis with the dizinc(II) complexes studied in this work may be attributed in part to the enhanced H-bonding effects, but the effects of other parameters in combination with H-bonding, needs further investigation.

Product Inhibition at the Active Site

Studies of the hydrolysis of phosphomonoesters using DNPP as model substrate in the substrate concentration dependence assays as well as in the TON assays revealed no acceleration of phosphoester hydrolysis compared to the autohydrolysis assay for the dizinc(II) complexes $[\text{Zn}^{\text{II}}_2(\text{L}^1)(\mu\text{-OAc})_2]^+$, $[\text{Zn}^{\text{II}}_2(\text{H}_2\text{L}^2)(\mu\text{-OAc})_2]^+$, $[\text{Zn}^{\text{II}}_2(\text{H}_2\text{SIM}^1)(\mu\text{-OAc})(\text{OH})]^+$, and $[\text{Zn}^{\text{II}}_2(\text{SIM}^2)(\mu\text{-OAc})_2]^+$.

Similar to the phosphate inhibition of phosphatases,^{289, 290} the formation of an adduct with a bridging phosphomonoester between the two Zn^{II} sites is known to lead to inhibition of phosphoester hydrolysis in model complexes.²⁹¹ Therefore, the influence of addition of DNPP to the reaction mixtures was explored. The presence of DNPP (1 mM) in the kinetic assays was shown to decrease the hydrolytic rate, independently of whether the phosphomonoester was added before or simultaneously with the substrate BDNPP (Figure 58).

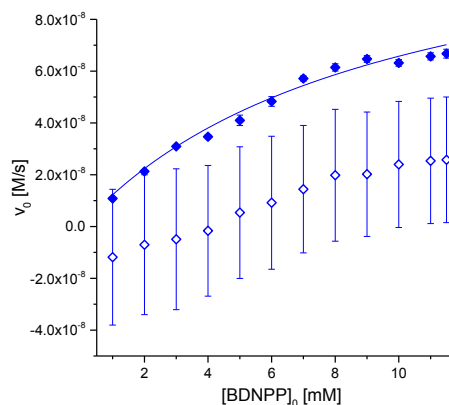


Figure 58: Initial rate vs. substrate concentration for the hydrolysis of BDNPP of $[\text{Zn}^{\text{II}}_2(\text{H}_2\text{L}^2)(\mu\text{-OAc})_2]\text{PF}_6$ with (unfilled symbols) and without (filled symbols) addition of DNPP.

The inhibited hydrolysis rates obtained in the presence of catalyst are, within the relatively large errors of these measurements, indistinguishable from the autohydrolysis rates under the same conditions (autohydrolysis experiments contain only phosphomono- and phosphodiester). These results demonstrate not only product inhibition but also that the hydrolysis product DNPP is more strongly bound to the complex than the phosphodiester substrate BDNPP.

Crystal Structure of an Asymmetric Dizinc(II) Complex with the Phosphomonoester PNPP

In order to explore the nature of product inhibition, the asymmetric complex $[\text{Zn}^{\text{II}}_2(\text{H}_2\text{SIM}^1)(\mu\text{-OAc})(\text{OH})]^+$ was treated with an excess of the phosphomonoester PNPP in acetonitrile. PNPP was chosen as phosphomonoester substrate mimic due to its higher stability towards autohydrolysis compared to DNPP. After the solvent was removed and the remaining oil dissolved in methanol, colorless crystals suitable for X-ray crystallography were obtained by slow evaporation. The structure reveals that the inhibited complex contains one μ -PNPP molecule, which forms a bridge between the two Zn^{II} centers of the same dizinc(II) complex (Figure 59; selected structural parameters are listed in Table 21), in contrast to a previously published complex $[\text{Zn}^{\text{II}}_4(\text{L}^{65})_2(\mu\text{-O}_3\text{POC}_6\text{H}_4\text{NO}_2)(\text{H}_2\text{O})_2](\text{PF}_6)_2$, in which the PNPP molecule forms not only an intramolecular bridge between the two Zn^{II} ions but also a intermolecular bridge between two Zn^{II} centers of adjacent dizinc(II) complexes.¹⁹⁵ In $[\text{Zn}^{\text{II}}_2(\text{H}_2\text{SIM}^1)(\mu\text{-O}_3\text{POC}_6\text{H}_4\text{NO}_2)]\text{PF}_6$, both Zn^{II} ions are bound to the bridging phenoxido residue, to the nitrogen atoms of two pyridine ligands, to a tertiary amine and additionally to an oxygen atom of the bridging PNPP molecule.

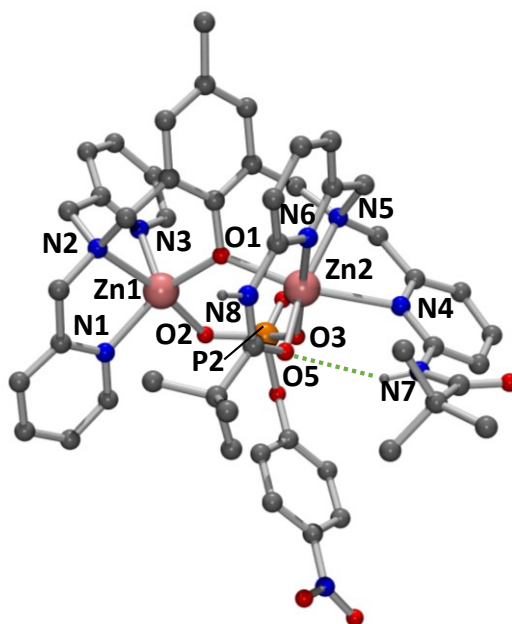


Figure 59: Structure of $[\text{Zn}^{\text{II}}_2(\text{H}_2\text{SIM}^1)(\mu\text{-O}_3\text{POC}_6\text{H}_4\text{NO}_2)]\text{PF}_6$ showing hydrogen bond formation (green dotted lines; counter ions, non-coordinated solvent molecules, and hydrogen atoms, not involved in hydrogen bonding, have been omitted for clarity; crystallographic data and ORTEP plots with 50% probability level of thermal ellipsoids appear in the Appendix, Table 34 and Figure 74).

Table 21: Selected bond lengths (Å) and angles (°) for $[\text{Zn}^{\text{II}}_2(\text{H}_2\text{SIM}^1)(\mu\text{-O}_3\text{POC}_6\text{H}_4\text{NO}_2)]\text{PF}_6$ compared to $[\text{Zn}^{\text{II}}_2(\text{H}_2\text{SIM}^1)(\mu\text{-OAc})(\text{OH})]\text{PF}_6$.

	$[\text{Zn}^{\text{II}}_2(\text{H}_2\text{SIM}^1)(\mu\text{-O}_3\text{POC}_6\text{H}_4\text{NO}_2)]^+$	$[\text{Zn}^{\text{II}}_2(\text{H}_2\text{SIM}^1)(\mu\text{-OAc})(\text{OH})]^+$
Zn(1)–Zn(2)	3.6971(8)	3.5422(7)
Zn(1)–O(1)	1.987(3)	1.954(3)
Zn(1)–O(2)	2.011(3)	2.003(3)
Zn(1)–N(1)	2.074(4)	2.057(3)
Zn(1)–N(2)	2.269(4)	2.233(2)
Zn(1)–N(3)	2.062(4)	2.102(3)
Zn(2)–O(1)	2.140(3)	2.120(2)
Zn(2)–O(3)	1.941(3)	2.133(3)
Zn(2)–N(4)	2.443(4)	2.322(3)
Zn(2)–N(5)	2.133(4)	2.136(3)
Zn(2)–N(6)	2.107(4)	2.336(3)
Zn(2)–O(6)	-	1.945(2)
Zn(2)–O(5)	2.122(3)	-
Zn(1)–O(1)–Zn(2)	127.16(17)	120.75(12)
O(1)–Zn(1)–N(1)	136.52(16)	118.71(12)
O(1)–Zn(1)–N(2)	89.85(14)	91.48(11)
O(1)–Zn(1)–N(3)	100.53(16)	124.82(11)
O(1)–Zn(1)–O(2)	98.94(13)	99.48(12)
O(1)–Zn(2)–N(4)	162.62(14)	88.66(10)
O(1)–Zn(2)–N(5)	91.55(14)	90.65(11)
O(1)–Zn(2)–N(6)	87.68(14)	161.27(10)
O(1)–Zn(2)–O(3)	93.42(13)	87.91(11)
O(1)–Zn(2)–O(6)	-	102.84(10)
O(5)–Zn(2)–O(1)	100.35(13)	-

Comparison with the structure of the corresponding acetate-bridged complex $[\text{Zn}^{\text{II}}_2(\text{H}_2\text{SIM}^1)(\mu\text{-OAc})(\text{OH})]\text{PF}_6$ (discussed in detail in Chapter 4.3), used as the starting material for the synthesis of $[\text{Zn}^{\text{II}}_2(\text{H}_2\text{SIM}^1)(\mu\text{-O}_3\text{POC}_6\text{H}_4\text{NO}_2)]\text{PF}_6$, illustrates important similarities: the Zn^{II} ions in both structures are on different sides of the phenoxido plane and exhibit different coordination geometries. In the catalyst-inhibitor adduct $[\text{Zn}^{\text{II}}_2(\text{H}_2\text{SIM}^1)(\mu\text{-O}_3\text{POC}_6\text{H}_4\text{NO}_2)]\text{PF}_6$, Zn(1) is also coordinated in a trigonal bipyramidal geometry (τ -value of 0.88), while Zn(2) is at the center of a six-coordinate site. In contrast to the catalyst complex, the remaining coordination site of Zn(2) is no longer completed by a terminal hydroxido group, but by the neighboring amide oxygen atom of the supporting dinucleating ligand. The coordination of the bulky PNPP inhibitor in $[\text{Zn}^{\text{II}}_2(\text{H}_2\text{SIM}^1)(\mu\text{-O}_3\text{POC}_6\text{H}_4\text{NO}_2)]\text{PF}_6$, compared to the acetate co-ligand in $[\text{Zn}^{\text{II}}_2(\text{H}_2\text{SIM}^1)(\mu\text{-OAc})(\text{OH})]\text{PF}_6$ leads to an increase of the $\text{Zn}^{\text{II}}\cdots\text{Zn}^{\text{II}}$ distance by 0.16 Å, accompanied by the widening of the Zn(1)-O(1)-Zn(2) angle by 6.4°. The structural differences in the dizinc(II) complexes of H_3SIM^1 , $[\text{Zn}^{\text{II}}_2(\text{H}_2\text{SIM}^1)(\mu\text{-O}_3\text{POC}_6\text{H}_4\text{NO}_2)]\text{PF}_6$ and $[\text{Zn}^{\text{II}}_2(\text{H}_2\text{SIM}^1)(\mu\text{-OAc})(\text{OH})]\text{PF}_6$, are mainly in the angles within the triangular plane of the trigonal bipyramidal site. Due to the bulkier 4-nitrophenolate residue of PNPP in $[\text{Zn}^{\text{II}}_2(\text{H}_2\text{SIM}^1)(\mu\text{-O}_3\text{POC}_6\text{H}_4\text{NO}_2)]\text{PF}_6$, compared to the acetate co-ligand in $[\text{Zn}^{\text{II}}_2(\text{H}_2\text{SIM}^1)(\mu\text{-OAc})(\text{OH})]\text{PF}_6$, the O(1)-Zn(1)-N(1) angle is widened (136.53(16)° vs. 118.77(16)°), and the O(1)-Zn(1)-N(3) angle is contracted (100.50(16)° vs. 124.76(15)°). However, the primary coordination sphere of the two complexes is similar.

Further investigation of the second coordination sphere in the amide-based complexes $[\text{Zn}^{\text{II}}_2(\text{H}_2\text{L}^2)(\mu\text{-OAc})_2]\text{PF}_6$, $[\text{Zn}^{\text{II}}_2(\text{H}_2\text{SIM}^1)(\mu\text{-OAc})(\text{OH})]\text{PF}_6$, $[\text{Zn}^{\text{II}}_2(\text{H}_2\text{SIM}^3)(\mu\text{-OAc})(\text{OH})]$ (discussed in detail in Chapter 4.3), and $[\text{Zn}^{\text{II}}_2(\text{H}_2\text{SIM}^1)(\mu\text{-O}_3\text{POC}_6\text{H}_4\text{NO}_2)]\text{PF}_6$ indicates that, while the symmetric ligand H_3L^2 forms two hydrogen bonds to the two bridging acetate co-ligands – one hydrogen bond to each acetate – the symmetric complexes, $[\text{Zn}^{\text{II}}_2(\text{H}_2\text{SIM}^1)(\mu\text{-OAc})(\text{OH})]\text{PF}_6$ and $[\text{Zn}^{\text{II}}_2(\text{H}_2\text{SIM}^3)(\mu\text{-OAc})(\text{OH})]$, form two hydrogen bonds to the hydroxido ligand, stabilizing this unusual structure. However, the introduction of the monophosphate PNPP, replacing the bridging acetate, leads to the coordination of one of the amide groups, stabilized by hydrogen bonding to the second amide function. The distance between these nitrogen and oxygen atoms of 3.210(6) Å is long compared to the corresponding distances in $[\text{Zn}^{\text{II}}_2(\text{H}_2\text{L}^2)(\mu\text{-OAc})_2]\text{PF}_6$ (2.982(4) Å and 2.977(5) Å), $[\text{Zn}^{\text{II}}_2(\text{H}_2\text{SIM}^1)(\mu\text{-OAc})(\text{OH})]\text{PF}_6$ (2.810(4) Å and 2.875(4) Å), and $[\text{Zn}^{\text{II}}_2(\text{H}_2\text{SIM}^3)(\mu\text{-OAc})(\text{OH})]$ (2.764(3) Å and 2.870(3) Å). It is assumed that steric hindrance by the *tert*-butyl groups causes this elongation. Interestingly, no hydrogen bonding to the bridging phosphate, as previously observed with the amino group-containing complex $[\text{Zn}^{\text{II}}_2(\text{L}^7)(\mu\text{-PNPP})]^+$, occurs.¹¹²

³¹P NMR Studies of Phosphoester Binding

Phosphomonoester Binding

In order to gain further insight into the catalytic mechanism, substrate binding was studied by ³¹P NMR spectroscopy. ³¹P NMR spectra of the hexafluorophosphate salts of the dizinc(II) complexes were measured with 85% H₃PO₄ as an external standard, and the ³¹P resonance of PF₆⁻ anion was then used as internal standard for the phosphoester binding experiments. First the spectra of the phosphoester substrates were measured to study the influence of the ester groups on the ³¹P chemical shifts (Figure 60a; NaPF₆ referenced to -144.30 ppm). Comparison of the ³¹P shifts in phosphoric acid, PNPP, BPNPP, DNPP, BDNPP, diphenyl phosphate and triphenyl phosphate show a linear correlation with the number of protons substituted by phenyl groups in H₃PO₄. Importantly, a comparison of the resonances of the phosphodiesters, BDNPP and BPNPP, as well as of the phosphomonoesters, DNPP and PNPP, indicates that the impact of an additional nitro substituent at the phenyl groups is rather small.

The ³¹P NMR spectrum of the crystallographically investigated complex [Zn^{II}₂(H₂SIM¹)(μ-O₃POC₆H₄NO₂)]⁺ in acetonitrile has a single resonance at 0.62 ppm compared to -5.05 ppm for the uncoordinated phosphoester. This effect was also studied using the phosphomonoester DNPP for the four dizinc(II) complexes, in order to gain deeper understanding on the product inhibited structure during the BDNPP hydrolysis; the detected resonances are summarized in Table 22.

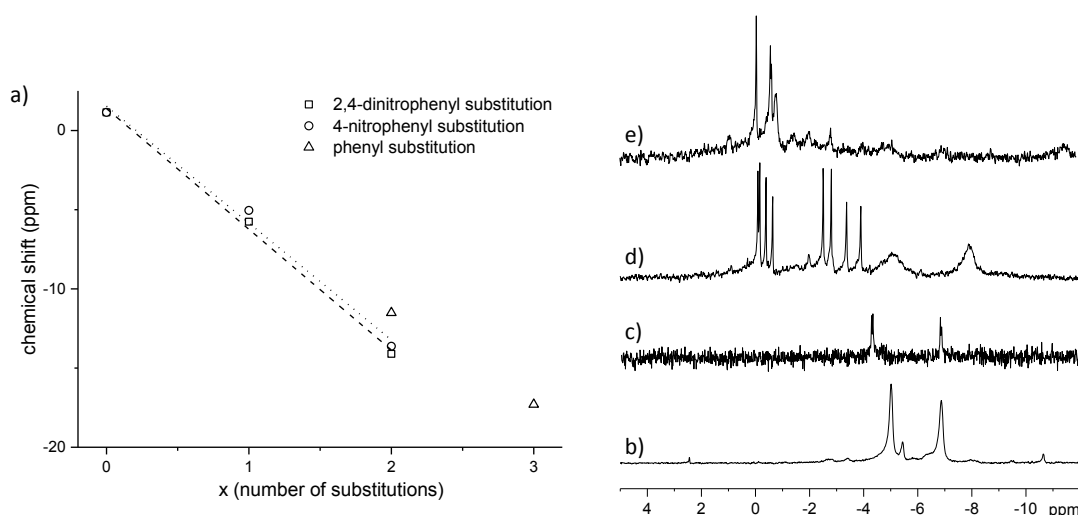


Figure 60: a) Chemical shifts of ³¹P NMR resonances for phosphoester substrates (OP(OH)_{3-x}(OR)_x) in water containing CD₃CN vs. extent of substitution (x) of phosphoric acid with 2,4-dinitrophenyl, 4-nitrophenyl and phenyl residues; Comparison of ³¹P NMR spectra in CD₃CN after addition of DNPP to b) [Zn^{II}₂(H₂SIM¹)(OAc)(OH)]⁺, c) [Zn^{II}₂(H₂L²)(OAc)₂]⁺, d) [Zn^{II}₂(SIM²)(OAc)₂]⁺ directly after addition, and e) [Zn^{II}₂(SIM²)(OAc)₂]⁺ after 48 hours.

Table 22: Phosphoester ^{31}P NMR resonances obtained before and after addition of dizinc(II) complexes $[\text{Zn}^{\text{II}}_2(\text{H}_2\text{L}^2)(\mu\text{-OAc})_2]^+$, $[\text{Zn}^{\text{II}}_2(\text{H}_2\text{SIM}^1)(\mu\text{-OAc})(\text{OH})]^+$, and $[\text{Zn}^{\text{II}}_2(\text{SIM}^2)(\mu\text{-OAc})_2]^+$.

ligand backbone in Zn^{II}_2 complex	phospho-ester	resonances arising from phosphoesters [ppm]								
		metal-free	treated with the Zn^{II}_2 complexes							
H_3SIM^1	PNPP	-5.05	0.62							
H_3SIM^1	DNPP	-5.76	-6.85	-5.01	-2.89					
after 98 d	DNPP		-6.85	-5.01						
H_3L^2	DNPP	-5.76	-6.80	-4.25						
after 98 d	DNPP		-6.80	-4.25	-2.93					
HSIM^2	DNPP	-5.76	-3.90	-3.37	-2.81	-2.50	-0.64	-0.40	-0.16	-0.09
after 48 h	DNPP						-0.63			-0.08
H_3L^2	BDNPP	-14.10								
	0.25eq		-10.25							
	0.5eq		-10.20							
	0.75eq		(-11.46)	-10.22	(-6.88)	(-4.58)				
after 24 h	0.75eq			-10.21	-6.95	-4.54	-1.40			
	1.0eq		-11.40	-10.20	-7.01	-4.48	-1.41			
after 21 d	1.0eq				-7.26	-4.45	-1.42			

The spectra recorded after the addition of DNPP to the amine-based complex $[\text{Zn}^{\text{II}}_2(\text{SIM}^2)(\mu\text{-OAc})_2]^+$ in deuterated acetonitrile (~20 vol% water content) show eight resonances shortly after addition (-3.90 ppm, -3.37 ppm, -2.81 ppm, -2.50 ppm, -0.64 ppm, -0.40 ppm, -0.16 ppm and -0.09 ppm) (Figure 60d). Over 48 hours further reaction results in the observation of only two resonances at -0.61 ppm and -0.08 ppm (Figure 60e). More detailed analysis of the spectrum obtained immediately after addition revealed a pattern of two sets of four resonances, in which always two resonances of the four are separated by about 0.3 ppm (50 Hz) or 0.5 ppm (78 Hz and 85 Hz). ^{31}P NMR studies performed with a series of cyclic phosphates disclosed that besides the electronegativity effect, the chemical shifts of ^{31}P NMR resonances are also significantly influenced by (i) the O-P-O angle, and (ii) the torsional angle R-O-P-O(R) of the phosphate.²⁹² Therefore, the eight resonances were attributed to four different species (-3.64 ppm, -2.66 ppm, -0.41 ppm and -0.25 ppm), each of them present in two conformers with varied positions of the 2,4-dinitrophenyl residue of the phosphoester. After 48 hours only the 'doublet' at -0.25 ppm remains. The chemical shift difference of 5.51 ppm between the resonances of DNPP in its free form and bound to complex $[\text{Zn}^{\text{II}}_2(\text{SIM}^2)(\text{solV})_x]^{\text{n}+}$ is in the same range as found by comparison of free PNPP and $[\text{Zn}^{\text{II}}_2(\text{H}_2\text{SIM}^1)(\mu\text{-O}_3\text{POC}_6\text{H}_4\text{NO}_2)]^+$. Therefore, a similar bridging coordination mode of DNPP to complex $[\text{Zn}^{\text{II}}_2(\text{SIM}^2)(\text{solV})_x]^{\text{n}+}$ as found in $[\text{Zn}^{\text{II}}_2(\text{H}_2\text{SIM}^1)(\mu\text{-O}_3\text{POC}_6\text{H}_4\text{NO}_2)]^+$ is proposed. Once more it should be emphasized that until this most stable phosphoester-bridged dizinc(II) complex was formed three different intermediate stages were detectable.

In contrast, when the amido-based complexes $[\text{Zn}^{\text{II}}_2(\text{H}_2\text{SIM}^1)(\mu\text{-OAc})(\text{OH})]^+$ and $[\text{Zn}^{\text{II}}_2(\text{H}_2\text{L}^2)(\mu\text{-OAc})_2]^+$ and solved in deuterated acetonitrile (~3.0 vol% water content for $[\text{Zn}^{\text{II}}_2(\text{H}_2\text{L}^2)(\mu\text{-OAc})_2]^+$ and ~1.2 vol% water content for $[\text{Zn}^{\text{II}}_2(\text{H}_2\text{SIM}^1)(\mu\text{-OAc})(\text{OH})]^+$) were treated with one equivalent of DNPP, two major resonances with similar chemical shifts appeared in the ^{31}P NMR spectra (-6.85 ppm, -5.01 ppm and -6.80 ppm, -4.25 ppm) (Figure 60b, c). Therefore, similar coordination modes of DNPP to $[\text{Zn}^{\text{II}}_2(\text{H}_2\text{L}^2)(\text{solvent})_x]^{n+}$ and $[\text{Zn}^{\text{II}}_2(\text{H}_2\text{SIM}^1)(\text{solvent})_x]^{n+}$ are assumed. Moreover, the resonances detected were downfield and upfield shifted, respectively, compared to the free phosphomonoester. The extent of the shifts (0.75 ppm to 1.51 ppm) are small compared to the cases discussed above. This suggests a rather different coordination mode of DNPP to $[\text{Zn}^{\text{II}}_2(\text{H}_2\text{SIM}^1)(\text{solvent})_x]^{n+}$ and $[\text{Zn}^{\text{II}}_2(\text{H}_2\text{L}^2)(\text{solvent})_x]^{n+}$ than observed in the X-ray structure of $[\text{Zn}^{\text{II}}_2(\text{H}_2\text{SIM}^1)(\mu\text{-O}_3\text{POC}_6\text{H}_4\text{NO}_2)]^+$. Studies with cyclic phosphoesters have shown that the O-P-O angle has a significant impact on the ^{31}P NMR chemical shift.²⁹² For example, an increase in the bond angle of phosphotriesters results in the better shielding of the phosphorus atom and therefore in an upfield shift of the ^{31}P NMR resonance.²⁹² Assuming the same binding mode for DNPP and PNPP, an upfield shift due to a larger O-P-O angle in the case of DNPP competes with a downfield shift due to coordination to two Zn^{II} ions, and this could explain the smaller extent of the downfield shifts in the cases of DNPP with $[\text{Zn}^{\text{II}}_2(\text{H}_2\text{L}^2)(\mu\text{-OAc})_2]^+$ and $[\text{Zn}^{\text{II}}_2(\text{H}_2\text{SIM}^1)(\mu\text{-OAc})(\text{OH})]^+$. The major resonances at around -6.8 ppm and -4 to -5 ppm can be attributed either to a complex structure with two DNPP ligands in two different electronic environments or to two different complex structures, each of them containing only one bound DNPP. Although the detection of the two major resonances upon binding DNPP by the amide-based complexes, $[\text{Zn}^{\text{II}}_2(\text{H}_2\text{L}^2)(\text{solvent})_x]^{n+}$ and $[\text{Zn}^{\text{II}}_2(\text{H}_2\text{SIM}^1)(\text{solvent})_x]^{n+}$, are similar, their ^{31}P NMR spectra are different: while the third resonance at -2.89 ppm was detected immediately after addition of DNPP to $[\text{Zn}^{\text{II}}_2(\text{H}_2\text{SIM}^1)(\mu\text{-OAc})(\text{OH})]^+$ and disappears after 14 weeks, a species with a similar signal was not observed with $[\text{Zn}^{\text{II}}_2(\text{H}_2\text{L}^2)(\mu\text{-OAc})_2]^+$, but, when a spectrum was measured after 14 weeks (-2.93 ppm). This implies that both complexes form different species with DNPP in different coordination modes, however, the equilibrium constants are dependent on the symmetry of the complex backbone. This could explain the different catalytic activity of the complexes $[\text{Zn}^{\text{II}}_2(\text{H}_2\text{L}^2)(\mu\text{-OAc})_2]^+$ and $[\text{Zn}^{\text{II}}_2(\text{H}_2\text{SIM}^1)(\mu\text{-OAc})(\text{OH})]^+$.

Phosphodiester Binding

The binding of BDNPP was investigated for the most active complex $[\text{Zn}^{\text{II}}_2(\text{H}_2\text{L}^2)(\mu\text{-OAc})_2]^+$ by stepwise addition of 0.25 equivalents of BDNPP and recording the ^{31}P NMR spectra at each step (~ 1.0 vol% water content) (Figure 61). Addition up to 0.5 equivalents BDNPP to a solution of the complex in CD_3CN resulted in the formation of only one phosphorus-containing species with a ^{31}P NMR resonance at -10.22 ppm (Figure 61b,c), in addition to free BDNPP with a resonance at -14.43 ppm (Figure 61a). After further addition of BDNPP two additional signals at -6.86 ppm and -4.58 ppm occurred in the ^{31}P NMR spectrum, and the signal integration increases upon increase of BDNPP concentration. Further reaction led to the disappearance of the initially detected species and formation of a new species with a resonance at -1.41 ppm.

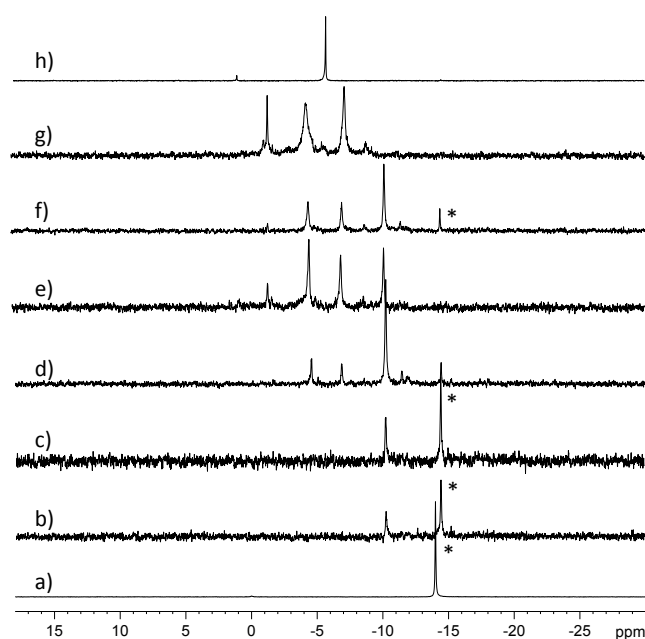


Figure 61. ^{31}P NMR measurements upon addition of BDNPP to $[\text{Zn}^{\text{II}}_2(\text{H}_2\text{L}^2)(\text{OAc})_2]^+$ in CD_3CN a) BDNPP reference, b) 0.25 eq BDNPP, c) 0.5 eq BDNPP, d) 0.75 eq BDNPP, e) 0.75 eq BDNPP after 24h, f) 1.0 eq BDNPP, g) 1.0 eq BDNPP after 16 days, and h) DNPP reference (* unreacted BDNPP).

Comparison to the spectra monitored after addition of the phosphomonoester DNPP to $[\text{Zn}^{\text{II}}_2(\text{H}_2\text{L}^2)(\mu\text{-OAc})_2]^+$ (Figure 61c), assigns the resonances at -6.86 ppm and -4.58 ppm to species containing DNPP. The increase of the integrals of these two species is accompanied by the decrease of the initially detected resonance at -10.22 ppm. Therefore, the resonance at -10.22 ppm is suggested to originate from a BDNPP-complex adduct. It follows that the binding of the phosphodiester to the Zn^{II} ion leads to a downfield shift by 4.2 ppm compared to free BDNPP, accompanied by the activation of the phosphodiester BDNPP. The following hydrolysis of BDNPP provides the phosphomonoester DNPP, which binds in the same way as by direct addition of DNPP to the complex. The decrease of the signal assigned to the BDNPP-complex

adduct is accompanied with an increase of a signal at -1.41 ppm. Although the structure of the corresponding species remains unclear, we speculate that this complex adduct is able to release the DNPP product and therefore continues to catalyze the BDNPP hydrolysis.

Mass Spectrometric Investigation of Phosphoester Binding

Phosphomonoester Binding

ESI⁺ mass spectrometric investigations were carried out with mixtures of the different dizinc(II) complexes with either the phosphomonoester DNPP or the phosphodiester BDNPP. Treatment of $[\text{Zn}^{\text{II}}_2(\text{H}_2\text{SIM}^1)(\mu\text{-OAc})(\text{OH})]^+$ in acetonitrile with the phosphomonoester DNPP resulted in a mass spectrum with the main peak at m/z 1201.2 corresponding to the species $[\text{Zn}^{\text{II}}_2(\text{HSIM}^1)(\text{DNPP})(\text{HOAc})(\text{HF})]^+$. This peak at m/z 1201.2 was also apparent in the spectrum recorded with the mixture of complex $[\text{Zn}^{\text{II}}_2(\text{H}_2\text{L}^2)(\mu\text{-OAc})_2]^+$ with DNPP ascribed to the species $[\text{Zn}^{\text{II}}_2(\text{HL}^2)(\text{DNPP})(\text{HOAc})(\text{HF})]^+$, respectively. An additional signal was found in this spectrum at m/z 1121.2 matching the mass of $[\text{Zn}^{\text{II}}_2(\text{HL}^2)(\text{DNPP})]^+$. Interestingly, treatment of complex $[\text{Zn}^{\text{II}}_2(\text{SIM}^2)(\mu\text{-OAc})_2]^+$ with the phosphomonoester DNPP resulted in a variety of signals in the region around m/z 1200, but those could not be ascribed to specific species due to overlapping of the signals. This finding is in agreement with the above discussed ³¹P NMR spectroscopic investigations supporting the various coordination modes of the phosphomonoester to the complex $[\text{Zn}^{\text{II}}_2(\text{SIM}^2)(\mu\text{-OAc})_2]^+$.

Phosphodiester Binding

Samples taken during the ³¹P NMR spectroscopic titration of BDNPP to the complex $[\text{Zn}^{\text{II}}_2(\text{H}_2\text{L}^2)(\mu\text{-OAc})_2]^+$ resulted in ESI⁺ mass spectra showing peaks at m/z 1121.2 and m/z 1201.2. These two species have also been detected in the mixture of the same dizinc(II) complex with the phosphomonoester DNPP and were ascribed to the species $[\text{Zn}^{\text{II}}_2(\text{HL}^2)(\text{DNPP})]^+$ and $[\text{Zn}^{\text{II}}_2(\text{HL}^2)(\text{DNPP})(\text{HOAc})(\text{HF})]^+$. Therefore, the coordination of the hydrolysis product has also been seen in the mass spectrometric investigations and supports the assignment during the ³¹P NMR spectroscopic investigations.

7.3 SUMMARY

Studying the phosphoester hydrolysis activity of a variety of model complexes with hydrogen bonding functionalities adjacent to the dizinc(II) core, but differing in (i) the type of the hydrogen bond donor, (ii) the position of the hydrogen bond donor, and (iii) the coordinating ligands in the primary coordination sphere, resulted in deeper insights in the impact of the second coordination sphere of phosphatases.

The impact of the hydrogen bond donors of the catalysts on their hydrolytic activity was clearly found to be pH dependent. Amino substitution of the two pyridine residues coordinated to one of the two Zn^{II} centers as in $[\text{Zn}^{\text{II}}_2(\text{SIM}^2)(\mu\text{-OAc})_2]^+$ leads to a lower pH maximum of the phosphoester hydrolysis activity, whilst substitution with pivaloyl-amide residues at the same positions as in $[\text{Zn}^{\text{II}}_2(\text{H}_2\text{SIM}^1)(\mu\text{-OAc})(\text{OH})]^+$ has not a significant effect. However, positioning of one pivaloyl-amide residue adjacent to each Zn^{II} center as in $[\text{Zn}^{\text{II}}_2(\text{H}_2\text{L}^2)(\mu\text{-OAc})_2]^+$ enables activity only under strong basic conditions.

The main impact of the secondary interactions was shown to be the increased substrate affinity, and this obviously depends on the hydrogen bonding sites and the type of the hydrogen bonding groups. At pH 7 the diamino derivative $[\text{Zn}^{\text{II}}_2(\text{SIM}^2)(\mu\text{-OAc})_2]^+$ is the most effective catalyst, possibly due to the flexibility in the binding mode of the phosphomonoester product, as seen in the ³¹P NMR spectroscopic investigations. While at pH 7 the positioning of both pivaloyl-amide residues proximal to one Zn^{II} center in $[\text{Zn}^{\text{II}}_2(\text{H}_2\text{SIM}^1)(\mu\text{-OAc})(\text{OH})]^+$ has a more positive effect towards the BDNPP hydrolysis than positioning one pivaloyl-amide adjacent to each Zn^{II} center in $[\text{Zn}^{\text{II}}_2(\text{H}_2\text{L}^2)(\mu\text{-OAc})_2]^+$; the finding at more basic condition is inversed. Moreover, the impact of a more electron-rich primary coordination sphere in $[\text{Zn}^{\text{II}}_2(\text{H}_2\text{SIM}^3)(\mu\text{-OAc})(\text{OH})]$ is found to surpass the effect of the hydrogen bonding effect of the secondary coordination sphere. However, at strong basic conditions the hydrolysis rate of the hydrogen bonding capable complexes $[\text{Zn}^{\text{II}}_2(\text{H}_2\text{SIM}^1)(\mu\text{-OAc})(\text{OH})]^+$, $[\text{Zn}^{\text{II}}_2(\text{H}_2\text{L}^2)(\mu\text{-OAc})_2]^+$ and $[\text{Zn}^{\text{II}}_2(\text{SIM}^2)(\mu\text{-OAc})_2]^+$ are significantly higher than for the parent complex $[\text{Zn}^{\text{II}}_2(\text{L}^1)(\mu\text{-OAc})_2]^+$ missing hydrogen bond donors.

Long-term catalytic studies revealed that at pH 9.5 the symmetrical, sterically hindered, amide-based system $[\text{Zn}_2(\text{H}_2\text{L}^2)(\mu\text{-OAc})_2]^+$ is the most efficient dizinc(II) complex employed in this work, and this is primarily due to less stable catalyst-inhibitor complexes. In contrast, incorporation of two pivaloyl-amide residues in an asymmetrical fashion as in $[\text{Zn}^{\text{II}}_2(\text{H}_2\text{SIM}^1)(\mu\text{-OAc})(\text{OH})]^+$ leads to the generation of a stable catalyst-inhibitor (hydrolysis

product) adduct. The reason for this behavior was found in the crystal structure of the corresponding complex with a bridging phosphomonoester co-ligand, which reveals one of the two pivaloyl-amide moieties to function as co-ligand for the remaining vacant coordination site of the proximal Zn^{II} center, stabilized by hydrogen bond formation to the second pivaloyl-amide residue.

Chapter 8

Phosphatase Activity of Diiron Complexes^g

^g Main parts of this chapter will be published in “An Approach to More Accurate Model Systems for Purple Acid Phosphatases (PAPs)”; Paul V. Bernhardt, [Simone Bosch](#), Peter Comba, Lawrence R. Gahan, Graeme R. Hanson, Valeriu Mereacre, Christopher J. Noble, Gerhard Schenk, Hubert Wadepohl; manuscript in preparation.

8.1 INTRODUCTION

The hydrolysis of phosphoesters in mammals is catalyzed by phosphatases with two iron centers in the active site, *i.e.* PAP. The oxidation state of the two iron centers in the active site of PAP was shown to be significant, with the homovalent Fe^{III}₂ form of ufPAP exhibiting phosphoester hydrolysis activity of less than 1% of that of the heterovalent Fe^{III}Fe^{II} form.²²¹ Although phosphodiester hydrolysis was observed with a wide range of model complexes, the biological relevant hydrolysis of phosphomonoesters with model systems has rarely been reported. Recently two dinuclear PAP model compounds were reported for which the hydrolysis of the phosphomonoester model substrate DNPP was achieved.^{108, 114} The two complexes, [Fe^{III}₂(L⁸)(μ-OH)(OH₂)₂](ClO₄)₄ and [Fe^{III}₂(L⁶)(μ-O)Cl₄](Cl)₂, depicted in Chart 25, differ from previously studied model systems in their ability to form hydrogen bonds to the putative substrate molecule bound to the metal centers; this was accomplished by incorporation of basic residues adjacent the dimetal core. At the same time a third complex, [Fe^{III}₂(L²)(μ-OH)](ClO₄)₄, was reported, and this complex included pivaloyl-amide moieties as mimics for the non-bonding histidine residues in the active site of PAPs.¹¹⁴ Investigations of the BDNPP hydrolysis with the Fe^{III}₂ complex of HL¹, missing hydrogen bond donors, as well as its derivatives [Fe^{III}₂(L⁸)(μ-OH)(OH₂)₂](ClO₄)₄ and [Fe^{III}₂(L²)(μ-OH)](ClO₄)₄ showed that the two complexes providing hydrogen bond donors exhibited faster hydrolysis rates than the Fe^{III}₂ complex formed with HL¹. However, it should be mentioned that the complexes [Fe^{III}₂(L⁸)(μ-OH)(OH₂)₂](ClO₄)₄ and [Fe^{III}₂(H₂L²)(μ-OH)](ClO₄)₄ exhibited similar catalytic efficiencies ($k_{\text{cat}}/K_{\text{M}}$) to the reference complex lacking a hydrogen bond donor; the differences were due to the higher substrate affinity of the complexes [Fe^{III}₂(L⁸)(μ-OH)(OH₂)₂](ClO₄)₄ and [Fe^{III}₂(H₂L²)(μ-OH)](ClO₄)₄ and subsequent larger substrate binding constants K_{M} , ascribed to hydrogen bond formation.¹¹⁴ In contrast, the complex [Fe^{III}₂(L⁶)(μ-O)Cl₄](Cl)₂ shows the highest catalytic efficiency $k_{\text{cat}}/K_{\text{M}}$ reported so far, with a similar substrate affinity compared to [Fe^{III}₂(L¹)(solvent)_x]⁵⁺, but a ten-fold higher hydrolysis rate.¹⁰⁸ Table 23 (page 170) lists kinetic data reported for different diiron complexes.

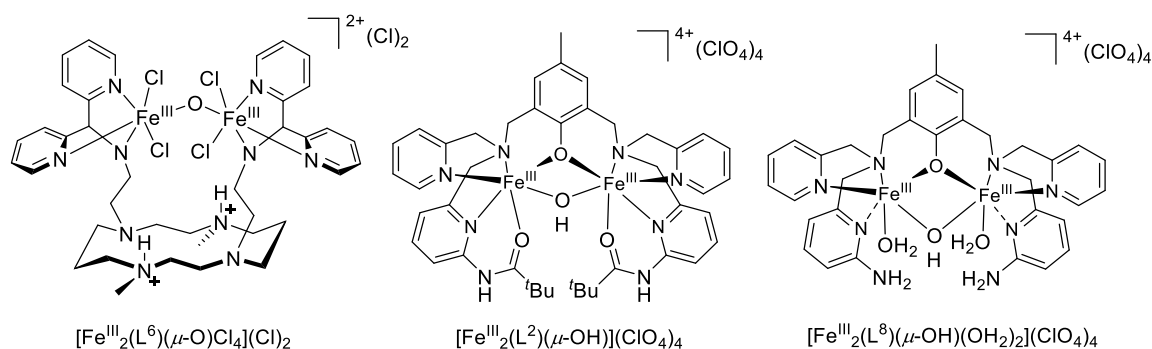


Chart 25: Previously reported diiron(III) complexes containing hydrogen bond donors.^{108, 114}

In order to understand the impact of the hydrogen bond donors the phosphoester binding of $[\text{Fe}^{\text{III}}_2(\text{L}^8)(\mu\text{-OH})(\text{OH}_2)_2](\text{ClO}_4)_4$, $[\text{Fe}^{\text{III}}_2(\text{H}_2\text{L}^2)(\mu\text{-OH})](\text{ClO}_4)_4$, and $[\text{Fe}^{\text{III}}_2(\text{L}^6)(\mu\text{-O})\text{Cl}_4](\text{Cl})_2$ was studied. These investigations revealed that (i) $[\text{Fe}^{\text{III}}_2(\text{L}^6)(\mu\text{-O})\text{Cl}_4](\text{Cl})_2$ and $[\text{Fe}^{\text{III}}_2(\text{L}^8)(\mu\text{-OH})(\text{OH}_2)_2](\text{ClO}_4)_4$ bind phosphomonoester DNPP in a bridging coordination mode, (ii) while the phosphodiester BDNPP was bound in a terminal fashion, and (iii) $[\text{Fe}^{\text{III}}_2(\text{H}_2\text{L}^2)(\mu\text{-OH})](\text{ClO}_4)_4$ did not indicate terminal coordination of phosphodiesters.¹⁰⁹ The difference in the coordination of phosphoesters of the phenolate-based complexes is reflected in their hydrolysis activity by a significantly larger activity of $[\text{Fe}^{\text{III}}_2(\text{L}^8)(\mu\text{-OH})(\text{OH}_2)_2](\text{ClO}_4)_4$ compared to $[\text{Fe}^{\text{III}}_2(\text{H}_2\text{L}^2)(\mu\text{-OH})](\text{ClO}_4)_4$.^{109, 114} The terminal coordination is rather unusual as many crystal structures show phenolate-based dinuclear complexes binding phosphodiesters in a bridging mode.^{293, 294} This unusual coordination mode of phosphoesters was attributed to the hydrogen bonding network provided by the ligand backbones^{108, 109, 114} supported by computational studies with $[\text{Fe}^{\text{III}}_2(\text{L}^6)(\mu\text{-O})\text{Cl}_4](\text{Cl})_2$. Commencing with a phosphomonoester molecule monodentately coordinated to complex $[\text{Fe}^{\text{III}}_2(\text{L}^6)(\mu\text{-O})(\text{solv})_3]^{4+}$, the activation barrier for bridging coordination was calculated to be considerably larger than for the hydrolysis reaction, especially in case the cyclam nitrogen atoms are protonated, thus illustrating the important role of the second coordination sphere on PAP like reactivity.^{108, 109}

With the complex $[\text{Fe}^{\text{III}}_2(\text{L}^8)(\text{solv})_x]^{5+}$ the generation of its reduced $\text{Fe}^{\text{III}}\text{Fe}^{\text{II}}$ form was achieved by bulk electrolysis. Kinetic studies revealed that the heterovalent diiron complex of ligand HL^8 exhibited a five-fold increased catalytic efficiency with respect to its corresponding homovalent Fe^{III}_2 counterpart.^{109, 114} $[\text{Fe}^{\text{III}}\text{Fe}^{\text{II}}(\text{L}^8)(\text{solv})_x]^{4+}$ revealed a lower substrate binding constant K_M and a faster hydrolysis rate than $[\text{Fe}^{\text{III}}_2(\text{L}^8)(\text{solv})_x]^{5+}$.¹¹⁴ As discussed above, the trend of a higher activity of the heterovalent diiron form compared to the homovalent Fe^{III}_2 form was also detected for the native PAP enzyme and ascribed to an increased ligand exchange rate of Fe^{II} compared to Fe^{III} .²⁷⁸ The release of the reaction product was proposed to be most likely the rate-

limiting step in the catalytic mechanism,^{21, 66, 266, 295} and this proposal is supported by the water exchange rates of Fe^{III} and Fe^{II} (10² s⁻¹ and 10⁶ s⁻¹, respectively).^{278, 296-298}

Although the complex [Fe^{III}₂(H₂L²)(μ-OH)](ClO₄)₄ provides two hydrogen bond donors similar to [Fe^{III}₂(L⁸)(μ-OH)(OH₂)₂](ClO₄)₄ and [Fe^{III}₂(L⁶)(μ-O)Cl₄](Cl)₂, this complex exhibited no phospho-monoester hydrolysis capacity and revealed no monodetate coordination of phosphodiester.¹⁰⁹

The latter was rather unexpected due to the sterically demanding pivaloyl-amide residues. In order to favor terminal coordination of phosphoesters an asymmetric ligand H₃SIM¹ was designed in this work bearing two pivaloyl-amide residues similar to H₃L², but both proximal to one of the two binding sites. In Chapter 2.4 the syntheses and characterization of the respective Fe^{II}₂ complexes, [Fe^{II}₂(H₂SIM¹)(μ-OAc)₂]PF₆ and [Fe^{II}₂(H₂L²)(μ-OAc)₂]PF₆, depicted in Chart 26, has been described as well as the generation of the Fe^{III}Fe^{II} complex of ligand H₃SIM¹.

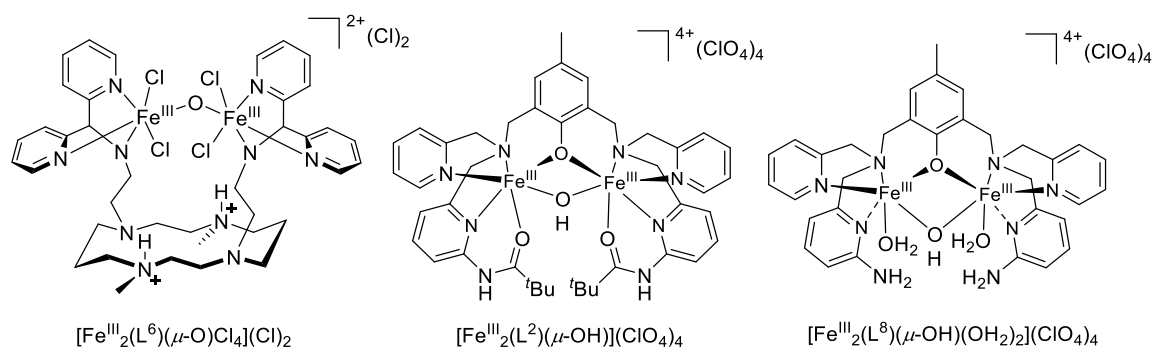


Chart 26: Diiron(II) complexes discussed in this chapter.

Comparison of those two Fe^{II}₂ complexes facilitates the study of the impact of the hydrogen bond donor position. Moreover, comparison of the Fe^{II}₂ complex and the reported Fe^{III}₂ complex of the ligand H₃L² will give an insight in the effect of the oxidation states of complexes providing hydrogen bonding capacity. Furthermore, the homovalent complexes [Fe^{II}₂(H₂SIM¹)(μ-OAc)₂]PF₆ and [Fe^{II}₂(H₂L²)(μ-OAc)₂]PF₆ and their corresponding heterovalent complexes generated by oxidation with ferrocenium hexafluorophosphate will enable to probe the effect of (i) the mixed oxidation state of the diiron core, and (ii) one or two hydrogen bond donors proximal to the Fe^{II} center. Therefore, kinetic studies with the substrate models BDNPP and DNPP have been conducted and the obtained results are presented in the following chapter.

8.2 PHOSPHOESTER HYDROLYSIS STUDIES OF DIIRON COMPLEXES

The sensitivity of the Fe^{II}₂ complexes to oxidation made it necessary to undertake the studies of the catalytic activity of the complexes [Fe^{II}₂(H₂SIM¹)(μ-OAc)₂]⁺ and [Fe^{II}₂(H₂L²)(μ-OAc)₂]⁺ under

inert atmosphere and therefore the experiments were carried out in a glovebox. It should be noted that the number of data points is smaller as well as the variance within the data points is significantly larger, compared to the investigations undertaken with the Zn^{II}_2 complexes owing to the more difficult procedures necessitated by manipulating the samples in the glovebox. The plots obtained for the dependence of the initial hydrolysis rate on the pH and on the initial substrate concentration are depicted in Figure 62. Unfortunately, the v_0 vs. pH curves could not be fitted following the procedures employed to model the analogous Zn^{II}_2 complexes and therefore only qualitative comparison is possible.

pH Dependence

The initial rate vs. pH profiles for $[\text{Fe}^{\text{II}}_2(\text{H}_2\text{SIM}^1)(\mu\text{-OAc})_2]^+$ and $[\text{Fe}^{\text{II}}_2(\text{H}_2\text{L}^2)(\mu\text{-OAc})_2]^+$ exhibited a similar shape. This finding is in contrast to the corresponding Zn^{II}_2 complexes of the ligands H_3SIM^1 and H_3L^2 (discussed in Chapter 7.2), which showed significantly different curve shapes. The $[\text{Fe}^{\text{II}}_2(\text{H}_2\text{L}^2)(\mu\text{-OAc})_2]^+$ complex exhibited lower hydrolysis rates compared to $[\text{Fe}^{\text{II}}_2(\text{H}_2\text{SIM}^1)(\mu\text{-OAc})_2]^+$ under the same condition. The curve shapes indicate that three active species are present in the pH range between pH 7 and pH 10. The first deprotonation step around pH 7 generates an active species; deprotonation of this species around pH 8.6 lowers its activity, while a third deprotonation at $\text{pH} > 9.5$ leads again to an increase of activity. This behavior is significantly different to the Zn^{II}_2 complexes $[\text{Zn}^{\text{II}}_2(\text{H}_2\text{SIM}^1)(\mu\text{-OAc})(\text{OH})]^+$ and $[\text{Zn}^{\text{II}}_2(\text{H}_2\text{L}^2)(\mu\text{-OAc})_2]^+$, which showed a bell-shaped and a sigmoidal profile, respectively (Chapter 7.2).

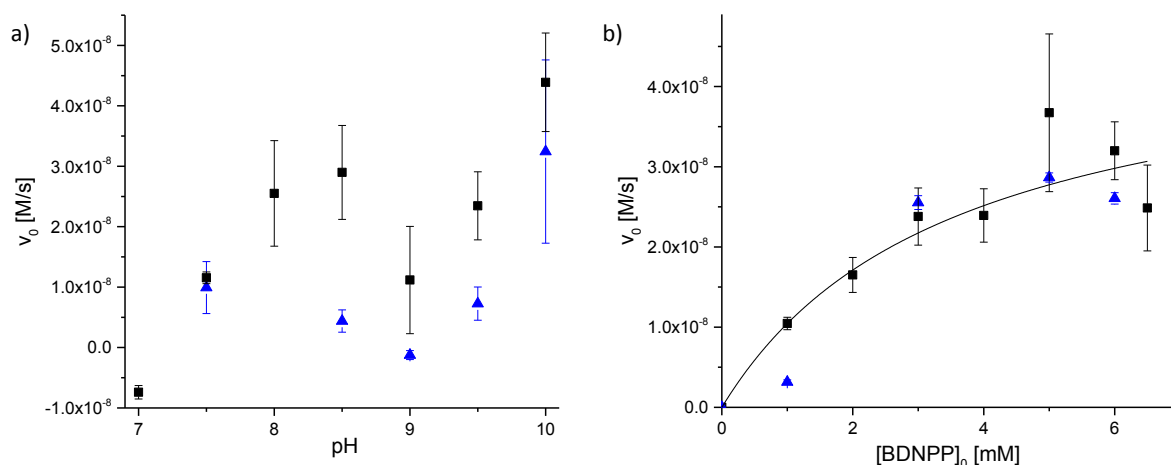


Figure 62: a) pH dependence and b) substrate concentration dependence at pH = 9.5 of BDNPP hydrolysis activity for $[\text{Fe}^{\text{II}}_2(\text{H}_2\text{SIM}^1)(\text{OAc})_2]^+$ (black squares) and $[\text{Fe}^{\text{II}}_2(\text{H}_2\text{L}^2)(\text{OAc})_2]^+$ (blue triangles).

In contrast to $[\text{Fe}^{\text{II}}_2(\text{H}_2\text{L}^2)(\mu\text{-OAc})_2]^+$, the Fe^{II}_2 complex of ligand H_3L^2 exhibited an initial rate vs. pH profile with a relatively sharp activity maximum at pH 6.5.¹⁰⁹ The activity maximum in the region between pH 7 and pH 9 for $[\text{Fe}^{\text{II}}_2(\text{H}_2\text{L}^2)(\mu\text{-OAc})_2]^+$ is at higher pH compared to

$[\text{Fe}^{\text{II}}_2(\text{H}_2\text{L}^2)(\text{solv})_x]^{5+}$. This activity shift to higher pH values is in agreement with the pK_a values of iron-bound water molecules ($\text{pK}_a = 9.5$ for Fe^{II} and $\text{pK}_a = 2.2$ for Fe^{III}) ascribed to the lower Lewis acidity of Fe^{II} compared to Fe^{III} .¹⁶⁵

Substrate Concentration Dependence

The dependence of the BDNPP hydrolysis rate on the substrate concentration was determined at $\text{pH} = 9.5$ to access a catalytic active species of the Fe^{II}_2 complexes and to allow comparison to the studies conducted with the respective Zn^{II}_2 complexes. The measurements with complex $[\text{Fe}^{\text{II}}_2(\text{H}_2\text{L}^2)(\mu\text{-OAc})_2]^+$, in which the two hydrogen bonding pivaloyl-amide residues are positioned in a symmetric manner, exhibited similar hydrolysis rates to $[\text{Fe}^{\text{II}}_2(\text{H}_2\text{SIM}^1)(\mu\text{-OAc})_2]^+$, the latter bearing the hydrogen bond donors in an asymmetric fashion. Therefore, the activity of these complexes within the first minutes of catalysis appears to be independent on the position of the hydrogen bond donors. The data obtained are depicted in Figure 62b and show Michaelis-Menten saturation behavior. Fitting the data of $[\text{Fe}^{\text{II}}_2(\text{H}_2\text{SIM}^1)(\mu\text{-OAc})_2]^+$ with the well-known Michaelis-Menten equation (Equation 22) provided values for the parameters k_{cat} , K_M , and k_{cat}/K_M . Table 23 lists these values and compares them to data for other diiron complexes.

Table 23: Kinetic data (k_{cat} in $[10^{-3} \text{ s}^{-1}]$, K_M in $[\text{mM}]$ and k_{cat}/K_M in $[\text{s}^{-1}\text{M}^{-1}]$) of BDNPP hydrolysis for $[\text{Fe}^{\text{II}}_2(\text{H}_2\text{SIM}^1)(\mu\text{-OAc})_2]^+$ and reported diiron complexes (all kinetic studies were undertaken in a mixture of acetonitrile:aqueous buffer solution (1:1)).

complex	$\text{pK}_a(\text{I})$	$\text{pK}_a(\text{II})$	k_{cat}	K_M	k_{cat}/K_M	$\text{pH}_{\text{MM}}^{\text{a}}$
$[\text{Fe}^{\text{II}}_2(\text{H}_2\text{SIM}^1)(\mu\text{-OAc})_2]^+$	n.a.	n.a.	2.37 ± 0.29	3.53 ± 0.68	0.67	9.5
$[\text{Fe}^{\text{III}}_2(\text{L}^1)(\text{solv})_x]^{5+}$ ¹¹⁴	5.00	7.15	0.17 ± 0.01	1.74 ± 0.35	0.10	6.35
$[\text{Fe}^{\text{III}}_4(\text{L}^{66})_2(\mu\text{-OAc})_2(\mu\text{-O})(\mu\text{-OH})(\text{OH}_2)_2]^{2+}$ ²⁷⁸	5.42	8.41	1.6 ± 0.2	7.4 ± 0.6	0.22	6.5
$[\text{Fe}^{\text{III}}_2(\text{H}_2\text{L}^2)(\text{solv})_x]^{5+}$ ¹¹⁴	5.16	7.43	0.47 ± 0.03	5.92 ± 0.62	0.08	6.45
$[\text{Fe}^{\text{III}}_2(\text{L}^{67})(\text{solv})_x]^{5+}$ ¹¹⁴	5.39	9.38	0.65 ± 0.03	7.38 ± 0.69	0.09	7.44
$[\text{Fe}^{\text{III}}_2(\text{H}_2\text{L}^6)(\mu\text{-O})\text{Cl}_2]^{2+}$ ¹⁰⁸	5.0	7.3	1.33 ± 0.08	1.94 ± 0.37	0.68	6.17
$[\text{Fe}^{\text{III}}\text{Fe}^{\text{II}}(\text{L}^4)(\mu\text{-OAc})_2]^{+}$ ¹⁴⁰	5.03	6.93	1.88	4.63	0.41	5.6
$[\text{Fe}^{\text{III}}\text{Fe}^{\text{II}}(\text{L}^{67})(\text{solv})_x]^{4+}$ ¹¹⁴	5.30	8.02	1.14 ± 0.04	2.30 ± 0.24	0.50	6.69

^a pH of aqueous buffer solution used for substrate dependence assays.

Compared to other examples of phenolate-bridged diiron complexes, $[\text{Fe}^{\text{II}}_2(\text{H}_2\text{SIM}^1)(\mu\text{-OAc})_2]^+$ exhibits the highest hydrolysis rate reported to date. In addition, the catalytic efficiency is the second highest reported for diiron(III) complexes after $[\text{Fe}^{\text{III}}_2(\text{H}_2\text{L}^6)(\mu\text{-O})\text{Cl}_2]^{2+}$. Although the latter complex exhibits a lower hydrolysis rate, it has a higher catalytic efficiency to $[\text{Fe}^{\text{II}}_2(\text{H}_2\text{SIM}^1)(\mu\text{-OAc})_2]^+$ due to higher substrate affinity. The Michaelis-Menten constant K_M and subsequently the substrate affinity of complex $[\text{Fe}^{\text{II}}_2(\text{H}_2\text{SIM}^1)(\mu\text{-OAc})_2]^+$ is in the medium range compared to the listed diiron complexes.

Comparison of the two complexes $[\text{Fe}^{\text{III}}_2(\text{H}_2\text{L}^2)(\text{solv})_x]^{5+}$ and $[\text{Fe}^{\text{II}}_2(\text{H}_2\text{L}^2)(\mu\text{-OAc})_2]^+$ with the same ligand backbone allows the identification of the impact of the oxidation state of the two iron

centers. The reduced form exhibits a higher hydrolysis rate, a higher substrate affinity and consequently a higher catalytic efficiency, but with the cost of the maximum activity at more basic conditions. Therefore, the higher activity of the two Fe^{II}₂ complexes studied in this work compared to the reference complexes listed in Table 23 can be attributed to an interplay of hydrogen bonding ability and the lower Lewis acidity of the two Fe^{II} centers (compared to the Fe^{III} centers in the reference complexes). However, it should be noted that the Fe^{II}₂ complexes are less reactive at physiological pH than under basic conditions used for these investigations.

The substrate concentration dependence measurements conducted with the Zn^{II}₂ complexes [Zn^{II}₂(H₂L²)(μ-OAc)₂]⁺ and [Zn^{II}₂(H₂SIM¹)(μ-OAc)(OH)]⁺ also under basic conditions (pH 9.5) resulted for both complexes in lower hydrolysis rates and higher Michaelis-Menten constants than the Fe^{II}₂ complex [Fe^{II}₂(H₂SIM¹)(μ-OAc)₂]⁺. Consequently, the catalytic efficiencies of [Zn^{II}₂(H₂L²)(μ-OAc)₂]⁺ and [Zn^{II}₂(H₂SIM¹)(μ-OAc)(OH)]⁺ are lowered compared to [Fe^{II}₂(H₂SIM¹)(μ-OAc)₂]⁺; two-fold in the case of [Zn^{II}₂(H₂L²)(μ-OAc)₂]⁺ and four-fold in the case of [Zn^{II}₂(H₂SIM¹)(μ-OAc)(OH)]⁺.

Turn Over Numbers

In order to probe the long-term catalytic behavior of the diiron complexes of ligand H₃SIM¹ and H₃L² studies of the TONs were conducted at 25°C with [complex]₀ = 10 μM and [BDNPP]₀ = 3.0 mM at different pH. The assays were prepared in the glovebox using 0.5 mM solutions of [Fe^{II}₂(H₂SIM¹)(μ-OAc)₂]⁺ and [Fe^{II}₂(H₂L²)(μ-OAc)₂]⁺ as well as 0.5 mM mixtures of [Fe^{II}₂(H₂SIM¹)(μ-OAc)₂]⁺ and [Fe^{II}₂(H₂L²)(μ-OAc)₂]⁺ with ferrocenium hexafluorophosphate (1:1), prepared 24 hours prior to the TON studies. Samples were taken from these assays at various intervals during the experiment, diluted with solvent, and their UV-vis spectra were recorded to determine the amount of phosphoester hydrolysis. The increase in the absorbance at 400 nm, assigned to the hydrolysis product 2,4-dinitrophenolate, was monitored over time and TON values were calculated after nine days using the Beer-Lambert Law. The resulting data obtained at pH 9.5 and pH 11 are given in Figure 63 and Table 24. [Zn^{II}₂(L¹)(μ-OAc)₂]⁺PF₆⁻ was also included in the process to ensure that there is no effect given by undertaking the experiments under inert atmosphere. In fact, this Zn^{II}₂ complex exhibit comparable TONs to those obtained under aerobic conditions (Chapter 7.2). Furthermore, the Zn^{II}₂ complex lacking hydrogen bond donors exhibited the highest TONs throughout the study.

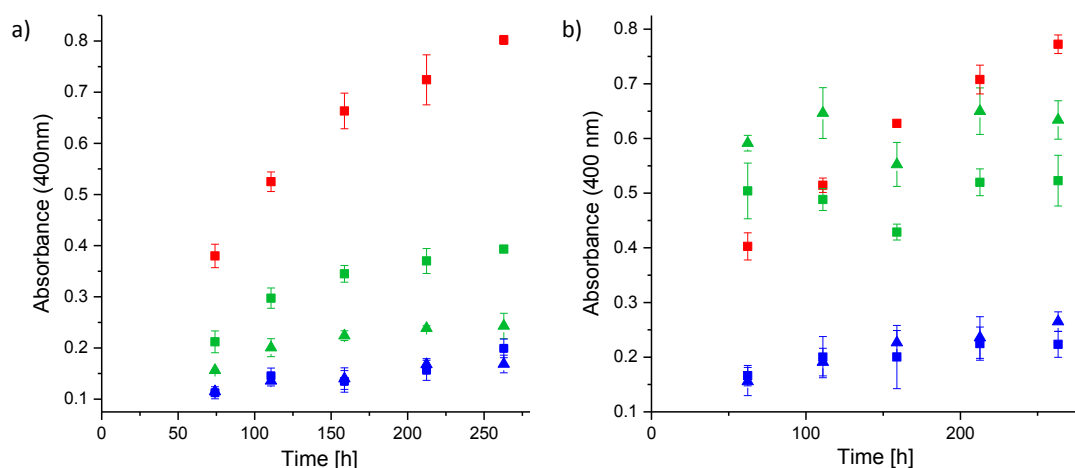


Figure 63: Time dependence of the absorbance band of 2,4-nitrophenolate (400 nm) a) at pH 9.5 and b) at pH 11 with [Zn^{II}₂(L¹)(μ-OAc)₂]⁺ (red), [Fe^{II}₂(H₂SIM¹)(μ-OAc)₂]⁺ (green), and [Fe^{II}₂(H₂L²)(μ-OAc)₂]⁺ (blue) with addition of 1 eq FeCp₂PF₆ (triangles) and without (squares).

The TONs for the diiron complexes increase with increasing pH, but it should be mentioned that all four iron containing assays show similar TONs when the experiments are conducted at pH < 9. However, under more basic condition the structural variations in the diiron complexes were reflected in the differences of their determined TONs. At basic conditions (pH > 9) the asymmetric diiron complex [Fe^{II}₂(H₂SIM¹)(μ-OAc)₂]⁺ (depicted in green in Figure 63) showed higher TONs than the symmetric counterpart [Fe^{II}₂(H₂L²)(μ-OAc)₂]⁺ (depicted in blue in Figure 63). This development seems independent on the oxidation state of the iron centers as the mixtures of the respective complexes with one equivalent of ferrocenium hexafluorophosphate followed the same trend. These findings lead to the conclusion that two hydrogen bond donors proximal to one Fe^{II} center in the Fe^{II}₂ model complex help to prevent more efficiently the complex being inhibited than one hydrogen bond donor proximal to each Fe^{II} center. Interestingly, the impact of the hydrogen bond donors was found to be reversed for the Zn^{II}₂ complexes: one hydrogen bond donor adjacent to each Zn^{II} center is more efficient in preventing complex inhibition than two hydrogen bond donors proximal to one of the two Zn^{II} centers.

Table 24: Turn over numbers (TONs) of BDNPP hydrolysis for [Fe^{II}₂(H₂SIM¹)(μ-OAc)₂]⁺ and [Fe^{II}₂(H₂L²)(μ-OAc)₂]⁺ as well as mixtures of those complexes with 1 eq FeCp₂PF₆.

complex	TON after 9 h		
	pH 9	pH 9.5	pH 11
[Fe ^{II} ₂ (H ₂ SIM ¹)(μ-OAc) ₂] ⁺	11 ± 2	61 ± 4	86 ± 4
[Fe ^{II} ₂ (H ₂ SIM ¹)(μ-OAc) ₂] ⁺ + 1 eq FeCp ₂ ⁺	6 ± 6	39 ± 1	107 ± 7
[Fe ^{II} ₂ (H ₂ L ²)(μ-OAc) ₂] ⁺	2 ± 2	26 ± 3	37 ± 5
[Fe ^{II} ₂ (H ₂ L ²)(μ-OAc) ₂] ⁺ + 1 eq FeCp ₂ ⁺	2 ± 2	28 ± 2	39 ± 6

Comparison of the TONs obtained with assays containing the same Fe^{II}₂ complex but differing in the presence of ferrocenium hexafluorophosphate enables to study the impact of the oxidation

states of the bound iron ions. The TON of the symmetric diiron complex bearing the H_3L^2 ligand backbone was found to be independent on the presence of ferrocenium hexafluorophosphate. This was different when the asymmetric complex $[Fe^{II}_2(H_2SIM^1)(\mu-OAc)_2]^+$ was used as catalyst. The long-term measurements at pH 9 and pH 9.5 resulted in higher TON values in the absence of ferrocenium hexafluorophosphate indicating that the heterovalent complex $[Fe^{III}Fe^{II}(H_2SIM^1)(solvent)_x]^{4+}$ is favored for bridging phosphate inhibition for the corresponding homovalent Fe^{II}_2 complex. This finding is in agreement with the higher water exchange rate of Fe^{II} compared to Fe^{III} ($10^6 s^{-1}$ and $10^2 s^{-1}$).^{278, 296-298} However, at strongly basic conditions (pH 11) the trend was reversed, *i.e.* the $Fe^{III}Fe^{II}$ complex revealed a higher TON than the Fe^{II}_2 complex of H_3SIM^1 .

Studies of the hydrolysis of phosphomonoesters using DNPP as model substrate in the TON assays revealed no acceleration of phosphoester hydrolysis compared to the autohydrolysis assay independent on (i) the symmetry, and (ii) the oxidation state of the diiron complexes.

8.3 SUMMARY

The investigation of the phosphoester hydrolysis undertaken with the Fe^{II}_2 complexes $[Fe^{II}_2(H_2SIM^1)(\mu-OAc)_2]^+$ and $[Fe^{II}_2(H_2L^2)(\mu-OAc)_2]^+$ and comparison with the corresponding Zn^{II}_2 and $Fe^{III}Fe^{II}$ complexes gave insights on the impact of (i) the secondary coordination sphere, and (ii) the Lewis acidity of the metal ion bound to the ligand backbone. The hydrolysis rate was found to be similar for both complexes $[Fe^{II}_2(H_2SIM^1)(\mu-OAc)_2]^+$ and $[Fe^{II}_2(H_2L^2)(\mu-OAc)_2]^+$; thus, the activity in the first minutes of catalysis seems to be independent on the hydrogen bond donor position. However, significant differences in long-term activity studies, *i.e.* the TONs, of $[Fe^{II}_2(H_2SIM^1)(\mu-OAc)_2]^+$ and $[Fe^{II}_2(H_2L^2)(\mu-OAc)_2]^+$ indicate that the steric hindrance of two pivaloyl-amide residues adjacent to one Fe^{II} center prevents inhibition by a bridging phosphomonoester molecule more efficiently than positioning one sterically demanding hydrogen bond donor proximal to each Fe^{II} center. Interestingly, the effect of the position of the pivaloyl-amide residues is found to be the opposite for the respective Zn^{II}_2 complexes (discussed in Chapter 7.2). Of the two influences of the pivaloyl-amide residues towards the bridging phosphoester coordination, (i) the hindered access to the metal ion, and (ii) the stabilization by hydrogen bond formation, the first appears more important for the Fe^{II}_2 complexes while the latter seems more important for the Zn^{II}_2 complexes. But it should be mentioned that both Fe^{II}_2 complexes exhibit lower TONs than the corresponding Zn^{II}_2 complexes, as expected due to the lower Lewis acidity and the faster water exchange rate of Zn^{II} compared to Fe^{II} . However, the Fe^{II}_2 complexes

revealed higher hydrolysis rates and catalytic efficiencies than the Zn^{II}_2 complexes. Therefore, the higher Lewis acidity of Fe^{II} compared to Zn^{II} appears to enhance not only the hydrolysis acceleration but also the binding of inhibiting phosphomonoesters. Similarly, the oxidation of one of the two Fe^{II} centers in $[Fe^{II}_2(H_2SIM^1)(\mu-OAc)_2]^+$ forming a more accurate $Fe^{III}Fe^{II}$ model system for PAP, lead to a lower TON. This is in agreement with the decreased water exchange rate and the higher Lewis acidity of Fe^{III} compared to Fe^{II} .^{164, 166} However, the Fe^{II}_2 complex of H_2L^2 reveals a more basic pH maximum of the hydrolysis activity than the respective Fe^{III}_2 complex supporting the presumption that the role of the Fe^{III} center in the active site of PAP is the provision of a nucleophilic hydroxide at low pH.

Chapter 9

Phosphatase Activity of

Heterovalent

Heterodinuclear Complexes^h

^h Main parts of this chapter will be published in "Asymmetric Mono- and Dinuclear Ga^{III} and Zn^{II} complexes as Models for Purple Acid Phosphatases (PAPs)"; [Simone Bosch](#), Peter Comba, Lawrence R. Gahan and Gerhard Schenk; manuscript in preparation.

9.1 INTRODUCTION

As a prototype of dinuclear metallohydrolases, PAPs catalyze the hydrolysis of phospho-monoesters containing two metal ions in close proximity in the active site of PAPs. More precisely, PAPs are the only dinuclear metallohydrolases which require a mixed-valent dinuclear site for their activity.²¹ While mammalian PAPs consist of a Fe^{III}Fe^{II} center,⁴⁹ the metal ion composition in PAPs isolated from plants was found to be either Fe^{III}Zn^{II} or Fe^{III}Mn^{II}.^{23, 24, 67, 68} It has been shown, however, that replacement of the Fe^{III} center in pig PAP and bovine spleen PAP by a Ga^{III} ion generates Ga^{III}Fe^{II} and Ga^{III}Zn^{II} derivatives that exhibit similar activities to the native enzymes,^{66, 142, 167, 299, 300} and showing that the diamagnetic Ga^{III} ion was able to act as a functional analog of paramagnetic Fe^{III} in PAPs.¹⁴⁶

Small heterodinuclear mixed-valent compounds modeling the structural and functional properties of metallohydrolases have been shown to be useful tools to study the roles of structural features within the active site of the corresponding enzymes. For example, the complex [Fe^{III}Zn^{II}(L⁴)(μ-OAc)₂]⁺ has shown that (i) the model substrate BDNPP only interacts with the Zn^{II} ion, and (ii) the bridging hydroxide is a much weaker nucleophile than the terminal Fe^{III}-bound hydroxide in the active species [(HO)Fe^{III}(μ-OH)M^{II}(OH₂)].⁹⁰ The respective isostructural complex [Ga^{III}Zn^{II}(L⁴)(μ-OAc)₂]⁺ was also studied and exhibited a higher TON than the analogous Fe^{III}Zn^{II} complex.⁶⁶ A similar result was observed from kinetic studies of the complexes [Fe^{III}Co^{II}(L⁴)(μ-OAc)₂]⁺ and [Ga^{III}Co^{II}(L⁴)(μ-OAc)₂]⁺, and Table 25 summarizes the reported kinetic data.¹⁴⁶ As in the case of the biomimetics, the Ga^{III} derivative of ufPAP revealed modest increased reactivity consistent with the increased nucleophilic character of the Ga^{III}-bound hydroxide compared to the Fe^{III}-bound hydroxide.¹⁴⁶ Moreover potentiometric titrations with [Fe^{III}Co^{II}(L⁴)(μ-OAc)₂]⁺ and [Ga^{III}Co^{II}(L⁴)(μ-OAc)₂]⁺ supports the terminal hydroxide being the reaction initiating nucleophile, as assumed previously for [Ga^{III}Zn^{II}(L⁴)(μ-OAc)₂]⁺ and [Fe^{III}Zn^{II}(L⁴)(μ-OAc)₂]⁺.^{146, 66} Hence, the mechanism that emerges for biomimetics involves the initial monodentate coordination of the substrate to the divalent metal ion, followed by a nucleophilic attack by the terminal M^{III}-bound hydroxide. This was supported by kinetic isotope effect and UV-vis spectroscopic substrate binding studies with [Fe^{III}Co^{II}(L⁴)(μ-OAc)₂]⁺ and [Ga^{III}Co^{II}(L⁴)(μ-OAc)₂]⁺.¹⁴⁶

Kinetic studies with a Fe^{III}Zn^{II} complex anchored to 3-aminopropyl-functionalized silica (Si3AP) resulted in increased substrate affinities compared to the free catalyst.¹⁵³ This effect was proposed to be caused by stabilization via hydrogen bonds with the residual amino-groups of the

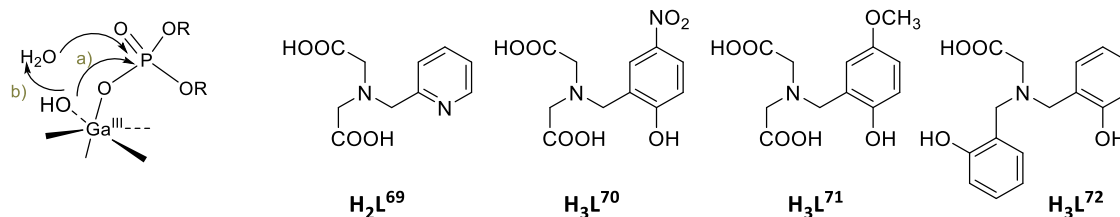
surface, supporting the role of the non-coordinating histidines in the active site of PAPs to bring the substrate in position suitable for hydrolysis.

Table 25: Kinetic data (k_{cat} in $[10^{-3} \text{ s}^{-1}]$, K_{M} in $[\text{mM}]$ and $k_{\text{cat}}/K_{\text{M}}$ in $[\text{s}^{-1} \text{ M}^{-1}]$) of BDNPP hydrolysis (all kinetic studies were undertaken in a mixture of acetonitrile:aqueous buffer solution (1:1)).

complex	pK _a (I)	pK _a (II)	k_{cat}	K_{M}	$k_{\text{cat}}/K_{\text{M}}$	pH _{MM} ^a
[Fe ^{III} Zn ^{II} (L ⁴)(μ-OAc) ₂] ⁺⁹⁵	4.8	7.5	0.73	8.10	0.09	6.1
[Fe ^{III} Zn ^{II} (L ⁴)(μ-OH) ₂] ⁺⁹⁰	5.3	8.1	0.91	4.20	0.22	6.5
[Ga ^{III} Zn ^{II} (L ⁴)(μ-OAc) ₂] ⁺⁶⁶	5.4	8.6	1.41	7.15	0.20	6.8
[Fe ^{III} Co ^{II} (L ⁴)(μ-OAc) ₂] ⁺¹⁴⁶	5.2	8.8	1.42	92.7	0.02	7.0
[Ga ^{III} Co ^{II} (L ⁴)(μ-OAc) ₂] ⁺¹⁴⁶	5.7	8.9	1.87	88.1	0.02	7.5
[Fe ^{III} Zn ^{II} (HL ⁶⁸)(μ-OH)(H ₂ O)] ²⁺¹⁵³	-	-	0.90	3.55	0.25	7.0
[Fe ^{III} Zn ^{II} (Si3AP-L ⁶⁸)(μ-OH)(H ₂ O)] ²⁺¹⁵³	-	-	0.14	1.54	0.09	7.0

^a pH of aqueous buffer solution used for substrate dependence assays.

Using monogallium(III) complexes of tripodal ligands, H₂L⁶⁹, H₃L⁷⁰, H₃L⁷¹, and H₃L⁷² among others (Scheme 22), the influence of the nature of the ligand donor sites on the reactivity of Ga^{III} (mimicking the Fe^{III} ion in PAPs) has been evaluated.⁷⁰ Thereby, the attack of the coordinated substrate by a Ga^{III}-bound hydroxide (Scheme 22, path a) was shown to be the catalytic mechanism rather than the alternative, where the metal-bound hydroxide acts as a general base deprotonating incoming water, which subsequently attacks the phosphoester substrate (Scheme 22, path b).⁷⁰



Scheme 22: Substrate activation and the two possibilities for the nucleophilic attack on the phosphorus atom during phosphoester hydrolysis by monogallium(III) model compounds and ligands H₂L⁶⁹, H₃L⁷⁰, H₃L⁷¹, and H₃L⁷² employed studying the influence of the nature of the ligand donor sites on the phosphoester hydrolysis activity of Ga^{III} complexes.⁷⁰

During the studies, it emerged that the reactivity of the monogallium(III) complexes was enhanced by replacement of neutral nitrogen donor atoms and carboxylate groups by phenolate groups. Specifically it was proposed that the presence of strongly electron-donating phenolate groups (H₃L⁷² > H₃L⁷¹ > H₃L⁷⁰ > H₂L⁶⁹) in the coordination sphere of Ga^{III} weakens the metal-hydroxide bond, thus giving rise to an enhanced nucleophilicity and higher activity of the corresponding Ga^{III} complexes.⁷⁰ Table 26 lists the reported kinetic data.⁷⁰

Table 26: Kinetic data (k_{cat} in $[10^{-3} \text{ s}^{-1}]$, K_{M} in $[\text{mM}]$ and $k_{\text{cat}}/K_{\text{M}}$ in $[\text{s}^{-1}\text{M}^{-1}]$) of BDNPP hydrolysis (all kinetic studies were undertaken in a mixture of methanol-aqueous buffer solution (1:5) at 37°C).⁷⁰

complex	$\text{p}K_{\text{a}}(\text{I})$	$\text{p}K_{\text{a}}(\text{II})$	k_{cat}	K_{M}	$k_{\text{cat}}/K_{\text{M}}$	$\text{pH}_{\text{MM}}^{\text{a}}$
$[\text{Ga}^{\text{III}}(\text{L}^{69})(\mu\text{-OH})_2]$	5.69	7.12	3.61	1.34	2.69	6.4
$[\text{Ga}^{\text{III}}(\text{L}^{70})(\text{H}_2\text{O})_2]$	5.43	8.59	21.2	541	0.04	7.0
$[\text{Ga}^{\text{III}}(\text{L}^{71})(\text{H}_2\text{O})_2]$	5.90	8.99	30.5	10.3	2.96	7.5
$[\text{Ga}^{\text{III}}(\text{L}^{72})(\text{H}_2\text{O})_2]$	7.26	9.72	46.4	7850	0.01	8.5

^a pH of aqueous buffer solution used for substrate dependence assays.

Comparison of the different monogallium(III) complexes emphasizes that the two most reactive complexes $[\text{Ga}^{\text{III}}(\text{L}^{71})(\text{H}_2\text{O})_2]$ and $[\text{Ga}^{\text{III}}(\text{L}^{72})(\text{H}_2\text{O})_2]$ have (i) the lowest Lewis acidities, thus providing the lowest substrate activation, and (ii) the strongest hydroxide nucleophile.⁷⁰ Apparently, this reveals that of the two effects of the metal ion in the hydrolysis of phosphoesters, (i) Lewis acid activation of the substrate and (ii) nucleophile activation, the latter is more important in determining the intrinsic reactivity.⁷⁰

In order to stabilize the heterovalent dinuclear core, the peptide backbone of the active site in PAPs forms two chemically distinct environments for the metal centers. In Chapter 3 the selective formation of the heterodinuclear heterovalent complexes $[\text{Ga}^{\text{III}}\text{Zn}^{\text{II}}(\text{H}_2\text{SIM}^1)(\text{solv})_x]^{4+}$ and $[\text{Ga}^{\text{III}}\text{Zn}^{\text{II}}(\text{H}_2\text{SIM}^4)(\text{solv})_x]^{3+}$, depicted in Chart 27, has been illustrated. These complexes combine the three essential structural features within the active site of PAPs: (i) the distinct coordination environment in the two binding sites, (ii) the mixed-valent dinuclear metal core, and (iii) the hydrogen bonding network provided by the second coordination sphere. With hydrogen bond donors proximal to the metal centers, mimicking the non-coordinating histidine residues in the active site of PAPs, the impact of hydrogen bonding capacity on the reactivity has been examined by comparison to each other and the reported complex $[\text{Ga}^{\text{III}}\text{Zn}^{\text{II}}(\text{L}^4)(\mu\text{-OAc})_2]^+$; the results are presented in the following chapter.

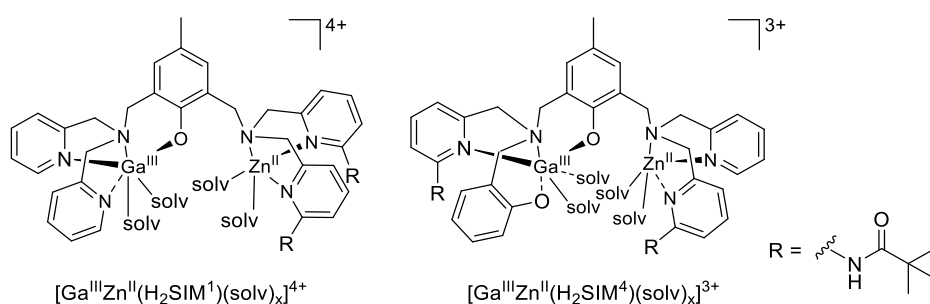


Chart 27: $\text{Ga}^{\text{III}}\text{Zn}^{\text{II}}$ complexes employed in this chapter.

Moreover, the ligands H_3SIM^1 and H_4SIM^4 have been shown to selectively form mononuclear Ga^{III} and Zn^{II} complexes (see Chapter 3). Therefore, the role of the specific structural aspect were investigated not only in their $\text{Ga}^{\text{III}}\text{Zn}^{\text{II}}$ complexes but also in their mononuclear Ga^{III} and Zn^{II} complexes as well as in their dizinc(II) complexes, depicted in Chart 28.

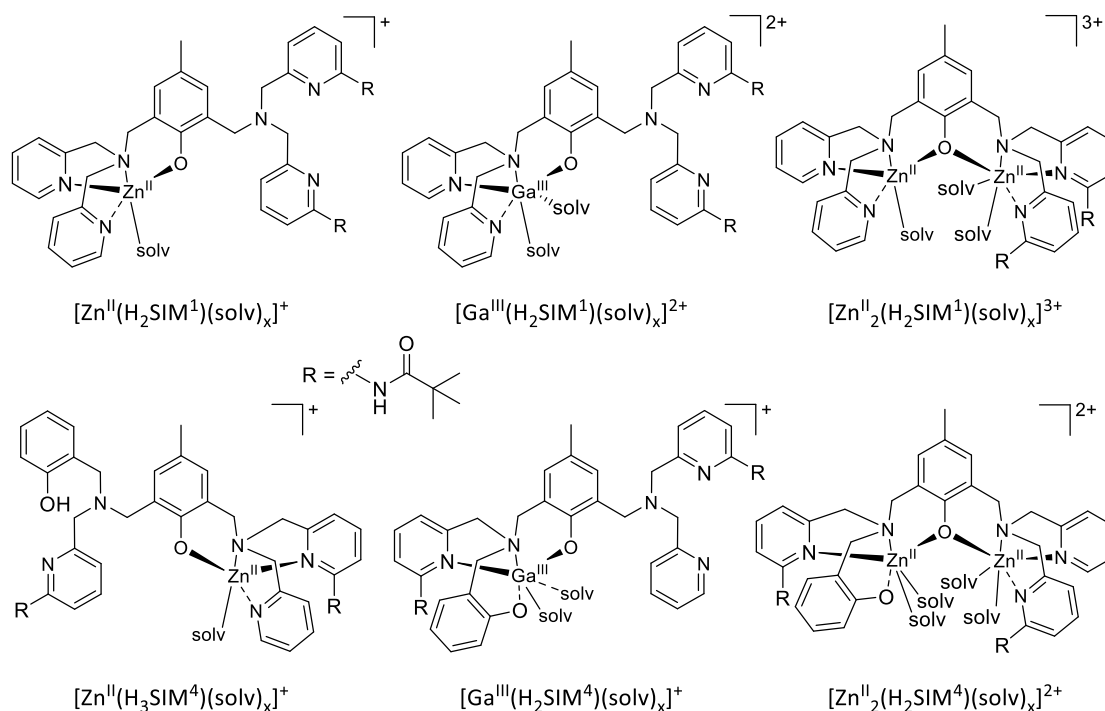


Chart 28: Zn^{II}, Ga^{III} and Zn^{II}₂ complexes referred to in this chapter.

Prior to the kinetic investigations the catalysts were prepared in solution. Separate 5 mM acetonitrile solutions of H₃SIM¹, H₄SIM⁴, zinc(II) perchlorate, and gallium(III) perchlorate were prepared. One equivalent of ligand solution was treated with either (i) one equivalent of zinc(II) perchlorate solution, (ii) two equivalents of zinc(II) perchlorate solution, or (iii) one equivalent of gallium(III) perchlorate solution. These mixtures were then heated at 50°C for one hour in the case of the zinc(II) containing mixtures and for six hours in the case of the gallium(III) containing mixtures in order to completely form the complexes $[Zn^{II}(H_2SIM^1)(solv)_x]^+$, $[Zn^{II}(H_3SIM^4)(solv)_x]^+$, $[Zn^{II}_2(H_2SIM^1)(solv)_x]^{3+}$, $[Zn^{II}_2(H_2SIM^4)(solv)_x]^{2+}$, $[Ga^{III}(H_2SIM^1)(solv)_x]^{2+}$, and $[Ga^{III}(H_2SIM^4)(solv)_x]^+$. The in this way previously prepared gallium(III) complexes of H₃SIM¹ and H₄SIM⁴, $[Ga^{III}(H_2SIM^1)(solv)_x]^{2+}$ and $[Ga^{III}(H_2SIM^4)(solv)_x]^+$, were treated with one equivalent of zinc(II) perchlorate and heated at 50°C for a further one hour to generate the Ga^{III}Zn^{II} complexes $[Ga^{III}Zn^{II}(H_2SIM^1)(solv)_x]^{4+}$ and $[Ga^{III}Zn^{II}(H_2SIM^4)(solv)_x]^{3+}$. All solutions were diluted with acetonitrile in the way that the final complex concentration was 1 mM.

9.2 PH BEHAVIOR OF $\text{Ga}^{\text{III}}\text{Zn}^{\text{II}}$ COMPLEXES

For determination of the pK_a values of metal-bound water deprotonation in the different complexes UV-vis spectroscopic titrations were undertaken. The investigations were carried out in acetonitrile:aqueous buffer mixtures (1:1) and the reported pH values refer to the pH of the buffer solution. Figure 64a depicts as an example the resulted UV-vis spectra for the complex $[\text{Ga}^{\text{III}}\text{Zn}^{\text{II}}(\text{H}_2\text{SIM}^1)(\text{solvent})_x]^{4+}$.

When the spectrum recorded at pH 5.5 is excluded, two isosbestic points are visible at 293 nm and 312 nm, indicating an equilibrium of two species. The absorbance vs. pH plots at different wavelengths are given in Figure 64b. These plots were fitted according to the procedure for the dizinc(II) complexes explained in Chapter 4.3. The pK_a values obtained for all complexes studied in this Chapter are given in Table 27.

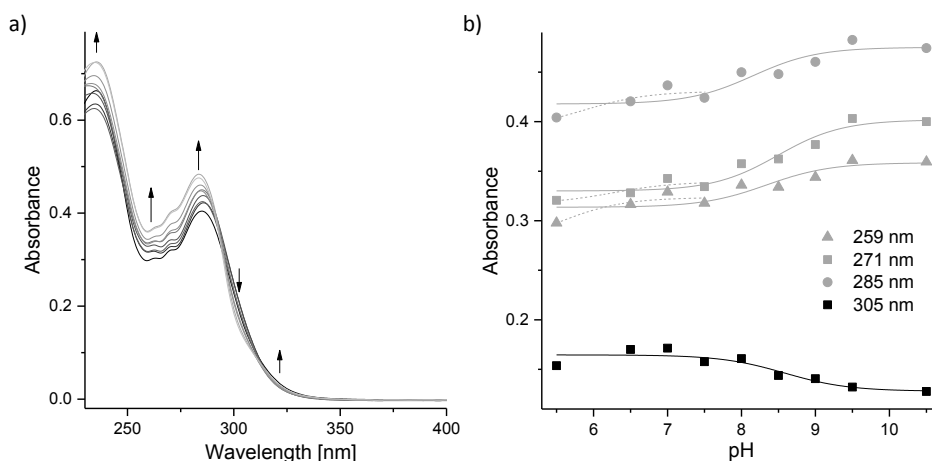


Figure 64: a) UV-vis spectroscopic titration spectra (25 μM in acetonitrile:aqueous buffer between pH 5.5 and 10.5) and b) absorbance vs. pH plot for $[\text{Ga}^{\text{III}}\text{Zn}^{\text{II}}(\text{H}_2\text{SIM}^1)(\text{solvent})_x]^{4+}$.

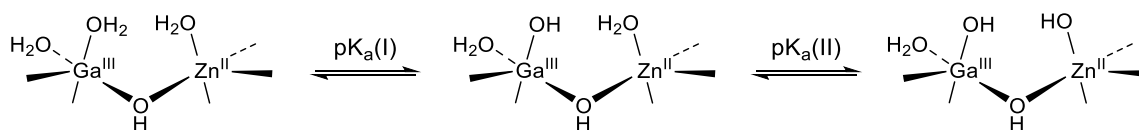
Table 27: pK_a values as determined by UV-vis-spectroscopic titration.

complex	pK_a	complex	pK_a
$[\text{Zn}^{\text{II}}(\text{H}_2\text{SIM}^1)(\text{solvent})_x]^+$	7.3 ± 0.2	$[\text{Zn}^{\text{II}}(\text{H}_2\text{SIM}^4)(\text{solvent})_x]$	8.4 ± 0.5
$[\text{Zn}^{\text{II}}_2(\text{H}_2\text{SIM}^1)(\text{solvent})_x]^{3+}$	6.9 ± 0.6	$[\text{Zn}^{\text{II}}_2(\text{H}_2\text{SIM}^4)(\text{solvent})_x]^{2+}$	9.8 ± 0.1
$[\text{Ga}^{\text{III}}(\text{H}_2\text{SIM}^1)(\text{solvent})_x]^{2+}$	6.7 ± 0.9	$[\text{Ga}^{\text{III}}(\text{H}_2\text{SIM}^4)(\text{solvent})_x]^+$	7.1 ± 0.7
	9.1 ± 0.4		
$[\text{Ga}^{\text{III}}\text{Zn}^{\text{II}}(\text{H}_2\text{SIM}^1)(\text{solvent})_x]^{4+}$	$(5.9 \pm 0.4)^a$	$[\text{Ga}^{\text{III}}\text{Zn}^{\text{II}}(\text{H}_2\text{SIM}^4)(\text{solvent})_x]^{3+}$	6.7 ± 0.4
	8.4 ± 0.2		$(10.6 \pm 0.1)^a$

^a determined pK_a values are close to limits of the examined pH range.

Fitting the data between pH 5.5 and pH 7.5 with a similar procedure resulted in a second pK_a value for $[\text{Ga}^{\text{III}}\text{Zn}^{\text{II}}(\text{H}_2\text{SIM}^1)(\text{solvent})_x]^{4+}$. Similarly, a second pK_a was found for $[\text{Ga}^{\text{III}}\text{Zn}^{\text{II}}(\text{H}_2\text{SIM}^4)(\text{solvent})_x]^{3+}$; these pK_a values should, however, be interpreted with care as they are close to the limits of the pH range studied. The respective pK_a values reported for

$[\text{Ga}^{\text{III}}\text{Zn}^{\text{II}}(\text{L}^4)(\mu\text{-OAc})_2]^+$, $\text{pK}_a(\text{I}) = 6.2$ and $\text{pK}_a(\text{II}) = 8.0$, were assigned to the equilibria depicted in Scheme 2.⁶⁶



Scheme 23: Illustration of the protonation equilibria for $\text{Ga}^{\text{III}}\text{Zn}^{\text{II}}$ complexes present in basic solution.⁶⁶

Comparison of the pK_a values obtained for $[\text{Ga}^{\text{III}}\text{Zn}^{\text{II}}(\text{H}_2\text{SIM}^4)(\text{solv})_x]^{3+}$ and $[\text{Ga}^{\text{III}}\text{Zn}^{\text{II}}(\text{L}^4)(\text{OAc})_2]^+$ indicate a shift of 0.5 pH units on account of a pivaloyl-amide residue proximal to the Ga^{III} center. This trend was also found, but was even more pronounced, for the monozinc(II) complexes $[\text{Zn}^{\text{II}}(\text{H}_2\text{SIM}^1)(\text{solv})_x]^+$ and $[\text{Zn}^{\text{II}}(\text{H}_3\text{SIM}^4)(\text{solv})_x]^+$.

9.3 PHOSPHOESTER HYDROLYSIS STUDIES WITH $\text{Ga}^{\text{III}}\text{Zn}^{\text{II}}$ COMPLEXES

The investigation of phosphatase-like activity of the two heterovalent heterodinuclear $\text{Ga}^{\text{III}}\text{Zn}^{\text{II}}$ complexes of the ligands H_3SIM^1 and H_4SIM^4 as well as their monogallium(III), monozinc(II), and dizinc(II) complexes were performed following the general procedure described in Chapter 6.3.

Kinetic Investigations with Complexes Bearing the H_3SIM^1 Backbone

pH Dependence

The pH dependence of the hydrolysis activity towards BDNPP of the complexes described above was investigated. Figure 65a shows the resulting v_0 vs. pH plot and Table 28 summarizes the pK_a and γ values obtained by fitting the data, assuming a monoprotic or diprotic system as explained in Chapter 6.3.

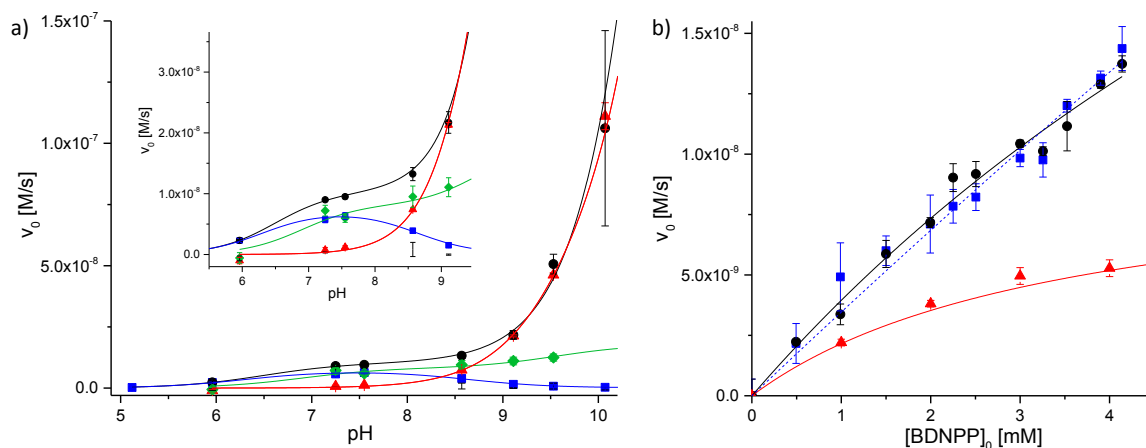


Figure 65: a) pH dependence and b) substrate concentration dependence at pH = 7 of BDNPP hydrolysis activity for mixtures of ligand H_3SIM^1 and with 1 eq of zinc(II) perchlorate (red triangles), 2 eq of zinc(II) perchlorate (green diamonds), 1 eq of gallium(III) perchlorate (blue squares), 1 eq zinc(II) perchlorate and 1 eq of gallium(III) perchlorate (black circles).

The examination of the BDNPP hydrolysis by the mono- and dinuclear complexes of H_3SIM^1 revealed differing pH dependencies. The monozinc(II) complex of H_3SIM^1 , $[\text{Zn}^{\text{II}}(\text{H}_2\text{SIM}^1)(\text{solv})_x]^+$, with Zn^{II} in the amide-free binding site B, was only active under basic conditions and showed very little activity below pH 7.5. Because the pK_a value for the deprotonation step of $[\text{Zn}^{\text{II}}(\text{H}_2\text{SIM}^1)(\text{solv})_x]^+$ is close or outside of the limits of the pH range examined in this study, the pK_a and γ values obtained from the fit to Equation 21 need to be interpreted with care. The dizinc(II) complex of HL^1 with two Zn^{II} centers in similar coordination environments to $[\text{Zn}^{\text{II}}(\text{H}_2\text{SIM}^1)(\text{solv})_x]^+$ and lacking hydrogen bond donors, revealed pK_a values of 6.5 and 10.3 and exhibited hydrolysis activity in the pH range between these two pK_a values. Therefore, the lack of activity at pH < 7.5 in the case of $[\text{Zn}^{\text{II}}(\text{H}_2\text{SIM}^1)(\text{solv})_x]^+$ seems to be due to the inability of cooperative interaction between two Zn^{II} centers. The pH dependence found for the dizinc(II) complex $[\text{Zn}^{\text{II}}_2(\text{H}_2\text{SIM}^1)(\text{solv})_x]^{3+}$, with both coordination sites of H_3SIM^1 occupied by Zn^{II} supports this proposal, as it exhibits BDNPP hydrolysis activity below pH 7.5, in contrast to the monozinc(II) complex $[\text{Zn}^{\text{II}}(\text{H}_2\text{SIM}^1)(\text{solv})_x]^+$.

In contrast to the mono- and dizinc(II) complexes of H_3SIM^1 , the monogallium(III) complex $[\text{Ga}^{\text{III}}(\text{H}_2\text{SIM}^1)(\text{solv})_x]^+$ shows a bell-shaped profile in the v_0 vs. pH plot. This complex is only catalytically active in the pH range between the two pK_a values of 6.3 and 8.6, indicating that the active species is $[\text{Ga}^{\text{III}}(\text{H}_2\text{SIM}^1)(\text{OH})(\text{OH}_2)]$. Both protonation and deprotonation of this active species lead to a decrease of activity.

Interestingly, when the second coordination site of the monogallium(III) complex is occupied by Zn^{II} in $[\text{Ga}^{\text{III}}\text{Zn}^{\text{II}}(\text{H}_2\text{SIM}^1)(\text{solv})_x]^{4+}$, a superposition of the profiles found for $[\text{Zn}^{\text{II}}(\text{H}_2\text{SIM}^1)(\text{solv})_x]^+$ and $[\text{Ga}^{\text{III}}(\text{H}_2\text{SIM}^1)(\text{solv})_x]^{2+}$ is observed but the initial rate at pH 7 was found to be higher than the

sum of the corresponding initial rates of $[\text{Zn}^{\text{II}}(\text{H}_2\text{SIM}^1)(\text{solv})_x]^+$ and $[\text{Ga}^{\text{III}}(\text{H}_2\text{SIM}^1)(\text{solv})_x]^{2+}$, indicating a cooperative effect of the two metal centers.

Comparison of the hydrolysis activity of the two mononuclear complexes of H_3SIM^1 , $[\text{Zn}^{\text{II}}(\text{H}_2\text{SIM}^1)(\text{solv})_x]^+$ and $[\text{Ga}^{\text{III}}(\text{H}_2\text{SIM}^1)(\text{solv})_x]$ demonstrates the role of the metal. While $[\text{Zn}^{\text{II}}(\text{H}_2\text{SIM}^1)(\text{solv})_x]^+$ shows only activity at high pH, $[\text{Ga}^{\text{III}}(\text{H}_2\text{SIM}^1)(\text{solv})_x]^+$ is active at low pH, indicating that in the case of a Zn^{II} in the active site, a high enough concentration of hydroxide is essential to ensure phosphoester hydrolysis. The fact that the metal-free ligand as well as the ligand-free zinc(II) perchlorate did not show any activity in the entire pH range illustrates the requirement for the Zn^{II} ion to be coordinated to the ligand for activation and subsequent hydrolysis of the phosphoester substrate. In the case of $[\text{Ga}^{\text{III}}(\text{H}_2\text{SIM}^1)(\text{solv})_x]^+$ the substrate hydrolysis detected at low pH can be explained by the ability of the Ga^{III} center to activate coordinated water and thereby to generate the nucleophilic hydroxide. Here, the nucleophile needed for phosphoester hydrolysis is provided even at near neutral pH. Moreover, ligand-free gallium(III) perchlorate was also tested for the hydrolysis of BDNPP but did not show any activity. The fact that at basic conditions only autohydrolysis is detectable with $[\text{Ga}^{\text{III}}(\text{H}_2\text{SIM}^1)(\text{solv})_x]^+$ indicates that the Ga^{III} ion in the doubly deprotonated species, most likely $[\text{Ga}^{\text{III}}(\text{H}_2\text{SIM}^1)(\text{OH})_2]$ is not able to activate the phosphoester substrate.

Substrate Concentration Dependence

The substrate concentration dependence was probed for $[\text{Zn}^{\text{II}}(\text{H}_2\text{SIM}^1)(\text{solv})_x]^+$, $[\text{Ga}^{\text{III}}(\text{H}_2\text{SIM}^1)(\text{solv})_x]^+$, and $[\text{Ga}^{\text{III}}\text{Zn}^{\text{II}}(\text{H}_2\text{SIM}^1)(\text{solv})_x]^{4+}$ at pH 7 ($0.5 \text{ mM} < [\text{BDNPP}]_0 < 4.14 \text{ mM}$). Saturation behavior was achieved for $[\text{Zn}^{\text{II}}(\text{H}_2\text{SIM}^1)(\text{solv})_x]^+$ and $[\text{Ga}^{\text{III}}\text{Zn}^{\text{II}}(\text{H}_2\text{SIM}^1)(\text{solv})_x]^{4+}$ that was not the case for $[\text{Ga}^{\text{III}}(\text{H}_2\text{SIM}^1)(\text{solv})_x]^+$ (k_{cat} , K_{M} and $k_{\text{cat}}/K_{\text{M}}$ are listed in Table 28).

Table 28: Kinetic data (k_{cat} in $[10^{-3} \text{ s}^{-1}]$, K_{M} in $[\text{mM}]$ and $k_{\text{cat}}/K_{\text{M}}$ in $[\text{s}^{-1}\text{M}^{-1}]$) of BDNPP hydrolysis with mixtures of the ligands H_3SIM^1 or H_4SIM^4 with 1 eq of zinc(II) perchlorate, 2 eq of zinc(II) perchlorate, 1 eq of gallium(III) perchlorate, 1 eq zinc(II) perchlorate and 1 eq of gallium(III) perchlorate (all kinetic studies were undertaken in a mixture of acetonitrile-aqueous buffer solution (1:1)).

complex	pK _a (I)	pK _a (II)	γ	$k_{\text{cat}}^{\text{a}}$	K_{M}^{a}	$k_{\text{cat}}/K_{\text{M}}^{\text{a}}$
$[\text{Zn}^{\text{II}}(\text{H}_2\text{SIM}^1)(\text{solv})_x]^+$	$(9.2 \pm 0.5)^{\text{c}}$	$(10.9 \pm 0.5)^{\text{c}}$	$(14.94 \pm 7.00)^{\text{c}}$	0.24 ± 0.02	4 ± 1	0.07
$[\text{Zn}^{\text{II}}_2(\text{H}_2\text{SIM}^1)(\text{solv})_x]^{3+}$	6.9 ± 0.4	9.6 ± 0.3	2.21 ± 0.64	n.a.	n.a.	n.a.
$[\text{Ga}^{\text{III}}(\text{H}_2\text{SIM}^1)(\text{solv})_x]^{2+}$	6.3 ± 0.2	8.6 ± 0.2	0.01 ± 0.07	- ^b	- ^b	- ^b
$[\text{Ga}^{\text{III}}\text{Zn}^{\text{II}}(\text{H}_2\text{SIM}^1)(\text{solv})_x]^{4+}$	6.5 ± 0.1	10.9 ± 0.1	90.34 ± 13.87	13.03 ± 3.51	12 ± 4	1.07
$[\text{Zn}^{\text{II}}(\text{H}_2\text{SIM}^4)(\text{solv})_x]$	$(12.4)^{\text{c}}$	-	-	0.12 ± 0.04	1 ± 1	0.10
$[\text{Zn}^{\text{II}}_2(\text{H}_2\text{SIM}^4)(\text{solv})_x]^{2+}$	-	-	-	n.a.	n.a.	n.a.
$[\text{Ga}^{\text{III}}(\text{H}_2\text{SIM}^4)(\text{solv})_x]^+$	6.7 ± 0.1	8.7 ± 0.2	0.01 ± 0.05	0.67 ± 0.14	7 ± 2	0.10
$[\text{Ga}^{\text{III}}\text{Zn}^{\text{II}}(\text{H}_2\text{SIM}^4)(\text{solv})_x]^{3+}$	6.5 ± 0.2	10.5 ± 0.3	12.84 ± 3.62	1.83 ± 0.21	7 ± 1	0.25

^a the assays were performed with aqueous buffer solution pH = 7, TONs were determined after 9 days.

^b the kinetic data for $[\text{Ga}^{\text{III}}(\text{H}_2\text{SIM}^1)(\text{solv})_x]^+$ could not be determined as Michaelis-Menten behavior was not observed.

^c determined pK_a values are close to limits if the examined pH range.

Mareque-Rivas *et al.* reported that a vacant second coordination site besides the coordination site occupied by Zn^{II} accelerates phosphoester hydrolysis in a similar way as providing metal...metal interaction. This effect was not observed for the phenolate-based complexes discussed in this chapter since the Zn^{II}_2 complexes of both, HL^1 and H_3SIM^1 , exhibit higher hydrolysis rates than $[Zn^{II}(H_2SIM^1)(solvent)_x]^+$.^{111, 193} The K_M values determined for $[Zn^{II}(H_2SIM^1)(solvent)_x]^+$ ($K_M = 4$ mM) and $[Zn^{II}_2(H_2SIM^1)(\mu-OAc)(OH)]^+$ ($K_M = 4$ mM; discussed in Chapter 7.2) are, however, in both cases much lower than for $[Zn^{II}_2(L^1)(\mu-OAc)_2]^+$ ($K_M = 123$ mM; discussed in Chapter 7.2), indicating an enhancement on the substrate affinity by the hydrogen bonding network.

Furthermore, the results obtained with the substrate concentration dependence measurements indicate that the exchange of the Zn^{II} ion present in binding site B in $[Zn^{II}(H_2SIM^1)(solvent)_x]^+$ by a Ga^{III} ion and the subsequent coordination of Zn^{II} in binding site C leads to a 50-fold increase in phosphoester hydrolysis rate, but simultaneously the value for K_M rises, *i.e.* the substrate affinity decreases. However, the catalytic efficiency of $[Ga^{III}Zn^{II}(H_2SIM^1)(solvent)_x]^{4+}$ is still 15-fold higher than the one detected for $[Zn^{II}(H_2SIM^1)(solvent)_x]^+$.

Comparison of the kinetic parameters for the $Ga^{III}Zn^{II}$ complex of H_3SIM^1 with those obtained for $[Zn^{II}_2(H_2SIM^1)(\mu-OAc)(OH)]^+$ ($k_{cat} = (0.57 \pm 0.04) \cdot 10^{-3} s^{-1}$; $K_M = (4 \pm 1)$ mM; $k_{cat}/K_M = 0.14 s^{-1}M^{-1}$;³⁰¹ discussed in Chapter 7.2) reveals that the heterodinuclear $Ga^{III}Zn^{II}$ complex hydrolyzes BDNPP twenty times faster at neutral pH. Although the substrate affinity of the $Ga^{III}Zn^{II}$ complex is significantly lower, the catalytic efficiency of $[Ga^{III}Zn^{II}(H_2SIM^1)(solvent)_x]^{4+}$ is increased six-fold compared to its Zn^{II}_2 counterpart illustrating the importance of the trivalent metal ion in the model complex.

Kinetic Investigations with Complexes Bearing the H_4SIM^4 Backbone

pH Dependence

The pH dependence experiments of the BDNPP hydrolysis for $[Zn^{II}(H_3SIM^4)(solvent)_x]^+$, $[Ga^{III}(H_2SIM^4)(solvent)_x]^+$ and $[Ga^{III}Zn^{II}(H_2SIM^4)(solvent)_x]^{3+}$ resulted in similar findings as for the corresponding complexes bearing the H_3SIM^1 ligand backbone, *i.e.* that (i) $[Zn^{II}(H_3SIM^4)(solvent)_x]^+$ is only active under strong basic conditions, (ii) $[Ga^{III}(H_2SIM^4)(solvent)_x]^+$ is active in a defined pH region between the two pK_a values, 6.74 and 8.68, and (iii) $[Ga^{III}Zn^{II}(H_2SIM^4)(solvent)_x]^{3+}$ exhibits a superposition of the behavior found for $[Zn^{II}(H_3SIM^4)(solvent)_x]^+$ and $[Ga^{III}(H_2SIM^4)(solvent)_x]^+$ (Figure 66a).

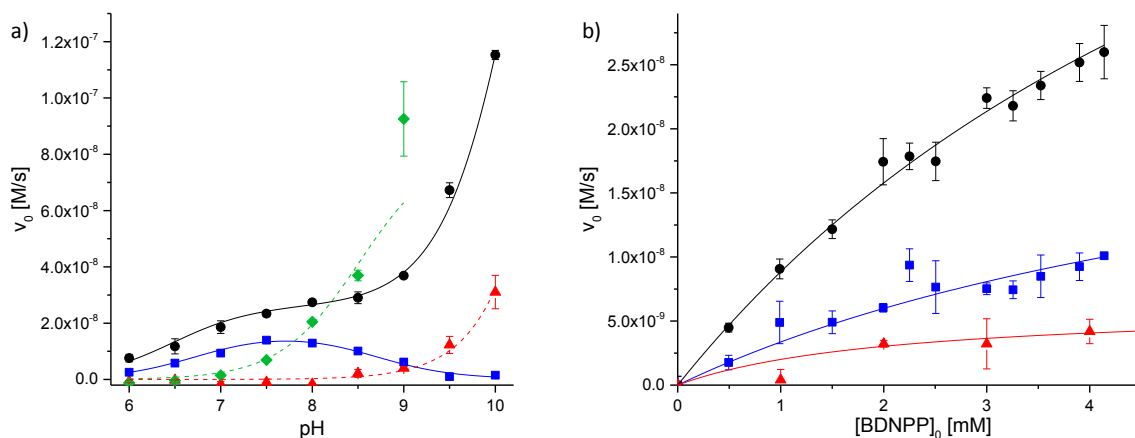


Figure 66: a) pH dependence and b) substrate concentration dependence at pH = 7 of BDNPP hydrolysis activity for mixtures of ligand H_4SIM^4 and with 1 eq of zinc(II) perchlorate (red triangles), 2 eq of zinc(II) perchlorate (green diamonds), 1 eq of gallium(III) perchlorate (blue squares), 1 eq zinc(II) perchlorate and 1 eq of gallium(III) perchlorate (black circles).

Substrate Concentration Dependence

The substrate concentration dependence measurements of $[Zn^{II}(H_3SIM^4)(solv)_x]^+$, $[Ga^{III}(H_2SIM^4)(solv)_x]^+$, and $[Ga^{III}Zn^{II}(H_2SIM^4)(solv)_x]^{3+}$ revealed that the hydrolysis rate of the $Ga^{III}Zn^{II}$ complex is increased three-fold compared to the monogallium(III) complex and increased six-fold compared to the monozinc(II) complex. However, the substrate affinity of the $Ga^{III}Zn^{II}$ complex is similar to that of the Ga^{III} complex and significantly lower to that of the Zn^{II} complex. Due to the much faster hydrolysis rate, the catalytic efficiency of $[Ga^{III}Zn^{II}(H_2SIM^4)(solv)_x]^{3+}$ is 2.5-times higher than those of $[Zn^{II}(H_3SIM^4)(solv)_x]^+$ and $[Ga^{III}(H_2SIM^4)(solv)_x]^+$.

In contrast to the corresponding complexes of H_3SIM^1 , $[Zn^{II}(H_3SIM^4)(solv)_x]^+$ bears the Zn^{II} in the same binding site as $[Ga^{III}Zn^{II}(H_2SIM^4)(solv)_x]^{3+}$, just like $[Ga^{III}(H_2SIM^4)(solv)_x]^+$ contains the Ga^{III} in the same binding site as $[Ga^{III}Zn^{II}(H_2SIM^4)(solv)_x]^{3+}$. Therefore, the fact that the $Ga^{III}Zn^{II}$ complex of H_4SIM^4 complex exhibit a higher catalytic activity than the sum of the hydrolysis rates of the monozinc(II) and monogallium(III) complexes can merely be attributed to a cooperative effect.

Comparison of the Zn^{II} , Zn^{II}_2 , Ga^{III} , and $Ga^{III}Zn^{II}$ Complexes with the Ligand Backbones H_3SIM^1 and H_4SIM^4

Independent on the ligand backbone of H_3SIM^1 and H_4SIM^4 , the two complexes with the same metal ions coordinated show similar pH dependencies of the initial hydrolysis rate. However, the initial hydrolysis rate of $[Zn^{II}(H_2SIM^1)(solv)_x]^+$ is higher at pH 10 than that for $[Zn^{II}(H_3SIM^4)(solv)_x]^+$ indicating a shift of the pK_a to higher pH by the pivaloyl-amide residue adjacent to the Zn^{II} center in $[Zn^{II}(H_2SIM^4)(solv)_x]$. The same is found for the Zn^{II}_2 complexes $[Zn^{II}_2(H_2SIM^1)(solv)_x]^{3+}$ and $[Zn^{II}_2(H_2SIM^4)(solv)_x]^{2+}$, *i.e.* $[Zn^{II}_2(H_2SIM^4)(solv)_x]^{2+}$ becomes active at higher pH than

$[\text{Zn}^{\text{II}}_2(\text{H}_2\text{SIM}^1)(\text{solvent})_x]^{3+}$, but the increase of the initial hydrolysis rate with increasing pH from 9 to 10 for the latter complex is more pronounced. The differences in the catalytic behavior of $[\text{Zn}^{\text{II}}_2(\text{H}_2\text{SIM}^1)(\text{solvent})_x]^{3+}$ and $[\text{Zn}^{\text{II}}_2(\text{H}_2\text{SIM}^4)(\text{solvent})_x]^{2+}$ could be a result of two structural features, (i) the unequal primary coordination sphere, and (ii) the different positioning of the hydrogen bond donors in the second coordination sphere.

Comparison of the Zn^{II}_2 complexes of H_3L^2 and H_4SIM^4 provides the opportunity to study the effect of changes to the first coordination sphere, with the secondary coordination sphere the same in both complexes. While H_3L^2 has two N_3O binding sites, H_4SIM^4 offers one N_3O^- and one N_2O_2 -coordination site. $[\text{Zn}^{\text{II}}_2(\text{H}_2\text{L}^2)(\mu\text{-OAc})_2]^+$ (see Chapter 7.2) and $[\text{Zn}^{\text{II}}_2(\text{H}_2\text{SIM}^4)(\text{solvent})_x]^{2+}$ exhibit similar behavior of their BDNPP hydrolysis activity; with increasing pH the initial hydrolysis rate for both increases significantly. However, the value of the initial hydrolysis rate measured at pH 9 is significantly higher for $[\text{Zn}^{\text{II}}_2(\text{H}_2\text{SIM}^4)(\text{solvent})_x]^{2+}$ than for $[\text{Zn}^{\text{II}}_2(\text{H}_2\text{L}^2)(\mu\text{-OAc})_2]^+$ and this is attributed to the exchange of one pyridine ligand by a more basic terminal phenolate ligand. Unfortunately, the absorbance at 400 nm increased to values near device limit when the experiments with $[\text{Zn}^{\text{II}}_2(\text{H}_2\text{SIM}^4)(\text{solvent})_x]^{2+}$ were undertaken at pH > 9. Based on these findings the higher initial hydrolysis rate of $[\text{Zn}^{\text{II}}_2(\text{H}_2\text{SIM}^4)(\text{solvent})_x]^{2+}$ compared to $[\text{Zn}^{\text{II}}_2(\text{H}_2\text{SIM}^1)(\text{solvent})_x]^{3+}$ is ascribed to the more basic phenolate donor in the former complex.

However, the most pronounced differences with respect to the two ligand backbones was found for the Ga^{III} complexes. In the pH profiles of Figure 67 it is clearly demonstrated that the complexes $[\text{Ga}^{\text{III}}(\text{H}_2\text{SIM}^4)(\text{solvent})_x]^+$ and $[\text{Ga}^{\text{III}}\text{Zn}^{\text{II}}(\text{H}_2\text{SIM}^4)(\text{solvent})_x]^{3+}$ show higher initial hydrolysis velocities than the corresponding H_4SIM^4 complexes $[\text{Ga}^{\text{III}}(\text{H}_2\text{SIM}^1)(\text{solvent})_x]^{2+}$ and $[\text{Ga}^{\text{III}}\text{Zn}^{\text{II}}(\text{H}_2\text{SIM}^1)(\text{solvent})_x]^{4+}$ in the entire pH range studied (Figure 67a).

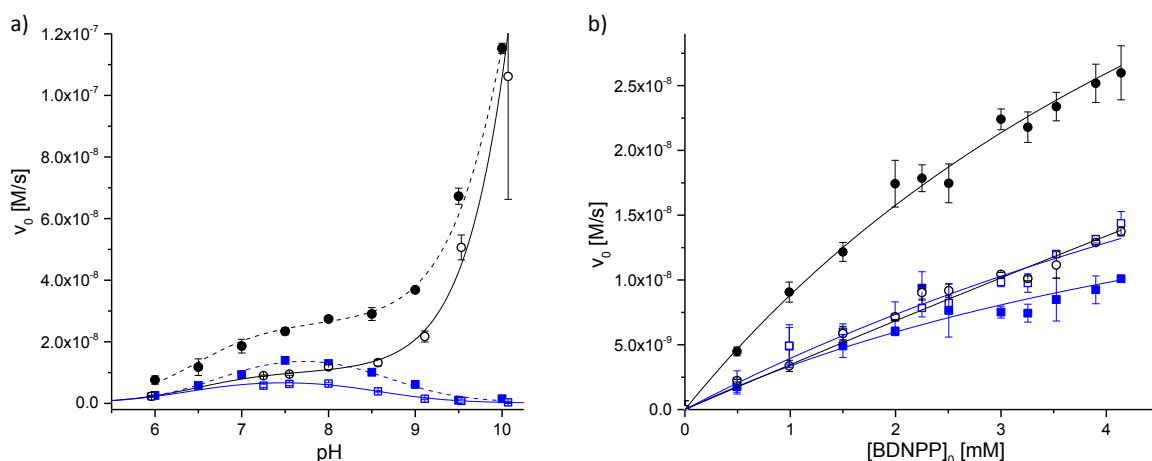


Figure 67: Comparison of a) pH dependence and b) substrate concentration dependence at pH = 7 of BDNPP hydrolysis activity for mixtures of ligand H_3SIM^1 (unfilled symbols) and H_4SIM^4 (filled symbols) with 1 eq of gallium(III) perchlorate (blue squares), 1 eq zinc(II) perchlorate and 1 eq of gallium(III) perchlorate (black circles).

The $\text{Ga}^{\text{III}}\text{Zn}^{\text{II}}$ complexes $[\text{Ga}^{\text{III}}\text{Zn}^{\text{II}}(\text{H}_2\text{SIM}^4)(\text{solv})]^{3+}$ and $[\text{Ga}^{\text{III}}\text{Zn}^{\text{II}}(\text{H}_2\text{SIM}^1)(\text{solv})]^{4+}$ differ in two structural features, (i) the primary coordination environment of the Ga^{III} center, and (ii) the position of the hydrogen bond donors mimicking the histidine residues in the second coordination sphere of the PAP active site. The previously reported complex $[\text{Ga}^{\text{III}}\text{Zn}^{\text{II}}(\text{L}^4)(\mu\text{-OAc})_2]^+$ helps to extract the specific impact of the structural variations.⁶⁶ The Ga^{III} environments in $[\text{Ga}^{\text{III}}\text{Zn}^{\text{II}}(\text{H}_2\text{SIM}^4)(\text{solv})]^{3+}$ and $[\text{Ga}^{\text{III}}\text{Zn}^{\text{II}}(\text{L}^4)(\mu\text{-OAc})_2]^+$ are similar with respect to the primary coordination sphere, but differ in the secondary coordination sphere as $[\text{Ga}^{\text{III}}\text{Zn}^{\text{II}}(\text{H}_2\text{SIM}^4)(\text{solv})]^{3+}$ bears a pivaloyl-amide residue adjacent to the Ga^{III} center while $[\text{Ga}^{\text{III}}\text{Zn}^{\text{II}}(\text{L}^4)(\mu\text{-OAc})_2]^+$ misses a proximal hydrogen bond donor. In contrast, the Ga^{III} center in both $[\text{Ga}^{\text{III}}\text{Zn}^{\text{II}}(\text{H}_2\text{SIM}^1)(\text{solv})]^{4+}$ and $[\text{Ga}^{\text{III}}\text{Zn}^{\text{II}}(\text{L}^4)(\mu\text{-OAc})_2]^+$, do not have a hydrogen bond donor in close proximity and therefore do not vary in the secondary coordination sphere, but the primary coordination sphere of the two complexes is different. Therefore, comparison of $[\text{Ga}^{\text{III}}\text{Zn}^{\text{II}}(\text{H}_2\text{SIM}^4)(\text{solv})]^{3+}$ with $[\text{Ga}^{\text{III}}\text{Zn}^{\text{II}}(\text{L}^4)(\mu\text{-OAc})_2]^+$ enables the elucidation of the effect of a hydrogen bonding donor adjacent to the Ga^{III} center. Similarly, comparison of $[\text{Ga}^{\text{III}}\text{Zn}^{\text{II}}(\text{H}_2\text{SIM}^1)(\text{solv})]^{4+}$ and $[\text{Ga}^{\text{III}}\text{Zn}^{\text{II}}(\text{L}^4)(\mu\text{-OAc})_2]^+$ gives an insight in the impact of the exchange of a pyridine by a phenolate residue in the primary coordination environment of the Ga^{III} center. In contrast to $[\text{Ga}^{\text{III}}\text{Zn}^{\text{II}}(\text{H}_2\text{SIM}^1)(\text{solv})_x]^{4+}$ and $[\text{Ga}^{\text{III}}\text{Zn}^{\text{II}}(\text{H}_2\text{SIM}^4)(\text{solv})_x]^{3+}$, $[\text{Ga}^{\text{III}}\text{Zn}^{\text{II}}(\text{L}^4)(\mu\text{-OAc})_2]^+$ exhibited a sigmoidal v_0 vs. pH curve with a relatively sharp activity maximum at $\text{pH} \sim 6.8$.⁶⁶ The differences in the pH profile curve shapes derived for $[\text{Ga}^{\text{III}}\text{Zn}^{\text{II}}(\text{H}_2\text{SIM}^1)(\text{solv})_x]^{4+}$ and $[\text{Ga}^{\text{III}}\text{Zn}^{\text{II}}(\text{H}_2\text{SIM}^4)(\text{solv})_x]^{3+}$ compared to $[\text{Ga}^{\text{III}}\text{Zn}^{\text{II}}(\text{L}^4)(\mu\text{-OAc})_2]^+$, more precisely the fact that the initial hydrolysis rate rises at pH values higher than nine for $[\text{Ga}^{\text{III}}\text{Zn}^{\text{II}}(\text{H}_2\text{SIM}^1)(\text{solv})_x]^{4+}$ and $[\text{Ga}^{\text{III}}\text{Zn}^{\text{II}}(\text{H}_2\text{SIM}^4)(\text{solv})_x]^{3+}$, in contrast to that of $[\text{Ga}^{\text{III}}\text{Zn}^{\text{II}}(\text{L}^4)(\mu\text{-OAc})_2]^+$, is attributed to the hydrogen bond donors adjacent to the Zn^{II} site in the former complexes.

The Ga^{III} coordination environments in both $[\text{Ga}^{\text{III}}\text{Zn}^{\text{II}}(\text{H}_2\text{SIM}^1)(\text{solv})_x]^{4+}$ and $[\text{Ga}^{\text{III}}\text{Zn}^{\text{II}}(\text{L}^4)(\mu\text{-OAc})_2]^+$ do not provide hydrogen bonding nearby, but they differ in the primary coordination sphere. The Ga^{III} center in $[\text{Ga}^{\text{III}}\text{Zn}^{\text{II}}(\text{H}_2\text{SIM}^1)(\text{solv})_x]^{4+}$ is bound in a N_3O -site, while the Ga^{III} ion in $[\text{Ga}^{\text{III}}\text{Zn}^{\text{II}}(\text{L}^4)(\mu\text{-OAc})_2]^+$ is coordinated to a N_2O_2 -site. Therefore, the shift of the pH maximum by 0.8 pH units with respect to the phosphoester hydrolysis activity in the region between pH 7 and pH 9 to more acidic conditions seems to be a result of the electron-rich phenolate coordinating ligand. However, it should be noted that this is in contrast to the results obtained with the monogallium(III) complexes of the tripodal ligands examined by Erxleben *et al.* (Scheme 22 and Table 26).⁷⁰

The Ga^{III} ions in $[\text{Ga}^{\text{III}}\text{Zn}^{\text{II}}(\text{H}_2\text{SIM}^4)(\text{solv})_x]^{3+}$ and $[\text{Ga}^{\text{III}}\text{Zn}^{\text{II}}(\text{L}^4)(\mu\text{-OAc})_2]^+$ have both the same primary coordination sphere but in $[\text{Ga}^{\text{III}}\text{Zn}^{\text{II}}(\text{H}_2\text{SIM}^4)(\text{solv})_x]^{3+}$ a pivaloyl-amide residue is positioned adjacent to the Ga^{III} ion that is missing in $[\text{Ga}^{\text{III}}\text{Zn}^{\text{II}}(\text{L}^4)(\mu\text{-OAc})_2]^+$. Interestingly, the pH maximum

for the hydrolysis activity in the region between pH 7 and pH 9 is shifted by 0.7 pH units to more basic conditions by the incorporation of a hydrogen bond donor proximal to the Ga^{III} center. Thus, the capacity of hydrogen bonding has a similar effect as a less electron-rich ligand in the primary coordination sphere, resulting in a more basic activity pH maximum.

Although, the pH maxima of the hydrolysis activity in the region between pH 6 and pH 9 is shifted to more basic conditions for the two complexes with hydrogen bond donors proximal to the dinuclear core, [Ga^{III}Zn^{II}(H₂SIM¹)(solv)]⁴⁺ and [Ga^{III}Zn^{II}(H₂SIM⁴)(solv)]³⁺ (see Table 28) exhibit at pH 7 (i) higher hydrolysis rates k_{cat} , (ii) higher K_M values and subsequently lower substrate affinity, and (iii) higher catalytic efficiencies than [Ga^{III}Zn^{II}(L⁴)(μ -OAc)₂]⁺ (see Table 25), lacking hydrogen bonding capacity.⁶⁶ This is most likely due to hydrogen bond formation. Moreover, the positioning of two hydrogen bond donors adjacent to the Zn^{II} binding site has the most pronounced effect.

Turn Over Numbers

In order to determine the TONs of the Zn^{II}, Zn^{II}₂, Ga^{III}, and Ga^{III}Zn^{II} complexes of H₃SIM¹ and H₄SIM⁴ a long-term study was conducted following the general procedure explained in Chapter 6.3. The assays were prepared with the aqueous-buffer solution of pH 7. TON values after nine days were calculated using the Beer-Lambert Law. The resulting data are given in Figure 68 and Table 29.

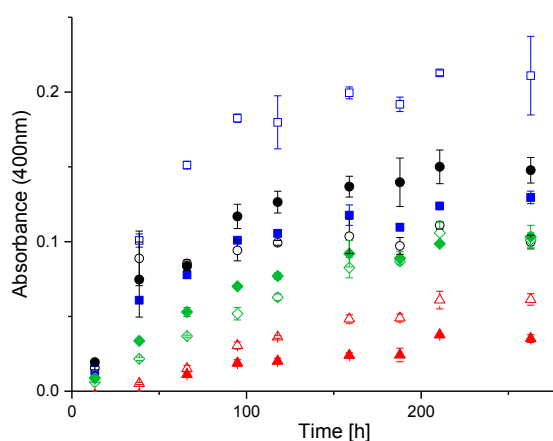


Figure 68: Time dependence of the absorbance band of 2,4-nitrophenolate (400 nm) at pH = 7 of BDNPP hydrolysis activity assays with mixtures of ligand H₃SIM¹ (unfilled symbols) and H₄SIM⁴ (filled symbols) with 1 eq zinc(II) perchlorate (red triangles), 2 eq zinc(II) perchlorate (green diamonds), 1 eq of gallium(III) perchlorate (blue squares), 1 eq zinc(II) perchlorate and 1 eq of gallium(III) perchlorate (black circles).

Comparing the complexes with the same metal content enables the formulation of conclusions about the impact of the structural variations given by the two ligand backbones. In the case of the monozinc(II) complexes [Zn^{II}(H₂SIM¹)(solv)_x]⁺ and [Zn^{II}(H₃SIM⁴)(solv)_x]⁺ the hydrolysis acceleration appears to be similar in the first 60 hours. But [Zn^{II}(H₃SIM⁴)(solv)_x]⁺, which has a Zn^{II} adjacent to a hydrogen bond donor, is, inhibited at lower product concentration than

$[\text{Zn}^{\text{II}}(\text{H}_2\text{SIM}^1)(\text{solv})_x]^+$ lacking hydrogen bond donors proximal to the Zn^{II} center, an effect possibly due to hydrogen bond formation.

Table 29: TONs of BDNPP hydrolysis with mixtures of the ligands H_3SIM^1 or H_4SIM^4 with 1 eq of zinc(II) perchlorate, 2 eq of zinc(II) perchlorate, 1 eq of gallium(III) perchlorate, 1 eq zinc(II) perchlorate and 1 eq of gallium(III) perchlorate (all kinetic studies were undertaken in a mixture of acetonitrile:aqueous buffer solution (1:1)).

complex	TON ^a
$[\text{Zn}^{\text{II}}(\text{H}_2\text{SIM}^1)(\text{solv})_x]^+$	10 ± 1
$[\text{Zn}^{\text{II}}_2(\text{H}_2\text{SIM}^1)(\text{solv})_x]^{3+}$	18 ± 1
$[\text{Ga}^{\text{III}}(\text{H}_2\text{SIM}^1)(\text{solv})_x]^{2+}$	35 ± 1
$[\text{Ga}^{\text{III}}\text{Zn}^{\text{II}}(\text{H}_2\text{SIM}^1)(\text{solv})_x]^{4+}$	23 ± 5
$[\text{Zn}^{\text{II}}(\text{H}_2\text{SIM}^4)(\text{solv})_x]$	6 ± 1
$[\text{Zn}^{\text{II}}_2(\text{H}_2\text{SIM}^4)(\text{solv})_x]^{2+}$	16 ± 1
$[\text{Ga}^{\text{III}}(\text{H}_2\text{SIM}^4)(\text{solv})_x]^+$	21 ± 1
$[\text{Ga}^{\text{III}}\text{Zn}^{\text{II}}(\text{H}_2\text{SIM}^4)(\text{solv})_x]^{3+}$	25 ± 2

^a the assays were performed with aqueous buffer solution pH = 7, TONs were determined after 9 days.

For the Ga^{III} complexes a similar result was observed since $[\text{Ga}^{\text{III}}(\text{H}_2\text{SIM}^4)(\text{solv})_x]^+$ with a pivaloyl-amide residue adjacent to the Ga^{III} center showed higher TONs than $[\text{Ga}^{\text{III}}(\text{H}_2\text{SIM}^1)(\text{solv})_x]^{2+}$, lacking a proximal hydrogen bond donor. However, compared to the respective monozinc(II) complexes both monogallium(III) complexes exhibited higher TONs as expected from the above discussed kinetic studies. Thus, the inhibiting phosphomonoester is bound in mononuclear complexes more strongly to a Zn^{II} ion than to a Ga^{III} ion and is stabilized by proximal hydrogen bond donors.

During the investigation of the TONs at pH 9.5 of various dizinc(II) complexes, discussed in Chapter 7.2, it was revealed that positioning one pivaloyl-amide residue proximal to each binding site prevents inhibition more reliably than with both at one binding site. Such an effect was not found comparing the TONs of $[\text{Zn}^{\text{II}}_2(\text{H}_2\text{SIM}^4)(\text{solv})_x]^{2+}$ and $[\text{Zn}^{\text{II}}_2(\text{H}_2\text{SIM}^1)(\text{solv})_x]^{3+}$; both exhibited similar TONs. Compared to $[\text{Zn}^{\text{II}}_2(\text{H}_2\text{L}^2)(\mu\text{-OAc})_2]^+$, discussed in Chapter 7.2, $[\text{Zn}^{\text{II}}_2(\text{H}_2\text{SIM}^4)(\text{solv})_x]^{2+}$ has a terminal phenolate residue instead of a pyridine in the primary coordination sphere, while the secondary coordination sphere is in both complexes arranged in a symmetrical fashion. Therefore, the lower TON of $[\text{Zn}^{\text{II}}_2(\text{H}_2\text{SIM}^4)(\text{solv})_x]^{2+}$ compared to $[\text{Zn}^{\text{II}}_2(\text{H}_2\text{L}^2)(\mu\text{-OAc})_2]^+$ is ascribed to the difference in the primary coordination sphere. Thus, the inhibition of dizinc(II) complexes by a phosphomonoester molecule seems to be favored by two hydrogen bond donors proximal to one binding site and an electron-rich phenolate residue in the primary coordination sphere. Comparing the two $\text{Ga}^{\text{III}}\text{Zn}^{\text{II}}$ complexes, $[\text{Ga}^{\text{III}}\text{Zn}^{\text{II}}(\text{H}_2\text{SIM}^1)(\text{solv})_x]^{4+}$ with two pivaloyl-amide residues proximal to the Zn^{II} center exhibited a lower TON. This suggests that sterical hindrance does not prevent from inhibition. The higher TON of $[\text{Ga}^{\text{III}}\text{Zn}^{\text{II}}(\text{H}_2\text{SIM}^4)(\text{solv})_x]^{3+}$ compared to $[\text{Ga}^{\text{III}}\text{Zn}^{\text{II}}(\text{H}_2\text{SIM}^1)(\text{solv})_x]^{4+}$ is assumed to be due to the lower product affinity of the Ga^{III} center coordinated to the electron-rich terminal phenolate residue.

The heterodinuclear complex $[\text{Ga}^{\text{III}}\text{Zn}^{\text{II}}(\text{H}_2\text{SIM}^4)(\text{solvent})_x]^{3+}$ revealed also a higher TON than the homodinuclear complex $[\text{Zn}^{\text{II}}_2(\text{H}_2\text{SIM}^4)(\text{solvent})_x]^{2+}$. It appears that a phosphoester bridge between two Zn^{II} centers coordinated in H_4SIM^4 is more easily formed than between a Ga^{III} and a Zn^{II} center, *i.e.* at lower product concentration. Interestingly, the TON of $[\text{Ga}^{\text{III}}\text{Zn}^{\text{II}}(\text{H}_2\text{SIM}^4)(\text{solvent})_x]^{3+}$ is also higher than for the two mononuclear complexes $[\text{Zn}^{\text{II}}(\text{H}_3\text{SIM}^4)(\text{solvent})_x]^+$ and $[\text{Ga}^{\text{III}}(\text{H}_2\text{SIM}^4)(\text{solvent})_x]^+$, indicating a positive interaction of the two metal ions in the heterodinuclear complex.

Comparing the different complexes of H_3SIM^1 without a terminal phenolate, the results suggests: the heterodinuclear complex $[\text{Ga}^{\text{III}}\text{Zn}^{\text{II}}(\text{H}_2\text{SIM}^1)(\text{solvent})_x]^{4+}$ exhibits a similar TON as the dizinc(II) complex $[\text{Zn}^{\text{II}}_2(\text{H}_2\text{SIM}^1)(\text{solvent})_x]^{3+}$ indicating that the inhibition is independent of the two metal ions bound in the two binding sites of H_3SIM^1 . However, $[\text{Ga}^{\text{III}}\text{Zn}^{\text{II}}(\text{H}_2\text{SIM}^1)(\text{solvent})_x]^{4+}$ shows a steeper increase of the absorbance at 400 nm with time, especially in the first forty hours, compared to $[\text{Zn}^{\text{II}}_2(\text{H}_2\text{SIM}^1)(\text{solvent})_x]^{3+}$. Thus, the hydrolysis rate depends strongly on the presence of the trivalent metal ion.

What emerged is that the $\text{Ga}^{\text{III}}\text{Zn}^{\text{II}}$ complex with H_4SIM^4 is the most active catalyst, with H_3SIM^1 the monogallium(III) complex is the most active one. Surprisingly, $[\text{Ga}^{\text{III}}(\text{H}_2\text{SIM}^1)(\text{solvent})_x]^{2+}$ exhibits the highest TON of all complexes studied, with a TON of 35 after nine days. The high TON of $[\text{Ga}^{\text{III}}(\text{H}_2\text{SIM}^1)(\text{solvent})_x]^{2+}$ is ascribed to (i) the lower product affinity of Ga^{III} compared to Zn^{II} , (ii) the lack of a proximal hydrogen bond donor, and (iii) the absence of a second metal ion and the resulting incapacity to bind efficiently the phosphomonoester product.

Phosphomonoester Hydrolysis Studies

Studies towards the phosphomonoester hydrolysis activity of the zinc(II), dizinc(II), gallium(III) and $\text{Ga}^{\text{III}}\text{Zn}^{\text{II}}$ complexes of H_3SIM^1 and H_4SIM^4 were conducted with the activated model substrate DNPP at different pHs (7, 8, 9 and 10). A significant phosphomonoester hydrolysis capacity was only observed for $[\text{Ga}^{\text{III}}\text{Zn}^{\text{II}}(\text{H}_2\text{SIM}^1)(\text{solvent})_x]^{4+}$, while a slight increase in the 2,4-phenolate concentration in the assays of $[\text{Ga}^{\text{III}}(\text{H}_2\text{SIM}^1)(\text{solvent})_x]^{4+}$ at pH 7 and $[\text{Zn}^{\text{II}}_2(\text{H}_2\text{SIM}^4)(\text{solvent})_x]^{2+}$ at pH 9.5 compared to autohydrolysis was detected. However, due to the instability of DNPP in the buffer solution, the deviations of the initial hydrolysis velocities obtained for $[\text{Ga}^{\text{III}}(\text{H}_2\text{SIM}^1)(\text{solvent})_x]^{4+}$ and $[\text{Zn}^{\text{II}}_2(\text{H}_2\text{SIM}^4)(\text{solvent})_x]^{2+}$ are too high to make an explicit statement about their hydrolysis capacity. The fact that only the $\text{Ga}^{\text{III}}\text{Zn}^{\text{II}}$ and Ga^{III} complex of H_3SIM^1 showed the ability to hydrolyze the phosphomonoester DNPP in contrast to the corresponding complexes of H_4SIM^4 , indicates that neither the strong electron-rich terminal phenolate nor the hydrogen bond donor proximal to the trivalent metal center cause the capacity of phosphomonoester hydrolysis in PAPs. Moreover, the dizinc(II) complex of ligand H_3SIM^1 did not reveal phosphomonoester hydrolysis.

This indicates that the trivalent metal ion is essential for the DNPP hydrolysis. Moreover, the only model complexes reported to cleave phosphomonoester bonds contained at least one Fe^{III} ion.^{108, 109, 114}

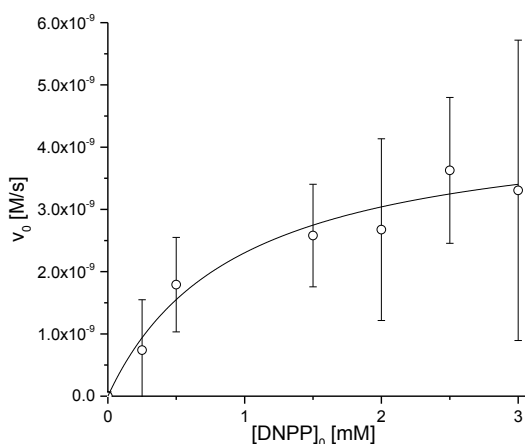
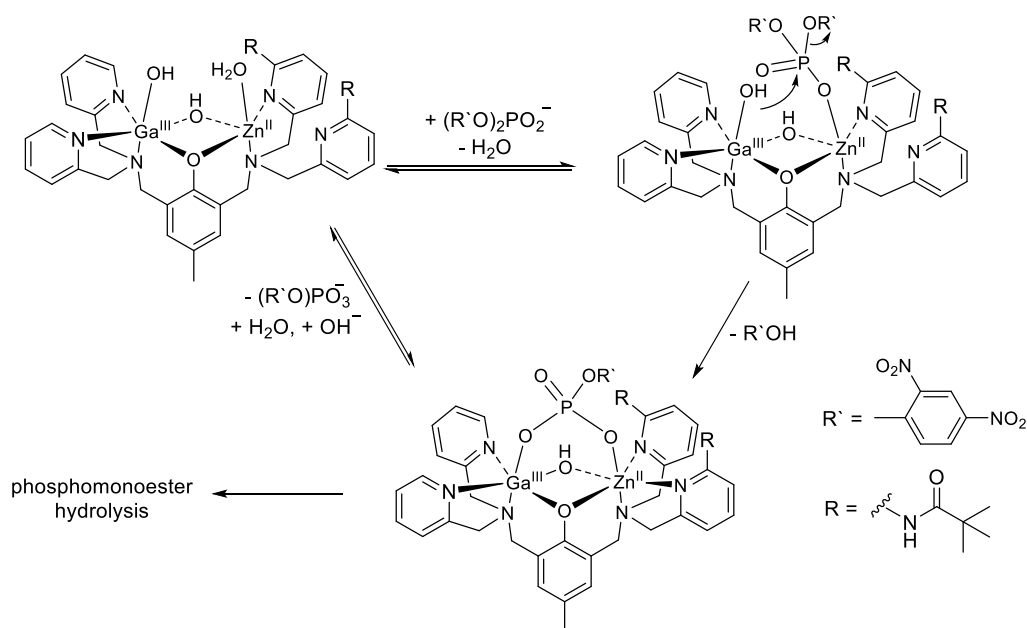


Figure 69: Substrate concentration dependence at pH = 7 of DNPP hydrolysis activity for the mixture of ligand H₃SIM¹ with 1 eq zinc(II) perchlorate and 1 eq of gallium(III) perchlorate.

The substrate concentration dependence measurements were conducted at pH 7 in order to mimic near physiological conditions. [Ga^{III}Zn^{II}(H₂SIM¹)(solv)_x]⁴⁺ showed Michaelis-Menten type behavior, and fitting the data determined the catalytic parameters $k_{\text{cat}} = (0.12 \pm 0.02) \cdot 10^{-3} \text{ s}^{-1}$, $K_{\text{M}} = (0.94 \pm 0.32) \text{ mM}$ and $k_{\text{cat}}/K_{\text{M}} = 0.12 \text{ s}^{-1}\text{M}^{-1}$. Although the activity of [Ga^{III}Zn^{II}(H₂SIM¹)(solv)_x]⁴⁺ is lower than those reported for the diiron complexes,^{108, 109, 114} [Ga^{III}Zn^{II}(H₂SIM¹)(solv)_x]⁴⁺ is to date the first heterodinuclear model complex able to hydrolyze phosphomonoesters.

9.4 SUMMARY

The investigations undertaken with the mono- and dinuclear complexes of the two asymmetric ligands H₃SIM¹ and H₄SIM⁴ with differing primary and secondary coordination spheres lead to a deeper insight in the reaction mechanism of phosphoester hydrolysis with heterodinuclear biomimetics. In the proposed mechanism the phosphoester is activated by the Zn^{II} center and the Ga^{III} is responsible for providing the hydroxide nucleophile at near physiological conditions (Scheme 24).



Scheme 24: Proposed mechanism for the BDNPP hydrolysis catalyzed by $[Ga^{III}Zn^{II}(H_2SIM^1)(solV)_x]^{4+}$.

It was shown that the monozinc(II) complexes are not able to hydrolyze phosphoesters at near physiological conditions, but coordination of a second Zn^{II} ion in the same ligand enables the hydrolysis. A similar cooperative effect was detected for the Ga^{III}Zn^{II} complexes. Although the substrate affinity of the complex $[Ga^{III}Zn^{II}(H_2SIM^1)(solV)_x]^{4+}$ was lower than of the corresponding Zn^{II}₂ complex, the heterodinuclear complex exhibits a 50-fold faster hydrolysis rate and a six-fold increased efficiency. Comparison of the activity of the two different Ga^{III}Zn^{II} complexes revealed a shift of the optimum pH to higher values with (i) an electron-poor coordinating ligand in the primary coordination sphere, or (ii) provision of hydrogen bonding by the second coordination sphere. Furthermore, the capacity of a hydrogen bonding network proximal to the dinuclear core results in (i) higher hydrolysis rates, (ii) lower substrate affinities, and (iii) higher efficiencies, especially when the two hydrogen bond donors were placed proximal to the Zn^{II} center. However, the long-time studies showed that such a sterically demanding complex is not prevented from inhibition. During the long-term studies an acceleration effect by the trivalent metal ion was detected. Furthermore, a Ga^{III} coordinating phenolate-residue results in a higher TON than pyridine for the Ga^{III}Zn^{II} complexes. However, the highest TON was found for the monogallium(III) complex without hydrogen bond donors in close distance to the metal center but with a vacant second amidated coordination site.

Investigation of the DNPP hydrolysis of the different complexes showed that only the complex $[Ga^{III}Zn^{II}(H_2SIM^1)(solV)_x]^{4+}$ is able to cleave phosphomonoesters efficiently. Therefore, this complex does not only combine the essential structural features of the active site of PAP, but is also the first heterodinuclear model complex mimicking the essential function of PAPs, the hydrolysis of phosphomonoesters.

Chapter 10

Conclusions and Outlook

In course of this work the ligands HL¹ and H₂L⁴, which have previously been accepted as a suitable basis for model complexes of phosphatases, were modified by the introduction of substituents capable of hydrogen bonding. In this way, the second coordination sphere of phosphatase metalloenzymes was mimicked in order to further improve the accuracy of phosphatase biomimetics as enzyme models. For the synthesis of the four asymmetric ligands, a selective procedure was evaluated, generating two different coordination sites. These ligands mimic the asymmetric peptide backbone that surrounds the dimetallic core in the active site of phosphatases.

The series of ligands studied, with no substituents, two asymmetrically disposed and two symmetrically disposed amide or two asymmetrically disposed amine anchor groups for hydrogen bonding, led to strikingly different structures of the corresponding dizinc(II) complexes. It became apparent that the steric hindrance caused by two pivaloyl-amide substituents adjacent to one coordination site, and the subsequent inability of the corresponding dizinc(II) complexes to bind two acetate co-ligands, resulted in a dizinc(II) structure similar to the active sites of phosphatases with two different Zn^{II} sites – one 6- and the other 5-coordinate. Moreover, these complexes represent rare examples of zinc(II) complexes with a hydroxido co-ligand - the potential nucleophile during the phosphoester hydrolysis reaction - stabilized by hydrogen bond formation. The desired hydrogen bonding network was also observed for the dizinc(II) and diiron(II) complexes studied, which revealed the common structure of phenoxido-bridged phosphatase models bearing two bridging acetate co-ligands.

Studying the phosphoester hydrolysis activity of the series of dizinc(II) and diiron(II) model complexes with hydrogen bonding functionalities proximal to the dimetal core enabled the analysis of the implications of (i) the type of the hydrogen bond donor, (ii) the position of the hydrogen bond donor, and (iii) the coordinating ligands in the primary coordination sphere. The main impact of the secondary interactions in the dizinc(II) complexes was found to be the increased substrate affinity, and this obviously depends on the hydrogen bonding sites and the type of the hydrogen bonding groups. In fact, at pH 7 the diamino derivative is the most effective catalyst, and positioning of both pivaloyl-amide residues proximal to one Zn^{II} center exhibited a more positive effect towards the BDNPP hydrolysis than positioning one pivaloyl-amide adjacent to each Zn^{II} center. Long-term catalytic studies showed that at pH 9.5 the symmetrical, sterically hindered, amide-based system is the most efficient dizinc(II) complex studied here, and this is primarily due to less stable catalyst-inhibitor complexes. Interestingly, the effect of the position of the pivaloyl-amide residues was shown to be the

opposite for the corresponding diiron(II) complexes. In fact, incorporation of two pivaloyl-amide residues in an asymmetric fashion into a dizinc(II) complex lead to the generation of a stable catalyst-inhibitor (hydrolysis product) adduct. Herein, one of the two pivaloyl-amide moieties fills the remaining vacant coordination site and is stabilized by hydrogen bond formation to the second pivaloyl-amide residue.

Although this work showed that the incorporation of sterically demanding amide moieties into dinuclear model complexes have a beneficial effect on the phosphoester cleavage capacity, it is still not completely understood which structural feature is accounted therefore: (i) the hydrogen bonding capacity, (ii) the sterical strain, or (iii) the electronic effect caused by potential coordination of the amide-oxygen donor. In order to circumvent the latter and to preserve the steric strain of the hydrogen bonding substituents, which might promote the hydrolysis, the efforts of future work could be put in the reduction of the pivaloyl-amide functionalities of the ligands developed in this thesis. For example, reduction of ligand H_3SIM^1 with lithium aluminium hydride should generate ligand H_4L^{73} with a sterically demanding amine substituent (Chart 29).¹⁹⁹ Using H_4L^{73} for the synthesis of a dizinc(II) complex supplies a biomimetic which maintains (i) the capacity to form hydrogen bonds as well as (ii) the steric strain comparable to H_3SIM^1 , but lacks the ability to stabilize a catalyst-inhibitor complex by coordination of an adjacent donor.

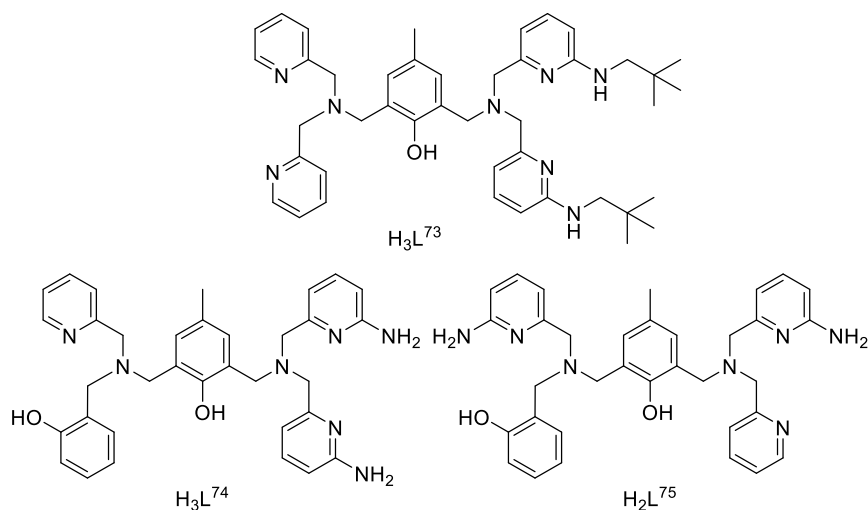


Chart 29: Depiction of the desired ligands for the generation of phosphatase biomimetics in future studies.

The more electron-rich primary coordination sphere and the amino hydrogen bond donors have been shown to support the phosphoester hydrolysis. Therefore, biomimetics which carry those structural features in tandem would be of considerable interest. The development of H_3L^{74} and H_3L^{75} (Chart 29), and complexes thereof, should have the potential to mimic the functionality of the native enzymes more accurately.

An interesting result during the characterization of the diiron(II) complexes was the reduction capacity of Fe^{III} bound to the ligand H_3SIM^1 under acidic conditions. A concerted proton-electron transfer mechanism was proposed for this reaction, but a direct proof remains to be provided. Therefore, a suitable experiment could be the use of EPR spectroscopy or radical scavengers which could support the proposed mechanism via the generation of a radical species.

In order to gain a more accurate model system for the active form of mammalian PAPs the formation of a heterovalent diiron core in an asymmetric coordination environment with the capacity to form a hydrogen bond network similar to the native enzymes was probed. In fact, the successful formation of an $\text{Fe}^{\text{III}}\text{Fe}^{\text{II}}$ species via chemical oxidation of the respective diiron(II) complex with ferrocenium hexafluorophosphate under anaerobic conditions was achieved. Comparison of the catalytic activity of the parent diiron(II) and the heterovalent diiron complex supported the presumption that the role of the Fe^{III} center in the active site of PAP is the provision of a nucleophilic hydroxide at low pH. Another milestone for the development of sophisticated model systems for the active form of mammalian PAPs could be the generation of diiron(II) complexes of H_4SIM^3 and H_4SIM^4 and the following study of the oxidation, analogous to the approach outlined in this thesis. Furthermore, reliable protocols for the isolation of the complexes obtained, such as extraction of the generated byproduct ferrocene need to be developed. These investigations are promising due to the provision of two chemically distinct coordination sites within these ligands.

The second strategy to generate heterovalent dinuclear model complexes which provide in parallel hydrogen bonding donors adjacent to the dimetal core was the selective generation of a $\text{Ga}^{\text{III}}\text{Zn}^{\text{II}}$ complex. Therefore, the coordination behavior of the three pivaloyl-amide containing ligands towards Zn^{II} , Cu^{II} , Ga^{III} and Fe^{III} was examined with various techniques. In this way, the selective formation of specific complexes was detected assigned to the asymmetry of the ligands. The trivalent Ga^{III} ion was shown to coordinate in the less hindered or the more electron-rich binding site, while the remaining binding site is selectively filled by the divalent Zn^{II} ion. Moreover, the catalytic activity of the monogallium(III), the monozinc(II), and the heterodinuclear $\text{Ga}^{\text{III}}\text{Zn}^{\text{II}}$ complexes was investigated. In this way, the previously proposed mechanism, in which the phosphoester is activated by the Zn^{II} center and the Ga^{III} is accountable for providing the hydroxide nucleophile even at near physiological conditions, was supported in this study and a cooperative effect was detected for the $\text{Ga}^{\text{III}}\text{Zn}^{\text{II}}$ complexes. Although the substrate affinity of the $\text{Ga}^{\text{III}}\text{Zn}^{\text{II}}$ complex was lower than for the respective Zn^{II}_2 complex, a 50-fold faster hydrolysis rate and a six-fold increased efficiency was detected in one case.

Comparing the activity of the two different Ga^{III}Zn^{II} complexes exhibited a shift of the optimum pH to higher values with (i) an electron-poor coordinating ligand in the primary coordination sphere, or (ii) provision of hydrogen bonding by the second coordination sphere. However, the capacity of a hydrogen bonding network proximal to the Ga^{III}Zn^{II} core resulted in (i) higher hydrolysis rates, (ii) lower substrate affinities, and (iii) higher efficiencies, especially when the two hydrogen bond donors were placed proximal to the Zn^{II} center.

With the use of long-term studies an acceleration effect by the trivalent metal ion was detected and a high TON was supported by the coordination of the Ga^{III} by a terminal phenolate-residue. However, the highest TON was found for the monogallium(III) complex bearing no hydrogen bond donors at close distance to the metal center but with a vacant second amidated coordination site. The lower TON of the respective Ga^{III}Zn^{II} was ascribed to the inhibitory effect of a bridging product molecule, stabilized via coordination of the adjacent amide residue, as found in a similar dizinc(II) complex. Therefore, the preparation of ligand H₃L⁷³ and its derivatives, in combination with the generation of a Ga^{III}Zn^{II} complex with the two different metal ions in distinct binding sites, may shed light into the coordination capacity of the amide oxygen atom.

The generation of the Ga^{III}Zn^{II} complex of ligand H₃L⁷³ is of particular interest due to the fact that the amidated counterpart [Ga^{III}Zn^{II}(H₂SIM¹)(solv)_x]⁴⁺ revealed the ability to cleave phosphomonoesters. Therefore, this complex does not only combine the essential structural features of the active site of PAP, but it is also the first heterodinuclear model complex found to mimic the essential function of PAPs, *i.e.* the hydrolysis of phosphomonoesters. However, the results of the phosphoester hydrolysis activity indicate fast inhibition, which makes the Ga^{III}Zn^{II} complex of ligand H₃L⁷³ a promising candidate for a more accurate structural and functional model of the heterovalent heterodinuclear active site of PAP, thus, leading us a step further to the well-directed development of more efficient osteoporosis therapeutic agents.

Chapter 11

Experimental Section

11.1 GENERAL REMARKS

The main part of this thesis is and will be published in several scientific journals. For the NMR spectra (^1H and ^{13}C) and mass spectra for the synthesized ligands as well as titration experiments it can be referred to the Supporting Information of each of the corresponding publications. The experimental structures reported in this thesis are deposited at the “Cambridge Crystallographic Data Centre”, the experimental data are not included in the Appendix, but can be obtained free of charge via www.ccdc.cam.ac.uk/data_request/cif. The corresponding CCDC-reference code of each complex is given in the Appendix.

11.2 MATERIAL AND METHODS

11.2.1 CHEMICALS

Chemicals and solvents used for synthesis and spectroscopy were purchased from Sigma-Aldrich and Acros. 2,4-Dinitrophenol was recrystallized and phosphoryl chloride was distilled before usage. All other chemicals were used without prior purification. Solvents for organic synthesis were of standard quality. Dry solvents were purchased from Sigma-Aldrich and Acros, stored over molecular sieves, and used without further purification. For complex syntheses and spectroscopy solvents of *p.a.* grade were utilized without further purification. In the kinetic assays MilliQ water was used.

11.2.2 PHYSICAL MEASUREMENTS

NMR Spectroscopy

Nuclear Magnetic Resonance (NMR) spectra were recorded with Bruker AV200, AV400, AV500 and AV600 spectrometers, for ^{13}C and ^{31}P NMR spectra with ^1H decoupling. Two-dimensional correlation spectroscopy (COSY), nuclear Overhauser-effect spectroscopy (NOESY), heterodinuclear single quantum correlation (HSQC) and heterodinuclear multiple bond connectivity (HMBC) experiments were used to assign each signal in the spectra. For ^1H and ^{13}C NMR spectra chemical shifts are reported in δ -units, relative to known solvent peak references: $\delta_{\text{H}} = 7.27$ ppm, $\delta_{\text{C}} = 77.00$ ppm for CDCl_3 ; $\delta_{\text{H}} = 1.94$ ppm, $\delta_{\text{C}} = 1.39$ ppm for CD_3CN ; $\delta_{\text{H}} = 3.30$ ppm, $\delta_{\text{C}} = 49.00$ ppm for CD_3OD and $\delta_{\text{H}} = 2.05$ ppm, $\delta_{\text{C}} = 29.92$ ppm for CD_3COCD_3 . 85 % phosphoric acid (0 ppm) was used as external reference for ^{31}P NMR spectra. The following abbreviations

were used: s (singlet), bs (broad singlet), d (doublet), t (triplet), dt (doublet of triplets), dd (doublet of doublets), ddd (doublet of doublets of doublets), td (triplet of doublets), sep (septet) and m (multiplet). The reported coupling constants nJ are for ${}^1\text{H}$ - ${}^1\text{H}$ couplings. The software package TopSpinTM from BRUKER was used for data processing.³⁰²

Magnetic Susceptibility Measurement by the Evans Method

Magnetic moments in solution were measured for a solution of known concentration of complex in deuterated solvent in a capillary which was in a NMR tube carrying the same solvent. The experiments were conducted with Bruker AV200 and AV500 instruments. Magnetic moments were evaluated using Equation 24 and Equation 25, whereby appropriate corrections were considered.

$$\text{Equation 24} \quad \chi_{\text{para,subst}} = \frac{3}{4\pi c} \left(\frac{\Delta\nu}{\nu} \right) + \chi_{\text{dia,solv}} + \chi_{\text{dia,subst}}$$

$$\text{Equation 25} \quad \mu = 2.828 \sqrt{\chi_{\text{para,subst}}} \text{ T}$$

Solid State Magnetic Susceptibility Measurement with SQUID

Magnetic susceptibility in solid state were examined with a MPMS-XL 5T superconducting quantum interference device (SQUID) from Quantum Design. The powdered samples were pressed into a PTFE band to avoid field-induced orientation and incorporated into two plastic straws as sample holder. Diamagnetic corrections for the PTFE band and the sample holder were applied.

X-Ray Structure Analyses

X-ray crystallographic data for the zinc(II) and gallium(III) complexes were collected with an Oxford Diffraction Gemini Ultra dual source (Mo or Cu) CCD diffractometer. The structures were solved by direct methods (SIR-92) using the SHELXS computer program and refined by the full-matrix least-squares method based on F^2 , with the SHELXL 97 computer program.³⁰³ These programs were accessed by the WINGX 1.70.01 crystallographic collective package.³⁰⁴ Crystallographic data for the iron complexes were collected with a Bruker AXS Smart 1000 CCD and an Agilent Technologies SuperNova-E dual source (Mo or Cu) CCD diffractometer. Using the software Olex2,³⁰⁵ the structures were solved with conventional direct methods and refined by full-matrix least squares based on F^2 . All non-hydrogen atoms were given anisotropic displacement parameters, unless they were disordered, and were placed at calculated positions. Hydrogen atoms were fixed geometrically and were not refined. The counter ion hexafluorophosphate was in some cases resolved into two disordered octahedral anions, which share the

same phosphorus central atom. For $[\text{Zn}^{\text{II}}_2(\text{H}_2\text{L}^2)(\mu\text{-OAc})_2]\text{PF}_6$, the structure was refined with acetone and water solvate, both with an occupancy of 50%. In case of $[\text{Fe}^{\text{II}}_2(\text{H}_2\text{L}^2)(\mu\text{-OAc})_2]\text{PF}_6$ the structure was refined with a diethylether solvate in the elemental cell. For $[\text{Fe}^{\text{II}}_2(\text{H}_2\text{SIM}^1)(\mu\text{-OAc})_2]\text{PF}_6$ and $\{\text{Na}[\text{Fe}^{\text{II}}_2(\text{H}_2\text{SIM}^3)(\mu\text{-OAc})_2]\}_2\text{PF}_6$ electron density attributed to disordered solvent molecules was removed from the structure with the BYPASS procedure as implemented in PLATON (SQUEEZE).^{306, 307} Partial structure factors from the solvent masks were included in the refinement as separate contributions to F_{obs} . The X-ray structural data of the published structures were deposited at the Cambridge Crystallographic Data Centre.

IR Spectroscopy

FT-Infrared spectroscopy was carried out with a Perkin Elmer FT-IR Spectrometer SPECTRUM 2000 equipped with a Smiths DuraSamplIR II ATR diamond window.

Mass Spectrometry

Electron ionization (EI) mass spectra were recorded with a JEOL JMS-700 instrument, Matrix-assisted laser desorption/ionization (MALDI) mass spectra were recorded with a Bruker ApexQe hybrid 9.4 FT-ICR instrument and Electrospray ionization (ESI) mass spectra were measured on a Finnigan LCQ spectrometer at the Institute of Organic Chemistry of the University of Heidelberg. High resolution mass spectra were collected with a Bruker microTOFQ ESI-MS spectrometer in the School of Chemistry and Molecular Biosciences of the University of Queensland and a Bruker Apex-Qe hybrid 9.4 T FT-ICR instrument at the Institute of Organic Chemistry at the University of Heidelberg. The data were processed with Bruker Compass Data Analysis software.

Elemental Analyses

Elemental microanalyses were performed in the analytic laboratories of the Institute of Organic Chemistry of the University of Heidelberg with an Elementar Vario Mikro cube machine and the Carlo Erba Elemental Analyzer model NA1500 in the School of Chemistry and Molecular Biosciences at the University of Queensland.

Cyclic Voltammetry

Cyclic voltammetric measurements were performed on a CH Instruments CHI660D electrochemical workstation equipped with a Faraday cage using a three-electrode setup consisting of a glassy carbon working electrode, a platinum wire as a counter electrode and a Ag/Ag⁺ (0.1 mM in NaCl) reference electrode. The complex solutions were prepared with

degassed solvents with 0.1 M (NBu₄)ClO₄ as electrolyte. The redox potentials of the obtained signals were determined by comparison to a ferrocen sample measured at the same conditions and referenced vs. SCE ($E(\text{Fc}/\text{Fc}^+) = 0.380\text{V vs. SCE}$).²⁵²

EPR Spectroscopy

X-band EPR spectra were measured with a Bruker Biospin ELEXSYS E500 spectrometer. The microwave frequency and magnetic field were calibrated with a Bruker frequency counter and an ER036 TM or an ER035M Tesla meter. Spin-Hamiltonian parameters were determined by computer simulations of the experimental spectra using the programs XSophe³⁰⁸ and MoSophe.³⁰⁹ The simulated and experimental spectra were visualized with the software suite XeprView.

UV-vis-NIR Spectroscopy

UV-vis-NIR spectra were recorded at 25°C with a TIDAS II J&M spectrophotometer and a Varian Cary50 Bio UV/visible spectrophotometer in 10 mm quartz cuvettes. Time-dependent UV-vis-NIR measurements were performed using a TIDAS II J&M spectrophotometer. Time-course measurements at fixed wavelengths were monitored by a JASCO V-570 spectrophotometer and a Varian Cary50 Bio UV/visible spectrophotometer with a Peltier temperature controller.

Mössbauer Spectroscopy

⁵⁷Fe Mössbauer spectra of frozen solutions were acquired with a conventional spectrometer incorporating an Oxford Instruments Mössbauer-Spectromag 4000 Cryostat, equipped with a ⁵⁷Co source (3.7 GBq) in a rhodium matrix in the constant-acceleration mode at 170 K. Isomer shifts are given relative to α -Fe at 300 K. Spectra were fitted using the NORMOS Mössbauer Fitting Program.

11.2.3 PHOSPHOESTER HYDROLYSIS EXPERIMENTS

General Procedure

Phosphoester hydrolysis activity of the complexes was probed with a spectrophotometric assay using BDNPP as phosphodiester model substrate and DNPP as phosphomonoester model substrate. Cleavage of the phosphorous-oxygen bond was followed at 25°C by monitoring the generated product, 2,4-dinitrophenolate, by its strong absorption at 400 nm ($\epsilon = 12,100 \text{ M}^{-1}\text{cm}^{-1}$). All measurements were carried out in 1:1 acetonitrile-buffer mixtures and performed in

triplicates. The complex was allowed to equilibrate in the acetonitrile-buffer mixture for one minute prior addition of substrate. When the substrate was added to the reaction mixture the starting hydrolysis activity was monitored in the time between 15 and 195 seconds and analyzed by linear regression. For each experiment autohydrolysis assays were conducted by measuring the hydrolysis rate under the same conditions, but without complex, and were subtracted from the derived data.

Preparation of the Multicomponent Buffer Solutions

The aqueous buffer consisted of 2-(*N*-morpholino)ethanesulfonic acid (MES) (50 mM; pH range: 5.5 – 6.7), 4-(2-hydroxyethyl)piperazine-1-ethanesulfonic acid (HEPES) (50mM; pH range: 6.8 – 8.2), 2-(cyclohexylamino)ethanesulfonic acid (CHES) (50 mM; pH range: 8.6 – 10.0), 3-(cyclohexylamino)-1-propanesulfonic acid (CAPS) (50 mM; pH range: 9.7 – 11.1) and lithium perchlorate (250 mM) for ionic strength control. The desired pH of the buffers was adjusted by addition of aqueous sodium hydroxide solution. Following treatment with Chelex® (Chelex 100 sodium form) overnight and filtration with 45 μ m syringe filters ensured the absence of metal ions in the buffer solutions. The pH values reported refer to the aqueous component; however, it should be noted that the pH of a 1:1 mixture of buffer and acetonitrile was the same within error as of the corresponding buffer solution itself.^{275, 276}

Phosphodiester Hydrolysis Assays

The activated model substrate BDNPP was initially prepared as 15 mM solution in acetonitrile and the complex solutions were 1 mM in acetonitrile. The pH dependence of the activity was studied by varying the pH value of the multicomponent buffer in the pH range of 5 to 11. In this process the assays contained the complex 0.04 mM and BDNPP 5 mM in the cuvette. The resulting pH profiles were fitted in the Origin (OriginLab) program using Equation 20 and Equation 21 (Chapter 6.3).²⁷⁷

Complex concentration dependency assays were 5 μ M in BDNPP and 0.01 – 0.09 mM in complex, respectively. The data derived were fitted with a linear function using the Origin software. Substrate concentration dependence of the catalytic rate was examined with a fixed complex concentration of 0.04 mM and the BDNPP concentration varied. The experimental data obtained were fitted in the Origin (OriginLab) program to the Michaelis-Menten equation (Equation 22). Studies of the turn over number (TON) were conducted 15 nM in complex and 5.25 μ M in BDNPP. Samples were taken at various intervals during the experiment, diluted with solvent, and their UV-vis spectra were recorded to determine the progress of phosphoester hydrolysis. The

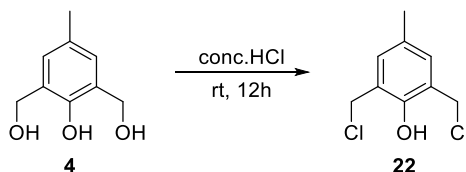
increase in the absorbance at 400 nm, assigned to the hydrolysis product 2,4-dinitrophenolate, was monitored over time and TON values were calculated using the Beer-Lambert Law.

Phosphomonoester Hydrolysis Assays

Phosphomonoester hydrolysis activity of the activated substrate DNPP was examined in a similar manner to the BDNPP assays, but DNPP was dissolved initially in aqueous buffer solution of the required pH. During the pH dependence measurements the final concentrations in the cuvette were 0.04 mM of complex and 0.5 mM in DNPP. Complex concentration dependent assays were 1 mM in DNPP and the complex concentration ranged from 0.03 to 0.09 mM. In order to study the substrate concentration dependency the concentration of complex was fixed at 0.04 mM and the DNPP concentration was varied between 0.1 and 1.5 mM. Turn-over experiment samples contained 0.01 mM complex and 3 mM DNPP.

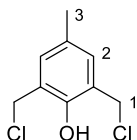
11.3 SYNTHESSES OF PRECURSORS

11.3.1 2,6-BIS(CHLOROMETHYL)-4-METHYLPHENOL (**22**)



2,6-Bis(chloromethyl)-4-methylphenol (**22**) was prepared according to a known literature procedure.³¹⁰

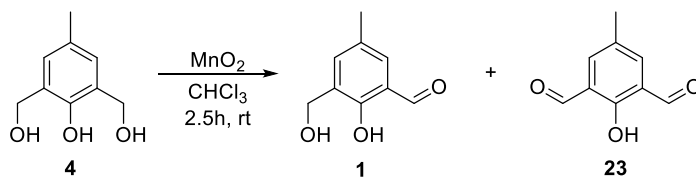
2,6-bis(hydroxymethyl)-4-methylphenol (**4**) (2.5 g, 14.9 mmol) was treated with concentrated hydrochloric acid (30 ml) and stirred at room temperature overnight. The product was extracted into dichloromethane (3 x 65 ml) and dried over sodium sulfate. Removal of the solvent gave 2,6-bis(chloromethyl)-4-methylphenol (**22**) in quantitative yield.



¹H NMR (199.92 MHz, CDCl₃): δ = 2.29 (s, 3H, H₃), 4.67 (s, 4H, H₁), 7.10 (s, 2H, H₂) ppm.

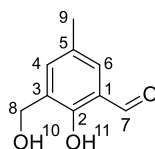
11.3.2 3-(CHLOROMETHYL)-2-HYDROXY-5-METHYLBENZALDEHYDE (5)

2-Hydroxy-3-(hydroxymethyl)-5-methylbenzaldehyde (1)



2-Hydroxy-3-(hydroxymethyl)-5-methylbenzaldehyde (**1**) was synthesized by modification of previously described procedures.^{120, 121}

To a solution of 2,6-bis(hydroxymethyl)-4-methylphenol (**4**) (50.0 g, 0.30 mol, 1.0 eq) in chloroform (1.6 l) was added activated manganese oxide (191 g, 2.2 mol, 7.3 eq) in portions and the resulting suspension was stirred for 2.5 hours at room temperature (progress was monitored by TLC (SiO₂; CH₂Cl₂:MeOH = 98:2)). The manganese dioxide was removed via filtration through a pad of Celite (∅ = 3 cm, L = 10 cm). The filtrate was concentrated to a brownish solid, which contained compound **1** and compound **23**. The mixture was separated by column chromatography (SiO₂; ∅ = 5 cm; L = 15 cm; CH₂Cl₂:MeOH = 98:2) yielding pure 2-hydroxy-3-(hydroxymethyl)-5-methylbenzaldehyde (**1**) (23.1 g, 46%) and 2-hydroxy-5-methylisophthalaldehyde (**23**) (12.8 g, 25 %), both as yellowish solids.



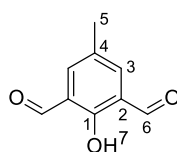
MS (EI⁺, direct): m/z = 166.06 ([C₉H₁₀O₃], *calcd.* 166.06).

¹H NMR (600.13 MHz, CDCl₃): δ = 2.33 (s, 3H, H₉), 2.44 (bs, 1H, H₁₀), 4.72 (s, 2H, H₈), 7.28 (s, 1H, H₆), 7.40 (s, 1H, H₄), 9.85 (s, 1H, H₇), 11.17 (s, 1H, H₁₁) ppm.

¹³C NMR (150.90 MHz, CDCl₃): δ = 20.2 (C₉), 60.5 (C₈), 120.0 (C₁), 129.0 (C₃/C₅), 129.1 (C₃/C₅), 132.6 (C₄), 136.9 (C₆), 157.3 (C₂), 196.7 (C₇) ppm.

Elemental analysis: *Calcd.* for C₉H₁₀O₃: C 65.05%; H 6.07%

Found: C 64.88%; H 6.29%.

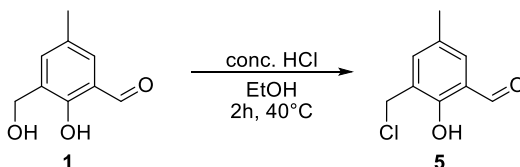


MS (EI⁺, direct): m/z = 164.04 ([C₉H₈O₃], *calcd.* 164.05).

¹H NMR (200.13 MHz, CDCl₃): δ = 2.40 (s, 3H, H₅), 7.78 (s, 2H, H₃), 10.23 (s, 2H, H₆), 11.47 (s, 1H, H₇) ppm.

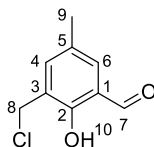
^{13}C NMR (100.55 MHz, CDCl_3): δ = 20.0 (C5), 122.9 (C2), 129.5 (C4), 137.9 (C3), 161.7 (C1), 192.1 (C6) ppm.

3-(Chloromethyl)-2-hydroxy-5-methylbenzaldehyde (**5**)



3-(Chloromethyl)-2-hydroxy-5-methylbenzaldehyde (**5**) was synthesized according to a known literature procedure.¹²¹

A solution of compound **1** (2.50 g, 15 mmol) in ethanol (12.5 ml) was added dropwise to warm concentrated hydrochloric acid (37.5 ml) and the mixture was then heated at 40°C for two hours. The resulting precipitate was filtered and washed with water until a pH value of 8 was reached. The yellowish solid, 3-(chloromethyl)-2-hydroxy-5-methylbenzaldehyde (**5**), was dried under vacuum until dryness (1.85 g, 67%).



MS (EI^+ , direct): m/z = 184.10 ($[\text{C}_9\text{H}_9\text{O}_2\text{Cl}]$, *calcd.* 184.03).

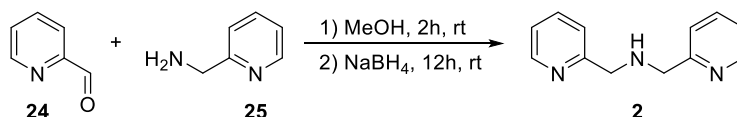
^1H NMR (200.13 MHz, CDCl_3): δ = 2.36 (s, 3H, H9), 4.68 (s, 2H, H8), 7.36 (s, 1H, H4), 7.47 (s, 1H, H6), 9.87 (s, 1H, H7), 11.26 (s, 1H, H10) ppm.

^{13}C NMR (50.32 MHz, CDCl_3): δ = 20.2 (C9), 39.8 (C8), 120.4 (C3), 125.8 (C1/C6), 129.2 (C1/C6), 134.0 (C5), 139.0 (C4), 157.3 (C2), 196.4 (C7) ppm.

Elemental analysis: *Calcd.* for $\text{C}_9\text{H}_9\text{O}_2\text{Cl}$: C 58.55%; H 4.91%

Found: C 58.34%; H 5.18%.

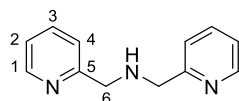
11.3.3 BIS(PYRIDIN-2-YLMETHYL)AMINE (**2**)



Bis(pyridine-2-ylmethyl)amine (**2**) was prepared according to known literature procedures.¹¹⁵

A solution of picolylaldehyde (**24**) (9.50 ml, 10.7 g, 0.10 mol, 1.0 eq) in methanol (225 ml) was cooled with a water-ice bath and 2-(aminomethyl)pyridine (**25**) (10.3 ml, 10.8 g, 0.10 mol, 1.0 eq) was added dropwise. Subsequently, the reaction mixture was allowed to warm up to room

temperature. After stirring the solution for two hours the mixture was again cooled with a water-ice bath before sodium borohydride (7.57 g, 0.20 mol, 2.0 eq) was added in portions. The reaction mixture was stirred overnight at room temperature. After the solution was concentrated under reduced pressure, the residue was treated with water (250 ml) and neutralized with 2M hydrochloric acid. The product was extracted into dichloromethane (3 x 75 ml), washed with brine and dried over sodium sulfate. The solvent was removed under reduced pressure to give bis(pyridine-2-ylmethyl)amine (**2**) as a brown oil (12.5 g, 63%).

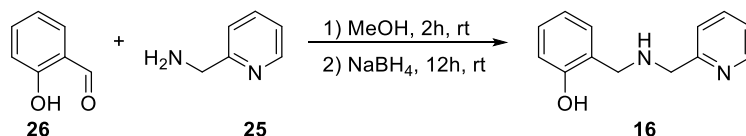


Molecular Formula: C₁₂H₁₃N₃

¹H NMR (200.13 MHz, CDCl₃): δ = 3.26 (s, 1H, NH), 4.03 (s, 4H, H₆), 7.17 (dd, ³J = 7.45 Hz, ³J = 4.93 Hz, 2H, H₂), 7.39 (d, ³J = 7.83 Hz, 2H, H₄), 7.66 (td, ³J = 7.46 Hz, ⁴J = 1.79 Hz, 2H, H₃), 8.59 (d, ³J = 4.93 Hz, 2H, H₁) ppm.

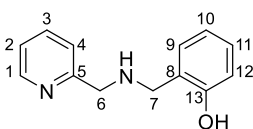
¹³C NMR (50.32 MHz, CDCl₃): δ = 54.0 (C₆), 121.6 (C₂/C₄), 121.9 (C₂/C₄), 135.9 (C₃), 148.8 (C₁), 158.7 (C₅) ppm.

11.3.4 2-(((PYRIDIN-2-YLMETHYL)AMINO)METHYL)PHENOL (**16**)



2-(((Pyridine-2-ylmethyl)amino)methyl)phenol (**16**) was prepared according to known literature procedures.^{124, 125}

Salicylaldehyde (**26**) (12.2 g, 0.10 mol, 1.0 eq) was dissolved in methanol (225.0 ml) and the solution was cooled in a water-ice bath. 2-(Aminomethyl)pyridine (**25**) (10.4 ml, 10.8 g, 0.10 mol, 1.0 eq) was added dropwise and the mixture was stirred for two hours at room temperature. Subsequently, sodium borohydride (7.57 g, 0.20 mol, 2.0 eq) was added in small portions while the solution was cooled in a water-ice bath. After completion of the addition, the reaction mixture was stirred overnight at room temperature. The solution was concentrated under reduced pressure and the residue was treated with water (250 ml) and neutralized with 2M hydrochloric acid. The product was extracted into dichloromethane (3 x 75 ml), washed with brine and dried over sodium sulfate. Removal of the solvent yielded 2-(((pyridine-2-ylmethyl)amino)methyl)phenol (**16**) as a brown oil (21.2 g, 99%).

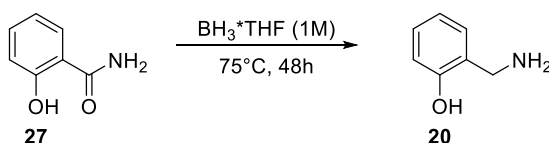


HRMS (ESI⁺, CH₃OH): m/z = 215.1179 ([C₁₃H₁₅N₂O]⁺, *calcd.* 215.1179).

¹H NMR (399.89 MHz, CDCl₃): δ = 3.92 (s, 2H, *H*7), 4.00 (s, 2H, *H*6), 6.78 (t, ³*J* = 7.40 Hz, 1H, *H*10), 6.87 (d, ³*J* = 8.03 Hz, 1H, *H*12), 6.98 (d, ³*J* = 7.28 Hz, 1H, *H*9), 7.15 - 7.24 (m, 3H, *H*2, *H*4, *H*11), 7.66 (td, ³*J* = 7.62 Hz, ⁴*J* = 1.19 Hz, 1H, *H*3), 8.58 (d, ³*J* = 3.76 Hz, 1H, *H*1) ppm.

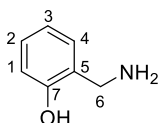
¹³C NMR (100.55 MHz, CDCl₃): δ = 51.7 (*C*7), 52.9 (*C*6), 116.3 (*C*12), 119.0 (*C*10), 122.3 (*C*8), 122.4 (*C*2), 122.6 (*C*4), 128.6 (*C*11), 128.7 (*C*9), 136.6 (*C*3), 149.3 (*C*1), 157.6 (*C*13), 158.1 (*C*5) ppm.

11.3.5 2-(AMINOMETHYL)PHENOL (**20**)



2-(Aminomethyl)phenol (**20**) was prepared according to published procedures with minor modifications.¹²⁶

Salicylamide (**27**) (2.68 g, 19.5 mmol, 1.0 eq) was treated with 1M borane tetrahydrofuran complex solution (100 ml, 100 mmol, 5.1 eq) under argon atmosphere and heated to 75°C for two days. After the mixture cooled to room temperature the reaction was quenched via dropwise addition of methanol. The solvent was removed under reduced pressure. The remaining tetrahydrofuran was stripped by addition of methanol (2 x 25 ml) followed by removal under vacuum to obtain 2-(aminomethyl)phenol (**20**) as a white solid in quantitative yield.



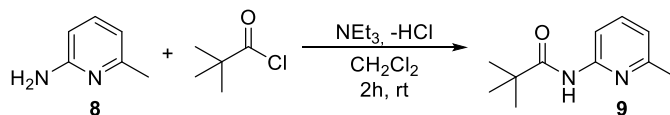
HRMS (EI⁺, direct): m/z = 123.0697 ([C₇H₉NO], *calcd.* 123.0684).

¹H NMR (600.13 MHz, CDCl₃): δ = 4.13 (s, 2H, *H*6), 6.79 (td, ³*J* = 7.42 Hz, ⁴*J* = 1.11 Hz, 1H, *H*3), 6.86 (dd, ³*J* = 8.07 Hz, ⁴*J* = 0.91 Hz, 1H, *H*1), 6.98 (dt, ³*J* = 7.44 Hz, ⁴*J* = 0.62 Hz, 1H, *H*4), 7.18 (td, ³*J* = 7.72 Hz, ⁴*J* = 1.61 Hz, 1H, *H*2) ppm.

¹³C NMR (150.90 MHz, CDCl₃): δ = 45.4 (*C*6), 116.7 (*C*1), 119.0 (*C*3), 123.9 (*C*5), 127.9 (*C*4), 128.7 (*C*2), 158.3 (*C*7) ppm.

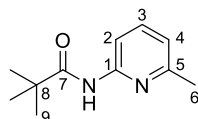
11.3.6 *N*-(6-IVALOYLAMIDO-2-PYRIDYLMETHYL)-*N*-(2-PYRIDYLMETHYL)AMIN (**18**)

N-(6-methylpyridin-2-yl)pivalamide (**9**)



N-(6-methylpyridin-2-yl)pivalamide (**9**) was prepared by slight modification of a previously described procedure.¹¹⁶

A solution of 2-amino-6-methylpyridine (**8**) (54.1 g, 0.50 mol, 1.0 eq) in dry dichloromethane (500 ml) was treated with triethylamine (90.1 ml, 65.8 g, 0.65 mol, 1.3 eq) and cooled to 0°C with an ice-water bath. Pivaloylchloride (67.2 ml, 66.3 g, 0.55 mol, 1.1 eq) was then added dropwise to the solution. The resulting mixture was warmed to room temperature and stirred for two hours. Afterwards, the reaction was quenched by addition of water (100 ml). The phases were separated and the aqueous phase was extracted with dichloromethane (2 x 50 ml). The combined organic phases were dried over sodium sulfate and concentrated under reduced pressure. The yellowish solid was recrystallized three times from diethylether to give *N*-(6-methylpyridin-2-yl)-pivalamide (**9**) as white crystals (95.6 g, 99%).



Molecular Formula: C₁₁H₁₆N₂O

MS (EI⁺, direct): *m/z* = 192.12 ([C₁₁H₁₆N₂O], *calcd.* 192.13).

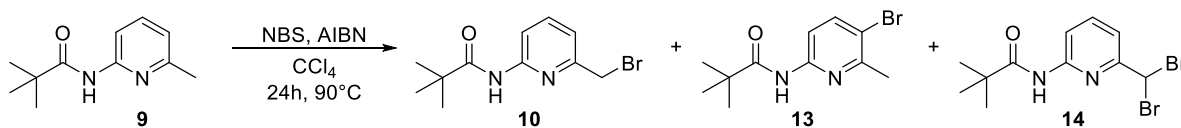
¹H NMR (199.92 MHz, CDCl₃): δ = 1.29 (s, 9H, *H*₉), 2.42 (s, 3H, *H*₆), 6.84 (d, ³*J* = 7.45 Hz, 1H, *H*₂), 7.54 (t, ³*J* = 7.89 Hz, 1H, *H*₃), 7.90 (bs, 1H, *NH*), 8.02 (d, ³*J* = 8.21 Hz, 1H, *H*₂) ppm.

¹³C NMR (100.55 MHz, CDCl₃): δ = 24.0 (*C*₆), 27.5 (*C*₉), 39.8 (*C*₈), 110.7 (*C*₂), 119.1 (*C*₃), 138.6 (*C*₄), 150.9 (*C*₁), 156.7 (*C*₅), 177.0 (*C*₇) ppm.

Elemental analysis: *Calcd.* for C₁₁H₁₆N₂O: C 68.72%; H 8.39%; N 14.57%

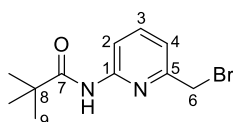
Found: C 68.75%; H 8.69%; N 14.64%.

N-(6-(bromomethyl)pyridin-2-yl)pivalamide (**10**) and *N*-(6-(dibromomethyl)pyridin-2-yl)pivalamide (**13**)



N-(6-bromomethyl)pyridin-2-yl)pivalamide (**10**) was synthesized by modification of previously published procedures.¹¹⁷⁻¹¹⁹

N-(6-methylpyridin-2-yl)pivalamide (**9**) (50.0 g, 0.26 mol, 1.0 eq) was dissolved under argon atmosphere in anhydrous carbon tetrachloride (500 ml) and was warmed to 70°C. *N*-bromosuccinimide (15.8 g) and a catalytic amount of AIBN was added and the mixture was heated for two hours with stirring while irradiated with a 150W UV lamp. Another portion of *N*-bromosuccinimide (15.8 g) and catalytic amount of AIBN were added. The additions were repeated every hour; in total seven additions of NBS (111 g, 0.62 mmol, 2.4 eq) were made. The mixture was then refluxed overnight. After cooling to room temperature the succinimide obtained was filtered and the filtrate concentrated under reduced pressure. The remaining brown oil was taken up in chloroform (400 ml), washed with water (3 x 300 ml), brine (300 ml) and dried over sodium sulfate. Removal of the solvent gave an orange oil containing a mixture of compound **9**, the desired products, **10** and **14**, and a ring-brominated species **13**. Column chromatography (SiO₂; Hexan:EtOAc = 4:1; R_f = 0.38) yielded a fraction of pure compound **10** next to a mixed fraction of compound **10**, compound **13** and compound **14** (R_f = 0.46). The latter was separated by column chromatography (SiO₂; Hexane:EtOAc = 10:1; R_f = 0.38). Ultra sonication of the orange oil obtained, treated with a small amount of hexane, yielded *N*-(6-bromomethyl)pyridin-2-yl)pivalamide (**10**) as a white solid (30.8 g, 44%). *N*-(6-(dibromomethyl)pyridin-2-yl)pivalamide (**14**) could not be isolated and was used in form of a mixture with the ring-brominated derivate **13** in the following reaction, after which the products were separated.



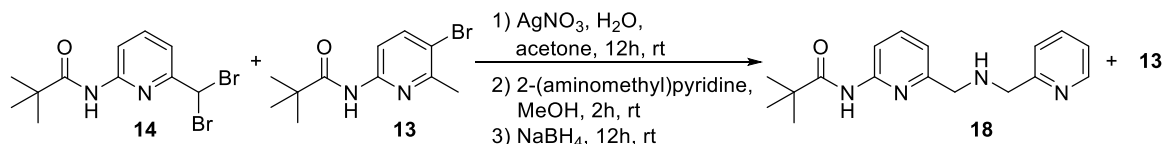
HRMS (ESI⁺, CH₃OH): *m/z* = 273.0421 ([C₁₁H₁₆N₂OBr]⁺, *calcd.* 273.0419).

¹H NMR (600.13 MHz, CDCl₃): δ = 1.34 (s, 9H, *H*₉), 4.43 (s, 2H, *H*₆), 7.15 (d, ³*J* = 7.47 Hz, 1H, *H*₄), 7.70 (t, ³*J* = 7.92 Hz, 1H, *H*₃), 8.02 (bs, 1H, *NH*), 8.19 (d, ³*J* = 8.38 Hz, 1H, *H*₂) ppm.

¹³C NMR (150.90 MHz, CDCl₃): δ = 27.5 (*C*₉), 33.4 (*C*₆), 39.8 (*C*₈), 113.3 (*C*₂), 119.2 (*C*₄), 139.4 (*C*₃), 151.3 (*C*₁), 154.8 (*C*₅), 177.2 (*C*₇) ppm.

Elemental analysis: *Calcd.* for C₁₁H₁₅N₂OBr: C 48.72%; H 5.58%; N 10.33%
 Found: C 48.58%; H 5.90%; N 10.27%.

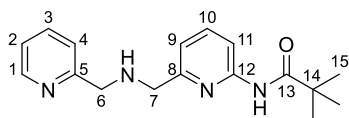
***N*-(6-pivaloylamido-2-pyridylmethyl)-*N*-(2-pyridylmethyl)amin (**18**)**



N-(6-formylpyridin-2-yl)pivalamide (**26**) and *N*-(6-pivaloylamido-2-pyridylmethyl)-*N*-(2-pyridylmethyl)amin (**18**) were synthesized following literature known procedures.^{114, 234}

Compound **14** (7.68 g, 21.9 mmol, 1.0 eq), in the form of a 32 w% mixture with compound **13**, was dissolved in acetone (210 ml) and the flask was covered with aluminium foil. Silver nitrate (33.6 g, 200 mmol, 9.0 eq) in water (18 ml) was added and the mixture stirred at room temperature overnight in the dark. The obtained precipitate was filtered and washed with dichloromethane. The yellow filtrate was concentrated to a brown oil, which was subsequently taken up in dichloromethane (300 ml), washed with water (100 ml), 0.5N sodium hydrogen-carbonate solution (100 ml), brine (100 ml) and dried over sodium sulfate. The successful conversion of *N*-(6-(dibromomethyl)pyridin-2-yl)pivalamide (**14**) to *N*-(6-formylpyridin-2-yl)pivalamide (**26**) was controlled via ¹H NMR spectroscopy.

In the next step the 33 w% mixture of *N*-(6-formylpyridin-2-yl)pivalamide (**26**) (3.26 g, 15.8 mmol, 1.0eq) with *N*-(5-bromo-6-methylpyridin-2-yl)pivalamide (**13**) were dissolved in methanol (64 ml). Then, 2-(aminomethyl)pyridine (1.78 ml, 1.87 g, 17.3 mmol, 1.1 eq) was added dropwise and the reaction mixture was stirred for 2.5 hours at room temperature. While cooling in an ice-water bath sodium borohydride (1.10 g, 29.0 mmol, 1.8 eq) was added in small portions and the mixture was stirred at room temperature overnight. The reaction was quenched by addition of water (70 ml) and the solution concentrated under reduced pressure. Water (20 ml) was added to the remaining oil and extracted with ethyl acetate. Removal of the solvent gave a brown oil, which was loaded onto a silica column. Elution with ethyl acetate removed the side products before the desired product *N*-(6-pivaloylamido-2-pyridylmethyl)-*N*-(2-pyridylmethyl)amin (**18**) was isolated by elution with methanol (4.48 g, 95%).

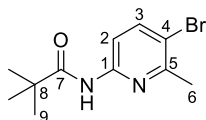


HRMS (ESI⁺, CH₃OH): *m/z* = 299.1863 ([C₁₇H₂₃N₄O]⁺, *calcd.* 299.1866).

¹H NMR (399.89 MHz, CDCl₃): δ = 1.31 (s, 9H, *H*₁₅), 2.73 (bs, 1H, *N*_{amin}*H*), 3.85 (s, 2H, *H*₇), 3.95 (s, 2H, *H*₆), 7.03 (d, ³*J* = 7.53 Hz, 1H, *H*₉), 7.15 (dd, ³*J* = 7.40 Hz, ³*J* = 4.64 Hz, 1H, *H*₂), 7.32 (d,

$^3J = 7.78$ Hz, 1H, *H4*), 7.63 (td, $^3J = 7.75$ Hz, $^4J = 1.97$ Hz, 2H, *H3*, *H10*), 8.03 (bs, 1H, *N_{amidH}*), 8.10 (d, $^3J = 8.28$ Hz, 1H, *H11*), 8.55 (d, $^3J = 4.64$ Hz, 1H, *H1*) ppm.

^{13}C NMR (100.55 MHz, CDCl_3): $\delta = 27.4$ (*C15*), 39.7 (*C14*), 54.2 (*C7*), 54.6 (*C6*), 112.0 (*C11*), 118.0 (*C9*), 122.0 (*C2*), 122.3 (*C4*), 136.4 (*C3*), 138.7 (*C10*), 149.2 (*C1*), 151.2 (*C12*), 157.7 (*C8*), 159.4 (*C5*), 177.0 (*C13*) ppm.



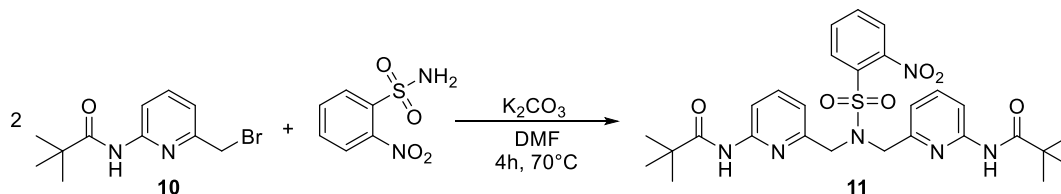
HRMS (EI^+ , direct): $m/z = 270.0374$ ($[\text{C}_{11}\text{H}_{15}\text{N}_2\text{OBr}]$, *calcd.* 270.0368)

^1H NMR (600.13 MHz, CDCl_3): $\delta = 1.31$ (s, 9H, *H9*), 2.54 (s, 3H, *H6*), 7.75 (d, $^3J = 8.68$ Hz, 1H, *H3*), 7.97 (d, $^3J = 8.73$, 2H, *NH*, *H2*) ppm.

^{13}C NMR (100.55 MHz, CDCl_3): $\delta = 24.4$ (*C6*), 27.4 (*C9*), 39.8 (*C8*), 112.5 (*C2*), 114.9 (*C4*), 141.8 (*C3*), 149.7 (*C1*), 155.2 (*C5*), 177.0 (*C7*) ppm.

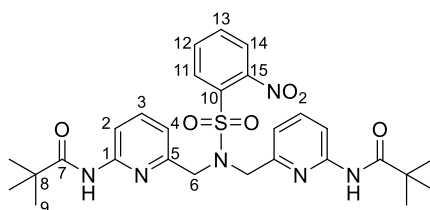
11.3.7 *N,N*-bis((2-pivaloylamidopyridin-6-yl)methyl)amin (3)

N,N-bis((2-pivaloylamidopyridin-6-yl)methyl)(2-nitrobenzene)sulfonamid (11)



N,N-bis((2-pivaloylamidopyridin-6-yl)methyl)(2-nitrobenzene)sulfonamide (**11**) was prepared according to a previously described procedure.¹¹⁹

Compound **10** (4.90 g, 18.1 mmol, 2.1 eq) was dissolved in dimethylformamide (86 ml) and then treated with potassium carbonate (2.97 g, 21.5 mmol, 2.5 eq) and 2-nitrobenzoyl-sulfonamide (1.74 g, 8.61 mmol, 1.0 eq). The resulting solution was heated at 70°C for 4 hours. After cooling to room temperature the reaction mixture was poured onto a saturated sodium bicarbonate solution (90 ml). Afterwards the phases were separated and the aqueous phase was extracted with ethyl acetate (5 x 50 ml). Then the combined organic phases were washed with half saturated sodium bicarbonate solution (4 x 25 ml) before being dried over sodium sulfate. Removal of the solvent under reduced pressure gave a brown oil which was purified by column chromatography (SiO_2 ; $\varnothing = 6$ cm; $L = 23$ cm; hexane:EtOAc = 5:4; $R_f = 0.17$). *N,N*-bis((2-pivaloylamidopyridin-6-yl)methyl)(2-nitrobenzene)sulfonamide (**11**) was obtained as a yellowish solid (4.91 g, 98%).



HRMS (ESI⁺, CH₃OH): m/z = 583.2331 ([C₂₈H₃₅N₆O₆S]⁺, *calcd.* 583.2333).

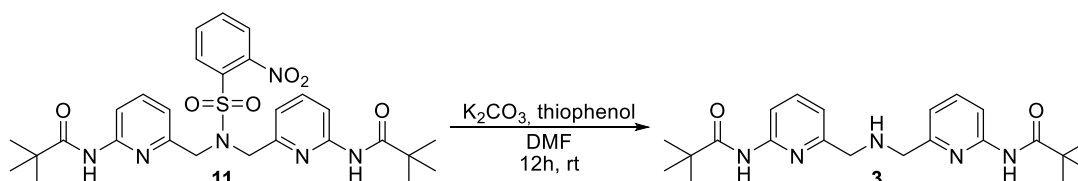
¹H NMR (600.13 MHz, CDCl₃): δ = 1.32 (s, 18H, *H*₉), 4.61 (s, 4H, *H*₆), 6.96 (d, ³*J* = 7.47 Hz, 2H, *H*₄), 7.53 (td, ³*J* = 7.67 Hz, ⁴*J* = 1.31 Hz, 2H, *H*₁₃), 7.59 (t, ³*J* = 7.87 Hz, 2H, *H*₃), 7.64 (td, ³*J* = 7.69 Hz, ⁴*J* = 1.26 Hz, 1H, *H*₁₂), 7.69 (dd, ³*J* = 7.98 Hz, ⁴*J* = 1.22, 1H, *H*₁₄), 7.89 (bs, 2H, NH), 7.98 (dd, ³*J* = 7.97 Hz, ⁴*J* = 1.11 Hz, 1H, *H*₁₁), 8.07 (d, ³*J* = 8.28 Hz, 2H, *H*₂) ppm.

¹³C NMR (150.90 MHz, CDCl₃): δ = 27.1 (*C*₉), 39.8 (*C*₈), 52.6 (*C*₆), 112.6 (*C*₂), 117.8 (*C*₄), 124.1 (*C*₁₄), 131.4 (*C*₁₁), 131.7 (*C*₁₃), 133.4 (*C*₁₂), 134.2 (*C*₁₀), 139.1 (*C*₃), 147.6 (*C*₁₅), 151.2 (*C*₁), 153.7 (*C*₅), 177.1 (*C*₇) ppm.

Elemental analysis: *Calcd.* for C₂₈H₃₄N₆O₆S · 0.3 C₄H₈O₂: C 57.58%; H 6.02%; N 13.80%

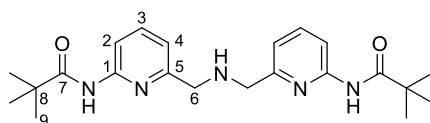
Found: C 56.92%; H 6.06%; N 14.10%.

***N,N*-bis((2-pivaloylamidopyridin-6-yl)methyl)amin (3)**



N,N-bis((2-pivaloylamidopyridin-6-yl)methyl)amin (**3**) was synthesized following a previously published procedure.¹¹⁹

A solution of compound **11** (16.0 g, 27.4 mmol, 1.0 eq) in anhydrous dimethylformamide (274 ml) was treated with potassium carbonate (5.70 g, 41.1 mmol, 1.5 eq) and thiophenol (3.10 ml, 30.1 mmol, 1.1 eq) before the reaction mixture was left stirring at room temperature overnight. Then, the reaction was quenched via decantation into a saturated sodium bicarbonate solution. Subsequently, the product was extracted into ethyl acetate, washed with half saturated sodium bicarbonate solution and dried over sodium sulfate. Removal of the solvent gave a crude product, which was purified by column chromatography (SiO₂; CH₂Cl₂:MeOH:NEt₃ = 980:14:8; R_f = 0.12) yielding *N,N*-bis((2-pivaloylamidopyridin-6-yl)methyl)amin (**3**) as a yellowish solid (8.78 g, 81 %).



HRMS (ESI⁺, CH₃OH): m/z = 398.2546 ([C₂₂H₃₂N₅O₂]⁺, *calcd.* 398.2551).

^{13}C NMR (100.55 MHz, CDCl_3): δ = 20.6 (C17), 27.5 (C36, C39), 39.8 (C35, C38), 54.7 (C13, C21), 59.0 (C27, C33), 59.9 (C6, C12), 111.7 (C23, C29), 118.0 (C25, C31), 121.9 (C2, C8), 122.7 (C4, C10), 123.8 (C14, C19), 127.6 (C16), 129.7 (C15, C18), 136.5 (C3, C9), 138.9 (C24, C30), 148.7 (C1, C7), 151.0 (C22, C28), 153.1 (C20), 157.3 (C26, C32), 159.4 (C5, C11), 177.1 (C34, C37) ppm.

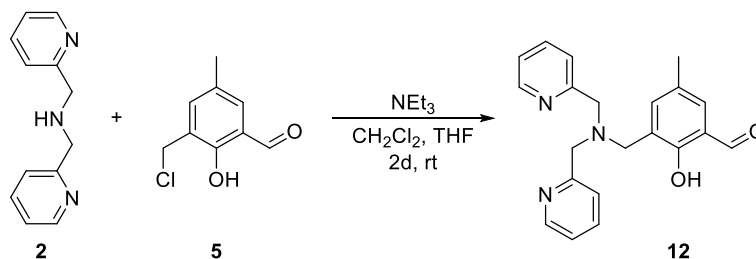
FT-IR spectroscopy: ν = 3438 ($\nu\{\text{N-H}\}$), 3389 ($\nu\{\text{O-H}\}$), 2964 ($\nu\{\text{C-H}\}$), 2869 ($\nu\{\text{C-H}\}$), 2817 ($\nu\{\text{C-H}\}$), 1686 ($\nu\{\text{C=O}\}$), 1523 ($\nu\{\text{C-N}\}$), $\delta\{\text{CNH}\}$, 1405 ($\nu\{\text{C-(CH}_3)_3\}$), 797 ($\delta\{\text{py-H}\}$) cm^{-1} .

Elemental analysis: *Calcd.* for $\text{C}_{43}\text{H}_{52}\text{N}_8\text{O}_3 \cdot \text{CH}_3\text{OH}$: C 69.45%; H 7.42%; N 14.73%

Found: C 69.47%; H 7.10%; N 14.98%.

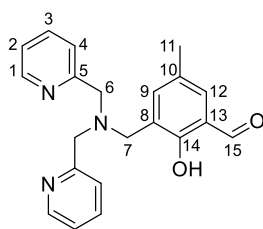
11.5 SYNTHESIS OF LIGAND H_3SIM^1

11.5.1 3-((BIS(PYRIDIN-2-YLMETHYL)AMINO)METHYL)-2-HYDROXY-5-METHYLBENZALDEHYDE (**12**)



3-((Bis(pyridine-2-ylmethyl)amino)methyl)2-hydroxy-5-methylbenzaldehyde (**12**) was synthesized by modification of the previously reported method.¹⁰⁶

3-(Chloromethyl)-2-hydroxy-5-methylbenzaldehyde (**5**) (0.54 g, 2.7 mmol, 1.0 eq) was dissolved in dichloromethane (4.0 ml) and cooled to 0°C in an water ice bath. A solution of bis(pyridin-2-ylmethyl)amine (**2**) (0.50 g, 2.7 mmol, 1.0 eq) in tetrahydrofuran (4.5 ml) which was treated with triethylamine (0.70 ml, 0.51 g, 5.0 mmol, 1.9 eq), was added dropwise. Afterwards, the reaction mixture was brought to room temperature and stirred for two days. The precipitate obtained was filtered and washed with a small amount of dichloromethane. The filtrate was concentrated under reduced pressure, taken up in dichloromethane (10 ml), washed with saturated sodium bicarbonate solution (10 ml) and dried over sodium sulfate. The yellow oil obtained after removal of the solvent solidified while keeping at -8°C . Recrystallisation from dichloromethane/hexane (1:1) yield 3-((bis(pyridine-2-ylmethyl)amino)methyl)2-hydroxy-5-methylbenzaldehyde (**12**) as a yellowish solid (0.57 g, 61%).

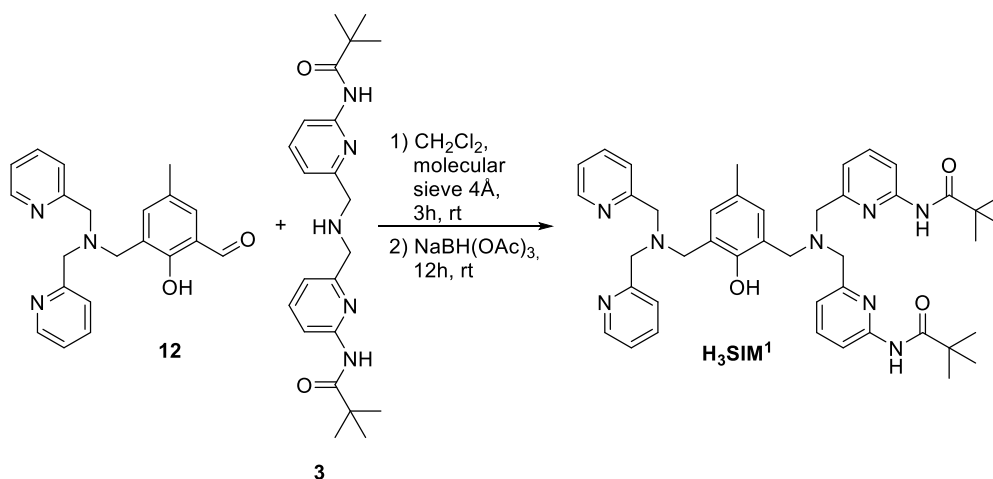


HRMS (ESI⁺, CH₃OH): $m/z = 348.1707$ ([C₂₁H₂₂N₃O₂]⁺, *calcd.* 348.1707).

¹H NMR (600.13 MHz, CD₃CN): $\delta = 2.25$ (s, 3H, H11), 3.78 (s, 2H, H7), 3.84 (s, 4H, H6), 7.22 (ddd, ³J = 7.42 Hz, ³J = 4.89 Hz, ⁴J = 1.01 Hz, 2H, H2), 7.27 (d, ⁴J = 2.32, 1H, H9), 7.36 (d, ³J = 7.87 Hz, 2H, H4), 7.40 (d, ⁴J = 1.61 Hz, 1H, H12), 7.69 (td, ³J = 7.69 Hz, ⁴J = 1.77 Hz, 2H, H3), 8.46 (ddd, ³J = 4.95 Hz, ⁴J = 1.64 Hz, ⁵J = 0.92 Hz, 2H, H1), 10.41 (s, 1H, H15) ppm.

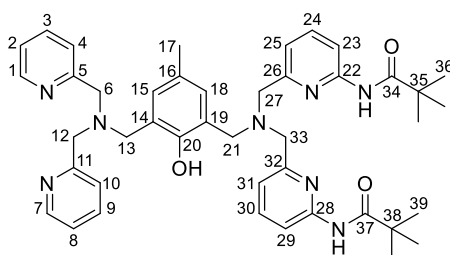
¹³C NMR (150.90 MHz, CD₃CN): $\delta = 20.3$ (C11), 56.1 (C7), 59.7 (C6), 123.4 (C2), 123.9 (C13), 124.2 (C4), 126.6 (C8), 128.3 (C12), 129.0 (C10), 137.9 (C3), 138.8 (C9), 149.8 (C1), 159.4 (C5), 160.3 (C14), 192.1 (C15) ppm.

11.5.2 LIGAND H₃SIM¹



Molecular sieves (4 Å) were added to a solution of compound **12** (3.13 g, 9.0 mmol, 1.0 eq) in anhydrous dichloromethane (23 ml), followed by the dropwise addition of a solution of compound **3** (3.58 g, 9.0 mmol, 1.0 eq) in anhydrous dichloromethane (10 ml). The mixture was stirred for three hours at room temperature. The solution was then treated with sodium triacetoxyborohydride (4.20 g, 20 mmol, 2.2 eq) by addition in portions and the mixture stirred at room temperature overnight. The reaction was quenched by addition of saturated sodium bicarbonate solution (30 ml) and stirring for 45 minutes. The pH value was subsequently adjusted to 8 by addition of solid sodium carbonate. The phases were separated and the aqueous phase was extracted with dichloromethane (3 x 30 ml). The combined organic phases were washed with saturated sodium carbonate solution (20 ml) and brine (20 ml) and dried over sodium sulfate. Removal of the solvent under reduced pressure gave a brownish foam. Purification by column

chromatography (SiO₂; DEE:NH₃ (7N in MeOH) = 98:2; R_f = 0.48) yielded H₃SIM¹ as a white solid (1.94 g, 30%).



HRMS (ESI⁺, CH₃CN): $m/z = 729.4232$ ([C₄₃H₅₃N₈O₃]⁺, *calcd.* 729.4235).

¹H NMR (CD₃CN, 500.13 MHz): $\delta = 1.25$ (s, 18H, H₃₆, H₃₉), 2.21 (s, 3H, H₁₇), 3.69 (s, 2H, H₂₁), 3.73 (s, 4H, H₂₇, H₃₃), 3.74 (s, 2H, H₁₃), 3.79 (s, 4H, H₆, H₁₂), 6.88 (d, ⁴J = 1.74 Hz, 1H, H₁₈), 7.10 (d, ³J = 8.06 Hz, 2H, H₂₅, H₃₁), 7.15 (d, ⁴J = 0.92 Hz, 1H, H₁₅), 7.15 (m, 2H, H₂, H₈), 7.50 (d, ³J = 8.07 Hz, 2H, H₄, H₁₀), 7.62 (t, ³J = 8.44 Hz, 2H, H₂₄, H₃₀), 7.64 (dt, ³J = 7.70 Hz, ⁴J = 1.83 Hz, 2H, H₃, H₉), 7.96 (d, ³J = 8.44 Hz, 2H, H₂₃, H₂₉), 8.28 (bs, 2H, NH), 8.46 (ddd, ³J = 4.83 Hz, ⁴J = 1.78 Hz, ⁵J = 1.05 Hz, 2H, H₁, H₇) ppm.

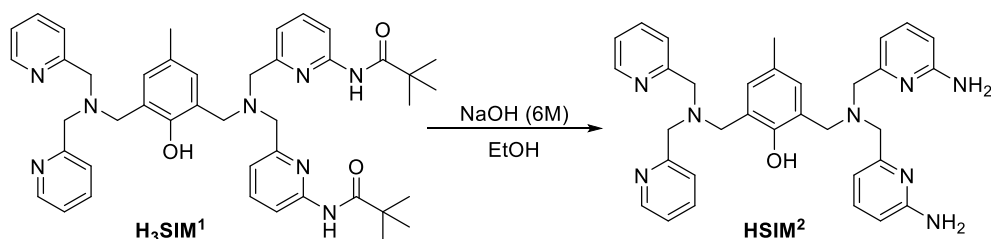
¹³C NMR (CD₃CN, 100.61 MHz): $\delta = 20.8$ (C₁₇), 27.7 (C₃₆, C₃₉), 40.5 (C₃₅, C₃₈), 54.4 (C₁₃), 56.3 (C₂₁), 59.6 (C₂₇, C₃₃), 60.8 (C₆, C₁₂), 112.5 (C₂₃, C₂₉), 119.2 (C₂₅, C₃₁), 123.1 (C₂, C₈), 123.8 (C₄, C₁₀), 124.7 (C₁₉), 125.6 (C₁₄), 128.5 (C₁₆), 130.7 (C₁₅), 131.0 (C₁₈), 137.4 (C₃, C₉), 139.9 (C₂₄, C₃₀), 149.9 (C₁, C₇), 152.3 (C₂₂, C₂₈), 154.4 (C₂₀), 158.7 (C₂₆, C₃₂), 160.6 (C₅, C₁₁), 177.9 (C₃₄, C₃₇) ppm.

FT-IR spectroscopy: $\nu = 3438$ (ν {N-H}), 3389 (ν {O-H}), 2964 (ν {C-H}), 2869 (ν {C-H}), 2817 (ν {C-H}), 1687 (ν {C=O}), 1517 (ν {C-N}, δ {CNH}), 1403 (ν {C-(CH₃)₃}), 798 (δ {py-H}) cm⁻¹.

Elemental analysis: *Calcd.* for C₄₃H₅₂N₈O₃: C 70.85%; H 7.19%; N 15.37%

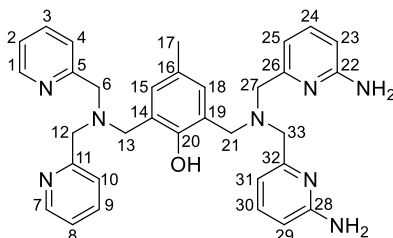
Found: C 70.63%; H 7.06%; N 15.29%.

11.6 SYNTHESIS OF LIGAND HSIM²



A solution of H₃SIM¹ (300 mg, 0.41 mmol) in ethanol (10 ml) was treated with aqueous sodium hydroxide solution (6M, 2.0 ml), after which the mixture was heated at 70°C for three days while stirring. Subsequently the solvent was removed under reduced pressure and the remaining solid was taken up in water (10 ml). Concentrated hydrochloric acid was added until the pH value

reached 1 and the pH value was subsequently adjusted to 7 using saturated sodium bicarbonate solution. After the product was extracted into dichloromethane (3 x 10 ml) the combined organic phases were washed with saturated sodium bicarbonate solution (10 ml) and dried over sodium sulfate. Removal of the solvent yielded a crude product which was purified by column chromatography (Alox_{neutral}; MeOH) yielding the desired product HSIM² as a white solid (109 mg, 47%).



HRMS (ESI⁺, CH₃CN): $m/z = 561.3080$ ([C₃₃H₃₇N₈O]⁺, *calcd.* 561.3085).

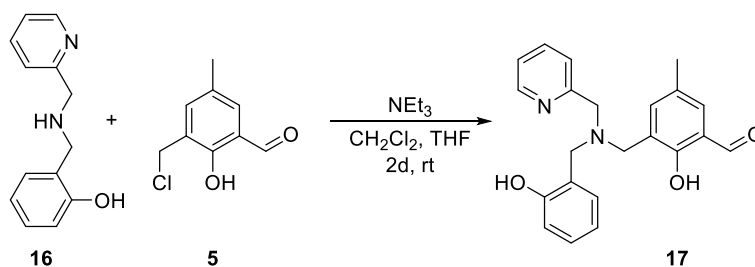
¹H NMR (CD₃CN, 500.13 MHz): $\delta = 2.18$ (s, 3H, H17), 3.51 (s, 4H, H27, H33), 3.57 (s, 2H, H21), 3.70 (s, 2H, H13), 3.77 (s, 4H, H6, H12), 6.35 (d, ³J = 8.07Hz, 2H, H23, H29), 6.61 (d, ³J = 6.97Hz, 2H, H25, H31), 6.88 (s, 1H, H18), 6.95 (s, 1H, H15), 7.17 (ddd, ³J = 6.24Hz, ³J = 5.14Hz, ⁴J = 1.10Hz, 2H, H2, H8), 7.33 (t, ³J = 7.70Hz, 2H, H24, H30), 7.46 (d, ³J = 7.70Hz, 2H, H4, H10), 7.66 (td, ³J = 7.70Hz, ⁴J = 1.83Hz, 2H, H3, H9), 8.48 (d, ³J = 5.14Hz, 2H, H1, H7) ppm.

¹³C NMR (CD₃CN, 100.61 MHz): $\delta = 20.5$ (C17), 52.5 (C13), 55.0 (C21), 60.2 (C27, C33), 60.5 (C6, C12), 107.8 (C23, C29), 113.1 (C25, C31), 123.2 (C2, C8), 124.2 (C4, C10), 124.7 (C14), 125.0 (C19), 131.2 (C15), 131.4 (C18), 137.7 (C3, C9), 139.2 (C24, C30), 149.9 (C1, C7), 157.9 (C26, C32), 160.0 (C5/C11/C22/C28), 160.2 (C5/C11/C22/C28) ppm.

FT-IR spectroscopy: $\nu = 3322$ (ν {N-H}), 3199 (ν {N-H}), 3059 (ν {Ar-H}), 3011 (ν {Ar-H}), 2917 (ν {C-H}), 2816 (ν {C-H}), 1594 (ν {C=C}), 1574 (ν {C=C}), 1466 (ν {C=C}), 1435 (ν {C=C}), 1299 (ν {C-N}), 1221 (ν {C-N}), 758 (δ {py-H}) cm⁻¹.

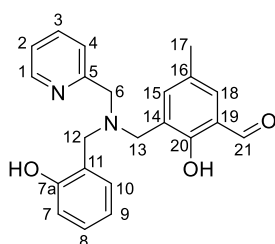
11.7 SYNTHESIS OF LIGAND H_4SIM^3

11.7.1 2-Hydroxy-3-(((2-hydroxybenzyl)(pyridin-2-ylmethyl)amino)methyl)-5-methylbenzaldehyde (**17**)



2-Hydroxy-3-(((2-hydroxybenzyl)(pyridine-2-ylmethyl)amino)methyl)-5-methylbenzaldehyde (**17**) was prepared according to a literature known procedures.³¹¹

3-(Chloromethyl)-2-hydroxy-5-methylbenzaldehyde (**5**) (4.62 g, 25.0 mmol, 1.0 eq) was dissolved in dichloromethane (40.0 ml) and the solution was cooled in a water-ice-bath. Then, a mixture of 2-(((pyridin-2-ylmethyl)amino)methyl)phenol (**16**) (5.36 g, 25.0 mmol, 1.0 eq) in tetrahydrofuran (45.0 ml), treated with triethylamine (12.8 ml, 9.29 g, 50.0 mmol, 2.0 eq), was added dropwise. After stirring the reaction mixture at room temperature for two days the precipitate obtained was filtered and washed with a small amount of dichloromethane. The filtrate was concentrated under reduced pressure and the residue taken up in dichloromethane (50 ml) before being washed with brine (30 ml) and dried over sodium sulfate. Removal of the solvent and recrystallization from dichloromethane/hexane (1:1) yielded 2-hydroxy-3-(((2-hydroxybenzyl)(pyridine-2-ylmethyl)amino)methyl)-5-methylbenzaldehyde (**17**) as a pale yellow solid (4.99 g, 55%).



HRMS (ESI⁺, CH₃OH): m/z = 363.1706 ([C₂₂H₂₃N₂O₃]⁺, *calcd.* 363.1703).

¹H NMR (600.13 MHz, CD₃CN): δ = 2.23 (s, 3H, H17), 3.74 (s, 2H, H13), 3.77 (s, 2H, H12), 3.85 (s, 2H, H6), 6.75 - 6.78 (m, 2H, H7, H9), 7.10 (dd, ³J = 7.27 Hz, ⁴J = 1.01 Hz, 1H, H10), 7.13 (td, ³J = 7.70 Hz, ⁴J = 1.67 Hz, 1H, H8), 7.27 - 7.30 (m, 2H, H2, H4), 7.31 (d, ⁴J = 1.82 Hz, H15), 7.36 (d, ⁴J = 1.61 Hz, H18), 7.74 (td, ³J = 7.67 Hz, ⁴J = 1.82 Hz, 1H, H3), 8.57 (dd, ³J = 4.95 Hz, ⁴J = 0.71 Hz, H1), 10.07 (s, 1H, H21), 11.09 (bs, 2H, OH) ppm.

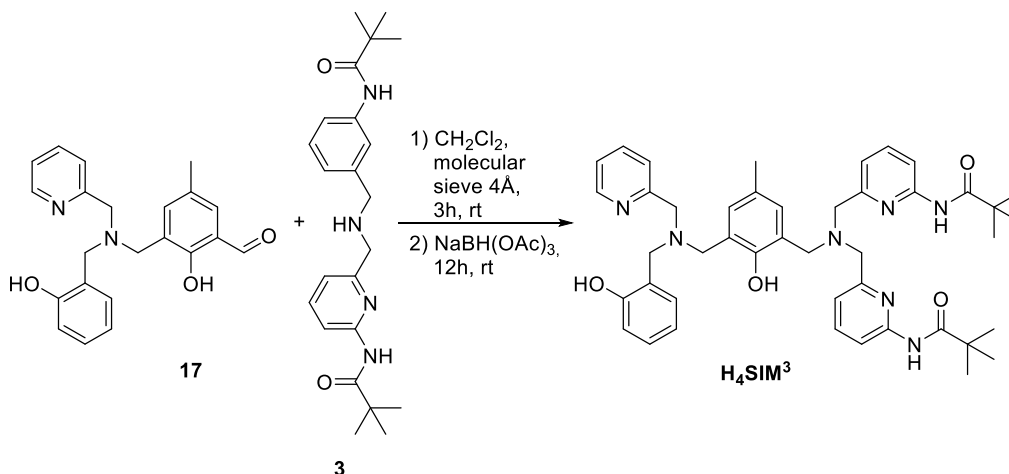
^{13}C NMR (150.90 MHz, CD_3CN): δ = 20.3 (C17), 54.0 (C13), 57.3 (C12), 58.5 (C6), 117.1 (C7), 120.0 (C9), 122.7 (C19), 123.6 (C11), 123.7 (C2), 124.6 (C4), 126.0 (C14), 129.7 (C16), 130.1 (C8), 131.3 (C10/C18), 131.3 (C10/C18), 138.4 (C3), 139.5 (C15), 149.3 (C1), 158.2 (C5), 158.5 (C7a), 159.3 (C20), 195.1 (C21) ppm.

Elemental analysis: *Calcd.* for $\text{C}_{22}\text{H}_{22}\text{N}_2\text{O}_3 \cdot 0.05 \text{CH}_2\text{Cl}_2$: C 72.23%; H 6.08%; N 7.64%

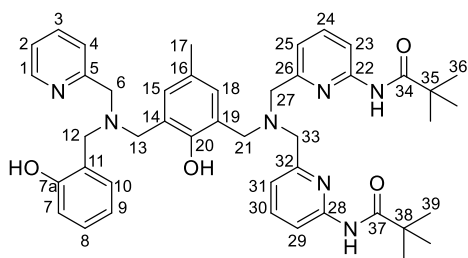
Found:

C 71.76%; H 6.31%; N 7.43%.

11.7.2 LIGAND H_4SIM^3



A solution of compound **17** (3.56 g, 9.80 mmol, 1.0 eq) in anhydrous dichloromethane (25 ml) was treated with molecular sieves (4 Å) before a solution of compound **3** (4.10 g, 10.3 mmol, 1.1 eq) in anhydrous dichloromethane (11 ml) was added dropwise. After the mixture was stirred for three hours at room temperature sodium triacetoxyborohydride (4.59 g, 21.7 mmol, 2.2 eq) was added in small portions and the reaction mixture was left to react at room temperature while stirring. The reaction was quenched by addition of saturated sodium bicarbonate solution (30 ml) and the mixture was stirred for 45 minutes before the pH value was adjusted to 8 by addition of solid sodium carbonate. The phases were separated and the aqueous phase was extracted with dichloromethane (3 x 30 ml). The combined organic phases were washed with saturated sodium carbonate solution (20 ml), brine (20 ml) and dried over sodium sulfate. Removal of the solvent under reduced pressure gave a orange foam. Purification by column chromatography (SiO_2 ; DEE:*n*-hexane: NH_3 (7N in MeOH) = 90:8:2; R_f = 0.57) yielded H_4SIM^3 as a white solid (4.50 g, 62%).



Molecular Formula: $C_{44}H_{53}N_7O_4$

HRMS (ESI⁺, CH₃CN): $m/z = 744.4231$ ($[C_{44}H_{54}N_7O_4]^+$, *calcd.* 744.4235).

¹H NMR (500.13 MHz, CD₃CN): $\delta = 1.26$ (s, 18H, *H*36, *H*39), 2.16 (s, 3H, *H*17), 3.69 (s, 2H, *H*21), 3.74 (s, 4H, *H*27, *H*33), 3.75 (s, 2H, *H*13), 3.76 (s, 2H, *H*6), 3.78 (s, 2H, *H*12), 6.74 (m, 2H, *H*7, *H*9), 6.85 (d, ⁴*J* = 1.83 Hz, 1H, *H*18), 6.99 (d, ⁴*J* = 1.47 Hz, 1H, *H*15), 7.05 (d, ³*J* = 7.34 Hz, 3H, *H*10, *H*25, *H*31), 7.11 (td, ³*J* = 7.70 Hz, ⁴*J* = 1.83 Hz, 1H, *H*8), 7.14 (d, ³*J* = 7.70 Hz, 1H, *H*4), 7.19 (ddd, ³*J* = 7.70 Hz, ³*J* = 6.60 Hz, ⁴*J* = 1.10 Hz, 1H, *H*2), 7.58 (td, ³*J* = 7.70 Hz, ⁴*J* = 1.83 Hz, 1H, *H*3), 7.61 (t, ³*J* = 7.70 Hz, 2H, *H*24, *H*30), 7.97 (d, ³*J* = 7.70 Hz, 2H, *H*23, *H*29), 8.33 (bs, 2H, *NH*), 8.52 (ddd, ³*J* = 4.95 Hz, ⁴*J* = 1.76 Hz, ⁵*J* = 0.91 Hz, 1H, *H*1) ppm.

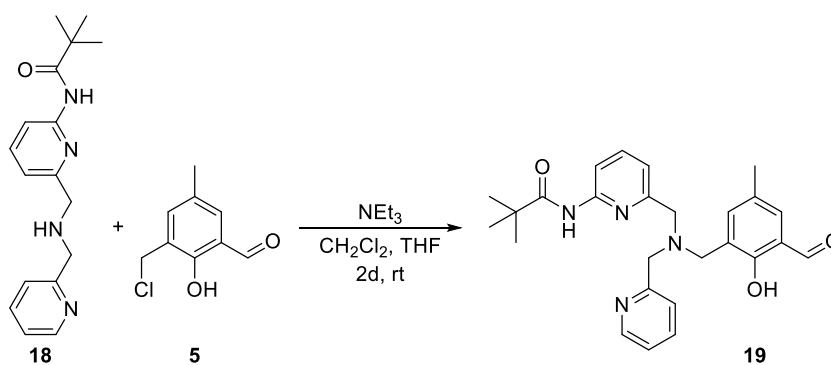
¹³C NMR (100.61 MHz, CD₃CN): $\delta = 20.6$ (*C*17), 27.7 (*C*36, *C*39), 40.5 (*C*35, *C*38), 53.2 (*C*13), 57.2 (*C*21), 57.9 (*C*12), 59.3 (*C*27, *C*33), 59.4 (*C*6), 112.6 (*C*23, *C*29), 116.9 (*C*9), 119.1 (*C*25, *C*31), 119.9 (*C*7), 123.3 (*C*2), 124.1 (*C*11), 124.4 (*C*4), 124.5 (*C*14/*C*19), 124.9 (*C*14/*C*19), 128.7 (*C*16), 129.7 (*C*8), 130.8 (*C*10), 131.3 (*C*18), 131.6 (*C*15), 137.7 (*C*3), 140.0 (*C*24, *C*30), 149.9 (*C*1), 152.4 (*C*22, *C*28), 154.5 (*C*20), 158.2 (*C*26, *C*32), 158.8 (*C*5/*C*11), 158.9 (*C*5/*C*11), 178.0 (*C*34, *C*37) ppm.

FT-IR spectroscopy: $\nu = 3392$ ($\nu\{N-H\}$), 2968 ($\nu\{C-H\}$), 2870 ($\nu\{C-H\}$), 2824 ($\nu\{C-H\}$), 1689 ($\nu\{C=O\}$), 1522 ($\nu\{C-N\}$, $\delta\{CNH\}$), 1450 ($\nu\{C-(CH_3)_3\}$), 751 ($\delta\{py-H\}$) cm⁻¹.

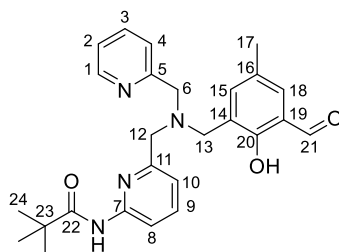
Elemental analysis: *Calcd.* for C₄₃H₅₂N₈O₃: C 71.04%; H 7.18%; N 13.18
 Found: C 71.11%; H 7.26%; N 12.93.

11.8 SYNTHESIS OF LIGAND H₄SIM⁴

11.8.1 *N*-(6-(((3-FORMYL-2-HYDROXY-5-METHYLBENZYL)(PYRIDIN-2-YLMETHYL)AMINO)METHYL)PYRIDIN-2-YL)PIVALAMIDE (**19**)



N-(6-pivaloylamido-2-pyridylmethyl)-*N*-(2-pyridylmethyl)amine (**18**) (4.92 g, 16.5 mmol, 1.0 eq) was dissolved in anhydrous dichloromethane (26.5 ml) and treated with triethylamine (4.30 ml, 3.09 g, 16.5 mmol, 1.0 eq). This solution was then added dropwise to a cold mixture of 3-(chloromethyl)-2-hydroxy-5-methylbenzaldehyde (**5**) (3.05 g, 16.5 mmol, 1.0 eq) in tetrahydrofuran (30.0 ml) at 0°C. Afterwards the mixture was stirred for two days at room temperature and the white precipitate obtained was filtered, washed with a small amount of dichloromethane and the filtrate was concentrated under reduced pressure. The remaining yellow oil was taken up in dichloromethane (50 ml), washed with half concentrated brine (20 ml) and dried over sodium sulfate. The solvent was evaporated under vacuum to yield *N*-(6-(((3-formyl-2-hydroxy-5-methylbenzyl)(pyridin-2-ylmethyl)amino)methyl)pyridin-2-yl)pivalamide (**19**) as a yellow solid (7.07 g, 96%).

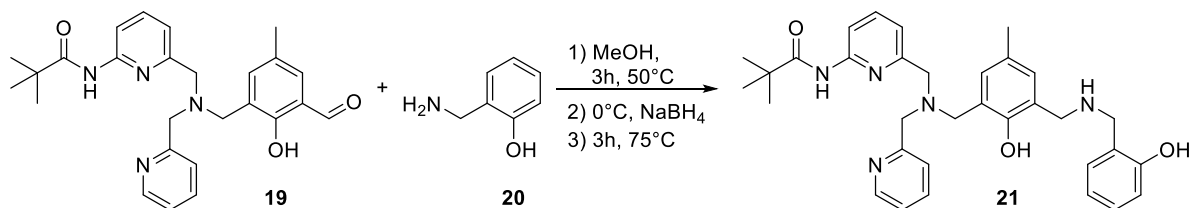


HRMS (ESI⁺, CH₃OH): *m/z* = 447.2391 ([C₂₆H₃₁N₄O₃]⁺, *calcd.* 447.2391).

¹H NMR (399.89 MHz, CDCl₃): δ = 1.38 (s, 9H, H₂₄), 2.29 (s, 3H, H₁₇), 3.81 (s, 2H, H₁₃), 3.89 (s, 4H, H₆, H₁₂), 6.98 (d, ³J = 7.53 Hz, 1H, H₁₀), 7.15 (dd, ³J = 7.28 Hz, ³J = 5.24 Hz, 1H, H₂), 7.20 (d, ⁴J = 1.51 Hz, 1H, H₁₅), 7.37 (d, ³J = 7.91 Hz, 1H, H₄), 7.49 (d, ⁴J = 1.63 Hz, 1H, H₁₈), 7.60-7.67 (m, 2H, H₃, H₉), 8.14 (d, ³J = 8.28 Hz, 1H, H₈), 8.46 (bs, 1H, NH), 8.52 (d, ³J = 4.77 Hz, 1H, H₁), 10.52 (s, 1H, H₂₁), 11.74 (bs, 1H, OH) ppm.

^{13}C NMR (100.55 MHz, CDCl_3): δ = 20.2 (C17), 27.4 (C24), 39.8 (C23), 55.7 (C13), 58.3 (C12), 59.4 (C6), 112.0 (C8), 118.0 (C10), 122.2 (C2), 122.9 (C4), 125.0 (C14), 128.1 (C16, C19), 128.3 (C18), 136.8 (C3), 137.8 (C15), 139.2 (C9), 148.8 (C1), 151.3 (C7), 156.1 (C11), 158.2 (C5), 158.7 (C20), 177.2 (C22), 191.1 (C21) ppm.

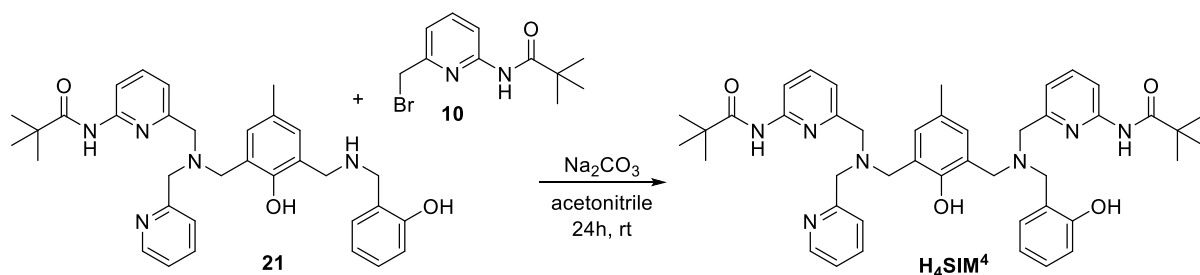
11.8.2 *N*-(6-(((2-hydroxy-3-(((2-hydroxybenzyl)amino)methyl)-5-methylbenzyl)(pyridin-2-ylmethyl)amino)-methyl)pyridin-2-yl)pivalamide (**21**)



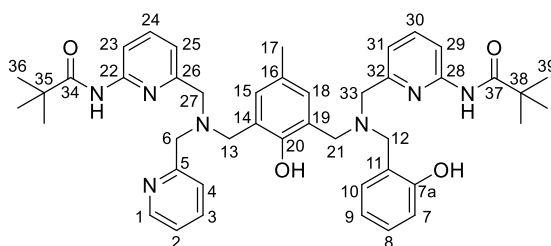
A mixture of compound **19** (6.25 g, 14.0 mmol, 1.0 eq) and 2-(aminomethyl)phenol (**20**) (2.42 g, 19.6 mmol, 1.4 eq) in methanol (300 ml) was heated at 50°C for three hours. The solution was cooled with an ice-water bath and sodium borohydride (1.99 g, 52.6 mmol, 3.8 eq) was added in portions. After addition, the reaction mixture was refluxed for three hours. After cooling to room temperature the solution was concentrated under vacuum. The remaining oil was taken up in dichloromethane (100 ml) and saturated sodium bicarbonate solution (100 ml) was added carefully. Using solid sodium carbonate the pH value was adjusted to 14. The phases were separated and the aqueous phase was extracted with dichloromethane (4 x 75 ml). The combined organic phases were washed with brine (20 ml) and dried over sodium sulfate. Removal of the solvent yielded *N*-(6-(((2-hydroxy-3-(((2-hydroxybenzyl)amino)methyl)-5-methylbenzyl)(pyridin-2-ylmethyl)amino)methyl)pyridin-2-yl)pivalamide (**21**) as a yellowish solid which was used in the next step without further purification.

HRMS (ESI⁺, CH_3OH): m/z = 554.3125 ($[\text{C}_{33}\text{H}_{40}\text{N}_5\text{O}_3]^+$, *calcd.* 554.3126).

^1H NMR (200.13 MHz, CDCl_3): δ = 1.27 (s, 6H, (CH_3)C), 1.30 (s, 3H, (CH_3)C), 2.17 (s, 3H, CH_3), 3.66 (s, 2H, CH_2), 3.75 (s, 2H, CH_2), 3.77 (s, 2H, CH_2), 3.82 (s, 2H, CH_2), 3.86 (s, 2H, CH_2), 4.69 (s, 1H, $\text{N}_{\text{amin}}\text{H}$), 6.76 (td, ^3J = 7.32, ^4J = 1.21, 1H, H_{aryl}), 6.84 – 6.94 (m, 4H, H_{aryl}), 7.03 (s, 1H, H_{aryl}), 7.09 – 7.22 (m, 3H, H_{aryl}), 7.26 – 7.34 (m, 1H, H_{aryl}), 7.52 – 7.68 (m, 2H, H_{aryl}), 8.13 (d, ^3J = 8.34, 2H, H_{aryl}), 8.45 (s, 1H, $\text{N}_{\text{amid}}\text{H}$), 8.51 (ddd, ^3J = 4.89, ^4J = 1.86, ^5J = 0.82, 1H, H_{aryl}) ppm.

11.8.3 LIGAND H₄SIM⁴

Compound **21** (7.75 g, 14.0 mmol, 1.0 eq) was dissolved in acetonitrile (400 ml) and treated with sodium carbonate (1.48 g, 14.0 mmol, 1.0 eq). Then, *N*-(6-bromomethyl)pyridine-2-yl)pivalamide (**10**) (3.80 g, 14.0 mmol, 1.0 eq) was added and the reaction mixture was stirred at room temperature for 24 hours. The solution was concentrated to a brown oil, which was taken up in dichloromethane (100 ml) and saturated sodium bicarbonate solution (100 ml). The product was extracted into dichloromethane (4 x 50 ml), washed with brine (30 ml) and dried over sodium sulfate. After removal of the solvent the crude product was purified via column chromatography (SiO₂; DEE:*n*-hexane:NH₃ (7N in MeOH) = 90:8:2; R_f = 0.48) to yield H₄SIM⁴ as yellowish solid (2.12 g, 22%).



HRMS (ESI⁺, CH₃OH): $m/z = 744.4237$ ([C₄₄H₅₄N₇O₄]⁺, *calcd.* 744.4232).

¹H NMR (500.13 MHz, CD₃CN): $\delta = 1.28$ (s, 9H, H_{36/39}), 1.28 (s, 9H, H_{36/39}), 2.13 (s, 3H, H₁₇), 3.67 (s, 2H, H_{13/21}), 3.73 (s, 2H, H_{13/21}), 3.74 (s, 4H, H₆, H_{27/H30}), 3.76 (s, 2H, H_{27/H30}), 3.77 (s, 2H, H₁₂), 6.74–6.79 (m, 2H, H_{7/H9}), 6.81 (d, ⁴J = 1.83 Hz, 1H, H_{15/H18}), 6.84 (dd, ³J = 7.70 Hz, ⁴J = 0.73 Hz, 1H, H_{25/H31}), 6.96 (d, ⁴J = 2.20 Hz, 1H, H_{15/H18}), 6.99 (dd, ³J = 7.70 Hz, ⁴J = 0.73 Hz, 1H, H_{25/H31}), 7.09 (dd, ³J = 7.34 Hz, ⁴J = 1.47 Hz, 1H, H₁₀), 7.12–7.15 (m, 2H, H_{2/H8}), 7.33 (d, ³J = 7.70 Hz, 1H, H₄), 7.56–7.61 (m, 2H, H₃, H_{24/H30}), 7.64 (t, ³J = 7.89 Hz, 1H, H_{24/H30}), 7.97 (d, ³J = 8.07 Hz, 1H, H_{23/H29}), 8.00 (d, ³J = 7.70 Hz, 1H, H_{23/H29}), 8.42 (bs, 1H, NH), 8.45 (ddd, ³J = 4.86 Hz, ⁴J = 1.82 Hz, ⁵J = 0.84 Hz, 1H, H₁), 8.48 (bs, 1H, NH) ppm.

¹³C NMR (125.76 MHz, CD₃CN): $\delta = 20.6$ (C₁₇), 27.6 (C_{36/C39}), 27.7 (C_{36/C39}), 40.5 (C_{35/C38}), 40.5 (C_{35/C38}), 52.9 (C_{13/C21}), 57.2 (C_{13/C21}), 58.0 (C₁₂), 58.7 (C_{27/C33}), 59.0 (C_{27/C33}), 59.8 (C₆), 112.3 (C_{23/C29}), 112.4 (C_{23/C29}), 116.8 (C_{7/C9}), 119.1 (C_{25/C31}), 119.3 (C_{25/C31}), 119.9 (C_{7/C9}), 123.1 (C₂), 123.9 (C₄), 124.29 (C_{14/C20}), 124.4 (C₁₁), 124.9 (C_{14/C20}), 128.5 (C₁₆), 129.7 (C₈), 131.0 (C₁₀, C_{15/C18}), 131.1 (C₁₀, C_{15/C18}), 131.4 (C₁₀, C_{15/C18}), 137.6 (C₃), 140.0

(C24/C30), 140.0 (C24/C30), 149.8 (C1), 152.3 (C22/C28), 152.4 (C22/C28), 154.5 (C20), 157.7 (C26/C32), 157.9 (C26/C32), 158.6 (C7a), 159.6 (C5), 177.9 (C34/C37).

FT-IR spectroscopy: $\nu = 3669$ ($\nu\{\text{O-H}\}$), 3388 ($\nu\{\text{N-H}\}$), 2971 ($\nu\{\text{C-H}\}$), 2901 ($\nu\{\text{C-H}\}$), 2819 ($\nu\{\text{C-H}\}$), 1688 ($\nu\{\text{C=O}\}$), 1520 ($\nu\{\text{C-N}\}$, $\delta\{\text{CNH}\}$), 1449 ($\nu\{\text{C-(CH}_3\text{)}_3\}$), 755 ($\delta\{\text{py-H}\}$) cm^{-1} .

Elemental analysis: *Calcd.* for $\text{C}_{44}\text{H}_{53}\text{N}_7\text{O}_4$: C 71.04%; H 7.18%; N 13.18%

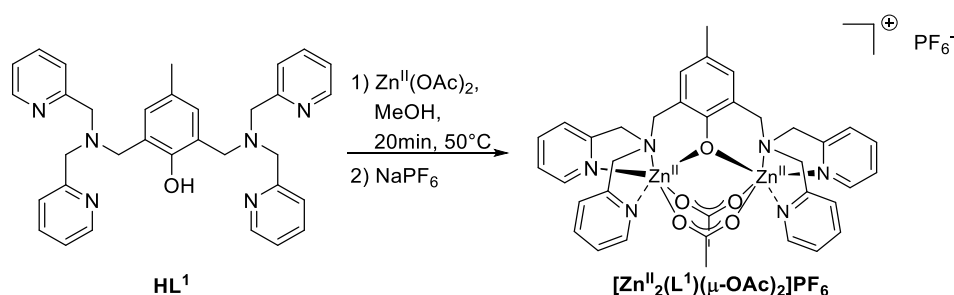
Found: C 70.66%; H 7.31%; N 13.35%.

11.9 SYNTHESIS OF DIZINC(II) COMPLEXES

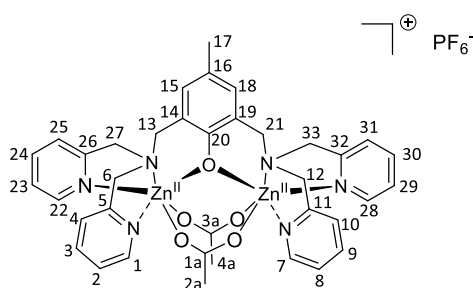
11.9.1 GENERAL PROCEDURE

The ligand (0.137 mmol, 1.0 eq) was dissolved in methanol (5.0 ml) (when H_4SIM^3 was used as ligand the solution was treated with 2M sodium hydroxide solution (69 μl , 1.0 eq)). After addition of Zn^{II} acetate (57.8 mg, 0.274 mmol, 2.0 eq) the mixture was heated to 50°C for 20 minutes. Sodium hexafluorophosphate (46.0 mg, 0.274 mmol, 2.0 eq) was added to the hot solution. The compounds were obtained as colourless crystals upon slow evaporation of solvent and these were collected by filtration.

11.9.2 SYNTHESIS OF $[\text{Zn}^{\text{II}}_2(\text{L}^1)(\mu\text{-OAc})_2]\text{PF}_6$



Yield: 102.5 mg (81%).



CCDC no.: 998888

HRMS (ESI⁺, CH_3CN): $m/z = 360.0704$ ($[\text{C}_{35}\text{H}_{36}\text{N}_6\text{O}_3\text{Zn}_2]^{2+}$, *calcd.* 360.0689); 765.1352 ($[\text{C}_{36}\text{H}_{37}\text{N}_6\text{O}_5\text{Zn}_2]^+$, *calcd.* 765.1360).

^1H NMR (500.13 MHz, CD_3CN): δ = 1.95 (s, 3H, *H*17), 1.99 (s, 6H, *H*2a, *H*4a), 3.17 (d, 2J = 11.37 Hz, 2H, *H*13, *H*21), 3.35 (d, 2J = 16.51 Hz, 2H, *H*12, *H*33), 3.48 (d, 2J = 16.14 Hz, 2H, *H*12, *H*33), 3.88 (d, 2J = 11.37 Hz, 2H, *H*13, *H*21), 3.97 (d, 2J = 14.31 Hz, 2H, *H*6, *H*27), 4.50 (d, 2J = 14.31 Hz, 2H, *H*6, *H*27), 6.40 (s, 2H, *H*15, *H*18), 6.44 (d, 3J = 7.70 Hz, 2H, *H*10, *H*31), 7.01 (dd, 3J = 7.34 Hz, 3J = 5.14 Hz, 2H, *H*8, *H*29), 7.29 (td, 3J = 7.70 Hz, 4J = 1.47 Hz, 2H, *H*9, *H*30), 7.43 (dd, 3J = 7.34 Hz, 3J = 5.14 Hz, 2H, *H*2, *H*23), 7.48 (d, 3J = 8.07 Hz, 2H, *H*4, *H*25), 7.92 (td, 3J = 7.79 Hz, 4J = 1.65 Hz, 2H, *H*3, *H*24), 8.24 (d, 3J = 4.77 Hz, 2H, *H*7, *H*28), 8.76 (d, 3J = 4.40 Hz, 2H, *H*1, *H*22) ppm.

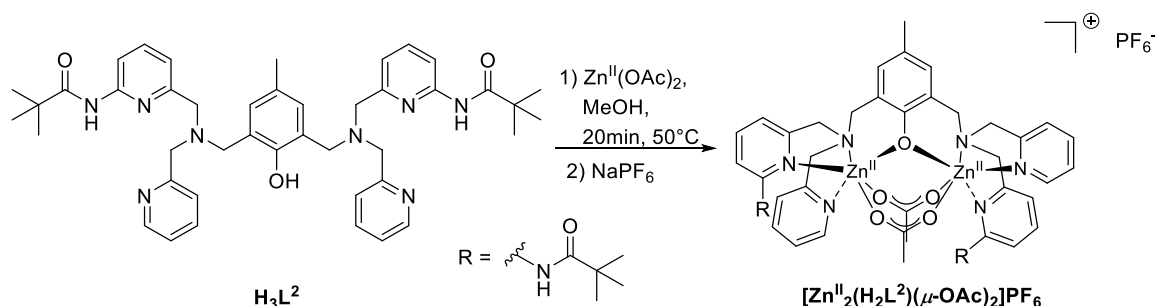
^{13}C NMR (100.61 MHz, CD_3CN): δ = 20.2 (*C*17), 24.9 (*C*2a, *C*4a), 58.5 (*C*12, *C*33), 60.7 (*C*13, *C*21), 60.8 (*C*6, *C*27), 121.9 (*C*10, *C*31), 123.6 (*C*8, *C*29), 124.3 (*C*14, *C*19), 125.0 (*C*2, *C*23), 125.1 (*C*16), 125.2 (*C*4, *C*25), 131.9 (*C*15, *C*18), 138.6 (*C*9, *C*30), 140.3 (*C*3, *C*24), 147.2 (*C*7, *C*28), 148.6 (*C*1, *C*22), 155.8 (*C*11, *C*32), 156.3 (*C*5, *C*26), 160.2 (*C*20), 179.3 (*C*1a, *C*3a) ppm.

FT-IR spectroscopy: ν = 2996 ($\nu\{\text{C-H}\}$), 2931 ($\nu\{\text{C-H}\}$), 2844 ($\nu\{\text{C-H}\}$), 1600 ($\nu_s\{\text{OAc}\}$), 1406 ($\nu_s\{\text{OAc}\}$), 831 ($\nu\{\text{P-F}\}$), 650 ($\delta\{\text{py-H}\}$), 556 ($\delta\{\text{F-P-F}\}$) cm^{-1} .

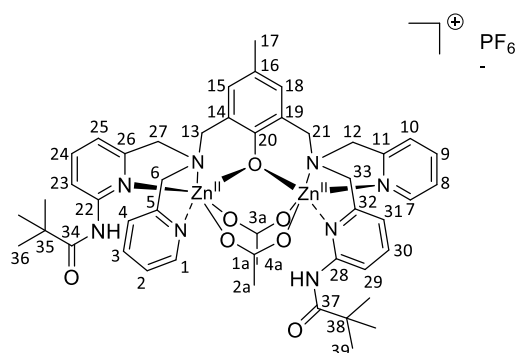
Elemental analysis: *Calcd.* for $\text{C}_{37}\text{H}_{39}\text{N}_6\text{O}_5\text{PF}_6\text{Zn}_2$: C 48.10%; H 4.26%; N 9.11%

Found: C 48.10%; H 4.50%; N 9.11%.

11.9.3 SYNTHESIS OF $[\text{Zn}^{\text{II}}_2(\text{H}_2\text{L}^2)(\mu\text{-OAc})_2]\text{PF}_6$



Yield: 116.6 mg (76%).



CCDC no.: 998889

HRMS (ESI^+ , CH_3CN): m/z = 429.1283 [$[\text{C}_{43}\text{H}_{50}\text{N}_8\text{O}_3\text{Zn}_2]^{2+}$, *calcd.* 429.1268).

^1H NMR (500.13 MHz, CD_3CN): δ = 1.27 (s, 18H, *H*36, *H*39), 1.91 (s, 3H, *H*17), 2.12 (s, 6H, *H*2a, *H*4a), 3.19 (d, 2J = 11.37 Hz, 2H, *H*13, *H*21), 3.42-3.56 (m, 4H, *H*6, *H*12), 3.82 (d, 2J = 11.74 Hz, 2H, *H*13, *H*21), 3.97 (d, 2J = 15.04 Hz, 2H, *H*27, *H*33), 4.59 (d, 2J = 15.04 Hz, 2H, *H*27, *H*33), 6.40 (s, 2H,

$^1\text{H NMR}$ (500.13 MHz, CD_3CN): δ = 6.59 (d, 3J = 7.70 Hz, 2H, H_4 , H_{10}), 7.05 (dd, 3J = 6.79 Hz, 3J = 6.05 Hz, 2H, H_2 , H_8), 7.16 (d, 3J = 7.70 Hz, 2H, H_{25} , H_{31}), 7.38 (td, 3J = 7.70 Hz, 4J = 1.47 Hz, 2H, H_3 , H_9), 7.85 (t, 3J = 7.70 Hz, 2H, H_{24} , H_{30}), 8.14 (d, 3J = 8.44 Hz, 2H, H_{23} , H_{29}), 8.39 (m, 2H, H_1 , H_7), 9.89 (s, 2H, NH) ppm.

$^{13}\text{C NMR}$ (100.61 MHz, CD_3CN): δ = 19.2 (C_{17}), 25.3 (C_{2a} , C_{4a}), 26.7 (C_{36} , C_{39}), 39.8 (C_{35} , C_{38}), 57.1 (C_6 , C_{12}), 60.2 (C_{13} , C_{21}), 61.1 (C_{27} , C_{33}), 115.9 (C_{23} , C_{29}), 119.1 (C_{25} , C_{31}), 121.7 (C_4 , C_{10}), 122.9 ($C_2/C_8/C_{14}/C_{19}$), 122.9 ($C_2/C_8/C_{14}/C_{19}$), 124.7 (C_{16}), 130.4 (C_{15} , C_{18}), 138.9 (C_3 , C_9), 141.0 (C_{24} , C_{30}), 146.2 (C_1 , C_7), 151.98 (C_{22} , C_{28}), 154.4 (C_{26} , C_{32}), 155.1 (C_5 , C_{11}), 159.0 (C_{20}), 177.8 (C_{34} , C_{37}), 178.9 (C_{1a} , C_{3a}) ppm.

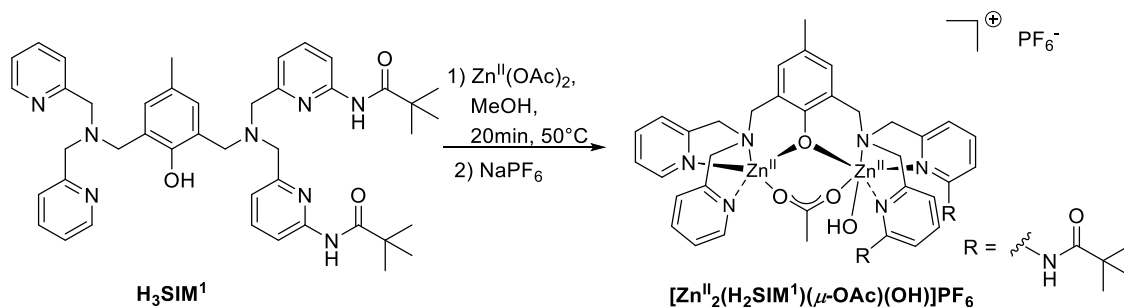
$^{31}\text{P NMR}$ (100.61 MHz, CD_3CN): δ = -144.3 (sep, PF_6^-) ppm.

FT-IR spectroscopy: ν = 3293 ($\nu\{\text{N-H}\}$), 2976 ($\nu\{\text{C-H}\}$), 2924 ($\nu\{\text{C-H}\}$), 2877 ($\nu\{\text{C-H}\}$), 1700 ($\nu\{\text{C=O}\}$), 1600 ($\nu_a\{\text{OAc}\}$), 1536 ($\nu\{\text{C-N}\}$, $\delta\{\text{CNH}\}$), 1458 ($\nu\{\text{C-(CH}_3)_3\}$), 1406 ($\nu_s\{\text{OAc}\}$), 1277 ($\nu\{\text{C-N}\}$), 841 ($\nu\{\text{P-F}\}$), 650 ($\delta\{\text{py-H}\}$), 557 ($\delta\{\text{F-P-F}\}$) cm^{-1} .

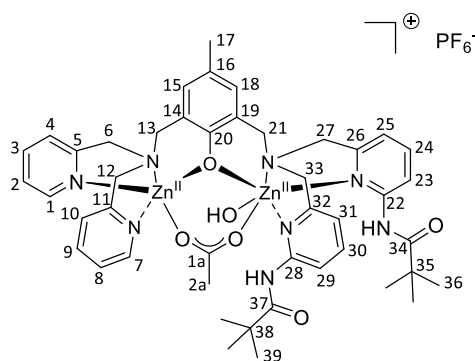
Elemental analysis: *Calcd.* for $\text{C}_{47}\text{H}_{57}\text{N}_8\text{O}_7\text{PF}_6\text{Zn}_2$: C 50.32%; H 5.12%; N 9.99%

Found: C 50.09%; H 5.26%; N 9.96%.

11.9.4 SYNTHESIS OF $[\text{Zn}^{\text{II}}_2(\text{H}_2\text{SIM}^1)(\mu\text{-OAc})(\text{OH})]\text{PF}_6$



Yield: 23.2 mg (16%).



CCDC no.: 998887

HRMS (ESI^+ , CH_3CN): m/z = 429.1298 ($[\text{C}_{43}\text{H}_{50}\text{N}_8\text{O}_3\text{Zn}_2]^+$, *calcd.* 429.1268); 877.2596 ($[\text{C}_{43}\text{H}_{50}\text{N}_8\text{O}_3\text{Zn}_2\text{F}]^+$, *calcd.* 877.2525).

$^1\text{H NMR}$ (500.13 MHz, CD_3CN): δ = 0.85 (s, 9H, H_{36}/H_{39}), 1.35 (s, 9H, H_{36}/H_{39}), 1.99 (s, 3H, H_{17}), 2.03 (s, 3H, H_{2a}), 3.36 (d, 2J = 11.74 Hz, 1H, H_{13}), 3.40 (d, 2J = 11.74 Hz, 1H, H_{21}), 3.56 (d,

$^2J = 15.77$ Hz, 1H, H_{27}), 3.67 (d, $^2J = 15.41$ Hz, 1H, H_{27}), 3.78 (d, $^2J = 16.87$ Hz, 1H, H_{12}), 3.84 (d, $^2J = 17.24$ Hz, 1H, H_{12}), 3.92 (d, $^2J = 14.31$ Hz, 1H, H_{33}), 4.03 (d, $^2J = 11.37$ Hz, 1H, H_{13}), 4.12-4.21 (m, 2H, H_6 , H_{21}), 4.28 (d, $^2J = 17.97$ Hz, 1H, H_6), 4.38 (d, $^2J = 14.31$ Hz, 1H, H_{33}), 6.29 (d, $^3J = 7.34$ Hz, 1H, H_{25}), 6.61 (d, $^4J = 1.83$ Hz, 1H, H_{15}), 6.64 (d, $^4J = 1.83$ Hz, 1H, H_{18}), 7.10 (d, $^3J = 7.70$ Hz, 1H, H_{31}), 7.14 (d, $^3J = 7.70$ Hz, 1H, H_{10}), 7.25 (dd, $^3J = 8.44$ Hz, $^3J = 7.70$ Hz, 1H, H_{24}), 7.36 (dd, $^3J = 6.20$ Hz, 1H, H_8), 7.53 (d, $^3J = 8.07$ Hz, 1H, H_4), 7.60 (dd, $^3J = 7.59$ Hz, $^3J = 6.20$ Hz, 1H, H_2), 7.80 (td, $^3J = 7.79$ Hz, $^4J = 1.65$ Hz, 1H, H_9), 7.81-7.87 (m, 2H, H_{23} , H_{30}), 8.08 (td, $^3J = 7.79$ Hz, $^4J = 1.65$ Hz, 1H, H_3), 8.33 (d, $^3J = 8.44$ Hz, 1H, H_{29}), 8.59 (d, $^3J = 4.77$ Hz, 1H, H_7), 8.80 (d, $^3J = 5.14$ Hz, 1H, H_1) ppm.

$^{13}\text{C NMR}$ (125.76 MHz, CD_3CN): $\delta = 20.2$ (C17), 27.8 (C16/C39), 27.9 (C16/C39), 40.5 (C35/C38), 41.2 (C35/C38), 57.7 (C12), 58.9 (C13), 59.9 (C27), 61.3 (C33), 61.4 (C6), 61.7 (C21), 114.6 (C23), 115.7 (C29), 117.7 (C25), 119.2 (C31), 124.7 (C10/C14), 124.7 (C10/C14), 125.0 (C4), 125.3 (C8/C19), 125.3 (C8/C19), 126.1 (C2), 127.4 (C16), 133.2 (C18), 133.4 (C15), 139.9 (C24), 141.4 (C30), 141.7 (C9), 142.6 (C3), 149.1 (C7), 149.8 (C1), 153.4 (C22/C28), 153.7 (C26), 154.3 (C32), 155.1 (C22/C28), 156.6 (C5), 157.1 (C11), 160.0 (C20), 179.60 (C34/C37), 179.6 (C34/C37), 180.7 (C1a) ppm.

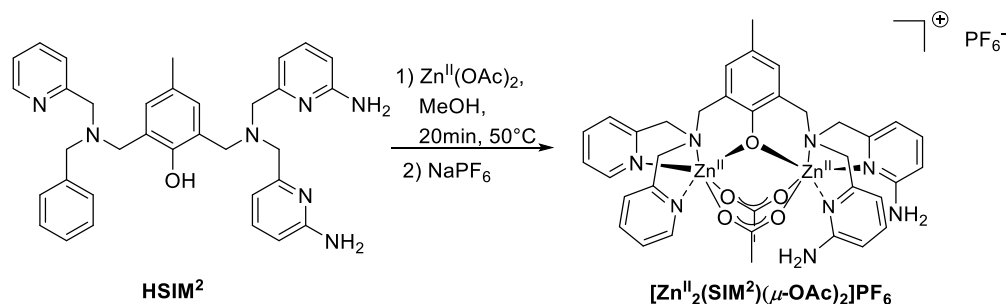
$^{31}\text{P NMR}$ (100.61 MHz, CD_3CN): $\delta = -144.3$ (sep, PF_6^-) ppm.

FT-IR spectroscopy: $\nu = 2982$ ($\nu\{\text{C-H}\}$), 2937 ($\nu\{\text{C-H}\}$), 2876 ($\nu\{\text{C-H}\}$), 1687 ($\nu\{\text{C=O}\}$), 1581 ($\nu_a\{\text{OAc}\}$), 1545 ($\nu\{\text{C-N}\}$, $\delta\{\text{CNH}\}$), 1461 ($\nu\{\text{C-(CH}_3)_3\}$), 1442 ($\nu_s\{\text{OAc}\}$), 1306 ($\nu\{\text{C-N}\}$), 834 ($\nu\{\text{P-F}\}$), 650 ($\delta\{\text{py-H}\}$), 556 ($\delta\{\text{F-P-F}\}$) cm^{-1} .

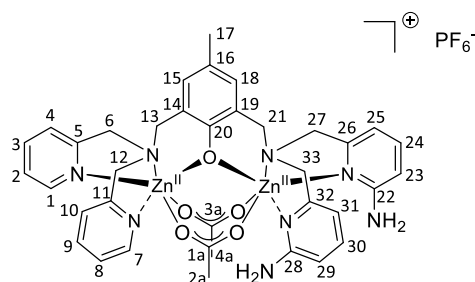
Elemental analysis: *Calcd.* for $\text{C}_{45}\text{H}_{55}\text{N}_8\text{O}_6\text{PF}_6\text{Zn}_2$: C 50.06%; H 5.13%; N 10.38%

Found: C 50.46%; H 5.38%; N 10.57%.

11.9.5 SYNTHESIS OF $[\text{Zn}^{\text{II}}_2(\text{SIM}^2)(\mu\text{-OAc})_2]\text{PF}_6$



Yield: 47.5 mg (50%).



CCDC no.: 998890

HRMS (ESI⁺, CH₃CN): $m/z = 344.0747$ ([C₃₃H₃₄N₈OZn₂]²⁺, calcd. 344.0698); 749.1529 ([C₃₃H₃₄N₈OZn₂CH₃COO]⁺, calcd. 749.1524).

¹H NMR (500.13 MHz, CD₃CN): $\delta = 1.85$ (s, 3H, H_{2a}/H_{4a}), 1.94 (s, 3H, H₁₇), 2.05 (s, 3H, H_{2a}/H_{4a}), 3.02 (d, ²J = 11.37 Hz, 1H, H₁₃/H₂₁), 3.17 (d, ²J = 15.77 Hz, 1H, H₃₃), 3.24 (d, ²J = 15.77 Hz, 1H, H₃₃), 3.28 (d, ²J = 10.64 Hz, 1H, H₁₃/H₂₁), 3.35 (d, ²J = 16.51 Hz, 1H, H₁₂), 3.50 (d, ²J = 16.51 Hz, 1H, H₁₂), 3.57 (d, ²J = 13.94 Hz, 1H, H₂₇), 3.80 (d, ²J = 11.37 Hz, 1H, H₁₃/H₂₁), 4.03 (d, ²J = 14.67 Hz, 1H, H₆), 4.33 (d, ²J = 10.64 Hz, 1H, H₁₃/H₂₁), 4.40 (dd, ²J = 14.12 Hz, ²J = 10.09 Hz, 2H, H₆, H₂₇), 5.58 (d, ³J = 7.34 Hz, 1H, H₃₁), 5.78 (bs, 2H, NH₂), 6.05 (d, ³J = 8.10 Hz, 1H, H₂₉), 6.29 (d, ⁴J = 1.83 Hz, 1H, H₁₅/H₁₈), 6.45-6.53 (m, 3H, H₁₀, H₁₅/H₁₈, H₂₃), 6.55 (d, ³J = 7.34 Hz, 1H, H₂₅), 6.67 (bs, 2H, NH₂), 6.88 (dd, ³J = 8.44 Hz, ³J = 7.34 Hz, 1H, H₃₀), 6.98-7.03 (m, 1H, H₈), 7.33 (td, ³J = 7.61 Hz, ⁴J = 1.65 Hz, 1H, H₉), 7.41-7.50 (m, 3H, H₂, H₄, H₂₄), 7.93 (td, ³J = 7.79 Hz, ⁴J = 1.65 Hz, 1H, H₃), 8.28 (m, 1H, H₇), 8.72 (m, 1H, H₁) ppm.

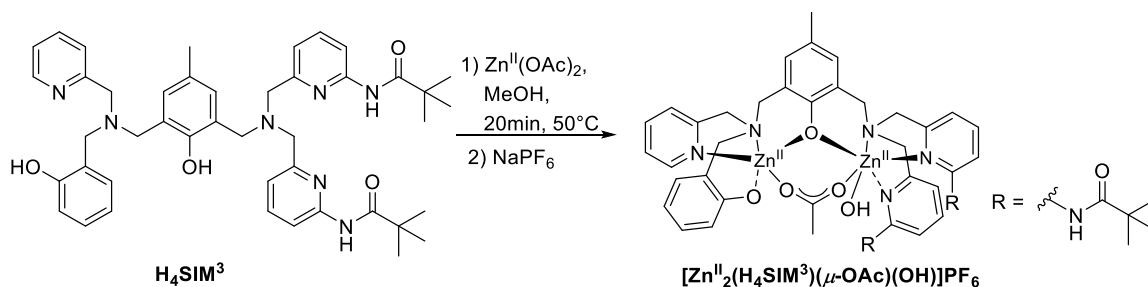
¹³C NMR (100.62 MHz, CD₃CN): $\delta = 20.2$ (C₁₇), 25.0 (C_{2a}/C_{4a}), 25.9 (C_{2a}/C_{4a}), 58.7 (C₁₂), 58.7 (C₃₃), 60.4 (C₁₃/C₂₁), 60.7 (C₆), 60.8 (C₂₇), 61.0 (C₁₃/C₂₁), 108.7 (C₂₉), 110.5 (C₃₁), 110.8 (C₂₃/C₂₅), 112.7 (C₂₃/C₂₅), 122.0 (C₁₀), 123.6 (C₈), 124.4 (C₁₉/C₁₄), 124.9 (C₂/C₁₉/C₁₄), 125.0 (C₂/C₁₉/C₁₄), 125.2 (C₄/C₁₆), 125.3 (C₄/C₁₆), 131.6 (C₁₅/C₁₈), 131.7 (C₁₅/C₁₈), 138.9 (C₉), 139.2 (C₃₀), 140.3 (C₃), 140.6 (C₂₄), 147.1 (C₇), 148.5 (C₁), 153.9 (C₂₆/C₃₂), 153.9 (C₂₆/C₃₂), 156.1 (C₅/C₁₁), 156.1 (C₅/C₁₁), 160.0 (C₂₈), 160.4 (C₂₂), 160.51 (C₂₀), 179.1 (C_{1a}/C_{3a}), 179.3 (C_{1a}/C_{3a}) ppm.

³¹P NMR (100.61 MHz, CD₃CN): $\delta = -144.3$ (sep, PF₆⁻) ppm.

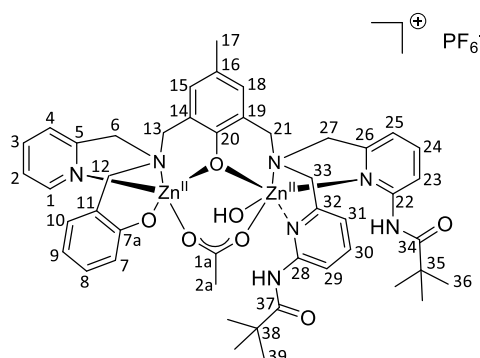
FT-IR spectroscopy: $\nu = 3484$ (ν {N-H}), 3332 (ν {N-H}), 3218 (ν {N-H}), 2984 (ν {C-H}), 2935 (ν {C-H}), 2906 (ν {C-H}), 1643 (δ {CNH}), 1606 (ν_a {OAc}), 1476 (ν_s {OAc}), 1275 (ν {C-N}), 827 (ν {P-F}), 658 (δ {py-H}), 557 (δ {F-P-F}) cm⁻¹.

Elemental analysis: Calcd. for C₃₇H₄₁N₈O₅PF₆Zn₂: C 46.61%; H 4.33%; N 11.75%

Found: C 46.42%; H 4.34%; N 11.74%.

11.9.6 SYNTHESIS OF $[\text{Zn}_2(\text{H}_2\text{SIM}^3)(\mu\text{-OAc})(\text{OH})]$ 

Yield: 85.7 mg (67%).



CCDC no.: 1009842

HRMS (ESI⁺, CH₃CN): $m/z = 434.6237$ [$\text{C}_{44}\text{H}_{51}\text{N}_7\text{O}_4\text{Zn}_2$]²⁺, *calcd.* 434.6287).

¹H NMR (500.13 MHz, CD₃CN (0.4 vol% HClO₄)): $\delta = 1.35$ (s, 18H, H₃₆, H₃₉), 1.95 (s, 3H, H_{2a}), 2.29 (s, 3H, H₁₇), 3.82 (d, ²J = 16.51 Hz, 2H, H₂₇, H₃₃), 3.96 (s, 2H, H₂₁), 4.11 (d, ²J = 16.14 Hz, 2H, H₂₇, H₃₃), 4.40 (s, 2H, H₆, H₁₂), 4.41 (s, 2H, H₆, H₁₂), 4.43 (s, 2H, H₁₃), 6.87 (d, ³J = 8.07 Hz, 1H, H₇), 6.92 (t, ³J = 7.34 Hz, 1H, H₉), 7.20–7.39 (m, 9H, H₄, H₈, H₁₀, H₁₅, H₁₈, H₂₃, H₂₅, H₂₉, H₃₁), 7.39 (dd, ³J = 6.97 Hz, ³J = 5.50 Hz, 1H, H₂), 7.82 (t, ³J = 7.70 Hz, 1H, H₃), 8.02 (t, ³J = 7.89 Hz, 2H, H₂₄, H₃₀), 8.48 (d, ³J = 4.40 Hz, 1H, H₁), 9.26 (s, 2H, NH) ppm.

¹³C NMR (125.76 MHz, CD₃CN (0.4 vol% HClO₄)): $\delta = 20.5$ (C₁₇), 20.7 (C_{2a}), 27.4 (C₃₆), 41.9 (C₃₅), 52.0 (C₂₁), 55.6 (C₂₇), 56.7 (C₆, C₁₂/C₁₃), 56.8 (C₆, C₁₂/C₁₃), 116.4 (C₂₃), 116.5 (C₇), 117.5 (C_{7a}), 121.8 (C₁₀), 121.9 (C₂₅), 125.3 (C₄), 125.5 (C₂), 132.2 (C₁₆), 132.7 (C₈/C₉), 133.2 (C₈/C₉), 135.2 (C₁₅/C₁₈), 137.1 (C₁₅/C₁₈), 139.9 (C₃), 143.5 (C₂₄), 149.4 (C₁), 153.4 (C₂₆), 153.8 (C₁₄/C₁₉), 156.4 (C₅/C₁₁), 180.8 (C_{1a}) ppm.

FT-IR spectroscopy: $\nu = 2978$ (ν(C-H)), 2932 (ν(C-H)), 2867 (ν(C-H)), 1681 (ν(C=O)), 1581 (ν_a(OAc)), 1453 (ν(C-(CH₃)₃)), 1433 (ν_s(OAc)), 1305 (ν(C-N)), 770 (δ(py-H)) cm⁻¹.

Elemental analysis: *Calcd.* for C₄₆H₅₅N₇O₇Zn₂: C 58.24%; H 5.84%; N 10.33%

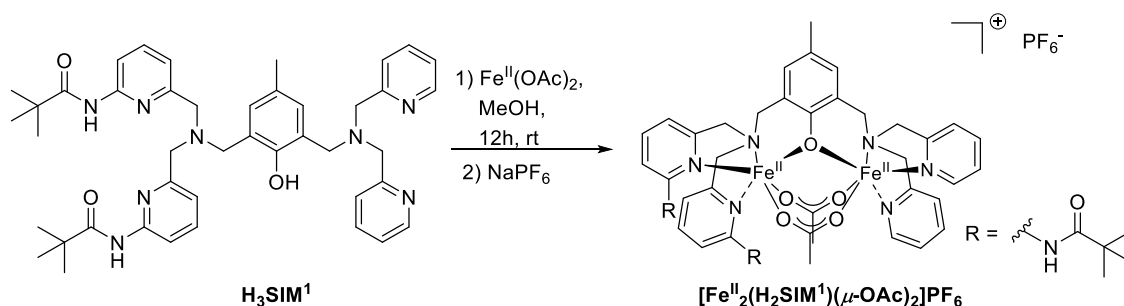
Found: C 58.02%; H 5.57%; N 10.19%.

11.10 SYNTHESIS OF DIIRON(II) COMPLEXES

11.10.1 GENERAL PROCEDURE

The ligand (68.6 μmol , 1.0 eq) was dissolved under inert atmosphere in anhydrous, degassed methanol (2.5 ml). The solution was treated with iron(II) acetate (137 μmol , 2.0 eq) and stirred at room temperature overnight. Sodium hexafluorophosphate (140 μmol , 2.0 eq) was added and the mixture stirred for ten minutes before filtration through a syringe filter. Crystallization from the filtrate was achieved with diffusion of diethyl ether, whereby yellow crystals were obtained, which were collected by filtration.

11.10.2 SYNTHESIS OF $[\text{Fe}^{\text{II}}_2(\text{H}_2\text{SIM}^1)(\mu\text{-OAc})_2]\text{PF}_6$



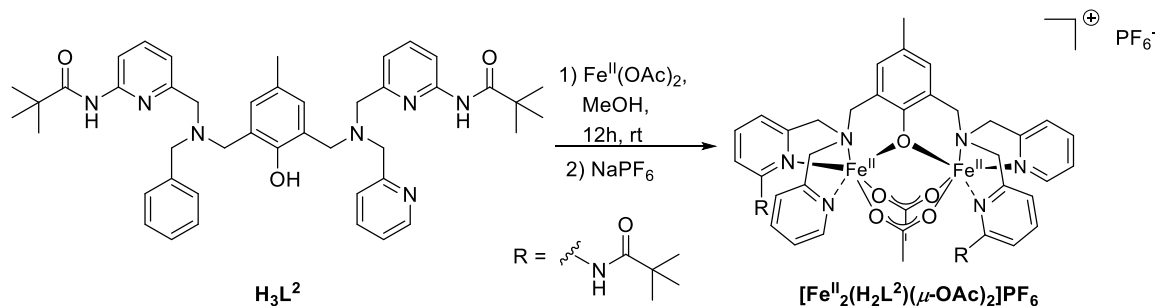
Yield: 37.0 mg (49%).

HRMS (ESI⁺, CH₂Cl₂): $m/z = 957.3087$ ($[\text{C}_{47}\text{H}_{57}\text{N}_8\text{O}_7\text{Fe}_2]^+$, *calcd.* 957.3046).

¹H NMR (500.13 MHz, CD₃CN): $\delta = -31.71$ (bs, 1H), -17.11 (bs, 1H), -12.52 (bs, 1H), -5.86 (bs, 1H), -1.20 (s, 1H), 3.86 (s, 9H), 4.08 (s, 9H), 7.49 (s, 1H), 9.48 (s, 1H), 9.67 (s, 1H), 12.52 (s, 1H), 17.21 (bs, 1H), 22.61 (s, 1H), 27.49 (s, 1H), 32.89 (s, 1H), 36.04 (s, 1H), 36.11 (s, 4H), 41.10 (s, 3H), 41.55 (s, 1H), 46.06 (s, 1H), 50.39 (s, 2H), 52.42 (s, 1H), 57.01 (s, 3H), 67.36 (s, 1H), 69.39 (s, 1H), 73.79 (s, 1H), 77.16 (s, 1H), 93.51 (s, 1H), 120.21 (bs, 1H), 148.20 (bs, 1H), 166.91 (s, 1H), 189.14 (s, 1H) ppm.

Elemental analysis: *Calcd.* for C₄₇H₅₇N₈O₇Fe₂PF₆: C 51.20%; H 5.21%; N 10.16%

Found: C 51.17%; H 5.30%; N 10.05%.

11.10.3 SYNTHESIS OF $[\text{Fe}^{\text{II}}_2(\text{H}_2\text{L}^2)(\mu\text{-OAc})_2]\text{PF}_6$ 

Yield: 48.2 mg (63%).

HRMS (ESI⁺, CH₂Cl₂): $m/z = 957.3074$ ($[\text{C}_{47}\text{H}_{57}\text{N}_8\text{O}_7\text{Fe}_2]^+$, *calcd.* 957.3046).

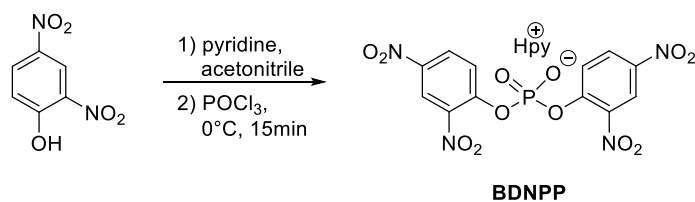
¹H NMR (500.13 MHz, CD₃CN): $\delta = 2.12$ (s, 2H), 5.40 (s, 18H), 5.68 (s, 2H), 5.76 (s, 2H), 10.70 (bs, 2H), 13.00 (bs, 2H), 17.06 (s, 2H), 26.15 (s, 2H), 29.54 (s, 3H), 41.15 (s, 3H), 41.37 (s, 5H), 45.70 (bs, 2H), 55.14 (s, 2H), 57.07 (s, 2H), 80.81 (bs, 2H), 107.33 (bs, 2H), 157.62 (bs, 2H), 188.50 (s, 2H) ppm.

Elemental analysis: *Calcd.* for $\text{C}_{47}\text{H}_{57}\text{N}_8\text{O}_7\text{Fe}_2\text{PF}_6$: C 51.20%; H 5.21%; N 10.16%

Found: C 51.28%; H 5.46%; N 10.20%.

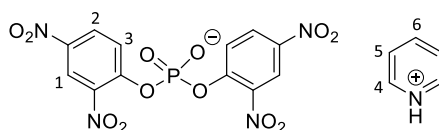
11.11 SYNTHESIS OF PHOSPHOESTER SUBSTRATES

11.11.1 SYNTHESIS OF BDNPP



BDNPP was synthesized following published procedures with minor modifications.³¹²

Dried 2,6-dinitrophenol (4.15 g, 22.5 mmol, 2.8 eq) was dissolved in anhydrous acetonitrile (45 ml) and anhydrous pyridine (3.60 ml, 3.68 g, 46.5 mmol, 5.7 eq) was added. The solution was cooled to 0°C with an ice-water bath and freshly distilled phosphoryl chloride (0.75 ml, 1.24 g, 8.1 mmol, 1.0 eq) was added dropwise. After stirring for 15 minutes the mixture was poured onto an ice-water mixture (400 ml) and the mixture was kept in the fridge overnight. The resulting precipitate was filtered and washed with a small amount of cold water. The crude product was recrystallized three times from hot acetone yielding BDNPP pyridinium salt as a white powder (2.81 g, 69%).



Molecular Formula: C₁₇H₁₂N₅O₁₂P

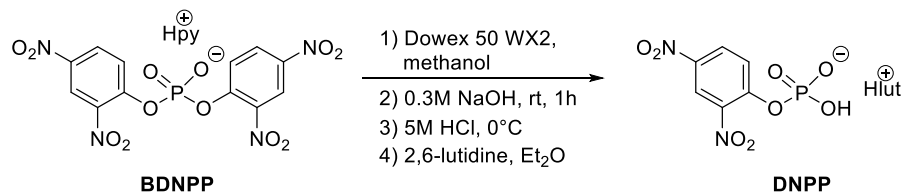
¹H NMR (399.89 MHz, CD₃COCD₃): δ = 8.12 (d, ³J = 9.25 Hz, 2H, H3), 8.25 (bs, 2H, H5), 8.50 (dd, ³J = 9.25 Hz, ⁴J = 3.13 Hz, 2H, H2), 8.71 (d, ⁴J = 2.78 Hz, 2H, H1), 8.77 (t, ³J = 7.65 Hz, 1H, H6), 9.03 (bs, 2H, H4) ppm.

³¹P NMR (161.88 MHz, CD₃COCD₃): δ = -14.2 ppm.

Elemental analysis: *Calcd.* for C₁₇H₁₂N₅O₁₂P: C 40.09%; H 2.37%; N 13.75%

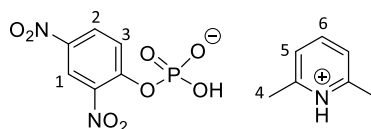
Found: C 40.06%; H 2.29%; N 13.65%.

11.11.2 SYNTHESIS OF DNPP



DNPP was synthesized following a published procedure.³¹³

BDNPP pyridinium salt (1.28 g, 2.83 mmol, 1.0 eq) dissolved in methanol (700 ml) was passed through a Dowex 50 WX2 ion exchange column (sodium form). The solvent was removed in vacuum ($T < 40^{\circ}\text{C}$) and the successful exchange of the pyridinium ion for sodium ion was controlled via ^1H NMR spectroscopy. BDNPP sodium salt was treated with 0.3M sodium hydroxide solution (50 ml) at room temperature for one hour. Then the solution was made strongly acidic by addition of 5M hydrochloric acid (~ 15 ml) and the resulting precipitate was removed by filtration. The filtrate was concentrated and the residue was taken up in diethyl ether (50 ml). The colorless solution was filtered and 2,6-lutidine (0.33 ml, 0.30 g, 2.83 mmol, 1.0 eq) was added dropwise while stirring until the solution turned slightly yellow. Filtration of the obtained precipitate and recrystallization from hot ethanol gave DNPP lutidinium salt as yellowish needles (0.16 g, 15%).



^1H NMR (400.13 MHz, CD_3CN): δ = 2.66 (s, 6H, H_4), 7.47 (d, $^3J = 7.92$ Hz, 2H, H_5), 7.93 (dd, $^3J = 9.39$ Hz, $^5J = 0.88$ Hz, 1H, H_3), 8.11 (t, $^3J = 7.92$ Hz, 1H, H_6), 8.32 (dd, $^3J = 9.24$ Hz, $^4J = 2.79$ Hz, 1H, H_2), 8.57 (dd, $^4J = 2.93$ Hz, $^5J = 0.88$ Hz, 1H, H_1) ppm.

^{31}P NMR (161.98 MHz, CD_3CN): δ = -5.0 ppm.

Elemental analysis: *Calcd.* for $\text{C}_{13}\text{H}_{14}\text{N}_3\text{O}_8\text{P}$: C 42.06%; H 3.80%; N 11.32%

Found: C 41.92%; H 3.81%; N 11.34%.

BIBLIOGRAPHY

1. Gass, M.; Dawson-Hughes, B., *Am. J. Med.* **2006**, *119*, 3-11.
2. O'Neill, S.; MacLennan, A.; Bass, S.; Diamond, T.; Ebeling, P.; Findlay, D.; Flicker, L.; Markwell, A.; Nowson, C.; Pocock, N.; Sambrook, P.; Singh, M. F., *Aust. Fam. Physician* **2004**, *33*, 910-919.
3. Sambrook, P.; Olver, I.; Goss, A., *Aust. Fam. Physician* **2006**, *35*, 801-803.
4. Halleen, J. M.; Alatalo, S. L.; Suominen, H.; Cheng, S.; Janckila, A. J.; Väänänen, H. K., *J. Bone Miner. Res.* **2000**, *15*, 1337-1345.
5. Moss, D. W.; Raymond, F. D.; Wile, D. B., *Crit. Rev. Clin. Lab. Sci.* **1995**, *32*, 431-467.
6. Hayman, A. R.; Jones, S. J.; Boyde, A.; Foster, D.; Colledge, W. H.; Carlton, M. B.; Evans, M. J.; Cox, T. M., *Development* **1996**, *122*, 3151-3162.
7. Angel, N. Z.; Walsh, N.; Forwood, M. R.; Ostrowski, M. C.; Cassady, A. I.; Hume, D. A., *J. Bone Miner. Res.* **2000**, *15*, 103-110.
8. Vääräniemi, J.; Halleen, J. M.; Kaarlonen, K.; Ylipahkala, H.; Alatalo, S. L.; Andersson, G.; Kaija, H.; Vihko, P.; Väänänen, H. K., *J. Bone Miner. Res.* **2004**, *19*, 1432-1440.
9. Oddie, G. W.; Schenk, G.; Angel, N. Z.; Walsh, N.; Guddat, L. W.; de Jersey, J.; Cassady, A. I.; Hamilton, S. E.; Hume, D. A., *Bone* **2000**, *27*, 575-584.
10. Valizadeh, M.; Schenk, G.; Nash, K.; Oddie, G. W.; Guddat, L. W.; Hume, D. A.; de Jersey, J.; Burke, T. R.; Hamilton, S., *Arch. Biochem. Biophys.* **2004**, *424*, 154-162.
11. Desbouis, D.; Troitsky, I. P.; Belousoff, M. J.; Spiccia, L.; Graham, B., *Coord. Chem. Rev.* **2012**, *256*, 897-937.
12. Schroeder, G. K.; Lad, C.; Wyman, P.; Williams, N. H.; Wolfenden, R., *Proc. Natl. Acad. Sci. USA* **2006**, *103*, 4052-4055.
13. Cozzone, A. J., *Annu. Rev. Microbiol.* **1988**, *42*, 97-125.
14. Chang, C.; Stewart, R. C., *Plant Physiol.* **1998**, *117*, 723-731.
15. Mildvan, A. S., *Proteins: Struct., Funct., Genet.* **1997**, *29*, 401-416.
16. Shenoy, A. R.; Sreenath, N.; Podobnik, M.; Kovacevic, M.; Visweswariah, S. S., *Biochemistry* **2005**, *44*, 15695-15704.
17. Shenoy, A. R.; Capuder, M.; Draskovic, P.; Lamba, D.; Visweswariah, S. S.; Podobnik, M., *J. Mol. Biol.* **2007**, *365*, 211-225.
18. Ghanem, E.; Li, Y.; Xu, C.; Raushel, F. M., *Biochemistry* **2007**, *46*, 9032-9040.
19. Jackson, C. J.; Carr, P. D.; Kim, H. K.; Liu, J. W.; Ollis, D. L., *Acta Cryst. F* **2006**, *62*, 659-661.
20. Jackson, C. J.; Carr, P. D.; Liu, J. W.; Watt, S. J.; Beck, J. L.; Ollis, D. L., *J. Mol. Biol.* **2007**, *367*, 1047-1062.
21. Mitic, N.; Smith, S. J.; Neves, A.; Guddat, L. W.; Gahan, L. R.; Schenk, G., *Chem. Rev.* **2006**, *106*, 3338-3363.
22. Schenk, G.; Mitic, N.; Gahan, L.; Smith, S.; Hadler, K., *Eurobic 9: Proceedings of the 9th European Biological Inorganic Chemistry Conference* **2008**, 29-38.
23. Durmus, A.; Eicken, C.; Sift, B. H.; Kratel, A.; Kappl, R.; Hüttermann, J.; Krebs, B., *Eur. J. Biochem.* **1999**, *260*, 709-716.
24. Schenk, G.; Ge, Y.; Carrington, L. E.; Wynne, C. J.; Searle, I. R.; Carroll, B. J.; Hamilton, S.; de Jersey, J., *Arch. Biochem. Biophys.* **1999**, *370*, 183-189.
25. Schenk, G.; Elliott, T. W.; Leung, E.; Carrington, L. E.; Mitic, N.; Gahan, L. R.; Guddat, L. W., *BMC Struct. Biol.* **2008**, *8*:6.
26. Guddat, L. W.; McAlpine, A. S.; Hume, D.; Hamilton, S.; de Jersey, J.; Martin, J. L., *Structure* **1999**, *7*, 757-767.

27. Sträter, N.; Jasper, B.; Scholte, M.; Krebs, B.; Duff, A. P.; Langley, D. B.; Han, R.; Averill, B. A.; Freeman, H. C.; Guss, J. M., *J. Mol. Biol.* **2005**, *351*, 233-246.
28. Daumann, L. J.; Schenk, G.; Ollis, D. L.; Gahan, L. R., *Dalton Trans.* **2014**, *43*, 910-928.
29. Schenk, G.; Mitić, N.; Hanson, G. R.; Comba, P., *Coord. Chem. Rev.* **2013**, *257*, 473-482.
30. Coleman, J. E., *Annu. Rev. Biochem.* **1992**, *61*, 897-946.
31. Millan, J. L., *Purinergic Signal.* **2006**, *2*, 335-341.
32. Millán, J. L., *Mammalian alkaline phosphatases: from biology to applications in medicine and biotechnology*, WILEY-VCH: Weinheim, **2006**.
33. Narisawa, S.; Huang, L.; Iwasaki, A.; Hasegawa, H.; Alpers, D. H.; Millan, J. L., *Mol. Cell. Biol.* **2003**, *23*, 7525-7530.
34. Narisawa, S.; Hoylaerts, M. F.; Doctor, K. S.; Fukuda, M. N.; Alpers, D. H.; Millan, J. L., *Am. J. Physiol.* **2007**, *293*, G1068-G1077.
35. Akiba, Y.; Mizumori, M.; Guth, P. H.; Engel, E.; Kaunitz, J. D., *Am. J. Physiol.* **2007**, *293*, G1223-G1233.
36. Mizumori, M.; Ham, M.; Guth, P. H.; Engel, E.; Kaunitz, J. D.; Akiba, Y., *J. Physiol.* **2009**, *587*, 3651-3663.
37. Poelstra, K.; Bakker, W. W.; Klok, P. A.; Hardonk, M. J.; Meijer, D. K. F., *Lab. Invest.* **1997**, *76*, 319-327.
38. Poelstra, K.; Bakker, W. W.; Klok, P. A.; Kamps, J. A.; Hardonk, M. J.; Meijer, D. K., *Am. J. Pathol.* **1997**, *151*, 1163-1169.
39. Goldberg, R. F.; Austen, W. G., Jr.; Zhang, X.; Munene, G.; Mostafa, G.; Biswas, S.; McCormack, M.; Eberlin, K. R.; Nguyen, J. T.; Tatlidede, H. S.; Warren, H. S.; Narisawa, S.; Millan, J. L.; Hodin, R. A., *Proc. Natl. Acad. Sci. USA* **2008**, *105*, 3551-3556.
40. Lalles, J.-P., *Nutr. Rev.* **2010**, *68*, 323-332.
41. Minkin, C., *Calcif. Tissue Int.* **1982**, *34*, 285-290.
42. Efstratiadis, T.; Moss, D. W., *Enzyme* **1985**, *34*, 140-143.
43. Hayman, A. R.; Bune, A. J.; Bradley, J. R.; Rashbass, J.; Cox, T. M., *J. Histochem. Cytochem.* **2000**, *48*, 219-227.
44. Nuttleman, P. R.; Roberts, R. M., *J. Biol. Chem.* **1990**, *265*, 12192-12199.
45. Kaija, H.; Alatalo, S. L.; Halleen, J. M.; Lindqvist, Y.; Schneider, G.; Kalervo Väänänen, H.; Vihko, P., *Biochem. Biophys. Res. Commun.* **2002**, *292*, 128-132.
46. Ek-Rylander, B.; Flores, M.; Wendel, M.; Heinegaard, D.; Andersson, G., *J. Biol. Chem.* **1994**, *269*, 14853-14856.
47. Raeisaenen, S. R.; Alatalo, S. L.; Ylipahkala, H.; Halleen, J. M.; Cassady, A. I.; Hume, D. A.; Vaeaenaenen, H. K., *Biochem. Biophys. Res. Commun.* **2005**, *331*, 120-126.
48. Mitic, N.; Valizadeh, M.; Leung, E. W. W.; de Jersey, J.; Hamilton, S.; Hume, D. A.; Cassady, A. I.; Schenk, G., *Arch. Biochem. Biophys.* **2005**, *439*, 154-164.
49. Schenk, G.; Guddat, L. W.; Ge, Y.; Carrington, L. E.; Hume, D. A.; Hamilton, S.; de Jersey, J., *Gene* **2000**, *250*, 117-125.
50. Bozzo, G. G.; Raghothama, K. G.; Plaxton, W. C., *Eur. J. Biochem.* **2002**, *269*, 6278-6286.
51. Bozzo, G. G.; Raghothama, K. G.; Plaxton, W. C., *Biochem. J.* **2004**, *377*, 419-428.
52. Bozzo, G. G.; Dunn, E. L.; Plaxton, W. C., *Plant Cell Environ.* **2006**, *29*, 303-313.
53. Zimmermann, P.; Regierer, B.; Kossmann, J.; Frossard, E.; Amrhein, N.; Bucher, M., *Plant Biol.* **2004**, *6*, 519-528.
54. Del Pozo, J. C.; Allona, I.; Rubio, V.; Leyva, A.; De la Pena, A.; Aragoncillo, C.; Paz-Ares, J., *Plant J.* **1999**, *19*, 579-589.
55. Li, D.; Zhu, H.; Liu, K.; Liu, X.; Leggewie, G.; Udvardi, M.; Wang, D., *J. Biol. Chem.* **2002**, *277*, 27772-27781.

56. Veljanovski, V.; Vanderbeld, B.; Knowles, V. L.; Snedden, W. A.; Plaxton, W. C., *Plant Physiol.* **2006**, *142*, 1282-1293.
57. Cashikar, A. G.; Kumaresan, R.; Rao, N. M., *Plant Physiol.* **1997**, *114*, 907-915.
58. Olczak, M.; Watorek, W., *Physiol. Plant.* **2003**, *118*, 491-498.
59. Duff, S. M. G.; Sarath, G.; Plaxton, W. C., *Physiol. Plant.* **1994**, *90*, 791-800.
60. Hegeman, C. E.; Grabau, E. A., *Plant Physiol.* **2001**, *126*, 1598-1608.
61. Wojtaszek, P.; Trethowan, J.; Bolwell, G. P., *FEBS Lett.* **1997**, *405*, 95-98.
62. Hayman, A. R.; Cox, T. M., *J. Biol. Chem.* **1994**, *269*, 1294-1300.
63. Sibille, J. C.; Doi, K.; Aisen, P., *J. Biol. Chem.* **1987**, *262*, 59-62.
64. Kim, E. E.; Wyckoff, H. W., *J. Mol. Biol.* **1991**, *218*, 449-464.
65. Weston, J., *Chem. Rev.* **2005**, *105*, 2151-2174.
66. Smith, S.; Casellato, A.; Hadler, K.; Mitić, N.; Riley, M.; Bortoluzzi, A.; Szpoganicz, B.; Schenk, G.; Neves, A.; Gahan, L., *J. Biol. Inorg. Chem.* **2007**, *12*, 1207-1220.
67. Schenk, G.; Boutchard, C. L.; Carrington, L. E.; Noble, C. J.; Moubaraki, B.; Murray, K. S.; de Jersey, J.; Hanson, G. R.; Hamilton, S., *J. Biol. Chem.* **2001**, *276*, 19084-19088.
68. Beck, J. L.; McConachie, L. A.; Summors, A. C.; Arnold, W. N.; De Jersey, J.; Zerner, B., *Biochim. Biophys. Acta, Protein Struct. Mol. Enzymol.* **1986**, *869*, 61-68.
69. Yang, Y.-S.; McCormick, J. M.; Solomon, E. I., *J. Am. Chem. Soc.* **1997**, *119*, 11832-11842.
70. Coleman, F.; Hynes, M. J.; Erxleben, A., *Inorg. Chem.* **2010**, *49*, 6725-6733.
71. Butler-Ransohoff, J. E.; Kendall, D. A.; Kaiser, E. T., *Proc. Natl. Acad. Sci. USA* **1988**, *85*, 4276-4278.
72. Chaidaroglou, A.; Brezinski, D. J.; Middleton, S. A.; Kantrowitz, E. R., *Biochemistry* **1988**, *27*, 8338-8343.
73. O'Brien, P. J.; Herschlag, D., *Biochemistry* **2001**, *40*, 5691-5699.
74. Funhoff, E. G.; Wang, Y.; Andersson, G.; Averill, B. A., *FEBS Journal* **2005**, *272*, 2968-2977.
75. Zhao, M.; Wang, H.-B.; Ji, L.-N.; Mao, Z.-W., *Chem. Soc. Rev.* **2013**, *42*, 8360-8375.
76. Youngme, S.; Chaichit, N.; Kongsaree, P.; van Albada, G. A.; Reedijk, J., *Inorg. Chim. Acta* **2001**, *324*, 232-240.
77. Daumann, L. J., *PhD Thesis: Spectroscopic and Mechanistic Studies of Dinuclear Metallohydrolases and their Biomimetic Complexes*, The University of Queensland, Brisbane, **2013**.
78. Holm, R. H.; Kennepohl, P.; Solomon, E. I., *Chem. Rev.* **1996**, *96*, 2239-2314.
79. Twitchett, M. B.; Geoffrey Sykes, A., *Eur. J. Inorg. Chem.* **1999**, *1999*, 2105-2115.
80. Wilcox, D. E., *Chem. Rev.* **1996**, *96*, 2435-2458.
81. Gahan, L. R.; Smith, S. J.; Neves, A.; Schenk, G., *Eur. J. Inorg. Chem.* **2009**, *2009*, 2745-2758.
82. Mitic, N.; Hadler, K. S.; Gahan, L. R.; Hengge, A. C.; Schenk, G., *J. Am. Chem. Soc.* **2010**, *132*, 7049-7054.
83. Klabunde, T.; Sträter, N.; Fröhlich, R.; Witzel, H.; Krebs, B., *J. Mol. Biol.* **1996**, *259*, 737-748.
84. Straeter, N.; Lipscomb, W. N.; Klabunde, T.; Krebs, B., *Angew. Chem. Int. Ed.* **1996**, *35*, 2025-2055.
85. Schenk, G.; Gahan, L. R.; Carrington, L. E.; Mitic, N.; Valizadeh, M.; Hamilton, S. E.; de Jersey, J.; Guddat, L. W., *Proc. Natl. Acad. Sci. USA* **2005**, *102*, 273-278.
86. Molenveld, P.; Engbersen, J. F. J.; Reinhoudt, D. N., *Chem. Soc. Rev.* **2000**, *29*, 75-86.
87. Williams, N. H.; Takasaki, B.; Wall, M.; Chin, J., *Acc. Chem. Res.* **1999**, *32*, 485-493.
88. Iranzo, O.; Kovalevsky, A. Y.; Morrow, J. R.; Richard, J. P., *J. Am. Chem. Soc.* **2003**, *125*, 1988-1993.

89. Chin, J., *Curr. Opin. Chem. Biol.* **1997**, *1*, 514-521.
90. Neves, A.; Lanznaster, M.; Bortoluzzi, A. J.; Peralta, R. A.; Casellato, A.; Castellano, E. E.; Herrald, P.; Riley, M. J.; Schenk, G., *J. Am. Chem. Soc.* **2007**, *129*, 7486-7487.
91. Belle, C.; Pierre, J.-L., *Eur. J. Inorg. Chem.* **2003**, *2003*, 4137-4146.
92. Lanznaster, M.; Neves, A.; Bortoluzzi, A.; Aires, V.; Szpoganicz, B.; Terenzi, H.; Severino, P.; Fuller, J.; Drew, S.; Gahan, L.; Hanson, G.; Riley, M.; Schenk, G., *J. Biol. Inorg. Chem.* **2005**, *10*, 319-332.
93. Schepers, K.; Bremer, B.; Krebs, B.; Henkel, G.; Althaus, E.; Mosel, B.; Müller-Warmuth, W., *Angew. Chem. Int. Ed.* **1990**, *29*, 531-533.
94. Neves, A.; Aires de Brito, M.; Drago, V.; Griesar, K.; Haase, W., *Inorg. Chim. Acta* **1995**, *237*, 131-135.
95. Lanznaster, M.; Neves, A.; Bortoluzzi, A. J.; Szpoganicz, B.; Schwingel, E., *Inorg. Chem.* **2002**, *41*, 5641-5643.
96. Karsten, P.; Neves, A.; Bortoluzzi, A. J.; Lanznaster, M.; Drago, V., *Inorg. Chem.* **2002**, *41*, 4624-4626.
97. Than, R.; Feldmann, A. A.; Krebs, B., *Coord. Chem. Rev.* **1999**, *182*, 211-241.
98. Jarenmark, M.; Carlsson, H.; Nordlander, E., *C. R. Chim.* **2007**, *10*, 433-462.
99. Albedyhl, S.; Averbuch-Pouchot, Marie T.; Belle, C.; Krebs, B.; Pierre, Jean L.; Saint-Aman, E.; Torelli, S., *Eur. J. Inorg. Chem.* **2001**, *2001*, 1457-1464.
100. Suzuki, M.; Kanatomi, H.; Murase, I., *Chem. Lett.* **1981**, *10*, 1745-1748.
101. Neves, A.; de Brito, M. A.; Vencato, I.; Drago, V.; Griesar, K.; Haase, W.; Mascarenhas, Y. P., *Inorg. Chim. Acta* **1993**, *214*, 5-8.
102. Horn Jr, A.; Vencato, I.; Bortoluzzi, A. J.; Hörner, R.; Silva, R. A. N.; Szpoganicz, B.; Drago, V.; Terenzi, H.; de Oliveira, M. C. B.; Werner, R.; Haase, W.; Neves, A., *Inorg. Chim. Acta* **2005**, *358*, 339-351.
103. Bortoluzzi, A. J.; Neves, A.; Rey, N. A., *Acta Crystallogr. C* **2007**, *63*, o84-o86.
104. Andruh, M.; Kahn, O.; Sinton, J.; Dromzee, Y.; Jeannin, S., *Inorg. Chem.* **1993**, *32*, 1623-1628.
105. Roth, A.; Spielberg, E. T.; Plass, W., *Inorg. Chem.* **2007**, *46*, 4362-4364.
106. Lambert, E.; Chabut, B.; Chardon-Noblat, S.; Deronzier, A.; Chottard, G.; Bousseksou, A.; Tuchagues, J.-P.; Laugier, J.; Bardet, M.; Latour, J.-M., *J. Am. Chem. Soc.* **1997**, *119*, 9424-9437.
107. Jarenmark, M.; Kappen, S.; Haukka, M.; Nordlander, E., *Dalton Trans.* **2008**, 993-996.
108. Comba, P.; Gahan, L. R.; Hanson, G. R.; Mereacre, V.; Noble, C. J.; Powell, A. K.; Prisecaru, I.; Schenk, G.; Zajaczkowski-Fischer, M., *Chem. Eur. J.* **2012**, *18*, 1700-1710.
109. Zajaczkowski-Fischer, M., *Dissertation: Second Generation Model Complexes for the Enzyme Purple Acid Phosphatase*, The University of Heidelberg, Heidelberg, **2010**.
110. Feng, G.; Mareque-Rivas, J. C.; Torres Martín de Rosales, R.; Williams, N. H., *J. Am. Chem. Soc.* **2005**, *127*, 13470-13471.
111. Feng, G.; Mareque-Rivas, J. C.; Williams, N. H., *Chem. Commun.* **2006**, 1845-1847.
112. Feng, G.; Natale, D.; Prabakaran, R.; Mareque-Rivas, J. C.; Williams, N. H., *Angew. Chem. Int. Ed.* **2006**, *45*, 7056-7059.
113. Linjalahti, H.; Feng, G.; Mareque-Rivas, J. C.; Mikkola, S.; Williams, N. H., *J. Am. Chem. Soc.* **2008**, *130*, 4232-4233.
114. Comba, P.; Gahan, L. R.; Mereacre, V.; Hanson, G. R.; Powell, A. K.; Schenk, G.; Zajaczkowski-Fischer, M., *Inorg. Chem.* **2012**, *51*, 12195-12209.
115. Carvalho, N. M. F.; Horn Jr, A.; Bortoluzzi, A. J.; Drago, V.; Antunes, O. A. C., *Inorg. Chim. Acta* **2006**, *359*, 90-98.
116. Ośmiałowski, B.; Kolehmainen, E.; Dobosz, R.; Gawinecki, R.; Kauppinen, R.; Valkonen, A.; Koivukorpi, J.; Rissanen, K., *J. Phys. Chem. A* **2010**, *114*, 10421-10426.

117. Soo, H. S.; Komor, A. C.; Iavarone, A. T.; Chang, C. J., *Inorg. Chem.* **2009**, *48*, 10024-10035.
118. Goswami, S.; Das, N. K.; Sen, D.; Hoong-Kun, F., *Supramol. Chem.* **2010**, *22*, 532-543.
119. Drewry, J. A.; Fletcher, S.; Hassan, H.; Gunning, P. T., *Org. Biomol. Chem.* **2009**, *7*, 5074-5077.
120. Carlsson, H.; Haukka, M.; Bousseksou, A.; Latour, J.-M.; Nordlander, E., *Inorg. Chem.* **2004**, *43*, 8252-8262.
121. Sun, G.-C.; He, Z.-H.; Li, Z.-J.; Yuan, X.-D.; Yang, Z.-J.; Wang, G.-X.; Wang, L.-F.; Liu, C.-R., *Molecules* **2001**, *6*, 1001-1005.
122. Abe, A. M. M.; Helaja, J.; Koskinen, A. M. P., *Org. Lett.* **2006**, *8*, 4537-4540.
123. Gisch, N.; Balzarini, J.; Meier, C., *J. Med. Chem.* **2008**, *51*, 6752-6760.
124. Johansson, A.; Abrahamsson, M.; Magnuson, A.; Huang, P.; Mårtensson, J.; Styring, S.; Hammarström, L.; Sun, L.; Åkermark, B., *Inorg. Chem.* **2003**, *42*, 7502-7511.
125. Krebs, B.; Schepers, K.; Bremer, B.; Henkel, G.; Althaus, E.; Mueller-Warmuth, W.; Griesar, K.; Haase, W., *Inorg. Chem.* **1994**, *33*, 1907-1914.
126. Woods, M.; Sherry, A. D., *Inorg. Chem.* **2003**, *42*, 4401-4408.
127. Xavier, F. R.; Bortoluzzi, A. J.; Neves, A., *Chem. Biodiversity* **2012**, *9*, 1794-1805.
128. Strater, N.; Klabunde, T.; Tucker, P.; Witzel, H.; Krebs, B., *Science* **1995**, *268*, 1489-1492.
129. Uppenberg, J.; Lindqvist, F.; Svensson, C.; Ek-Rylander, B.; Andersson, G., *J. Mol. Biol.* **1999**, *290*, 201-211.
130. Egloff, M.-P.; Cohen, P. T. W.; Reinemer, P.; Barford, D., *J. Mol. Biol.* **1995**, *254*, 942-959.
131. Tainer, J. A.; Getzoff, E. D.; Richardson, J. S.; Richardson, D. C., *Nature* **1983**, *306*, 284-287.
132. Tainer, J. A.; Getzoff, E. D.; Beem, K. M.; Richardson, J. S.; Richardson, D. C., *J. Mol. Biol.* **1982**, *160*, 181-217.
133. Ghosh, D.; Kundu, N.; Maity, G.; Choi, K.-Y.; Caneschi, A.; Endo, A.; Chaudhury, M., *Inorg. Chem.* **2004**, *43*, 6015-6023.
134. Carlsson, H.; Nordlander, E.; Jarenmark, M., *C. R. Chim.* **2007**, *10*, 433-462.
135. Jarenmark, M.; Csapo, E.; Singh, J.; Wockel, S.; Farkas, E.; Meyer, F.; Haukka, M.; Nordlander, E., *Dalt. Trans.* **2010**, *39*, 8183-8194.
136. Carboni, M.; Latour, J.-M., *Coord. Chem. Rev.* **2011**, *255*, 186-202.
137. Jarenmark, M.; Haukka, M.; Demeshko, S.; Tuzcek, F.; Zuppiroli, L.; Meyer, F.; Nordlander, E., *Inorg. Chem.* **2011**, *50*, 3866-3887.
138. Lee, J.; Jung, D. J.; Lee, H.-J.; Lee, K.-B.; Hur, N. H.; Jang, H. G., *Bull. Korean Chem. Soc.* **2000**, *21*, 1025-1030.
139. Borovik, A. S.; Papaefthymiou, V.; Taylor, L. F.; Anderson, O. P.; Que, L., *J. Am. Chem. Soc.* **1989**, *111*, 6183-6195.
140. Smith, S. J.; Peralta, R. A.; Jovito, R.; Horn, A.; Bortoluzzi, A. J.; Noble, C. J.; Hanson, G. R.; Stranger, R.; Jayaratne, V.; Cavigliasso, G.; Gahan, L. R.; Schenk, G.; Nascimento, O. R.; Cavalett, A.; Bortolotto, T.; Razzera, G.; Terenzi, H.; Neves, A.; Riley, M. J., *Inorg. Chem.* **2012**, *51*, 2065-2078.
141. Batista, S. C.; Neves, A.; Bortoluzzi, A. J.; Vencato, I.; Peralta, R. A.; Szpoganicz, B.; Aires, V. V. E.; Terenzi, H.; Severino, P. C., *Inorg. Chem. Commun.* **2003**, *6*, 1161-1165.
142. Schenk, G.; Peralta, R. A.; Batista, S.; Bortoluzzi, A. J.; Szpoganicz, B.; Dick, A. K.; Herrald, P.; Hanson, G. R.; Szilagy, R.; Riley, M. J.; Gahan, L. R.; Neves, A., *J. Biol. Inorg. Chem.* **2008**, *13*, 139-155.
143. Danford, J. J.; Dobrowolski, P.; Berreau, L. M., *Inorg. Chem.* **2009**, *48*, 11352-11361.

144. Peralta, R. A.; Bortoluzzi, A. J.; de Souza, B.; Jovito, R.; Xavier, F. R.; Couto, R. A. A.; Casellato, A.; Nome, F.; Dick, A.; Gahan, L. R.; Schenk, G.; Hanson, G. R.; de Paula, F. v. C. S.; Pereira-Maia, E. C.; de P. Machado, S.; Severino, P. C.; Pich, C.; Bortolotto, T.; Terenzi, H. n.; Castellano, E. E.; Neves, A.; Riley, M. J., *Inorg. Chem.* **2010**, *49*, 11421-11438.
145. Xavier, F. R.; Peralta, R. A.; Bortoluzzi, A. J.; Drago, V.; Castellano, E. E.; Haase, W.; Tomkowicz, Z.; Neves, A., *J. Inorg. Biochem.* **2011**, *105*, 1740-1752.
146. Xavier, F. R.; Neves, A.; Casellato, A.; Peralta, R. A.; Bortoluzzi, A. J.; Szpoganicz, B.; Severino, P. C.; Terenzi, H.; Tomkowicz, Z.; Ostrovsky, S.; Haase, W.; Ozarowski, A.; Krzystek, J.; Telser, J.; Schenk, G.; Gahan, L. R., *Inorg. Chem.* **2009**, *48*, 7905-7921.
147. Karsten, P.; Neves, A.; Bortoluzzi, A. J.; Strähle, J.; Maichle-Mössmer, C., *Inorg. Chem. Commun.* **2002**, *5*, 434-438.
148. Smith, S. J.; Riley, M. J.; Noble, C. J.; Hanson, G. R.; Stranger, R.; Jayaratne, V.; Cavigliasso, G.; Schenk, G.; Gahan, L. R., *Inorg. Chem.* **2009**, *48*, 10036-10048.
149. Belle, C.; Gautier-Luneau, I.; Karmazin, L.; Pierre, J.-L.; Albedyhl, S.; Krebs, B.; Bonin, M., *Eur. J. Inorg. Chem.* **2002**, *2002*, 3087-3090.
150. Belle, C.; Gautier-Luneau, I.; Gellon, G.; Pierre, J.-L.; Morgenstern-Badarau, I.; Saint-Aman, E., *Dalton Trans.* **1997**, 3543-3546.
151. de Souza, B.; Kreft, G. L.; Bortolotto, T.; Terenzi, H.; Bortoluzzi, A. J.; Castellano, E. E.; Peralta, R. A.; Domingos, J. B.; Neves, A., *Inorg. Chem.* **2013**, *52*, 3594-3596.
152. Retegan, M.; Milet, A.; Jamet, H., *J. Phys. Chem. A* **2010**, *114*, 7110-7116.
153. Piovezan, C.; Jovito, R.; Bortoluzzi, A. J.; Terenzi, H. n.; Fischer, F. L.; Severino, P. C.; Pich, C. T.; Azzolini, G. G.; Peralta, R. A.; Rossi, L. M.; Neves, A., *Inorg. Chem.* **2010**, *49*, 2580-2582.
154. Vallee, B. L.; Auld, D. S., *Proc. Natl. Acad. Sci. USA* **1990**, *87*, 220-224.
155. Christianson, D. W., *Adv. Protein Chem.* **1991**, *42*, 281-355.
156. McCall, K. A.; Huang, C.-c.; Fierke, C. A., *J. Nutr.* **2000**, *130*, 1437S-1446S.
157. Kövári, E.; Krämer, R., *Chem. Ber.* **1994**, *127*, 2151-2157.
158. Kovari, E.; Heitker, J.; Kramer, R., *J. Chem. Soc., Chem. Commun.* **1995**, 1205-1206.
159. Kövári, E.; Krämer, R., *J. Am. Chem. Soc.* **1996**, *118*, 12704-12709.
160. Rossi, L. M.; Neves, A.; Bortoluzzi, A. J.; Hoerner, R.; Szpoganicz, B.; Terenzi, H.; Mangrich, A. S.; Pereira-Maia, E.; Castellano, E. E.; Haase, W., *Inorg. Chim. Acta* **2005**, *358*, 1807-1822.
161. Osório, R. E. H. M. B.; Peralta, R. A.; Bortoluzzi, A. J.; de Almeida, V. R.; Szpoganicz, B.; Fischer, F. L.; Terenzi, H.; Mangrich, A. S.; Mantovani, K. M.; Ferreira, D. E. C.; Rocha, W. R.; Haase, W.; Tomkowicz, Z.; Anjos, A. d.; Neves, A., *Inorg. Chem.* **2012**, *51*, 1569-1589.
162. Wall, M.; Linkletter, B.; Williams, D.; Hynes, R. C.; Chin, J., *J. Am. Chem. Soc.* **1999**, *121*, 4710-4711.
163. Comba, P.; Gahan, L. R.; Hanson, G. R.; Westphal, M., *Chem. Commun.* **2012**, *48*, 9364-9366.
164. Lide, D. R., *CRC handbook of chemistry and physics: a ready-reference book of chemical and physical data*, 89. ed.; CRC Press: Boca Raton, **2008**.
165. Baes, C. F.; Mesmer, R. E., *The hydrolysis of cations*, Wiley: New York, **1976**.
166. Richens, D. T., *The chemistry of aqua ions: synthesis, structure and reactivity; a tour through the periodic table of the elements*, Wiley: Chichester, **1997**.
167. Merckx, M.; Averill, B. A., *Biochemistry* **1998**, *37*, 8490-8497.
168. Mareque Rivas, J. C.; Torres Martin de Rosales, R.; Parsons, S., *Dalton Trans.* **2003**, 2156-2163.

169. Smith, S. J.; Noble, C. J.; Palmer, R. C.; Hanson, G. R.; Schenk, G.; Gahan, L. R.; Riley, M. J., *J. Biol. Inorg. Chem.* **2008**, *13*, 499-510.
170. Lötzbeyer, L., *Dissertation: Synthese neuer Patellamid-Derivate und Eigenschaften ihrer Kupfer(II)-Komplexe*, Ruprecht-Karls Universität Heidelberg, Heidelberg, **2001**.
171. Addison, A. W.; Rao, T. N.; Reedijk, J.; van Rijn, J.; Verschoor, G. C., *Dalton Trans.* **1984**, 1349-1356.
172. Kozlevcar, B.; Segedin, P., *Croat. Chem. Acta* **2008**, *81*, 369-379.
173. Kahn, O., *Molecular magnetism*, VCH: New York, **1993**.
174. Clarke, J.; Braginski, A. I., *The SQUID Handbook, Vol. II: Applications of SQUIDs and SQUID Systems*, Wiley-VCH: Weinheim, **2006**.
175. de Almeida, V. R.; Xavier, F. R.; Osorio, R. E. H. M. B.; Bessa, L. M.; Schilling, E. L.; Costa, T. G.; Bortolotto, T.; Cavalett, A.; Castro, F. A. V.; Vilhena, F.; Alves, O. C.; Terenzi, H.; Eleutherio, E. C. A.; Pereira, M. D.; Haase, W.; Tomkowicz, Z.; Szpoganicz, B.; Bortoluzzi, A. J.; Neves, A., *Dalton Trans.* **2013**, *42*, 7059-7073.
176. Rey, N. A.; Neves, A.; Bortoluzzi, A. J.; Haase, W.; Tomkowicz, Z., *Dalton Trans.* **2012**, *41*, 7196-7200.
177. Chaudhuri, P.; Wagner, R.; Weyhermueller, T., *Inorg. Chem.* **2007**, *46*, 5134-5136.
178. Ruiz, E.; Alemany, P.; Alvarez, S.; Cano, J., *Inorg. Chem.* **1997**, *36*, 3683-3688.
179. Ruiz, E.; Alemany, P.; Alvarez, S.; Cano, J., *J. Am. Chem. Soc.* **1997**, *119*, 1297-1303.
180. Paine, T. K.; Weyhermueller, T.; Wieghardt, K.; Chaudhuri, P., *Inorg. Chem.* **2002**, *41*, 6538-6540.
181. Grillo, V. A.; Hanson, G. R.; Hambley, T. W.; Gahan, L. R.; Murray, K. S.; Moubaraki, B., *J. Chem. Soc., Dalton Trans.* **1997**, 305-311.
182. Holman, T. R.; Wang, Z.; Hendrich, M. P.; Que, L., *Inorg. Chem.* **1995**, *34*, 134-139.
183. Yan, S.; Pan, X.; Taylor, L. F.; Zhang, J. H.; O'Connor, C. J.; Britton, D.; Anderson, O. P.; Que Jr, L., *Inorg. Chim. Acta* **1996**, *243*, 1-8.
184. Mareque-Rivas, J. C.; Prabakaran, R.; Martin de Rosales, R. T., *Chem. Commun.* **2004**, 76-77.
185. Vallee, B. L.; Auld, D. S., *Acc. Chem. Res.* **1993**, *26*, 543-551.
186. Bertini, I.; Luchinat, C.; Rosi, M.; Sgamellotti, A.; Tarantelli, F., *Inorg. Chem.* **1990**, *29*, 1460-1463.
187. Kodama, M.; Kimura, E., *Dalton Trans.* **1977**, 2269-2276.
188. Zompa, L. J., *Inorg. Chem.* **1978**, *17*, 2531-2536.
189. Kimura, E.; Shiota, T.; Koike, T.; Shiro, M.; Kodama, M., *J. Am. Chem. Soc.* **1990**, *112*, 5805-5811.
190. Mareque-Rivas, J. C.; Prabakaran, R.; Parsons, S., *Dalton Trans.* **2004**, 1648-1655.
191. Chiu, Y.-H.; Canary, J. W., *Inorg. Chem.* **2003**, *42*, 5107-5116.
192. Christianson, D. W.; Fierke, C. A., *Acc. Chem. Res.* **1996**, *29*, 331-339.
193. Hernandez-Gil, J.; Ferrer, S.; Salvador, E.; Calvo, J.; Garcia-Espana, E.; Mareque-Rivas, J. C., *Chem. Commun.* **2013**, *49*, 3655-3657.
194. Huang, F.; Cheng, C.; Feng, G., *J. Org. Chem.* **2012**, *77*, 11405-11408.
195. Daumann, L. J.; Dalle, K. E.; Schenk, G.; McGearry, R. P.; Bernhardt, P. V.; Ollis, D. L.; Gahan, L. R., *Dalton Trans.* **2012**, *41*, 1695-1708.
196. Adams, H.; Bradshaw, D.; Fenton, D. E., *Inorg. Chim. Acta* **2002**, *332*, 195-200.
197. Das, B.; Haukka, M.; Nordlander, E., *Acta Cryst. E* **2014**, *70*, m120-m121.
198. Selmeczi, K.; Michel, C.; Milet, A.; Gautier-Luneau, I.; Philouze, C.; Pierre, J.-L.; Schnieders, D.; Rompel, A.; Belle, C., *Chem. Eur. J.* **2007**, *13*, 9093-9106.
199. Berreau, L. M.; Saha, A.; Arif, A. M., *Dalton Trans.* **2006**, 183-192.
200. Matsufuji, K.; Shiraishi, H.; Miyasato, Y.; Shiga, T.; Ohba, M.; Yokoyama, T.; Okawa, H., *Bull. Chem. Soc. Jpn.* **2005**, *78*, 851-858.

201. Hough, E.; Hansen, L. K.; Birknes, B.; Jynge, K.; Hansen, S.; Hordvik, A.; Little, C.; Dodson, E.; Derewenda, Z., *Nature* **1989**, *338*, 357-360.
202. Goldberg, J.; Huang, H.-b.; Kwon, Y.-g.; Greengard, P.; Nairn, A. C.; Kuriyan, J., *Nature* **1995**, *376*, 745-753.
203. M. Hesse; H. Meier; Zeeh, B., *Spectroscopic methods in organic chemistry*, G. Thieme: NY, **1997**.
204. H. Günzler; H.-U. Gremlich, *IR Spectroscopy An Introduction*, 1. ed.; **2002**.
205. Nakamoto, K., *Infrared and Raman spectra of inorganic and coordination compounds*, Wiley: NY, **1978**.
206. Deacon, G. B.; Phillips, R. J., *Coord. Chem. Rev.* **1980**, *33*, 227-250.
207. Gross, F., *Iron Metabolism: An International Symposium*, Springer: Berlin, Heidelberg, **1964**.
208. Lippard, S. J., *Angew. Chem. Int. Ed.* **1988**, *27*, 344-361.
209. Vincent, J. B.; Olivier-Lilley, G. L.; Averill, B. A., *Chem. Rev.* **1990**, *90*, 1447-1467.
210. Fontecave, M.; Ménage, S.; Duboc-Toia, C., *Coord. Chem. Rev.* **1998**, *178-180*, 1555-1572.
211. Friedle, S.; Reisner, E.; Lippard, S. J., *Chem. Soc. Rev.* **2010**, *39*, 2768-2779.
212. Merx, M.; Kopp, D. A.; Sazinsky, M. H.; Blazyk, J. L.; Müller, J.; Lippard, S. J., *Angew. Chem. Int. Ed.* **2001**, *40*, 2782-2807.
213. Sazinsky, M. H.; Lippard, S. J., *Acc. Chem. Res.* **2006**, *39*, 558-566.
214. Stubbe, J.; Nocera, D. G.; Yee, C. S.; Chang, M. C. Y., *Chem. Rev.* **2003**, *103*, 2167-2201.
215. Nordlund, P.; Reichard, P., *Annu. Rev. Biochem.* **2006**, *75*, 681-706.
216. Kurtz, D. M., Jr., *Dalton Trans.* **2007**, 4115-4121.
217. Antanaitis, B. C.; Aisen, P.; Lilienthal, H. R., *J. Biol. Chem.* **1983**, *258*, 3166-3172.
218. Hill, H. A. O.; Sadler, P. J.; Thomson, A. J., *Metal Sites in Proteins and Models*, 1. ed.; Springer: Berlin, Heidelberg, **1997**; Vol. 89.
219. Averill, B. A.; Davis, J. C.; Burman, S.; Zirino, T.; Sanders-Loehr, J.; Loehr, T. M.; Sage, J. T.; Debrunner, P. G., *J. Am. Chem. Soc.* **1987**, *109*, 3760-3767.
220. Wilkins, R. G., *Chem. Soc. Rev.* **1992**, *21*, 171-178.
221. Merx, M.; Averill, B. A., *Biochemistry* **1998**, *37*, 11223-11231.
222. Wang, D. L.; Holz, R. C.; David, S. S.; Que, L., Jr.; Stankovich, M. T., *Biochemistry* **1991**, *30*, 8187-8194.
223. Bernhardt, P. V.; Schenk, G.; Wilson, G. J., *Biochemistry* **2004**, *43*, 10387-10392.
224. Debrunner, P. G.; Hendrich, M. P.; Jersey, J. d.; Keough, D. T.; Sage, J. T.; Zerner, B., *Biochim. Biophys. Acta, Protein Struct. Mol. Enzymol.* **1983**, *745*, 103-106.
225. Rodriguez, J. H.; Ok, H. N.; Xia, Y. M.; Debrunner, P. G.; Hinrichs, B. E.; Meyer, T.; Packard, N. H., *J. Phys. Chem.* **1996**, *100*, 6849-6862.
226. Day, E. P.; David, S. S.; Peterson, J.; Dunham, W. R.; Bonvoisin, J. J.; Sands, R. H.; Que, L., *J. Biol. Chem.* **1988**, *263*, 15561-15567.
227. Crowder, M. W.; Vincent, J. B.; Averill, B. A., *Biochemistry* **1992**, *31*, 9603-9608.
228. Dietrich, M.; Münstermann, D.; Suerbaum, H.; Witzel, H., *Eur. J. Biochem.* **1991**, *199*, 105-113.
229. Eulerling, B.; Ahlers, F.; Zippel, F.; Schmidt, M.; Nolting, H. F.; Krebs, B., *Chem. Commun.* **1995**, 1305-1307.
230. Nie, H.; Aubin, S.; Mashuta, M. S.; Wu, J.; Richardson, J. F.; Hendrickson, D. N.; Buchanan, R. M., *Inorg. Chem.* **1995**, *34*, 2382-2388.
231. Suzuki, M.; Uehara, A.; Oshio, H.; Endo, K.; Yanaga, M.; Kida, S.; Saito, K., *Bull. Chem. Soc. Jpn.* **1987**, *60*, 3547-3555.
232. Yim, S. H.; Lee, H. J.; Lee, K.-B.; Kang, S. J.; Hur, N. H.; Jang, H. G., *Bull. Korean Chem. Soc.* **1998**, *19*, 654-660.

233. Maeda, Y.; Yamamoto, M.; Hayami, S., *J. Radioanal. Nucl. Chem.* **2007**, *272*, 651-656.
234. Inomata, T.; Shinozaki, K.; Hayashi, Y.; Aarii, H.; Funahashi, Y.; Ozawa, T.; Masuda, H., *Chem. Commun.* **2008**, 392-394.
235. Borovik, A. S.; Que, L., Jr., *J. Am. Chem. Soc.* **1988**, *110*, 2345-2347.
236. O'Connor, C. J.; Lippard, S. J., *Prog. Inorg. Chem.* **1982**, 203-283.
237. Jang, H. G.; Hendrich, M. P.; Que, L., Jr., *Inorg. Chem.* **1993**, *32*, 911-918.
238. Tolman, W. B.; Liu, S.; Bentsen, J. G.; Lippard, S. J., *J. Am. Chem. Soc.* **1991**, *113*, 152-164.
239. Satcher, J. H., Jr.; Balch, A. L.; Olmstead, M. M.; Droege, M. W., *Inorg. Chem.* **1996**, *35*, 1749-1750.
240. Hayashi, Y.; Kayatani, T.; Sugimoto, H.; Suzuki, M.; Inomata, K.; Uehara, A.; Mizutani, Y.; Kitagawa, T.; Maeda, Y., *J. Am. Chem. Soc.* **1995**, *117*, 11220-11229.
241. Dong, Y.; Menage, S.; Brennan, B. A.; Elgren, T. E.; Jang, H. G.; Pearce, L. L.; Que, L., Jr., *J. Am. Chem. Soc.* **1993**, *115*, 1851-1859.
242. Evans, D. F., *J. Chem. Soc.* **1959**, 2003-2005.
243. Bertini, I.; Luchinat, C.; Parigi, G., *Solution NMR of paramagnetic molecules: applications to metalloproteins and models*, 1. ed.; Elsevier: Amsterdam, **2001**.
244. Carboni, M.; Clémancey, M.; Molton, F.; Pécaut, J.; Lebrun, C.; Dubois, L.; Blondin, G.; Latour, J. M., *Inorg. Chem.* **2012**, *51*, 10447-10460.
245. Wang, Z.; Holman, T. R.; Que, L., *Magn. Reson. Chem.* **1993**, *31*, S78-S84.
246. Gonsor, U., *Mössbauer spectroscopy*, Springer: Berlin, **1975**.
247. Gütlich, P., *Chem. unserer Zeit* **1970**, *4*, 133-144.
248. Brant, R. A. *NORMOS Mössbauer Fit. Progr. Pack.*, Duisburg, Germany, **1994**.
249. Dong, Y.; Fujii, H.; Hendrich, M. P.; Leising, R. A.; Pan, G.; Randall, C. R.; Wilkinson, E. C.; Zang, Y.; Que, L., Jr.; et, a., *J. Am. Chem. Soc.* **1995**, *117*, 2778-2792.
250. Rhile, I. J.; Markle, T. F.; Nagao, H.; DiPasquale, A. G.; Lam, O. P.; Lockwood, M. A.; Rotter, K.; Mayer, J. M., *J. Am. Chem. Soc.* **2006**, *128*, 6075-6088.
251. Markle, T. F.; Tronic, T. A.; DiPasquale, A. G.; Kaminsky, W.; Mayer, J. M., *J. Phys. Chem. A* **2012**, *116*, 12249-12259.
252. Pavlishchuk, V. V.; Addison, A. W., *Inorg. Chim. Acta* **2000**, *298*, 97-102.
253. Manago, T.; Hayami, S.; Oshio, H.; Osaki, S.; Hasuyama, H.; Herber, R. H.; Maeda, Y., *J. Chem. Soc., Dalton Trans.* **1999**, 1001-1012.
254. Alimi, M.; Allam, A.; Selkti, M.; Tomas, A.; Roussel, P.; Galardon, E.; Artaud, I., *Inorg. Chem.* **2012**, *51*, 9350-9356.
255. Rivas, J. C. M.; Hinchley, S. L.; Metteau, L.; Parsons, S., *Dalton Trans.* **2006**, 2316-2322.
256. Aarii, H.; Nagatomo, S.; Kitagawa, T.; Miwa, T.; Jitsukawa, K.; Einaga, H.; Masuda, H., *J. Inorg. Biochem.* **2000**, *82*, 153-162.
257. Zheng, S.; Berto, T. C.; Dahl, E. W.; Hoffman, M. B.; Speelman, A. L.; Lehnert, N., *J. Am. Chem. Soc.* **2013**, *135*, 4902-4905.
258. Yan, S.; Cheng, P.; Wang, Q.; Liao, D.; Jiang, Z.; Wang, G., *Sci. China, Ser. B: Chem.* **2000**, *43*, 405-411.
259. Ainscough, E. W.; Brodie, A. M.; Plowman, J. E.; Brown, K. L.; Addison, A. W.; Gainsford, A. R., *Inorg. Chem.* **1980**, *19*, 3655-3663.
260. Gaber, B. P.; Miskowski, V.; Spiro, T. G., *J. Am. Chem. Soc.* **1974**, *96*, 6868-6873.
261. Weil, J. A.; Bolton, J. R., *Electron paramagnetic resonance: elementary theory and practical applications*, 2. ed. ed.; Wiley-Interscience: Hoboken, NJ, **2007**.
262. Suzuki, M.; Oshio, H.; Uehara, A.; Endo, K.; Yanaga, M.; Kida, S.; Saito, K., *Bull. Chem. Soc. Jpn.* **1988**, *61*, 3907-3913.
263. Stec, B.; Hehir, M. J.; Brennan, C.; Nolte, M.; Kantrowitz, E. R., *J. Mol. Biol.* **1998**, *277*, 647-662.

264. Stec, B.; Holtz, K. M.; Kantrowitz, E. R., *J. Mol. Biol.* **2000**, *299*, 1303-1311.
265. Aquino, M. A. S.; Lim, J. S.; Sykes, A. G., *J. Chem. Soc., Dalton Trans.* **1994**, 429-436.
266. Twitchett, M. B.; Schenk, G.; Aquino, M. A. S.; Yiu, D. T. Y.; Lau, T.-C.; Sykes, A. G., *Inorg. Chem.* **2002**, *41*, 5787-5794.
267. Smoukov, S. K.; Quaroni, L.; Wang, X.; Doan, P. E.; Hoffman, B. M.; Que, L., *J. Am. Chem. Soc.* **2002**, *124*, 2595-2603.
268. Wang, X.; Ho, R. Y. N.; Whiting, A. K.; Que, L., Jr., *J. Am. Chem. Soc.* **1999**, *121*, 9235-9236.
269. Merckx, M.; Averill, B. A., *J. Am. Chem. Soc.* **1999**, *121*, 6683-6689.
270. Wang, X.; Randall, C. R.; Que, L., Jr., *Biochemistry* **1996**, *35*, 13946-13954.
271. Kimura, E., *Curr. Opin. Chem. Biol.* **2000**, *4*, 207-213.
272. Wynne, C. J.; Hamilton, S. E.; Dionysius, D. A.; Beck, J. L.; de Jersey, J., *Arch. Biochem. Biophys.* **1995**, *319*, 133-141.
273. Neverov, A. A.; Lu, Z.-L.; Maxwell, C. I.; Mohamed, M. F.; White, C. J.; Tsang, J. S. W.; Brown, R. S., *J. Am. Chem. Soc.* **2006**, *128*, 16398-16405.
274. Richard, J. P.; Amyes, T. L., *Bioorg. Chem.* **2004**, *32*, 354-366.
275. Daumann, L. J.; Gahan, L. R.; Comba, P.; Schenk, G., *Inorg. Chem.* **2012**, *51*, 7669-7681.
276. Daumann, L. J.; Marty, L.; Schenk, G.; Gahan, L. R., *Dalton Trans.* **2013**, *42*, 9574-9584.
277. Segel, I. H., *Enzyme Kinetics: Behavior and analysis of rapid equilibrium and steady-state enzyme systems*, Wiley-Interscience: NY, **1975**.
278. Kantacha, A.; Buchholz, R.; Smith, S.; Schenk, G.; Gahan, L., *J. Biol. Inorg. Chem.* **2011**, *16*, 25-32.
279. Michaelis, L.; Menten, M. L., *Biochem. Z.* **1913**, *49*, 333-369.
280. Johnson, K. A.; Goody, R. S., *Biochemistry* **2011**, *50*, 8264-8269.
281. Meyer, F., *Eur. J. Inorg. Chem.* **2006**, 3789-3800.
282. Parkin, G., *Chem. Rev.* **2004**, *104*, 699-768.
283. Breslow, R.; Berger, D.; Huang, D. L., *J. Am. Chem. Soc.* **1990**, *112*, 3686-3687.
284. He, J.; Sun, J.; Mao, Z.-W.; Ji, L.-N.; Sun, H., *J. Inorg. Biochem.* **2009**, *103*, 851-858.
285. Mareque-Rivas, J. C.; Torres Martin de Rosales, R.; Parsons, S., *Chem. Commun.* **2004**, 610-611.
286. Fan, Y.; Gao, Y. Q., *J. Am. Chem. Soc.* **2007**, *129*, 905-913.
287. Mohamed, M. F.; Brown, R. S., *J. Org. Chem.* **2010**, *75*, 8471-8477.
288. Aoki, S.; Kimura, E., *Rev. Mol. Biotechnol.* **2002**, *90*, 129-155.
289. Coburn, S. P.; Mahuren, J. D.; Jain, M.; Zubovic, Y.; Wortsman, J., *J. Clin. Endocrinol. Metab.* **1998**, *83*, 3951-3957.
290. H. N. Fernley, P. G. W., *Biochem. J.* **1967**, *104*, 1011-1018.
291. Kinoshita, E.; Takahashi, M.; Takeda, H.; Shiro, M.; Koike, T., *Dalton Trans.* **2004**, 1189-1193.
292. Gorenstein, D. G., *Phosphorus-31 NMR: principles and applications*, Acad. Pr.: Orlando, **1984**.
293. Norman, R. E.; Yan, S.; Que, L., Jr.; Backes, G.; Ling, J.; Sanders-Loehr, J.; Zhang, J. H.; O'Connor, C. J., *J. Am. Chem. Soc.* **1990**, *112*, 1554-1562.
294. Turowski, P. N.; Armstrong, W. H.; Liu, S.; Brown, S. N.; Lippard, S. J., *Inorg. Chem.* **1994**, *33*, 636-645.
295. Duboc-Toia, C.; Menage, S.; Vincent, J.-M.; Averbuch-Pouchot, M. T.; Fontecave, M., *Inorg. Chem.* **1997**, *36*, 6148-6149.
296. Helm, L.; Merbach, A. E., *Chem. Rev.* **2005**, *105*, 1923-1959.
297. Tanaka, M.; Yamada, S., *Chem. Commun.* **1976**, 178-179.
298. Grant, M.; Jordan, R. B., *Inorg. Chem.* **1981**, *20*, 55-60.

299. Davis, J. C.; Averill, B. A., *Proc. Natl. Acad. Sci. USA* **1982**, *79*, 4623-4627.
300. David, S. S.; Que, L., Jr., *J. Am. Chem. Soc.* **1990**, *112*, 6455-6463.
301. Bosch, S.; Comba, P.; Gahan, L. R.; Schenk, G., *Inorg. Chem.* **2014**, *53*, 9036-9051.
302. Bruker *TopSpin 2.0 Software for NMR data processing*.
303. Sheldrick, G. M. *SHELXL97: Program for the refinement of crystal structures*, University of Gottingen: Germany, **1997**.
304. Farrugia, L. J., *J. Appl. Crystallogr.* **1999**, *32*, 837-838.
305. Dolomanov, O. V.; Bourhis, L. J.; Gildea, R. J.; Howard, J. A. K.; Puschmann, H., *J. Appl. Crystallogr.* **2009**, *42*, 339-341.
306. Van der Sluis, P.; Spek, A. L., *Acta Cryst. A* **1990**, *A46*, 194-201.
307. Spek, A. L., *J. Appl. Crystallogr.* **2003**, *36*, 7-13.
308. Hanson, G. R.; Gates, K. E.; Noble, C. J.; Griffin, M.; Mitchell, A.; Benson, S., *J. Inorg. Biochem.* **2004**, *98*, 903-916.
309. Hanson, G. R. *Molecular sophe simulation suite*, Bruker Biospin: Germany, Switherland, France, U.S., **2007**.
310. Paine, R. T.; Tan, Y.-C.; Gan, X.-M., *Inorg. Chem.* **2001**, *40*, 7009-7013.
311. Jovito, R.; Neves, A.; Bortoluzzi, A. J.; Lanznaster, M.; Drago, V.; Haase, W., *Inorg. Chem. Commun.* **2005**, *8*, 323-327.
312. Bunton, C. A.; Farber, S. J., *J. Org. Chem.* **1969**, *34*, 767-772.
313. Rawji, G.; Milburn, R. M., *J. Org. Chem.* **1981**, *46*, 1205-1206.

APPENDIX

Table 30: Crystallographic data for $[\text{Ga}^{\text{III}}(\text{H}_2\text{SIM}^1)(\mu\text{-OH})]_2(\text{ClO}_4)_2 \cdot \text{CH}_3\text{CN} \cdot \text{Et}_2\text{O}$, $[\text{Ga}^{\text{III}}\text{Zn}^{\text{II}}(\text{H}_2\text{SIM}^1)(\text{OAc})_2(\text{OH})]\text{PF}_6 \cdot \text{Et}_2\text{O}$ and $[\text{Cu}^{\text{II}}_2(\text{HSIM}^1)(\mu\text{-OAc})]\text{PF}_6$.

	$[\text{Ga}^{\text{III}}(\text{H}_2\text{SIM}^1)(\mu\text{-OH})]_2(\text{ClO}_4)_2 \cdot \text{CH}_3\text{CN} \cdot \text{Et}_2\text{O}$	$[\text{Ga}^{\text{III}}\text{Zn}^{\text{II}}(\text{H}_2\text{SIM}^1)(\text{OAc})_2(\text{OH})]\text{PF}_6 \cdot \text{Et}_2\text{O}$	$[\text{Cu}^{\text{II}}_2(\text{HSIM}^1)(\mu\text{-OAc})]\text{PF}_6$
Empirical formula	$\text{C}_{49}\text{H}_{65}\text{Cl}_2\text{GaN}_9\text{O}_{13}$	$\text{C}_{51}\text{H}_{68}\text{F}_6\text{GaN}_8\text{O}_9\text{PZn}$	$\text{C}_{45}\text{H}_{53}\text{Cu}_2\text{F}_6\text{N}_8\text{O}_5\text{P}$
Formula weight	1128.72	1217.19	1058.00
Temperature (K)	120(1)	200(2)	100(1)
Wavelength (Å)	1.54184	0.71073	0.71073
Crystal system	Triclinic	Monoclinic	Triclinic
Space group	P -1	C 1 2/c 1	P -1
a (Å)	10.5436(3)	18.8817(7)	12.887(7)
b (Å)	13.6018(4)	18.7090(10)	13.394(8)
c (Å)	19.3106(6)	32.536(2)	15.137(9)
α (°)	78.857(3)	90	79.960(13)
β (°)	82.0085(3)	103.756(5)	73.452(17)
γ (°)	77.117(3)	90	70.673(11)
Vol (Å ³)	2635.77(15)	11163.9(10)	2354(2)
Z	2	8	2
μ (mm ⁻¹)	2.248	1.022	1.015
F(000)	1182	5056	1092
P (Mg/m ³)	1.422	1.448	1.492
Reflections collected	59276	23354	56089
Independent reflections [R_{int}]	9785 [0.0736]	9829 [0.0556]	14368 [0.0424]
Θ range for data collection (°)	3.777 – 70.622	2.91 - 29.24	1.727 – 30.555
GOOF on F ²	1.059	1.035	1.014
Final R indices [$I > 2\sigma(I)$]	$R_1 = 0.0827$ $wR_2 = 0.2212$	$R_1 = 0.0772$ $wR_2 = 0.1893$	$R_1 = 0.0382$ $wR_2 = 0.0873$
R indices (all data)	$R_1 = 0.1090$ $wR_2 = 0.2400$	$R_1 = 0.1089$ $wR_2 = 0.2103$	$R_1 = 0.0632$ $wR_2 = 0.0993$
Largest diff. peak and hole (e Å ⁻³)	1.347 and -0.796	1.223 and -0.695	0.669 and -0.394
Identification code	co_sb15	-	co_sb14
CCDC number	-	1024620	-

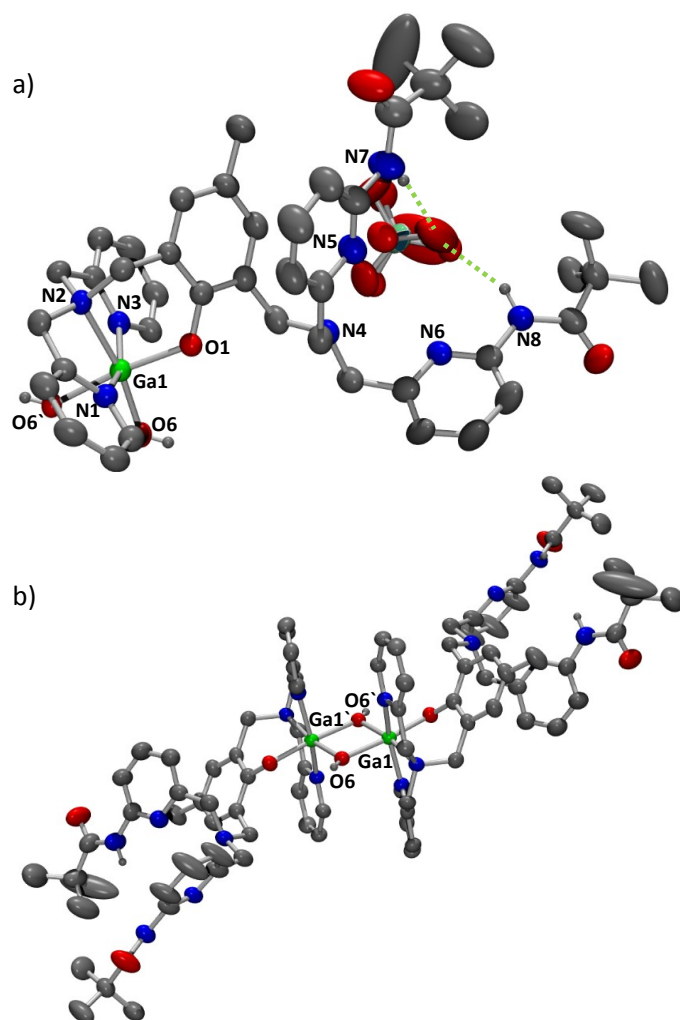


Figure 70: ORTEP plots of a) $[\text{Ga}^{\text{III}}(\text{H}_2\text{SIM}^1)(\mu\text{-OH})]\text{ClO}_4$ and b) the respective dimer $[\text{Ga}^{\text{III}}(\text{H}_2\text{SIM}^1)(\mu\text{-OH})]_2^{2+}$ with 50% probability level of thermal ellipsoids. Counter ions, non-coordinated solvent molecules and hydrogen atoms not involved in hydrogen bonding are omitted for clarity.

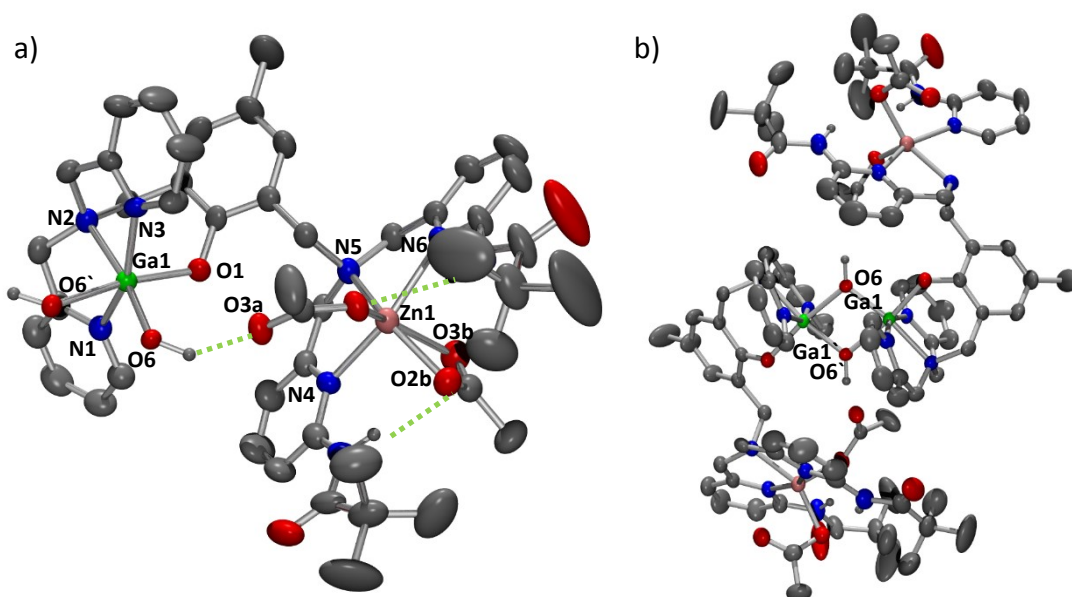


Figure 71: ORTEP plots of a) $[\text{Ga}^{\text{III}}\text{Zn}^{\text{II}}(\text{H}_2\text{SIM}^1)(\text{OAc})_2(\text{OH})]\text{PF}_6$ and b) the respective dimeric structure with 50% probability level of thermal ellipsoids showing hydrogen bonds as green, dotted lines. Counter ions, non-coordinated solvent molecules and hydrogen atoms not involved in hydrogen bonding are omitted for clarity.

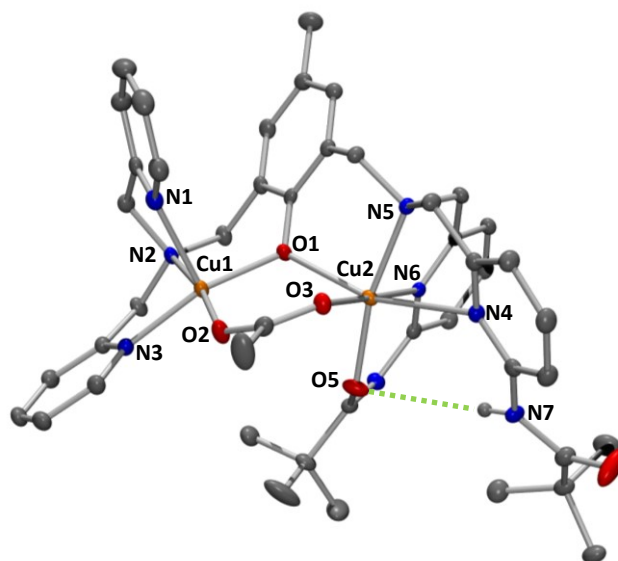


Figure 72: ORTEP plot of $[\text{Cu}^{\text{II}}_2(\text{HSIM}^1)(\mu\text{-OAc})]\text{PF}_6$ with 50% probability level of thermal ellipsoids showing hydrogen bonds as green, dotted lines. Counter ion and hydrogen atoms not involved in hydrogen bonding are omitted for clarity.

Table 31: Crystallographic data for $\{\text{Na}[\text{Fe}^{\text{III}}(\text{H}_2\text{SIM}^2)]_2(\mu\text{-OAc})(\mu\text{-OH}_2)\}(\text{BF}_4)_2 \cdot 3\text{H}_2\text{O}$.

	$\{\text{Na}[\text{Fe}(\text{H}_2\text{L}^4)]_2(\mu\text{-OAc})(\mu\text{-OH}_2)\}(\text{BF}_4)_2 \cdot 3\text{H}_2\text{O}$
Empirical formula	$\text{C}_{45}\text{H}_{53}\text{N}_7\text{O}_6\text{BF}_4\text{Na}_{0.5}\text{Fe}$
Formula weight	942.10
Temperature (K)	293(2)
Wavelength (\AA)	0.71073
Crystal system	Triclinic
Space group	$P\bar{1}$
a (\AA)	17.6526(17)
b (\AA)	17.6900(17)
c (\AA)	19.16(3)
α ($^\circ$)	77.164(10)
β ($^\circ$)	63.144(12)
γ ($^\circ$)	84.177(8)
Vol (\AA^3)	5204(8)
Z	4
μ (mm^{-1})	0.357
F(000)	1970
P (Mg/m^3)	1.202
Reflections collected	39653
Independent reflections [R_{int}]	18269 [0.1091]
Θ range for data collection ($^\circ$)	2.84 - 25.00
GOOF on F^2	0.976
Final R indices	$R_1 = 0.1245$
$[I > 2\sigma(I)]$	$wR_2 = 0.2919$
R indices	$R_1 = 0.2396$
(all data)	$wR_2 = 0.3768$
Largest diff. peak and hole (e \AA^{-3})	0.667 and -0.507

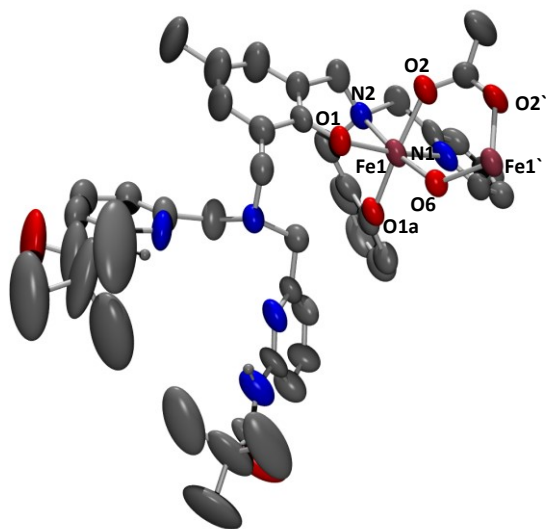


Figure 73: ORTEP plot of the monomeric structure of $\{\text{Na}[\text{Fe}^{\text{III}}(\text{H}_2\text{SIM}^2)]_2(\mu\text{-OAc})(\mu\text{-OH}_2)\}(\text{BF}_4)_2$ including bridging acetate and aqua ligands with 50% probability level of thermal ellipsoids. Counter ion and hydrogen atoms not involved in hydrogen bonding are omitted for clarity.

Table 32: Atomic coordinates ($\cdot 10^4$) and equivalent isotropic displacement parameters ($\text{\AA}^2 \cdot 10^3$) for $\{\text{Na}[\text{Fe}^{\text{III}}(\text{H}_2\text{SIM}^2)]_2(\mu\text{-OAc})(\mu\text{-OH}_2)\}(\text{BF}_4)_2$; $U(\text{eq})$ is defined as one third of the trace of the orthogonalized U^{ij} tensor.

	x	y	z	U(eq)
Fe(1)	6817(1)	1666(1)	2786(1)	53(1)
Fe(2)	7525(1)	617(1)	4202(1)	53(1)
C(28')	9046(5)	4446(5)	3652(6)	73(3)
O(1)	7668(3)	1468(3)	1778(3)	56(1)
O(1A)	6990(3)	2797(3)	2502(3)	54(1)
O(1A')	6852(3)	1026(3)	5114(3)	60(2)
O(1')	8592(3)	983(3)	4059(3)	54(1)
C(29)	9814(5)	4897(5)	1163(6)	81(3)
C(34')	13920(6)	1685(6)	1044(8)	88(3)
N(5)	9373(4)	2569(3)	364(4)	54(2)
O(6)	7464(3)	1472(3)	3402(3)	49(1)
N(6')	9211(4)	3817(4)	3348(4)	64(2)
C(37)	11742(6)	4812(7)	476(8)	96(4)
C(3)	4193(6)	2608(5)	4695(8)	89(4)
N(2)	5930(4)	1810(4)	2246(4)	57(2)
O(2)	6367(3)	570(3)	3195(4)	68(2)
O(4')	14449(4)	1808(5)	1249(5)	112(3)
N(4')	11868(4)	2042(4)	2538(5)	64(2)
N(5')	10029(4)	2241(4)	3172(4)	59(2)
O(2')	6495(4)	72(3)	4295(4)	75(2)
C(28)	10300(5)	4298(5)	830(6)	69(3)
C(23')	13110(7)	2646(6)	2376(8)	88(3)
N(6)	9993(4)	3669(4)	801(4)	66(2)
N(2')	7687(4)	-457(3)	4967(4)	55(2)
N(1)	5641(4)	1934(4)	3739(5)	67(2)
C(14')	9220(5)	-171(4)	4466(5)	57(2)
C(20')	9279(4)	541(4)	3970(5)	54(2)
C(33')	10197(5)	2955(4)	2551(5)	61(2)
N(7')	13099(4)	1826(4)	1466(5)	79(2)
N(8')	8200(4)	4634(4)	4117(5)	80(3)
N(4)	10631(6)	2804(5)	-1148(5)	84(3)
C(4)	4231(5)	2347(5)	4068(7)	70(3)
C(32)	9139(5)	3625(4)	1085(5)	54(2)
C(16')	10724(5)	-414(5)	3699(6)	69(3)
C(32')	10021(5)	3673(5)	2885(5)	60(2)
C(11')	6640(5)	-3(6)	6210(5)	65(2)
N(1')	8269(4)	-103(4)	3369(4)	62(2)

APPENDIX

C(24`)	12657(9)	2951(7)	3013(9)	108(4)
C(39A)	12926(8)	4295(12)	-653(12)	197(10)
C(11)	5864(5)	3251(5)	2168(6)	63(3)
O(5)	11481(4)	5386(4)	710(6)	121(4)
C(19)	8466(6)	1516(5)	439(6)	71(3)
C(26)	9852(7)	3004(5)	-1097(6)	76(3)
C(18`)	10760(5)	299(5)	3228(5)	63(2)
F(4)	1712(5)	3813(4)	5661(4)	128(3)
C(5)	4967(5)	2021(5)	3586(5)	60(2)
C(7)	6275(5)	3945(5)	2876(5)	69(3)
C(21`)	10128(5)	1536(5)	2791(5)	63(2)
C(13`)	8373(5)	-395(4)	5189(5)	56(2)
C(38)	12663(7)	4617(8)	112(12)	138(7)
C(22`)	12703(5)	2182(5)	2160(6)	69(3)
O(5`)	7490(4)	3561(4)	4355(5)	106(3)
C(33)	8847(5)	2847(4)	1125(5)	58(2)
C(15`)	9929(5)	-627(5)	4335(6)	67(3)
C(21)	9255(5)	1713(4)	443(5)	62(2)
C(13)	6113(5)	1218(6)	1777(5)	69(3)
N(8)	11199(4)	4277(4)	532(5)	87(3)
C(19`)	10066(4)	784(4)	3341(5)	51(2)
F(1)	2375(5)	3124(6)	4759(7)	205(5)
N(7)	12038(6)	2577(7)	-1872(6)	136(4)
C(27`)	10522(6)	2187(5)	3642(6)	77(3)
C(25)	9691(7)	3159(5)	-1722(7)	80(3)
F(2)	1057(6)	2959(4)	5449(6)	171(4)
C(17`)	11472(6)	-929(6)	3566(7)	97(4)
F(3)	1561(6)	4028(4)	4585(6)	168(4)
C(26`)	11444(6)	2364(5)	3173(7)	74(3)
C(7A)	6398(5)	3331(5)	2511(5)	62(2)
C(7A`)	6624(5)	782(6)	5890(6)	68(3)
C(27)	9208(6)	3051(6)	-270(6)	78(3)
C(30)	8957(6)	4841(5)	1420(6)	77(3)
C(35)	13574(14)	2320(20)	-2341(11)	230(14)
C(38`)	6677(6)	4635(6)	4854(8)	91(4)
C(31)	8610(5)	4193(5)	1393(6)	69(3)
C(12`)	6879(5)	-616(5)	5728(5)	69(3)
C(18)	8496(7)	1395(7)	-277(7)	100(4)
C(22)	11271(7)	2787(5)	-1871(6)	83(3)
O(4)	12893(7)	2658(8)	-3172(6)	181(5)
C(14)	6961(5)	1299(5)	1058(6)	67(2)

C(12)	6009(5)	2608(5)	1729(6)	78(3)
C(1)	5604(5)	2190(5)	4357(6)	61(2)
C(4`)	8971(7)	-1322(5)	3234(7)	98(4)
C(2`)	9307(8)	-326(6)	2105(6)	110(4)
C(37`)	7502(6)	4235(6)	4413(6)	81(3)
C(5`)	8386(6)	-849(5)	3696(5)	66(2)
C(8`)	6096(7)	1088(8)	7184(7)	111(4)
C(23)	11137(8)	2966(6)	-2542(7)	93(3)
C(2)	4900(6)	2519(5)	4854(6)	67(3)
C(6)	5067(4)	1693(5)	2913(6)	67(3)
C(31`)	10676(6)	4150(5)	2689(7)	84(3)
C(8)	5669(7)	4473(6)	2890(7)	89(4)
C(24)	10321(8)	3155(6)	-2462(7)	97(3)
C(39D)	5952(6)	4100(7)	5122(8)	129(6)
C(35`)	14183(7)	1403(8)	308(8)	98(4)
C(6`)	7830(6)	-1105(4)	4548(5)	66(3)
C(9)	5175(7)	4429(7)	2546(8)	111(5)
C(25`)	11818(9)	2820(6)	3422(8)	97(4)
C(36B)	13596(10)	2943(16)	-1864(14)	253(14)
C(20)	7697(5)	1416(4)	1113(5)	62(2)
C(7`)	6366(5)	1326(6)	6377(6)	81(3)
C(10)	5241(5)	3797(6)	2192(7)	92(4)
C(10`)	6389(6)	-209(7)	7036(6)	88(3)
C(16)	7809(9)	1219(9)	-337(8)	131(5)
C(9`)	6109(7)	328(8)	7516(7)	103(4)
C(3`)	9478(9)	-1067(6)	2432(8)	129(6)
C(1`)	8715(6)	134(5)	2599(6)	75(3)
C(39C)	13161(8)	5357(9)	-122(12)	200(9)
C(2A)	5507(8)	-491(7)	4067(8)	136(5)
C(39E)	6593(7)	5391(7)	4311(10)	142(6)
C(1A)	6178(6)	87(5)	3828(6)	69(3)
C(29`)	9655(6)	4935(5)	3510(8)	110(5)
C(36D)	15111(7)	1124(9)	16(9)	146(6)
C(34)	12799(10)	2559(11)	-2512(9)	166(8)
C(15)	7031(7)	1202(8)	336(7)	117(4)
C(39B)	12856(7)	3990(10)	662(11)	198(10)
C(39F)	6695(7)	4825(9)	5562(9)	149(6)
C(36E)	13644(8)	749(9)	425(9)	139(5)
C(36F)	14073(9)	2053(10)	-308(8)	168(7)
B(1)	1723(8)	3461(8)	5115(8)	79(4)
C(17)	7872(9)	1066(11)	-1100(8)	189(9)

APPENDIX

C(30')	10477(7)	4779(7)	3034(10)	132(6)
C(36A)	13523(17)	1564(14)	-1878(14)	305(19)
C(36C)	14383(10)	2522(15)	-3127(11)	265(14)
F(5)	603(3)	1941(3)	884(4)	99(2)
F(6)	1773(4)	1479(7)	942(5)	182(4)
F(8)	1702(5)	2623(7)	491(15)	393(16)
B(2)	1490(12)	1989(11)	605(12)	174(13)
F(7)	1807(8)	1875(13)	-150(6)	299(9)
O(9)	8545(4)	2292(3)	4613(4)	79(2)
Na(1)	8251(3)	2827(3)	2974(3)	133(2)
O(8)	9030(20)	3694(18)	-4100(20)	259(14)
O(7)	11161(13)	6458(12)	3191(16)	165(8)

Table 33: Crystallographic data for $[\text{Zn}^{\text{II}}_2(\text{L}^1)(\mu\text{-OAc})_2]\text{PF}_6$, $[\text{Zn}^{\text{II}}_2(\text{H}_2\text{L}^2)(\mu\text{-OAc})_2]\text{PF}_6 \cdot 0.5\text{H}_2\text{O} \cdot 0.5 \text{CH}_3\text{COCH}_3$ and $[\text{Zn}^{\text{II}}_2(\text{SIM}^2)(\mu\text{-OAc})_2]\text{PF}_6$.

	$[\text{Zn}_2(\text{L}^1)(\mu\text{-OAc})_2]\text{PF}_6$	$[\text{Zn}_2(\text{H}_2\text{L}^2)(\mu\text{-OAc})_2]\text{PF}_6 \cdot 0.5\text{H}_2\text{O} \cdot 0.5 \text{CH}_3\text{COCH}_3$	$[\text{Zn}_2(\text{SIM}^2)(\mu\text{-OAc})_2]\text{PF}_6$
Empirical formula	$\text{C}_{37}\text{H}_{39}\text{F}_6\text{N}_6\text{O}_5\text{PZn}_2$	$\text{C}_{48.50}\text{H}_{61}\text{F}_6\text{N}_8\text{O}_8\text{PZn}_2$	$\text{C}_{37}\text{H}_{41}\text{F}_6\text{N}_8\text{O}_5\text{PZn}_2$
Formula weight	923.45	1159.76	953.49
Temperature (K)	293(2)	293(2)	200(2)
Wavelength (Å)	1.54180	0.71073	0.71073
Crystal system	Triclinic	Monoclinic	Orthorhombic
Space group	P-1	$\text{P}2_1/\text{n}$	$\text{P}21\ 21\ 21$
a (Å)	10.2562(4)	16.2410(10)	11.1444(6)
b (Å)	12.5876(5)	21.5930(10)	17.0144(9)
c (Å)	16.7528(7)	16.3693(8)	20.6731(8)
α (°)	89.561(3)	90	90
β (°)	74.354(3)	100.533(6)	90
γ (°)	74.696(3)	90	90
Vol (Å ³)	2004.11(14)	5643.9(5)	3919.9(3)
Z	2	4	4
μ (mm ⁻¹)	2.531	0.953	1.348
F(000)	944	2404	1952
P (Mg/m ³)	1.530	1.365	1.616
Reflections collected	17469	25999	10212
Independent reflections [R_{int}]	6308 [0.0222]	9929 [0.0342]	6482 [0.0394]
Θ range for data collection (°)	3.65 - 62.25	3.10 - 25.00	2.94 - 25.00
GOOF on F^2	1.026	1.058	1.025
Final R indices [$I > 2\sigma(I)$]	$R_1 = 0.0303$ $wR_2 = 0.0792$	$R_1 = 0.0564$ $wR_2 = 0.1520$	$R_1 = 0.0523$ $wR_2 = 0.1185$
R indices (all data)	$R_1 = 0.0362$ $wR_2 = 0.0847$	$R_1 = 0.0775$ $wR_2 = 0.1643$	$R_1 = 0.0629$ $wR_2 = 0.1263$
Largest diff. peak and hole (e Å ⁻³)	0.371 and -0.251	1.013 and -0.340	1.087 and -0.363
CCDC number	998888	998889	998890

Table 34: Crystallographic data for $[\text{Zn}^{\text{II}}_2(\text{H}_2\text{SIM}^1)(\mu\text{-OAc})(\text{OH})]\text{PF}_6$, $[\text{Zn}^{\text{II}}_2(\text{H}_2\text{SIM}^3)(\mu\text{-O}_3\text{POC}_6\text{H}_4\text{NO}_2)]\text{PF}_6 \cdot \text{H}_2\text{O} \cdot \text{CH}_3\text{OH}$ and $[\text{Zn}^{\text{II}}_2(\text{H}_2\text{SIM}^3)(\mu\text{-OAc})(\text{OH})]$.

	$[\text{Zn}_2(\text{H}_2\text{SIM}^1)(\mu\text{-OAc})(\text{OH})]\text{PF}_6$	$[\text{Zn}_2(\text{H}_2\text{SIM}^1)(\mu\text{-O}_3\text{POC}_6\text{H}_4\text{NO}_2)]\text{PF}_6 \cdot \text{H}_2\text{O} \cdot \text{CH}_3\text{OH}$	$[\text{Zn}_2(\text{H}_2\text{SIM}^3)(\mu\text{-OAc})(\text{OH})]$
Empirical formula	$\text{C}_{45}\text{H}_{55}\text{F}_6\text{N}_8\text{O}_6\text{PZn}_2$	$\text{C}_{50}\text{H}_{61}\text{F}_6\text{N}_9\text{O}_{11}\text{P}_2\text{Zn}_2$	$\text{C}_{46}\text{H}_{55}\text{N}_7\text{O}_7\text{Zn}_2$
Formula weight	1079.68	1270.76	948.71
Temperature (K)	293(2)	190(2)	200(2)
Wavelength (Å)	1.54180	0.71073	1.54180
Crystal system	Monoclinic	Monoclinic	Triclinic
Space group	$\text{P}2_1/\text{n}$	$\text{P}2_1/\text{n}$	P-1
a (Å)	16.8815(6)	14.5695(6)	13.3627(8)
b (Å)	13.5366(5)	23.3831(8)	14.0727(8)
c (Å)	21.8837(9)	17.1987(5)	14.7688(10)
α (°)	90	90	70.854(6)
β (°)	105.077(4)	107.817(4)	66.835(6)
γ (°)	90	90	62.523(6)
Vol (Å ³)	4828.7(3)	5578.2(3)	2228.5(2)
Z	4	4	2
μ (mm ⁻¹)	2.215	1.004	1.803
F(000)	2232	2624	992
P (Mg/m ³)	1.485	1.513	1.414
Reflections collected	53093	22528	20772
Independent reflections [R_{int}]	7633 [0.0738]	9829 [0.0664]	6963 [0.0508]
Θ range for data collection (°)	2.96 - 62.39	2.89 - 25.00	3.31 - 62.41
GOOF on F ²	1.018	1.030	1.051
Final R indices [$I > 2\sigma(I)$]	$R_1 = 0.0485$ $wR_2 = 0.1198$	$R_1 = 0.0671$ $wR_2 = 0.1291$	$R_1 = 0.049$ $wR_2 = 0.127$
R indices (all data)	$R_1 = 0.0669$ $wR_2 = 0.1324$	$R_1 = 0.1115$ $wR_2 = 0.1482$	$R_1 = 0.0563$ $wR_2 = 0.1359$
Largest diff. peak and hole (e Å ⁻³)	0.513 and -0.386	0.883 and -0.690	1.038 and -0.382
CCDC number	998887	998891	1009842

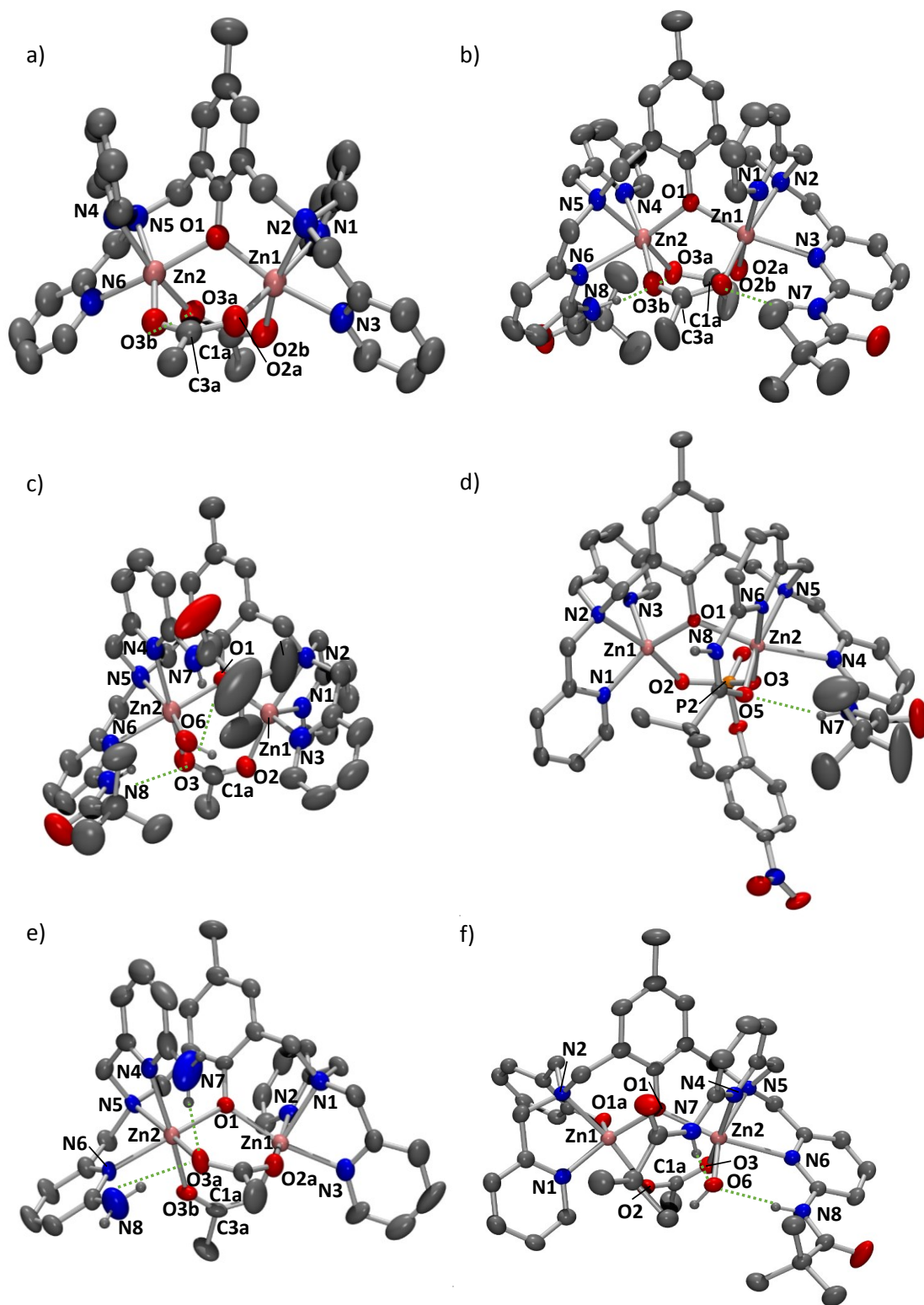


Figure 74: ORTEP plots of a) $[\text{Zn}^{\text{II}}_2(\text{L}^1)(\mu\text{-OAc})_2]\text{PF}_6$, b) $[\text{Zn}^{\text{II}}_2(\text{H}_2\text{L}^2)(\mu\text{-OAc})_2]\text{PF}_6$, c) $[\text{Zn}^{\text{II}}_2(\text{H}_2\text{SIM}^1)(\mu\text{-OAc})(\text{OH})]\text{PF}_6$, d) $[\text{Zn}^{\text{II}}_2(\text{H}_2\text{SIM}^1)(\mu\text{-O}_3\text{POC}_6\text{H}_4\text{NO}_2)]\text{PF}_6$, e) $[\text{Zn}^{\text{II}}_2(\text{SIM}^2)(\mu\text{-OAc})_2]\text{PF}_6$ and f) $[\text{Zn}^{\text{II}}_2(\text{H}_2\text{SIM}^3)(\mu\text{-OAc})(\text{OH})]$ with 50% probability level of thermal ellipsoids. Counter ions, non-coordinated solvent molecules and hydrogen atoms not involved in hydrogen bonding are omitted for clarity.

Table 35: Crystallographic data for $[\text{Fe}^{\text{II}}_2(\text{H}_2\text{SIM}^1)(\mu\text{-OAc})_2]\text{PF}_6$, $[\text{Fe}^{\text{II}}_2(\text{H}_2\text{L}^2)(\mu\text{-OAc})_2]\text{PF}_6 \cdot \text{Et}_2\text{O}$ and $\{\text{Na}[\text{Fe}^{\text{II}}_2(\text{H}_2\text{SIM}^3)(\mu\text{-OAc})_2]_2\}\text{PF}_6$.

	$[\text{Fe}^{\text{II}}_2(\text{H}_2\text{SIM}^1)(\mu\text{-OAc})_2]\text{PF}_6$	$[\text{Fe}^{\text{II}}_2(\text{H}_2\text{L}^2)(\mu\text{-OAc})_2]\text{PF}_6 \cdot \text{Et}_2\text{O}$	$\{\text{Na}[\text{Fe}^{\text{II}}_2(\text{H}_2\text{SIM}^3)(\mu\text{-OAc})_2]_2\}\text{PF}_6$
Empirical formula	$\text{C}_{47}\text{H}_{57}\text{F}_6\text{Fe}_2\text{N}_8\text{O}_7\text{P}$	$\text{C}_{51}\text{H}_{67}\text{F}_6\text{Fe}_2\text{N}_8\text{O}_8\text{P}$	$\text{C}_{96}\text{H}_{114}\text{F}_6\text{Fe}_4\text{N}_{14}\text{NaO}_{16}\text{P}$
Formula weight	1102.67	1176.79	2111.36
Temperature (K)	120(1)	110(1)	100(1)
Wavelength (Å)	0.71073	0.7107	0.71073
Crystal system	Monoclinic	Monoclinic	Monoclinic
Space group	P 21/n	P 21/n	P 21/n
a (Å)	14.9220(5)	14.79581(6)	20.237(9)
b (Å)	19.7653(5)	22.51003(10)	25.243(12)
c (Å)	18.4489(5)	16.47614(8)	23.062(12)
α (°)	90	90	90
β (°)	91.110(3)	94.4616(4)	109.169(16)
γ (°)	90	90	90
Vol (Å ³)	5440.3(3)	5470.82(4)	11128(9)
Z	4	4	4
μ (mm ⁻¹)	0.637	0.639	0.603
F(000)	2288	2456	4400
P (Mg/m ³)	1.346	1.429	1.260
Reflections collected	77359	236690	195127
Independent reflections [R_{int}]	9711 [0.0887]	13964 [0.0358]	21219 [0.0778]
Θ range for data collection (°)	3.298 - 25.142	3.243 - 28.909	1.336 - 25.740
GOOF on F^2	1.031	1.038	1.024
Final R indices [$I > 2\sigma(I)$]	$R_1 = 0.0908$ $wR_2 = 0.2418$	$R_1 = 0.0437$ $wR_2 = 0.1087$	$R_1 = 0.0634$ $wR_2 = 0.1589$
R indices (all data)	$R_1 = 0.1223$ $wR_2 = 0.2675$	$R_1 = 0.0499$ $wR_2 = 0.1125$	$R_1 = 0.0859$ $wR_2 = 0.1733$
Largest diff. peak and hole (e Å ⁻³)	1.714 and -0.890	1.044 and -0.867	1.655 and -1.052
Identification code	co_sb12	co_sb4	co_sb5

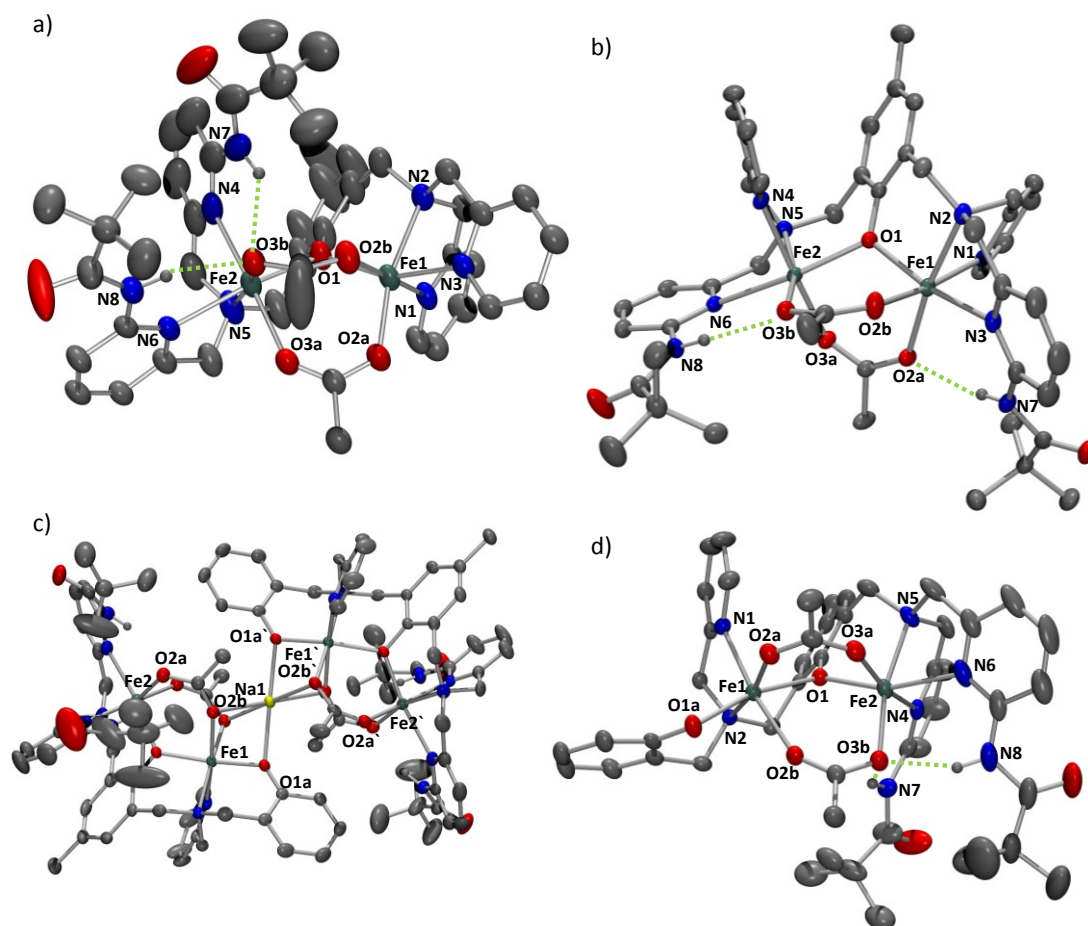


Figure 75: ORTEP plots of a) $[\text{Fe}^{\text{II}}_2(\text{H}_2\text{SIM}^1)(\mu\text{-OAc})_2]\text{PF}_6$, b) $[\text{Fe}^{\text{II}}_2(\text{H}_2\text{L}^2)(\mu\text{-OAc})_2]\text{PF}_6$, c) $\{\text{Na}[\text{Fe}^{\text{II}}_2(\text{H}_2\text{SIM}^3)(\mu\text{-OAc})_2]_2\}\text{PF}_6$ and d) the respective monomer $[\text{Fe}^{\text{II}}_2(\text{H}_2\text{SIM}^3)(\mu\text{-OAc})_2]$ with 50% probability level of thermal ellipsoids showing hydrogen bonds as green, dotted lines. Counter ions, non-coordinated solvent molecules and hydrogen atoms not involved in hydrogen bonding are omitted for clarity.

Table 36: Crystallographic data for $[\text{Fe}^{\text{III}}\text{Na}(\text{H}_2\text{SIM}^1)(\mu\text{-OAc})_2]\text{PF}_6$.

	$[\text{Fe}^{\text{III}}\text{Na}(\text{H}_2\text{SIM}^1)(\mu\text{-OAc})_2]\text{PF}_6$
Empirical formula	$\text{C}_{47}\text{H}_{57}\text{F}_6\text{FeN}_8\text{NaO}_7\text{P}$
Formula weight	1069.81
Temperature (K)	110(1)
Wavelength (\AA)	0.7107
Crystal system	Monoclinic
Space group	P 21/c
a (\AA)	22.1770(3)
b (\AA)	14.66804(16)
c (\AA)	15.3946(2)
α ($^\circ$)	90
β ($^\circ$)	99.1136(12)
γ ($^\circ$)	90
Vol (\AA^3)	4944.54(11)
Z	4
μ (mm^{-1})	0.428
F(000)	2228
P (Mg/m^3)	1.437
Reflections collected	156660
Independent reflections [R_{int}]	15102 [0.0720]
Θ range for data collection ($^\circ$)	3.214 - 30.548
GOOF on F^2	1.035
Final R indices	$R_1 = 0.0424$
[$I > 2\sigma(I)$]	$wR_2 = 0.0957$
R indices	$R_1 = 0.0568$
(all data)	$wR_2 = 0.1027$
Largest diff. peak and hole ($e \text{\AA}^{-3}$)	0.625 and -0.440
Identification code	co_sb8

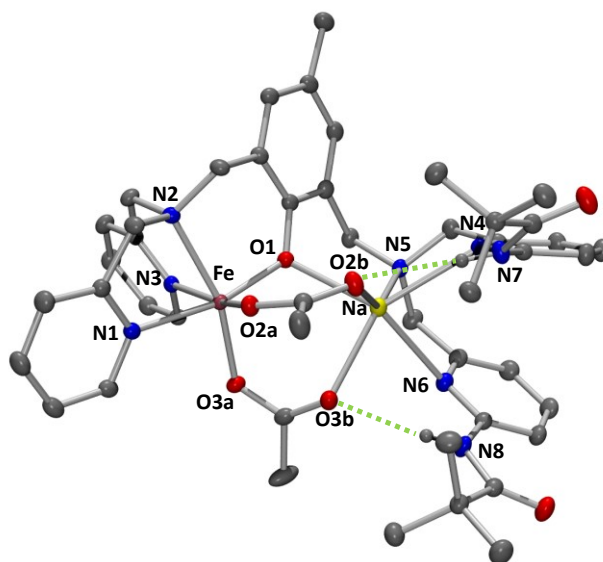


Figure 76: ORTEP plot of $[\text{Fe}^{\text{III}}\text{Na}(\text{H}_2\text{SIM}^1)(\mu\text{-OAc})_2]\text{PF}_6$ with 50% probability level of thermal ellipsoids showing hydrogen bonds as green, dotted lines. Counter ions, non-coordinated solvent molecules and hydrogen atoms not involved in hydrogen bonding are omitted for clarity.

**Eidesstattliche Versicherung gemäß § 8 der Promotionsordnung der
Naturwissenschaftlich-Mathematischen Gesamtfakultät
der Universität Heidelberg**

1. Bei der eingereichten Dissertation zum Thema

The Impact of the Second Coordination Sphere in Phosphatase Model Complexes

handelt es sich um meine eigenständig erbrachte Leistung.

2. Ich habe nur die angegebenen Quellen und Hilfsmittel benutzt und mich keiner unzulässigen Hilfe Dritter bedient. Insbesondere habe ich wörtlich oder sinngemäß aus anderen Werken übernommene Inhalte als solche kenntlich gemacht.

3. Die Arbeit oder Teile davon werde ich an einer Hochschule des In- oder Auslands als Bestandteil einer Prüfungs- oder Qualifikationsleistung im Rahmen eines binationalen Promotionsverfahren vorlegen.

Titel der Arbeit: The impact of the Second Coordination Sphere in Phosphatase Model Complexes

Hochschule und Jahr: The University of Queensland, Australia in 2015

Art der Prüfungs- oder Qualifikationsleistung: Degree of Doctor of Philosophy (PhD)

4. Die Richtigkeit der vorstehenden Erklärungen bestätige ich.

5. Die Bedeutung der eidesstattlichen Versicherung und die strafrechtlichen Folgen einer unrichtigen oder unvollständigen eidesstattlichen Versicherung sind mir bekannt.

Ich versichere an Eides statt, dass ich nach bestem Wissen die reine Wahrheit erklärt und nichts verschwiegen habe.

Ort und Datum

Unterschrift